



# Impact of the topology of the zeolite structure on the mechanism and selectivity of ethylcyclohexane bifunctional isomerization: experiments, ab initio calculations and multi-scale kinetic modelling

Ester Gutierrez Acebo

## ► To cite this version:

Ester Gutierrez Acebo. Impact of the topology of the zeolite structure on the mechanism and selectivity of ethylcyclohexane bifunctional isomerization: experiments, ab initio calculations and multi-scale kinetic modelling. Catalysis. Université de Lyon, 2018. English. NNT: 2018LYSE1240. tel-02373422

**HAL Id: tel-02373422**

**<https://theses.hal.science/tel-02373422>**

Submitted on 21 Nov 2019

**HAL** is a multi-disciplinary open access archive for the deposit and dissemination of scientific research documents, whether they are published or not. The documents may come from teaching and research institutions in France or abroad, or from public or private research centers.

L'archive ouverte pluridisciplinaire **HAL**, est destinée au dépôt et à la diffusion de documents scientifiques de niveau recherche, publiés ou non, émanant des établissements d'enseignement et de recherche français ou étrangers, des laboratoires publics ou privés.



N°d'ordre NNT : xxx

## **THESE de DOCTORAT DE L'UNIVERSITE DE LYON**

opérée au sein de  
**l'Université Claude Bernard Lyon 1**

**Ecole Doctorale ED 206**  
**Ecole Doctorale de Chimie de Lyon**

**Spécialité de doctorat** : Catalyse  
**Discipline** : Chimie

Soutenue publiquement le 20/11/2018, par :  
**GUTIERREZ ACEBO Ester**

---

# **Impact of the topology of the zeolite structure on the mechanism and selectivity of ethylcyclohexane bifunctional isomerization : experiments, ab initio calculations and multi-scale kinetic modelling**

---

Devant le jury composé de :

FONGARLAND, Pascal, Professeur à l'Université Claude Bernard 1  
RIBEIRO, Filipa, Professeure à l'Universidade Técnica de Lisboa  
BERTHOMIEU, Dorothée, Directrice de Recherche CNRS à l'Institut Charles Gerhardt de Montpellier  
PINARD, Ludovic, Maître de Conférences à l'Université de Poitiers  
CHIZALLET, Céline, Chef de projet à IFP Energies nouvelles  
SCHUURMAN, Yves, Directeur de Recherche CNRS à l'IRCELyon  
BOUCHY, Christophe, Chef de projet à IFP Energies nouvelles

Examineur  
Rapporteuse  
Rapporteuse

Examineur  
Examineur  
Directeur de thèse  
Invité



## REMERCIEMENTS

Je tiens à remercier en premier lieu M. Tivadar Cséri, Chef du département *Catalyse par les métaux et les solides acido-basiques*, et M. Denis Guillaume et Luc Nougier directeurs successifs de la direction *Catalyse et séparation* pour m'avoir accueillie au sein de leur département et direction à l'IFP Energies nouvelles, respectivement.

Je remercie également messieurs Prof. Pascal Fongarland, Directeur du Laboratoire de Génie des Procédés Catalytiques et Dr. Ludovic Pinard pour avoir accepté de juger ce travail. Je voudrais remercier aussi mesdames Prof. Filipa Ribeiro professeure à l'Universidade técnica de Lisboa et Dr. Dorothée Berthomieu, directrice de recherche CNRS, d'avoir accepté d'être les rapporteurs de cette thèse.

Deux gros merci à mes encadrants : Christophe Bouchy et Céline Chizallet pour m'avoir non seulement encadré ces trois années mais aussi pour tout leur aide et soutien, leur engagement infini pendant la thèse et leurs critiques toujours constructives qui m'ont fait beaucoup apprendre et grandir en tant que scientifique. Merci aussi pour leur passion et leur enthousiasme pour ce métier et leur capacité à les transmettre. Pour tout cette aide vraiment enrichissante, je leur témoigne de ma profonde reconnaissance. Je ne pourrais pas oublier Dr. Yves Schuurman, mon directeur de thèse qui bien que n'étant pas sur le même site, a été toujours présent et disponible pour me conseiller et m'éclairer pendant nos discussions scientifiques ainsi que pour mettre à notre disposition tous les moyens dont il disposait.

Merci Charles, pour ton aide, patience et engagement infatigable. Pour me faire partager tes expériences et tes savoirs afin de bien mener ma thèse toujours avec un gros sourire. Merci aussi pour ton soutien humain, pour rester toujours à l'écoute et pour toutes ces discussions enrichissantes qui m'ont éclairé beaucoup de fois.

Je tiens à remercier très chaleureusement Christophe James et Veronique Delattre pour leur aide et compétences apportées sur l'unité EHD. Pour leur disponibilité, les discussions et pour l'intérêt porté sur mon sujet.

Un grand merci aussi à Jérôme. Pour ta disponibilité, pour être toujours prêt à t'investir dans mes calculs et dans mon projet de manière désintéressée. Merci pour tous les discussions et pour m'apprendre énormément de choses.

Gros merci aussi aux techniciens et ingénieurs de la direction d'analyse qui m'ont toujours écouté et sont restés disponibles pour m'éclairer et répondre aux questions que



## REMERCIEMENTS

j'avais. Mickael Rivallan, pour tous ces moments passés à en discuter et chercher sans laisser tomber une explication satisfaisante aux résultats d'IR pyridine, merci aussi Laurent Lemaître, Emmanuel Soyer et Lucie Bussod à ce propos-là. Je tiens à remercier aussi à Anne-Lise Taleb (MEB), Isabel Clemençon (DRX), Thomas Coquet, Sebastian Selles et Sylvain Carbonneaux (XPS), Nathalie Texier (ICP), Frederic Neyret-Martinez et Oliver Delpoux (RMN), Denis Rouge et Mickael Legast (adsorption d'azote et titrage  $\text{H}_2\text{O}_2$ ) et Nicolas Girod (TPD- $\text{NH}_3$ ).

Merci Raquel, Eric et Monique pour votre disponibilité et votre aide si précieux sur les zéolithes.

Je ne peux pas oublier vous deux : Marie Claude Beaufils et Nathalie Farrenq, merci pour faire de les démarches administratives quelque chose de moins fastidieux. Pour votre disponibilité à m'aider toujours, merci.

Pascal, Denis, Sophie, Eugenie, Charles, Larissa, Laetitia, Lydie, Amandine et Karine merci pour partager les repas du Lundi et m'entendre râler autant, vous avez fait preuve redoutable de patience. Merci aussi à tous les personnes du département CATMAB avec lesquelles j'ai pu partager de très bons moments au café et qui ont été toujours là pour aider si nécessaire.

Ana, Sophie...sans vous, ces deux dernières années n'auront été pareilles. Merci pour les rigolades, et pour tous les moments vécus. Vous allez me manquer énormément. Merci également à tous les thésards avec qui j'ai partagé ces trois années. Spécialement je tiens à te remercier Anilla pour me soutenir, écouter et aider comme pas possible. J'avoue que je sais pas comment je ferais sans toi.

Je tiens finalement à remercier très chaleureusement ma famille. Pas seulement ma famille du sang mais cette autre que l'on trouve dans les amis. Natalia, Pablo, Raquel, Luis, Maria, David, July, merci de m'avoir soutenu ces trois dernières années et de m'avoir aidé à garder le moral même si ce n'était pas toujours facile. Maria, Lorena, Mel, Fran, Albert merci pour être là malgré la distance. A mon oncle, ma tante et à ma sœur merci pour me conseiller, me soutenir et m'écouter même si parfois vous ne compreniez presque rien de ce que je disais. Maman, merci à toi simplement pour m'avoir soutenu dans tous mes choix même si parfois tu n'étais pas d'accord.

A ti abuelo,



<b>INTRODUCTION</b>	<b>13</b>
<b>1. STATE OF THE ART</b>	<b>17</b>
1.1. Context: C <sub>8</sub> aromatic cut isomerization	17
1.1.1. EB Hydrodealkylation	17
1.1.2. EB Isomerization	18
1.2. Bifunctional catalyst	20
1.2.1. Zeolites as acidic function	20
1.2.1.1. Structure	21
1.2.1.2. Acidity (type, strength, amount)	24
1.2.1.3. Diffusion and adsorption effects	25
1.2.2. Metal as hydro/dehydrogenation function	26
1.2.2.1. Metal particle size and dispersion	26
1.2.2.2. Metal deposition	27
1.3. Hydroconversion of naphthenes: mechanistic aspects	27
1.3.1. Isomerization reaction: elementary steps	27
1.3.2. Undesired side reactions	28
1.3.2.1. Ring opening	29
1.3.2.2. Cracking	32
1.3.2.3. Disproportionation	32
1.3.3. Ideal hydroconversion catalyst	33
1.3.3.1. Influence of the metal/acid balance	33
1.3.3.2. Intimacy criterion	34
1.3.3.4. Metal/support interaction	36
1.4. Insights from ab initio calculations	37
1.4.1. Models for protonic sites in zeolites	37
1.4.2. General aspects of carbenium chemistry on zeolites	39
1.4.3. Works dealing with olefins isomerization	42
1.4.4. Works dealing with olefins cracking	43
1.5. Multiscale kinetic modelling	46
1.6. Conclusions and scope of the work	46
<b>2. EXPERIMENTAL and MODELING PART</b>	<b>49</b>
2.1. Zeolite bifunctional catalysts	49
2.1.1. Zeolite as solid acid	50
2.1.2. Platinum deposition	51
2.1.2.1. On the EU-1 zeolite	51
2.1.2.2. On the alumina	52
2.1.3. Mechanical mixtures	52
2.2. Characterization techniques	53
2.2.1. X-Ray diffraction (XRD)	53
2.2.2. N <sub>2</sub> Physisorption	54
2.2.3. X-Ray Fluorescence	55
2.2.4. Atomic absorption spectroscopy (AAS)	56
2.2.5. CO chemisorption monitored by FTIR	57
2.2.6. Nuclear Magnetic Resonance (NMR)	57
2.2.7. H <sub>2</sub> /O <sub>2</sub> titration	58
2.2.8. Electron microscopy	59

## RESUME

2.2.8.1. Scanning electron microscopy (SEM)	59
2.2.8.2. Scanning transmission electron microscopy (STEM)	60
2.2.9. Ammonia temperature-programmed desorption (NH <sub>3</sub> -TPD)	61
<b>2.3. Catalytic testing of ethylcyclohexane hydroconversion</b>	<b>61</b>
2.3.1. Unit description	61
2.3.2. Test conditions	62
2.3.2.1. Feedstock composition	62
2.3.2.2. Operation conditions	62
2.3.2.3. Reactor loading	65
2.3.3. GC analysis	66
2.3.4. Expressions of catalytic performance	69
2.3.5. Typical catalytic test procedure	70
<b>2.4. Ab initio calculations</b>	<b>70</b>
2.4.1. Resolution of Schrödinger equation	71
2.4.2. Periodic calculations and plane wave database	71
2.4.3. Geometry optimizations	72
2.4.4. Nudged Elastic Band	72
2.4.5. Vibrational frequency calculations	74
2.4.6. Intrinsic reaction coordinate (IRC)	74
2.4.7. Line minimization procedure	74
2.4.8. Thermodynamic calculations	76
2.4.9. Rate constant calculations	77
<b>2.5. Kinetic modelling</b>	<b>78</b>
<b>3. METAL/ACID BIFUNCTIONAL CATALYSIS AND INTIMACY CRITERION</b>	<b>81</b>
ABSTRACT	83
<b>3.1. Introduction</b>	<b>84</b>
<b>3.2. Materials and methods</b>	<b>88</b>
3.2.1. Catalysts preparation	88
3.2.2. Materials characterization	89
3.2.3. Catalytic test	91
3.2.4. Thermodynamic and kinetic modeling	92
<b>3.3. Results</b>	<b>93</b>
3.3.1. Characterizations of the samples	93
3.3.1.1. Pt/HEU-1 samples	93
3.3.1.2. Pt/Al <sub>2</sub> O <sub>3</sub> samples	95
3.3.2. Catalytic tests	96
3.3.2.1. Catalytic behavior of Pt-HEU-1/Al <sub>2</sub> O <sub>3</sub> catalysts	96
3.3.2.2. Catalytic behavior of Pt- Al <sub>2</sub> O <sub>3</sub> / HEU-1 catalysts	100
<b>3.4. Discussion</b>	<b>102</b>
3.4.1. Ethylcyclohexane isomerization pathway over EU-1	102
3.4.2. Impact of the metal to acid sites distance	102
3.4.3. Impact of the metal to acid sites ratio	103
<b>3.5. Conclusions</b>	<b>105</b>
<b>4. LOCATION OF THE ACTIVE SITES IN THE EUO FRAMEWORK</b>	<b>107</b>
ABSTRACT	109

## RESUME

4.1. Introduction	110
4.2. Experiments and methods	115
4.2.1. DFT calculations	115
4.2.2. Catalyst preparation	117
4.2.3. Material characterizations	118
4.2.4. Catalytic tests	119
4.2.5. Diffusion measurements	119
4.3. Results and discussion	120
4.3.1. The adsorbed cycloalkene species: $\pi$ -complex <i>versus</i> carbenium <i>versus</i> alkoxide species	120
4.3.2. Isomerization pathway at the T10O12 intersection site	123
4.3.3. Comparison between the different active sites within the EUO framework	127
4.3.4. Gibbs free energy profiles	131
4.3.5. Experimental characterization and catalytic evaluation of the EU-1 and ZSM-50 zeolites	133
4.4. Conclusions	135
<b>5. KINETIC STUDY and KINETIC MODEL</b>	<b>137</b>
5.1. Introduction	137
5.2. Experimental kinetic study on the ECH hydroconversion	137
5.2.1. General features	138
5.2.2. Focus on the isomerization kinetics	140
5.2.3. Focus on the ring opening kinetics	146
5.3. Ab initio Kinetic study on the ECH hydroconversion	148
5.3.1. Isomerization ab initio kinetics	149
5.3.1.1. General features	149
5.3.1.2. The secondary carbeniums issue: stability and comparison with the corresponding $\pi$ -complexes	151
5.3.1.3. Isomerization energy profiles	154
5.3.2. Ring opening ab initio kinetics	160
5.4. Microkinetic model	162
5.5. Conclusion	171
<b>6. ECH HYDROISOMERIZATION: Evaluation of various zeolite topologies</b>	<b>175</b>
6.1. Introduction	175
6.2. Zeolites characterization	176
6.3. Well-balanced bifunctional catalysts selection	179
6.4. Performances of the well-balanced bifunctional catalysts	182
6.4.1. Catalytic activity	182
6.4.2. Catalytic selectivity	189
6.4.2.1. Contribution of dehydrogenation reactions	189
6.4.2.2. Evaluation of catalysts selectivity isomerization vs ring opening and cracking	191
6.5. DFT analysis of the stability of key intermediates and TS for isomerization and ring opening	195
6.6. Comparison between experimental and calculated catalytic features	199
6.7. Conclusion	202

<b>CONCLUSIONS AND PERSPECTIVES</b>	<b>205</b>
<b>REFERENCES</b>	<b>215</b>
<b>APPENDIX</b>	<b>i</b>
<b>APPENDIX I</b>	<b>i</b>
I.I. TEMPERATURE PROFILES FOR CALCINATION	i
I.II. LOSS ON IGNITION	iv
I.III. WATER UPTAKE VOLUME (WUV)	iv
<b>APPENDIX II</b>	<b>vi</b>
II.I. DIFFERENT TYPES OF ISOTHERMS	vi
II.II. H <sub>2</sub> /O <sub>2</sub> DOUBLE TITRATION PRODEDURE	vii
<b>APPENDIX III</b>	<b>viii</b>
<b>APPENDIX IV</b>	<b>xxi</b>
<b>APPENDIX V</b>	<b>xliii</b>
V.I. GENERAL FEATURES	xliii
V.II. HYDRIDE- AND METHYL- SHIFT	xliv
V.III. DFT STUDY	xlvi
<b>APPENDIX VI</b>	<b>lxi</b>
VI.I CHARACTERIZATION	lxi
VI.II CATALYTIC TESTS	lxiii
VI.III PROII RESULTS	lxxxi
VI.IV PRODUCTS DISTRIBUTION	lxxxi
VI.I ZEOLITES STRUCTURES BY MATERIALS STUDIO	lxxxvii
<b>REFERENCES</b>	<b>xcviii</b>

## RESUME

---

Le paraxylène (pX), utilisé dans la fabrication de l'acide téréphtalique pour la production de polyester, est principalement produit par isomérisation de la coupe aromatique C<sub>8</sub>. Cette dernière est principalement composée des trois isomères du xylènes (para, ortho et méta) et de l'éthylbenzène (EB). L'EB est transformé en xylènes grâce à un catalyseur bifonctionnel comprenant à la fois une fonction acide comme la zéolithe EU-1 et une fonction hydrodéshydrogénante (HD/DHD) comme le platine. L'hydrogénation de l'EB conduit également à la production d'éthylcyclohexane, qui peut subir des réactions non désirées d'ouverture de cycle et de craquage sur la fonction acide du catalyseur. Au cours de ce travail, nous avons cherché à comprendre les facteurs influant sur la sélectivité du catalyseur bifonctionnel en hydroconversion de l'éthylcyclohexane (ECH), et à identifier des phases acides zéolithiques très sélectives. L'effet de paramètres tels que le ratio et la proximité entre sites acides et sites HD/DHD, la localisation des sites acides au sein du réseau zéolithique, et la topologie de ce réseau zéolithique, a été examiné. Des études catalytiques ont été mises en œuvre sur des séries de catalyseurs bifonctionnels à base de zéolithe EU-1, et interprétées à la lueur de calculs *ab initio* focalisés sur les mécanismes d'isomérisation et d'ouverture de cycle de l'ECH sur la phase acide EU-1. L'intégration de données thermocinétiques déterminées *ab initio* dans un modèle cinétique en champ moyen a permis de valider l'approche et d'identifier les étapes réactionnelles clés dictant la sélectivité. Un criblage rationnel de structures zéolithes a ensuite été proposé pour identifier les paramètres topologiques influant.



## ABSTRACT

---

The paraxylene (pX), used in the manufacture of terephthalic acid for the production of polyester, is mainly produced by isomerization of the C8 aromatic cut. The latter is mainly composed of the three xylene isomers (para, ortho and meta) and ethylbenzene (EB). EB is converted into xylenes by mean of a bifunctional catalyst comprising both an acid function, such as EU-1 zeolite, and a hydro-dehydrogenating function (HD / DHD), such as platinum. The hydrogenation of EB also leads to the production of ethylcyclohexane, which can undergo undesired ring-opening and cracking reactions on the acid function of the catalyst. In this work, we tried to understand the factors influencing the selectivity of the bifunctional catalyst in the hydroconversion of ethylcyclohexane (ECH), and to identify very selective zeolitic acid phases. The effect of parameters such as the ratio and proximity between acid and HD / DHD sites, the location of acid sites within the zeolite network, and the topology of this zeolite network, was evaluated. Catalytic studies have been carried out over bifunctional catalysts series based on the EU-1 zeolite, and interpreted considering *ab initio* calculations focused on the isomerization and ring-opening mechanisms of ECH on the EU-1 acid phase. The integration of thermokinetic data (determined by *ab initio* calculations) in a mean field kinetic model made it possible to validate the approach and to identify the key reaction steps dictating the selectivity. A rational screening of zeolite structures was then proposed to identify the influential topological parameters.

## INTRODUCTION

The para-xylene (pX) is a highly sought-after product since it is used in the manufacture of the terephthalic acid employed in the polyester production. pX is mainly produced by isomerization of the C<sub>8</sub> aromatic cut. This C<sub>8</sub> aromatic cut is usually originated from a reforming or vapocracking unit and is mainly composed by the three xylenes isomers (para, ortho and meta xylene) and the ethylbenzene (EB). After pX separation, the aromatic cut is sent to an isomerization unit to perform the EB isomerization into xylenes and xylenes isomerization into pX<sup>1</sup>.

It is well established that EB isomerization requires a bifunctional catalyst providing both an acidic and a hydro-dehydrogenating (HD/DHD) functions<sup>2,3</sup>. Figure 0.1. represents the simplified mechanism of the ethylbenzene isomerization reaction. The HD/DHD function enables the EB hydrogenation into ethyl-cyclohexenes. The ethylcyclohexenes are then isomerized over the acidic sites into dimethylcyclohexenes. Finally, the dimethylcyclohexenes are dehydrogenated into xylenes over the HD/DHD function. Noticeably the EB hydrogenation also lead to the production of ethylcyclohexane (ECH). Naphthenes like ECH can undergo ring opening and cracking reactions. Such reactions should be minimized as they are generating undesired products (i.e. paraffins).

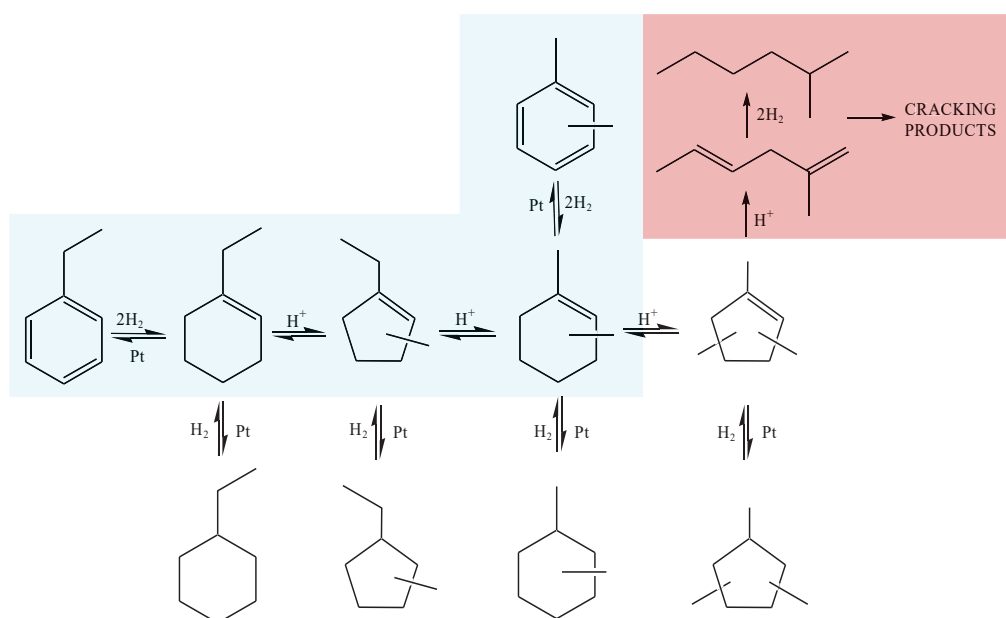


**Figure 0.1.** Simplified mechanism for the isomerization reaction of ethylbenzene into xylenes on a bi-functional catalyst (desired reaction, blue) and side reactions, in particular ring opening and cracking of the ring-opening products (red). Hydro-dehydrogenation reactions take place on the metallic phase, ring contractions, expansions, opening and cracking on the acidic phase.

## INTRODUCTION

It is known that isomerization, ring opening and cracking reactions are taking place on the acidic function of the bifunctional catalyst. A promising way to improve the catalyst selectivity towards isomerization is therefore to select the most suitable acidic phase for this purpose. Nowadays, the bifunctional catalysts employed for the C<sub>8</sub> aromatic cut isomerization have a zeolitic phase, for example the EU-1 zeolite, as an acidic function.<sup>4</sup> It is expected that shape selectivity, induced by the topology of the microporous network, is of prime importance for the zeolite selectivity towards isomerization (versus ring opening and cracking side reactions). Other factors can also have an impact on the zeolite selectivity such as acid sites location in the microporous network<sup>5</sup>, extraframework aluminium<sup>3</sup> etc. Improving our knowledge about the key factors governing the zeolite selectivity towards isomerization is required before a rational screening of zeolites. With this purpose, the mechanism of naphthenes isomerization and ring opening has to be revealed, with advanced knowledge about key intermediates, and quantification of the corresponding kinetics. In order to do that, the hydroconversion of the key C<sub>8</sub> naphthene, namely ethylcyclohexane (ECH), is studied. *Ab initio* and experimental kinetic studies of ECH over bifunctional catalysts using EU-1 zeolite are performed in order to shed light on the key factors governing the zeolite selectivity.

Several bifunctional catalyst associating the zeolite EU-1 as acid function and Pt as metallic phase will be tested in the ECH hydroisomerization. The metal-acid site balance and the distance between them will be studied with two different groups of catalyst. The objective of this study is to find a “well balanced” catalyst in which the acid phase was rate controlling and the distance between metal/acid sites fitted the “Weisz intimacy criterion”. With this catalysts we will have access to the intrinsic kinetics of the zeolite that will be afterward studied by Density Functional Theory (DFT) *ab initio* calculations.

A preliminary study of the all products distribution (isomerization, ring opening and cracking) will be performed with the purpose of revealing an isomerization apparent reaction scheme. Such scheme will be taken into consideration for the DFT study. Based on experimental results, the possible ring opening pathways will be identified in order to study them after with DFT methods.

The preliminary DFT study will be carried out to unravel the reaction mechanisms and calculate the thermodynamic data and the kinetic constants of the key reactions of the mechanism. These data will be then employed in the construction of a microkinetic model.

The last part of this study corresponds to the screening of the catalytic properties of bifunctional catalysts for ECH hydroisomerization. A high throughput catalytic test unit will

## INTRODUCTION

be used for this specific study. Eleven different zeolites will be tested in order to evaluate the influence of the topology of the zeolite structure on the hydroisomerization of ECH.

With this purpose the present work is structured in the following parts:

- Chapter 1 summarizes the state of the art. A brief overview of the isomerization of the C<sub>8</sub> aromatic cut and the catalysts employed are provided. Also a particular focus is done on bifunctional catalyst and the napthens hydroconversions reaction. Finally, insight into DFT calculation and perspectives is given in this chapter.
- Chapter 2 corresponds to the experimental and computational part. The different preparation methods and characterization techniques are described, as well as the detailed description of the catalytic test for ECH hydroconversion, and the principles of Density Functional Theory calculations and kinetic modelling.
- In Chapter 3 is found the article already published: *“Metal/acid bifunctional catalysis and intimacy criterion for thylcyclohexane hydroconversion : when proximity does not matter.”*
- In Chapter 4 is found the article to be published: *“Location of the Active Sites for Ethylcyclohexane Hydroisomerization by Ring Contraction and Expansion in the EUO Zeolitic Framework”*
- Chapter 5 provides the kinetic study done experimentally and ab initio, and the microkinetic model built from the ab initio calculation to reproduce experimental results.
- Chapter 6 summarizes the results of the catalytic screening of various bifunctionnal catalyst using eleven different zeolites.



## 1. STATE OF THE ART

---

### 1.1. Context: C<sub>8</sub> aromatic cut isomerization

The C<sub>8</sub> aromatic cut is constituted basically of metaxylene (mX), paraxylene (pX), orthoxylene (oX) and ethylbenzene (EB)<sup>1,5</sup>. These aromatic hydrocarbons are essentially obtained by catalytic reforming or steam cracking processes which provide a mixture of aromatic compounds. Nevertheless, in this mixture, the proportion of each aromatic molecule is not adapted to the market demand. In particular, the global demand of pX as raw material for the manufacture of terephthalic acid (PTA) has been continually increasing. The production of pX only by separating it from the other aromatics cannot meet the demand.

Therefore, it is necessary to proceed with complementary transformations. Conversion processes were developed in order to transform the less valuable aromatics into the high sought-after aromatics, like pX. One of this process is the isomerization of the C<sub>8</sub> aromatic cut, currently applied at the industrial level.

Whereas every industrial process allow the xylenes isomerization, the EB conversion depends on the considered process. Nowadays, there are two different types of processes: those which involve the EB dealkylation into Benzene (evoked in section 1.1.1). and those which involve the isomerization of EB in a mixture of C<sub>8</sub> isomers (detailed in section 1.1.2). The process selection is based on market requirements i.e., the price differential between the C<sub>8</sub> aromatics and benzene (high benzene prices favour the dealkylation process whereas high C<sub>8</sub> aromatics prices will favour the isomerization process). This work is taking place in the context of EB conversion *via* isomerization.

When the target reaction is the EB isomerization, a metal-acid bifunctional catalyst is required. On the other hand, when dealkylation is the desired reaction, an acid catalyst is needed. In both cases, a metallic phase incorporation to the catalyst allows to improve its stability concerning the coking. Therefore, isomerization industrial processes use heterogeneous bifunctional catalysts consisting in an acidic phase and a hydro/dehydrogenation metallic phase.

#### 1.1.1. EB Hydrodealkylation

The EB Hydrodealkylation reaction target is the benzene production from ethylbenzene. The main reaction is shown in Figure 1.1.

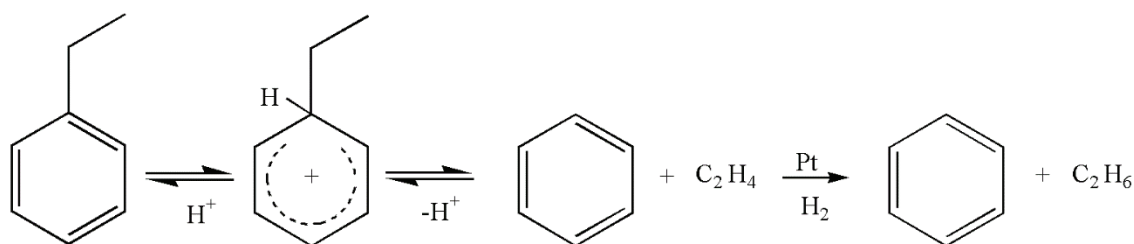


**Figure 1.1. EB Hydrodealkylation.**<sup>1</sup>

As told before, when the target reaction is the EB hydrodealkylation, it is only performed over an acidic function. Nevertheless, the presence of a hydro/dehydrogenation function in the catalyst allows to hydrogenate immediately the ethylene formed avoiding any possible realkylation of the aromatic molecule by ethylene. The catalyst employed in the EB hydrodealkylation involves basically an intermediate pore size zeolite such as ZSM-5. The catalyst are often constituted by a small noble metal amount dispersed over a shaped support containing the zeolite. Typically, the industrial process aiming at xylenes isomerization and EB hydrodealkylation is operated under the following conditions: temperature from 370 to 430°C, total pressure from 0.5 to 1.5 MPa, H<sub>2</sub> to hydrocarbon ratio from 2 to 4 mol/mol, and a weight hourly space velocity (WHSV) from 3 to 12 h<sup>-1</sup>.<sup>6</sup>

### 1.1.2. EB Isomerization

The EB isomerization requires the presence of a bifunctional catalyst<sup>5</sup>. Figure 1.2. shows a simplified mechanism of the EB isomerization, which is now widely accepted in the literature. This transformation over the acid sites was reported first in 1955 by Pitts et al.<sup>7</sup>. However, it was not before 1962 that Weisz<sup>8</sup> proposed the associated mechanism to proceed by ring contraction-expansion *via* carbenium ions.

The EB is hydrogenated over the metallic sites in ethylcyclohexenes. After, the latter leave the metallic sites by diffusion and are isomerized over the acid sites by ring contraction and expansion. Finally, the dimethylcyclohexenes are dehydrogenated over the metallic sites into xylenes.

It must be emphasized that the formation of naphthenic compounds cannot be avoided because of the strong hydrogenating function of the catalyst. Undesired side reactions include disproportionation and hydrodealkylation of aromatic compounds, ring opening and cracking of naphthenes. The two latter are considered as “fatal losses” since once than the ring is opened and cracked it becomes really hard to recover it. Thus, in order to rise the isomers

production to the maximum, these “fatal losses” have to be avoided. Efficient catalysts will be therefore, those minimizing the loss of naphthenes *via* these side reactions.

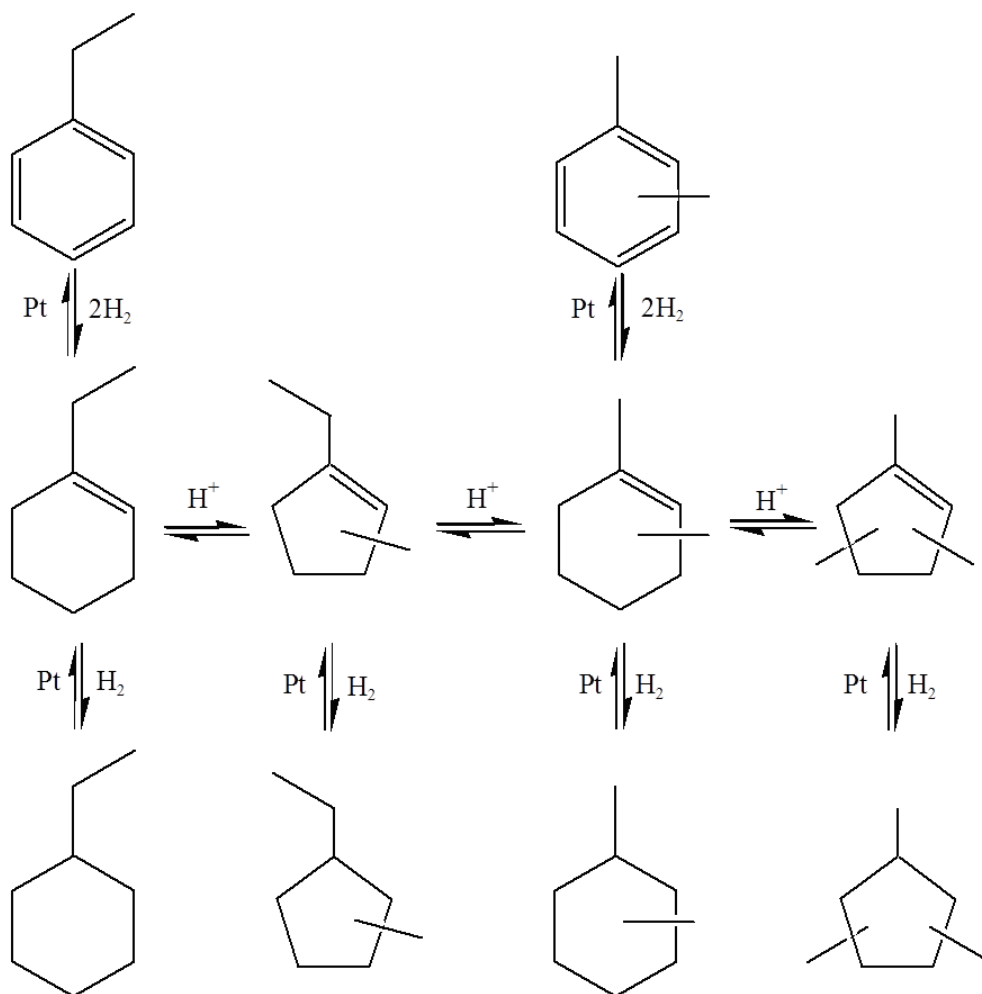


**Figure 1.2. Simplified mechanism for the ethylbenzene isomerization reaction.**

The catalysts for the EB isomerization have evolved a lot through the time. Isomerization catalysts have historically included amorphous silica–alumina, zeolites, and metal-loaded oxides<sup>9</sup>. The feature in common for all of them is the acidity, which isomerizes the xylenes and if strong enough can even crack EB and xylenes to benzene and toluene. Besides, bifunctional catalysts, contain a metal able to convert EB into xylenes. Bifunctional catalytic processes use an acidic oxide support, such as alumina, loaded with a metal such as Pt to isomerize the xylenes as well as convert EB to xylenes<sup>9</sup>. The apparition of zeolitic bifunctional catalysts changed completely the outlook. Mainly, the first ones were based on mordenite due to its high activity, thermal stability and special porosity<sup>10–13</sup>. Nevertheless, these mordenite-based catalysts undergo most of the secondary acidic reactions such as disproportionation, dealkylation, transalkylation and hydrocracking<sup>5,10</sup>. Some modifications of



these catalysts have been done, but the gain in activity and selectivity remained limited<sup>11,14</sup>. Thus, the investigation of new zeolitic structures had led to the use of EU-1 zeolite<sup>5,15</sup>. This zeolite possesses several particular properties that make it special such as a strong isomerization selectivity attributed to a progressive blockage of the pores leading to an external surface catalysis also called pore mouth catalysis<sup>16,17</sup>. Interesting results have been obtained with this zeolite compared with the mordenite based-catalysts<sup>15</sup>. Nonetheless, it remains still challenging to achieve lower fatal losses. Therefore, it is necessary to reveal which are the parameters governing these undesired side reactions. Typically, the industrial process aiming at xylenes isomerization and EB isomerization operates under the following conditions: temperature from 370 to 430°C, total pressure from 0.7 to 1.5 MPa, H<sub>2</sub> to hydrocarbon ratio from 3 to 10 mol/mol, and a WHSV from 3 to 5 h<sup>-1</sup>.<sup>6</sup>

### 1.2. Bifunctional catalyst

A bifunctional catalyst is a catalyst with two functions: in the present case, an acid function generally provided by a zeolite and/or silica/alumina; and a hydro/dehydrogenation function provided by a noble metal such as Pt, Pd, or a sulfide metal (Mo, W) promoted by Ni or Co.

The choice of the acid and metal functions is specific of each catalytic reaction. In the case of xylenes and EB isomerization, the acidic function is provided by a zeolite, and the metallic function by Pt.

#### 1.2.1. Zeolites as acidic function

There is a large number of reactions which are catalyzed by acid sites, and their importance from an industrial point of view has motivated the interest of the fundamental scientific community. It can be said that solid acids are the most widely solid catalysts used today, considering both the total amount used and the final economic impact<sup>18,19</sup>. Among the acid catalysts, zeolites have been widely employed as acid catalysts in heterogeneous catalysis and their merits have been extensively discussed in literature<sup>19-21</sup>. The advantage of zeolites is that their acid sites are mostly inside a microporosity structure. Thus, these sites have special properties different from those of other acid solids such as amorphous silica-aluminas<sup>22</sup>.

Zeolites are microporous crystalline silicates and aluminosilicates linked through oxygen atoms producing a three-dimensional network containing channels and cavities of molecular dimensions. The system of channels of these molecular sieves produces solids with a very

high surface area and pore volume. This fact combined with the possibility to generate active sites inside of the channels and zeolites cavities, gives rise to a very unique type of catalyst.

In a catalytic reaction, the reactant follows a sequence of events before it becomes a desorbed product. In the case of a zeolite, the sequence consists in: the diffusion of the reactant through the zeolite micropores to reach an active site, the reactant adsorption on the active site, the chemical reaction to give the adsorbed product, the product desorption and, finally the product diffusion through the zeolite channels.

The zeolite catalytic activity and selectivity are due to the complex interaction of several factors such as their structure, acidity, diffusion through them and adsorption effects. These features will be described in the following sections. The acidity has been considered as the main characteristic of zeolites influencing on their catalytic performance. Therefore it has been extensively studied. Nonetheless, in 2001 Patrigeon et al.<sup>23</sup> studied different acid solids in n-heptane hydroconversion. They showed the porosity as the major factor influencing on selectivities whereas the acidity did not appear like a key parameter. This conclusion was drawn because all the studied open solids had led to same selectivities although working at different temperatures. This reveals that there are some other factors than acidity affecting the zeolite performance in catalysis.

### 1.2.1.1. Structure

Generally, zeolites are classified in four different groups depending on their pore structure: small pores when the pore opening has a maximum of 8 MR (8 membered-ring i.e. the ring is formed by eight oxygen atoms), intermediate pores if there are 10 MR, large pores if there are 12 MR and ultra-large pore if there are more than 12 MR.

The microporous volumes in most opened zeolites can be as large as 0.5 to 0.55 cm<sup>3</sup>/g of zeolite. This volume consists of an extremely dense network of channels running in one, two or three dimensions, depending on the structures. With two- or three-dimensional porous systems, the channels are generally interconnected<sup>22</sup>. In Figure 1.3 are shown three zeolites with one-, two- and three-dimensional structures corresponding to MTT (ZSM-23), MFS (ZSM-57) and MFI (ZSM-5) frameworks.

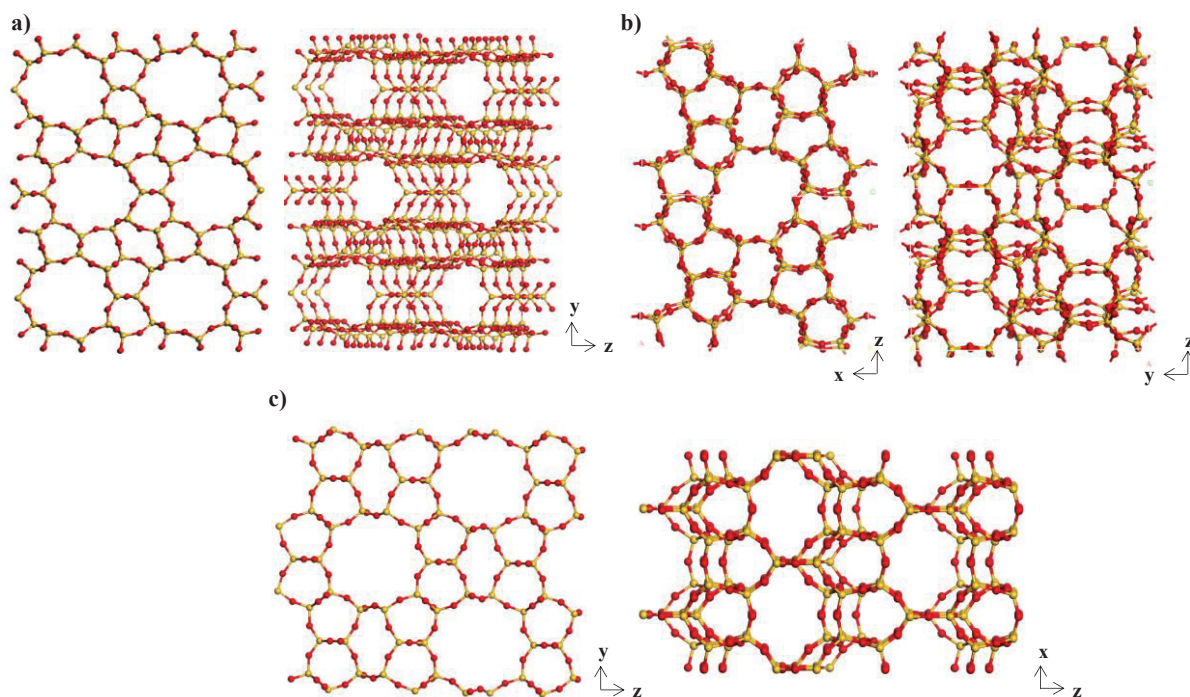


Figure 1. 3. Zeolites framework employed in this study. a) MTT (ZSM-23), b) MFS (ZSM-57), c) MFI (ZSM-5)

Characteristics such as the size and shape of the channels, which determine the space available around each site, play an important role in the zeolite's behavior. It can be distinguished various types of shape selectivities depending on whether pore size limits the entrance of the reacting molecule, the departure of the product molecule, or the formation of certain transition states<sup>21</sup>:

- **Reactant selectivity** occurs when only part of the reactant molecules are small enough to diffuse through the catalyst pores. It is for instance, the case of linear and branched paraffins as illustrated in Figure 1.4. While the linear paraffin is able to pass through the pores and reacts, the branched paraffin does not react at all. This type of reactant selectivity can appear in the case of small and medium pore size zeolites whereas in large and ultra-large pore size, it is not the case.

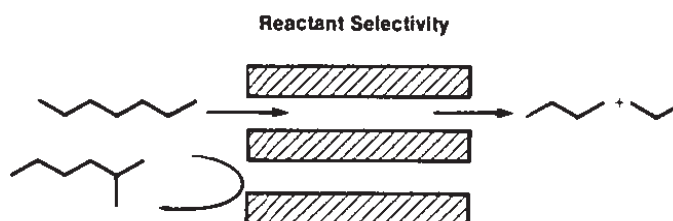


Figure 1.4. Reactant selectivity<sup>21</sup>.

- **Product selectivity** occurs when some of the products formed within the pores are too bulky to diffuse out. They are either converted to less bulky molecules or eventually they deactivate the catalyst by blocking the pores as schematized in Figure 1.5.

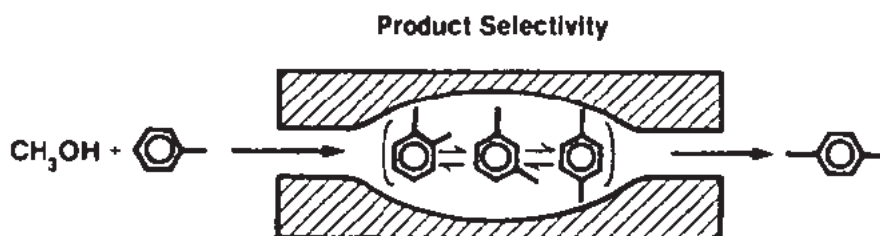


Figure 1.5. Product selectivity<sup>21</sup>.

- **Restricted transition-state selectivity** occurs when certain reactions are prevented because the corresponding transition state would require more space than available in the cavities. Neither reactant nor potential product molecules are prevented from diffusing through the pores. Reactions requiring smaller transition states proceed unhindered.

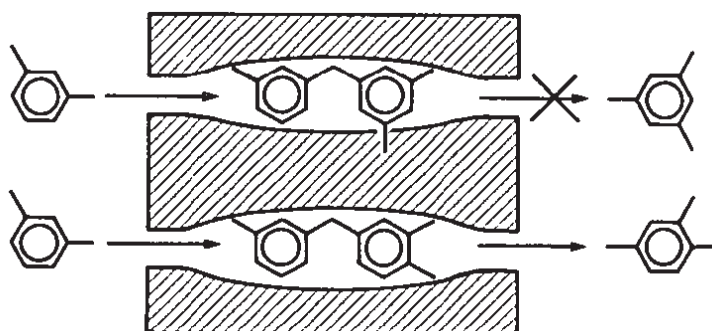
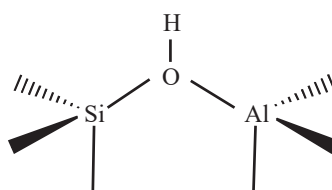


Figure 1.6. Restricted transition-state selectivity<sup>21</sup>.

There is another type of catalysis associated to the zeolite structure and reported by many authors.<sup>17,24,25</sup> It is named pore mouth catalysis. This is characteristic because in this case all the catalysis is taking place near the surface of the zeolite crystal. The reactants do not enter the zeolite porosity reacting only in the active sites of the zeolite near the external surface of the crystal (at the pore mouth). This is particularly relevant in the case of the conversion of reactants which are too bulky to enter the pores, or when the microporosity of a zeolite is poisoned upon filling by coke for example.

**1.2.1.2. Acidity (type, strength, amount)**

The zeolite structure containing only  $\text{SiO}_4$  tetrahedron would be electrically neutral and no acidity would be developed on its surface. Brønsted acid sites are developed when  $\text{Si}^{4+}$  is isomorphically substituted by a trivalent metal cation such as  $\text{Al}^{3+}$  and a negative charge is created in the lattice which is compensated by a cation, for instance, a proton. This proton,  $\text{H}^+$  produces the Brønsted acidity of the solid. Consequently, to each aluminate tetrahedron corresponds potentially one Brønsted acid site. The protons are fixed on the oxygen of the framework belonging to an aluminate tetrahedron, forming Brønsted acid hydroxyl groups as illustrated in Figure 1.7.



**Figure 1.7. Brønsted acid hydroxyl group.**

On the other hand, the Lewis acid sites in zeolites are electron deficient sites exhibiting the ability to accept electrons during interaction with molecules. Lewis acidity due to aluminum in a zeolite generally results from extra-framework aluminum (EFAL). Extra-framework aluminum is aluminum which is not tetrahedrally bounded in the framework. The nature of these EFAL is really complex and variable. It has been the subject of many investigations and two forms have been proposed: cationic particles adsorbed in anionic zeolites ( $\text{Al}^{3+}$ ,  $\text{AlO}^+$ ,  $\text{Al}(\text{OH})^{2+}$ ,  $\text{Al}(\text{OH})^{+2}$ ) and neutral or polymerized forms ( $\text{AlO}(\text{OH})$ ,  $\text{Al}(\text{OH})_3$ ,  $\text{Al}_2\text{O}_3$ )<sup>26</sup>.

In the case of bifunctional catalysis, hydrocarbon isomerization is believed to involve the formation of carbocations after protonation of the olefinic intermediates. Therefore, the Brønsted acidity of the zeolites is of prime importance.

Then, the global acidity of a given zeolite is the result, among other things, of two parameters characteristic of Brønsted sites: their density and strength.

The concentration of Brønsted acid sites of the framework depends on its aluminum content, it decreases when the Si/Al ratio of the zeolitic framework increases. However, any traces of residual alkali metals, not eliminated by ion exchange, will neutralize a corresponding fraction of the Brønsted acidity.

The strength of the Brønsted sites depends on the interaction between the proton and the zeolitic framework (the stronger the interaction, the lower the acidity).

### 1.2.1.3. Diffusion and adsorption effects

In the case of hydrocarbon reactions on zeolites where the size of a molecule closely matches the pore size, the first step (i.e. the diffusion of the reactant) can play an important role in the overall reaction rate. In fact, in this case, it is impossible to think in terms of molecular and Knudsen diffusion. Thus, Weisz<sup>27</sup> introduced the term “configurational diffusion” to denote intracrystalline migration. This configurational diffusion is strongly dependent on the site and nature of the reactant, the type of molecular sieve, and temperature.

The dimensions of the diffusing molecules have to be lower than the dimensions of the pores in order to diffuse through them. However, it should be kept in mind that due to the lattice vibrations, the effective pore size is slightly larger than the crystallographic one<sup>28</sup>.

When the size of the molecule and pore dimensions allow the reactant diffusion, the temperature has an important effect on the rate. This is due to the fact that molecular diffusion is an activated process.

Diffusion of molecules within the zeolites is thought to proceed by thermally activated jumps from one site to the nearby site<sup>29,30</sup>. Thus, the zeolite pore geometry also plays an important role. As an example, in zeolites with unidirectional channels the diffusivities will be lower than in the case of two-dimensional or three-dimensional pore systems. This is called molecular traffic control<sup>31</sup>.

The tortuosity of the channels also has an effect on the diffusion of molecules close in size to the diameter of the pores. For instance, flat and large molecules diffusion is expected to be easier in straight channels than in sinusoidal ones<sup>31</sup>.

Differences in diffusivities can be used to increase the selectivity to a given product by the adequate selection of the pore size of the zeolite catalyst. This comes into the field of shape-selective catalyst explained before (section 1.2.1.1).

When a reactant molecule has diffused inside the zeolite channel, it interacts with its walls and acid sites. These series of interactions involve the following energy terms: the attractive and repulsive contributions from the van der Waals interactions (mainly determined by the geometry of the acid sites environment), the polar, field-dipole, and field gradient-quadrupole (terms which are mostly affected by the environment chemical composition), the

sorbate-sorbate intermolecular energy and the intrinsic-reactant-acid site interaction<sup>19</sup>. The van der Waals interactions play an important role in the “confinement effect” proposed by Derouane<sup>32</sup>. He suggested that due to this confinement effect, sorbate-molecules in zeolites led to optimize these van der Waals interactions with the environment. Besides, he proposed that its importance was increased by the surface curvature of the pore walls interacting with the reactant<sup>33</sup>.

Therefore, it can be easily understood that by changing the chemical composition and the structure of the zeolite, the relative contribution of these interaction energy terms will be modified. Consequently, the adsorption characteristics of a given molecule will be changed. This flexibility in modifying the adsorption characteristic of zeolites will also allow discrimination between competing reactants and products by modifying their relative adsorption interaction.

### **1.2.2. Metal as hydro/dehydrogenation function**

Transition metals supported on zeolites have been found to be active for many processes<sup>2,15,34–37</sup>. Pd or Pt can be employed, especially when the feedstock is free of sulfur compounds. These metals are of interest due to their strong hydro/dehydrogenating activity essential for the bifunctional catalysis. The performance and selectivity of the catalyzed processes depend not only on the zeolite but also on the nature of the metal. The particle size, their location and the electronic state of the supported metal ( which are consequences of the metal/support interaction) are important factors that can affect the catalytic activity of the catalyst.

#### **1.2.2.1. Metal particle size and dispersion**

Platinum and palladium are expensive metals. Hence, they should be used in such a way that provides a surface to volume ratio as high as possible i.e. the smallest possible metal crystallites. The fraction of atoms at the surface is frequently termed as dispersion<sup>37,38</sup>. Thus, the smallest the metal particles, the higher the fraction of metal atoms and therefore the higher the dispersion.

However, Boudart<sup>39</sup> reported that the particle size could have an influence on the catalytic performance when it was below 5 nm. Beyond that, the metal particle size was no longer expected to have an effect on the intrinsic catalytic activity, nevertheless, large metal particles could affect secondary reactions such as hydrogenolysis.<sup>40</sup> However, this was only



applicable in the case of structure-sensitive reactions. Boudart<sup>39</sup> defined the term structure-sensitive reaction as a reaction whose TOF (turnover frequency) varies with metal dispersion over an inert support. According to his rating, aromatic hydrogenation was a structure-insensitive reaction<sup>41</sup> and it occurred the same with cyclohexene hydrogenation<sup>42</sup>.

### **1.2.2.2. Metal deposition**

Several methods are used to load the metal on a support. The most widely used are incipient wetness impregnation, ion exchange and deposition-precipitation<sup>43,44</sup>. Because of the dependence of ion-exchange capacity on the molar  $\text{SiO}_2/\text{Al}_2\text{O}_3$  ratio, this method is not suitable for obtaining a high metal concentration on zeolites. In this case, incipient wetness impregnation is preferred. Nevertheless, when incipient wetness impregnation is used, large metal particles can be obtained. The loading method has direct or indirect influence on various characteristics of the catalysts such as metal dispersion, size and location of the metal particles, metal-surface interactions or acidity<sup>45</sup>.

## **1.3. Hydroconversion of naphthenes: mechanistic aspects**

The well-known bifunctional mechanism of hydroisomerization and hydrocracking reactions proceeding through olefinic intermediates<sup>22</sup> is widely accepted for describing the product distribution. The feed molecules are adsorbed into the zeolites porosity from the surrounding fluid phase, which can be gas or liquid depending upon the reactor operating conditions. In the context on this work, the attention is focused on naphthenic species. For which, there are different reaction pathways available. In the following subsections some are going to be described.

### **1.3.1. Isomerization reaction: elementary steps**

With a bifunctional catalyst, it is believed that the naphthenic species are adsorbed in the zeolite and then diffused to the metal sites (when the Pt is deposited on the zeolite porosity). They are then chemisorbed in the metal sites and dehydrogenated into the corresponding olefinic species, which migrate from the metal sites to the nearby Brønsted acidic sites. They are later protonated into naphthenic carbenium ions (Figure 1.8.).<sup>46</sup> The olefinic species adsorbed in the zeolite pores are assumed to be in equilibrium with the chemisorbed olefins on the metal sites, as well as with the surface carbenium ions on the acid sites (Figure 1.88.a). The cyclic carbenium ions thus produced are isomerized by hydride shift (Figure 1.88.b),



methyl shift (Figure 1.8.c) and ring contraction expansion *via* protonated cyclopropane (PCP) steps (Figure 1.8 d,e). This scheme can be found extensively in literature<sup>47–53</sup>.

The alkylnaphthenes rearrangements have been classified in two main categories: type A and type B isomerization as suggested by Weitkamp<sup>49</sup>. In type A isomerization, the number of substituents does not change whereas in type B isomerization the degree of branching is altered. It can be noticed from Figure 1.8.d and 1.8.e. that ring contraction-expansion steps can be type A or type B isomerization respectively. In general, type A reactions are faster<sup>49</sup>.

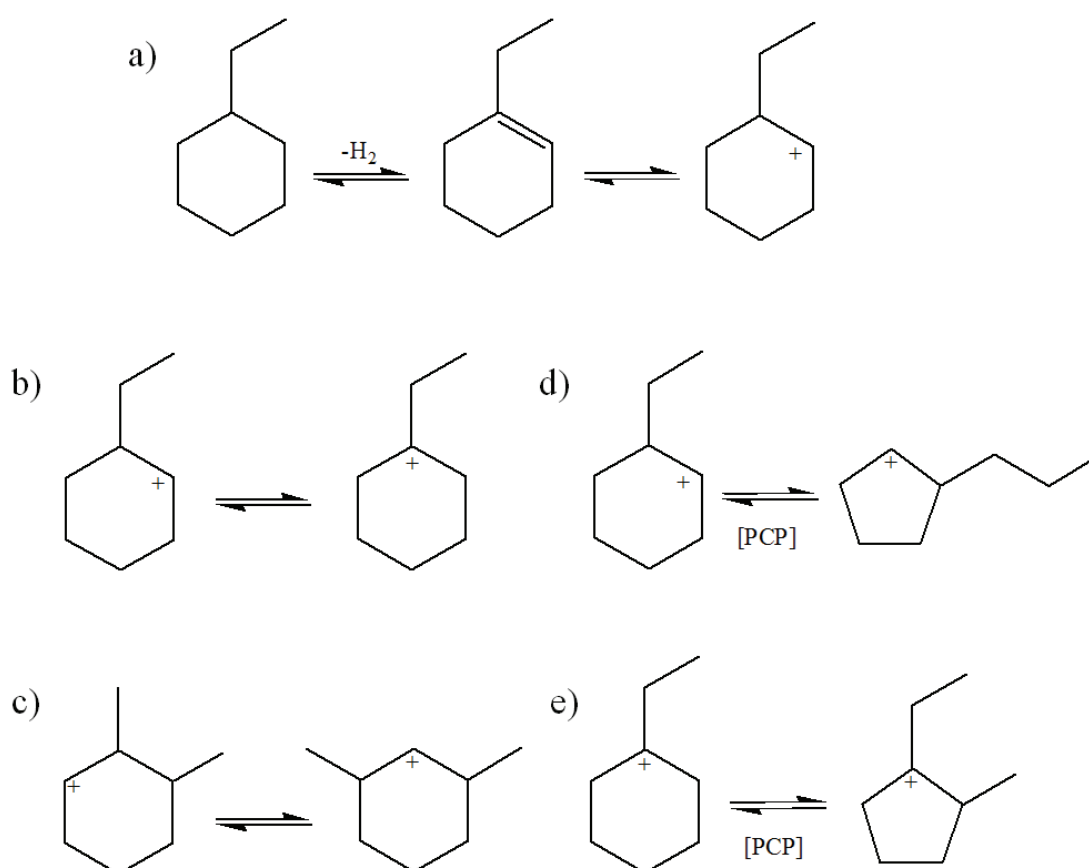


**Figure 1.8. Bifunctional-catalyzed steps for the naphthenes isomerization – case of ethylcyclohexane. a) ECH dehydrogenation and protonation; b) Hydride shift; c) methyl shift; d) Type A isomerization; e) Type B isomerization.**

### 1.3.2. Undesired side reactions

Nonetheless, naphthenes isomerization is not the sole reaction taking place. Concurrently, several other undesired side reactions appear, such as ring opening, cracking and possibly disproportionation. Ring opening and cracking are considered as “net losses” because once

that the ring is opened and cracked it is not recoverable<sup>46</sup>. Therefore, they should be avoided as much as possible in order to increase the yield towards the isomers.

### 1.3.2.1. Ring opening

The ring opening can occur according to three different mechanisms: thermal, acid (monofunctional or bifunctional) and metallic. In the cases of naphthenes hydroconversion, the thermal mechanism seems unlikely since the temperatures are milder compared to those necessities for this mechanism ( $> 500^{\circ}\text{C}$ ). In addition, the reaction time to reach relevant conversions is really high<sup>54</sup>. Regarding the metal mechanisms, Gault<sup>55</sup> identified three different paths (non-selective, selective and partially selective) for ring opening *via* hydrogenolysis. This is basically a C-C bonds breakage reaction taking place over the metallic function. Nevertheless, whereas the non-selective mechanism required well dispersed catalysts, the other two needed not well-dispersed catalyst. Therefore, as in this project well-dispersed catalysts are going to be used, the only possible mechanism is the non-selective one. This mechanism involves the cleavage of a C-C substituted bond through  $\pi$ -adsorbed olefin and metallocyclobutane intermediates. With regard to the acidic mechanisms, some related literature have been found for acid<sup>56</sup> and bifunctional<sup>37,57</sup> mechanisms. However, these studies were done with chlorinated alumina. It was not until some years ago that Cerqueira et al.<sup>50</sup> reported an acid ring opening mechanism catalyzed by zeolites. They explained the ring opening such as a product of a  $\beta$ -scission reaction (Figure 1.9.) where the first carbocation came either from protolytic dehydrogenation or cracking, or by hydrogen transfer. Sometime after, a bifunctional mechanism for the methylcyclopentane (MCp) was considered as possible by Galperin et al<sup>58</sup>. as illustrated in Figure 1.9. They found out that the most acid bifunctional catalyst provided as primary reaction the MCp isomerization into cyclohexane (CH) followed by the latter dehydrogenation into benzene. Following this scheme, cyclohexane (CH) was isomerized into methylcyclopentane (MCp) on the acid sites whereas the following ring opening and cracking were performed over both acid and metal sites.

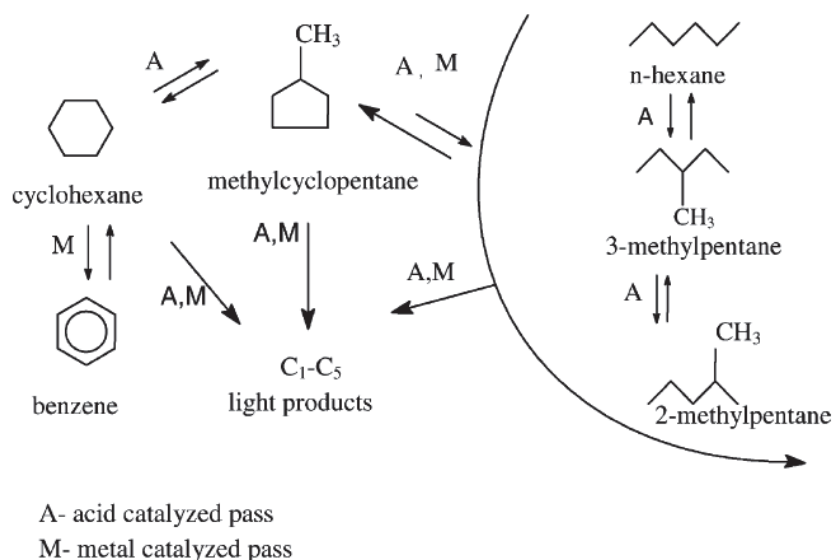


**Figure 1.9. Flow scheme for MCP conversion<sup>58</sup>.**

These results suggest that cycle expansion from the 5C-ring to the 6C-ring is faster than the ring opening reactions and the hydrogenation of CH into benzene seems faster than the CH ring opening.

If the ring opening happens on the acid sites, the naphthenic carbenium ions can be opened through endocyclic  $\beta$ -scission towards an unsaturated carbenium ion as illustrated in 10. Nonetheless, depending on the location of the positive charge, the naphthenic carbenium ions can also undergo an exocyclic  $\beta$ -scission (Figure 1.10) producing a naphthenic olefin and cutting the long alkyl chain as a paraffinic carbenium ion.

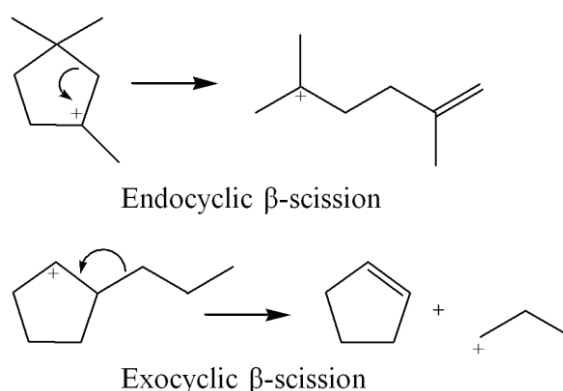


**Figure 1.10. Endocyclic and exocyclic  $\beta$ -scission**

On the other hand, if the ring opening is governed by the metal sites, hydrogenolysis will happen with a product distribution that highly depends of parameters such as metal particle size or metal-support interaction.<sup>40</sup>

Much work along this line has been done with alkanes<sup>23,59-61</sup> and lately with naphthenes<sup>47-51,62</sup> as well. Nevertheless, in this work it is going to be taken into account as reported by Sozinho<sup>46</sup> that under the process conditions, using a EU-1 catalyst, ring opening and cracking seem to take place on the acid phase *via* a bifunctional mechanism. This conclusion was based on the different nature of the ring-opening products and the cracking products following this opening.

It seems that the rate difference between ring opening and consecutive cracking of the opened products, is quite related to the most promising  $\beta$ -scission allowed for the paraffins cracking reaction than the ring  $\beta$ -scission.

Marcilly<sup>22</sup> proposed an approximate classification of the methylnaphthenes  $\beta$ -scission ring opening rates as a function of the carbocations stability as illustrated in Figure 1.11.

Mode	$m \geq$	Reactants (methylnaphthenes)	Ring opening products	Ions involved	Rate classification
A	8		$\begin{array}{c} \text{C} \quad \text{C} \\   \quad   \\ \text{C}=\text{C}-\text{C}-\text{C}-\text{C}_+-\text{C} \end{array}$	T $\rightarrow$ T	$V_O < V_C$
B1	7		$\begin{array}{c} \text{C} \\   \\ \text{C}=\text{C}-\text{C}-\text{C}-\text{C}_+-\text{C} \end{array}$	S $\rightarrow$ T	$V_O = V_C$
B2	7		$\begin{array}{c} \text{C} \\   \\ \text{C}=\text{C}-\text{C}-\text{C}-\text{C}_+-\text{C} \end{array}$	T $\rightarrow$ S	$V_O = V_C$
C	6		$\text{C}=\text{C}-\text{C}-\text{C}-\text{C}_+-\text{C}$	S $\rightarrow$ S	$V_O > V_C$
D	5		$\text{C}=\text{C}-\text{C}-\text{C}-\text{C}_+$	S $\rightarrow$ P	(No data)

**Figure 1.11. Approximate classification of the methylnaphthenes ring opening by  $\beta$ -scission into the corresponding isoparaffines ( $V_O$ : ring opening rate.  $V_C$ : rate of the isoparaffines  $\beta$ -scission)<sup>22</sup>.**

Taking into account the model reaction performed in this project i.e. ethylcyclohexane hydroisomerization, the reactant of interest in Figure 1.11. is the trimethylcyclopentane. In this case, the ring opening rate is expected to be lower than the isoparaffin cracking rate, despite the fact that the ring opening involves a type A  $\beta$ -scission (with two tertiary carbenium ions, see section 1.3.2.2.). The sluggishness of the carbon-carbon bond breaking inside a naphthenic ring is well known in the literature and is commonly attributed to an unfavorable orbital orientation for the corresponding  $\beta$ -scission<sup>63</sup>.

### 1.3.2.2. Cracking

As told in the previous section, cracking reactions are believed to occur through the acid function of the bifunctional catalyst. Thus, like the acid isomerization, the cracking reaction of non-naphthenic compounds is believed to occur by  $\beta$ -scission *via* the scission of the carbon – carbon bond in  $\beta$  position of the positively charged carbon atom of the carbocation.

This  $\beta$ -scission was classified in five types by Weitkamp<sup>64</sup> taking into account the carbocation stability i.e. tertiary-tertiary (A), secondary-tertiary (B1), tertiary-secondary (B2), secondary-secondary (C) and secondary-primary (D) (Figure 1.12.).

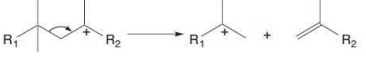
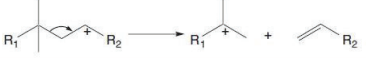
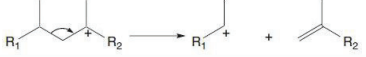
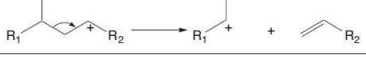
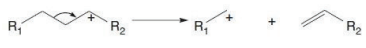
Type	Minimal number of C-atoms in chain	Carbenium ions involved	Example
A	$\geq 8$	tert $\rightarrow$ tert	
B1	$\geq 7$	sec $\rightarrow$ tert	
B2	$\geq 7$	tert $\rightarrow$ sec	
C	$\geq 6$	sec $\rightarrow$ sec	
D	$\geq 5$	sec $\rightarrow$ prim	

Figure 1.12. Types of  $\beta$ -scission<sup>65</sup> for non-naphthenic compounds.

He concluded from the product distribution and as expected regarding the carbocations stability, that under the so-called ideal hydrocracking conditions (see later section 1.3.3), tertiary-tertiary, secondary-tertiary and tertiary-secondary are the dominant  $\beta$ -scissions, in line with the stability of the carbocations involved.

### 1.3.2.3. Disproportionation

Naphthenes disproportionation in which a bimolecular transition state is formed and cracked after, has not been largely reported. Nevertheless, Weitkamp<sup>47</sup> studied naphthenes conversion on bifunctional catalyst and he reported some naphthenes with nine or less carbon atoms disproportionation on large-pore catalysts. Nevertheless, with medium pore catalyst no naphthenes disproportionation is found as medium pore zeolites cannot accommodate the bulky intermediates inside the microporous structure<sup>47</sup>.

### 1.3.3. Ideal hydroconversion catalyst

An ideal hydroconversion catalyst was firstly reported by Weitkamp<sup>66</sup>. It was defined as a catalyst where the acid and hydro/dehydrogenation functions are well balanced and the rate determining step of the reaction takes place on the acidic function. When the catalytic functions are well balanced, the catalyst activity and selectivity are independent of the concentration and the dispersion of the noble metal and are solely related to the catalytic properties of the acidic phase. In addition, no diffusional limitations may occur in ideal hydroconversion, i.e. the distance between acid and metal sites should be below a critical value under which there are no diffusional problems (Weisz intimacy criterion)<sup>8</sup>.

Nevertheless, Thybaut et al.<sup>67</sup> suggested that not only the acid-metal balance affected the ideality of the hydroconversion reaction, if not also the operating conditions such as total pressures, temperatures, hydrogen to hydrocarbon molar ratios and the reactant carbon number. It suggested that for each reaction and corresponding catalytic system to be studied, the formulation of an ideal bifunctional catalyst should be determined experimentally (if there was no kinetic model available).

#### 1.3.3.1. Influence of the metal/acid balance

To measure the metal/acid balance, the amount of accessible surface metal and the Brønsted acid sites of the acid solid are evaluated, then the metal/acid sites ratio is calculated. Several authors<sup>12,52,68–70</sup> have described the impact of the metal/acid balance on the bifunctional catalyst activity and selectivity following a typical bifunctional mechanism. In this mechanism, activity and selectivity increase as the metal/acid ratio increases which is in agreement with a bifunctional process limited by the Pt catalyzed steps at lower ratios. Then a quasi-equilibrium of the hydro-dehydrogenation reaction is reached above a critical metal/acid ratio. In these conditions the rate determining step takes place on the zeolite i.e. activity and selectivity changes are limited by the acid function. Optimal catalytic characteristics are obtained when metal/acid values are high enough i.e. when a “plateau” in activity (Figure 1.12) and selectivity is reached. Some authors<sup>71,72</sup>, reported some values of this ratio. A ratio  $n(\text{Pt})/n(\text{H}^+) \geq 0.03$  appeared as necessary to reach the plateau and  $n\text{Pt}/n\text{H}^+ \geq 0.17$  to provide a stability in the products selectivity in the hydroisomerization and hydrocracking of n-heptane on Pt zeolites. Nevertheless, these values do not seem very generalizable since as reported before,<sup>67</sup> the operational conditions and the reactant molecule impact as well the ideality of a catalyst. However, Mignard et al.<sup>73</sup>, studied the influence of

the  $n\text{Pt}/n\text{H}^+$  ratio in the methylcyclohexane hydroconversion with a Pt/USY catalyst revealing no influence of the amount of Pt in the results even with a low amount of Pt (0.03%). However, they did not reported the  $n(\text{Pt})/n(\text{H}^+)$ . On the other hand, Batalha et al.<sup>69</sup> observed that the optimal stability (to deactivation by coking) and selectivity required metal/acid ratios higher than those necessary for an optimal activity in the n-alkane hydroisomerization reaction. This suggested not only the acidic reaction as the rate limiting step but also only one skeletal rearrangement or cracking had to happen during the molecules diffusion from the platinum sites on which they were generated to those on which they were hydrogenated. Hence, a selectivity plateau where the reactions of hydro/dehydrogenation had reached the equilibrium with regard to the reaction products was obtained.

To conclude, before any kinetic investigation on bifunctional catalysis, regarding the acidic phase properties, one has to be sure that the plateau is reached. Otherwise, the comparison between several catalysts may be biased by limitations inherent to the metallic phase.

### 1.3.3.2. Intimacy criterion

More than 50 years ago, Weisz<sup>8</sup> established the so called “intimacy criterion”. It is based on the fact that a critical distance exists between the acid and metal functions, below which, the performance of the catalyst remains constant. Commonly, this has been assumed as “the closer the better” between the two catalytic functions.

An graphical illustration of the intimacy criterion concept is depicted in Figure 1.13. Two catalyst with different distance between acid and metal sites (shorter and larger) are considered. On the left part of the picture is illustrated evolution of the catalytic activity versus the metal accessible sites per acid sites micromole ratio for the two catalysts. Following the intimacy criterion, larger distance will provide a plateau of activity (green dots) lower than the one corresponding to shorter distances (blue dots). When the intimacy criterion is fulfilled (blue dots) the diffusion of the olefinic intermediates between the two functions is not a limiting step in the bifunctional mechanism.

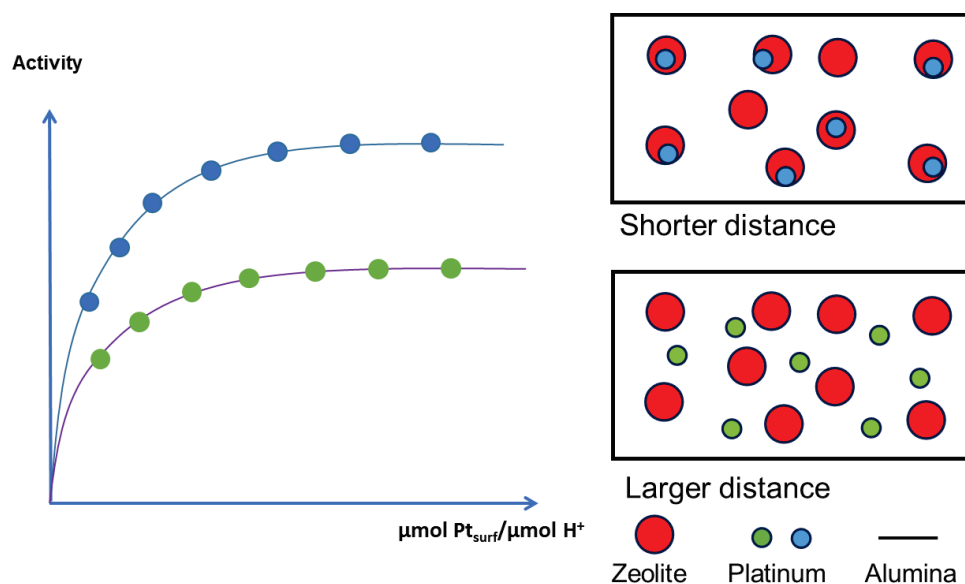


**Figure 1.13. Illustration of the impact of the expected metal to acid site ratio and of the proximity between the two functions (Weisz intimacy criterion) on a bifunctional catalyst activity.**

For many years, a great number of publications supporting this “intimacy criterion” and some more recently<sup>52,68–70</sup> have been published. However, it has been recently reported that proximity can be detrimental for catalysts selectivity towards hydroisomerization of paraffins<sup>74</sup>. These authors studied different hydrocarbons (*n*-decane (*n*-C<sub>10</sub>), *n*-nonadecane (*n*-C<sub>19</sub>) and pristane (2,6,10,14-tetramethylpentadecane, *i*-C<sub>19</sub>)) hydroconversion with two different catalysts with Pt particles located either inside the zeolite Y pores or on the alumina binder. Their results revealed that when Pt is located inside the zeolite rather than on the alumina support, the isomerization selectivity decreased. It was proposed that the probability of secondary reactions increased (essentially cracking) when the alkene intermediates were formed in the metal sites deposited inside the zeolites. The explanation proposed was their trapping on the zeolite pores due to the strong adsorption and concurrent slow diffusion through the pores. In the same spirit, Samad et al.<sup>61</sup> studied the effect of metal-acid proximity in Pt/silica-alumina catalysts for *n*-heptane isomerization with four different distances: atomic- (<10<sup>-9</sup>m), nano- (10<sup>-9</sup>-10<sup>-6</sup>m), micro- (10<sup>-6</sup>-10<sup>-3</sup>m) and millimeter- scale (>10<sup>-9</sup>m). They found out that both nano and micro-scale proximity provided the same results fulfilling the “intimacy criterion” whereas it was not the case of the atomic distance. In this case, more cracking products were found in detriment of the isomerization ones. Nevertheless, in recent times, another study of the of metal-acid proximity in Pt/Alumina and Pt/Beta-zeolite



catalysts for n-heptane isomerization revealed that regardless of the position of the Pt particles (zeolite or alumina) no influence on the conversion was observed. This meant that even if the Pt is deposited on the alumina, the reaction was limited by the isomerization on the acid sites and not by the intermediates diffusion.<sup>70</sup>

### **1.3.3.3. Zeolite structure influence**

It has been observed experimentally how the zeolite topology have a significant impact on the relative rates of type A and type B for naphthenes isomerization. Weitkamp<sup>47</sup> reported that MOR favored type B isomerization compared to type A, as propylcyclopentane did not appeared as the primary product of ethylcyclohexane isomerization. MOR structure has channels located in one crystallographic plane with side pockets evenly space. By contrast, for other three-dimensional zeolites such as FAU<sup>49</sup> or MFI<sup>48</sup> propylcyclopentane was indeed the primary isomerization product. The pores shape, or the dimension of the structure can create some constraints related to the transition states or even to the reactant and the products<sup>21</sup> as explained in the section 1.2.1.1.

### **1.3.3.4. Metal/support interaction**

The support is able to generate a modification in the metal electronic density and so in its activity. Thus, generally, the changes in catalytic activity are ascribed to this modification of the electronic properties of the metal particles and several models have been proposed; Mojet<sup>75</sup> studied a model to describe the metal–support interaction in noble metal catalysts. He concluded that the metal-support interaction affected the electronic properties of the metal. It was revealed as well, a decrease of the neopentane hydrogenolysis activity when the support alkalinity increased due to a decrease in the ionization potential of the metal particles directly induced by the Coulomb potential of the support. Following with that idea, Regali et al.<sup>76</sup> investigated the hydroconversion of n-hexadecane on Pt/silica-alumina catalysts. They found better hydrogenolysis activities by using a catalyst with a more acidic support than with a less acidic one, even if the Pt dispersions were similar. They attributed this increase in activity to an influence of the support acidity on the platinum crystallites. However, and contrary to the above explanations, Samant and Boudart<sup>77</sup> related the electron deficiency of the metal to the intrinsic small size of the Pt clusters. Therefore, questions such as how metal-support interaction affects the electronic structure and properties of the metal particles upon adsorption remains somewhat ambiguous.

### 1.4. Insights from *ab initio* calculations

The reactions evoked previously can be the object of *ab initio* calculations. We will focus here on reactions taking place on the acidic phase (zeolite) considering that in this study, an ideal bifunctional catalyst is employed.

#### 1.4.1. Models for protonic sites in zeolites

An important issue in modeling zeolite electronic structures is how to represent its extended nature with adjustable calculations. The challenge is double since it is not only to model the zeolites structural complexity (the infinite dimension of solids), if not the necessity to take into account the weak chemical interactions, such as van der Waals interactions, and the hydrogen bonding of reactants to Brønsted acid sites<sup>78</sup>.

The computational expense of electronic structure calculations is not negligible. This restricts often the size of a molecular model to only those atoms essential to capture the chemical phenomena of interest. For instance, in zeolites, the use of a truncated model or cluster approximation has been largely employed<sup>79–84</sup>. A cluster is a finite, generally small environment of the active sites described on the basis of quantum-chemical or density functional approaches. Nevertheless, even when the clusters are constrained to mimic the target zeolite, qualitative errors can arise<sup>82,83,85</sup> such as the edge effect, the inaccurate reproducibility of the topology and the absence of long distance effects. Therefore, larger models with embedded clusters have appeared as alternative to the small clusters<sup>82,85</sup>.

The investigation of properties and the local geometry of the bridged hydroxyl acid sites of zeolites has been an area of interest for theoretical studies. Hartree-Fock (HF) molecular orbital methods has been used in most of the historical work (70's and 80's) using small clusters to represent the bridged hydroxyl groups<sup>86</sup>. Later studies<sup>87,88</sup>, have employed Density Functional Theory approaches to include the electron correlation. However, these theoretical models are limited regarding the cluster size that can be used in the calculations. On the other hand, semi-empirical methods allow to manage with larger clusters reaching a more accurate illustration of the zeolite crystal lattice structure, but with a lower precision on energies and forces. For instance, Farnworth et al.<sup>89</sup> studied the bridged hydroxyl group model in two different clusters ( $\text{H}_3\text{Al}(\text{OH})\text{SiH}_3$  and  $(\text{HO})_3\text{Si}(\text{OH})\text{Al}(\text{OH})_3$ ) with HF, density functional and semi-empirical methods including crystal lattice constraints. Density functional methods, especially B3LYP improved the HF theory in the description of the zeolite bridged hydroxyl group. Constraining the crystal lattice, the Si-O-Al bond angle results were closer to the

reality (experiments), achieving a more realistic local geometry and therefore, more accurate acidity measurements. On the other hand, semi-empirical methods were not as conclusive as DFT ones because of the poor prediction of proton affinity accuracy, atomic charges and bond lengths. Only PM3 might be useful in the case of larger cluster zeolite models. A similar study reported by Gu. et al.<sup>90</sup> revealed, in agreement with Farnworth, the B3LYP exchange correlation-functional as reliable for the study of Brønsted acidity on zeolites. Besides, these authors reported the importance of the chosen system configuration, above all for the OH-terminated models. This was due to the huge influence of the H bond formed between the acidic proton and its closer neighbor oxygen on the aluminum atom (the acidic OH bond length and its stretching frequency).

The artificial termination of clusters was as well, remarked by Hafner et al.<sup>78</sup> suggesting periodic models as an important step forward regarding the cluster approach. Actually, these periodic models are the most commonly used since the year 2000 to model the zeolites<sup>78,91</sup>. In Figure 1.14 a 3T cluster and a periodic cell are represented.

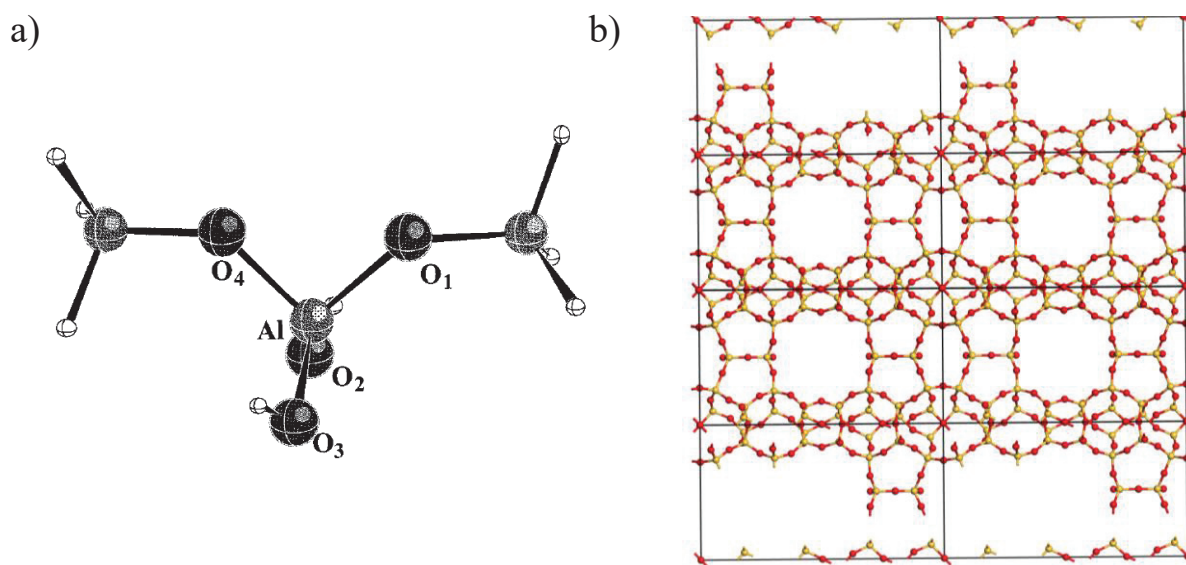


**Figure 1.14. Representation of a) a 3T cluster,<sup>92</sup> b) a periodic cell.**

Even if DFT has rapidly become the main computational approach for the solids electronic structure<sup>93</sup>, finding an adequate approximation to the electron density functional is not straightforward. For instance, the local density approximation (LDA) is known to give high cohesive energies and too small lattice constants due to its tendency to overbind. This is a serious default in the case of zeolites because, for instance, the hydrogen bond energy between the Brønsted acid sites and saturated molecules is overestimated. This overbinding tendency is well corrected by the generalized gradient approximation (GGA). In spite of this

improvement, it underestimates the HOMO-LUMO gap. A solution to this problem are hybrid functional such as B3LYP and PBE nonetheless, the computational expense is higher compared to LDA or GGA.

Based on several zeolites structural optimizations reported<sup>91,94,95</sup>, GGA is considered as a well-adapted electron density functional not only for predicting in an accurate way the structural parameters but also for its ability to analyze the active sites structure and reactivity in proton-exchanged and metal-activated zeolites. Nevertheless, it should be bear on mind the continuous development of the exchange correlation functionals with the aim of get closer to reality that still remains a challenge.

#### 1.4.2. General aspects of carbenium chemistry on zeolites

It is not always clear from experiments whether carbenium ions exists as free or adsorbed species inside the zeolite pores, or if they are covalently bonded to framework oxygen forming alkoxide intermediates. This depends on the zeolite but also on the nature of the olefin and carbenium (substitution, delocalized nature)<sup>96</sup>. In Figure 1.15 are illustrated the possible species appearing on the zeolites: a  $\pi$ -complex, a carbenium and an alkoxide in the case of a naphthene.

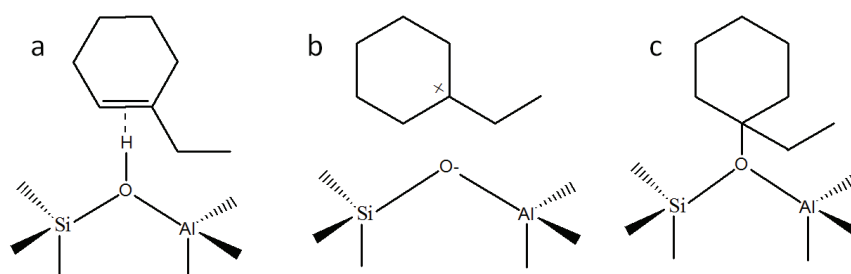


**Figure 1.15. Ethylcyclohexene a.  $\pi$ -complex; b. carbenium and c. alkoxide.**

Some time ago, ab initio quantum chemical calculations at B3LYP/6-31G\* level using a T3 cluster without any symmetry constrains, of acid-catalyzed transformations of hydrocarbons on zeolites were performed. They revealed that adsorbed carbenium and carbonium ion active intermediates were not the highly reactive species really existing, but the transition states of the corresponding elementary steps<sup>97</sup>.

Rigby and Frash<sup>98</sup> studied the isobutene chemisorption to a zeolite Brønsted site using HF calculations and MP2 approximation, with the cluster and periodic approach. The results showed the same geometry trends passing through alkoxide intermediates in both,

cluster and periodic electronic structure calculations. It was well-described that olefin physisorbed to the acid Brønsted site of a zeolite crystal was not a very stable situation since olefin was readily protonated<sup>98</sup>. Because charge separation in an acidic zeolite was energetically costly, a free carbocation was believed in same case not to exist. At the same time that the olefin protonation occurred, an alkoxy bond was formed between an olefin carbon atom and an a zeolite oxygen atom so as to stabilize the positive charge.

Nonetheless, using more recent DFT theory (nonlocal hybrid BH&HLYP with 6.31G(d,p) basis set) and both a 3T cluster approximation and a bigger embedded cluster, Vollmer and Troung<sup>92</sup> remarked the increase on the carbocationic nature of the transition state due to the explicit presence of the zeolite. The steric constraints provided by the zeolite framework played an important role since the stabilization of the adsorbed complexes (specially alkoxides) was very sensitive to the local site geometry. The latter was also observed more recently by Rozanska<sup>99</sup> et al. in a GGA periodic study of isobutene chemisorption in proton-exchanged zeolites. They observed carbocations as transition states (TS) whose stabilization was favored by short-range electrostatic contributions and by fitting its shape with the zeolite micropore size. Tuma et Sauer<sup>100</sup> took into account the influence of the temperature in the stability of the reaction intermediates and transition states. Employing DFT/PBE calculations with a plane wave basis set and a periodic cell, the carbenium was revealed as the most stable species when the temperature was raised over 120K. It was a local minimum in the potential energy surface (PES). More recently studies<sup>101</sup> by the team of Van Speybroeck et al., about the stability of adsorbed pentene in HZSM-5 using static and molecular dynamic methods for measuring were reported. A more stable  $\pi$  complex was found in the case of static calculations without finite temperature effects, whereas in the dynamic calculations at 323K, both  $\pi$  complex and alkoxide had similar stabilities. On the opposite, the carbenium was not observed in the simulations at 323K. However, it was observed as transient specie higher in energy during the transformation from a stable  $\pi$  complex to an alkoxide. Another recent study<sup>102</sup> investigated the effect of the temperature in the stability of the C<sub>4</sub>-C<sub>5</sub> alkene cracking intermediates in HZSM-5. Interesting results were found. At 323K, linear alkoxides, alkene  $\pi$  complex and tertiary carbenium ions were found as the favored intermediates. Nonetheless, at 773K secondary and tertiary alkoxides were not stable. The carbenium (especially tertiary carbenium) was found as a stable intermediate.

On the other hand, Boronat and Corma<sup>103</sup> reported alkoxides as intermediates and carbeniums as TS for linear alkanes isomerization. Besides, they remarked the possible

existence of the tert-butyl cation as a true reaction intermediate. This cation appeared because of a certain stability reached due to its position inside the zeolite microporosity. They emphasized the importance of the zeolite geometry as crucial for the TS stabilities. Moreover, as the accuracy of the methods increased, the carbenium was revealed as the most stable intermediate against the alkoxide. Nonetheless, higher level (but very demanding) calculations (MP2/hybrid) were performed by Tuma et al.<sup>104</sup>. They found the tert-butyl carbenium ion as intermediate of the reaction but being the least stable specie on the PES (potential energy surface) as compared to the pi complex and alkoxides. They performed as well, lower accuracy calculations (PBE+dispersion corrections) revealing that this method was not expected to give reliable relative stabilities and energy barriers due to its inefficacy in the standard self-interaction correction (SIC) error.

To sum up, in spite of all the performed studies, the question of whether the reaction intermediates and transition states are carbenium or alkoxides still remains elusive.

Whereas many work has been done about olefins chemisorption on acidic zeolites<sup>92,99,103,105</sup>, the reactivity of naphthenes from a DFT point of view have not been highly investigated. Most of the experimental studies showed that the carbocations inside the zeolite were not stable species. Nonetheless, lately, some cyclic cations have been experimentally observed to be important long-lived intermediates in some reactions of hydrocarbons on zeolites<sup>106,107</sup>. In recent years, a DFT study of the cyclohexene interactions pathways over HZSM-5<sup>83</sup> revealed the formation of ionic intermediate species instead of alkoxides. The explanation comes from the more restricted structure of bigger models since the sensibility of the alkoxy product stabilization depended on the local geometry of the active site. When a small model environment is used, it is easier to performed the different structural changes to accommodate the bulky alkoxy species around the active site. On the other hand, this becomes more difficult when the active site in the catalyst is restricted by the rest of the zeolite framework when the molecule is too bulky.

Nevertheless, concerning the mechanism of ring contraction, expansion, and cracking of cyclic olefins over the acid sites, no DFT work has been published to date, to the best of our knowledge. We will however in the following analyze the existing DFT literature about non-cyclic olefin isomerization and cracking.

### 1.4.3. Works dealing with olefins isomerization

2-pentene isomerization in H-ZSM-22 has been studied with GGA/PW91 approximation by Demuth et al.<sup>94</sup>, by periodic calculations. They reported two isomerization mechanisms: *via* alkyl-shift reaction and *via* dimethylcyclopropane intermediate, or *via* edge-protonated dimethylcyclopropane transition state as shown in Figures 1.16 and 1.17 respectively.

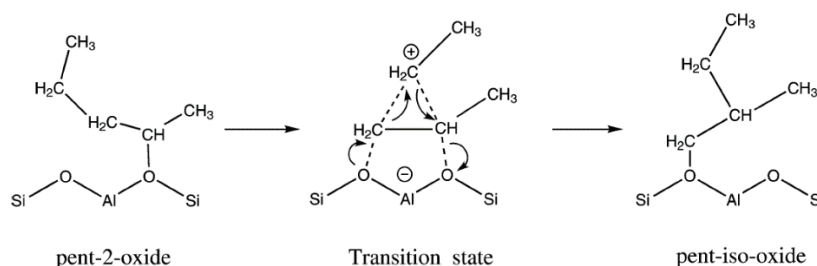


**Figure 1.16. C<sub>5</sub> isomerization reaction *via* alkyl-shift reaction<sup>94</sup>.**

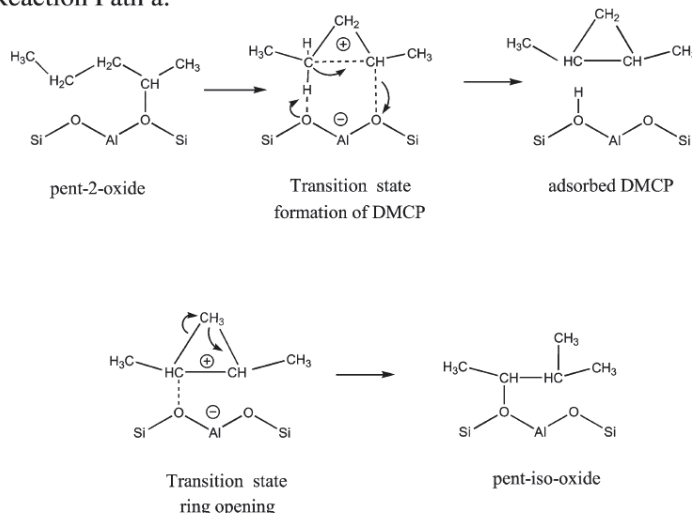
In the alkyl-shift reaction (Figure 1.16), a terminal alkyl ion was separated from the molecule and reattached at a different carbon atom of the remaining hydrocarbon chain being the product an isopentyl oxide. The transition state was characterized by a triangular arrangement of the carbenium ion and the activation energy found was 180 kJ/mol. Nevertheless, this mechanism was found to be improbable by the authors since the transition state(alkyl ion) was a high-energy specie inducing too high activation energies. Note that the reactants and products were found in the form of alkoxides, and not carbenium ions, which could have an influence on the reaction profile.

In Figure 1.17 is illustrated the second mechanism proposal, certainly more complex compared to the one shown before. This pathway involved three different transition states and two intermediates (in path a: a secondary carbenium ion and a neutral DMCP).

Path a concerned a complex series of molecular rotations, thereby, the alternative path b may be kinetically preferred. Besides, this mechanism is generally considered in isomerization and cracking reactions. These reactions *via* DMCP had lower activation energies (100 kJ/mol) than the ones involving alkyl shifts. Thus, the alkyl-shift pathway must be discarded in this case.



## Reaction Path a:



## Reaction Path b:

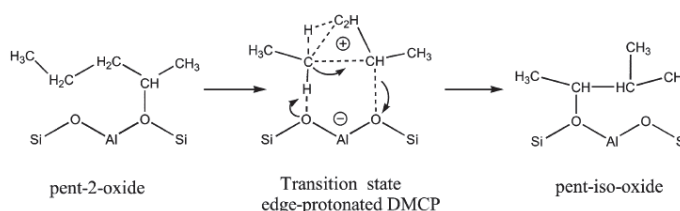


**Figure 1.17. C<sub>5</sub> skeletal isomerization. Path a: *via* a dimethylcyclopropane (DMCP) intermediate. Path b: *via* an edge-protonated DMCP transition state (PCP type)<sup>94</sup>.**

#### 1.4.4. Works dealing with olefins cracking

Catalytic cracking of olefins is a very important reaction in the refining and petrochemical industry. Generally, zeolites are used as solid-acid catalyst in the cracking process because they provide high catalytic activities and selectivities. The nature of the intermediates for olefin cracking reactions is not yet elucidated. Many works have been done but very different results have been reported.

In 1996, Kazansky et al.<sup>80</sup> studied by HF calculations and a T and 3T clusters the isobutene cracking on zeolites. They reported that the tert-butyl carbenium ions and isobutyl carbonium ions were not the reaction intermediates but the transition state of the corresponding elementary reactions. For the beta-scission reaction, activation energies of 240 kJ/mol were found. Nevertheless, the opposite was reported by Guo et al.<sup>81</sup> in their study of  $\alpha$ -olefins cracking. They found that the intermediates in the  $\beta$ -scission process were adsorbed short-lifetime carbocations and not the alkoxides as largely reported before<sup>92,98</sup>. They suggested that the real activation energy of olefin cracking was almost independent of the



olefin chain length, being around 185kJ/mol. Nevertheless, under certain reaction conditions, the alkoxide pathway could also occur. The DFT calculations in this case were performed with a B3LYP/6-31G(d,p) hybrid approach and a 3T cluster. Figure 1.18 shows a transition state (TS) for linear C4–C10  $\alpha$ -olefin cracking concerning the latter study.<sup>81</sup>

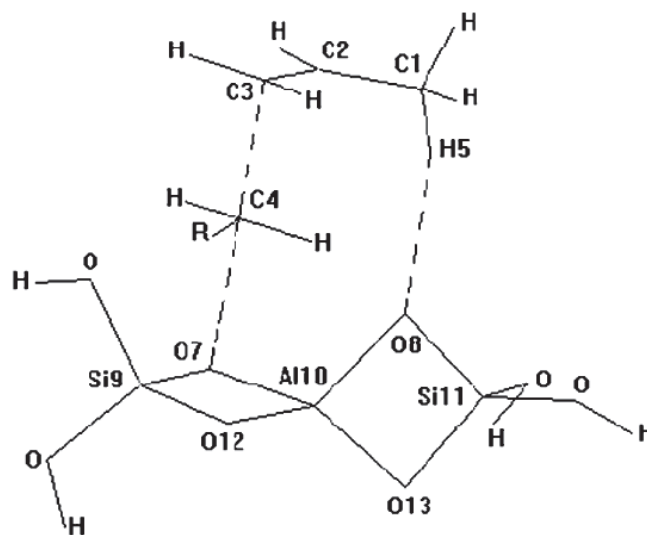


Figure 1.18. TS for linear C4–C10  $\alpha$ -olefin cracking.<sup>81</sup>

Jeffrey et al.<sup>108</sup> studied the C-C  $\beta$ -scission of pentene on zeolites with HF/6-31G\* and DFT/B3LYP calculations of the HF optimized structures. They found similar results with regards to the pentene and methylpentene transition state energies (251 kJ/mol and 230 kJ/mol respectively) passing through an alkoxide intermediate in a 3T cluster. Guo et al.<sup>109</sup> studied the cracking of 1-hexene over HZSM-5 with ONIOM(B3LYP/6-31G (d,p)) with a 88T cluster model and the B3LYP/6-31G(d,p) method with a 5T cluster. They found out that no stable carbenium was observed in the case of the smaller cluster while that was not the case with the larger cluster in which a very stable carbenium was obtained. Nevertheless in both cases, carbenium intermediates existed in the reaction pathway following a two-step mechanism. They noteworthy mentioned the fact that the zeolite environment was really important regarding the stability of the hexyl carbenium ion. Therefore, the apparent energy barriers found were quite different depending on the cluster employed; 105 kJ/mol in the case of the 88T cluster and 150 kJ/mol in the smaller one (5T).

On the other hand, another group of authors<sup>110–112</sup> studied the alkenes dimerization, which is of interest to us as this is the reverse reaction with respect to cracking. Two different mechanisms were investigated: stepwise and concerted. In the first one, the dimerization

reaction occurred through two elementary steps: protonation of the adsorbed alkene to form the alkoxide and the formation of the C-C bond between the alkoxide and the second alkene whereas in the second one, the protonation of the C=C and new C-C formation occurred concurrently. For instance, Svelle et al.<sup>110</sup> studied these two methods for the alkene dimerization with a 4T cluster using B3LYP and MP2 combined with larger, triple- $\zeta$  basis sets. They observed that the alkoxides formation had the lowest energy barrier. Besides, the C-C bond formation step had higher activation energy than the single barrier of the concerted mechanism which involved primary or secondary carbenium ion-like transition state. Nevertheless they were not able to discriminate between the two mechanisms since more detailed knowledge regarding the alkoxides species stability was required. Later, Namuangruk et al.<sup>111</sup> studied the ethylene dimerization over Faujasite zeolite but in this case with a larger cluster (84T) and employing a more accurate model ONIOM3(MP2/6-311++G-(d,p)/HF/6.31G(d):UFF). They were able to conclude that the stepwise mechanism was the one dominating in the ethylene dimerization since the rate-determining step of the stepwise mechanism (the protonation of the ethylene to form the alkoxide intermediate) energy barrier was 128 kJ/mol whereas in the concerted mechanism the energy barrier was 159 kJ/mol. On the other hand, Chu et al.<sup>112</sup> highlighted the influence of the acid strength and the confinement effect on the latter reaction on zeolites ZSM-5 and ZSM-22 by mean of a DFT study. Their calculations demonstrated that acid strength governed the reactivity independently of the mechanism (stepwise or concerted). Also the calculations showed that the zeolite structure could stabilize the ionic transition states. Regarding the activation energies, higher activation energies were found in this work, the stepwise mechanism showed always lower energy barriers than the concerted mechanism indicating that the former mechanism was preferred for the ethylene dimerization reaction.

Interesting studies of the influence of the basicity of the catalyst on the  $\beta$ -scission of carbenium ions was published by Li et al.<sup>113,114</sup>. They used several catalysts with different basicity finding different intermediates: stable neutral alkenes or alkylcyclopropanes on the most basic catalyst( $\text{AlH}_2(\text{OH})_2^-$ ) whereas protonated alkylcyclopropanes were reaction intermediates in the case of a less basic catalyst ( $\text{AlHCl}_3^-$ ). The energy barriers found for both cases are respectively 280 and 155-159 kJ/mol.

Leydier et al.<sup>115</sup>. performed a DFT study to compare the 2,4,4-trimethyl-2-pentene cracking pathway between an amorphous silica-alumina(ASA) and mordenite zeolite. In this study, only the intermediates were identified but not the transition states. They remarked that

the carbocationic pathway was preferred in mordenite due to its confinement effects whereas in the case of ASA was the alkoxide route the most favored. In this study, the pathway involving the tertiary alkoxide was the preferred one. Nevertheless, an alternative route involving both carbocations and alkoxides intermediates was not discarded in the case of ASA. Nonetheless, in both supports the activation energy barrier was higher than 70 kJ/mol. In addition, for both as well, protonation and  $\beta$ -scission were the rate limiting steps of the reaction, on the basis of the analysis of the stability of the intermediates.

The reaction energies calculated for several alkenes  $\beta$ -scission steps occurring on zeolites, and reported in the literature differ quite strongly from one study to another. As illustrated here, these energies vary from 10 kJ mol<sup>-1</sup> to more than 100 kJ/mol with a very strong impact of the model size and the zeolite type, as well as of steric and confinement effects.

### 1.5. Multiscale kinetic modelling

Investigating multi-step reaction pathways by ab initio calculations does not always lead to simple conclusions about the quantitative selectivity / activity that will be reached at the macroscopic scale. To make a direct relation between the atomic and the reactor scales, multi-scale modeling proved to be an efficient tool for several kinds of chemical systems,<sup>116–131</sup> including catalytic systems. In particular, it was successfully applied to alcohol dehydration in zeolites,<sup>132–134</sup> but was never used for the reactions we are aiming at investigating in the present work. First, accurate rate constants have to be calculated thanks to the transition state theory for example, using ab initio calculations, including entropic components. For carbenium chemistry within zeolites, as illustrated before, this can be a challenge.

### 1.6. Conclusions and scope of the work

The growing demand for paraxylene due to its importance in the manufacture of the terephthalic acid, has made the processes related to its production of great interest. Paraxylene can be produced by process involving the isomerization of meta, orthoxylene and ethylbenzene. In particular, ethylbenzene isomerization is a well-known reaction that follows a bifunctional mechanism which requires the use of a bifunctional catalyst.

A bifunctional catalyst is made up by two functions: an acidic function and a metallic one. In the case of ethylbenzene (EB) isomerization, one of the catalyst employed in the industry nowadays exhibits EU-1 zeolite as the acidic function and Pt as the metallic function.

## CHAPTER I. STATE OF THE ART

According to the widely accepted bifunctional mechanism, EB isomerization is expected to occur as follows. Firstly EB is hydrogenated over the Pt into ethylcyclohexenes. Then, ethylcyclohexenes diffuse to the zeolite acid sites where they are isomerized into the different isomers by ring contraction-expansion. The products are finally dehydrogenated on the Pt sites into xylenes. However, because of the strong hydrogenation function, the formation of naphthenic compounds cannot be avoided. These naphthenic compounds are suffering undesirable side reactions such as ring opening and cracking. The loss generated by these two reactions decreases the selectivity towards the desired products, the isomerization ones. It is believed that these side reactions are occurring on the acidic sites of the zeolite.

It is therefore of great importance to understand the key features of the zeolite affecting the C<sub>8</sub> naphthenes isomerization, ring opening and cracking, and their reaction rates. This is the first purpose of this work. To do so, the hydroconversion of a model C<sub>8</sub> naphthene, namely ethylcyclohexane, will be studied. The catalysts employed will be a bifunctional catalysts based in a mixture of zeolite EU-1 and alumina with Pt deposited either over the zeolite or over the alumina. Thereby, an ideal bifunctional catalyst is necessary in order to establish the mechanism of those side reactions, and to quantify the rate constants of the kinetically relevant steps. This ideal catalysts has the acid function as rate limiting and no diffusional problems (according to Weisz). In other terms, it's necessary that only the zeolite controls the evolution of activity and selectivity of the reaction in order to reveal which are their characteristics affecting directly to the isomerization, ring opening and consecutive cracking.

Finding the appropriate catalyst to gather these conditions, in terms of metal loading and location, will be our first aim. Then, we will undertake a cautious kinetic study on the selected catalyst, investigating the effect of contact time and temperature on the activity and selectivities. At this stage, this should allow to propose a reaction mechanism, with the quantification of apparent rate constants. In parallel, DFT calculations will be performed to identify the structure and nature of relevant intermediates and transition states for the isomerization (ring contraction and expansion) and ring opening within the EU-1 zeolite. Such reactions suffers from a quasi-absence of computed data at the atomic scale in the literature. We will also aim at calculating rate constants for each elementary steps. First, in order to be compared with experimental results, and next so as to introduce them in a micro-kinetic model to compare activities and selectivities for the multi-step reactions involved. Note that this computational investigation will first require to unravel the most plausible form

## CHAPTER I. STATE OF THE ART

(carbenium or alkoxide) for the protonated olefins within the EU-1 structure. DFT study should allow us to gain knowledge about the key factors governing the zeolite selectivity towards isomerization.

Afterwards, a selection of zeolite structures of potential interest for EB isomerization, beyond the EU-1 zeolite, will be carried out. The approach will combine an high-throughput experimental screening of the several different structures chosen, and a DFT study of the stability of the most representative transition states and intermediates of the reaction mechanisms for isomerization and cracking steps.

## 2. EXPERIMENTAL and MODELING PART

---

### 2.1. Zeolite bifunctional catalysts

For the first part of the thesis, two groups of bifunctional catalyst were synthesized either with the Pt impregnated over the Alumina or over the EU-1 from different precursors depending on the protocol followed as described in the section 2.1.2.

The bifunctional catalysts based on the zeolite EU-1 were obtained by mechanical mixture of 20% of zeolite and 80% of alumina in two different ways:

- Mechanical mixture of alumina impregnated with platinum, and zeolite.
- Mechanical mixture of zeolite impregnated with platinum, and alumina.

The zeolite and the alumina containing one of them the Pt are first milled and sieved in order to obtain a powder with a size below 63 $\mu$ m and mixed after in the desired proportion. The mechanical mixture was done at 300 rpm during 2min in a Fischer Scientific MM20 mixer. After, the mechanical mixture is pelletized in an hydraulic press Carver C (4 bar), crushed and sieved at the desired size (250-500 microns).

For the high throughput experimentation (HTE), another group of bifunctional catalyst was synthesized. These bifunctional catalysts were mechanical mixtures of alumina impregnated with platinum, and a zeolite: ZSM-23, ZSM-12, mordenite, ZSM-57, IZM-2, ZSM-5, ZSM-50, NU-86 and Beta. The alumina containing the Pt and the different zeolites are first milled and sieved in order to obtain a powder with a size below 63 $\mu$ m and mixed after in the desired proportion. The mechanical mixture is done in the same way as explained before for the EU-1 bifunctional catalyst. The acidic solids chosen in this work are enclosed in Table 2.1

**Table 2.1. Acidic solids employed in this study**

Zeolite	Supplier	Framework type	Ring-size	Dimension
ZSM-23	Zeolyst	MTT	10MR	1-D
EU-1	Zeolyst	EUO	10MR-12 MR pockets	1-D
ZSM-12	Zeolyst	MTW	12MR	1-D
ZSM-5	Zeolyst	MFI	10MR	3-D
ZSM-57	IFPEN	MFS	10-8MR	2-D
IZM-2	IFPEN	Unknown	10-12MR*	1-2D?*
NU-86	IFPEN	—	10-11-12MR	3-D
BETA	PQ	BEA	12MR	3-D
MORDENITE15	TOSOH	MOR	12MR-8MR	2-D
MORDENITE50	Zeolyst	MOR	12MR-8MR	2-D
ZSM-50	IFPEN	EUO	10MR	1-D

\* IZM-2 structure is unknown at the moment. IZM-2 is believed to possess 10 and 12 MR pores and a low dimensionality.<sup>135</sup>

### 2.1.1. Zeolite as solid acid

The EU-1 is provided by Zeolyst and is delivered uncalcined. Therefore, it has to be calcined before impregnation in order to remove the remaining template (organic molecule employed for the synthesis of the zeolite, hexamethonium (HM) in the case of the EU-1) making thus, the porosity and acidity available. The temperature profile for calcination of EU-1 under air flow (2 Nl/g) at 520°C is shown in appendix I, Figure 1.

Besides, a  $\text{NH}_4^+$  ionic exchange is carried out to remove the remaining  $\text{Na}^+$  ions. The zeolite is placed in an Erlenmeyer containing a previously prepared solution of  $\text{NH}_4\text{NO}_3$  using a volume of solution (ml)/dried catalyst weight(g) (V/P) ratio of 10. The slurry is heated under stirring (400 rpm) at 85°C for 4 h and then centrifuged at a rotation speed of 10000 rpm for 10 min. The solid is then washed three times with distilled water and centrifuged again. Then it is dried overnight at 100°C.

This procedure is repeated three times in order to guarantee high cationic exchange levels. The calcination after ionic exchange it is a little bit different from the previous calcination. In this case, the air flow is 1 Nl/g h at 520°C and follows the ramp of the appendix I, Figure 2.

ZSM-12, ZSM-23 and ZSM-5 are provided by Zeolyst and they are delivered directly in the protonic form. No ammonium or calcination are performed before their evaluation in the catalytic test. Mordenite15 and EU-1 are as well provided by Zeolyst, nevertheless they are not directly delivered in the protonic form. Thus, mordenite have undergone the same process

as the EU-1: calcination, ionic exchange and a last calcination. Beta zeolite has been delivered containing the template and then, a calcination has been performed (Appendix I). On the other hand, NU-86, IZM-2 and ZSM-57 have been synthesized at IFPEN (Divided Materials Engineering Department). The non-protonic zeolites have undergone a similar process as the EU-1: calcination, ionic exchange and a last calcination (Appendix I).

### 2.1.2. Platinum deposition

#### 2.1.2.1. On the EU-1 zeolite

When the deposition of the metal is done on the zeolite the wetness incipient impregnation has been used.

The incipient wetness impregnation allows the metal deposition over a solid without looking for an optimal dispersion. The metal in an aqueous solution is deposited directly over the solid, a zeolite in our case. When this impregnation is used, large metal particles could be obtained but it allows to deposit higher amounts of metal. In this case, the platinum precursor is  $[\text{Pt}(\text{NH}_3)_4\text{Cl}_2] \cdot \text{H}_2\text{O}$ .

A LOI and a WUV (water uptake volume) have to be performed before the impregnation. (see in the Appendix I. the different protocols). LOI has to be done in order to see which amount of water has the zeolite allowing to correct the humid mass weight and WUV to know how amount of water is necessary to saturate the solid.

Once known the LOI, for a dry mass  $m_d$  to impregnate the humid mass  $m_h$  to weight is given by the Eq. 2.1.

$$m_h = \frac{m_d \cdot 100}{100 - \text{LOI}} \quad \text{Eq. 2.1.}$$

The amount of precursor,  $[\text{Pt}(\text{NH}_3)_4\text{Cl}_2] \cdot \text{H}_2\text{O}$  is chosen in order to achieve the desired amount deposited over the support. It is calculated with the Eq. 2.2.

$$m_p = m_d \cdot x_{\text{Pt}} \cdot \frac{m_{w p}}{m_{w \text{Pt}}} \quad \text{Eq. 2. 2.}$$

The volume of the impregnation solution is determined by the WUV (Eq. 2. 3)

$$V = \text{WUV} \cdot m_d \quad \text{Eq. 2. 3}$$

$m_h$  support humid mass (g);  $m_d$  support dry mass (g);  $m_p$  precursor mass (g);  $m_{w p}$  precursor molecular weight(g/mol);  $m_{w \text{Pt}}$  Pt molecular weight (g/mol);  $x_{\text{Pt}}$  desired Pt %(g)



Once the Pt solution is prepared, it is added dropwise over the support (which has been previously introduced in a rotatory vessel) until the solid starts to be sticky showing a physical behavior in between a liquid and a solid. In this moment it will be introduced in an humidifier during one hour and then, dried overnight at 100°C. A calcination (Appendix I, Figure 3) has been done after impregnation.

### **2.1.2.2. On the alumina**

The excess impregnation is used in this work to impregnate the alumina provided by Axens. It has as objective to obtain a well dispersed platinum. Hexachloroplatinic acid ( $\text{H}_2\text{PtCl}_6 \cdot 9\text{H}_2\text{O}$ ) is the precursor in this impregnation.

A LOI (Appendix I) has to be performed before the impregnation.

First of all, a chlorination of the support is done in order to introduce the Cl as a competitor to obtain a better dispersion of the metal over the solid. With this purpose a solution of HCl with a 3%wt of Cl is necessary (4 ml of solution per gram of solid. The HCl solution is added to the support and stirred 1h with a shaker and after centrifuged once.

The precursor solution is done with 4 ml of solution per gram of solid. Then, it is added in the support already chlorinated and it is left during 24 hours under stirring at 300 rpm.

The day after, centrifugation and washing are done 3 times. Finally, the solid is dried overnight at 110°C and calcined (Appendix I, Figure 3).

### **2.1.3. Mechanical mixtures**

As it was told before mechanical mixture of 20% of zeolite and 80% of alumina in two different ways were performed: a mechanical mixture of alumina impregnated with platinum or a mechanical mixture of zeolite impregnated with platinum, and alumina. The zeolite and the alumina containing one of them the Pt are first milled and sieved in order to obtain a powder with a size below 63 $\mu\text{m}$  and mixed after in the desired proportion. The mechanical mixture was done at 300 rpm during 2min in a Fischer Scientific MM20 mixer. After, the mechanical mixture is pelletized in an hydraulic press Carver C (4 bar), crushed and sieved at the desired size (250-500 microns).

## 2.2. Characterization techniques

A series of techniques were carried out with the aim to characterize the different bifunctional catalysts employed in the catalytic test. A brief description of each technique employed is given below.

### 2.2.1. X-Ray diffraction (XRD)

XRD reveals detailed information about the crystallographic structure of different acidic solids. In the current project, it was used to investigate the crystallinity of the zeolites before and after impregnation<sup>136</sup>.

The X-Ray diffraction is based on the incidence of a monochromatic X-Ray beam on the solid sample to analyze. The X-Ray diffraction takes place when the distance between atom layers is approximately of the same magnitude as the wavelength of the radiation employed. Besides, there is a regular distribution of the scattering planes. These measurements provide useful information about the structure of the solid.

In 1912, W.L. Bragg studied the X-Ray diffraction of crystalline solids: focusing a monochromatic X-Ray beam at an incidence angle,  $\theta$ , on the sample. With the aim of the reflected radiation is in phase and therefore gives rise to the diffraction, it is necessary that the difference between two beams routes is a multiple of the wavelength.

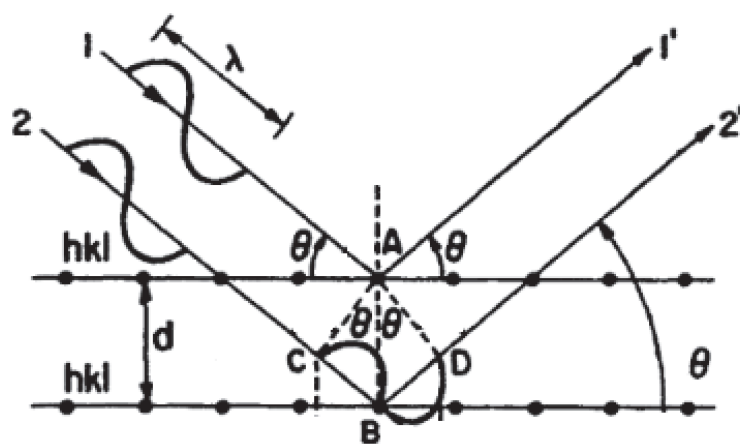


Figure 2.1. X-Ray diffraction of consecutive crystalline planes.<sup>137</sup>

In Figure 2.1. the route followed by the incident beam and the reflected one are depicted. Whether the distance  $CB + BD$  is equal to  $n\lambda$ , and, besides  $CB = CD = d \cdot \sin\theta$ , the condition for a constructive interference of the beam with the angle, can be written as shown in the Eq. 2.4.

$$2 d \sin \theta = n \lambda \quad \text{Eq. 2. 4.}$$

$d$  interplanar distance (nm);  $\theta$  incidence angle of the X-ray (°);  $n$  integer number which represents the diffraction order ;  $\lambda$  wavelength of the X-Ray source(nm)

The. Eq. 2.4. is at the basis of the interpretation of X-ray diffraction. It is the so-called Bragg 's Law.

Only if the incidence angle satisfies the condition:  $\sin \theta = n \lambda / 2 d$ , the interference will be constructive, in other angles the interferences are destructive. That is, only when the incident angle satisfies Bragg equation, the X-ray diffraction is produced.

The measurements of X-ray diffraction were registered using a X'Pert Pro diffractometer from Philips Analytical supplier, using a Cu Ka radiation ( $\lambda = 1.5406 \text{ \AA}$ ). Diffraction profiles were scanned using the step mode over a range  $2\theta$  of 5–40°, in steps of 0.02° during 6 hours with a step time of 5 seconds at each point. The identification of the zeolite crystalline phases is derived from the comparison to the JCPDS (Joint Committee on Powder Diffraction Standards) cards. The crystallinity is then calculated by dividing the intensity of the crystalline peaks by the sum of the crystallinity and amorphous peaks intensity.

### 2.2.2. N<sub>2</sub> Physisorption

The N<sub>2</sub> Physisorption allowed to determine the specific surface area, the microporous and mesoporous volume and the average particle diameter of all the zeolites.

During the adsorption process, different phenomena can occur such as adsorption of the gas in a monolayer and after, in a multilayer according to the N<sub>2</sub> pressure and another phenomenon occurring is the capillarity. This occurs in mesoporous materials, due to the fast filling of some specific pore sizes because of the formation of adsorbate-adsorbate interactions. The isotherms obtained (N<sub>2</sub> adsorbed volume vs. N<sub>2</sub> relative pressure) represents the N<sub>2</sub> adsorption-desorption on the sample surface. There are different types of isotherms depending on the material porosity (Appendix II)

The Brunauer-Emmett-Teller (BET)<sup>138</sup> method is the most common technique to determine the specific surface area of porous materials. The linear. Eq. 2.5 is shown below.

$$\frac{P}{V.(P^{\circ}-P)} = \frac{1}{V_m.C} + \frac{P.(C-1)}{V_m.C.P^{\circ}} \text{Eq. 2.5.}$$

$V$  volume adsorbed at a determined relative pressure  $P/P^{\circ}$  (volume units);  $V_m$  monolayer volume (volume units);  $C$  BET constant, it is exponentially related to the adsorption enthalpy of the first layer adsorption.

The specific surface area BET is calculated from the adsorbed volume on the monolayer according to Eq. 2.6.

$$S_{BET} = n_m \cdot N_A \cdot a_m \quad \text{Eq. 2.6.}$$

$N_A$  Avogadro number ( $\text{mol}^{-1}$ );  $a_m$  area required for every  $N_2$  adsorbed molecule ( $0,162\text{nm}^2$  at  $77\text{K}$ );  $n_m$  amount of  $N_2$  in the monolayer (mol)

The t-plot method is used to calculate the microporous volume and the external surface by comparing with a reference adsorption isotherm of a nonporous material in terms of adsorbed thickness<sup>139</sup> (Appendix II). This method is based on the use of standard adsorption isotherms i.e. the so-named t-curve which relates the statistical film thickness  $t(P)$  on a flat surface as a function of pressure,  $P$  for the same adsorbate and temperature. The reference system have to possess a surface without no micro- or mesoporosity so that curvature effects (such as capillary condensation) can be neglected<sup>140</sup>.

$N_2$  Physisorption analyses were performed with a with an automatic Micromeritics ASAP 2420. A pretreatment of the zeolite was carried out under vacuum with a temperature ramp of  $1^{\circ}\text{C}/\text{min}$  up to  $100^{\circ}\text{C}$ . for 30 minutes and then a ramp of  $5^{\circ}\text{C}/\text{min}$  up to  $500^{\circ}\text{C}$ . for 6 hours.

### 2.2.3. X-Ray Fluorescence

With this technique, the amount of Pt present in the zeolite and in the alumina after impregnation was measured, as well as the amount of Al and Si present in the zeolites.

The X-Ray Fluorescence consists in the exposure of the sample to an electron beam or X-Rays which causes the removal of a core electron and the formation of an ion. The ion can return to its ground state as one of the outer electrons falls into the vacancy, and, in the process, X-Rays of a certain wavelength that is characteristic for that atom are emitted. The intensity measured for a given energy is connected to the mass concentration of the concerned element.

The analysis were performed with a Thermo scientific ARL Perform'X apparatus.

#### 2.2.4. Atomic absorption spectroscopy (AAS)

Atomic absorption spectrometry is a method of elemental analysis which exploits the property of atoms of being excited by external energy in the form of electromagnetic radiation (photons) with well-defined frequencies.

The absorption of a photon of frequency  $\nu$  by a given atom is only possible if the energy difference between the initial level  $E_b$  and the level  $E_h$  after absorption corresponds to a transition between two energy levels of this atom as depicted in Figure 2.2. and expressed by the Eq. 2.7.

$$\nu = E_h \frac{E_b}{h} \quad \text{Eq. 2. 7.}$$

$h$  Planck's constant

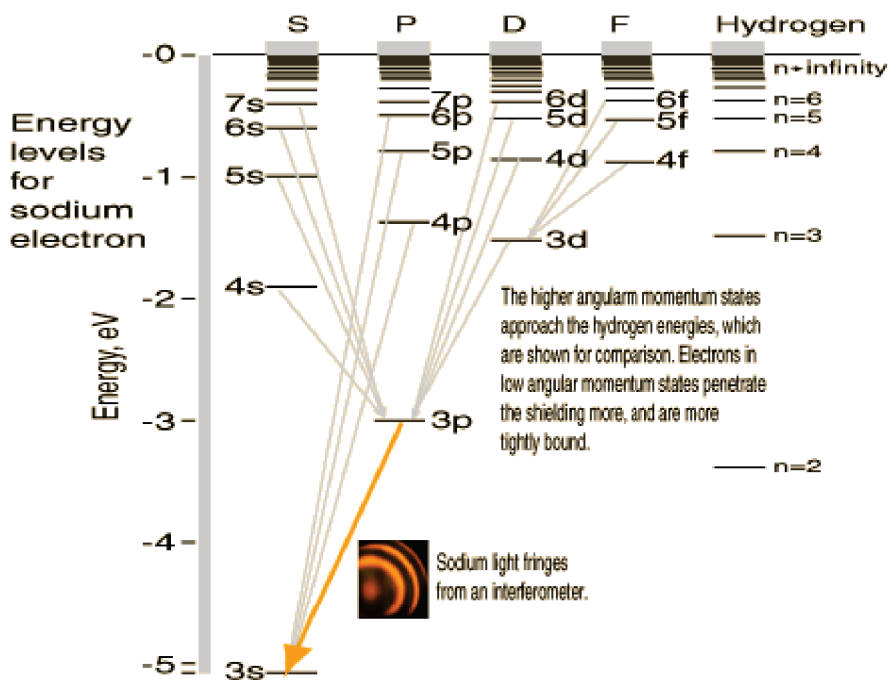


Figure 2.2. Spectrum of sodium electron orbital transitions associated with optical absorption.<sup>141</sup>

Here we will be dealing with transitions where the lower level is the ground state, since this is the most populated state. It is thus possible to make a quantitative determination of the presence of an element by measuring the quantity of light absorbed. To quantify individually

the amount of an element in the presence of others, a specific light source is used and the wavelength is selected<sup>139</sup>.

The device employed for the measurements was a Varian AA240FS. This technique was used to determine the amount of Na on the zeolites.

### 2.2.5. CO chemisorption monitored by FTIR

Infrared spectroscopy has been widely used to study adsorbed molecules on metal surfaces<sup>142</sup>. CO can adsorb on oxide surfaces, in cationic sites and in reduced metals forming carbonyls<sup>143</sup> and the C-O stretching frequency is sensitive to the oxidation and coordination states of metal ions. Most of the information obtained when using CO as an IR probe is derived from the C-O fundamental stretching frequency and from the stability of the surface carbonyls. This technique allows to related band intensities of the observed IR spectra to the surface concentration of the adsorbed CO.

In this study the measurements were performed with a Bruker Vertex 70. The CO chemisorption is carried out with pulses under vacuum from 5 mbar to 1000 mbar until saturation. The pressure in the chamber was then reduced and kept at 120 mbar. This method has been employed to calculate the Pt dispersion on zeolites considering that one CO molecule is adsorbed per platinum surface atom.

### 2.2.6. Nuclear Magnetic Resonance (NMR)

The <sup>27</sup>Al MAS (Magic Angle Spinning) NMR is widely used in the study of Aluminum-based zeolite systems. This technique gives information about the nature of the aluminum species: Al<sup>IV</sup> (usually framework aluminum, although extraframework Al<sup>IV</sup> may exist), Al<sup>V</sup> (distorted framework Al) and Al<sup>VI</sup> (extraframework aluminum).

NMR is based on the magnetic properties of atoms nuclei. When placed in a magnetic field, NMR active nuclei resonate at a specific frequency. This frequency depends on the local chemical environment of the studied nuclei. In solid-state NMR, the three main interactions, namely chemical shift anisotropy, dipolar and quadrupolar interactions can be averaged by physically spinning the sample at the “magic angle” of  $\theta_m=54.74^\circ$  with respect to the static magnetic field  $B_0$  yielding  $(3\cos^2\theta-1=0)$  as shown in the Figure 2.3. When the sample is spun at the magic angle, the anisotropic part produces NMR sidebands and with fast rotation, the

sidebands are shifted away, and the spectrum consists of narrow lines at the isotropic shifts. High resolution spectra are obtained in solid state<sup>144</sup>.

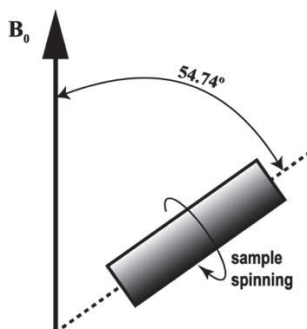


**Figure 2.3. Schematic representation of the MAS technique<sup>144</sup>.**

A Bruker Ultrashield 400WB plus was used for the analysis. The rotation frequency was 12 kHz, the rotor diameter 4 mm. The sequence used for Al was a zg sequence and the reference used to calibrate the 0 ppm was a molar solution of  $\text{Al}(\text{NO}_3)_3$ .

### 2.2.7. $\text{H}_2/\text{O}_2$ titration

This method allowed to calculate the dispersion of a metal over the alumina based on the selective adsorption of the gas.

Then, in order to calculate the Pt dispersion  $D$ , the following equation was employed.

$$D = \frac{v \cdot n \cdot m_{mPt}}{22400 \cdot x_{Pt}} \quad \text{Eq. 2. 8.}$$

$v$ : volume adsorbed per g of metal ( $\text{cm}^3/\text{g}$ );  $n$ : is the number of metal atoms on which a gas molecule is chemisorbed; ;  $m_{mPt}$ : Pt molar mass (195.08 g/mol); **22400** : molar volume of an ideal gas ( $\text{cm}^3$ );  $x_{Pt}$ : weight Pt content of the solid.

$\text{H}_2/\text{O}_2$  titration was firstly proposed by Benson and Boudart<sup>145</sup> as a method with increased sensibility compared to the  $\text{H}_2$  chemisorption<sup>146</sup>. In this project, double titration measurements were carried out. Before the first titration, a calcination was done following the curve illustrated in appendix II. Later, the sample was cooled down to room temperature and purged with He. The first reduction with  $\text{H}_2$  was then done at  $500^\circ\text{C}$  for 2h (reaction 1). After a decrease of the temperature to room temperature and a purge with He, pulses of oxygen were provided until saturation occurred and no further adsorption was obtained (reaction 2).  $\text{VO}_1$  corresponded to the  $\text{O}_2$  uptake in this first titration was measured. Again, a purge of He was

performed before the second H<sub>2</sub> reduction which was carried out for 1 hour, in this case at room temperature (reaction 3). After purging with He, a second O<sub>2</sub> chemisorption was carried out and its volume was recorded as VO<sub>2</sub> (reaction 2). The stoichiometry invoked in reactions (1) to (3) is commonly employed<sup>145,147,148</sup>



The device employed for the measurements was a Gira Xisorb. There have been problems of reproducibility on zeolites, and incompatibility results with the TEM dispersions. This led us to reserve the use of this technique to Pt/Alumina.

### 2.2.8. Electron microscopy

Electron microscopy can be used to monitor the shape and size of the particles, and also can give information about their composition. For instance, by the detection of the X-ray produced by the interactions between the electrons and the matter, or by the analysis of how the electrons are diffracted. Figure 2.4. shows the behavior of the sample when an incident beam impacts the matter.

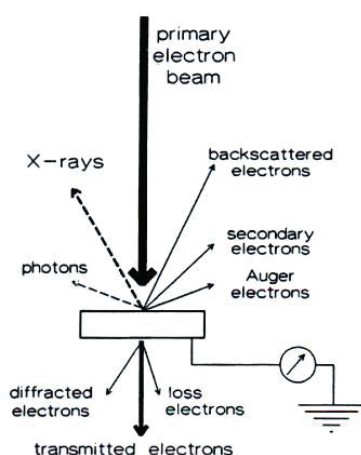


Figure 2.4. Interaction of a primary electron with the sample.

#### 2.2.8.1. Scanning electron microscopy (SEM)

The scanning electron microscopy is based on the bombardment of the surface by an electron beam. This beam of electrons, focused by electromagnetic lenses through a high



vacuum tower, is projected on the surface of the sample where the electrons bounce or cause the emission of secondary electrons. The secondary electrons have low energies (10-50 eV) and they are formed on the sample surface. The bounced electrons come from the deeper layers and give information about the composition of the sample.

SEM can be used to image over a very large magnification range from 1 pm to 100 pm, allowing study of particle morphology and size, surface texture and detail and surface defects such as faults and cavities<sup>149</sup>. In the present study, these measurements allowed to know the morphology of the zeolite and the crystallite size.

### 2.2.8.2. Scanning transmission electron microscopy (STEM)

This technique combines characteristics of the TEM (high resolution) and the SEM (surface scanning) to produce a superior instrument. Transmission electron microscopy (TEM) technique consists in a microscope that uses an electron beam to visualize an object. The images are formed by the recombination of the beams adsorbed by the sample<sup>139</sup>. Thus, TEM provides an image of the sample that depends on the electron interactions. The STEM can be used not only for imaging but also for analytical work since several scanning signals are collected simultaneously, the contrast is enhanced relative to the standard instruments. The high-resolution picture gives information on structure, absorbed species and depth.

Then, in order to calculate the dispersion, D the following equations (Eq. 2.9, Eq. 2.10 and Eq. 2.11) were employed.

$$d = \frac{F}{s_{Pt} \rho_{Pt}} \quad \text{Eq. 2. 9.} \quad s_{Pt} = \frac{n_{Pt}}{s_{dPt} x_{Pt}} \quad \text{Eq. 2. 10.} \quad D = \frac{n_{Pt} m_m}{x_{Pt}} \quad \text{Eq. 2. 11.}$$

**d** : particle diameter deduced from STEM (m); **F**: shape factor, 5 (when the metal particle is considered a cube with a one side non-exposed as it is deposited on the catalyst support) ; **s<sub>Pt</sub>**: specific metal surface area; **ρ<sub>Pt</sub>** : density of bulk platinum, 21090 kg/m<sup>3</sup>; **n<sub>Pt</sub>** : amount of accessible metal per catalyst mass (μmol/g); **s<sub>dPt</sub>** : metal surface density 20.75 μmol/m<sup>2</sup><sup>150</sup>; **x<sub>Pt</sub>**: weight Pt content of the solid; **m<sub>mPt</sub>**: Pt molar mass (195.08 g/mol)

In this work, a microscope JEOL 2100F TEM was used. The voltage employed was 15 kV. The samples were observed in TEM mode but also in STEM mode. STEM was employed to calculate the dispersion of the Pt on the zeolites.

### 2.2.9. Ammonia temperature-programmed desorption (NH<sub>3</sub>-TPD)

Quantification of the global acidity of the zeolite was assessed by ammonia temperature programmed desorption (NH<sub>3</sub>-TPD).

TPD of ammonia is an extensively used method for the acidity characterization of solid acids due to the simplicity of the technique. The number of ammonia molecules chemisorbed on the acid sites gives the number of acid sites<sup>151</sup>. Due to its small molecular size, ammonia is able to penetrate into all pores of the solid whereas is not the case of larger molecules. On the other hand, ammonia is a very basic molecule, able to titrate even weak acid sites which may not contribute to the activity of catalysts.

In this work, NH<sub>3</sub>-TPD was performed on an Autochem II 2920 apparatus, equipped with a TCD detector, coupled with a Pfeiffer mass spectrometer. The samples were first pre-treated at 500°C under Helium (50 mL min<sup>-1</sup>, 2 h), before adsorption of 10% NH<sub>3</sub>/He at 150°C during 30 minutes (50 mL min<sup>-1</sup>), followed by a purge under helium (150°C, 60 minutes, 50 mL min<sup>-1</sup>). The TPD was performed under a flow of helium (50 mL min<sup>-1</sup>) from 150°C to 600°C, with a 10°C min<sup>-1</sup> ramp.

## 2.3. Catalytic testing of ethylcyclohexane hydroconversion

The ethylcyclohexane (ECH) hydro-conversion test was developed in order to obtain data enough to establish a detailed apparent kinetic reaction scheme.

### 2.3.1. Unit description

The diagram flow of the unit used for this test is presented in Figure 2.5. It consists in a steel fixed bed reactor covered by a heating shell (furnace). To the entrance of the reactor arrive four different gas lines of H<sub>2</sub> and N<sub>2</sub> (two of high pressure (HP) and two of low pressure (LP)) and the ECH line. The ECH is stored in a reservoir and is boosted by a pump. There is a sieve as well to dry the charge before performing the test. At the reactor outlet there is a line going to the GC (gas chromatograph) to analyze the products and another one going to a condenser and a splitter in charge of release the products.

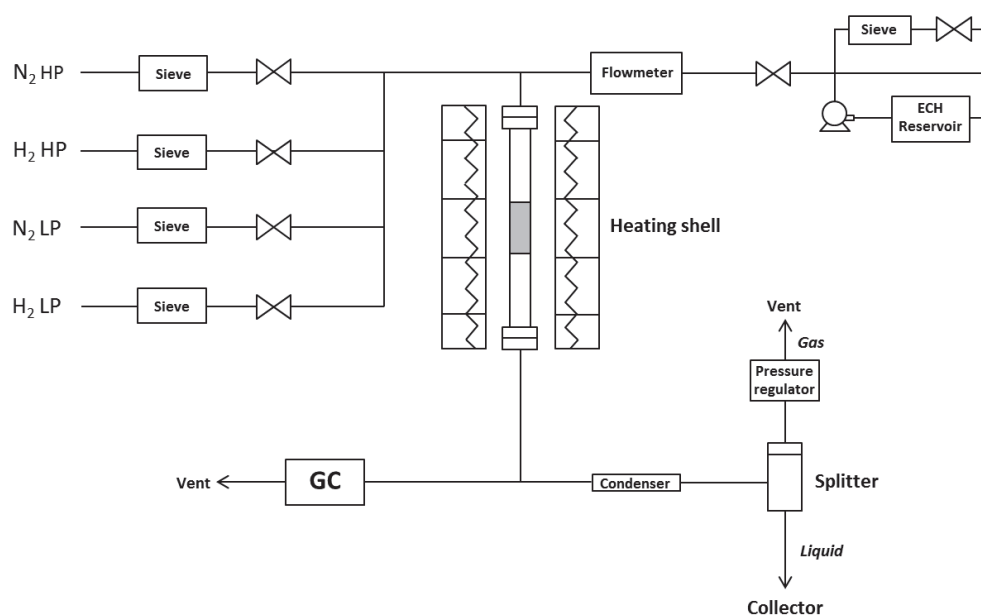


**Figure 2.5. Scheme of the ECH hydroconversion catalytic test unit.**

The hydroconversion of ethylcyclohexane was also performed in a high-throughput catalytic test with sixteen parallel, fixed-bed downflow reactor system. The objective using this tool was to evaluate the behavior of bifunctional catalysts involving Brønsted acidity. With this purpose, twelve different zeolites were tested.

### 2.3.2. Test conditions

#### 2.3.2.1. Feedstock composition

The feedstock composition consisted in ethylcyclohexane (ECH) at 99% of purity commercialized by Sigma-Aldrich,  $H_2$  from Air Liquid (99.99%) and  $N_2$  from Air Liquid (99.99%) used as inert gas.

#### 2.3.2.2. Operation conditions

The operational conditions of the catalytic test are enclosed in the Table 2.2.

**Table 2.2. Catalytic test operating conditions.**

Temperature	230-330	°C
Pressure	10	bar g
H <sub>2</sub> /ECH	40	mol/mol
WHSV*	0.125-4	g <sub>ECH</sub> g cat <sup>-1</sup> h <sup>-1</sup>
Catalyst mass	5	g

\* ECH Weight Hourly Space Velocity

They were established as standard conditions (after testing several other options) because they showed better catalytic performances. For instance, several H<sub>2</sub>/ECH ratio were tested with PROII at different pressures as depicted in Figure 2.6.

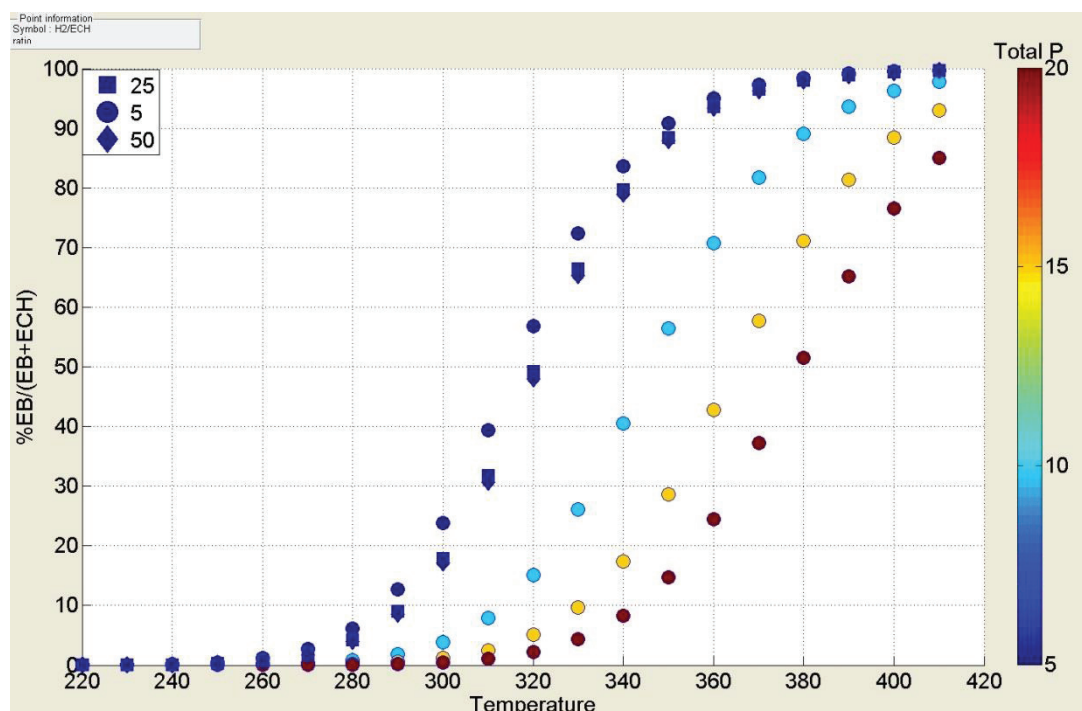


**Figure 2.6. Ethylbenzene (EB) conversion depending on the temperature, pressure and H<sub>2</sub>/ECH ratio measured with PROII.**

Figure 2.6 represents the Ethylbenzene (EB) conversion depending on the temperature, pressure and H<sub>2</sub>/ECH ratio. As expected, the aromatics concentration was increased at higher temperatures and pressures. Nevertheless, it appeared that the H<sub>2</sub>/ECH ratio had a very slight effect on the EB conversion, being scarcely smaller at H<sub>2</sub>/ECH higher ratios. From this

analysis, the choice of the temperature and the pressure were done in order to limit the aromatics in our products and favored the naphthenes isomerization.

In addition, some hydrodynamic tests were carried out in the catalytic unit. The purpose was to find the particle size avoiding mass and heat transfer problems in the reactor. In Figure 2.7. it can be observed how the particles with size in the range 250-500  $\mu\text{m}$  were the most efficient ones. The smallest ones (10-100  $\mu\text{m}$ ) were even worse than the biggest ones (750-1000  $\mu\text{m}$ ) because of overpressure.

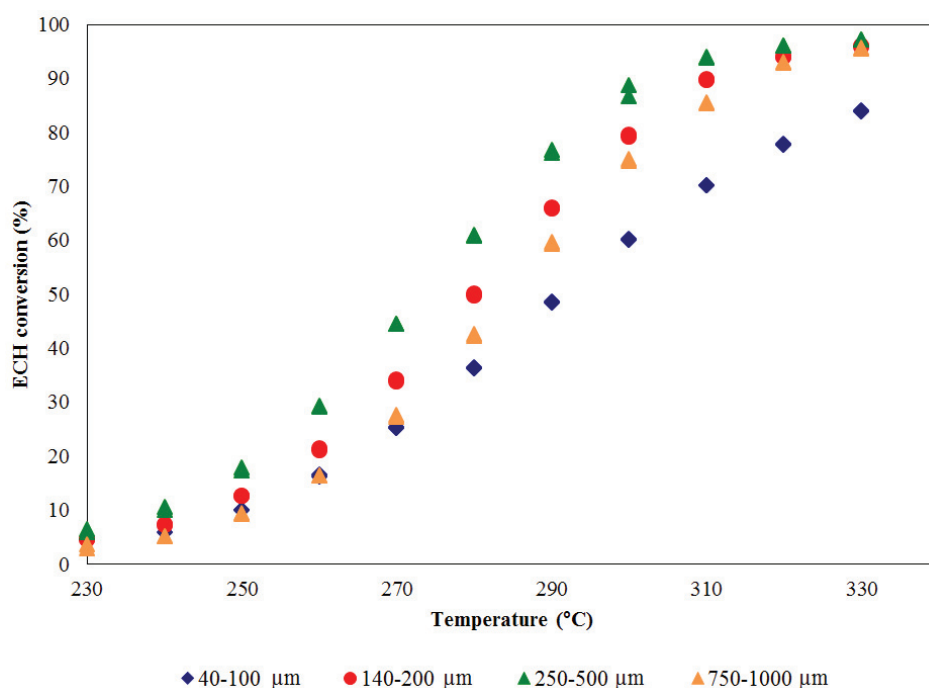


**Figure 2.7. Ethylcyclohexane (ECH) conversion depending on the temperature, pressure and  $\text{H}_2$ /ECH ratio in the catalytic unit for four different particle sizes.**

Another test was afterwards carried out with half the catalyst mass (2.5 g) and half  $\text{H}_2$  and ECH flows. The results almost overlapped to those obtained with 5 g. of catalyst. These results supported the idea that there were no diffusional problems in the catalytic unit.

In the case of the HTE unit, the feedstock composition consisted in the same ethylcyclohexane (ECH) feed as in section 2.3.2.1. The operational conditions of the catalytic test are enclosed in the Table 2.3.

**Table 2.3. Catalytic HTE test operating conditions.**

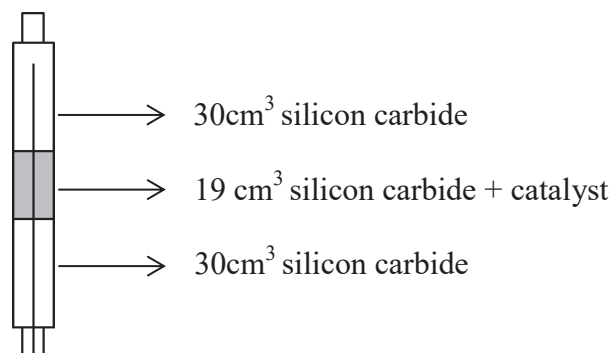
<b>Temperature</b>	200-330	°C
<b>Pressure</b>	10	bar g
<b>H<sub>2</sub>/ECH</b>	30	mol/mol
<b>WHSV</b>	2	h <sup>-1</sup>
<b>Catalyst mass</b>	150	mg

They have been established as standard conditions since they were the more similar conditions to the standard test ones achievable with this unit.

### 2.3.2.3. Reactor loading

Before filling the reactor, the catalyst had to be pelletized with the desired size between 250-500  $\mu\text{m}$  by grinding and sieving, and dried for 2 h at 100°C. The catalyst (5 g generally) was mixed with silicon carbide (9.5  $\text{cm}^3$ ) to get a volume of 19  $\text{cm}^3$  corresponding to a catalytic bed height of around 5 cm. The catalytic bed was diluted because it was considered to improve heat transfer<sup>152</sup>. Nevertheless, the catalytic bed should not be diluted more than five to ten times.<sup>152</sup> Besides, the height of the catalytic bed was calculated according to the hydrodynamic constraints. The first one considers that the reactor diameter should be ten times higher than the particle diameter whereas the second one considers that the catalytic bed height should be about fifty times higher than the particle diameter.

The bottom part of the reactor was filled with 30  $\text{cm}^3$  of silicon carbide, then the catalytic bed was added and finally another layer of 30  $\text{cm}^3$  of silicon carbide filled completely the reactor (Figure 2.8). Before the first layer of silicon carbide, a little bit of quartz-fiber had to be put in order to avoid the blockage of the reactor outlet. The temperature inside the reactor was measured by a thermocouple.

**Figure 2.8. Reactor loading protocol.**

In the HTE unit, before filling the reactor, the catalyst had to be shaped in 355-500  $\mu\text{m}$ . The catalyst (150 mg) was mixed with alumina (500 mg) to get a catalytic bed height of around 20 cm. The catalytic bed had a diameter of 2.6 mm. The bottom part of the reactor was filled with ceramic beads of Zirblast® until reaching a height around 5 cm, then the catalytic bed was added and finally a cord filled completely the reactor (Figure 2.9).

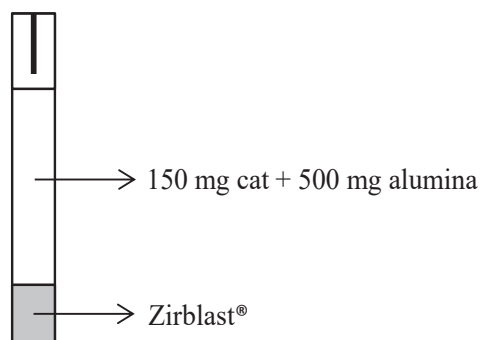


**Figure 2.9. Reactor loading protocol in the HTE unit.**

### 2.3.3. GC analysis

The reaction product analysis was done on-line using a GC chromatograph with a FID detector and a capillary column DB-1 (20x100x0.4) with 100% dimethyl polysiloxane as stationary phase. The vector gas is He. The duration of the GC analysis is 32 min and the ramp is defined in Table 2.4.

**Table 2.4. GC Ramp conditions.**

Rate( $^{\circ}\text{C}/\text{min}$ )	T ( $^{\circ}\text{C}$ )	Hold time (min)	Run time (min)
—	40	0	0
3	85	0	15
15	260	5	31.67

Figure 2.10. illustrates a typical chromatograph of the ECH hydroconversion. Lower retentions times correspond to the paraffins with lower molecular weight followed by the ring opening and isomerization ones. At higher retentions times, the heavier dehydrogenation products appear.





**Table 2.5. List of products of ECH hydroconversion.**

Reaction	Product Family	Products
Isomerization	TMCP	1,1,3-trimethylcyclopentane
		1-trans-2-cis-4-trimethylcyclopentane
		1-cis-2-cis-4-trimethylcyclopentane <sup>*a</sup>
		1,trans-2-cis-3-trimethylcyclopentane
		1,1,2-trimethylcyclopentane
	DMCH	1,trans-4-dimethylcyclohexane
		1,cis-3-dimethylcyclohexane*
		1,trans-3-dimethylcyclohexane
		1,trans-2-dimethylcyclohexane
		1,cis-4-dimethylcyclohexane
		1,1-dimethylcyclohexane
		1,cis-2-dimethylcyclohexane
	EMCP	1-methyl-trans-3-ethylcyclopentane
		1-methyl-cis-3-ethylcyclopentane
		1-methyl-trans-2-ethylcyclopentane
		1-methyl-cis-2-ethylcyclopentane
		1-ethyl-1-methylcyclopentane
	PCP	isocyclopentane
		n-propylcyclopentane*
	MCHP	methylcycloheptane
Ring opening	P8	2-methylheptane
		4-methylheptane
		2,3-dimethylhexane
		2,4-dimethylhexane
		2,5-dimethylhexane*
		n-Octane
		3,4-dimethylhexane
Cracking	C1	ethane
	C2	methane
	C3	propane
	C4	n-butane
		isobutane
	C5	n-pentane
		isopentane
		cyclopentane
	C6	methylcyclopentane
		2-methylpentane
		3-methylpentane
		cyclohexane
		n-hexane
	C7	1,1-dimethylcyclopentane
		1,cis-3-dimethylcyclopentane
		1,trans-3-dimethylcyclopentane
		2-methylhexane
		3-methylhexane
		3-methylpentane
		ethylcyclohexane
		n-heptane
Dehydrogenation	A8	ethylbenzene
		m-xylene
		p-xylene
		o-xylene

\* In coelution with low amounts of paraffin C<sub>8</sub>\*<sup>a</sup> In coelution with low amounts of 3-methylheptane\*<sup>b</sup> In coelution with the ECH. Product negligible

In the HTE unit the products were analyzed on-line by 2 flame ionization detector (FID) and one thermal conductivity detector (TCD) using a GC chromatograph equipped with two DB-1 capillary columns (20m x 0.1mm x 0.4μm). The ramp conditions were the ones of Table 2.2.

The identification of the integrated peaks was carried out by a special method developed for this project.

### 2.3.4. Expressions of catalytic performance

The ECH conversion and product selectivities were calculated from the integration of peak areas from the chromatograph. It was assumed that the total peak area corresponded to the total amount of products. All the peak areas were corrected with a calculated response factor, specific for each family product. Thus the conversion, selectivities and yields were calculated as shown in the Eq. 2.12. Eq. 2.13. and Eq. 2.14.

$$x_{ECH} (\%) = \frac{A_{ECH \text{ peak}}}{\sum A_{peaks_t}} \cdot 100 \quad \text{Eq. 2.12.}$$

$$s(\%) = \frac{\sum A_{peaks_{isomers}}}{\sum A_{peaks_t} - A_{ECH \text{ peak}}} \cdot 100 \quad \text{Eq. 2.13.}$$

$$Y(\%) = x_{ECH} \cdot s \cdot 100 \quad \text{Eq. 2.14.}$$

$x_{ECH}$  ethylcyclohexane conversion;  $A_{ECH \text{ peak}}$  ECH corrected peak area (s.a.u);  $\sum A_{peaks_t}$  total corrected peak area (s.a.u);  $\sum A_{peaks_{isomers}}$  corrected isomers peak area(s.a.u);  $s$  selectivity;  $Y$  Yield.

Regarding the TOF, it was calculated as defined in Eq. 2.15.

$$TOF(s^{-1}) = \frac{F_0(ECH)}{w_{cat} \cdot n_A} \ln \left( \frac{1}{1 - x_{ECH}} \right) \quad \text{Eq. 2.15.}$$

$F_0(ECH)$  molar flow of ECH at the entrance of the reactor ( $\mu\text{mol s}^{-1}$ ),  $w_{cat}$  amount of catalyst (g),  $n_A$  amount of Brønsted acid sites per gram of catalyst ( $\mu\text{mol g}^{-1}$ ).

### 2.3.5. Typical catalytic test procedure

When the reactor was filled and the possible leaks tested on the catalytic unit, a flow of  $N_2$  was passed through the catalyst to dry it at  $150^\circ\text{C}$ . Then the reduction of the catalyst was carried out under  $H_2$  (4 NL/h/g), with a plateau of 2 h at  $480^\circ\text{C}$  with a ramp of  $5^\circ\text{C}/\text{min}$ . Once the reduction was performed, the temperature was decreased keeping the  $H_2$  flow and the unit was stabilized for 2 hours at the initial temperature for starting the catalytic test ( $230^\circ\text{C}$ ), before ECH was injected.

The conversion and selectivities were measured at each temperature varying from 230 to  $330^\circ\text{C}$  first with a temperature step of  $20^\circ\text{C}$  until reached a conversion higher than 5% and later with a temperature step of  $10^\circ\text{C}$ . With this purpose two GC injections were done at each temperature. The first injection was done after a stabilization period of 1h and the second one 45 minutes after in order to test the stability of the catalyst. In several tests some return points were realized to verify that the catalyst was not deactivated.

In the HTE unit, the catalytic test was fully automated, with the operating conditions of the catalytic bed of each reaction being monitored individually. The catalysts powder was pretreated using a  $H_2$  flow rate of 4 NL/h/g and heated at  $5^\circ\text{C min}^{-1}$  to a final reduction temperature of  $450^\circ\text{C}$ . over 1h.

The conversion and selectivities were measured at each temperature varying from 200 to  $330^\circ\text{C}$  first with a temperature step of  $10^\circ\text{C}$ . With this purpose two GC injections are done at each temperature.

## 2.4. Ab initio calculations

We performed *ab initio* calculations, using a static approach. The static approach is based on the analysis of potential energy surfaces at  $T = 0\text{ K}$ . In this approach, the reactant, product and intermediate states are identified as local minimums whereas the transition states are saddle points on the potential energy surface. The energy difference between saddle point and minimum connected by a path described by an intrinsic reaction coordinate, provided the reaction barrier. Afterwards, thermodynamic calculations were performed in order to obtain free energies and entropies at finite temperature. It was taking into account the hypothesis that nuclear degrees of freedom of different types are fully decoupled and gathered in vibrational, rotational, or translational categories. Then, rate constants were calculated within the transition state theory. This static approach is popular because it is less expensive than ab

initio molecular dynamic techniques, and it can provide useful information about potential energy surfaces and reaction paths.

#### 2.4.1. Resolution of Schrödinger equation

The computational study performed consisted in *ab initio* calculations, in the framework of the Density Functional Theory (DFT). These calculations are based on an approximate resolution of the Schrödinger equation (Eq. 2.16). Indeed, this equation exhibits some analytical solutions for monoelectronic systems only.

$$H\psi = E\psi \quad \text{Eq. 2.16.}$$

**H** Hamiltonian; **Ψ** wave function; **E** total energy

$\Psi$  is a function related to the electron and nucleus coordinates and  $H$  consists of kinetic energy terms and potential energy of nucleus and electrons for molecular systems. DFT methods are useful for quantum calculation on large chemical systems. These methods use an approximation of the Hamiltonian instead of working with the hypotheses of specific expressions of the wave function like the Hartree-Fock method. In DFT, the terms within the Hamiltonian leading to difficulties in the resolution of the Schrödinger equations, are gathered in what is called the exchange-correlation functional. The quality of the calculation, but also the computational cost, are linked to the choice of the exchange-correlation functional. One popular family of exchange-correlation functionals is the GGA one (Generalized Gradient Approximation), expressed as a function of the local electronic density and its gradient. More accurate choices can be made (hybrid functionals for instance), but in practice a compromise between accuracy and computational cost has to be made. In the present work we performed calculations with the Perdew, Burke and Ernzerhof<sup>153</sup> (PBE, GGA family) exchange-correlation functional and a D2<sup>154</sup> correction for the dispersion interactions.

#### 2.4.2. Periodic calculations and plane wave database

The Kohn-Sham equations<sup>155</sup> can be solved by extending the orbitals in one of two main types of basis set: atom-centered Gaussian-type orbitals (GTO) or plane waves (PW). In the case of crystals which are three-dimensional periodic array of atoms it is necessary to find a basis set that accounts for the periodicity. Therefore, the plane wave approach is more suitable.

Plane wave basis sets are used along with pseudopotentials<sup>156</sup>, for example with the projector augmented wave<sup>157</sup> (PAW) method, to account for core electrons while making the calculation quicker (frozen core approximation). They have many advantages: the basic functions are orthonormal by definition, showing no prejudice by the atomic positions, thus describing any point in the crystalline cell with the same quality, having therefore the ability to accurately treat different kinds of structure. The convergence of the calculation with respect to the size of the truncated PW basis set can be checked by increasing the electronic kinetic energy cutoff. i.e. the higher the cut off energy, the more plane waves included and therefore the faster the convergence. Nevertheless this is computationally more expensive.

Periodic calculations were performed in this project, i.e. a primitive cell was propagated in the three space dimensions as well as its properties; with the VASP (Vienna Ab initio Simulation Package) code.<sup>158</sup> Brillouin zone sampling was restricted to the  $\Gamma$  point. The cut-off energy was of 400eV, except for the optimization of the all structure of the zeolite (framework extracted from IZA database<sup>159</sup>) that was performed at 800 eV. This cut-off value determined the energy and the number of plane waves included in the expansion of the basis set. The SCF cycles are the steps of the electronic optimization (for a given geometry). The convergence criterion for the SCF cycles was set to  $10^{-7}$  eV for zeolitic cells and  $10^{-9}$  eV for the gas phase molecules.

### 2.4.3. Geometry optimizations

Once the electronic energy of the fundamental state is calculated, geometry relaxation can be performed, leading to minimize the forces on each atom .i.e.  $\sum F=0$ . As described in Eq. 2.17 the force due to the movement of an atom in the direction  $r$  is the derivative of the energy compared to this movement.

$$F = -\frac{\delta E}{\partial r} \quad \text{Eq. 2.17}$$

The geometry optimizations of the local minimums were performed with a conjugate-gradient algorithm as implemented in VASP. The convergence was achieved when the forces on all atoms were lower than a predefined criterion, 0.005 eV/Å in this thesis.

### 2.4.4. Nudged Elastic Band

The Nudged Elastic Band (NEB) method is used to find the transition states when both the initial and final states (which are local energy minima) are known. Using this method, the

minimum energy path (MEP) for any given chemical process may be calculated. The code Opt'n Path<sup>160</sup> works by linearly interpolating a set of images between the known initial and final states (as a "guess" at the MEP), using either Cartesian coordinates or internal coordinates (or a mixing of both), and then the NEB minimizes the energy of this string of images. Each "image" corresponds to a specific geometry of the atoms on their way from the initial to the final state, a snapshot along the reaction path. Thus, once the energy of this string of images has been minimized, the true MEP is revealed. A scheme of a potential energy surface of an arbitrary reaction and its NEB and MEP are shown in Figure 2.11.

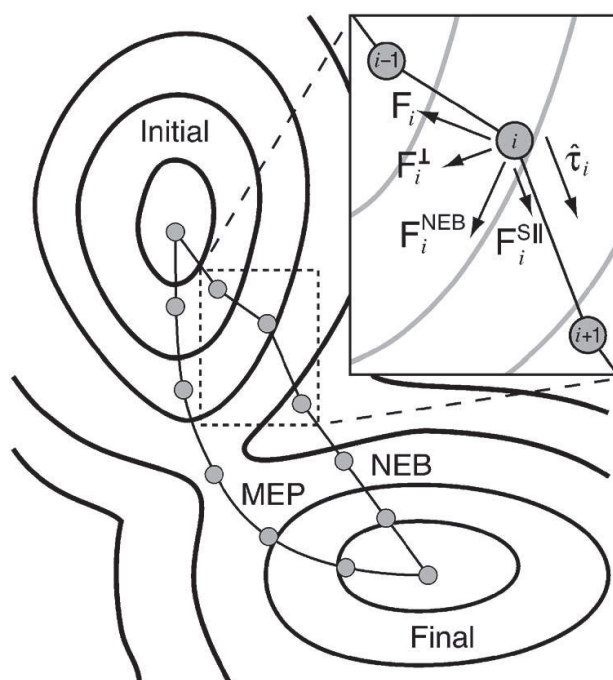


Figure 2.11. NEB and MEP for an arbitrary reaction.<sup>161</sup>

NEB calculations were performed with VASP. The number of NEB images to investigate reaction pathways was 10 (including the reactant and the product, both local energy minima). 50 NEB steps were performed before optimizing the structure of highest energy. In some complex cases we performed a special climbing image<sup>162</sup> to approach the TS in a closer manner. When all forces in the intermediate states fell below 0.02 eV/Å, the system with highest energy in the reaction pathway (MEP) was optimized separately with a quasi-Newton algorithm (convergence criterion: 0.005 eV/Å). In some occasions, the Quasi-Newton failed and another algorithm, Dimer<sup>163,164</sup> appeared to be more adequate for our systems.

#### 2.4.5. Vibrational frequency calculations

After convergence, in order to verify if the optimized configuration was a true transition state, a vibrational analysis of the transition state was performed. It was required that all the frequencies were positive except one imaginary frequency corresponding to the unstable mode. Residual imaginary frequencies that could occur in the vibrational spectrum of the relaxed configuration were removed using a line minimization procedure (section 2.5.7).

A system composed of  $N$  atoms was defined by the position of each of its atoms, described by 3 spatial coordinates. An atom was moved away from its optimized position by a small displacement in one of the three directions of space. The total energy and the forces exerted on each atom were then calculated. In principle, in the optimized structure, the force exerted on each atom was zero. Vibrational frequency values were calculated from a second derivative of the nuclei energy of the optimized structure at 0 K.

In the present study, harmonic frequency calculations were performed with an energy cutoff of 400 eV on optimized structures (all atoms of the cell moving) under the same conditions with a displacement of  $\pm 0.02$  Å around the equilibrium atomic positions.

#### 2.4.6. Intrinsic reaction coordinate (IRC)

When a chemical reaction is studied theoretically, to determine the stationary points, i.e. reactants, transition state and products on the potential energy surface, becomes essential. Once a transition state has been determined, it is necessary to verify if it is related to the expected reactant and product. The intrinsic reaction coordinate (IRC) approach defines the reaction path on the potential energy surface connecting reactants, transition states and products. This concept introduced by Fukui<sup>165</sup> is the sheerest descent path. It starts from the transition state and follow the direction of the transition vector corresponding to the imaginary vibrational frequency which has to be calculated before, in this case, *via* vibrational analysis.

In this work, the damped velocity Verlet algorithm for the IRC determination<sup>166</sup> was used, as implemented in VASP by Tomas Bucko (Univ. Bratislava). This method is specially favorable for large systems<sup>166</sup>.

#### 2.4.7. Line minimization procedure

This procedure lets to explore energy throughout a particular direction in the  $3N$  dimensional configuration space. This technique is used to eliminate the residual imaginary

frequencies, usually remaining after geometry optimizations. These imaginary frequencies are generally due to an incomplete energy minimization along one or more directions. This problem is commonly related to a relative flatness of potential energy landscape in some parts of the configuration space. Therefore, even very tight convergence criteria in atomic relaxations might not head to the removal of all undesired imaginary frequencies.

There are 3 global translations and no global rotations for a periodic solid with  $N$  atoms. The total momentum in simulations is considered to be zero, and there are  $3N - 3$  vibrational degrees of freedom.<sup>167</sup> Significantly, the potential energy of the system is translationally and rotationally changeless. With the aim to identify and efficiently take out the residual imaginary vibrations, the translational degrees of freedom have to be dissociated from vibrations. Nonetheless, this is not done by the VASP code since the  $3N$  modes are considered to be vibrational modes, so a program specific for this purpose was employed (developed by Tomas Bucko in Bratislava). This program reads the forces in the output file of the VASP calculation and computes and diagonalizes the Hesse and dynamical matrices in translationally and rotationally changeless internal coordinates. Hence, translations are effectively dissociated from vibrations. Then, the energy landscape is sampled along the direction of the eigenvector with the largest undesired eigenvalue by a sequence of single point energy calculations. For example, in Figure 2.13 it is shown a successive sampling during the optimization of a transition state (TS5 T1O1 chapter 5). The energy minimum structure was re-optimized and the vibrational frequencies re-computed at each step. The procedure was repeated until a configuration with only one imaginary frequency corresponding to the unstable mode was identified (typically 1 to 6 repeated cycles were required).

This line minimization method was successfully applied to some TS and some products and reactants investigated in this thesis.



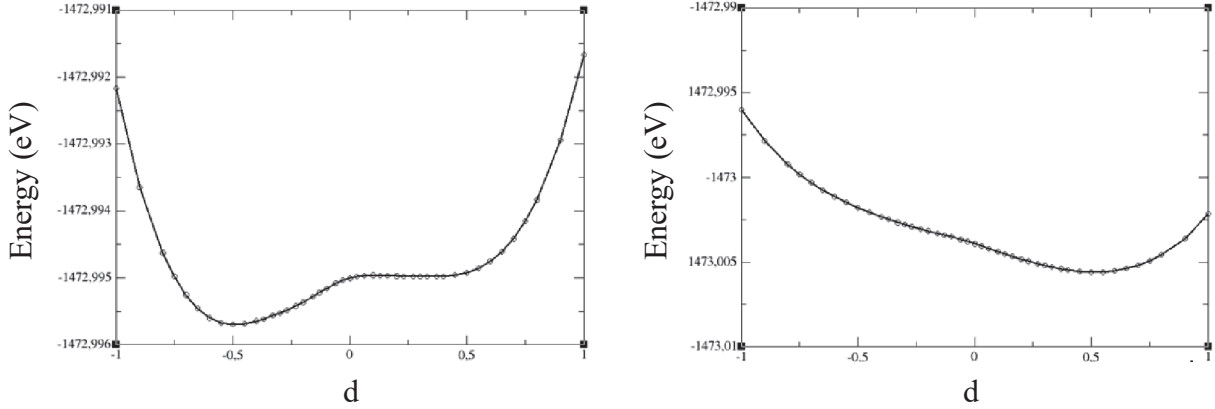


**Figure 2.13.** Successive sampling of the potential energy along Hesse matrix eigenvector with negative eigenvalue.  $d$  is a scaling dimensionless parameter for displacement. Two successive line minimizations for the same transition state are shown. Upon each line minimization, the structures with the lowest energy (for  $d = -0.55$  (left) and  $d = 0.50$  (right)) have been re-optimized and the Hesse matrix has been re-calculated.

#### 2.4.8. Thermodynamic calculations

The thermodynamic calculations were carried out taking into account the hypothesis that nuclear degrees of freedom of different types are fully dissociated and fall into vibrations, rotations, or translations categories as it has been explained in the section below (2.5.7).

Gibbs free energy was calculated with the following equation,

$$G(T, p) = E + U_{trans}(T, p) + U_{vib}(T, p) + U_{rot}(T, p) + PV_m - T(S_{trans}(T, p) + S_{vib}(T, p) + S_{rot}(T, p)) \quad \text{Eq. 2.18}$$

**E:** electronic energy, **S:** entropies, **U:** internal energies, **P:** pressure and **V<sub>m</sub>:** molar volume.

The first term  $E$  is the result of the DFT calculation described above in section 2.5.3. The other energy terms can be calculated using results from statistical thermodynamics according to the harmonic approximation.

The first term of  $H_{vib}$  corresponds to the vibrational energy and is obtained from the knowledge of all the whole set of vibration waves numbers,  $\mathbf{v}_n$  of a system with the following equation:

$$H_{vib}(T) = N_A \left[ \sum_n \frac{1}{2} h \nu_n + \sum_n \frac{h \nu_n \exp\left(-\frac{h \nu_n}{k_B T}\right)}{1 - \exp\left(-\frac{h \nu_n}{k_B T}\right)} \right] \quad \text{Eq. 2.19}$$

**h:** Planck constant, **k<sub>B</sub>:** Boltzmann constant, **T** absolute temperature, **N<sub>A</sub>:** Avogadro constant

The first term of  $H_{\text{vib}}$ , corresponds to the vibrational energy at 0K of the system and is called "Zero Point Energy" (ZPE).

For gas phase ethylcyclohexene, Eq. 2.20 is used. In the case of condensed systems, these terms are considered to be zero, as well as rotational and translational entropies given by equations 2.22 and 2.23.

$$U_{\text{trans}}(T) + U_{\text{rot}}(T) + PV_{\text{m}}(T) = 4RT \quad \text{Eq. 2.20}$$

$$S_{\text{vib}}(T) = N_A k_B \left[ \sum_n \frac{\frac{h\nu_n}{k_B T} \times \exp\left(-\frac{h\nu_n}{k_B T}\right)}{1 - \exp\left(-\frac{h\nu_n}{k_B T}\right)} - \sum_n \ln \left( 1 - \exp\left(-\frac{h\nu_n}{k_B T}\right) \right) \right] \quad \text{Eq. 2.21}$$

$$S_{\text{rot}}(T) = N_A k_B \left( \frac{3}{2} + \ln \left[ \frac{\sqrt{\pi}}{\sigma} \left( \frac{8\pi^2 k_B T}{h^2} \right)^{\frac{3}{2}} \sqrt{A_e \times B_e \times C_e} \right] \right) \quad \text{Eq. 2.22}$$

$$S_{\text{trans}}(T, p) = N_A k_B \left( \frac{5}{2} + \ln \left( \frac{RT}{p} \left( \frac{2\pi M}{h^2} k_B T \right)^{3/2} \right) \right) \quad \text{Eq. 2.23}$$

**M**: molar weight, **σ**: corresponds to the symmetry number of the system and **A<sub>e</sub>**, **B<sub>e</sub>** and **C<sub>e</sub>** : moments of inertia according to the eigenaxes of the molecule.

#### 2.4.9. Rate constant calculations

The determination of the rate constant of an elementary step is not limited to calculate only the activation energy at 0 K. If this calculations are considered within the framework of Eyring's theory<sup>168</sup> or "transition state theory" the following features have to be taken into account: Eyring rate equation takes account of equilibria between activated complexes (saddle points) and its reactant and product.

This "transition state theory" corresponds to a theoretical model based on statistical thermodynamics. The Eyring-equation defined the rate constant as follows:

$$k = \frac{k_B T}{h} e^{-\frac{\Delta G^\ddagger}{k_B T}} \quad \text{Eq. 2.26}$$

$\Delta G^\ddagger$ : activation free enthalpy

## 2.5. Kinetic modelling

Once the kinetic constants for all elementary steps have been calculated by ab initio methods, the complete sequence of all elementary steps has to be solved to calculate the exit flows of the reactants and products for a fixed bed reactor. The calculated exit flows can then be compared to the experimental data. This approach is referred to as microkinetic modeling.<sup>169,170</sup> Here it is based on a mean field approach and calculating the reaction rates by applying the law of mass action. The reactor model was based on a one-dimensional fixed-bed plug-flow reactor without heat and mass transfer limitations.

The material balance of each species is established on an elementary section of the tubular reactor containing a  $\delta w$  mass of catalyst. This section is small enough that the composition is considered uniform. The molar balance for each species is written according to equation 2.27.

$$r_j = \frac{1}{\gamma_j} \frac{\partial F_j}{\partial w} \quad \text{Eq. 2.27}$$

$r_j$ : rate of formation or disappearance of the species  $j$ ,  $\gamma_j$ : the stoichiometric coefficient of the species  $j$ ,  $F$ : the molar flow rate.

A catalytic cycle, as defined by M. Boudart and G. Djega-Mariadassou,<sup>39</sup> is a reaction sequence consisting of elementary steps. The first step converts an active site into a superficial intermediate species and the last elementary step restores this catalytic site. These elementary steps multiplied by an appropriate factor called stoichiometric number and added member-to-limb lead to the stoichiometric equation.

For each elementary stage  $i$ , the net velocity of the species  $j$  is denoted  $r_{ij}$ . The same species  $j$  can participate in several stages  $i$ . Its velocity is then, the sum of the velocities of the reactions in which it appears. For  $q$  reactions, the net velocity of species  $j$  is expressed by equation 2.28.

$$r_j = \sum_{i=1}^q r_{ij} \quad \text{Eq. 2.28}$$

From the expression of the velocities of the elementary steps, it is a matter of expressing the speed of the overall reaction solely as a function of the accessible experimentally concentrations. For that, two hypotheses can be adopted.

The first hypothesis is to assume the existence of a quasi-stationary state where the intermediate species is very reactive and therefore has a limited lifetime. Also, its concentration can be considered as being low. The quasi-stationary state assumption is that the rate of formation of the intermediate species is zero. The overall velocity is then obtained by removing all the concentration terms of the adsorbed species.

- In the case of a mechanism consisting of two elementary steps, the manual resolution of the equation system is easy.
- In the case of a mechanism consisting of many elementary steps (as it is the case of a microkinetic study for example), the application of the quasi-stationary state hypothesis to each adsorbed species gives a system of non linear equations difficult to solve manually. Nevertheless, the resolution is possible by numerical methods.

The system of non-linear equations for the surface intermediates is coupled to the differential equations for the gas phase species (i.e. equation 2.27). This set of mixed equations is solved numerically by a home-made FORTRAN code. Note that this approach does not involve any assumption on the rate determining step, which can actually be determined a posteriori. The outcome of the microkinetic modeling not only leads to the values of the exit flows for all reactants and products but also to the concentration of all surface intermediates and the rate of the forward and reverse steps. This allows a detailed analysis of the reaction network.

Not all rate constants in the reaction mechanism could be determined by ab initio calculations. Thus a small number of rate constants were estimated by regression analysis of the experimental data. A least-squares multi-response non-linear regression routine was implemented based on the Marquard-Levenberg method.<sup>171,172</sup> After the regression analysis a statistical analysis of the overall fit (F-test) and of the parameter estimates (student t-test, binary correlation coefficients) was performed.<sup>173</sup>

For the modeling the experimental data on 13 products were used (13-EMCP, 12-EMCP, 11-EMCP, 14-DMCH, 13-DMCH, 12-DMCH, 11-DMCH, 113-TMCP, 112-TMCP, 124-TMCP, 123-TMCP, PCP and CRACK. The latter one is the lumped sum of ring-opening and cracking products) as a function of  $W/F_{ECH}$  at three temperatures (18 data sets in total). The objective function for the multi-response regression analysis consisted of the yield of the 13 products, excluding the ECH conversion (giving 13\*18 datapoints). No weighting factors were applied. The data at the three temperatures were regressed simultaneously.

## CHAPTER II. EXPERIMENTAL AND MODELLING PART

Although for the most products separate concentrations for the trans and cis isomers could be determined by the GC analysis, the cis and trans isomers were assumed to be in quasi-equilibrium and therefore lumped together. The GC analysis did not allow to separate trans-14-DMCH and trans-13-DMCH. By using PROII the equilibrium composition of cis and trans 13-DMCH was calculated as a function of temperature. In the model the equilibrium fraction corresponding to trans-13-DMCH as estimated by PROII was added to the 14-DMCH yield and subtracted from the trans 13-DMCH yield.

### 3. METAL/ACID BIFUNCTIONAL CATALYSIS AND INTIMACY CRITERION

---

Before undertaking any detailed kinetic investigation of ethylcyclohexane hydroconversion on a bifunctional Pt / EU-1 catalyst, one has to check that the measured kinetics will be driven by the acid phase and not by the HD/DHD phase. This chapter presents the results of the study to analyze the influence of the metal acid balance and distance between the two types of sites in two different groups of metal acid bifunctional catalysts. Both groups of catalysts contained Pt as metal function and the zeolite EU-1 as acid function. The catalysts consisting in mechanical mixtures of zeolite plus alumina had different metal/acid distances because the Pt was deposited either over the alumina or over the zeolite (micro- and nano- scale distance respectively). Besides, in each group the metal-acid balance was varied by changing the amount of impregnated Pt. Furthermore, a dual-function kinetic model<sup>174</sup> was employed to quantify the effect on the metal to acid sites ratio on the catalytic performance. The overall objective is to identify a well-balanced catalyst with not diffusion limitations between the two kinds of sites, so as to access preliminary mechanistic information about desired isomerization reactions and undesired ring opening reactions. The supporting information of this chapter is enclosed in appendix III.

This study is the subject of a publication published in ACS Catalysis 2018, 8, 6035-6046 (DOI: 10.1021/acscatal.8b00633), which constitutes the essence of this chapter.

### CHAPTER III. METAL/ACID BIFUNCTIONAL CATALYSIS AND INTIMACY CRITERION

## Metal/acid bifunctional catalysis and intimacy criterion for ethylcyclohexane hydroconversion: when proximity does not matter

*Ester Gutierrez-Acebo,<sup>1</sup> Charles Leroux,<sup>1</sup> Céline Chizallet,<sup>1</sup> Yves Schuurman,<sup>2</sup> Christophe Bouchy<sup>1\*</sup>*

<sup>1</sup>IFP Energies nouvelles, Rond-point de l'échangeur de Solaize, BP 3, Solaize, 69360, France

<sup>2</sup>IRCELYON, Institut de recherches sur la catalyse et l'environnement de Lyon, CNRS, UMR 5256, Université Lyon 1, 2 avenue Albert Einstein, F-69626 Villeurbanne, France

### ABSTRACT

The apparent kinetics in metal/acid bifunctional catalysis is generally strongly affected by the metal to acid site ratio and their proximity. However, these two key parameters have not been systematically investigated in the scientific literature. Such a study is provided here for bifunctional catalysts using platinum as the metallic function and EU-1 zeolite as the acidic function. Two series of bifunctional catalysts with different metal to acid site ratios and different metal to acid site distances were prepared and tested in ethylcyclohexane hydroconversion. On increase in the metal to acid site ratio, the catalytic activity and isomerization selectivity increased until a plateau was reached, an observation which is in agreement with the classical bifunctional mechanism. At the same time, the intimacy criterion of Weisz was evaluated: strikingly, for a given metal to acid site ratio, activities and selectivities are not affected by their distance (up to a micrometer scale). A dual-function kinetic model was successfully applied in order to quantify the effect of the metal to acid site ratio on the catalyst activity and isomerization properties. The application of this model showed that the metal to acid site ratio needed to reach the catalytic activity plateau is higher than the ratio needed to reach the selectivity plateau. This was interpreted as a consequence of the lower kinetic constant rate for the naphthene ring-opening reaction in comparison to the naphthene isomerization reaction.



### 3.1. Introduction

Bifunctional catalysts containing both, a hydro/dehydrogenation and acid functions are used in several industrial refining processes,<sup>22,175</sup> such as the hydroisomerization of C<sub>5</sub>-C<sub>6</sub> *n*-paraffins (to produce high-octane gasoline),<sup>176,177</sup> and the production of diesel by hydrocracking of heavy oil.<sup>178,179</sup> In the petrochemical field, ethylbenzene hydroisomerization is important for the paraxylene production. Paraxylene is a highly sought-after product used in the manufacture of the terephthalic acid, which is used for polyester production.

Bifunctional catalysts also play a key role in the production of alternative liquid fuels: produced either by hydroisomerization of hydrotreated vegetable oils<sup>180,181</sup> or by hydroisomerization and hydrocracking of Fischer Tropsch waxes.<sup>65,182,183</sup> They are also promising catalyst candidates for biomass conversion.<sup>184–186</sup> Their complex behavior, due to the multi-step nature of the reactions, has been the object of deep investigations for decades.<sup>8,49,61,74</sup> In spite of all these works, several key questions are still highly debated.<sup>49,74</sup>

A bifunctional catalyst is typically composed of a metallic compound dispersed over an acidic support. The metallic compound provides the hydro-dehydrogenation function and the support provides the isomerization and cracking functions. The hydro-dehydrogenation (HD/DHD) component can either be a noble metal (Pt, Pd) or a combination of non-noble metal-sulphides from Group VI A (Mo, W) and at least one from Group VIII A (Co, Ni). The acidic component can be an amorphous oxide like silica-alumina, a zeolite or a mesoporous material. The proper choice of the HD/DHD and the acidic component is dictated by the targeted application. For example, zeolites of the FAU type<sup>187</sup> (USY zeolites) are used in hydrocracking whereas zeolites of the mordenite (MOR zeolites) and EUO types (EU-1 zeolites) can be used for ethylbenzene hydroisomerization.<sup>5</sup>

In the present work, we focus on EU-1 zeolite. The choice of EU-1 is firstly motivated by the fact that this zeolite is industrially used for the xylene and ethylbenzene isomerization processes to form para-xylene. Besides, interesting results have been obtained with EU-1 compared to mordenite-based catalysts.<sup>15</sup> During the process, some naphthenes are formed by hydrogenation of the aromatics compounds on the HD/DHD function. For instance, ethylcyclohexane can be formed by ethylbenzene hydrogenation.

The classical bifunctional mechanism for the case of ethylcyclohexane hydroconversion is depicted in Figure 1. A first dehydrogenation reaction is required in order to provide olefinic reactants for the acidic catalyzed reaction to happen. Once the ethylcyclohexane is

### CHAPTER III. METAL/ACID BIFUNCTIONAL CATALYSIS AND INTIMACY CRITERION

dehydrogenated into olefin, it diffuses towards the Brønsted acid sites and is protonated to form carbocations. These carbocations can in turn be isomerized, hydrogenated to their corresponding naphthene counterparts, or opened as C<sub>8</sub> paraffins that can be cracked.

For a given HD/HDH and acidic component, the bifunctional catalyst performances are driven by two factors: the balance between the metal and acid function activities (further referred as metal/acid balance)<sup>44</sup> and the distance between metal and acid sites.<sup>8</sup> The metallic to acidic sites ratio is a convenient way to experimentally describe the metal/acid balance.<sup>71</sup> When the metal function activity is high enough compared to the acid function activity (“well-balanced” catalyst) a plateau, where the HD/DHD reactions are at quasi-equilibrium, is reached. At this point, activity and selectivity are both dependent on the acid function. On the other hand, metal and acid sites should be sufficiently close to insure that the diffusion of olefinic intermediates does not impede the kinetics. A long time ago, Weisz<sup>8</sup> established the so called “intimacy criterion”, suggesting that it exists a certain critical distance between metal and acid sites. Below such distance, the catalyst performance is not impacted by the diffusion of olefinic intermediates. A well-balanced catalyst that fulfills the intimacy criterion can also be defined as an ideal bifunctional catalyst according to Weitkamp’s terminology.<sup>44</sup>

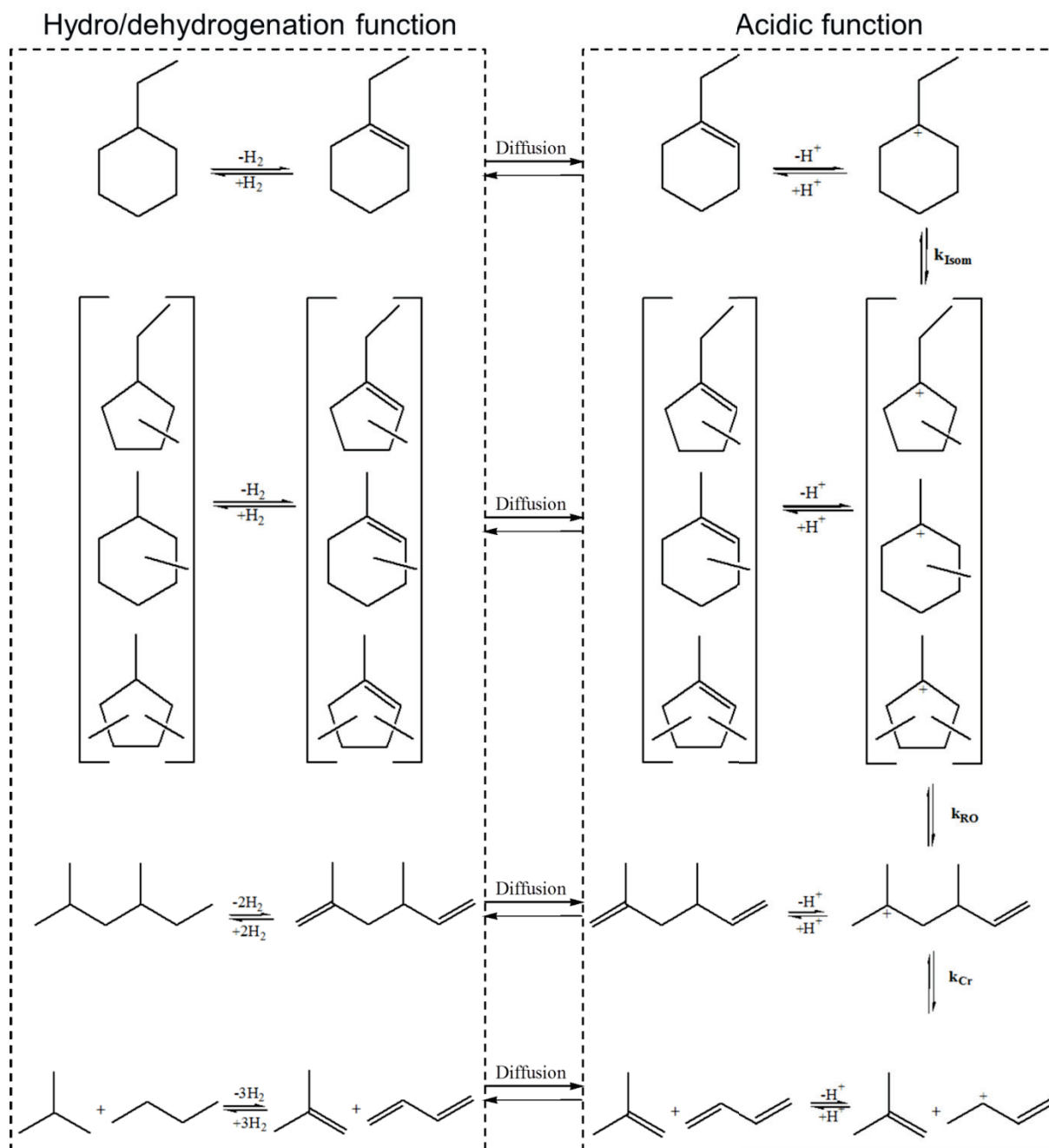


**Figure 1. Simplified bifunctional mechanism for the hydroconversion of ethylcyclohexane. Alternative ring opening and cracking products are omitted for clarity.**

For many years, several publications supporting this “intimacy criterion” have been published. This “intimacy criterion” has been often considered as “the closer the better”.<sup>52,68,69</sup> This “intimacy criterion” has been often considered as “the closer the better”. Zečević et al.<sup>74</sup> have recently studied the hydroconversion of different paraffins with bifunctional catalysts, containing platinum and USY zeolite. In this work, they reported closer distances between the two functions as detrimental to the isomerization selectivity. This decrease in selectivity was

### CHAPTER III. METAL/ACID BIFUNCTIONAL CATALYSIS AND INTIMACY CRITERION

attributed to the long residence time of the molecules inside the zeolite porosity., which will generate more cracking products. More recently, Samad et al.,<sup>61</sup> studied this phenomenon for n-heptane isomerization using a bifunctional catalyst (Pt dispersed over an acidic silica-alumina support). Their results pointed out in the same direction, showing lower activity at atomic distance between metal and acid sites than with larger ones, such as nano- and micro-meter distances. The same tendency was observed for the isomerization selectivity.

Regarding the balance between both functions, Batalha et al.<sup>69</sup> reported that the latter has to be high enough to reach the plateau, where the rate limiting step of reaction takes place on the acidic function. Following that idea, Guisnet<sup>52</sup> published later that this condition is necessary to obtain optimal catalytic performances.

Consequently, in order to achieve a general understanding, an unified view on the effects of the metal/acid balance and distance between sites is required. With this purpose, a systematic investigation of a combination of these two parameters has to be performed. Moreover, whereas their influence has been widely studied for paraffins hydroconversion,<sup>61,68,69,74</sup> naphthenes hydroconversion has remained somehow in the background. To our knowledge, not many studies have been published.<sup>49</sup> This reaction is of practical importance, since during ethylbenzene hydroisomerisation, naphthenes ring opening and cracking have been identified as the main side reactions impacting isomerization yields.<sup>5</sup>

In the present study, the influence of the distance and the balance between metal/acid functions for ethylcyclohexane (ECH) hydroconversion over different platinum/EU-1 zeolite catalysts is investigated. The distance is tuned by impregnating platinum either on the zeolite, or on an alumina support. Although there are different ways to change the metal to acid sites ratio, we decided to change the amount of metal while keeping the number of acid sites constant. The metal to acid sites ratio could be also modified by tuning the zeolite Si/Al molar ratio. However, this is far less reliable since changing the Si/Al ratio while keeping all other properties (such as crystallinity, particle size, aluminum zoning, etc.) constant is not straightforward. For the trends investigated here, variations in these properties may be detrimental, as it was observed in the case of n-heptane hydroconversion catalyzed by Pt/FAU bifunctional catalysts.<sup>188</sup>

A reaction mechanism is proposed on the basis of a detailed analysis of the reaction products, and the trends observed are explained by a dual-function kinetic model.

### 3.2. Materials and methods

#### 3.2.1. Catalysts preparation

Commercial zeolite EU-1 (CP742-1) was supplied by Zeolyst. The zeolite was first calcined at 520°C for 20 h to remove the organic template. To obtain the protonic form (HEU-1), it was then ion-exchanged with a solution of  $\text{NH}_4\text{NO}_3$  (10 ml per gram of zeolite) at 85°C for 4 h. under stirring. Afterwards, the solid was calcined under air flow of  $1 \text{ NL h}^{-1}\text{g}^{-1}$  at 150, 250, 350, 450°C for 1 h. at each temperature and a final plateau at 520°C for 20 h. A heating rate of  $5^\circ\text{C min}^{-1}$  was used. The introduction of platinum on the zeolites (Pt/HEU-1) was performed by incipient wetness impregnation of  $[\text{Pt}(\text{NH}_3)_4\text{Cl}_2]\cdot\text{H}_2\text{O}$  (99.5%), supplied by Sigma-Aldrich. Three Pt contents were aimed for: 0.5, 0.8 and 1 wt.%. The platinum introduction on alumina (Pt/ $\text{Al}_2\text{O}_3$ ) was carried out by competitor impregnation of  $[\text{H}_2\text{PtCl}_6]\cdot 6\text{H}_2\text{O}$  (99.9%) supplied by Strem chemical, HCl being the competitor, and resulting in four Pt contents: 0.1, 0.26, 1.05 and 2.3 wt.%. The impregnated materials (Pt/HEU-1 and Pt/ $\text{Al}_2\text{O}_3$ ) were dried overnight at 110°C and then calcined in an air flow of  $1 \text{ NL h}^{-1}\text{g}^{-1}$  at 150, 250 and 350°C for 1 h. at each temperature and finally at 520°C for 2 h. A heating rate of  $5^\circ\text{C min}^{-1}$  was used. Ex situ reduction was performed to ensure a stable and consistent platinum state to all the catalytic tests and some characterization techniques. Reduction was performed at 480°C for 2 h., using a heating rate of  $5^\circ\text{C min}^{-1}$  and under a hydrogen flow of  $20 \text{ NL h}^{-1}\text{g}^{-1}$ . Mechanical mixtures of 80% of  $\text{Al}_2\text{O}_3$  (loaded or not with Pt) and 20% of zeolite (loaded or not with Pt), with a pellet size below 60  $\mu\text{m}$ , were performed. The distance between metal and acid sites was considered as “microscale” when platinum is deposited on alumina (Pt- $\text{Al}_2\text{O}_3$ /HEU-1), and as “nanoscale” when platinum is deposited on the zeolite (Pt-HEU-1/ $\text{Al}_2\text{O}_3$ ) (See figure 2). The mechanical mixtures were pelletized with a hydraulic press, crushed and sieved to obtain a pellet size between 250 and 500  $\mu\text{m}$ . Table 1 summarizes all the catalysts employed in this study.

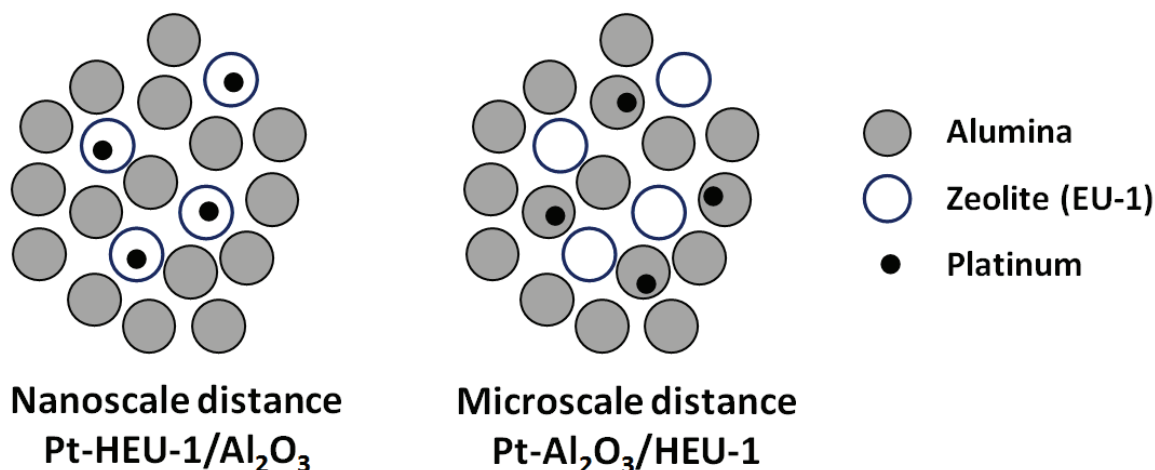


**Figure 2.** Schemes of the two catalysts groups employed in this study showing different degrees of intimacy between metal and acid sites.

**Table 1.** Bifunctional catalysts used in this study.

Pt location	metal/acid sites distance	Composition (wt %)	Catalyst name	nA	nPt <sub>s</sub>	nPt <sub>s</sub> /nA
				(μmol Al g <sup>-1</sup> cat)	(μmol Pt/g <sup>-1</sup> cat)	
Alumina (Pt-Al <sub>2</sub> O <sub>3</sub> )	Microscale distance	80% 0.10 wt%Pt-Al <sub>2</sub> O <sub>3</sub> - 20% HEU-1	0.1%Pt-Al <sub>2</sub> O <sub>3</sub> /HEU-1	135	3.4	0.03
		80% 0.26 wt%Pt-Al <sub>2</sub> O <sub>3</sub> - 20% HEU-1	0.3%Pt-Al <sub>2</sub> O <sub>3</sub> /HEU-1	129	9.1	0.07
		80% 1.05 wt%Pt-Al <sub>2</sub> O <sub>3</sub> - 20% HEU-1	1%Pt-Al <sub>2</sub> O <sub>3</sub> /HEU-1	142	38.1	0.27
		80% 2.30 wt%Pt-Al <sub>2</sub> O <sub>3</sub> - 20% HEU-1	2.3%Pt-Al <sub>2</sub> O <sub>3</sub> /HEU-1	142	68.7	0.48
Zeolite (Pt/HEU-1)	Nanoscale distance	80% Al <sub>2</sub> O <sub>3</sub> - 20% 0.51 wt%Pt/HEU-1	0.5%Pt-HEU-1/Al <sub>2</sub> O <sub>3</sub>	132	4.3	0.03
		80% Al <sub>2</sub> O <sub>3</sub> - 20% 0.82 wt%Pt/HEU-1	0.8%Pt-HEU-1/Al <sub>2</sub> O <sub>3</sub>	132	6.9	0.05
		80% Al <sub>2</sub> O <sub>3</sub> - 20% 0.95 wt%Pt/HEU-1	1%Pt-HEU-1/Al <sub>2</sub> O <sub>3</sub>	129	8.1	0.06

n<sub>A</sub>: micromoles of Brønsted acid sites per gram of catalyst

n<sub>Pt<sub>s</sub></sub>: micromoles of surface Pt per gram of catalyst

### 3.2.2. Materials characterization

Zeolites were characterized by X-ray fluorescence to determine the global Si/Al molar ratio. <sup>27</sup>Al magic angle spinning nuclear magnetic resonance (MAS NMR) was employed to determine the percentage of framework and extra-framework aluminum. XRF analyses were performed with a Thermo scientific ARL Perform'X. NMR experiments were performed using a Bruker Ultrashield 400 MHz spectrometer equipped with a 4 mm CP MAS probe head at room temperature. The MAS rate was 12 kHz for all experiments, the sequence used for Al is a zg sequence and a delay time of 0.5 s. The number of Brønsted acid sites was calculated from these two techniques (number of Al<sup>IV</sup> equal to number of Brønsted sites). For this calculation, Na residual presence, measured by atomic absorption spectroscopy (AAS) has been considered. Quantification of the zeolite global acidity was also assessed by ammonia Temperature Programmed Desorption (NH<sub>3</sub>-TPD). NH<sub>3</sub>-TPD was performed on an Autochem

### CHAPTER III. METAL/ACID BIFUNCTIONAL CATALYSIS AND INTIMACY CRITERION

II 2920 apparatus, equipped with a TCD detector, coupled with a Pfeiffer mass spectrometer. The samples were first pre-treated at 500°C under Helium (50 mL min<sup>-1</sup>, 2 h), before adsorption of 10% NH<sub>3</sub>/He at 150°C during 30 min. (50 mL min<sup>-1</sup>), followed by a purge under helium (150°C, 60 min., 50 mL min<sup>-1</sup>). The TPD was performed under a flow of helium (50 mL min<sup>-1</sup>) from 150°C to 600°C, with a 10°C min<sup>-1</sup> ramp.

Crystallinity was measured by X-ray diffraction (XRD) using a X'Pert Pro diffractometer from Philips Analytical, using a Cu Ka radiation ( $\lambda = 1.5406 \text{ \AA}$ ). Diffraction profiles were scanned using the step mode over a  $2\theta$  range of 5–40°, in steps of 0.02° for six hours with a step time of 5 s. at each point. Nitrogen adsorption measurements were carried out at -200°C on an automatic Micromeritics ASAP 2420 apparatus. Before adsorption, zeolite samples were degassed under vacuum at 500°C for 6 h. The total porous volume ( $V_{\text{total}}$ ) was calculated from the adsorbed volume of nitrogen at a relative pressure  $P/P_0$  of 0.98 whereas the microporous volume ( $V_{\text{micro}}$ ) was determined using the t-plot method.<sup>140</sup> The mesoporous volume ( $V_{\text{meso}}$ ) was obtained by the difference between  $V_{\text{total}}$  and  $V_{\text{micro}}$ .

Platinum dispersion on alumina was determined by hydrogen titration of chemisorbed oxygen (H<sub>2</sub>–O<sub>2</sub> titration) in a Gira Xisorb apparatus with a thermal conductivity detector. The samples were first calcined under air at 530°C for 2 h. at 5°C min<sup>-1</sup>, then cooled down to room temperature and purged with He. The first reduction with H<sub>2</sub> was done at 450°C for 2 h. with a flow of 20 NmL min<sup>-1</sup>. After cooling down to room temperature and purging with He, 15 pulses with pressures from 0.5 to 60 kPa of oxygen were added until saturation occurred (oxygen titration). Another He purge was done before a second reduction with H<sub>2</sub> at room temperature. Then 10 pulses with pressures from 0.5 to 60 kPa of hydrogen were added until saturation (hydrogen titration). Platinum dispersion on zeolite was determined by scanning transmission electron microscopy (STEM) performed using a JEOL 2100 TEM microscope operated at 15 kV. The Pt particles average size was estimated using a shape factor for a cube with one non-exposed side ( $F=5$ ) as recommended in literature for supported metal particles.<sup>150</sup> IR spectroscopy of adsorbed CO measurements were performed with a Bruker Vertex 70 with the purpose to characterize the Pt electronic state. The sample was reduced before analysis at 480°C for 15 min. under static hydrogen and 15 min. for purging (this process was repeated three times). The CO chemisorption was carried out with pulses under vacuum from 5 mbar. to 1000 mbar. until saturation. The pressure in the chamber was then reduced and kept at 120 mbar. This method also allowed to calculate the Pt dispersion. The



molar amount of CO adsorbed was considered as equal to the molar amount of exposed Pt on the surface.

### 3.2.3. Catalytic test

Ethylcyclohexane hydroconversion was performed between 230 and 330°C at a total pressure of 10 bar, using a steel fixed bed reactor. The reactor effluent was analyzed on-line with a gas chromatograph (GC) equipped with a 20 m. DB-1 capillary column from Agilent Technologies and a flame ionization detector (FID). 5 g. of catalyst were loaded in the reactor for each catalytic test. Before reaction, the catalyst was reduced under hydrogen (20 NL h<sup>-1</sup> g<sup>-1</sup>) at 480°C for 2 h. using a heating rate of 5°C min<sup>-1</sup>. The hydrogen to ethylcyclohexane molar ratio was 40, and the weight hourly space velocity (WHSV) was set to 4 g. of ethylcyclohexane per gram of catalyst per hour. The conversion was changed by increasing the temperature. For each temperature two GC analyses were performed in order to check the catalyst stability. Return points confirmed that catalyst deactivation was negligible during the test. The ECH conversion and product selectivities were calculated from the integration of peak areas coming from the chromatograph. It was assumed that the total peak area corresponded to the total amount of products. All the peak areas were corrected with a calculated response factor, specific for each family product depending on their number of carbon atoms and type of compounds. For instance, the naphthenic C<sub>8</sub> isomers were lumped into their corresponding families, i.e. all the dimethylcyclohexane (DMCH) isomers were lumped into the so-called DMCH family, the trimethylcyclopentane (TMCP) and ethylmethylcyclopentane (EMCP) ones into the TMCP and EMCP families, respectively (see supporting information, Table S1) and the propylcyclopentanes into the PCP family. The apparent kinetic constant for first-order ethylcyclohexane consumption per catalyst gram per unit of time was calculated at each temperature by using the integrated form of the rate equation. Selectivity towards a product or a family of products was calculated as the weight of the specific product or family of products divided by the total products weight. The turnover frequency (TOF, in s<sup>-1</sup>) per acid site was calculated according to Eq. 1.<sup>174</sup>

$$TOF = \frac{F_0(ECH)}{W_{cat} n_A} \ln\left(\frac{1}{1-X}\right) \quad \text{Eq. 1}$$

$F_0(ECH)$  is the molar flow of ECH at the entrance of the reactor (μmol s<sup>-1</sup>),  $W_{cat}$  is the amount of catalyst (g),  $n_A$  is the amount of Brønsted acid sites per gram of catalyst (μmol g<sup>-1</sup>) and  $X$  is the ethylcyclohexane conversion.



### 3.2.4. Thermodynamic and kinetic modeling

Thermodynamic simulations were performed with SimSci Pro/II v 9.2 (Schneider Electric). The thermodynamic equation of state used was SRK (Soave-Redlick-Kwong). The compounds database was that from SimSci. The equilibrium between the different compounds was evaluated with a Gibbs reactor (outlet pressure 10 bar, T between 230 and 330°C, 50 iterations max, convergence tolerance -based on the relative change of Gibbs free energy between two iterations:  $10^{-6}$ , Fibonacci tolerance: 0.01).

The kinetic modeling was based on the scheme depicted in figure 3 that represents the main reactions occurring for our system according to a bifunctional mechanism.

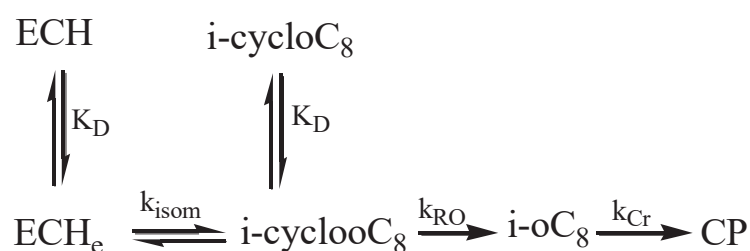


**Figure 3. Representative scheme of the bifunctional mechanism for the main reactions appearing in the ECH hydroconversion.  $K_D$ ,  $k_{\text{isom}}$ ,  $k_{\text{RO}}$  and  $k_{\text{Cr}}$  are the apparent equilibrium ( $K_D$ ) and rate constants for dehydrogenation, isomerization, ring opening and cracking steps, respectively.**

In order to describe this system, a dual-function kinetic model published recently by Mendes et al.<sup>174</sup> for the hydroisomerization of paraffins was applied to our results.

With this model it is possible to quantify the impact of the metal to acid sites ratio on the catalyst performance. Nevertheless, the proximity between the two functions is not taken into account into the model.

The two descriptors of the catalytic performances are the turnover frequency per Brønsted acid site (TOF in  $\text{s}^{-1}$ ) and the maximal yield of naphthenic isomers ( $Y_{\text{i-cycloC}_8, \text{max}}$ , in wt.%) representing the maximal yield (i-cycloC<sub>8</sub> isomers selectivity multiplied by the conversion) of C<sub>8</sub> naphthenes isomers obtained during the reaction. Their expressions are given by Eq.2 and 3.

$$\text{TOF} = \frac{\alpha}{1 + \beta \cdot \left( \frac{n_A}{n_{PtS}} \right)} \quad \text{Eq. 2}$$

$$Y_{i-cycloC8,max} = \frac{\gamma}{1 + \varepsilon \cdot \left( \frac{n_A}{n_{PtS}} \right)} \quad \text{Eq. 3}$$

Where  $\left( \frac{n_A}{n_{PtS}} \right)$  is the catalyst amount of Brønsted acid sites per number of surface Pt.

These equations were derived based on the reaction scheme shown in Figure 3 for a plug-flow reactor and assuming first order isomerization and ring opening/cracking reactions. The DH/HDH reaction rates were assumed to be a function of: the fractional vacancy and the total number of metal sites, as well as of the difference between paraffin partial pressure and the corresponding equilibrium pressure. Furthermore it was assumed that the fraction of occupied acid sites is low and unaffected by olefins partial pressures. Further details are provided in ref 30.

Four parameters describe the kinetic model.  $\alpha$  corresponds to the intrinsic  $TOF_{Al}$  of the zeolite, where  $TOF_{Al}$  is the average turnover frequency per Brønsted site along the reactor.  $\beta$  is a measurement of the  $n_{PtS}/n_A$  ratio required to reach the intrinsic  $TOF_{Al}$  of the zeolite. In the expression of the maximum yield i-cycloC<sub>8</sub>,  $\gamma$  reflects the highest value of  $Y_{i-cycloC8,max}$  that can be reached. and so the intrinsic zeolite selectivity towards hydroisomerization.  $\varepsilon$  is a measurement of the  $n_{PtS}/n_A$  ratio required to attain such value. In the model of Mendes et al.<sup>174</sup>  $\varepsilon$  and  $\beta$  are related to the kinetic constants of cracking and isomerization respectively, i.e.  $\varepsilon/\beta$  equals  $k_{Cr}/k_{isom}$ . When a naphtene molecule like ethylcyclohexane is considered, ring opening is required before cracking can occur. Moreover, ring opening is a limiting step compared to the cracking (see. 3.2). Therefore in this case  $\varepsilon/\beta$  equals  $k_{RO}/k_{isom}$ .

### 3.3. Results

#### 3.3.1. Characterizations of the samples

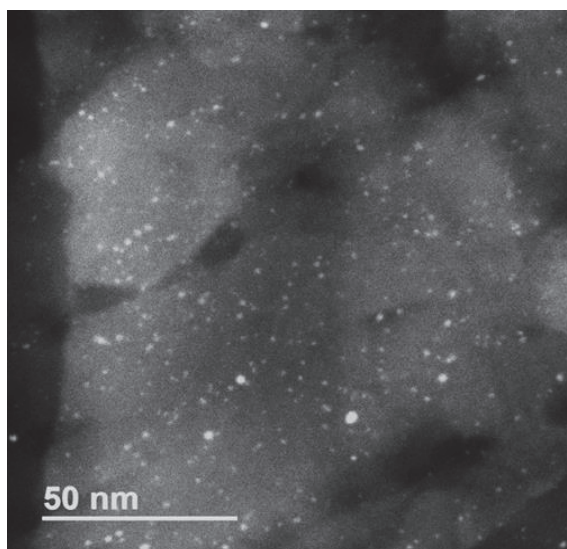
##### 3.3.1.1. Pt/HEU-1 samples

Table 2 reports the main physical-chemical properties of the non-impregnated and impregnated zeolites. After zeolites impregnation, crystallinity remained constant, around 100% (figure S1). The amount of sodium after ionic exchange was low, below 100 ppm. The microporous and mesoporous volumes were in all cases around 0.13 and 0.21 mL g<sup>-1</sup> respectively, meaning that the Pt deposition had no influence on these physical properties of

### CHAPTER III. METAL/ACID BIFUNCTIONAL CATALYSIS AND INTIMACY CRITERION

the zeolite. Concerning the acidity, once again no effect was observed after Pt impregnation, as illustrated by the constant total amount of acid sites in both zeolites (based on the amount of  $\text{Al}^{\text{IV}}$ ), of about  $650 \mu\text{mol g}^{-1}$ . The negligible impact of the platinum deposition on the acidity was also confirmed by ammonia temperature programmed desorption experiments. The initial calcined zeolite and the one loaded with the highest Pt content (1% Pt-HEU-1/ $\text{Al}_2\text{O}_3$ ), that one with the highest pore blockage effect expected, were characterized and compared revealing similar  $\text{NH}_3$  desorption profiles. Afterwards, the profiles were decomposed in order to quantify the amount of acid sites corresponding to the highest temperature peak. These results demonstrated a negligible decrease of the amount of acid sites (within the experimental error, of  $\pm 10 \%$ ) for the impregnated zeolite sample ( $678 \mu\text{mol g}^{-1}$ ) compared to the initial one ( $710 \mu\text{mol g}^{-1}$ ). These values were in agreement with the acid site concentration calculated from Si/Al ratio and  $^{27}\text{Al}$  NMR (Table 2). Thus, we can conclude that the platinum particles are located in such a way that they do not affect the access to the acid sites.

According to STEM characterization (figure 4), platinum was rather well dispersed over the zeolite and the average particle size was 1.2 nm corresponding to 82% dispersion. Similar dispersions were obtained (Table 2) regardless of the amount of impregnated Pt. In all samples, some larger particles were found representing less than 10% of the total particle population.



**Figure 4. STEM image of 1%Pt/HEU-1.**

In the case of the 0.5% Pt/HEU-1 sample, the CO adsorption monitored by FTIR revealed only a stretching band at  $2090 \text{ cm}^{-1}$ , corresponding to CO adsorbed over Pt in a reduced

# CHAPTER III. METAL/ACID BIFUNCTIONAL CATALYSIS AND INTIMACY CRITERION

state.<sup>189</sup> In the samples with higher amounts of Pt, especially in the case of 1% Pt/HEU-1, some stretching bands at 2130-2110 cm<sup>-1</sup> appeared (figure S2). They are attributed to CO in interaction with Pt<sup>+</sup> species.<sup>189</sup> A very good linear correlation was found between the peak area of the Pt<sup>0</sup>-CO species and the total number of Pt atoms (figure S3). This number has been calculated by taking into account the percentage of Pt present in each sample, measured by the XRF technique. This linear correlation sustained the fact that the dispersion was similar for all samples.

**Table 2. Physical-chemical properties of the non-impregnated and impregnated zeolites.**

Sample	S <sub>BET</sub> (m <sup>2</sup> g <sup>-1</sup> )	V <sub>micro</sub> (mL g <sup>-1</sup> )	V <sub>meso</sub> (mL g <sup>-1</sup> )	Pt (wt %)	Na (wt %)	Si/Al	Al <sup>IV</sup> (%)	n <sub>A</sub> (μmol g <sup>-1</sup> )	D <sub>Pt</sub>	n <sub>PtsZ</sub> (μmolPt g <sup>-1</sup> )
HEU-1	404	0.12	0.20	—	0.003	18.3	80	644	—	—
0.5% Pt/HEU-1	393	0.14	0.23	0.51	0.005	18.1	80	659	82	21
0.8% Pt/HEU-1	389	0.13	0.21	0.82	0.005	18.1	80	659	82	34
1% Pt/HEU-1	412	0.13	0.23	0.95	0.003	18.3	80	644	82	41

n<sub>A</sub>: micromoles of acid sites per gram of zeolite

n<sub>PtsZ</sub>: micromoles of surface Pt per gram of zeolite

D<sub>Pt</sub>: dispersion

## 3.3.1.2. Pt/Al<sub>2</sub>O<sub>3</sub> samples

The Pt/Al<sub>2</sub>O<sub>3</sub> samples were analyzed after Pt deposition by nitrogen physisorption, XRF, H<sub>2</sub>-O<sub>2</sub> titration and STEM. Nitrogen physisorption revealed that the surface area and mesoporous volume remained constant compared to the non-impregnated alumina (Table 3).

**Table 3. Physical-chemical properties for the non-impregnated and impregnated alumina samples.**

Sample	S <sub>BET</sub> (m <sup>2</sup> g <sup>-1</sup> )	V <sub>meso</sub> (mL g <sup>-1</sup> )	Pt (wt %)	D <sub>Pt</sub> (%)	n <sub>PtsA</sub> (μmolPt g <sup>-1</sup> )
Alumina	190	0.53	—	—	—
0.1% Pt/Al <sub>2</sub> O <sub>3</sub>	194	0.52	0.1	81	4
0.3% Pt/Al <sub>2</sub> O <sub>3</sub>	200	0.55	0.26	85	11
1.1% Pt/ Al <sub>2</sub> O <sub>3</sub>	200	0.55	1.05	89	48
2.3% Pt/ Al <sub>2</sub> O <sub>3</sub>	203	0.52	2.3	73	86

n<sub>PtsA</sub>: micromoles of surface Pt sites per gram of alumina

## CHAPTER III. METAL/ACID BIFUNCTIONAL CATALYSIS AND INTIMACY CRITERION

Pt dispersion was calculated by  $\text{H}_2\text{-O}_2$  titration, a typical technique employed to determine platinum dispersion over alumina.<sup>190</sup> Dispersions around 85% were found regardless of the amount of impregnated Pt (see Table 3). CO adsorption analysis revealed only the presence of Pt in the reduced state (figure S5).

### 3.3.2. Catalytic tests

#### 3.3.2.1. Catalytic behavior of Pt-HEU-1/ $\text{Al}_2\text{O}_3$ catalysts

The catalytic test was carried out with the three different catalysts of this group, 0.5%, 0.8% and 1% Pt-HEU-1/ $\text{Al}_2\text{O}_3$ . The evolution of the conversion was measured as a function of the temperature (figure 5 a).

According to the bifunctional mechanism first advanced by Weisz,<sup>8</sup> the higher the metal/acid ratio, the higher the conversion until reaching a plateau. This was well observed for this catalyst group: as the metal/acid balance increased the conversion increased (figure 5 a). However, a plateau was not reached in this metal content range. The apparent activation energy was around 119 kJ/mol (figure S6) in the case of 1% Pt-HEU-1/ $\text{Al}_2\text{O}_3$  and the maximal conversion reached was 93% at 330°C.

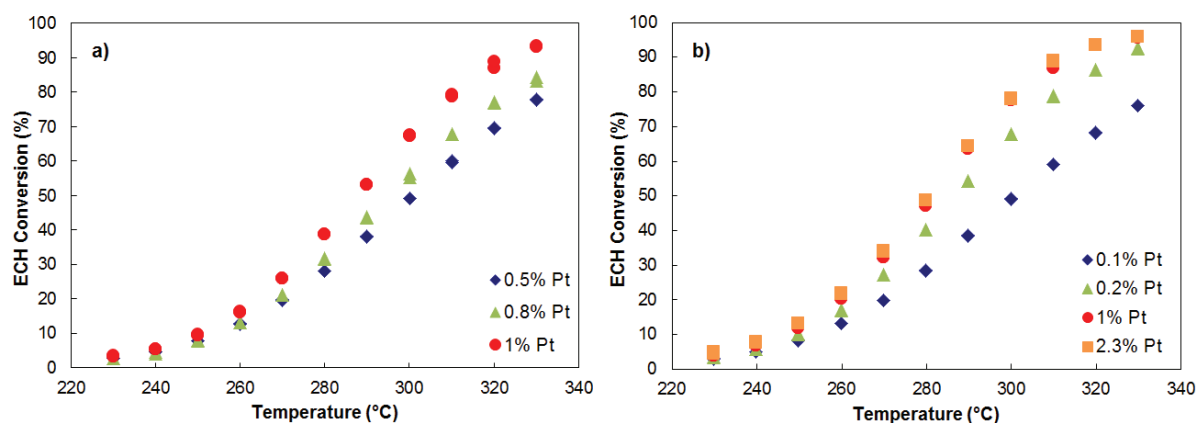


**Figure 5.** Evolution of the conversion versus temperature for a) the Pt-HEU-1/ $\text{Al}_2\text{O}_3$  catalysts; b) the Pt- $\text{Al}_2\text{O}_3$ /HEU-1 catalysts.

### CHAPTER III. METAL/ACID BIFUNCTIONAL CATALYSIS AND INTIMACY CRITERION

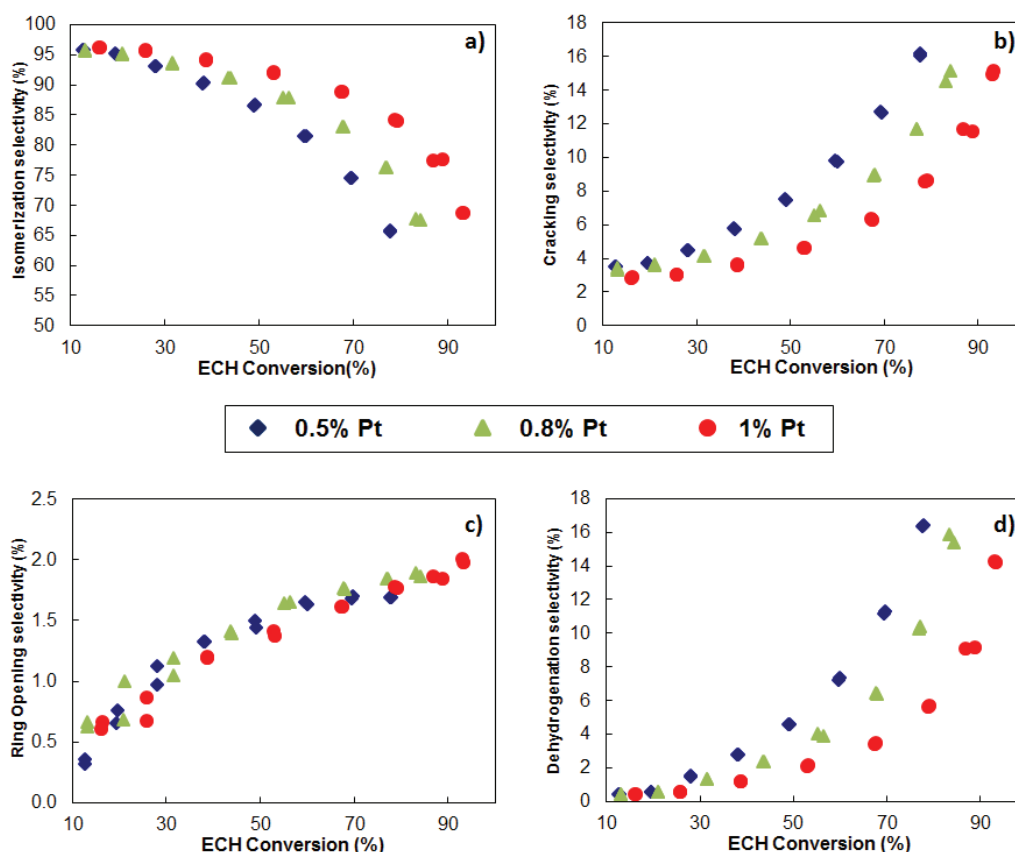


**Figure 6. Evolution of the selectivity versus ECH conversion for the Pt-HEU-1/Al<sub>2</sub>O<sub>3</sub> catalysts; a) isomerization; b) cracking; c) ring opening; d) dehydrogenation.**

In Figure 6 the evolution of the isomerization is depicted as a function of the ECH conversion. The same tendency as that observed for the conversion was found, i.e., the higher the metal/acid balance, the higher the isomerization selectivity. As a consequence, the selectivities towards the undesired side reactions, such as ring opening, cracking and dehydrogenation, decreased as long as the metal/acid balance increased (Figures 6b, 6c and 6d).

Based on these curves, the primary products were easily identifiable as the isomerization ones, almost the only compounds appearing at low ECH conversions. Ring opening products were present only in very low amounts (lower than 2%, figure 6c) whereas the cracking and dehydrogenation ones increased with the ECH conversion. This was consistent with the fact that naphthene ring opening is slow<sup>47</sup> compared to naphthene isomerization and paraffin cracking (by beta scission). Thus, from these results, a first apparent reaction mechanism is proposed in Figure 7a. Product selectivities were also studied vs the contact time at a given temperature (285°C), and basically the same conclusions were drawn.

### CHAPTER III. METAL/ACID BIFUNCTIONAL CATALYSIS AND INTIMACY CRITERION

For a deeper understanding of the isomerization reaction scheme, the various isomers were lumped according to their branching degree into different families (see section 2.3). The evolution of their mole fractions with temperature is reported in Figure 8a in the case of the 1% Pt-HEU-1/Al<sub>2</sub>O<sub>3</sub> catalyst. The thermodynamic equilibrium product distribution as a function of temperature was also calculated with PRO II (see section 2.4).

In the catalytic unit, this equilibrium was reached at higher temperatures (last point of figure 8a).

a)  $\text{ECH} \rightleftharpoons \text{ISOMERIZATION products} \rightarrow \text{RING OPENING products} \rightarrow \text{CRACKING products}$

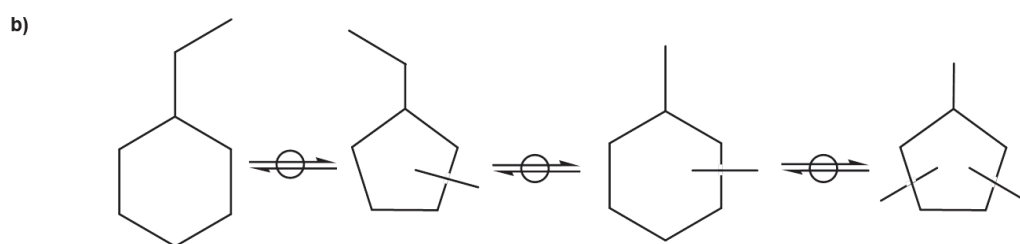


Figure 7.a) Apparent reaction mechanism for the hydroconversion of ECH and b) Apparent isomerization reaction scheme.

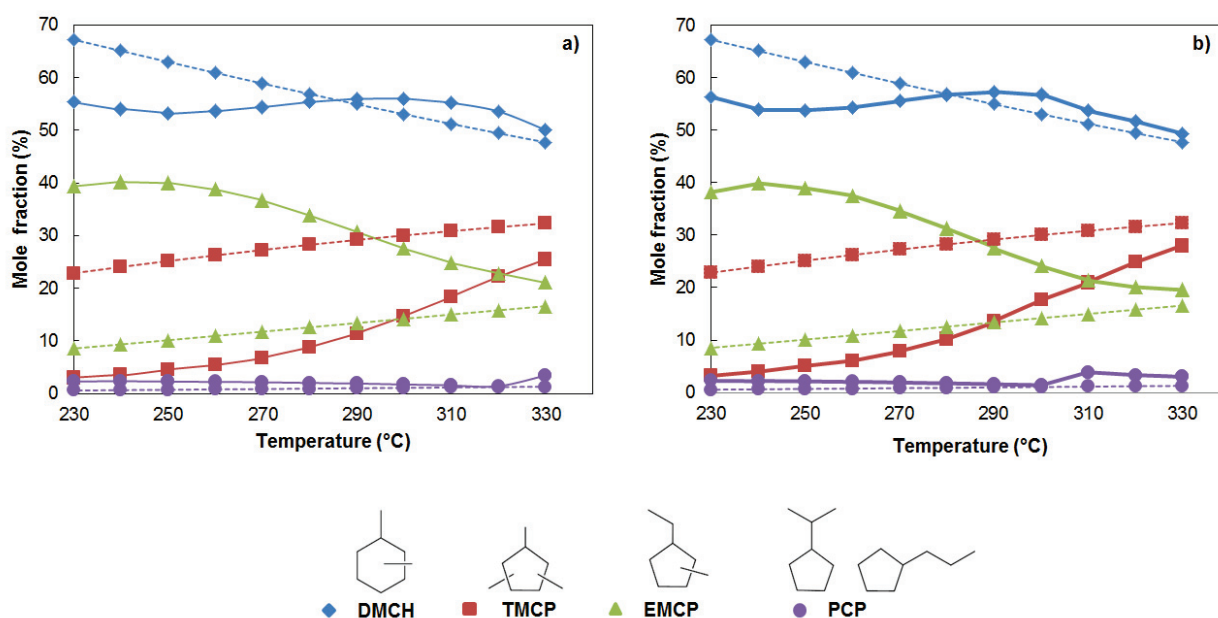


Figure 8. Evolution of the lumped isomers mole fraction versus temperature at thermodynamic equilibrium (dashed line, PRO II simulation) and observed experimentally (full line) for a) 1% Pt-HEU-1/Al<sub>2</sub>O<sub>3</sub> and b) 1% Pt-Al<sub>2</sub>O<sub>3</sub>/ HEU-1 catalysts.



### CHAPTER III. METAL/ACID BIFUNCTIONAL CATALYSIS AND INTIMACY CRITERION

DMCH and EMCP were the major reaction products at low ECH conversion, as inferred from Figure 8a. It can also be observed that the EMCP mole fraction at low conversion (i.e. low temperature) was much higher experimentally than at the thermodynamic equilibrium. Nonetheless, in the case of DMCH, the experimental mole fraction was lower than the one at the thermodynamic equilibrium. This suggests that the primary isomerization products are EMCP and not DMCH. The presence of DMCH at very low levels of conversion pointed out a fast isomerization from EMCP to DMCH. It means, the ring expansion reaction (formation of DMCH from EMCP) seems to be faster than the ring contraction reaction (formation of EMCP from ECH), otherwise DMCH would not appear as apparent primary products.

As the conversion increased, the EMCP mole fraction decreased as the TMCP mole fraction increased, while the DMCH mole fraction remained almost constant. This suggests that some DMCH is transformed into TMCP and concurrently EMCP into DMCH. Such fact can explain the constant DMCH mole fraction. On the other hand, the PCP concentration was negligible regardless of the conversion level, contrary to previous findings for zeolite Y.<sup>49</sup>

Based on these experimental observations, an apparent reaction scheme for the ECH isomerization is depicted in Figure 7b.

The products molar distribution with carbon numbers other than 8 is depicted Figure 9. No larger paraffins than C<sub>8</sub> were observed. Typical products from hydrogenolysis, such as C<sub>1</sub>, C<sub>2</sub>, C<sub>7</sub> and C<sub>6</sub>, were found in low amounts. C<sub>3</sub>-C<sub>5</sub> compounds are normally produced by the hydrocracking of C<sub>8</sub> paraffins *via* a bifunctional mechanism (figure 1). These compounds were by far the most abundant ones, suggesting that the formation of cracked products mainly occurs *via* the bifunctional mechanism whereas the hydrogenolysis mechanism remains marginal. Besides, according to Weitkamp and Ernst,<sup>49</sup> the higher amount of C<sub>5</sub> with respect to C<sub>3</sub> can be due to disproportionation followed by cracking reaction. According to these reactions, two C<sub>8</sub> molecules dimerize and then crack into C<sub>5</sub>+C<sub>4</sub>+C<sub>6</sub> or 2C<sub>5</sub>+C<sub>6</sub> compounds. The existence of the disproportionation pathway was also sustained by the presence of C<sub>9</sub> naphthenes.



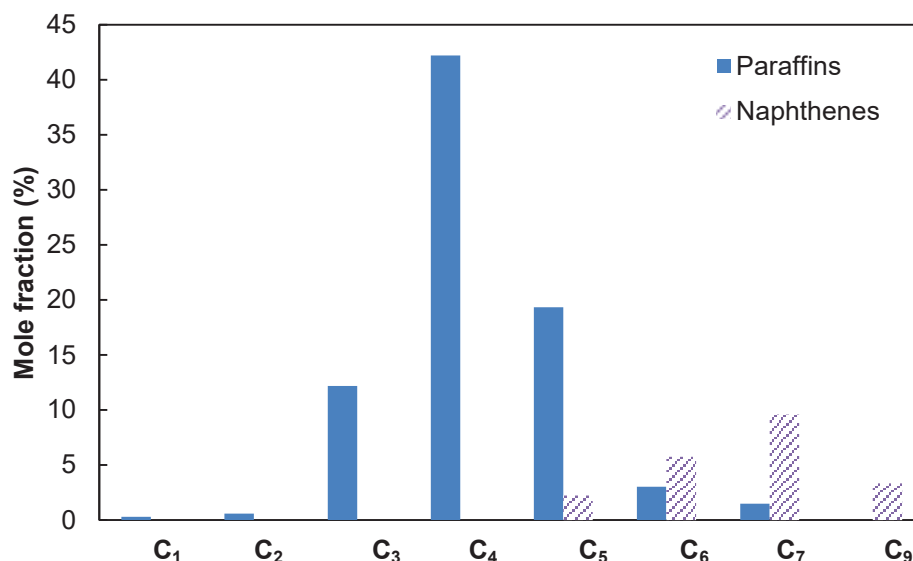


**Figure 9. Molar distribution of products with carbon number other than eight at 300°C with the 1% Pt-HEU-1/ Al<sub>2</sub>O<sub>3</sub> catalyst. The yield of products with carbon number other than eight is equal to 4.2 %.**

Ethylbenzene (EB) was the dehydrogenation product appearing first (260°C) (figure S7), although its percentage remained low regardless of the temperature. The three xylenes: meta- (m-Xyl), para- (p-Xyl), and ortho-xylene (m-Xyl), appeared around 290°C and their concentration increased with higher temperatures (specially meta-xylene). This behavior was expected, since due to the endothermic character of the dehydrogenation, at higher temperatures the equilibrium is always shifted towards the formation of aromatics.

### 3.3.2.2. Catalytic behavior of Pt- Al<sub>2</sub>O<sub>3</sub>/ HEU-1 catalysts

Four different catalysts with 0.1, 0.2, 1.0 and 2.3 wt.% Pt supported on alumina and mixed with the HEU-1 zeolite, were tested under standard conditions (section 2.3). The conversion was measured as a function of temperature and depicted in Figure 5 b. Again, the salient feature of the bifunctional mechanism was well observed: the higher the metal to acid sites ratio, the higher the conversion until reaching a plateau. This conversion plateau was reached when the curves related to the two catalysts containing 1 and 2.3% of Pt overlap as shown in Figure 5 b. At this plateau, the hydro/dehydrogenation reactions (metal function) are at quasi-equilibrium and the limiting step of the reaction takes place on the acid sites. The 1% Pt-Al<sub>2</sub>O<sub>3</sub>/HEU-1 catalyst was considered as the reference system concerning this catalysts group, reaching a maximal ECH conversion of 96%. The activation energy obtained with this catalyst was of 123 kJ/mol. These results revealed the importance of the metal/acid balance.

## CHAPTER III. METAL/ACID BIFUNCTIONAL CATALYSIS AND INTIMACY CRITERION

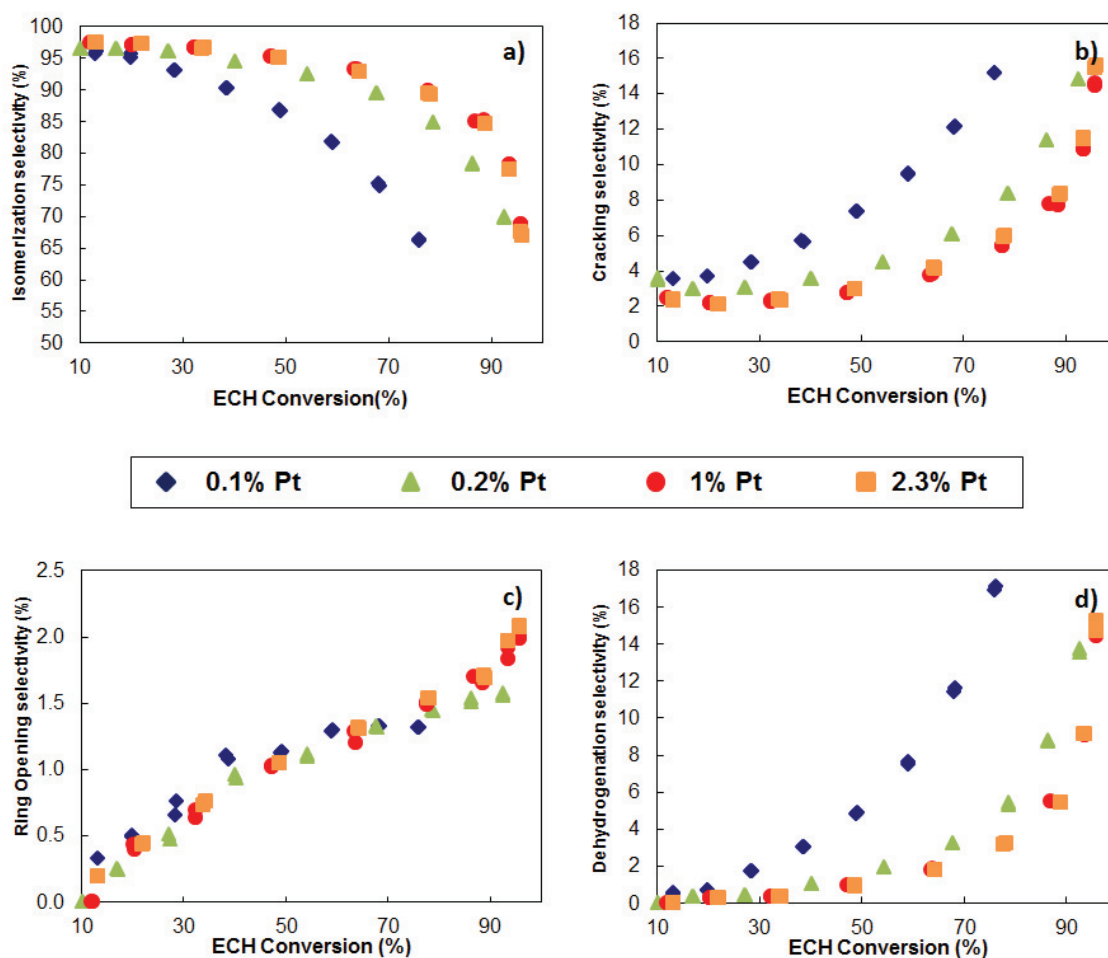


**Figure 10.** Evolution of the selectivity versus ECH conversion for the Pt-Al<sub>2</sub>O<sub>3</sub>/HEU-1 catalysts group; a) isomerization; b) cracking; c) ring opening; d) dehydrogenation.

Figure 10 shows that the selectivity also reached a plateau for the isomerization and the undesired side reactions. This selectivity plateau means that the quasi-equilibrium of the hydro/dehydrogenation reactions was reached for the products too. It is important to notice that the selectivity towards the undesired products (ring opening and cracking) remained really low. In particular, the selectivity for ring opening product was extremely low (below 2%), regardless the ECH conversion.

These results were similar to those corresponding to the Pt-HEU-1/Al<sub>2</sub>O<sub>3</sub> group. Thus, the apparent reaction mechanism is the same as defined for the Pt-Al<sub>2</sub>O<sub>3</sub>/HEU-1 group, depicted in Figure 7a.

The isomers evolution was monitored experimentally (full line) over 1% Pt-Al<sub>2</sub>O<sub>3</sub>/HEU-1 (Figure 8b). The data in Figure 8b is almost overlapping with those of Figure 8a. This implies that the evolution of the isomerization products with conversion was the same, regardless

where the platinum was located. Therefore, the apparent isomerization reaction scheme is identical to that corresponding to the Pt-HEU-1/Al<sub>2</sub>O<sub>3</sub> series (figure 7b).

Concerning the evolution of cracking and dehydrogenation products, the results were almost the same as the ones corresponding to the 1% Pt-HEU-1/Al<sub>2</sub>O<sub>3</sub> catalyst (figure S9 and S10).

### 3.4. Discussion

#### 3.4.1. Ethylcyclohexane isomerization pathway over EU-1

As for non-cyclic alkanes, two kinds of isomerization can be distinguished for naphthenes.<sup>22</sup> On the one hand, type A isomerization does not change the naphthene branching degree. It corresponds for instance, to the ethylcyclohexane transformation into propylcyclopentanes. On the other hand, type B isomerization changes the naphthene branching degree. It corresponds for instance, to the ethylcyclohexane transformation into ethyl-methylcyclopentanes. Type A isomerization is generally reported to occur much faster than type B.<sup>22,191–193</sup> However the zeolite topology has a significant impact on the relative rates of type A and type B isomerization. According to Weitkamp,<sup>30</sup> mordenite favored type B isomerization compared to type A, as propylcyclopentane did not appear as the primary product of ethylcyclohexane isomerization. By contrast, for other zeolites such as faujasite<sup>17</sup> or ZSM-5,<sup>48</sup> propylcyclopentane was indeed the primary isomerization product. The pore shape, or the structure dimension, can create some constraints related to the transition states or even to the reactant and the products.<sup>21</sup> In the present study, for the EUO framework, the propylcyclopentanes do not appear as primary products. As for MOR, it is tempting to explain this result by an acceleration of type B isomerization compared to type A over EUO. However, such interpretation should be considered cautiously, since under our reaction conditions, the propylcyclopentanes formation is extremely disfavored from a thermodynamic point of view (figure 8). This point could be further investigated but is beyond the scope of this work.

#### 3.4.2. Impact of the metal to acid sites distance

The impact of the metal/acid balance has been already highlighted in the previous sections. In order to evaluate the impact of the distance between both functions, the evolution of the turnover frequency per Brønsted acid site, TOF, and the maximal i-cycloC<sub>8</sub>

## CHAPTER III. METAL/ACID BIFUNCTIONAL CATALYSIS AND INTIMACY CRITERION

isomerization yield for both catalyst series *versus* the metal/acid balance is reported in Figure 11. Pt-Al<sub>2</sub>O<sub>3</sub>/HEU-1 corresponds to the catalysts with a “microscale distance” between the two functions whereas Pt-HEU-1/Al<sub>2</sub>O<sub>3</sub> corresponds to the catalyst with a “nanoscale distance” between the two functions. The metal/acid balance is represented by the molar ratio of surface platinum sites to Brønsted acid sites. For a given metal/acid balance, comparable turnover frequencies are obtained regardless of the platinum location (figure 11a). This suggests that the intimacy criterion is fulfilled even when the platinum and acid sites are at “microscale” distance. The same has been also observed before in Figure 5b.

Figure 11b represents the evolution of the maximal C<sub>8</sub> isomerization yield vs. the metal/acid balance. As it occurs for the TOF, the same trend is observed for the two catalyst series. For a given metal/acid balance, comparable maximal i-cycloC<sub>8</sub> isomerization yields are obtained regardless of the platinum location. Noticeably, the isomerization yield plateau seems to be reached at lower metal to acid ratio than the TOF. In this case study, the key parameter governing the activity and the selectivity of the bifunctional catalyst appears to be the metal/acid balance rather than the metal to acid sites distance.

Note that the desorption of the multibranched intermediates and products may be an issue under some operating conditions. The zeolite channels are indeed composed of 10 MR, even if side pockets are 12MR. Similar trends in terms of activity and selectivity are obtained for both catalysts series, while the diffusion path is likely not the same for all samples. This fact makes us confident that diffusion limitations in the microporosity are not occurring under our operating conditions. Note that they were carefully chosen to avoid the formation of aromatics. First to better study the intrinsic isomerization/cracking kinetics, but also to prevent the catalyst coking. The latter is known to occur when aromatics are produced in significant amounts.

### 3.4.3. Impact of the metal to acid sites ratio

To further quantify the impact of the metal to acid sites ratio on the catalytic performance, a dual-function kinetic model for the hydroisomerization of ethylcyclohexane was applied (section 2.4).

Figure 11a compares the evolution of the turnover frequency calculated by the kinetic model to the experimental data for both catalyst series, as a function of the metal/acid sites balance. The model describes the experimental behavior with good accuracy ( $R^2 = 0.85$ ). Such model reveals the following fitted values for the parameters describing the kinetic model

### CHAPTER III. METAL/ACID BIFUNCTIONAL CATALYSIS AND INTIMACY CRITERION

curve:  $\alpha = 0.03 \text{ s}^{-1}$  and  $\beta = 0.02$ .  $\alpha$  equals the intrinsic turnover frequency per Brønsted acid site whereas  $\beta$  is a measure of the  $n_{\text{Pts}}/n_{\text{A}}$  required to reach the plateau of the turnover frequency.

To further quantify the impact of the metal to acid sites ratio on the catalytic performance, a dual-function kinetic model for the hydroisomerization of ethylcyclohexane was applied (section 2.4).

Figure 11a compares the evolution of the turnover frequency calculated by the kinetic model to the experimental data for both catalyst series, as a function of the metal/acid sites balance. The model describes the experimental behavior with good accuracy ( $R^2 = 0.85$ ). Such model reveals the following fitted values for the parameters describing the kinetic model curve:  $\alpha = 0.03 \text{ s}^{-1}$  and  $\beta = 0.02$ .  $\alpha$  equals the intrinsic turnover frequency per Brønsted acid site whereas  $\beta$  is a measure of the  $n_{\text{Pts}}/n_{\text{A}}$  required to reach the plateau of the turnover frequency.

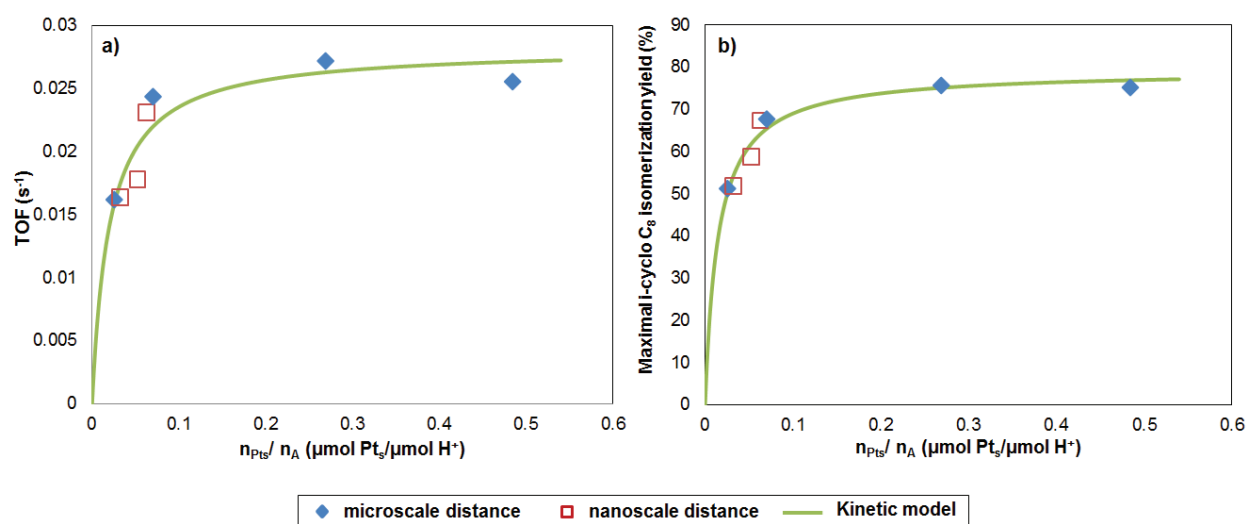


**Figure 11. a) Experimental (270°C) and model (according to the scheme first proposed in <sup>174</sup>) evolution of the a) TOF ( $\text{s}^{-1}$ ) and b) maximal i-cyclo  $\text{C}_8$  isomerization yield, vs the metal/acid balance ( $\mu\text{mol Pt}_s/\mu\text{mol H}^+$ ) for both series of catalysts.**

The fitting of the maximal i-cyclo $\text{C}_8$  isomerization yield against the metal/acid balance (figure 11 b), also shows a very good agreement ( $R^2 = 0.94$ ) with the experimental points. In this case, the values for the parameters describing the kinetic model are  $\gamma = 79.2\%$  and  $\varepsilon = 0.015$ .  $\gamma$  represents the highest i-cyclo $\text{C}_8$  isomerization yield that can be reached and being intrinsic to the zeolite.  $\varepsilon$  is a measure of  $n_{\text{Pts}}/n_{\text{A}}$  required to reach the plateau for the maximal i-cyclo $\text{C}_8$  isomerization yield.

## CHAPTER III. METAL/ACID BIFUNCTIONAL CATALYSIS AND INTIMACY CRITERION

The values obtained for  $\beta$  and  $\varepsilon$  are quite different. This reveals that the requirement in terms of metal to acid ratio, are not the same to reach the plateau for the turnover frequency and for the maximal i-cycloC<sub>8</sub> isomerization yield. The  $\varepsilon/\beta$  ratio is around 0.75. It means that the  $n_{\text{Pts}}/n_{\text{A}}$  ratio required to reach the plateau for the turnover frequency is higher compared to the one required to reach the plateau of maximal i-cycloC<sub>8</sub> isomerization yield. The  $\varepsilon/\beta$  ratio is equal to the ratio of the apparent kinetic constants  $k_{\text{RO}}/k_{\text{isom}}$ . The value of the kinetic constant for isomerization is thus 4/3 times higher than that for ring opening. It is in agreement with the sluggishness of the ring opening reaction compared to the isomerization one.

The dual function kinetic model was initially developed by Mendes<sup>174</sup> for n-paraffins hydroconversion and applied for n-hexadecane hydroconversion over FAU and BEA zeolites. In that case the  $\varepsilon/\beta$  ratio is equal to the ratio of the apparent kinetic constant for isomerization and for cracking,  $k_{\text{Cr}}/k_{\text{isom}}$ , and was found equal to 2. It means that the  $n_{\text{Pts}}/n_{\text{A}}$  ratio required to reach the plateau for the turnover frequency is now lower compared to the one required to reach the plateau of maximal iC<sub>16</sub> isomerization yield, i.e., the kinetic constant for isomerization is half the one of cracking. This is in agreement with the fact that type A beta-scission occurs faster than type A or type B isomerization.<sup>22</sup> The different requirements in terms of metal to acid ratio necessary to reach the plateaus, are the consequence of the fundamental reactivity differences between hexadecane and ethylcyclohexane.

So, as a brief general conclusion, in the present study it is shown that the catalytic activity and selectivity depend strongly on the metal to acid sites ratio. Nevertheless, they are marginally affected by the distance between the active sites, and hence, by the diffusion path of the reaction intermediates. Despite such a simple model fits the data is somehow surprising, it reveals that indeed, the metal/acid balance is the key factor to rationalize the trends, from one sample to another. Note that we are not claiming that such a model is sufficient to precisely render the detailed feature of each catalyst one by one. In particular, it does not render the apparent mechanisms summarized in Figure 7. Additional investigations will be needed in the future to propose a detailed mechanism.

### 3.5. Conclusions

Bifunctional catalysts using platinum as metallic function and EU-1 zeolite as acidic function were prepared, characterized and evaluated for the ethylcyclohexane hydroconversion. Two groups of bifunctional catalysts with different metal/acid distances

### CHAPTER III. METAL/ACID BIFUNCTIONAL CATALYSIS AND INTIMACY CRITERION

(nano-scale and micro-scale) were tested in this study. Within each group, the metal to acid sites ratio was varied.

We have shown that the catalytic activity and selectivity are strongly influenced by the metal to acid sites ratio. On the other hand, it was observed no influence of the distance between both functions, up to micrometer scale. This means that both groups of catalysts, either at nano- and micro- scale distances exhibit the same catalytic performance, provided that the metal to acid sites ratio is the same. Thus, the intimacy criterion is fulfilled in both cases. An ideal bifunctional catalyst is obtained when the metal to acid sites ratio is sufficiently high. In this case the rate limiting step of the reaction is taking place on the acidic function.

To quantify the impact on the metal to acid sites ratio on the catalytic performances (activity and isomerization selectivity), a dual function kinetic model was employed. The model describes the experimental catalytic performances with good accuracy. It shows that the catalyst activity plateau is reached at higher metal to acid sites ratio than the catalyst isomerization selectivity plateau. This is interpreted as a consequence of the lower value of the ring opening kinetic constant compared to the isomerization one.

## 4. LOCATION OF THE ACTIVE SITES IN THE EUO FRAMEWORK

---

Within the EUO framework there are many possible active sites. Revealing which active sites are the most active ones is of importance for the future construction of the microkinetic model. Then, the objective of this chapter is to investigate the reactivity of the cycle contraction-expansion in the context of the ethylcyclohexene isomerization (itself obtained from the dehydrogenation of ethylcyclohexane), identifying the location of the most active sites of an EUO type zeolite for this reaction. To do so, first the stability of the different forms of the adsorbed reactant (carbenium, alkoxide and  $\pi$ -complex) have been evaluated, as well as the intermediates and transition states for the studied mechanism. An exhaustive screening of all the possible active sites of an EUO type zeolite has been as well performed. Furthermore, an experimental evaluation of the activity of zeolites EU-1 and ZSM-50 (both zeolites possess the EUO structure, but with different location of the acid sites) has been carried out for the ethylcyclohexane hydroconversion, so as to challenge the calculated features in terms of location of the most active sites. The supporting information of this chapter is enclosed in appendix IV.

This study is the subject of a publication just accepted in ACS Catalysis, which constitutes the essence of this chapter.





## Location of the Active Sites for Ethylcyclohexane Hydroisomerization by Ring Contraction and Expansion in the EUO Zeolitic Framework

*Ester Gutierrez-Acebo,<sup>1</sup> Jérôme Rey,<sup>1</sup> Christophe Bouchy,<sup>1</sup> Yves Schuurman,<sup>2</sup> Céline Chizallet<sup>1,\*</sup>*

<sup>1</sup>IFP Energies nouvelles, Rond-point de l'échangeur de Solaize, BP 3, Solaize, 69360, France

<sup>2</sup>Université Lyon 1, CNRS, UMR 5256, IRCELYON, Institut de recherches sur la catalyse et l'environnement de Lyon, 2 avenue Albert Einstein, F-69626 Villeurbanne, France

### ABSTRACT

Identifying the location of the active sites in a zeolite is a current challenge, impeding the design of optimal catalysts. In this work, we identify the location of the most active sites of 1-ethylcyclohexene isomerization in the EUO framework (10 MR channels, 12 MR side pockets), thanks to DFT calculations corroborated by experiments. Skeletal isomerization of cycloalkenes is a crucial industrial reaction for the bifunctional isomerization of ethylbenzene. Ethylcyclohexene is protonated by framework protons into cyclic carbenium ions, which undergo ring contraction-expansion reactions through protonated cyclopropane (PCP) like transition states. Ab initio calculations clearly show that the acid sites located at the intersection between the channel and the pocket stabilize much less the cyclic carbenium ions involved in the reaction than 12 MR pockets and 10 MR channel sites, due to stronger dispersion stabilizing interactions. This computational finding is fully confirmed experimentally by the comparison of the catalytic performances of the H-EU-1 and H-ZSM-50 zeolites in ethylcyclohexane hydroisomerization. Both zeolites possess the EUO structure, but with different location of the acid sites. The ratio in turnover frequencies is quantitatively rendered by the DFT calculated free energy profiles. Diffusion measurements reveal similar ethylcyclohexane diffusion times for the two zeolites, supporting that the difference in activity is primarily driven by the location of the active sites.

#### 4.1. Introduction

Zeolites are aluminosilicates very powerful as catalysts for a variety of reactions in refining, petrochemistry,<sup>4</sup> pollution abatement,<sup>194</sup> and also very promising candidates for biomass conversion.<sup>195</sup> Their crystalline nature and the large variety of structures makes possible the design of catalysts from structural considerations.<sup>196,197</sup> For acid catalyzed reactions, such as isomerization and cracking, the active sites are protons related to the aluminum atoms. A main challenge however consists in the identification of the precise location of the active sites of a given zeolite, as the local topology may strongly differ from one T site to another.<sup>198</sup> This is first of all due to the limited number of zeolites with more or less known location of aluminum atoms.<sup>196,199–207</sup> Then, even once the location is known, it is generally not unique so that identifying the precise location of the most stable intermediates and transition states is not straightforward. This is however a condition for the design of better catalysts. The case of the EUO framework is illustrative in that respect. This structure is composed of a monodimensional channel pore system (10 MR) with side pockets (12 MR). Two zeolites exhibiting this structure type, EU-1 and ZSM-50 were deeply investigated, in particular by neutron diffraction.<sup>208,209</sup> In the case of ZSM-50, the aluminum atoms are located mainly in the intersection between the channel and the pocket whereas in the case of the EU-1,<sup>208,209</sup> they are found either inside the pocket or in the channels. In contrast with EU-1, the synthesis of ZSM-50 at low Si/Al ratio is challenging.<sup>15</sup>

Naphthenes (cycloalkanes) are an important part of the feedstock converted in refineries and therefore, a matter of interest for oil industry. Nevertheless, their reactivity has not been deeply studied contrary to the case of paraffins. Naphthenes have a more complex reactivity than linear paraffins. This fact is due to the possibility of forming tertiary carbons by adding additional alkyl groups, and to the higher number of possible conversion pathways (including dehydrogenation into cycloalkenes, then isomerization, ring opening and cracking).<sup>22</sup> Typically, the most abundant naphthenic components in the hydrocarbons produced from oil are 5- and 6- carbon rings,<sup>22</sup> due to minimum tension in the ring compared to the 3 and 4 carbons rings. In petrochemistry, ethylbenzene hydroisomerization is of importance in the paraxylene production. Paraxylene is a highly sought-after product used in the manufacture of the terephthalic acid, employed for polyester production. Traditionally, this reaction employs a bifunctional catalyst<sup>9</sup> composed by a metal compound (responsible of the hydro/dehydrogenation function, HD/DHD) dispersed over an acidic support (isomerization and cracking function). The EU-1 zeolite is industrially used as acidic function for

ethylbenzene hydroisomerization.<sup>4</sup> The location of the active sites is an important question for this zeolite family, as the confinement effect is expected to differ significantly between the 10 MR channel, the 12MR side-pockets and the intersection between the channels and the pockets.

Ethylbenzene hydroisomerization over bifunctional catalysts involves the isomerization of ethylcyclohexenes over the Bronsted acid phase (the zeolite).<sup>52</sup> Reactions involving these cycloalkenes are expected to implicate carbocations. These cyclic carbenium ions can be isomerized by hydride shift, methyl shift and ring contraction expansion *via* protonated cyclopropane (PCP) steps.<sup>47–53</sup> The alkylnaphthenes rearrangements have been classified by Weitkamp<sup>49</sup> in two main categories: type A and type B isomerizations. In type A isomerization, the branching degree remains constant whereas in type B isomerization the branching degree is modified. Type A isomerization is considered to be faster than type B isomerization.<sup>22,49,191–193</sup> Molecular insight is strongly lacking for these reactions, regarding not only the relevant mechanisms if not as well, the intermediate / transition states involved and the quantification of their stability.

In the present work, we propose a Density Functional Theory (DFT) approach to determine these features in the EUO framework. We also aim at identifying the location of the most active sites for these reactions with the same approach, complemented with experimental comparison of the catalytic performances of the EU-1 and ZSM50 zeolites. Furthermore, some diffusion measurements have been performed in order to evaluate the possible influence of the diffusion in the catalytic performance.

The chosen reaction is the isomerization of ethylcyclohexene ( $\text{ECH}^-$ , obtained from the dehydrogenation of ethylcyclohexane (ECH), or the hydrogenation of ethylbenzene) into other branched substituted cycloalkenes. We showed experimentally<sup>210</sup> that a relevant apparent reaction pathway consists in the transformation of  $\text{ECH}^+$  (ethyl-cyclohexenium) into  $\text{EMCP}^+$  (ethylmethyl-cyclopentenium), then into  $\text{DMCH}^+$  (dimethyl-cyclohexenium) and finally into  $\text{TMCP}^+$  (trimethyl-cyclopentenium). Experimentally, many products are obtained (16 re-hydrogenated products, meaning an even higher number of alkene structures), belonging to the three EMCP, DMCH, TMCP families. It prevents, preventing the exhaustive computational investigation of the formation of all of them on all the sites of the zeolite. Thus, we decided to make a relevant choice so as to represent the three families of products. The reaction sequence selected here (Figure 1) takes into account members of each of the three families, focusing on tertiary carbenium ions, which are expected to be stable species.

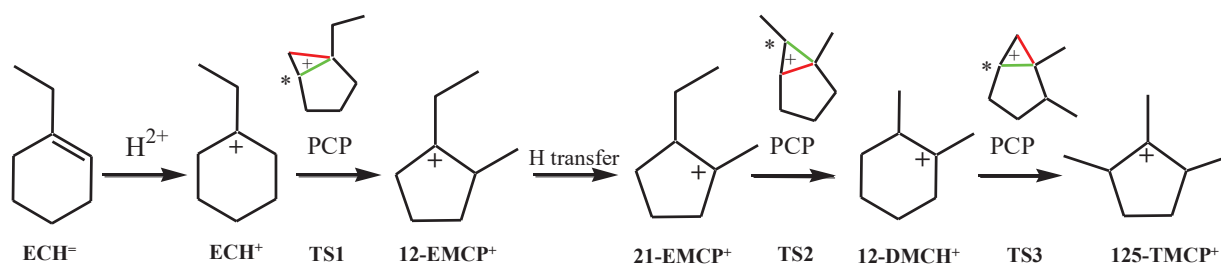


**Figure 1. One ethylcyclohexene isomerization reaction pathway, passing through tertiary carbocations. \* Hydrogen moving. The bond to be broken (in the forward direction) is depicted in red and the forming bond in green.**

For non-cyclic species it is not clear from experiments whether carbenium ions exist as free or adsorbed species inside the zeolite pores, or if they are covalently bonded to framework oxygen forming alkoxide intermediates (Figure 2). This depends on the zeolite but also on the nature of the olefin and the carbenium (substitution, delocalized nature).<sup>96</sup> From catalytic hydrocracking experiments, carbenium appears as the most probable intermediates.<sup>248, 249</sup>

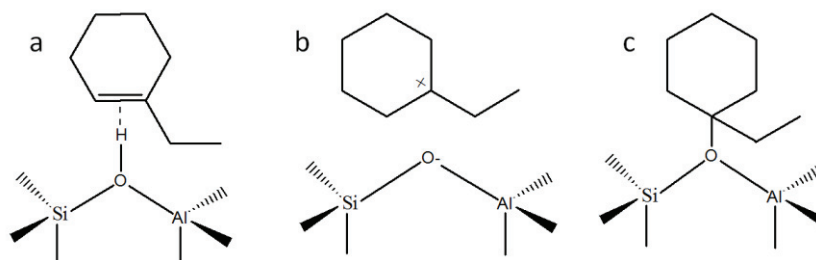


**Figure 2. Three possible forms for adsorbed 1-ethylcyclohexene at the bridging acid site of a zeolite: a)  $\pi$ -complex; b) carbenium, c) alkoxide.**

Earliest *ab initio* calculations used small clusters. These calculations indicated that adsorbed carbenium and carbonium ions (active intermediates of acid-catalyzed transformations of small hydrocarbons up to C<sub>4</sub>) on zeolites were not reaction intermediates. Indeed, they were the transition states of the alkene protonation elementary step, whose products were their corresponding alkoxides, avoiding charge separation.<sup>97,98</sup> The same conclusion was obtained for PCP species,<sup>211</sup> isolated as transition states only.

However, the steric constraints and electrostatic field provided by the zeolite framework play an important role which cannot be taken into account by very small clusters as the one used in the earliest studies. These factors are better considered by periodic approaches or by

big clusters simulations. Both factors can affect not only the stability of alkoxides, which is very sensitive to the local site geometry,<sup>103,105</sup> but also the stability of carbenium ions, sensitive to the electrostatic field intensity.<sup>99,115,212</sup> Depending on the level of theory (DFT-GGA *versus* DFT-GGA plus dispersion corrections *versus* hybrid functionals) and on the location of the Brønsted acid site (itself function of the considered zeolite framework), the carbenium species can however still be considered as transition states for the protonation of alkenes to alkoxides,<sup>99,105</sup> or as local energy minima, thus reaction intermediates.<sup>105,115</sup> Periodic studies of the isomerization through PCP species are very scarce. Demuth et al.,<sup>94</sup> focused on the isomerization of 2-pentene in H-ZSM-22. Huang et al. recently reported about hex-3-ene isomerization in H-ZSM-5.<sup>250</sup> The PCP was found as a transition structure, alkoxides being the reaction intermediates in both studies.

Higher level calculations, such as the hybrid MP2 calculations performed by Tuma et al.<sup>104</sup> revealed the tert-butyl carbenium ion as a reaction intermediate, which was not the case at the PBE level. Nonetheless, it was less stable as compared to the  $\pi$  complex and alkoxides. The consideration of thermal effects was also shown to affect the conclusions about the stability of carbenium ions as intermediates. Tuma and Sauer<sup>100</sup> took into account the influence of the temperature in the stability of the reaction intermediates and transition states, starting from periodic static DFT - PBE calculations. The carbenium appeared as the most stable species with respect to alkoxides when the temperature was raised over 120K. More recently studies from van Speybroeck et al.<sup>101,102</sup> compared static and molecular dynamic methods for measuring the stability of adsorbed butene and pentene in HZSM-5. By *ab initio* molecular dynamics at 323 K, linear alkoxides, alkene  $\pi$  complex and tertiary carbenium ions were found as the favored intermediates. Nonetheless, at 773K, secondary and tertiary alkoxides were not stable, contrary to the carbenium which was found as a stable intermediate.

To sum up, in spite of all the performed studies, the answer to the question if carbenium ions are reaction intermediates or transition states remains elusive. Very scarce are the studies devoted to reactions proceeding via PCP species. Moreover, whereas many work has been done about olefins chemisorption on acidic zeolites,<sup>92,94,99-105,115</sup> the reactivity of naphthenes was only very barely investigated by DFT. Some cyclic cations have been experimentally observed to be important long-lived intermediates in some reactions of hydrocarbons on zeolites.<sup>106,107</sup> A DFT study of the cyclohexene interaction in HZSM-5<sup>83</sup> revealed the formation of carbenium species instead of alkoxides as local energy minima. The bulkiness of

cyclic carbenium with respect to non-cyclic ones may indeed be a factor of easier stabilization of cyclic carbenium, preventing the approach to framework oxygen atoms.

Concerning the mechanism of ring contraction and expansion of cyclic olefins, over the acid sites, no DFT work has been published to date, to the best of our knowledge. Ring contraction-expansion reactions are also of interest in the Methanol to Olefin context, and were looked at by computational approaches, but the nature of the reaction intermediates and transition state differs as in MTO the starting points are protonated aromatics, whereas we start here from protonated cycloalkenes.<sup>251- 255</sup> As mentioned previously, the single periodic study of isomerization reactions through PCP concerned a non-cyclic short molecule, namely 2-pentene, in H-ZSM-22, at the GGA (PW91) level, by Demuth et al.<sup>94</sup> Note that the reactants and products were found in the form of alkoxides, and not carbenium ions, which may have had an influence on the reaction profile. The lower-activated (about 100 kJ.mol<sup>-1</sup>) mechanism proposal involved up to three different transition states (among which an edge-protonated PCP) and two intermediates (a secondary carbenium ion and a neutral dimethylcyclopropane DMCP).

Therefore, the objective of this study is to investigate the reactivity of the cycle contraction-expansion in the context of the ethylcyclohexene isomerization (itself obtained from the dehydrogenation of ethylcyclohexane), identifying the location of the most active sites of an EUO type zeolite for this reaction. To do so, first the stability of the different forms of the adsorbed reactant (carbenium, alkoxide and  $\pi$ -complex) have been evaluated, as well as the intermediates and transition states for the mechanism shown in Figure 1. An exhaustive screening of all the possible active sites of an EUO type zeolite has been as well performed (Figure 3). Furthermore, an experimental evaluation of the activity of zeolites H-EU-1 and H-ZSM-50 has been carried out for the ethylcyclohexane hydroconversion, to challenge the calculated features in terms of location of the most active sites. To complete this evaluation, Temporal Analysis of Products (TAP) experiments<sup>213</sup> of ethylcyclohexane in both zeolites H-EU-1 and H-ZSM-50 has been performed, to check if this parameter can also affect the difference between the two zeolites.

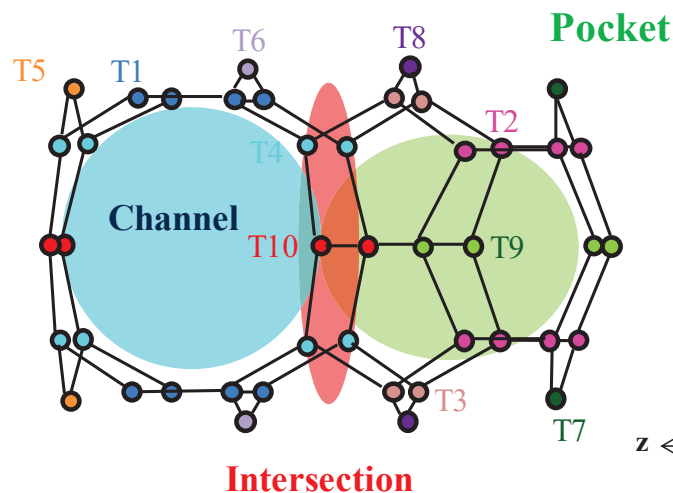


Figure 3. Section of the EUO framework structure showing the different active sites analyzed in this study: pocket -green zone (light green T9, dark pink T2, light pink T3, dark green T7, and dark purple T8), channel -blue zone (dark blue T1, orange T5, and light purple T6) and intersection between the pocket and the channel -red zone (red T10 and light blue T4) [1 0 0]. Adapted from ref.<sup>209</sup>. The oxygen atoms are not included and the silicon atoms are represented as colored circles.

## 4.2. Experiments and methods

### 4.2.1. DFT calculations

Periodic DFT calculations were performed with the PBE (Perdew, Burke and Ernzerhof) exchange-correlation<sup>153</sup> as implemented in VASP 5.3.<sup>214</sup> The projected augmented wave (PAW) method<sup>215</sup> was used to describe the core-electron interactions, and the plane wave basis set was limited to a kinetic cutoff energy of 400 eV except for the optimization of the cell dimensions, for which the cutoff was set at 800 eV. Van der Waals corrections as proposed within the D2 Grimme formalism<sup>154</sup> were applied. The convergence criterion for the electronic self-consistent field relaxation was fixed to  $10^{-7}$  eV. All calculations were performed at the gamma point.

The bulk cell parameters and ionic positions of EU-1 and ZSM50 (EUO type) were obtained from International Zeolite Association (IZA) database<sup>159</sup> and then reoptimized in the purely siliceous form with an increased energy cutoff of 800 eV (initial parameters from IZA:  $a = 13.3778$  Å,  $b = 13.3778$  Å,  $c = 20.5820$  Å,  $\alpha = \beta = 90^\circ$ ,  $\gamma = 62.6^\circ$ , parameters after optimization:  $a = 13.2189$  Å,  $b = 13.3266$  Å,  $c = 20.3045$  Å,  $\alpha = 90.0^\circ$ ,  $\beta = 89.9^\circ$ ,  $\gamma = 62.8^\circ$ ). The amount of aluminum atoms (together with a proton per Al) in the zeolite framework came



from a Si/Al equal to 15, commonly considered experimentally,<sup>5,210,216</sup> and representative of the EU-1 used in the present study. Since the primitive EUO structure cell possesses 112 T sites, the number of aluminum atoms needs to be between 3 and 4. As a matter of simplicity it has been chosen 3. In the beginning of the study two different cells with three different locations of the Al on each were investigated. The sites choice was basically considering the most different locations in the structure: the pocket, the channel, and their intersection. The sites are named from the number (IZA) of the T atom substituted by Al, and the number of the oxygen atom holding the proton. The first cell contains exchanged T10O12, T1O1, and T9O6 sites, whereas the second one contains exchanged T4O12, T1O2 and T9O20 sites. Afterwards, in order to test the other active T sites all the silicon atoms were successively substituted (Table S1), whereas the oxygen ones chosen were located in an accessible position. The relative stability of the aluminations configurations considered (Table S1) ranges over 44 kJ.mol<sup>-1</sup>, consistently with previous observations made on other frameworks.<sup>68,91,212</sup> Full geometry optimizations (zeolite plus hydrocarbons) of the reaction intermediates were performed using a conjugate gradient algorithm, with a convergence criterion on forces of 0.005 eV.Å<sup>-1</sup>.

The Nudged Elastic Band (NEB) method<sup>161</sup> was used to locate the transition states. The number of images to investigate reaction pathways between the reactant and the product is 8. To start with, an interpolation scheme involving both Cartesian and internal coordinates was used (Opt'n-Path developed by Paul Fleurat-Lessard).<sup>160</sup> We basically perform 50 NEB steps before optimizing the structure of highest energy image. The optimization consists in a quasi-Newton calculation,<sup>217</sup> sometimes followed by a Dimer calculation<sup>163,164</sup> if the quasi-Newton had difficulties to converge.

Harmonic frequency calculations were performed on optimized structures (all atoms of the cell moving) with a displacement of  $\pm 0.02$  Å around the equilibrium atomic positions. The objective of these calculations was double: i) to identify the true local energy minimum / saddle point nature of the optimized intermediates and transition structure, ii) to deduce vibrational free energies.

To achieve objective i), most of the time some refinements of the intermediate and transition structures had to be performed, to get zero (in the case of intermediates) or only one (in the case transition structures) imaginary frequencies, which is scarcely the case right after the Dimer or quasi-Newton optimizations, despite stringent convergence criteria. Line minimization methods were applied, thanks to algorithms developed by Tomas Bucko (Univ.

Bratislava).<sup>218</sup> The procedure is repeated until the configuration with a correct vibrational spectrum is identified (typically 1 to 6 repeated cycles are needed). An example of such a sequence is given in Supporting Information S1.

For each transition structure, the connection with the expected reactants and products was established thanks to the intrinsic reaction coordinate (IRC) approach. This concept has been introduced by Fukui<sup>165,219</sup> and was successfully applied within VASP in the case of hydrocarbon reactions in zeolites.<sup>218</sup> The IRC is the steepest descent path, starting from the transition state in the direction of the transition vector (corresponding to the imaginary vibrational frequency determined *via* vibrational analysis). Examples are given in Supporting Information S2. The algorithm stops if the energy increases over 20 successive steps. Structures identified at the end of the IRC were re-optimized with a convergence criterion on forces of 0.005 eV.Å<sup>-1</sup>.

The adsorption energy  $E_{\text{ads}}$  of all the considered species was calculated, using isolated ethylcyclohexene and the empty zeolite as references. For each of these species, the Gibbs free energy was then calculated according to the equations given in Supporting Information S3 by considering the rotational, translational, and vibrational degrees of freedom for gas-phase ethyl-cyclohexene and the vibrational degrees of freedom only for the zeolite models. The translational (and rotational) degrees of freedom were again decoupled from the vibrational one before estimating vibration partition functions.

#### 4.2.2. Catalyst preparation

Commercial zeolite EU-1 supplied by Zeolyst was obtained in the protonic form according to the procedure described in reference <sup>210</sup>. ZSM-50 was synthesized according to the protocol given in reference <sup>209</sup>. ZSM-50 was obtained in the protonic form as follows. The zeolite was first calcined in order to remove the dibenzyltrimethylammonium organic template. The calcination was done under an air flow (2 NL h<sup>-1</sup> g<sup>-1</sup>) at 150°C (1h), 250°C (1h), 550°C (1h), 650°C (1h), 750°C (1h) and finally at 800°C for 10 h. The zeolite was then exchanged with an ammonium nitrate solution and calcined with the same protocol used for EU-1.<sup>210</sup>

The H-EU-1 and H-ZSM-50 bifunctional catalysts were obtained by mixing 20% wt. of the corresponding zeolite with 80% wt. of alumina loaded with 1% wt. platinum. The experimental protocol is described elsewhere.<sup>210,209</sup> The mechanical mixtures were pelletized

with a hydraulic press, crushed, and sieved to obtain a pellet size between 350 and 500  $\mu\text{m}$  before catalytic tests. Main features of the two bifunctional catalyst are provided Table 1 .

**Table 1. Bifunctional catalysts used in this study.**

Metallic function	Acidic function	Catalyst composition	Catalyst name	$n_{\text{Pt}}$ ( $\mu\text{mol/g}$ )	$n_{\text{A}}$ ( $\mu\text{mol/g}$ )	$n_{\text{Pt}}/n_{\text{A}}$
1.05%wt Pt-Al <sub>2</sub> O <sub>3</sub>	H-EU-1	80%wt Pt-Al <sub>2</sub> O <sub>3</sub> / 20%wt HEU-1	1%Pt-Al <sub>2</sub> O <sub>3</sub> /HEU1	43	147	0.29
1.05%wt Pt-Al <sub>2</sub> O <sub>3</sub>	H-ZSM-50	80%wt Pt-Al <sub>2</sub> O <sub>3</sub> / 20%wt HZSM-50	1%Pt-Al <sub>2</sub> O <sub>3</sub> /HZSM50	43	106	0.42

\* micromoles of platinum surface sites per gram of catalyst, \*\* micromoles of Brønsted acid sites per gram of catalyst

### 4.2.3. Material characterizations

Zeolites were characterized by X-ray fluorescence to determine the global Si/Al molar ratio. XRF analyses were performed with a Thermo scientific ARL Perform'X. <sup>27</sup>Al magic angle spinning nuclear magnetic resonance (MAS NMR) was employed to determine the percentage of framework and extra-framework aluminum. NMR experiments were performed using a Bruker Ultrashield 400 MHz spectrometer equipped with a 4 mm CP MAS probe head at room temperature. The MAS rate was 12 kHz for all experiments, the sequence used for Al is a zg sequence and a delay time of 0.5 s. The number of Brønsted acid sites was calculated from these two techniques (number of Al<sup>IV</sup> considered to be equal to the number of Brønsted sites). For this calculation, Na residual presence, measured by atomic absorption spectroscopy (AAS) has been considered. Crystallinity was measured by X-ray diffraction (XRD) using a X'Pert Pro diffractometer from Philips Analytical, using a Cu K $\alpha$  radiation ( $\lambda = 1.5406 \text{ \AA}$ ). Diffraction profiles were scanned using the step mode over a  $2\theta$  range of 5–40°, in steps of 0.02° for six hours with a step time of 5 s at each point. Nitrogen adsorption measurements were carried out at -200°C on an automatic Micromeritics ASAP 2420 apparatus. Before adsorption, zeolite samples were degassed under vacuum at 500°C for 6 h. The total porous volume ( $V_{\text{total}}$ ) was calculated from the adsorbed volume of nitrogen at a relative pressure  $P/P_0$  of 0.98 whereas the microporous volume ( $V_{\text{micro}}$ ) was determined using the t-plot method.<sup>120</sup> The mesoporous volume ( $V_{\text{meso}}$ ) was obtained by the difference between  $V_{\text{total}}$  and  $V_{\text{micro}}$ .

Platinum dispersion on alumina was determined by hydrogen titration of chemisorbed oxygen (H<sub>2</sub>–O<sub>2</sub> titration) in a Gira Xisorb apparatus with a thermal conductivity detector. The samples were first calcined under air at 530°C for 2 h at 5°C min<sup>-1</sup>, then cooled down to room

temperature and purged with He. The first reduction with H<sub>2</sub> was done at 450°C for 2 h with a flow of 20 NmL min<sup>-1</sup>. After cooling down to room temperature and purging with He, 15 pulses with pressures from 0.5 to 60 kPa of oxygen were added until saturation occurred (oxygen titration). Another He purge was done before a second reduction with H<sub>2</sub> at room temperature. The number of platinum surface sites was calculated based on the platinum dispersion and the total amount of platinum measured by XRF.

#### 4.2.4. Catalytic tests

Ethylcyclohexane (ECH) hydroconversion tests were performed in a high-throughput catalytic test unit with sixteen fixed-bed downflow reactors. This test was performed at a total pressure of 11 bar absolute. The hydrogen to ethylcyclohexane molar ratio was set to 30, and the weight hourly space velocity (WHSV) was set to 2 grams of ethylcyclohexane per gram of catalyst per hour. The conversion was changed by changing the temperature in the 200-330°C range. For each temperature two gas chromatography (GC) analyses were performed in order to check the catalyst stability. Return points confirmed that catalyst deactivation was negligible during the test. ECH conversion, product selectivities, and turnover frequencies per acid site were calculated according to reference 210. Catalytic tests demonstrated that the chosen amount of platinum was sufficient to properly balance the zeolite.<sup>8,44</sup>

#### 4.2.5. Diffusion measurements

Temporal Analysis of Products (TAP) experiments were carried out to estimate the characteristic diffusion time of ethyl-cyclohexane inside EU-1 and ZSM-50 zeolites.<sup>213</sup> 6 mg of the zeolite sample (200 – 300 µm) was placed between two layers of quartz particles (200 – 300 µm). A thermocouple was placed inside the reactor close to the zeolite layer. The sample was heated to 400°C (10°C/min) under vacuum and kept for 30 minutes to desorb all water. Pulse experiments were then carried out between 150 - 250°C. At the end of the temperature cycle an experiment at 175°C was repeated to check if the sample had not changed. A mixture of 50% ethyl-cyclohexane and 50% Ar was used and the m/e of 55 and 40 were monitored. Single pulse experiments were performed with 10 pulses averaged to improve the signal over noise ratio. Data acquisition times amounted to 20 seconds with pulses rates of 0.04 Hz. Before the experiments the Knudsen regime was verified by changing the pulse intensity and normalizing the Ar data. The pulse size was below 5 nmol per pulse. Details on the modeling procedure of the data can be found in the SI section.

### 4.3. Results and discussion

#### 4.3.1. The adsorbed cycloalkene species: $\pi$ -complex *versus* carbenium *versus* alkoxide species

A systematic DFT study of the stability of adsorbed cycloalkenes involved in the reaction network was performed at the T10O12 site, located at the intersection between 12 MR pockets and the 10 MR channel of EU-1 (Figure 4). The carbenium species (including some chair and boat conformations) depicted in Figure 1 were considered, as well as the corresponding  $\pi$ -complexes. Some of the optimized structures are depicted in Figure 5. In all attempts to stabilize alkoxides, the optimization failed and provided the corresponding  $\pi$ -complexes. Considering that we were performing static calculations, this conclusion differs strongly from previous investigations performed at similar level of theory for non-cyclic alkoxide species.<sup>115,212</sup> This suggests that the rigidity of the cycle with respect to mobile alkyl chains is a factor that hinders species that are the closest to the framework (such as alkoxides). Performing a detailed AIMD analysis of the reaction network was beyond the scope of the present work, in particular due to the significant size of the cell and number of atoms (nearly 200 per cell<sup>o</sup>). Even though, we can anticipate that the stabilization of the carbenium species with respect to alkoxides will even be enhanced by a refined approach, as this was shown for non-cyclic species.<sup>101,102</sup>

Some secondary carbocations were as well analyzed and the results showed either a worse stability compared to the tertiary carbocations or the direct transformation into a tertiary carbocation by hydride shift during the geometry optimization.

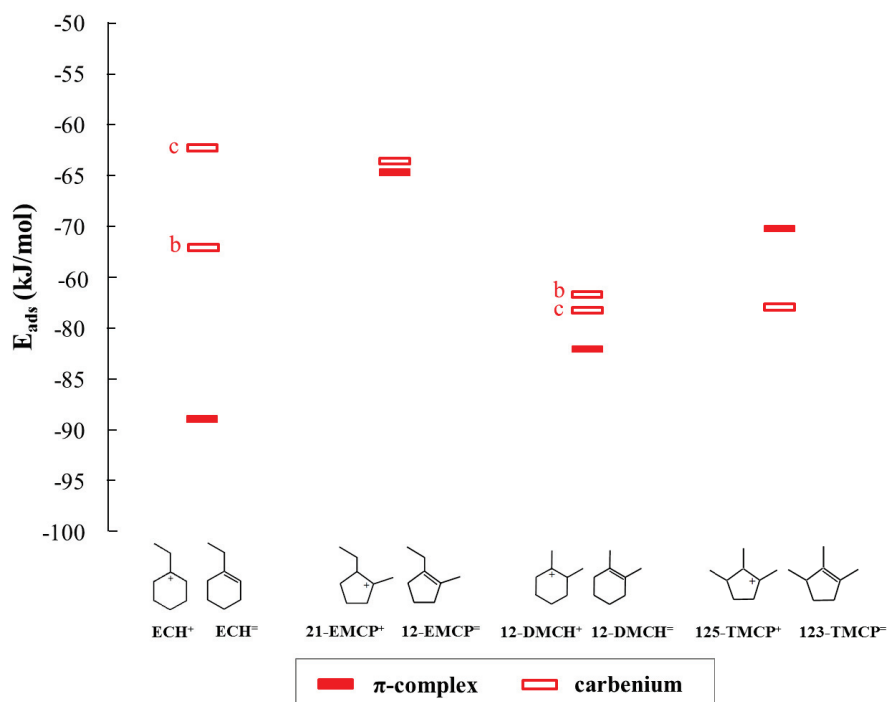


Figure 4. Adsorption energies for  $\pi$ -complexes and carbenium for the  $\text{C}_8$  species considered in the present work, at the T10O12 intersection Brønsted acid site. For  $\text{C}_6$  cycles, two conformations were considered: the chair conformation is noted “c” whereas a distorted boat one is noted “b”.

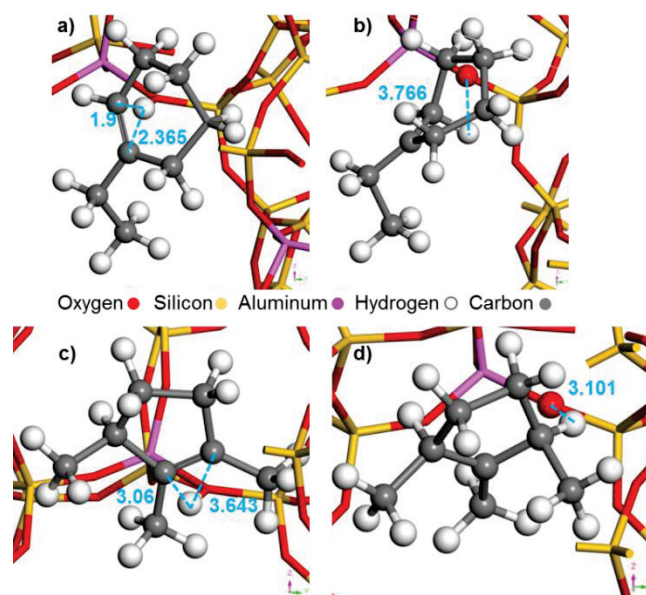


Figure 5. Structures of selected species at the T10O12 site, at the intersection between the channel and the side pocket: a)  $\text{ECH}^-$   $\pi$ -complex; b)  $\text{ECH}^+$  carbenium; c)  $123\text{-TMCP}^-$   $\pi$ -complex; b)  $125\text{-TMCP}^+$  carbenium. For  $\pi$ -complexes, the distance ( $\text{\AA}$ ) between the proton and the carbons belonging to the double bond is given. For carbenium ions, the distance ( $\text{\AA}$ ) between the hydrogen which left the zeolite and the corresponding oxygen is given.

The energy of the carbenium species did not vary too much as compared with the one of  $\pi$ -complexes. In the case of the ECH skeleton, the  $\pi$ -complex are at least 25 kJ/mol more stable than the carbenium regardless the conformation. For the carbenium, two configurations were investigated due to their relevance in further isomerization reactions (see later): chairs and distorted boats. The chair conformation is 10 kJ/mol more stable than the distorted boat conformation. 12-EMCP and 12-DMCH related carbenium and  $\pi$ -complexes, are very close in energy. In the case of 12-DMCH<sup>+</sup> chair and boat conformation energies were almost the same. Finally, for 123-TMCP, the  $\pi$ -complex was about 10 kJ/mol less stable than the carbenium.

In order to explain such relative energy differences, we performed structural analysis. The stability of the four  $\pi$ -complexes is directly correlated to the distance between the molecule and the zeolite framework: the closer to the framework, the more stable the  $\pi$ -complexes. The latter was quantified by the average distance between the framework proton and the carbons belonging to the C=C double bond (Figure 6 and Table S2). The ECH  $\pi$ -complex was more stable than the corresponding carbocation and also closer to the zeolite. For bulkier structures, such 123-TMCP, the  $\pi$ -complex is slighter higher in energy compared to the corresponding carbenium. The three methyl groups of this molecule are likely at the origin of a steric constraint to approach the framework.

However, such a correlation between stability and distance was not valid for carbenium species. For these species, some other correlations with the local electrostatic field were looked at, but did not reveal clear trends, contrary to previous findings for smaller hydrocarbons.<sup>115</sup> This suggests that the stability of these charged bulky species is a combination of several factors (likely electrostatics, van der Waals interaction, etc.) making simple descriptors irrelevant for the prediction of the nature of the most stable species at a given site in the zeolite.



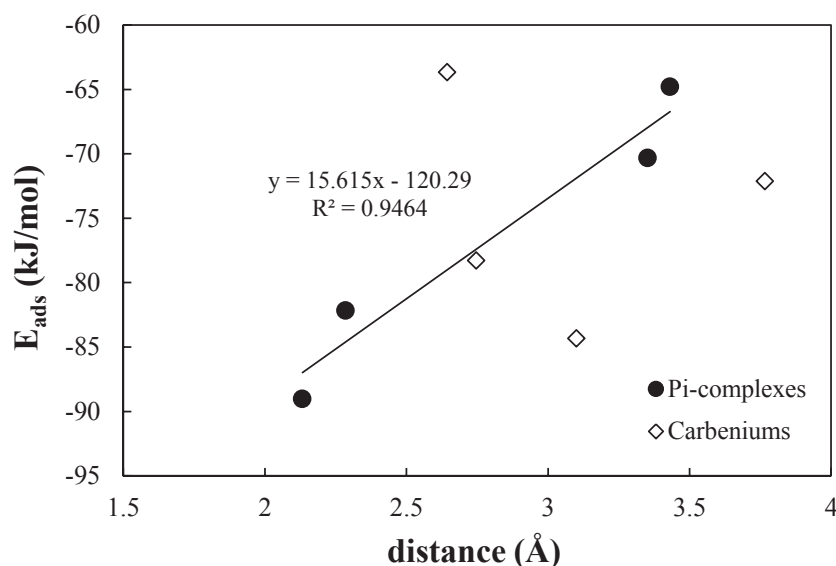


**Figure 6.** Correlation between adsorption energy and distance between pi-complex / carbenium ions and the zeolite framework at the intersection channel-pocket site (T10O12).

#### 4.3.2. Isomerization pathway at the T10O12 intersection site

At the T10O12 intersection site between the channel and the pocket, a full study of the ethylcyclohexene isomerization pathway including proton transfer, hydride transfer and cycle contraction-expansions (Figure 1) has been performed. Starting from 1-ethylcyclohexene (ECH=) the different isomers families considered were the ethylmethylcyclopentenium (EMCP+), dimethylcyclohexenium (DMCH+) and trimethylcyclopentenium (TMCP+). They were obtained via type B isomerization, expected to take place via PCP species.

A first proton transfer from the zeolite framework to the  $\text{ECH}^- \pi$ -complex is needed in order to start the isomerization reaction. This elementary step (via ts1) exhibits an energy barrier (Figure 7) around 15 kJ/mol and leads to a carbenium with a distorted chair conformation. A conformational change from a chair to a boat  $\text{ECH}^+$  has been found as necessary before any cycle contraction step. The energetic barrier corresponding to this conformational change (via ts2) is around 22 kJ/mol (Figure 7).

Then, the cycle contraction from  $\text{ECH}^+$  to the 12-EMCP<sup>+</sup> happens through a PCP (TS1), by a bond formation between carbons 1 and 2. The latter was obtained as a transition state, being an edge protonated cyclopropyl species (Figure 7 and Figure 8 a), with an energy barrier of 57 kJ/mol. In the course of the isomerization, the proton from carbon 2 moved to carbon 3 while the C1-C3 bond was broken. The skeleton of the transition state resembles that of the ring contraction-expansion intermediates in MTO,<sup>251-255</sup> with a three carbon cycle



connected by an edge to a five carbon cycle. However, due to different saturation levels (number of H atoms connected to each C atom on the rings), the spatial arrangement is very different as well as the charge delocalization.

Hydride transfer from the methyl to the ethyl of the 12-EMCP<sup>+</sup> is then required in order to start the next cycle contraction (via ts3). The energetic barrier of this step was found at around 12 kJ/mol. ts1, ts2 and ts3 structures are depicted in Figure S3. Then, it appears that the cycle contraction step is by far the most energy demanding step, as compared to proton and hydride transfers, and cycle conformation change. Thus, for the following steps, transition states for cycle contractions and expansions only were looked at.

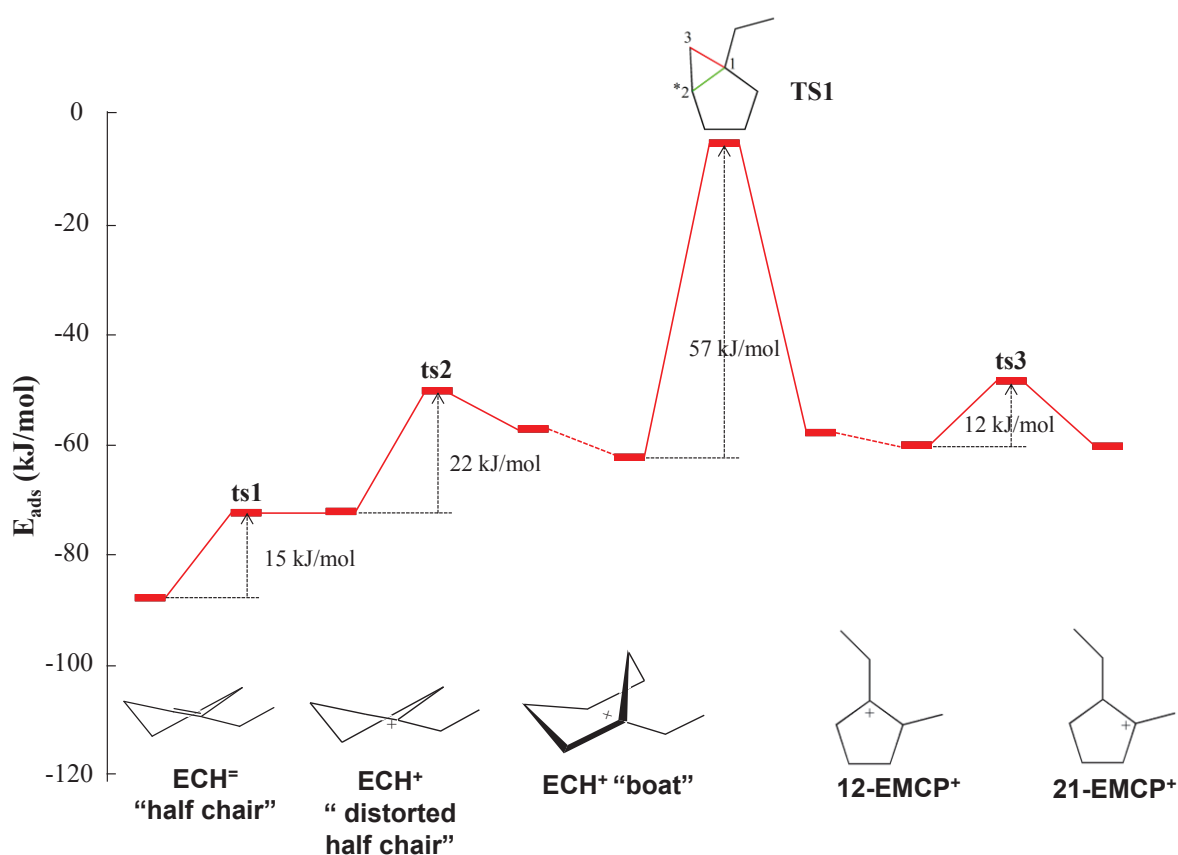


**Figure 7.** Energy profile at the T10O12 intersection site for the proton transfer, conformational change, first cycle contraction and hydride transfer reactions. Full lines represent the different intermediates with their corresponding TS whereas the dashed lines connect the same intermediates coming from different TS, i.e. obtained by two different IRCs. \* Hydrogen moving. The bond to be broken (in the forward direction) is depicted in red and the forming bond in green.

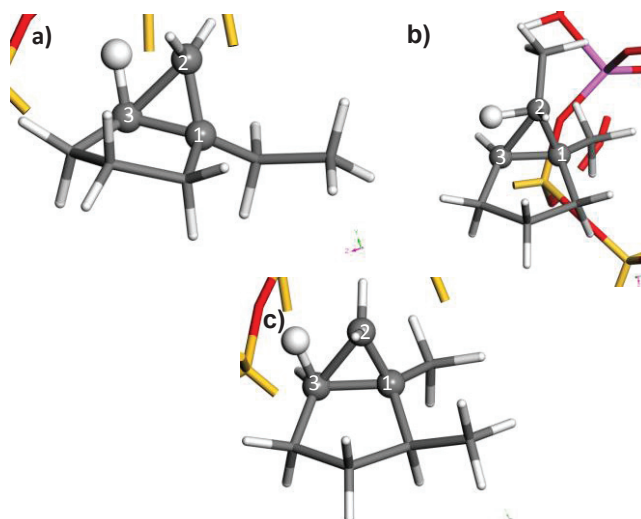


**Figure 8.** Different transition states at the intersection active site T10O12 a) TS1, b) TS2 and c) TS3. The carbons numbered are the ones corresponding to the PCP and the white ball corresponds to the Hydrogen atom moving between the reactant and the product. Same color code as Figure 5.

Figure 9 (red curve for the T10O12 site) depicts the energy barriers associated to the PCP transition states, corresponding to the different cycle contraction-expansion reactions. Each transition structure was connected to a reactant and a product from the IRC. Two consecutive TS should have had in common the species that is at the same time the product of the first step and the reactant of the next one. Due to small conformation changes, the energies of the two identical species obtained from the two IRCs may differ somehow, as depicted in two cases in Figure 7. In this case, we have reported the intermediate with the lowest adsorption energy hereafter.

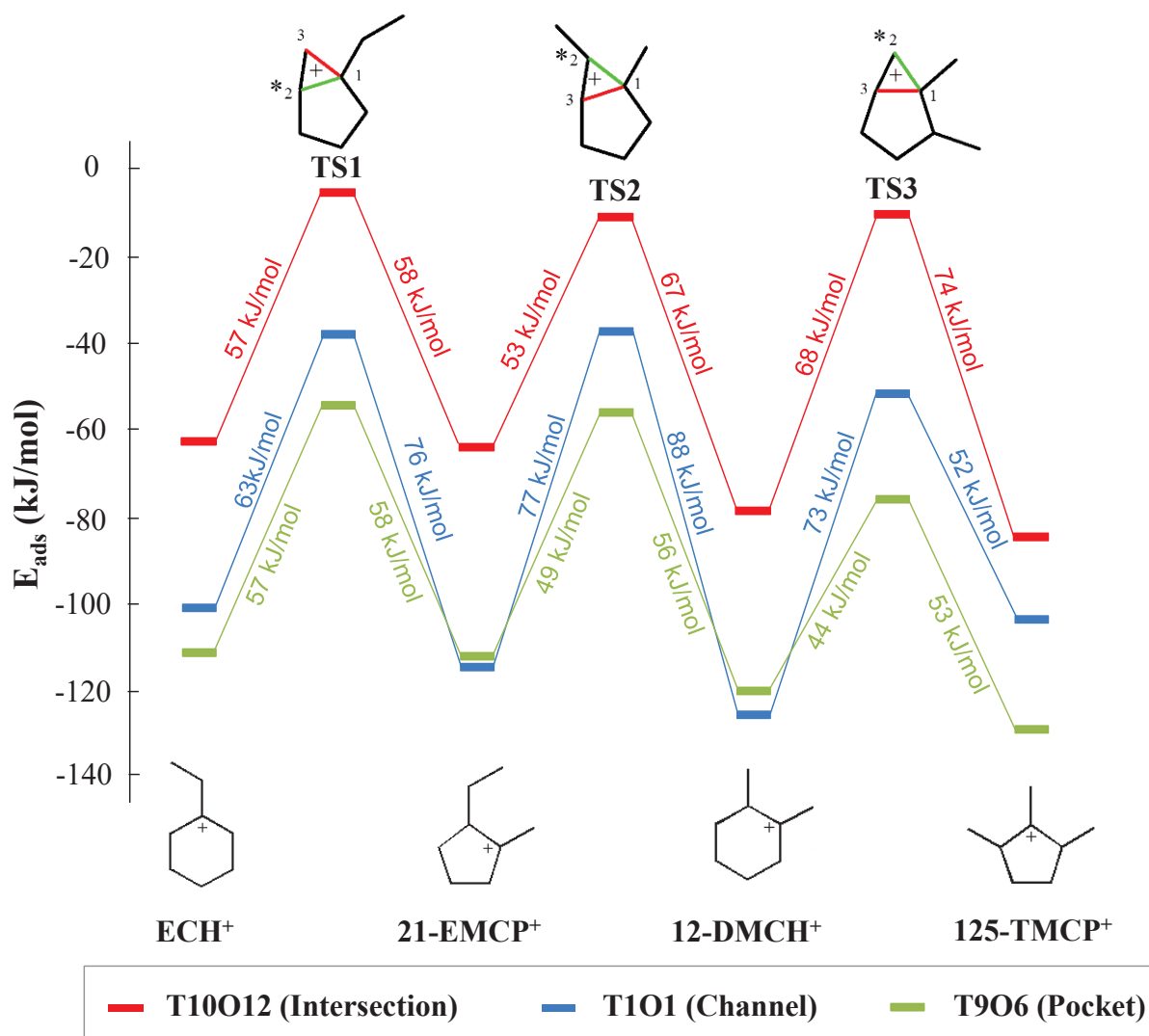


**Figure 9.** Energy profile for the cycle contraction-expansions through PCPs, at three sites of the EUO framework located at the 10 MR channel, the 12 MR pocket, and at their intersection. \* Hydrogen moving. The bond to be broken (in the forward direction) is depicted in red and the forming bond in green.

At this intersection site, the expansion from  $21\text{-EMCP}^+$  to  $12\text{-DMCH}^+$  exhibits a 53 kJ/mol energy barrier, very similar to the contraction barrier from  $\text{ECH}^+$  to  $12\text{-EMCP}^+$  (57 kJ/mol). The following contraction from  $12\text{-DMCH}^+$  to  $125\text{-TMCP}^+$  exhibits a barrier around 68 kJ/mol. All transition structures consisted in a cyclopentane with a PCP connected edge-to-edge with the cyclopentane, and containing one of the branches in one of their vertices. The distances between the atoms in the PCP exhibited close values for all the transition states (Table 2). TS2 is slightly different since the distance between  $\text{C}_2\text{-H}$  and  $\text{C}_3\text{-H}$  were inversed compared to the other transition states (see terminology in Figure 8). These similarities in distance, supports the close adsorption energies found for all of them, i.e. independently of the

contraction or expansion of the cycle. The TS are so close than the different energy barriers are led mainly by the energy differences of the intermediates and not by the TS themselves. Moreover, the transition states are not early nor late transition states.

**Table 2. Distances between atoms in the PCP for all optimized transition structures for contraction-expansion steps, at the T10O12 intersection active site. The imaginary frequencies for the transition structures are also given (one single imaginary frequency per transition structure).**

	Distance (Å)					fi (cm <sup>-1</sup> )
	C <sub>1</sub> -C <sub>2</sub>	C <sub>2</sub> -C <sub>3</sub>	C <sub>1</sub> -C <sub>3</sub>	C <sub>2</sub> -H	C <sub>3</sub> -H	
TS1	1.470	1.737	1.559	1.449	1.217	386
TS2	1.557	1.806	1.479	1.208	1.453	419
TS3	1.476	1.741	1.551	1.415	1.225	451

Demuth et al.<sup>94</sup> studied the 2-pentene isomerization in H-ZSM-22 with GGA/PW91 approximation by periodic calculations. Their most likely mechanism goes through an edge-protonated dimethylcyclopentane transition state (PCP type) similar to our TS. The energy barrier reported is 100 kJ/mol, higher than ours. Similarly, Huang et al.<sup>250</sup> report a barrier of 94 kJ mol<sup>-1</sup> for hex-3-oxide isomerization into 3-methylpent-2-oxide, also higher than ours. The difference is not unexpected as the reactant and products are considered as alkoxides in both studies, whereas in our case, carbenium ions are intermediates.

### 4.3.3. Comparison between the different active sites within the EUO framework

First, an analysis of the stability of TS2 and of the reactants (21-EMCP<sup>+</sup>) and products (12-DMCH<sup>+</sup>) connected to it, has been performed over all the possible active sites of the EUO type zeolite (Figure 3). This TS had the particularity that a methyl was linked to the carbon of the PCP edge that was not a part of the five-member ring. Figure 10 shows the energy profiles obtained for this reaction step. We failed in optimizing the transition state for two sites at the channel, T5 and T6, likely due to the difficulty of the protonated molecule to get close to the deprotonated active site, located in a poorly accessible area.

We first discuss the behavior of the sites located in the 12MR pocket. Significant differences in energy were found from one site to another, despite the structural similarities for the transition state in terms of C-C and C-H bond lengths (supporting information S4).

Nevertheless, the position of this TS in the pocket differs from one active site to another (Figure S7). The energy difference could be due to the different accommodation of the TS inside the pocket, i.e. if the PCP is oriented towards the exit of the pocket (channel) or to the bottom of the pocket and if the methyl- bonded to the edge-carbon oriented or not towards the active site. The species at T3 and T9 have similar low energies and their positions inside the pocket provided a similar local geometry for the accommodation of the TS: the PCP is oriented towards the channel and the methyl -bonded to the edge- carbon oriented in the opposite site of the active site (towards the channel). This is not the case of the other active sites.

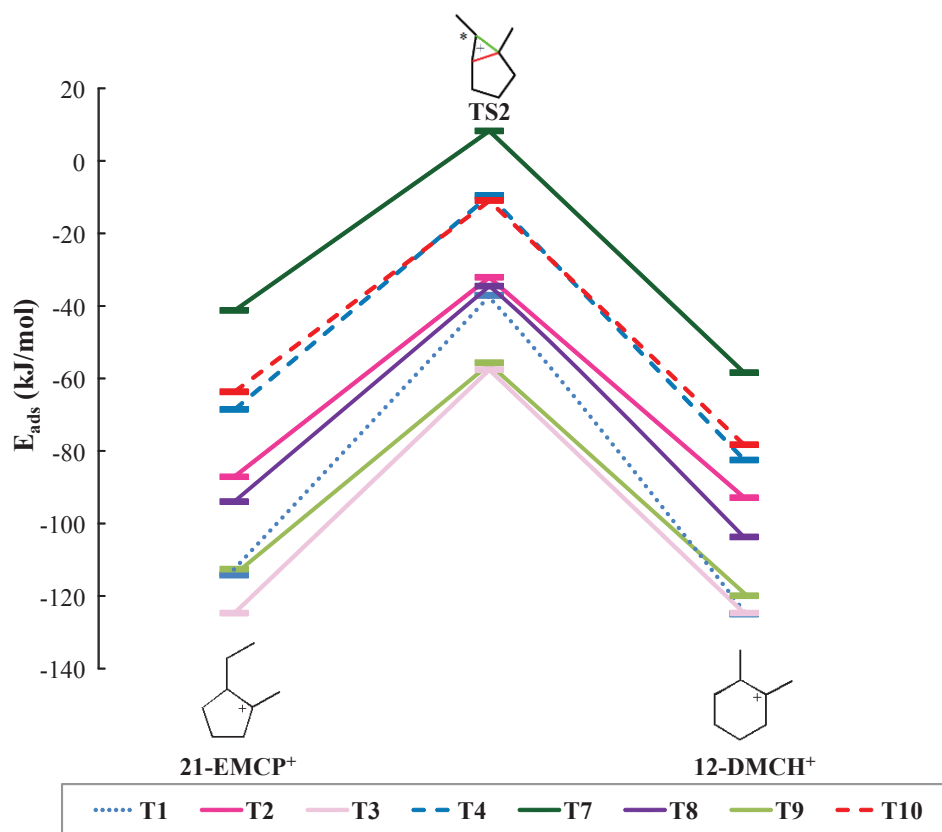


**Figure 10.** Energy profile for the expansions through the TS2 PCP at all the sites of the EUO type zeolite represented in Figure 3. Pocket sites: full lines, intersection sites: dashed lines, channel sites: dot lines. \* Hydrogen moving. The bond to be broken (in the forward direction) is depicted in red and the forming bond in green.

Regarding the sites located at the intersection, species located at T4 and T10 exhibited close energies, in line with their similar position at the intersection. The distance from the PCP to the active site position is however different in both sites as illustrated in Table S6, which seems to have no influence in the adsorption energy of the TS.

The T1 site was found as the single site able to stabilize the PCP in the channel, as explained previously. Comparing the stability of TS2 and the related reactants and products, the pocket exhibits the most stabilizing sites (T3 and T9), followed by the channel (T1), whereas the intersection had less favorable interaction with the cationic species (T4 and T10). Some other sites of the pocket (such as T7) did not stabilize much the intermediates. Comparing the barriers from one site to the other, there are rather close (varying from 50 to 77 kJ/mol forward and from 61 to 88 kJ/mol backward, table S7). Thus, in most cases what differs the most between the different active sites are the absolute energies of the intermediates and transition states, but not so much the energy barriers of this step. This reflects a strong site-dependent confinement effect, which does not strongly depend on the nature of the carbenium species (reactant, PCP transition state, product) for a given step.

Table 3 reports the dispersion contribution to the adsorption energy for the reactant, transition state and product of this reaction step. This contribution appears to be strongly negative in all cases, but much more at the pocket and channel sites (from -134 to -101 kJ.mol<sup>-1</sup>) than at the intersection sites (from -84 to -59 kJ.mol<sup>-1</sup>). However, the dispersion term does only slightly vary along the reaction pathway, which means that the strong energy differences between transition states and intermediates are held by non-dispersive term, due to the PCP nature of the TS.

**Table 3. Dispersion contribution to the adsorption energy of the 21-EMCP<sup>+</sup>, TS2 and 12-DMCH<sup>+</sup> species. Note that the no transition state was identified at the T5 and T6 sites.**

Site		E <sub>ads</sub> (disp) (kJ.mol <sup>-1</sup> )		
Al siting	zone	21-EMCP <sup>+</sup>	TS2	12-DMCH <sup>+</sup>
T1	Channel	-127	-124	-121
T2	Pocket	-113	-105	-105
T3	Pocket	-119	-112	-118
T4	Intersection	-59	-59	-61
T7	Pocket	-127	-106	-134
T8	Pocket	-101	-112	-121
T9	Pocket	-117	-111	-112
T10	Intersection	-75	-77	-84

Thus, the respective behaviors of the intersection versus the channel and pocket sites are well rendered by the dispersion interaction. For the molecules considered, these make the intersection site disfavored with respect to the two other kinds of sites. This is in agreement with the notion of confinement effect, which variation according to the local topology is often

considered to be of van der Waals origin,<sup>32</sup> and with previous computational work addressing the comparison of the stabilization of various hydrocarbons in various zeolites.<sup>256-258</sup>

We extended the comparison of various active sites to the whole reaction pathways, taking into account only the cycle contractions and expansions, and selecting one favorable site per location: one in the channel (T1O1), one in the pocket (T9O6), one at the intersection (T10O12, already investigated in section 3.2). The energy profiles are reported in Figure 9. They confirmed the much higher stability of species at the pocket and the channel as compared to the intersection, regardless the reaction intermediates and the transition states. A slight difference in terms of energy for intermediates (2-11 kJ/mol) is observed between the channel and the pocket sites, except the 125-TMCP<sup>+</sup> which was clearly more stable in the pocket than in the channel (25 kJ/mol). All transition states are lower in energy in the pocket than in the channel (16-24 kJ/mol). Similar as for TS2, the dispersion contribution to the adsorption energy was extracted for the three sites along the hole reaction pathway (Table 4). The same feature is revealed, suggesting that the dispersion interactions are favoring the pocket and channel sites versus the intersection site. Note however that along a given pathway at a given site, the dispersion contribution is not a sufficient feature to anticipate the stability of the ionic species considered, as shown in section 3.1. This is in agreement with previous findings devoted to the investigation of various non-cyclic carbocations.<sup>92,99,115,212,256-259</sup>

**Table 4. Dispersion contribution (kJ.mol<sup>-1</sup>) to the adsorption energy of all the species considered in the pathway, for selected sites at the intersection, channel and pocket zone in EUO.**

Species	Site		
	T10O12 Intersection	T1O1 Channel	T9O6 Pocket
ECH <sup>+</sup>	-66	-113	-136
TS1	-61	-118	-141
21-EMCP <sup>+</sup>	-75	-127	-117
TS2	-77	-124	-111
12-DMCH <sup>+</sup>	-84	-121	-112
TS3	-73	-127	-149
125-TMCP <sup>+</sup>	-76	-121	-150

These observations generalize our findings made before in the case of TS2 tested at all the active sites, even if the step corresponding to TS2 is not the rate-determining one for all sites. Indeed, it appears that the main differences between the three investigated acid sites is not the precise respective energy of TS1, TS2 or TS3, but the absolute energy levels of all the species (close to 50 kJ/mol in difference between the pocket and the intersection site). The

origin of this is found to be the dispersion interaction term between the intermediates/transition states and the zeolite. Moreover, the maximal forward barriers are slightly lower for the pocket (57 kJ/mol) as compared to the other sites (73 kJ/mol in the channel and 68 kJ/mol at the intersection).

All these results suggest that the most probable active site for carrying out the reaction is the one located in the pocket. Thanks to an optimal confinement effect, this site stabilizes all intermediates and transition states, affecting only slightly the barriers of each elementary step. An impact on the macroscopic kinetic feature is thus expected on apparent activation energies, but mainly due to adsorption terms. Note also that we can retrospectively consider that the protonation barriers (such as the one investigated in section 3.2.) will not be strongly different from one site to another, and will thus stay negligible with respect to the contraction-expansion barriers.

#### **4.3.4. Gibbs free energy profiles**

The Gibbs free energy profiles at 277 °C, calculated according to the methods exposed in section 2 and Supporting Information S3, are depicted in Figure 11, for the T10O12, T9O6 and T1O1 sites. This temperature was chosen as it is a central temperature in the present experimental investigation (see later, section 3.4).



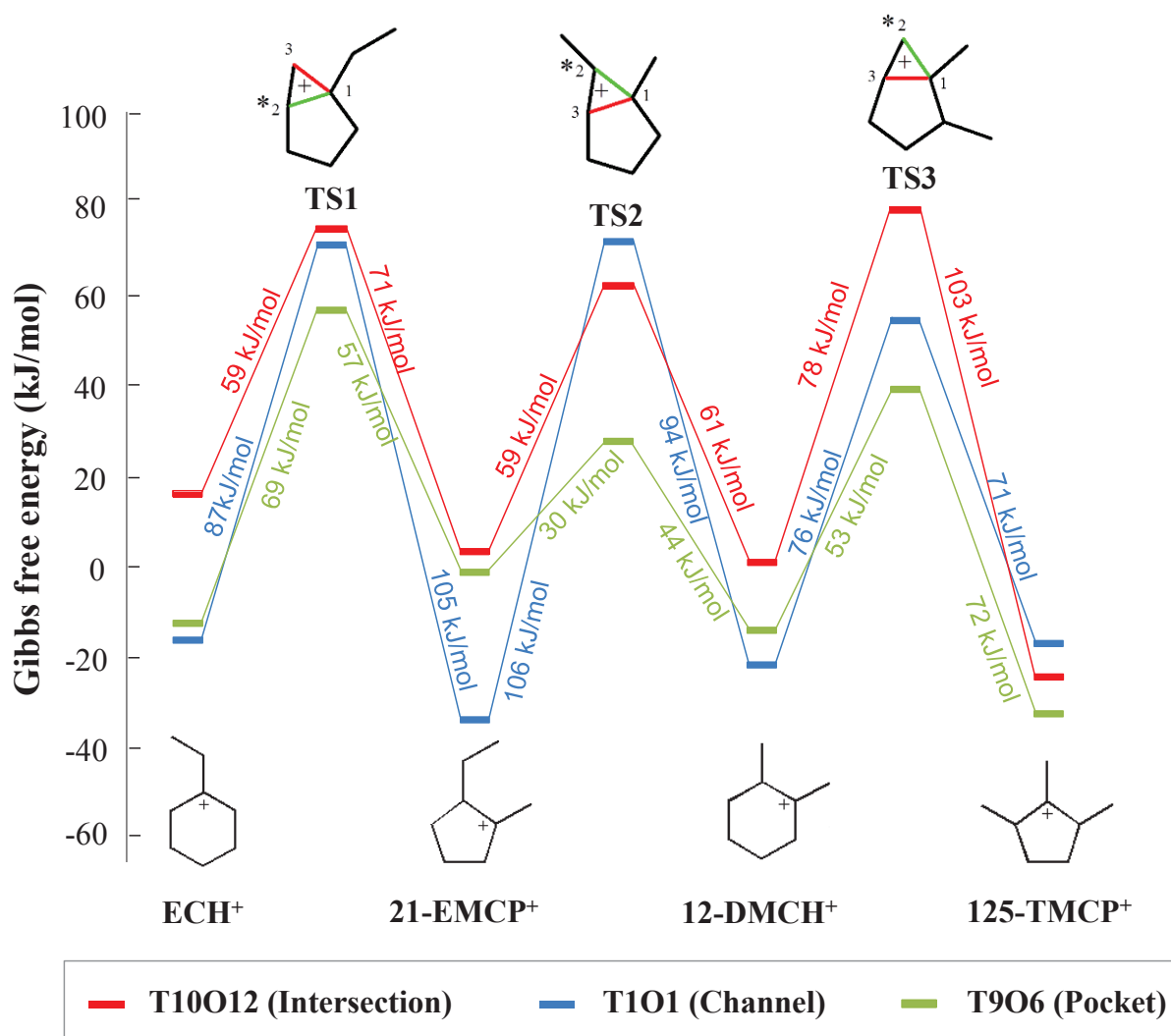


Figure 11. Adsorption Gibbs free energy profiles at the pocket (green), the channel (blue) and the intersection (red) at 277°C. \* Hydrogen moving. The bond to be broken (in the forward direction) is depicted in red and the forming bond in green.

Whereas most energies are negative (Figure 10), entropy contributions lead to positive values of free energies for transition structures, as well as for some of the intermediates. The shape of the profiles is also affected: the Gibbs free energy profile reveals again the pocket as the most favorable site whereas the channel exhibits much higher Gibbs free energy barriers. The intersection remains a noncompetitive site with respect to the pocket and channel sites. Table S7 includes all the Gibbs energies for all the intermediates and TS. Table S8 gives all the activation data estimated from the DFT calculations.

In the case of the free energy profile at the pocket site intrinsic energy barrier to pass from ECH<sup>+</sup> to TS1 is 69 kJ/mol (Figure 11). In the case of the intersection site, this barrier is of 59 kJ/mol. Thus, the intrinsic activation free energy difference between the two sites is

expected to be close to 10 kJ/mol, for the consumption of the reactant. If we consider the apparent activation free energies for the first step, the adsorption free energy of the reactant has to be removed. At the pocket site, the apparent activation free energy is close to 56 kJ/mol, while at the intersection it is 74 kJ/mol. The difference is then 18 kJ/mol.

#### 4.3.5. Experimental characterization and catalytic evaluation of the EU-1 and ZSM-50 zeolites

XRD characterization confirmed that both solids are well crystallized and corresponded to EU-1 and ZSM-50 respectively (Supporting Information S6). The physicochemical properties of the zeolites in the protonic form are provided Table 5. The very low amount of Na compared to framework Al (less than 4% molar) demonstrates the efficiency of the ammonium exchange. For both zeolites, the percentage of extraframework aluminum was the same, 9%, according to  $^{27}\text{Al}$  NMR. The total amount of Brønsted acid sites per gram is 1.5 time higher for the HEU-1 zeolite. This is a consequence of the lower Si/Al molar ratio of HEU-1 compared to HZSM-50. Microporous volume is comparable. However, the external surface area and the mesoporous volume of the H-EU-1 are substantially higher compared to HZSM-50. The high H-EU-1 external surface area and the significant mesoporous volume are induced by the agglomeration of round nano crystals (30-60 nm) as revealed by SEM analysis (Supporting Information S6). Such phenomenon was reported for other zeolites such as Beta<sup>220</sup> or IZM-2.<sup>135</sup> H-ZSM-50 particles are much bigger rods (several nm of length and 200 nm of thickness).

**Table 5. Physicochemical properties of the H-EU-1 and H-ZSM-50 zeolites**

Sample	$S_{\text{BET}}$ ( $\text{m}^2 \text{g}^{-1}$ )	$S_{\text{ext}}$ ( $\text{m}^2 \text{g}^{-1}$ )	$V_{\text{micro}}$ ( $\text{mL g}^{-1}$ )	$V_{\text{mes}}$ ( $\text{mL g}^{-1}$ )	(Si/Al) <sub>g</sub> (mol/mol)	Na/Al <sup>IV</sup> (%)	Al <sup>IV</sup>	$n_{\text{A}}$ ( $\mu\text{mol/g}$ )
H-EU-1	438	75	0.14	0.19	18	0.3%	91%	807
H-ZSM-50	356	28	0.13	0.05	29	3.9%	91%	581

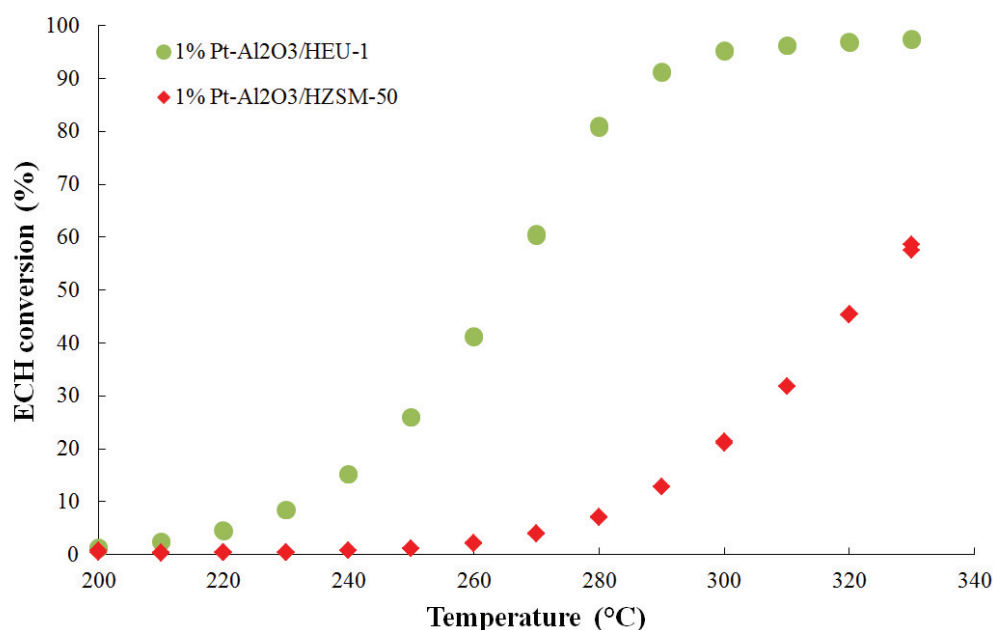
$n_{\text{A}}$ : calculated with % weight Al, % Al<sup>IV</sup> from NMR and corrected for the residual Na content

Figure 12 represents the evolution of the ECH (ethylcyclohexane) conversion as a function of the temperature for both zeolites H-ZSM-50 and HEU-1. The H-EU-1 zeolite is significantly more active than the H-ZSM-50 zeolite on a weight basis. Comparable level of ECH conversions could be obtained for temperature typically 70°C lower with H-EU-1. The different amount of Brønsted acid sites per gram for the two zeolites cannot account for such

difference. For instance, at 270°C the turnover frequency per acid site equals 0.03 s<sup>-1</sup> for HEU-1 and 0.002 s<sup>-1</sup> for HZSM-50. Thus, the acid sites in HEU-1 are on average, fifteen times more active than those in HZSM-50. This represents a difference in apparent activation free energy of 12 kJ/mol. Applying the Eyring's equation,<sup>168</sup> one can deduce the link between the ratio of TOFs  $\frac{TOF_{H-EU-1}}{TOF_{H-ZSM-50}}$  and the difference in apparent activation free energy between the two materials  $\Delta_r G_{HEU-1}^{\ddagger} - \Delta_r G_{HZSM-50}^{\ddagger}$  (eq.1).

$$\frac{TOF_{H-EU-1}}{TOF_{H-ZSM-50}} = e^{-\frac{\Delta_r G_{H-EU-1}^{\ddagger} - \Delta_r G_{H-ZSM-50}^{\ddagger}}{RT}} \quad \text{Eq.1}$$

This represents a difference in apparent activation free energy of  $\Delta_r G_{H-EU-1}^{\ddagger} - \Delta_r G_{H-ZSM-50}^{\ddagger} = -12$  kJ/mol.



**Figure 12. Ethylcyclohexane conversion versus temperature for the HEU-1 and for the HZSM-50 zeolites.**

At this stage, the extremely higher turnover frequency per acid site observed for H-EU-1 compared to H-ZSM-50 could be explained either by the different location of the active sites for the two zeolites or by increased diffusional limitations for H-ZSM-50 induced by its bigger crystallites size. Indeed, diffusion limitations were indeed assigned an important role in the hydroconversion of n-heptane in H-EU-1.<sup>60</sup>

In order to evaluate the possible diffusional limitations, TAP experiments were carried out. Figure S1-S2 compares the experimental and model normalized TAP pulse responses for

ethyl-cyclohexane over H-ZSM-50 and H-EU-1 as a function of temperature. As shown in the figures, an adequate description of the experimental data was obtained by the model. Table S1 lists the parameter estimates from the TAP data. Rather similar adsorption enthalpies were found for both zeolite samples, as expected for zeolites with similar structures. The characteristic diffusion times are, on the other hand, different for the two zeolites. At equal crystallite sizes, the diffusion of ethyl-cyclohexane inside the micropores of H-ZSM-50 is faster than for H-EU-1 at 175°C. However, when the values are extrapolated to the reaction temperatures applied in this study, the characteristic diffusion times become similar for both zeolites, due to the difference in activation energy for micropore diffusion. The difference in catalytic performance between the two zeolites can thus not be attributed to transport phenomena.

Thus, the location of the active site remains to explain the difference in performance between the two zeolites. It is known from literature that the active sites of the EU-1 are located in the channel and in the pocket whereas in the ZSM-50 are located in the intersection.<sup>208,209</sup>. Thus, in full consistence with our *ab initio* calculations, the zeolite possessing active sites in the channel and in the pocket (EU-1) is much more active than the zeolite possessing active sites in the intersection (ZSM-5). The free energy difference of 12 kJ/mol between the two zeolites, given by the ratio of turnover frequencies, is in excellent agreement with the computational estimation of 10 kJ/mol, according to the difference in intrinsic activation free energy for the first step of the reaction (section 3.4). Considering apparent activation free energies, the difference was estimated at 18 kJ/mol, also close to the experimental value of 12 kJ/mol. This makes our conclusions based on DFT calculations even stronger, regarding the difference in activity of both samples, as a tracer of the difference in confinement effect between the side pockets and the channel. Note that the uncertainty of DFT calculations may be higher than 10 kJ/mol, making the estimation of difference in computed activation free energy approximate. However, the fact that the order of magnitude is the same make us confident in the conclusion.

Hence, this work suggests that DFT calculations of such reaction pathways is a relevant method for determining the location of the active sites. It also provides new insights in the mechanism of cyclic alkene transformations by Brønsted acid catalysts, which was never investigated at the atomic scale in the past.

#### 4.4. Conclusions

In the present contribution, the location of the most active sites (for ethylcyclohexene isomerization, within the ethylcyclohexane hydroconversion bi-functional framework) within a given zeolitic framework (EUO) is elucidated by DFT calculations, and confirmed experimentally by the experimental catalytic evaluation of two zeolites (EU-1 and ZSM50) depicting this framework but with different positions of the Brønsted acid sites. The active sites in the EU-1 zeolite are mainly found inside 12MR side-pockets and in 10MR channels, whereas in the ZSM-50 zeolite they are located at the intersection between the channel and the side-pocket. The DFT evaluation of the stability of intermediates and transition states revealed the intersection between the channel and the pocket as the most unfavorable active site for the reaction. On the contrary the side pocket is found as the preferred place for the reaction to happen. The origin of the differences was found to be mainly the dispersion interactions between the intermediates/transition states and the zeolite. These results were as well confirmed by the calculation of the Gibbs adsorption energy profile. Consistently, in the experimental hydroconversion of ethylcyclohexane HEU-1 shows an activity fifteen times higher than HZSM50. This difference in activity could be attributed either to diffusional limitations or to the active site location. However, TAP experiments revealed that the difference in catalytic performance between the two zeolites can thus not be attributed to transport phenomena. Hence, the difference of activity can be attributed to the different active sites location. The experimental difference in activation free energy for the two solids very nicely matched the value computed by DFT.

This study also provides detailed computational information about the reaction network for the bi-functional isomerization of naphthenes. The transition structures are PCP-like, the cyclopropane being connected edge-to-edge to a cyclopentane unit. A typical feature of the transition states is the presence of an edge proton, migrating along the cycle contraction-expansion step. This work opens the door to the computational design of zeolitic catalysts from ab initio investigations.

## 5. KINETIC STUDY and KINETIC MODEL

### 5.1. Introduction

In this chapter, the target is to build a microkinetic model from ab initio calculations, to be compared with experiments, so as to get a deep knowledge of the reaction mechanism and identify kinetically relevant intermediates and steps. With this purpose, the general mechanism and the isomerization and ring opening mechanisms have to be deeper analyzed by mean of an experimental kinetic approach, to investigate in more detail the composition of the isomerization and ring opening products lumps. Besides, a deep knowledge of the mechanism is pursued by ab initio calculations which allow to calculate the rate constants of some key steps of the reaction. Including these rate constants in the microkinetic model, a correlation between the experimental and modelled data has been sought for describing the global and the isomerization mechanisms.

### 5.2. Experimental kinetic study on the ECH hydroconversion

In chapter 3, we investigated the reactivity of ethylcyclohexane on platinum-HEU-1 bifunctional catalysts, by changing the reaction temperature to vary the conversion. The apparent reaction and isomerization schemes deduced from the experimental are depicted in Figure 5.1.

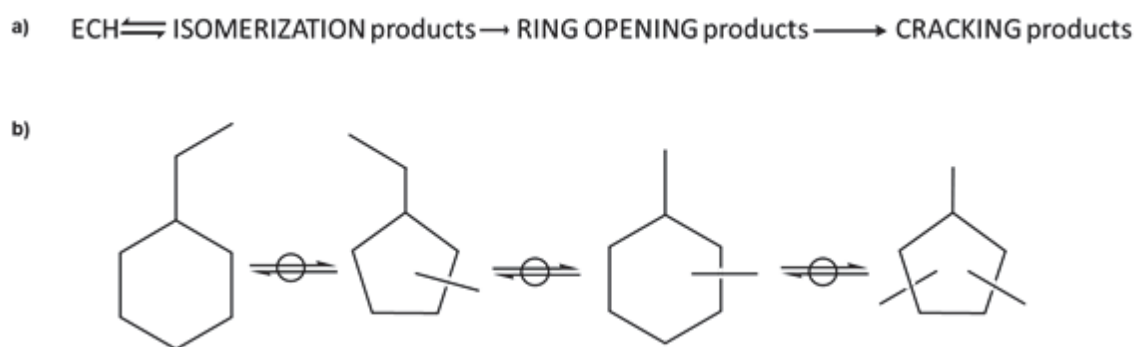


**Figure 5.1. Apparent reaction scheme (a) and apparent isomerization reaction scheme (b).**

Whereas in chapter 3, the conversion and selectivity were changed for a given contact time by changing the reaction temperature, in this chapter the evolution of the conversion and selectivity vs the contact times at some given temperatures was measured. The target was to study deeper the kinetics of the reactions taking place. With this purpose, the reference catalyst 1% Pt/Al<sub>2</sub>O<sub>3</sub>-HEU-1 was employed. The goal of the present work is: (i) to confirm

the apparent mechanisms proposed by a more rigorous kinetic investigation; (ii) to investigate in more detail the composition of the isomerization and ring opening products lumps.

### 5.2.1. General features

In this test, for three given temperatures the conversion is varied by changing the ECH contact time. Total pressure (10 bar) and hydrogen to ECH molar ratio (40 mol/mol) are kept constant. Periodically the catalyst is tested again at the initial operating conditions in order to test the catalyst stability. The deactivation during all the test is found to be negligible. As expected, and depicted in Figure 5.2. the higher the contact time, the higher the conversion. The same trend is observed with regards to the temperature, the higher the temperature, the higher the conversion. Nevertheless, ring opening and cracking selectivities do not change with the temperature for a given conversion (Appendix V). The isomerization and dehydrogenation selectivities change slightly for a given conversion when the temperature is increased: isomerization selectivity decreases whereas dehydrogenation selectivity increases. This subtle change in isomerization and dehydrogenation selectivities is explained by the fact that at higher temperatures, the equilibrium is more displaced towards the dehydrogenation products. Then, the loss of isomerization selectivity results in a gain on the dehydrogenation selectivity (dehydrogenation of the isomerization products). As these changes remain marginal, the evolution of the products selectivities with conversion are represented for a single temperature, 285°C (Figure 5.3).

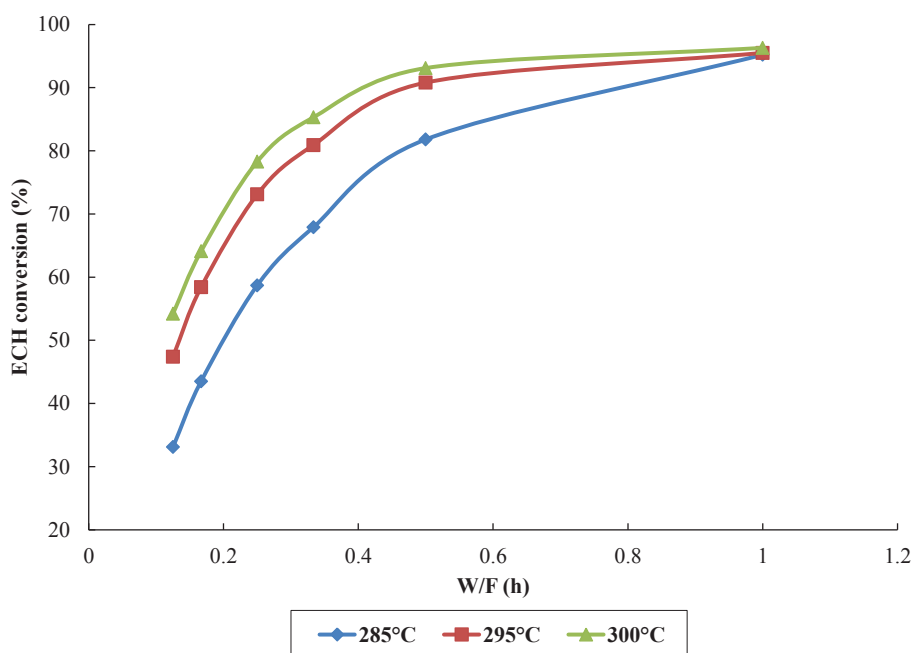


**Figure 5.2.** ECH conversion vs ECH contact time (catalyst mass divided by the ECH mass flowrate) at different temperatures for the 1% Pt/Al<sub>2</sub>O<sub>3</sub>–HEU-1 catalyst.

Figure 5.3. confirms that the primary products are the isomerization ones since they are the only products appearing at low ECH conversion. The ring opening and dehydrogenation products are almost inexistent, whereas the amount of cracking products increases as the contact time increases. This confirms the apparent reaction mechanism proposed in Chapter 3. The very low amount of ring opening products is due to the fact that they are immediately transformed in cracked products. Thus, we confirm the apparent reaction scheme depicted in Figure 5.1.(a). The ethylcyclohexane is easily transformed into the different isomers which are then opened as the contact time increases and very quickly thereafter the ring opening products are cracked.



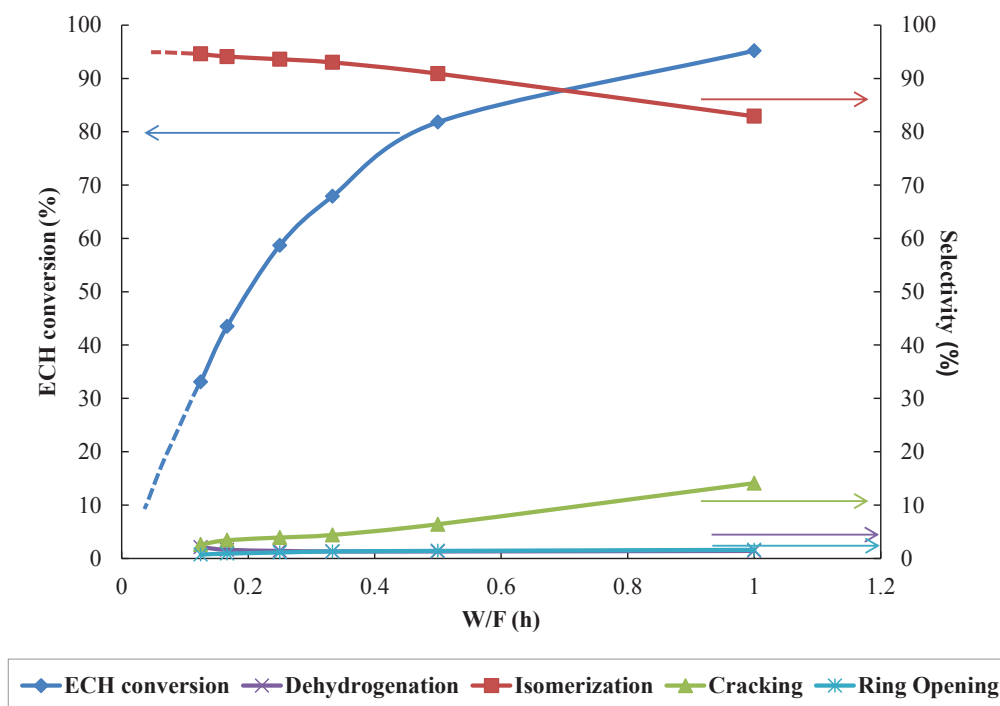


**Figure 5.3.** ECH conversion and selectivity vs contact time (catalyst mass divided by the ECH flow) at 285°C for the 1% Pt/Al<sub>2</sub>O<sub>3</sub>–HEU-1 catalyst.

### 5.2.2. Focus on the isomerization kinetics

In order to study the isomerization kinetics, the evolution of the isomers lumped in their different families (chapter 2 table 2.5) is monitored experimentally at different ECH conversions (varying the contact time) at 285°C.

The trend of the curves represented in Figure 5.4. is fully compatible with the apparent isomerization reaction scheme for the ECH isomerization proposed in chapter 3 and depicted in Figure 5.1.b).

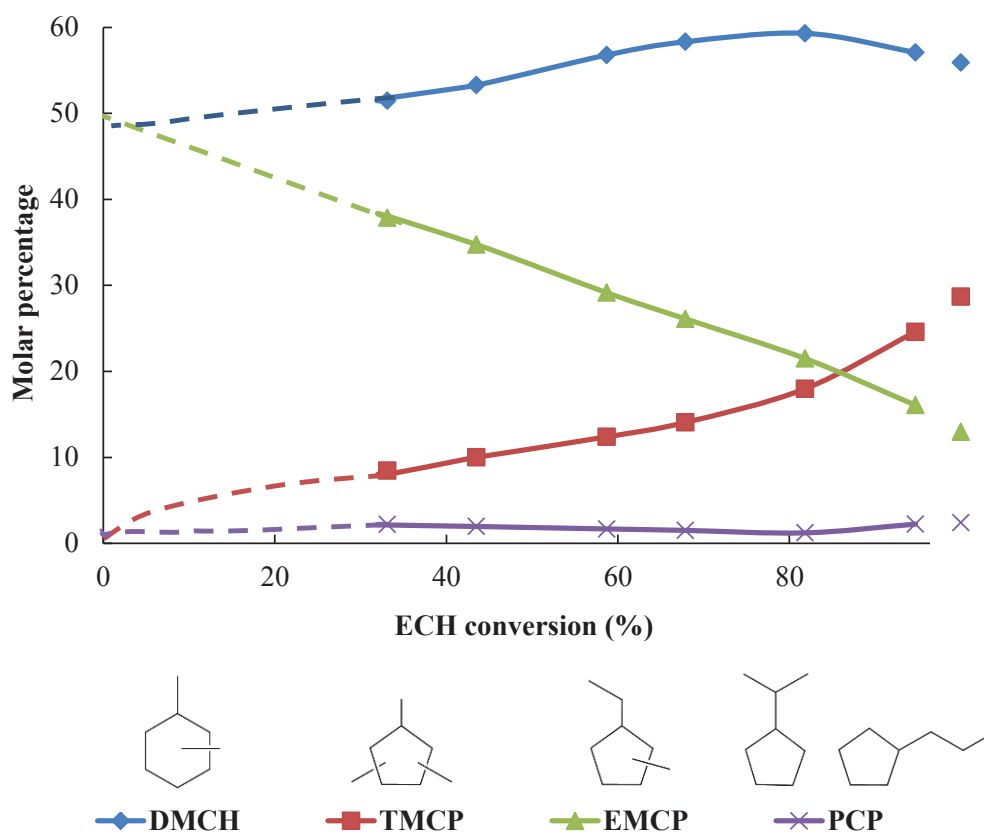


**Figure 5.4. Experimental isomers mole percentage vs ECH conversion at 285°C in full lines. The free dots on the right correspond to the isomers mole percentage at thermodynamic equilibrium at 285°C according to PROII.**

The thermodynamic equilibrium of the different isomers lumped in their different families was before calculated with PRO II at different temperatures as explained in section 3.3.2.1. That evolution allowed a first approximation to the isomerization mechanism. However, a deeper investigation about each isomer distribution within its corresponding lump is required if a microkinetic model is targeted.

Figure 5.5. depicts the evolution of the mole percentage of all EMCP family isomers with ECH conversion. 13-EMCP appears as the major primary product of this family, regardless the position of the substituents (cis and trans i.e. C1E3MCP and T1E3MCP). The trans-1-ethyl,2-methyl-cyclopentane (T1E2MCP) mole percentage appears in lower amount than 13-EMCP at the beginning and it increases as the conversion increases in detriment of 13-EMCP. The same tendency was observed concerning cis-1-ethyl-2-methyl-cyclopentane (C1E2MCP) and 1-ethyl,1-methyl-cyclopentane (1E1MCP). Nevertheless, their mole percentages remain lower and almost negligible compared to T1E2MCP and 13-EMCP (cis and trans) mole

percentages. Only T1E3MCP and T1E2MCP mole percentages are slightly far from equilibrium for ECH conversion higher than 90%. As expected, the mole percentage of each molecule tends to approach the thermodynamic equilibrium value as the conversion increases.

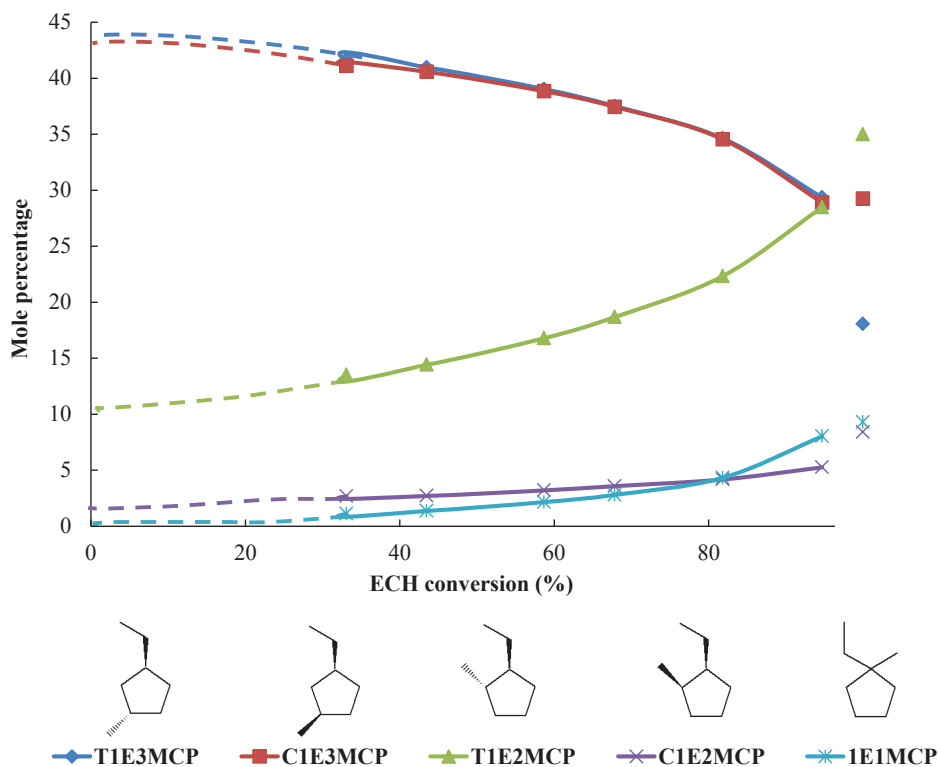


**Figure 5.5. Isomers mole percentage within the EMCP family vs ECH conversion at 285°C in full lines. The free dots on the right correspond to the isomers mole percentage in equilibrium at 285°C according to PROII.**

Figure 5.6 depicts the evolution of DMCH isomers with conversion. In this case, both, cis-1,3-dimethylcyclohexane (C13DMCH) and cis-1,4-dimethyl-cyclohexane (C14DMCH) are the primary products of the DMCH isomers family with a small fraction of trans-1,3-dimethylcyclohexane (T13DMCH) plus trans-1,4-dimethyl-cyclohexane (T14DMCH). Note that T13DMCH and T14DMCH cannot be separated as they are coeluted in the GC. Nonetheless, C13DMCH is the major product at lower conversion. The mole percentage of T13DMCH plus T14DMCH increases with the ECH conversions in detriment of the C13DMCH, whereas the C14DMCH slightly decreases, and the trans-1,2-dimethyl-cyclohexane (T12DMCH) increased reaching its highest mole percentages (14%) at higher conversions. The amounts of cis-1,2-dimethyl-cyclohexane (C12DMCH) and 1,1-dimethyl-

cyclohexane (11DMCH) remain lower at all the range of ECH conversions reaching their higher mole percentage at higher conversions, 4 and 7% respectively.

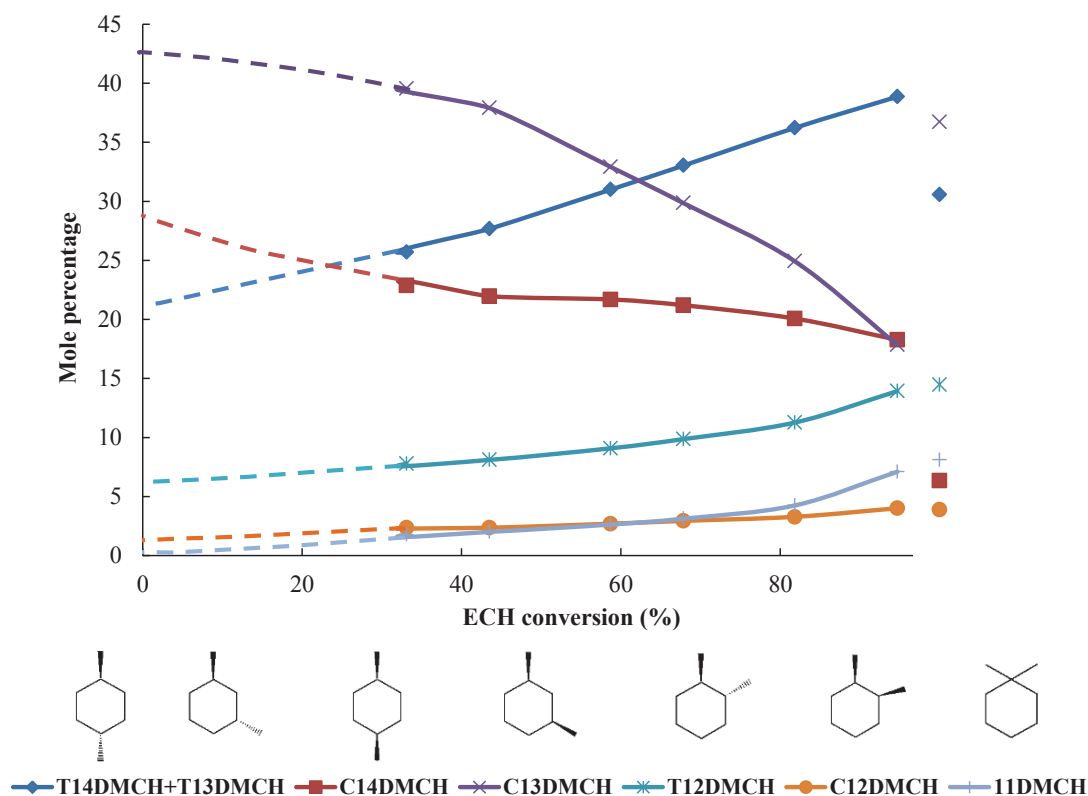


**Figure 5.6.** Isomers within the DMCH family mole percentage vs ECH conversion at 285°C in full lines. The free dots on the right correspond to the isomers mole percentage in equilibrium at 285°C according to PROII.

With regards to the mole percentage at equilibrium in this group, half of the isomers are rather far from equilibrium even for a conversion higher than 90%. Only the isomers appearing experimentally at lower mole percentages such as C12DMCH, 11DMCH and T12DMCH get close to equilibrium. Regarding the major isomers T14DMCH plus T13DMCH and C14DMCH mole percentages are higher than their corresponding value at equilibrium. In the case of C13DMCH, the experimental mole percentage is far lower than the thermodynamic one. The main idea extracted from this Figure 5.6 is that the mole percentages of C13DMCH and T14DMCH + T13DMCH are moving further from the thermodynamic equilibrium value as the conversion increases. At the moment we cannot provide satisfactory explanation for such phenomenon.

In the case of the TMCP isomers family (figure 5.7.), clearly trans-1,2-cis-2,4-trimethylcyclopentane (T12C24TMCP) is the major primary product appearing at low conversion. At

the same time, it seems that cis-1,2-cis-2,4-trimethyl-cyclopentane (C12C24TMCP), trans-1,2-cis-2,3-trimethyl-cyclopentane (T12C23TMCP) and 1,1,3-trimethyl-cyclopentane (113TMCP) are primary products as well, but in lower amounts than T12C24TMCP. Besides, 1,1,2-trimethyl-cyclopentane (112-TMCP) is not a primary product in this family group. For conversions higher than 90% the isomers with lower mole percentages are close to equilibrium, contrary to the isomers appearing in higher amounts. The same tendency was observed in the previous group (DMCH). In this case, T12C24TMCP experimental mole percentage is slightly higher than at equilibrium whereas T12C23TMCP mole percentage is lower than the equilibrium one. The most striking fact is that the experimental 113-TMCP mole percentage is much higher than the thermodynamic mole percentage. Thus, the production of this isomer seems favored by the intrinsic kinetics of the zeolite.

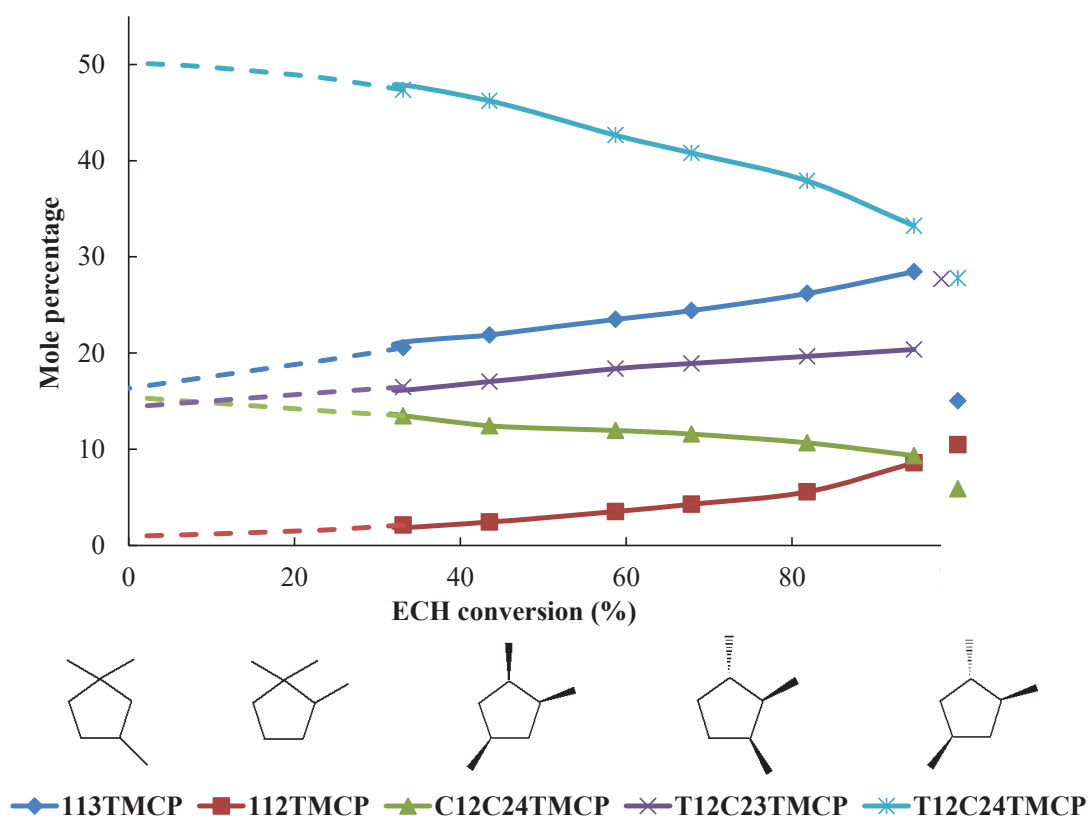


**Figure 5.7.** Isomers within the TMCP family mole percentage vs ECH conversion at 285°C in full lines. The free dots on the right correspond to the isomers mole percentage in equilibrium at 285°C according to PROII.

If we do not differentiate stereoisomers, a scheme with the order of isomers appearance in each lump can be depicted as shown in Figure 5.8.

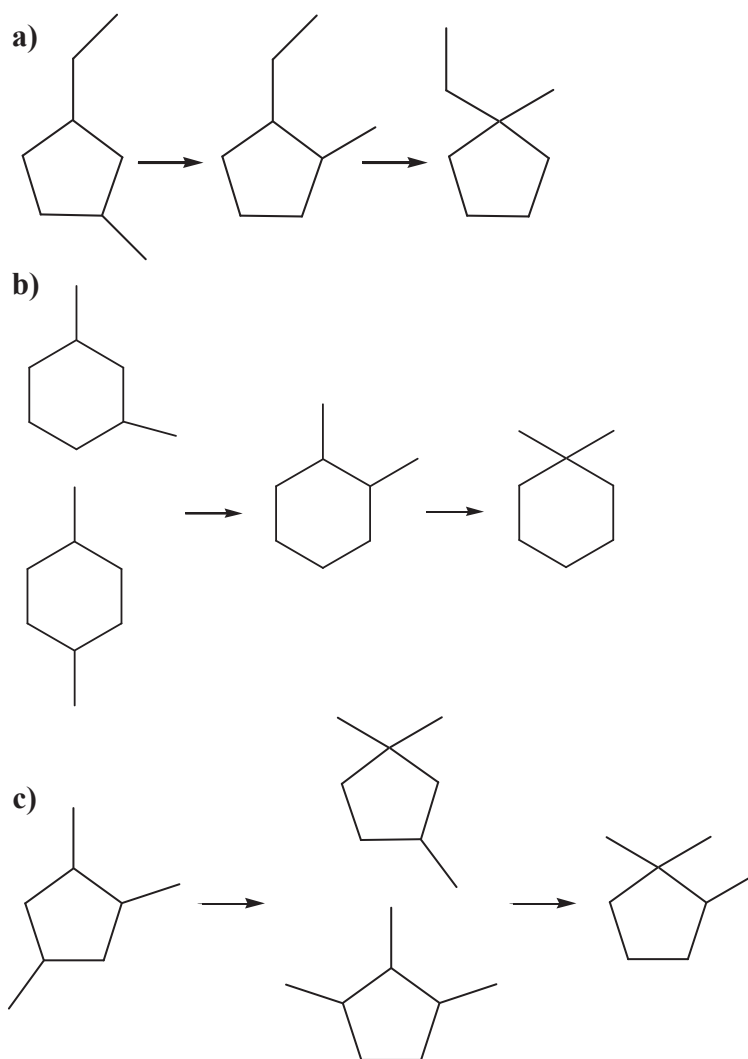


**Figure 5.8. Isomers apparition order in a) EMCP family , b) DMCH family and c) TMCP family.**

Concerning the primary isomerization products family (EMCP) (Figure 5.8.a), the 13-TMCP appears first, followed by 12-EMCP and at last, 11EMCP. Consecutively, the DMCH family (Figure 5.8.b) has 13-DMCH and 14-DMCH as first products appearing, followed by 12-DMCH and 11-DMCH at last. Regarding the TMCP family, the first isomer appearing is the 124-TMCP followed by 113-TMCP and 123-TMCP and 112-TMCP appearing at last. Note that for the EMCP and TMCP family the order of appearance of the isomers is in accordance with successive carbon to carbon methyl shift. For DMCH family such observations cannot be made because of the 13 and 14 DMCH coelution on GC analysis. From this products analysis it will be depicted the possible isomerization mechanism paths analyzed in Section 5.2.1.

### 5.2.3. Focus on the ring opening kinetics

In order to gain some information on the ring opening and cracking kinetics, an analysis of the distribution of these products has been done. It was based on the effluent composition obtained at 300°C at a contact time of 0.25 h. This temperature has been chosen in order to have significant amount of cracking and ring opening products in the effluent (1.5wt.% of ring opening and 5.6wt.% of cracking products).

The ring opening product distribution is provided Figure 5.9. It must be emphasized that the results should be considered cautiously as not all the ring opening products are identified by GC. This is due for instance, to coelution with other compounds during GC analysis (see table 2.5). Although, some salient features can be observed. First of all, the C<sub>8</sub> paraffins are mainly branched ones (n-octane stands for only 20% of the identified products). Secondly, the amounts of monobranched and dibranched products are about the same (about 40%) and no tribranched products are observed. 2-methyl-heptane and 2,5-dimethyl-hexane are the main principal isomerized products: these two molecules represent half of the total identified ring opening products. The ring opening products distribution calculated at thermodynamic equilibrium with PROII, included ring opening isomers not appearing experimentally or appearing in coelution with another products. Thus, in order to compare experimental and PROII results, from PROII results only the isomers appearing experimentally have been taking into account and normalized to 100. (Figure 5.9. hatched line bars). From Figure 5.9, it can be observed that the mono-branched products are really close to the equilibrium. In the case of the multibranched isomers, 25-dimethylcyclohexane and 23-dimethylcyclohexane appear in lower amount experimentally than at equilibrium (5 and 3% respectively) whereas 24-dimethylcyclohexane appears experimentally higher than at the equilibrium (5%). Concerning the n-octane, experimental results are close to equilibrium.

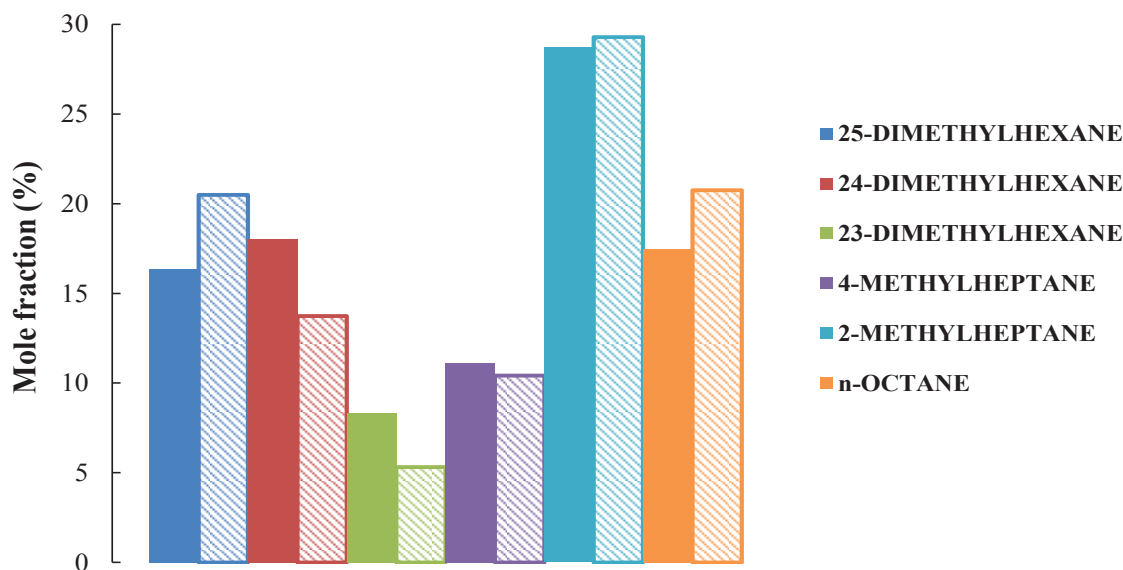


**Figure 5.9. Ring opening (RO) product distribution at 300°C in the standard test with the reference catalyst 1% Pt/Al<sub>2</sub>O<sub>3</sub>–EU-1 at a contact time of 0.25h. in full lines. Ring opening (RO) product distribution at 300°C with PROII in hatched lines. RO global yield at 300°C= 1.16%**

Regarding the carbocations stability as reported in 1.3.2.2., tertiary-tertiary, secondary-tertiary and tertiary-secondary are the dominant mode of  $\beta$ -scissions<sup>22</sup>. Therefore it can be expected that 113TMCP is particularly prone to form the 2,5-dimethyl-hexane by ring opening<sup>46</sup> as a tertiary-tertiary  $\beta$ -scission is involved in this case as depicted in the Figure 5.10.a. Following the same guideline, 1,1-dimethyl-cyclohexane or 1,3-dimethyl-cyclohexane can form the 2-methyl-heptane by secondary-tertiary or secondary-tertiary  $\beta$ -scission (Figure 5.10.b.). Indeed, the products depicted in Figure 5.10 a and b, appear experimentally as the dominant ones (Figure 5.9.). Note that these products can themselves undergo bifunctional isomerization reactions, leading to other mono/di/tribranched products. Concerning the presence of the n-octane product, it could come either by the isomerization of the branched ring opening product or by the opening of a naphthenic ring isomer such as ECH<sup>+</sup>.<sup>48</sup>(Figure 5.10.c) Nonetheless, the latter possibility seems quite unlikely since n-octane coming from the naphthenic ring opening, involves a primary carbocation. As explained in Section 1.3.2.2. reactions involving primary carbocations are the most unlikely ones.<sup>22</sup>



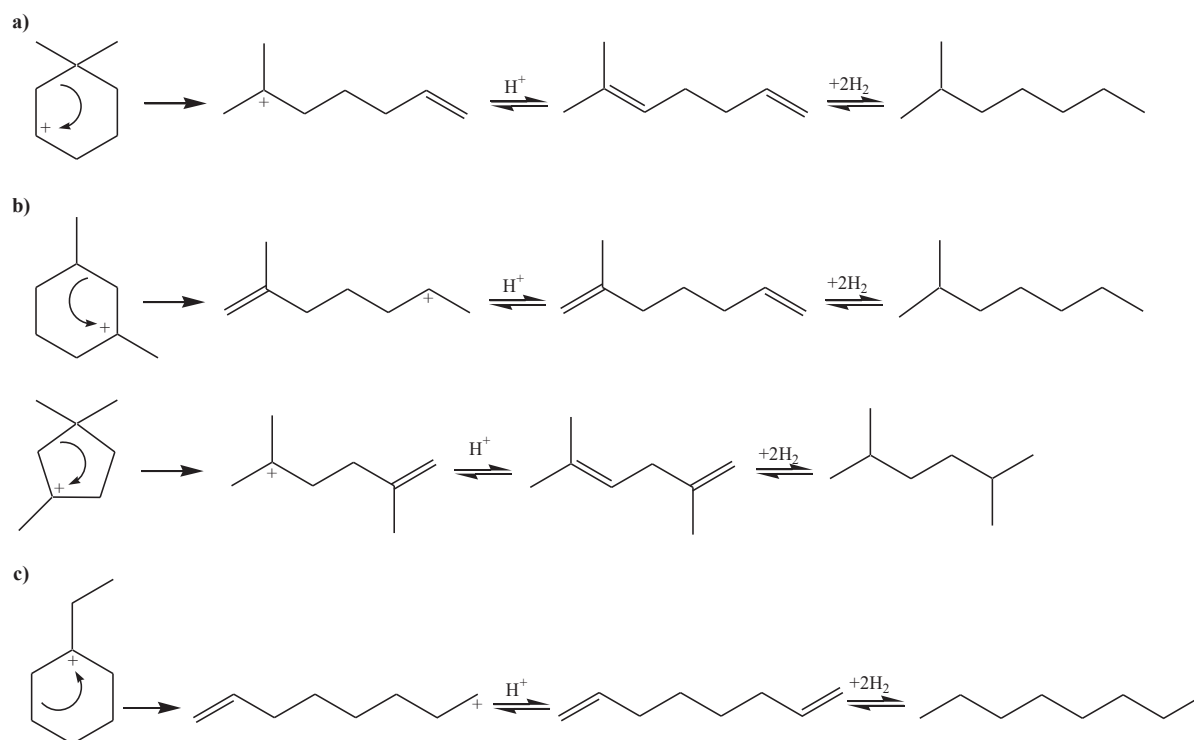


**Figure 5.10.** Ring opening pathway providing a) 2,5-dimethylhexane and b) 2-methylheptane c) n-octane.

Therefore we propose to focus the future DFT study on the ring opening pathway depicted in Figure 5.10 a and b.

### 5.3. Ab initio Kinetic study on the ECH hydroconversion

In order to understand better the evolution of our products during the reaction and to provide values for the kinetic constants of each individual step, an ab initio investigation of part of the reaction network has been done. Figure 5.11 represents the considered cycle contraction-expansion reactions. The whole scheme considered also contains isomerization reactions by methyl-shifts and hydride shifts (Appendix V) that will also be implemented in the kinetic model later (section 5.3). Nevertheless, the latter are fast compared to the cycle contraction-expansion reactions as already shown in chapter 4. According to Brouwer and Hogeveen,<sup>63</sup> the hydride shift between consecutive carbons is extremely fast and its rate depends on the type of start and end carbons, being more favorable for tertiary carbocation. However, with some complex cyclic carbenium ions this hydride shift can be impeded by steric constraints.<sup>22</sup> The migration of the methyl- group, was reported as occurring easily due to its low energy barrier (around 5 kJ/mol).<sup>221</sup> Nonetheless, it was considered as being more difficult and slower than the hydride migration.<sup>222</sup> Again, as it occurred with the hydride shift,

the methyl-shift rate depended on the type of starting and ending carbons. Similar rates were found for hydride and methyl- shifts when the start and end carbons were tertiary, whereas the methyl-shift was much slower than hydride shift when one of the carbons was secondary and the other tertiary.<sup>63</sup>

The considered isomerization reactions (Figure 5.11) were selected because they can explain the formation of the main products observed experimentally. Furthermore, the protonation/deprotonation, adsorption/desorption on the zeolite and hydro/dehydrogenation reactions (taking place on platinum, not simulated in the present work) are represented. Figure 5.11 includes secondary and tertiary carbocations, pi-complex and naphthenes involved in the reaction. Regarding the ring opening reaction, the pathways depicted in Figure 5.10 a and b have been as well investigated since they have been identified as the most likely pathways to obtain the ring opening products.

### **5.3.1. Isomerization ab initio kinetics**

#### **5.3.1.1. General features**

Figure 5.12 shows all reaction pathways involving PCP considered in the kinetic study. Part of Path I was already investigated in chapter 4, from the a) to the e) intermediate. From a technical point of view, this part of the pathway was the most simple to optimize by static approaches, as it deals only with tertiary carbocations. Nevertheless, the experimental product distribution made clear that this part of the pathway is not sufficient to explain all the reaction products. For example, the formation of 13EMCP (Figure 5.5.) or 13DMCH (Figure 5.6.) are not explained by Path I only. Two hypotheses can be proposed to explain the formation of these compounds:

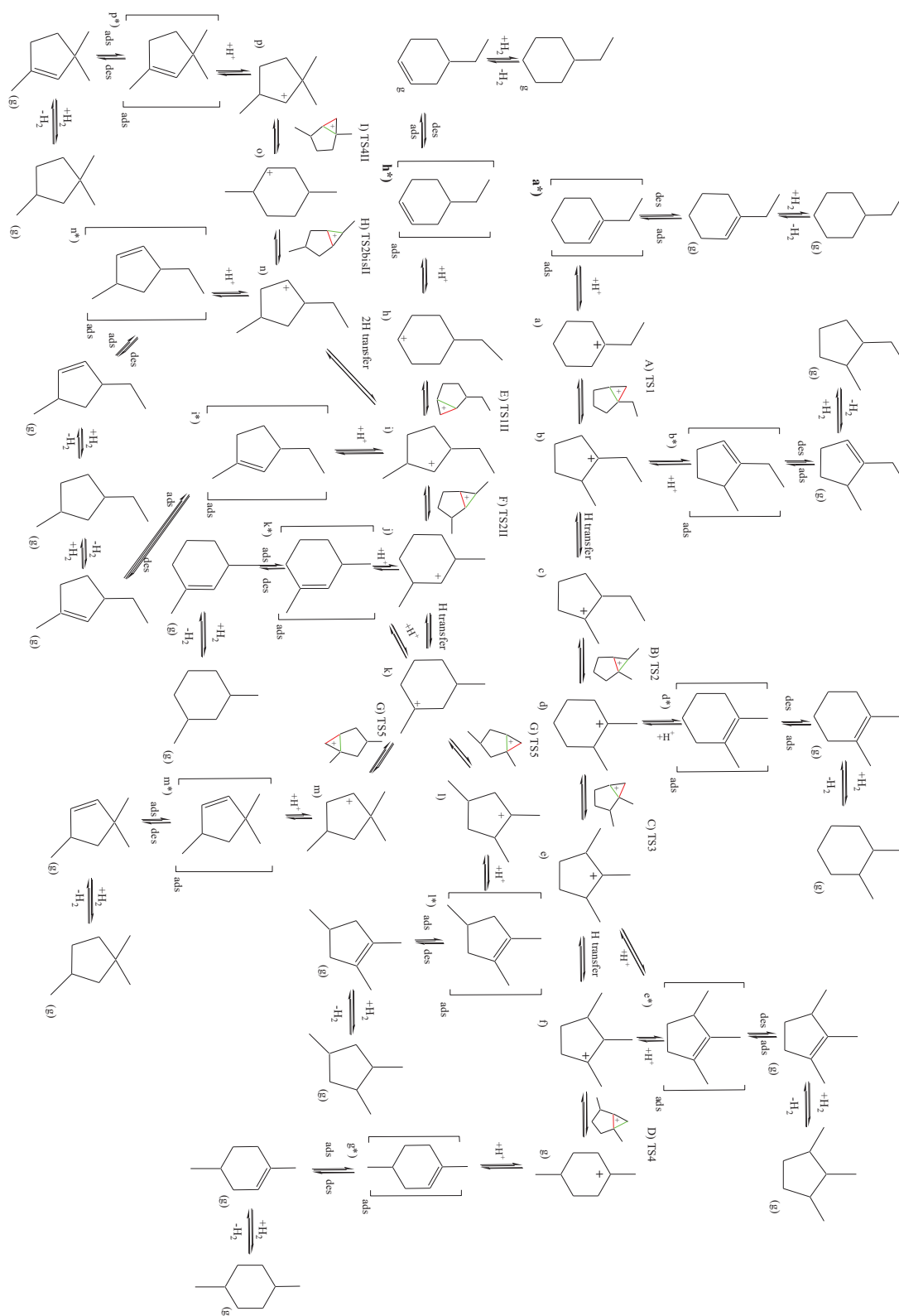


Figure 5.11. Reaction scheme considered in *ab initio* calculations and kinetic model for the hydroisomerization of ECH. Only isomers obtained through cycle contraction-expansion are shown, but methyl and hydride shifts were also considered in the micro-kinetic model.

- Either they are formed from 12EMCP<sup>+</sup> / 12DMCH<sup>+</sup> by a sequence of hydride and methyl shifts. Such a sequence needs secondary carbenium to appear in the reaction sequence (Appendix V). This is however not compatible with the experimental observation of 13EMCP (Figure 5.5.) or 13DMCH (Figure 5.6.) as primary reaction products
- Either they are formed by another sequence of type B isomerization reactions. This is featured in Path II, which also requires some secondary carbenium ions to be invoked.

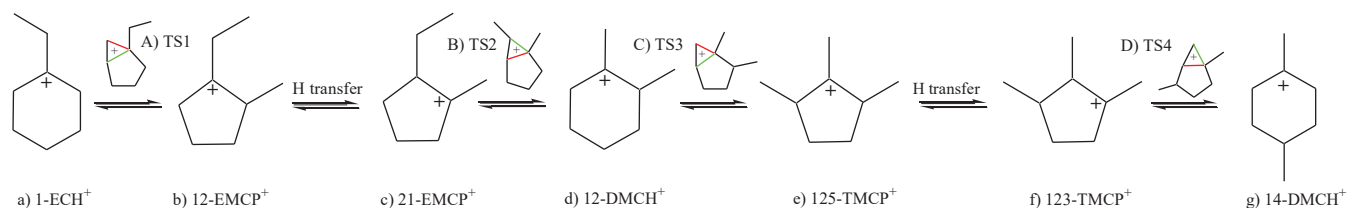
Moreover, Path II bis and ter were added to account for the formation of 113TMCP, observed experimentally and thought to be a key intermediate (in its carbenium form, see figure 5.10.a) for ring opening.

#### **5.3.1.2. The secondary carbeniums issue: stability and comparison with the corresponding $\pi$ -complexes**

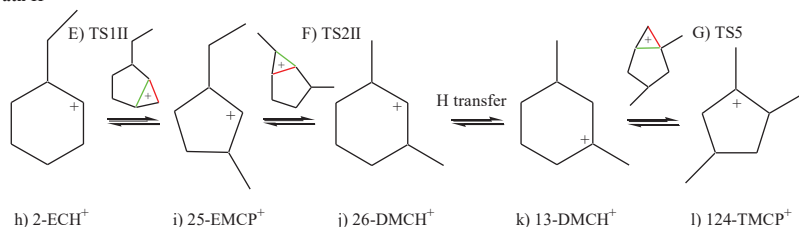
We managed to optimize some secondary carbocations as reaction intermediates in some cases. However, we encountered many difficulties to optimize some others. This problem can be explained by the fact that they are not always local energy minima, if not that they are located on flat areas of a descending potential energy profile.<sup>223</sup>

Their adsorption energies (quantified in a similar manner as in chapter 4) remain very high compared to their corresponding  $\pi$ -complex (Figure 5.13). Thus, from a kinetic point of view, it can be anticipated that when a secondary carbenium is needed to convert one species in another, the relevant kinetic intermediate will be the corresponding  $\pi$ -complex, as will be shown latter in section 5.2.1.3.

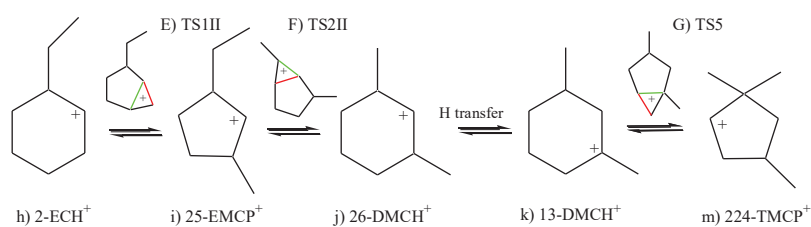
## Path I



## Path II



## Path II bis



## Path II ter

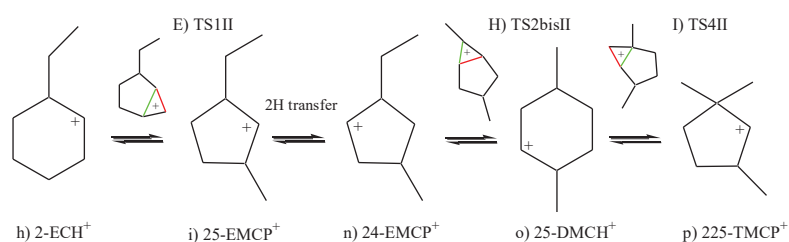


**Figure 5.12. Isomerization pathways considered in the kinetic study. The red and green line depicts the bond breaking and formation taking place from the PCP to the product.**

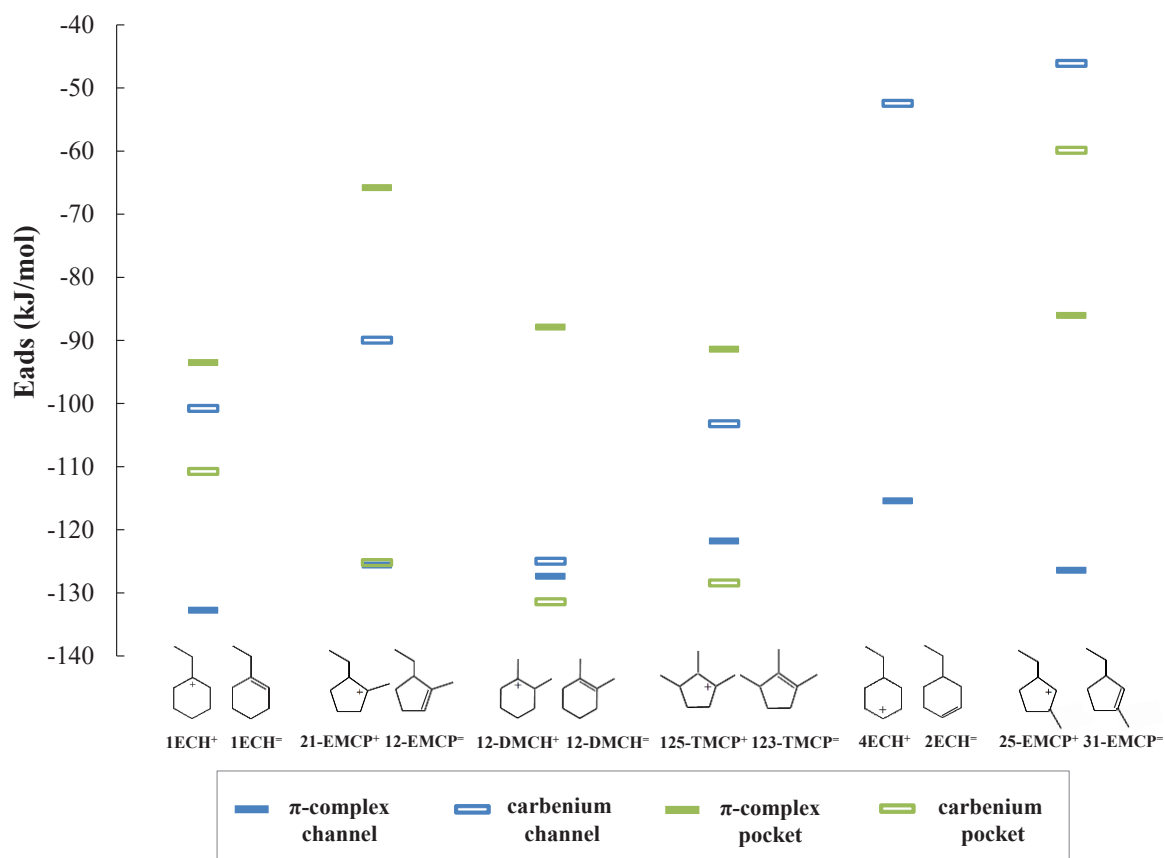


**Figure 5.13. Adsorption energies for C8  $\pi$ -complexes, tertiary and secondary carbeniums at the T1O1 channel Brønsted site (blue) and at the T9O6 pocket Brønsted site (green).**

In any case, the energy of the secondary carbenium species is further higher than the one corresponding to  $\pi$ -complexes. Nevertheless, this difference is extremely high in the channel, compared to the pocket active site. In the case of the ECH skeleton (only stabilized in the channel), the  $\pi$ -complex is more than 60 kJ/mol more stable than the carbenium. 13-EMCP related carbenium and  $\pi$ -complexes in the channel and in the pocket, are as well far in terms of adsorption energy (80 kJ/mol). However, in the pocket this difference is only of 27 kJ/mol. The fact that  $\pi$ -complex are more stable in the channel was not surprising since as explained in chapter 4,  $\pi$ -complexes are more stable when the distance from them to the framework is short. The local geometry of the pocket made especially difficult for the  $\pi$ -complex to get close to the framework whereas the channel local geometry was more favorable.

Figure 5.14. shows the distance values between pi-complex / carbenium ions and the zeolite framework at the channel T1O1 and pocket T9O6 sites. Even if the correlation is not linear as in chapter 3, it is easy observable two groups of points corresponding to the two different active sites. Closer distances correspond to the channel T1O1 active site whereas larger distances correspond to pocket T9O6 active site. The fact of the linear correlation in chapter 3

and not in here is not surprising since in chapter 3 all the  $\pi$ -complexes corresponded to the same Path, having then, a similar location. In this case,  $\pi$ -complexes correspond to different paths and then different locations.

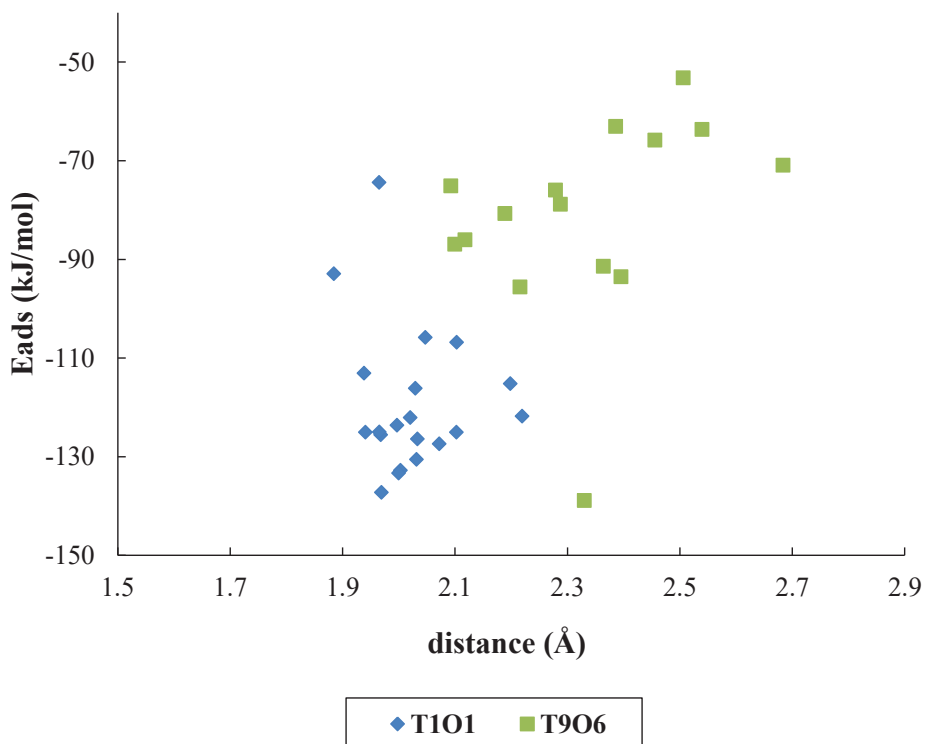


**Figure 5.14. Distance values between pi-complex and the zeolite framework at the channel (T1O1) and at the pocket (T9O6) sites.**

Another comparison in between pi-complex and tertiary carbocations (counterpart of Figure 4 from chapter 4) was done in order to verify if this tendency was followed as well (Figure 5.13). As it is observed for secondary carbocations, again the  $\pi$ -complexes are much more stable in the channel than the tertiary carbeniums. However, the opposite tendency is observed in the pocket i.e the tertiary carbocations are much more stable than  $\pi$ -complexes. Thus, it can be concluded that the channel is a more favorable site for  $\pi$ -complex species than the pocket while the pocket is a more favorable site for tertiary carbocations than the channel.

### 5.3.1.3. Isomerization energy profiles

Therefore, T1O1 channel and T9O6 pocket sites were chosen to perform a full study of the different ethylcyclohexene isomerization pathways including type B isomerization (Figure 5.12). Path I (already studied in part in chapter 4) starts from 1-ethylcyclohexium (1-ECH<sup>+</sup>),

whereas Path II, Path II bis and Path II ter start from 4-ethylcyclohexenium (4-ECH<sup>+</sup>). TS1II which is a common species for all the Path II (Path II-, -bis and -ter) is the only TS that differed the most from the other TS. Not only because it is a TS connecting two secondary carbeniums, but also because it is the only PCP not connected to any alkyl- group. The structure of TS1II is shown in Figure 5.15 for both active sites: the channel T1O1 and the pocket T9O6. Besides, Table 5.1 enclosed the distance values for each PCP.

**Table 5.1. TSIII distances at the channel active site T1O1 and pocket active site T9O6 and their imaginary frequencies.**

	Distance (Å)					
	C <sub>1</sub> -C <sub>2</sub>	C <sub>2</sub> -C <sub>3</sub>	C <sub>1</sub> -C <sub>3</sub>	C <sub>2</sub> -H	C <sub>3</sub> -H	fi
T1O1	1.466	1.771	1.548	1.440	1.208	404
T9O6	1.470	1.705	1.532	1.370	1.232	244

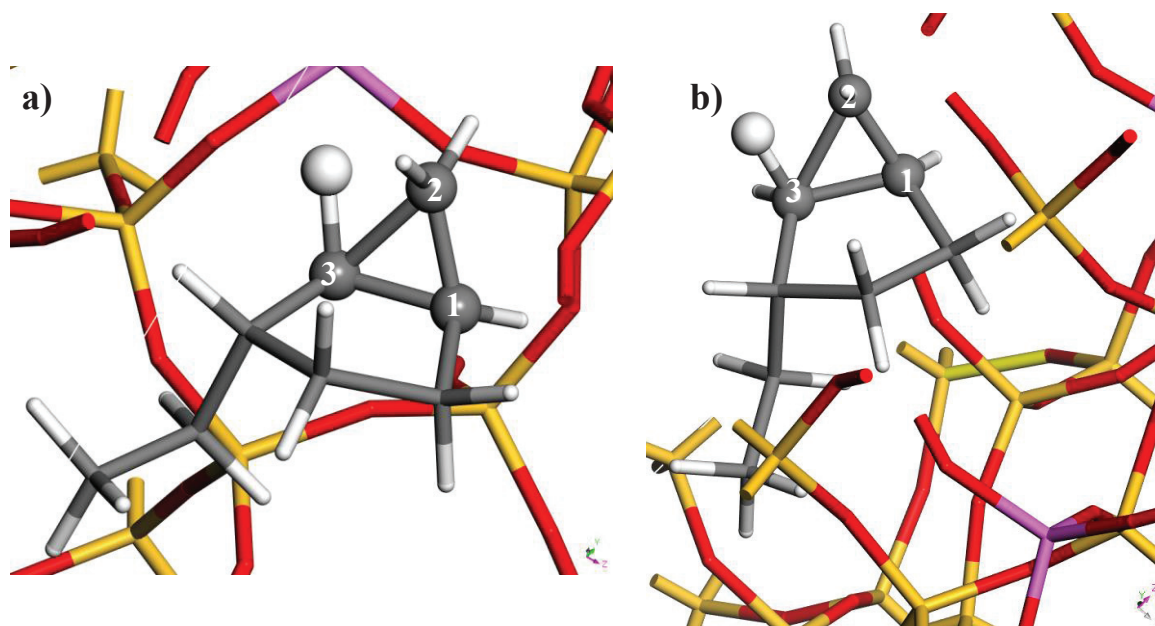


**Figure 5.15. TS1II a) at the pocket active site T9O6 and b) at the channel T1O1 active site.**

The distance of the PCP are really close to those already defined for other TS in the intersection T10O12 active site (Chapter 4).

Figure 5.16 depicts the energy profiles and barriers associated to the PCP transition states, corresponding to the different cycle contraction-expansions at the channel. In Path I, each transition structure is connected to a reactant and a product; in the same way as



explained in chapter 4 (IRC). It occurred similarly for the individual steps concerning TS connecting tertiary carbocations in the other paths. In the case of the TS involving secondary carbocations as intermediates, some of them were connected to the reactant and a product being those secondary carbocations. When secondary carbocations are involved, the  $\pi$ -complexes corresponding to the protonation of those secondary carbeniums is kinetically relevant. The energy level corresponding to carbocations is linked through dashed lines to the corresponding  $\pi$ -complexes (Figure 5.16).

In the T1O1 channel active site, it seemed that Path I is likely the first appearing since the energy barrier for reaching the first TS (TS1) is 57 kJ/mol and the corresponding  $\pi$ -complex is really stable (-133 kJ/mol). Even if kinetically relevant intermediates energies (corresponding to TS1) are higher than the ones corresponding to TS1II, the energy barrier was around 30 kJ/mol lower than the first energy barrier of Path II (TS1II). For the following steps of the reaction scheme, similar forward energy barriers were found regardless the Path followed. Regarding backward energy barriers, they are usually higher than the forward barriers with some exceptions such is the case of the second elementary step of Path II and Path II ter where the backward energies were 10 kJ/mol lower than the forward ones. The intermediates stability is not so different concerning the two first elementary steps of each Path. However, the last reaction intermediate of Path I is somehow more unstable than the other intermediates whereas the last intermediate of Path II ter is slightly more stable than the others. Concerning Path II the intermediates corresponding to TS2II and TS5 are quite unstable suggesting that this path is less likely than Path I and Path II ter. In spite of this analysis, a kinetic model will be necessary to clarify which is the predominant path.

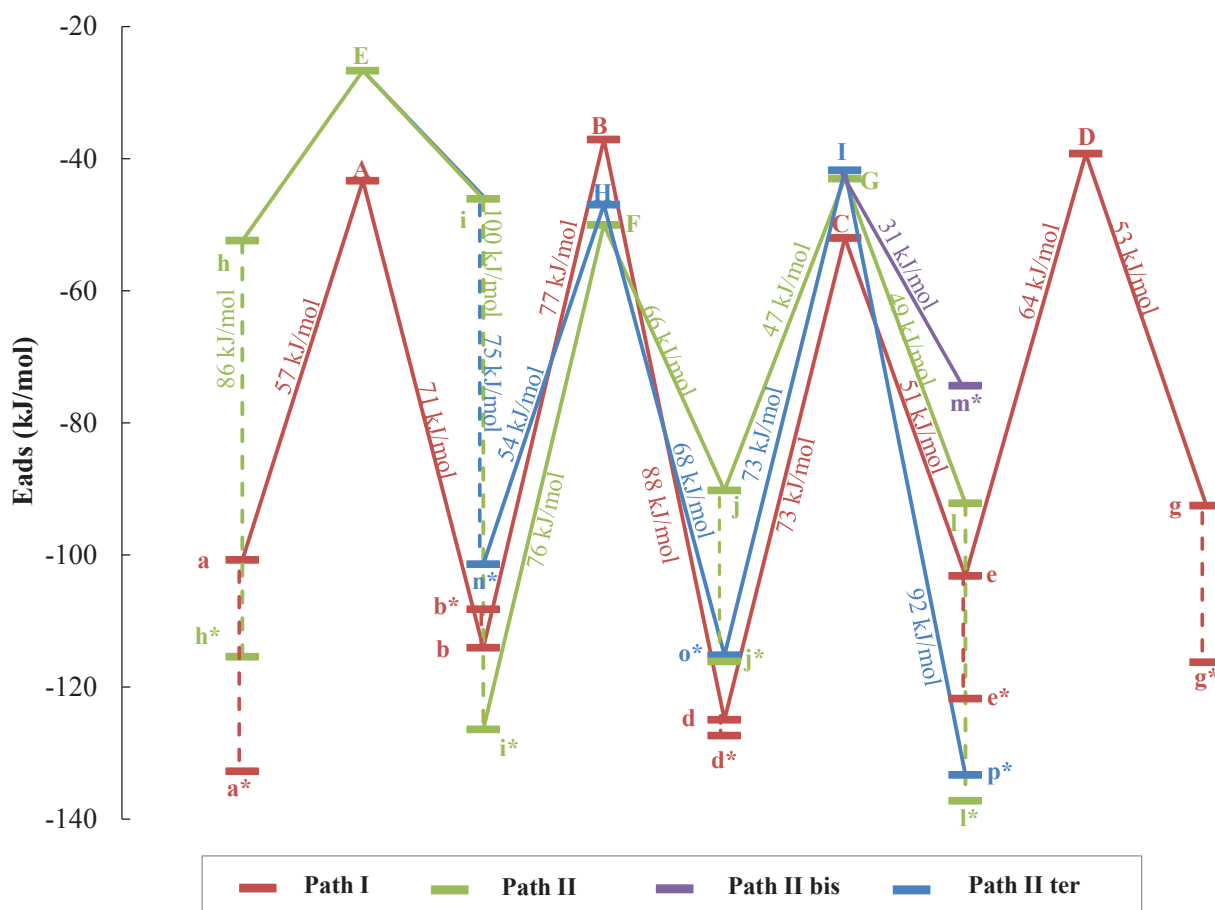
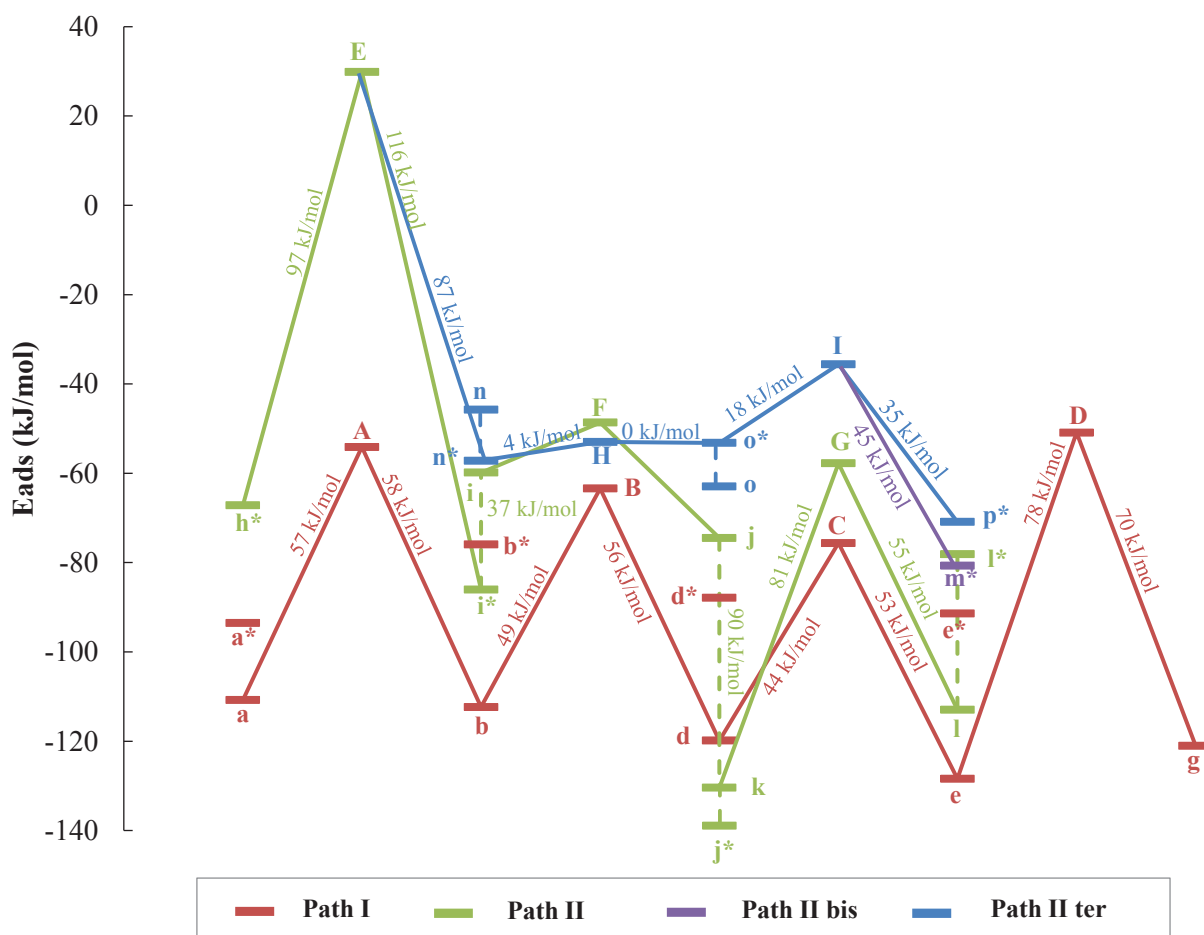


Figure 5.16. Energy profile for the cycle contraction-expansions pathways through PCPs, at the channel T1O1 active site. (\* pi-complex, vertically connected to the corresponding carbenium ion)

In the same way, all the TS are similar in energy except TS1II. Its energy is higher, which is likely associated to the non-substituted nature of the PCP. The presence of alkyl  $\sigma$ -donor substituents in the PCP is indeed expected to compensate the instability of the charged PCP. From a general point of view, the multi-step nature of the pathways, and their multiple crossing in energetic terms, makes it hard to conclude about a preferred one. For this reason, integrating the calculated ab initio kinetic data in a kinetic model will be helpful to identify the most abundant intermediates.



**Figure 5.17.** Energy profile for the cycle contraction-expansions pathways through PCPs, at the pocket T9O6 active site. (\* $\pi$ -complex)

The same analysis was carried out for the pocket active site (Figure 5.17). The marked difference between Figure 5.16 and 5.17 is eye-catching. In the pocket active site, a huge energy barrier is found to reach the first TS (TS1II) from Path II, Path II bis and ter. This makes these paths unlikely compared to Path I. The other important feature in this profile comes from the instability of  $\pi$ -complex intermediates compared to tertiary carbocations. As it was explained before, for all the reactions involving secondary carbocations,  $\pi$ -complex are the kinetically relevant intermediates from a kinetic point of view. Nonetheless, in this active site the  $\pi$ -complexes are much more unstable than tertiary carbocations. This fact explained then the difference between intermediates in terms of energy.

From experimental work, it has been observed that Path I and Path II are required in order to find all the products found experimentally. Then, this active site is not chosen for building up the kinetic model. Note that another option would be that the first step of Path II takes place in the channel. Then, the isomerized product i would transform into i\* (corresponding

$\pi$ -complex), which would later migrate to the pocket. Once in the pocket, the  $\pi$ -complex would transform easily into a stable carbenium which would react with a much lower barrier than in the channel. For the sake of time, this option was not analyzed in the micro-kinetic approach, but this is a short-term open perspective of the work.

Therefore, in order to create a microkinetic model, the data at the channel active sites is considered. With the help of frequency calculations, the thermodynamic data such as Gibbs adsorption energies, enthalpy and entropy energies are calculated. Figure 5.18 is the counterpart of Figure 5.16 but considering Gibbs adsorption energies instead of adsorption energies. However, some systems are not accurately optimized enough to do this analysis due to the presence of more than one imaginary frequency (due to the lack of time, line minimizations were performed only on selected cases). Then, some points are not represented in this figure.

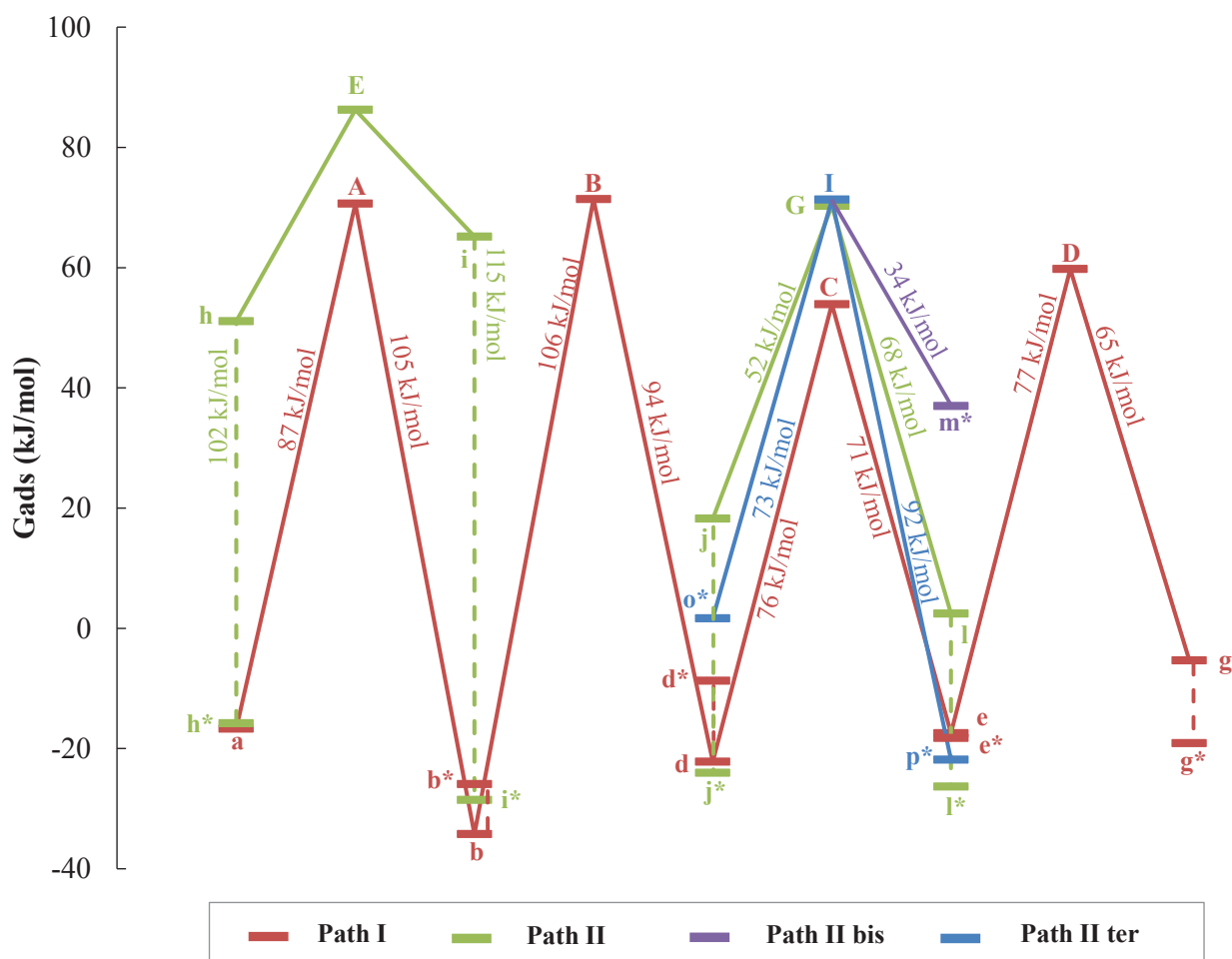


**Figure 5.18.** Adsorption Gibbs energy profile for the cycle contraction-expansions pathways through PCPs, at the channel T1O1 active site. (\*  $\pi$ -complex)

Again this profile does not allow to discriminate between Paths. Table 1 of appendix V includes the thermodynamic data to feed the microkinetic model explained in section 2.6.

### 5.3.2. Ring opening ab initio kinetics

From our experimental investigation, the ring opening reactions likely to take place are the one depicted in Figure 5.9. Nevertheless, the reaction starting from 1,1-DMCH<sup>+</sup> is not considered since this product appears in low amount experimentally. Then, only the other two reactions are considered for an ab initio investigation. For this part of the study we consider the channel T1O1 and pocket T9O6 sites as for the isomerization part, but also the T10O12 intersection site. The latter was shown to lead to unfavorable isomerization TS and intermediates with respect to channel and pocket sites (chapter 4), but its reactivity remains to be unraveled concerning the ring opening.

At the intersection site, the opening of the 133-TMCP<sup>+</sup> carbocation was successfully carried out whereas that was not the case for the 13-DMCH<sup>+</sup> carbocation ring opening. In the latter case, a secondary carbocation is involved as reaction product. Due to the instable character of secondary carbocations for aliphatic species, even if forcing the cycle to open, it is reformed spontaneously. At this point of the study, this problem of stability concerning the secondary carbocations is not only attributed to the real instability of these species but also to the limitations of the static approach to stabilize these species.<sup>223</sup>

The 133-TMCP<sup>+</sup> ring opening into 25-DmHx<sup>+</sup> was successfully carried out. Nevertheless, the transition state is not isolated because the energy of the product is so close to the TS one that is not possible to differentiate. Since this is the only successful ring opening reaction, it was tested as well in the other active sites i.e. channel T1O1 and pocket T9O6 active sites.

In those active sites, the same problem to find the TS as that found in the intersection site is again encountered. Then, the energy barrier is considered as the energy difference between the product and the reactant. The energy barrier found is gathered in Table 5.2.

**Table 5.2. Energy barriers for the 133-TMCP<sup>+</sup> ring opening reaction.**

	$\Delta E_{\text{ads}}$ (kJ/mol)
Intersection T10O12	93
Channel T1O1	89
Pocket T9O6	60

Regarding the ring opening energy barriers, the pocket active site is revealed as the one where the ring opening products are produced most easily (60kJ/mol) whereas the other two active sites exhibit barriers around 90 kJ/mol. The energy barrier in the pocket is competitive with the isomerization ones. However, the feedback reaction is very fast, so indeed the RO is difficult. What makes RO feasible is in reality the consecutive cracking reaction since the cracking products are more stable in terms of energy. Note that the respective selectivities in terms of isomerization versus cracking of the pocket, channel versus intersection sites in EUO, will be discussed again in chapter 6, considering also additional experimental data.

On the other hand, the barriers for ring opening are higher than the barriers for the isomerization for the active sites located in the channel and at the intersection between channel and pocket. This phenomenon could be related to the unfavorable local geometry inside the pocket for  $\pi$ -complex. On one hand, the likely carbocations located more in the middle of the pocket had place enough to be opened. Besides, as the deprotonation is expected to be not favored (due to the higher distances of the  $\pi$ -complex to the active site), there would be no other reaction competing with the ring opening. In the case of the channel both ring opening and dehydrogenation could occur. However, since the  $\pi$ -complex are much more stable, the ring opening would be more impeded.

Figure 5.19. represents the reactive ( $133\text{-TMCP}^+$ ) and the product ( $25\text{-DmHx}^+$ ), intermediates of the ring opening reaction in the channel T1O1 active site.

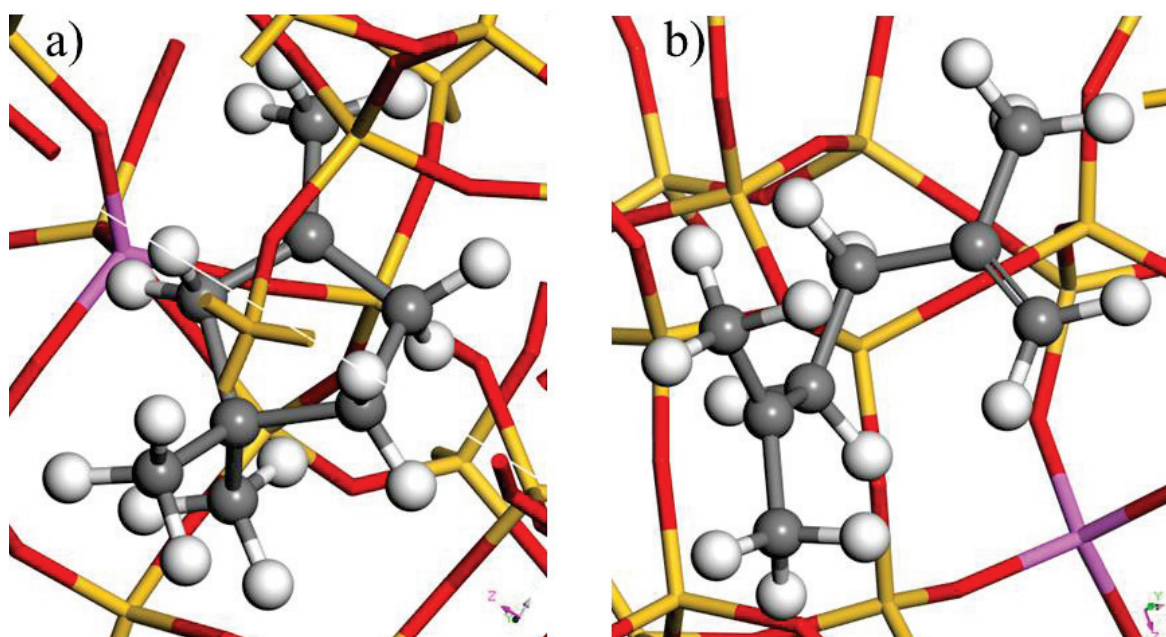


Figure 5.19.a)  $133\text{-TMCP}^+$  and b)  $25\text{-DmHx}^+$  structures in the channel T1O1 active site.

In the appendix V, there are two figures showing the energy profile for the cycle contraction-expansions pathways through PCPs plus the ring opening at the channel T1O1 and in the pocket T9O6 active site.

#### 5.4. Microkinetic model

In order to compare the results of the ab-initio calculations with the experimental data, the net reaction rates of all steps presented in Figure 5.11 need to be calculated to predict the flows of the products at the reactor exit. As detailed in Section 2.6, a microkinetic model considering the kinetic constants from the ab initio calculations has been built based on the figure 5.11. The steps with their corresponding kinetic constants are defined in Table 5.3 and steps from 15 to 35 are represented in Figure 5.20. The corresponding  $\pi$ -complexes, secondary and tertiary carbenium ions are assumed to be in quasi-equilibrium and thus only one surface intermediate is considered for each product, except for ethyl-cyclohexane where two intermediates have been used. For the first microkinetic model several simplifications with respect to the scheme in Figure 5.11 have been applied. In order to reduce the number of intermediates in the model, the dehydrogenation/hydrogenation, adsorption/desorption and protonation/deprotonation steps for all products are lumped into one single step (steps (3)-(14) in Table 5.3). This lumped step is in quasi-equilibrium and is described by an equilibrium rate constant, which value does not depend on temperature. This is a significant simplification of the model, but at the initial stage it allows only one parameter instead of 28 parameters to be estimated. These parameter values will be refined in a later optimization. The reaction starts with the dehydrogenation of ethyl-cyclohexane, which takes place in two parallel paths, leading to two different  $\pi$ -complexes. These two paths have been taken into account by two sets of parameters. The energy difference between the 2  $\pi$ -complexes (a\* and h\*) is about 20 J/mol. The same energy difference is maintained between the parameters of step (1) and (2) in Table 5.3. The rate parameters for step (21), (24), (27), (28) and (29) were not included in the ab initio calculations and therefore the values of the pre-exponential factors were optimized. The initial values for the parameters of these steps were taken from a similar step in the reaction mechanism. All the pre-exponential factors for methyl shifts (steps (30)-(36)) were optimized. After parameter optimization the ratio of the forward and reverse rate for steps (1)-(14) and (30)-(36) was found equal to 1.0, indicating that these steps are in quasi-equilibrium. Therefore only the equilibrium constant value is given in Table 5.3.



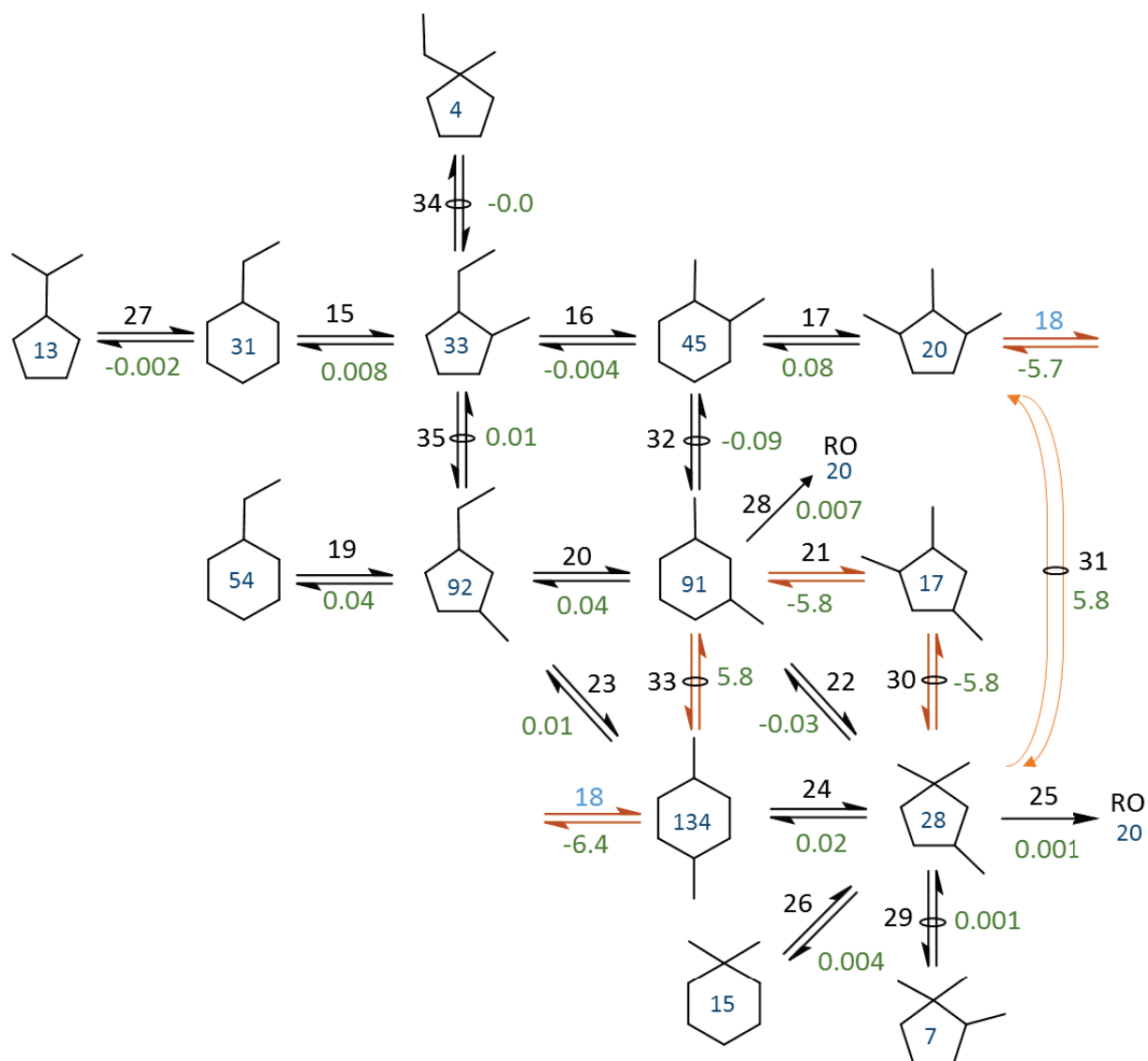
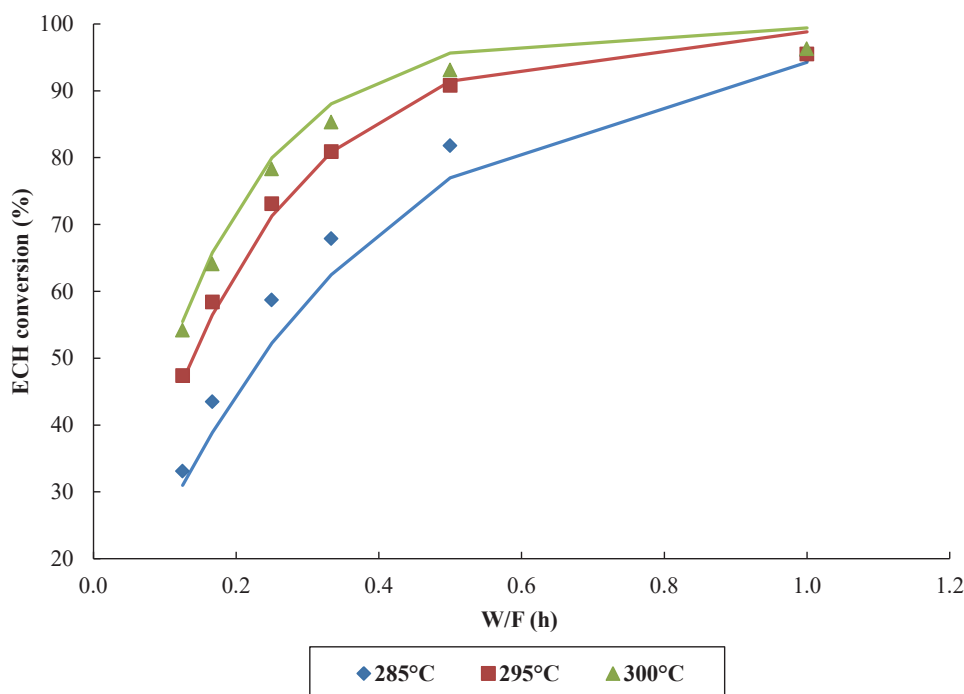


Figure 5.26. Reaction network for the carbenium ions taken into account in the microkinetic model. All carbenium ions are in quasi-equilibrium with their corresponding gas phase products using the same equilibrium constant for all species, except for ECH (reactions 1-14 not shown). The reactions are numbered by the black numbers close to the arrows. The green numbers represent the net turnover frequency for each elementary step (calculated at the reactor exit). Positive rates go from right to left and from top to bottom; negative rates go in the opposite direction. The blue numbers inside the species correspond to the concentration of the carbenium ions in nanomol/kg. Reactions 25 & 28 are the ring opening reactions and are assumed irreversible leading to a lumped group of ring opening and cracking products. Arrows that contain the symbol  $\circ$  are quasi-equilibrated step, for which is  $r_f/r_r=1.00$ . Step 18 on the top right continues in the middle (towards the bottom eg: 123-TMCP  $\rightleftharpoons$  1,4-DMCH). The orange arrow represent very fast net reactions. Conditions experiment, T= 285°C, X=68%.



In the following Figures experimental and kinetic data are going to be compared. For this purpose, equivalent figures to those of section 5.1 are going to be depicted. Full lines represent kinetic data whereas the points represent the experimental data.



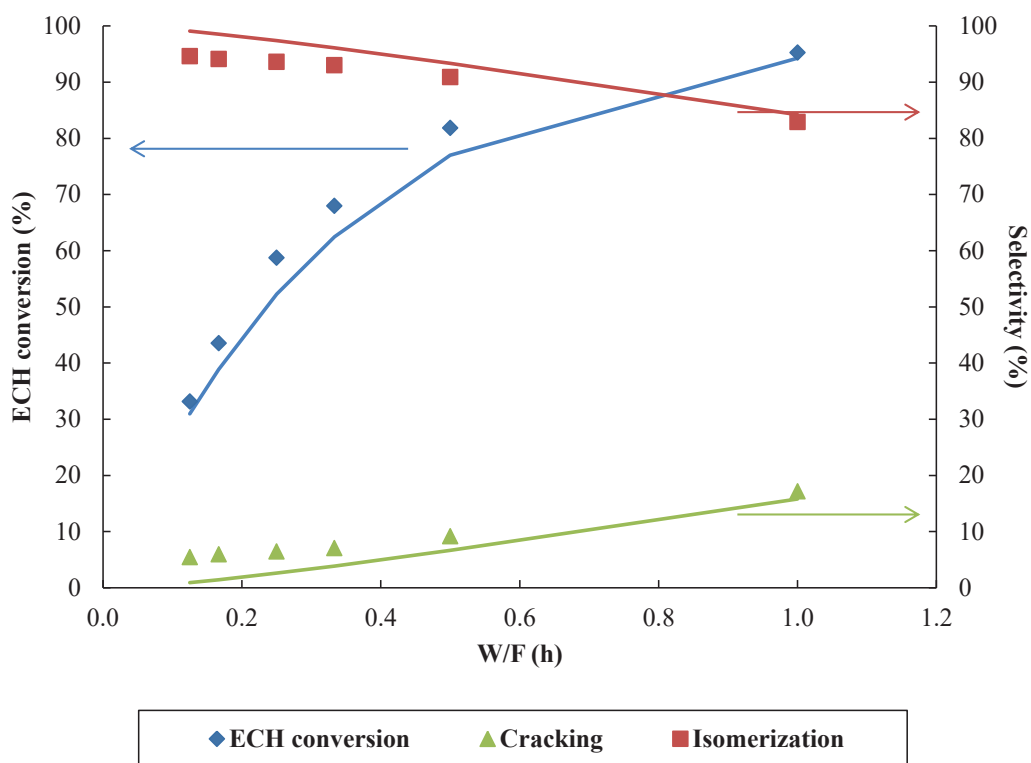
**Figure 5.21. ECH conversion vs contact time (catalyst mass divided by the ECH flow). Full lines: kinetic data; dots: experimental data.**

Figure 5.21 shows that the model fits the conversion as a function of W/F at the three temperatures adequately, although it underestimates the conversion at 285°C and slightly overestimates it at 300°C. By using only the experimental conversion at the lowest W/F, an activation energy of 115 kJ/mol was calculated assuming a first order reaction and using the integral rate equation for a fixed bed reactor. Applying this procedure to the calculated conversion, gives an activation energy of 131 kJ/mol. The initial activation barrier to convert ethyl-cyclohexane in the model equals 127 kJ/mol for steps (1a) + (15) and 147 kJ/mol for steps (1b) + (19), respectively.

**Table 5.3.** Reaction mechanism and the pre-exponential factor, activation energy and rate constants concerning each single step considered in the kinetic model. Green color represents the reactions of dehydrogenation and adsorption, blue color represents the cycle contraction-expansion reactions, red color represents the ring opening reactions and orange color the methyl-shift reactions. The bold characters represent the prefactors fitted by the model. In the case of the cycle contraction-expansion reactions the initial prefactor values are considered from similar reactions with data available.

	Reaction	$k_f^0 (s^{-1})$	$k_b^0 (s^{-1})$	$E_f (kJ mol^{-1})$	$E_b (kJ mol^{-1})$
		$K^0 (bar^{-1})$ or (-)			
1a	$ECH + H^+ \rightleftharpoons ECH^+$	<b><math>1.64 \pm 0.03 \cdot 10^{-2}</math></b>		38	0
1b	$ECH + H^+ \rightleftharpoons ECH^+$	<b><math>3.67 \pm 0.07 \cdot 10^0</math></b>		58	0
2	$13-EMCP + H^+ \rightleftharpoons 13-EMCP^+$	<b><math>7.36 \pm 0.15 \cdot 10^{-5}</math></b>		0	0
3	$12-EMCP + H^+ \rightleftharpoons 12-EMCP^+$	<b><math>7.36 \pm 0.15 \cdot 10^{-5}</math></b>		0	0
4	$11-EMCP + H^+ \rightleftharpoons 11-EMCP^+$	<b><math>7.36 \pm 0.15 \cdot 10^{-5}</math></b>		0	0
5	$14-DMCH + H^+ \rightleftharpoons 14-DMCH^+$	<b><math>7.36 \pm 0.15 \cdot 10^{-5}</math></b>		0	0
6	$13-DMCH + H^+ \rightleftharpoons 13-DMCH^+$	<b><math>7.36 \pm 0.15 \cdot 10^{-5}</math></b>		0	0
7	$12-DMCH + H^+ \rightleftharpoons 12-DMCH^+$	<b><math>7.36 \pm 0.15 \cdot 10^{-5}</math></b>		0	0
8	$11-DMCH + H^+ \rightleftharpoons 11-DMCH^+$	<b><math>7.36 \pm 0.15 \cdot 10^{-5}</math></b>		0	0
9	$113-TMCP + H^+ \rightleftharpoons 113-TMCP^+$	<b><math>7.36 \pm 0.15 \cdot 10^{-5}</math></b>		0	0
10	$112-TMCP + H^+ \rightleftharpoons 112-TMCP^+$	<b><math>7.36 \pm 0.15 \cdot 10^{-5}</math></b>		0	0
11	$124-TMCP + H^+ \rightleftharpoons 124-TMCP^+$	<b><math>7.36 \pm 0.15 \cdot 10^{-5}</math></b>		0	0
12	$123-TMCP + H^+ \rightleftharpoons 123-TMCP^+$	<b><math>7.36 \pm 0.15 \cdot 10^{-5}</math></b>		0	0
13	$IPCP + H^+ \rightleftharpoons IPCP^+$	<b><math>7.36 \pm 0.15 \cdot 10^{-5}</math></b>		0	0
14	$CRACK + H^+ \rightleftharpoons CRACK^+$	<b><math>7.36 \pm 0.15 \cdot 10^{-5}</math></b>		0	0
15	$ECH^+ \rightleftharpoons 12-EMCP^+$	$4.54 \cdot 10^{12}$	$3.13 \cdot 10^9$	89.0	71.0
16	$12-EMCP^+ \rightleftharpoons 12-DMCH^+$	$1.39 \cdot 10^{10}$	$8.25 \cdot 10^{11}$	77.0	87.9
17	$12-DMCH^+ \rightleftharpoons 123-TMCP^+$	$9.46 \cdot 10^{11}$	$3.34 \cdot 10^9$	73.5	51.7
18	$123-TMCP^+ \rightleftharpoons 14-DMCH^+$	$1.27 \cdot 10^{10}$	$2.03 \cdot 10^{11}$	63.9	53.3
19	$ECH^+ \rightleftharpoons 13-EMCP^+$	$6.81 \cdot 10^{12}$	$1.67 \cdot 10^{11}$	89.4	99.7
20	$13-EMCP^+ \rightleftharpoons 13-DMCH^+$	<b><math>4.51 \pm 0.1 \cdot 10^{11}</math></b>	$2.54 \cdot 10^{10}$	76.0	66.0
21	$13-DMCH^+ \rightleftharpoons 124-TMCP^+$	$2.22 \cdot 10^{12}$	$1.52 \cdot 10^{12}$	87.4	52.8
22	$13-DMCH^+ \rightleftharpoons 113-TMCP^+$	$2.22 \cdot 10^{12}$	$2.74 \cdot 10^{13}$	87.4	91.4
23	$13-EMCP^+ \rightleftharpoons 14-DMCH^+$	<b><math>3.48 \pm 0.07 \cdot 10^{11}</math></b>	$1.82 \cdot 10^{12}$	77.0	87.9
24	$14-DMCH^+ \rightleftharpoons 113-TMCP^+$	$9.67 \cdot 10^{10}$	$3.37 \cdot 10^{12}$	74.5	91.6
25	$113-TMCP^+ \rightleftharpoons CRACK^+$	$1.59 \cdot 10^{11}$	0	88.5	0
26	$113-TMCP^+ \rightleftharpoons 11-DMCH^+$	<b><math>1.24 \pm 0.02 \cdot 10^7</math></b>	$2.22 \cdot 10^{12}$	31.4	87.4
27	$ECH^+ \rightleftharpoons IPCP^+$	<b><math>3.28 \pm 0.07 \cdot 10^{11}</math></b>	$1.39 \cdot 10^{10}$	87.9	77.0
28	$13-DMCH^+ \rightleftharpoons CRACK^+$	<b><math>5.64 \pm 0.11 \cdot 10^{11}</math></b>	0	88.5	0
29	$113-TMCP^+ \rightleftharpoons 112-TMCP^+$	<b><math>3.07 \pm 0.07 \cdot 10^{-1}</math></b>		0	0
30	$113-TMCP^+ \rightleftharpoons 124-TMCP^+$	<b><math>4.53 \pm 0.1 \cdot 10^{-1}</math></b>		0	0
31	$113-TMCP^+ \rightleftharpoons 123-TMCP^+$	<b><math>2.11 \pm 0.04 \cdot 10^0</math></b>		0	0
32	$12-DMCH^+ \rightleftharpoons 13-DMCH^+$	<b><math>2.01 \pm 0.04 \cdot 10^0</math></b>		0	0
33	$13-DMCH^+ \rightleftharpoons 14-DMCH^+$	<b><math>1.45 \pm 0.03 \cdot 10^0</math></b>		0	0
34	$12-EMCP^+ \rightleftharpoons 11-EMCP^+$	<b><math>2.16 \pm 0.1 \cdot 10^{-1}</math></b>		0	0
35	$12-EMCP^+ \rightleftharpoons 13-EMCP^+$	<b><math>2.94 \pm 0.12 \cdot 10^0</math></b>		0	0

The evolution of the ECH conversion and the selectivities towards the isomerization and cracking products versus contact times are represented in Figure 5.22.



**Figure 5.22. ECH conversion and selectivity vs contact time at 285°C (catalyst mass divided by the ECH flow). Full lines: kinetic data; dots: experimental data.**

Since ring opening and dehydrogenation products selectivities are close to 0 they are not represented. In this figure, it can be observed that the kinetic model provides results in good accuracy with the experimental results for ECH conversion and for isomerization and cracking products. In view of these encouraging finding, accuracy of the kinetic model was analyzed in further details. First, the evolution of the different isomers lumps with ECH conversion is considered.

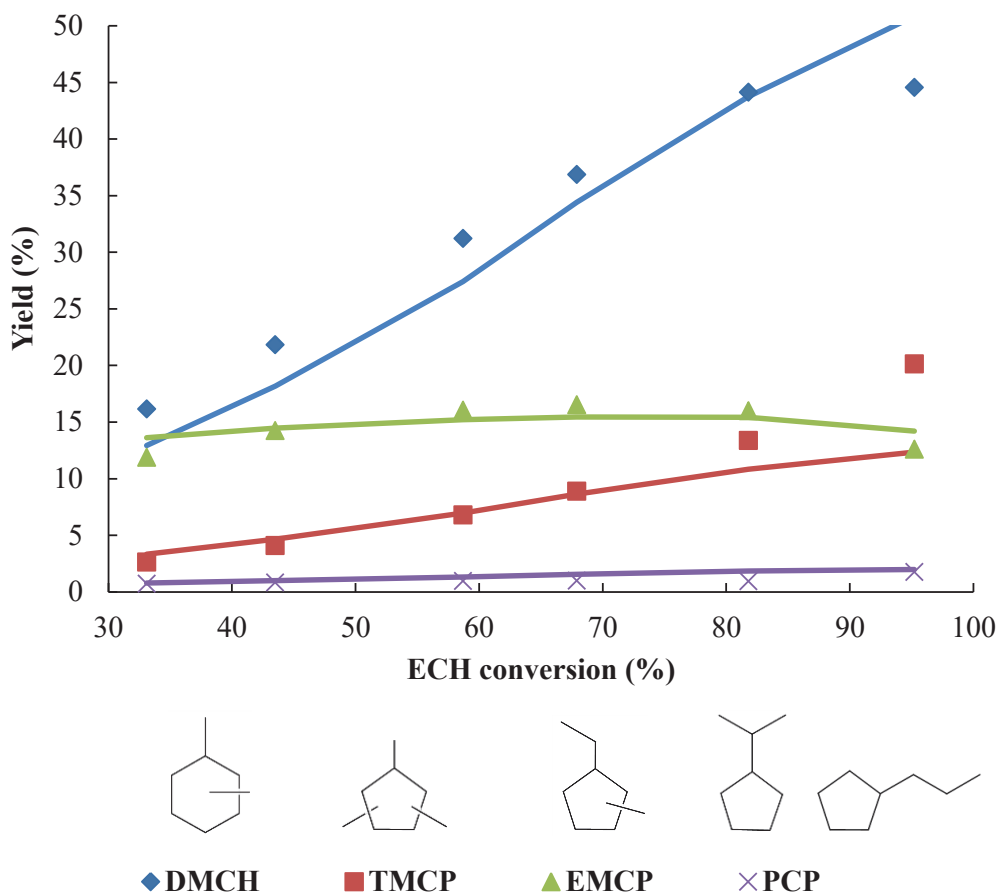


**Figure 5.23. Yield of lumped isomers families vs ECH conversion at 285°C. Full lines: kinetic data; dots: experimental data.**

Figure 5.23 represents the evolution of the yield percentage of each family of isomers as a function of the ECH conversion for both experimental and model data. The model fits pretty well the experimental data, even though at higher ECH conversion the model DMCH yield estimation is slightly higher than experimental data whereas in the case of the TMCP family, the model yield estimation is slightly lower than experimental data.

In order to go deeper in the study, the evolution of each isomer within its own family has been analyzed. It should be kept in mind that in the DFT data, there are no discrimination in between cis and trans isomers. Then, in the following analysis both cis and trans isomers are lumped together.

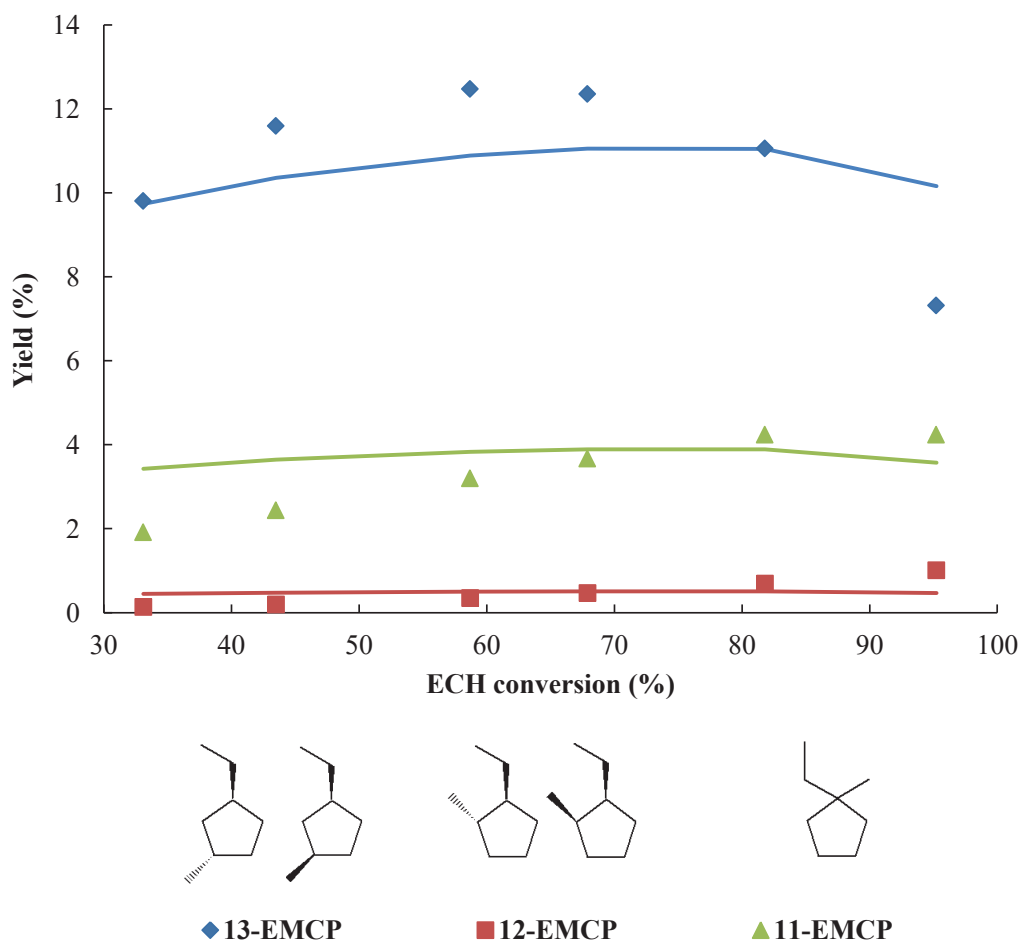


**Figure 5.24. Isomers yield within the EMCP family vs ECH conversion at 285°C. Full lines: kinetic modeling data; dots: experimental data.**

The evolution of EMCP isomers yield within the EMCP family is shown in Figure 5.24 as a function of the ECH conversion. In this family the experimental evolution of 12-EMCP and 11-EMCP yield is well defined by the kinetic model whereas is not so in the case for 13-EMCP. Within a range between 30-80 % of ECH conversion, the model underestimates the 13-EMCP yield while at higher conversion (where the equilibrium in the catalytic unit was reached) the kinetic model overestimates it if compared to the experience.

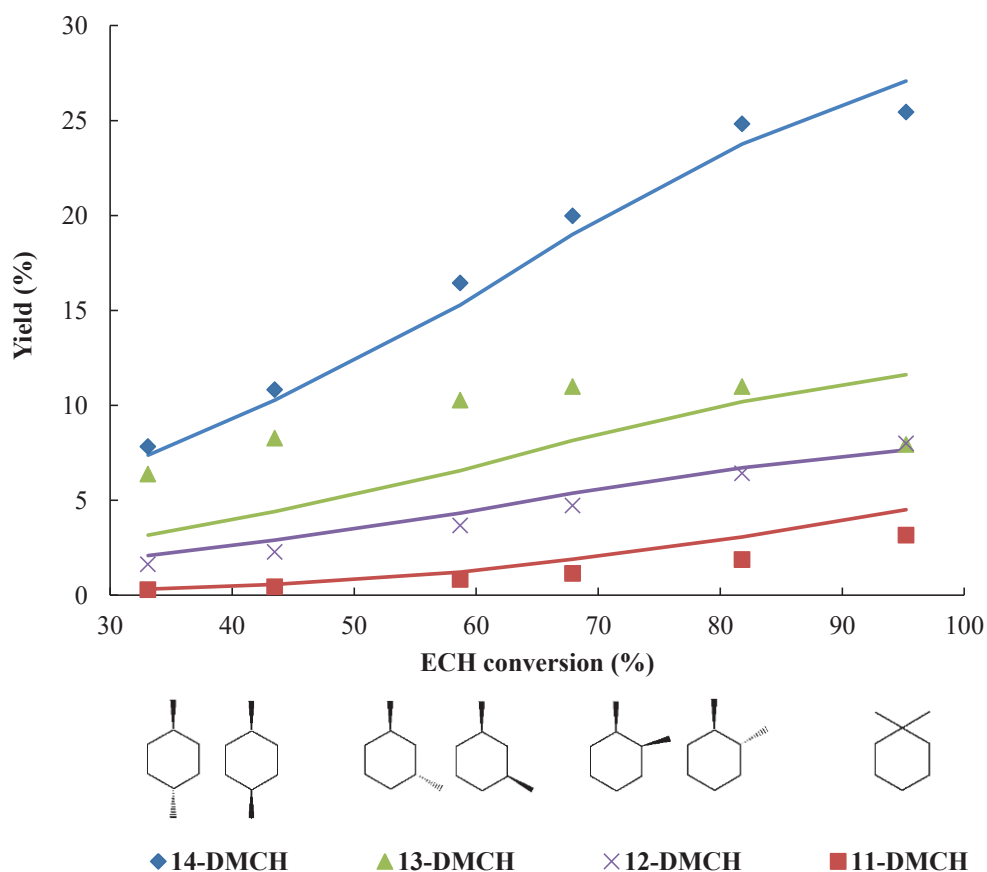


**Figure 5.25. Isomers yield within the DMCH family vs ECH conversion at 285°C. Full lines: kinetic modeling data; dots: experimental data.**

Concerning the DMCH family (Figure 5.25), the kinetic model fits quite well the experimental yields. Only at lower conversion 13-DMCH is underestimated with the model compared to experimental data whereas at higher conversion the model 13-DMCH yield percentage is overestimated.

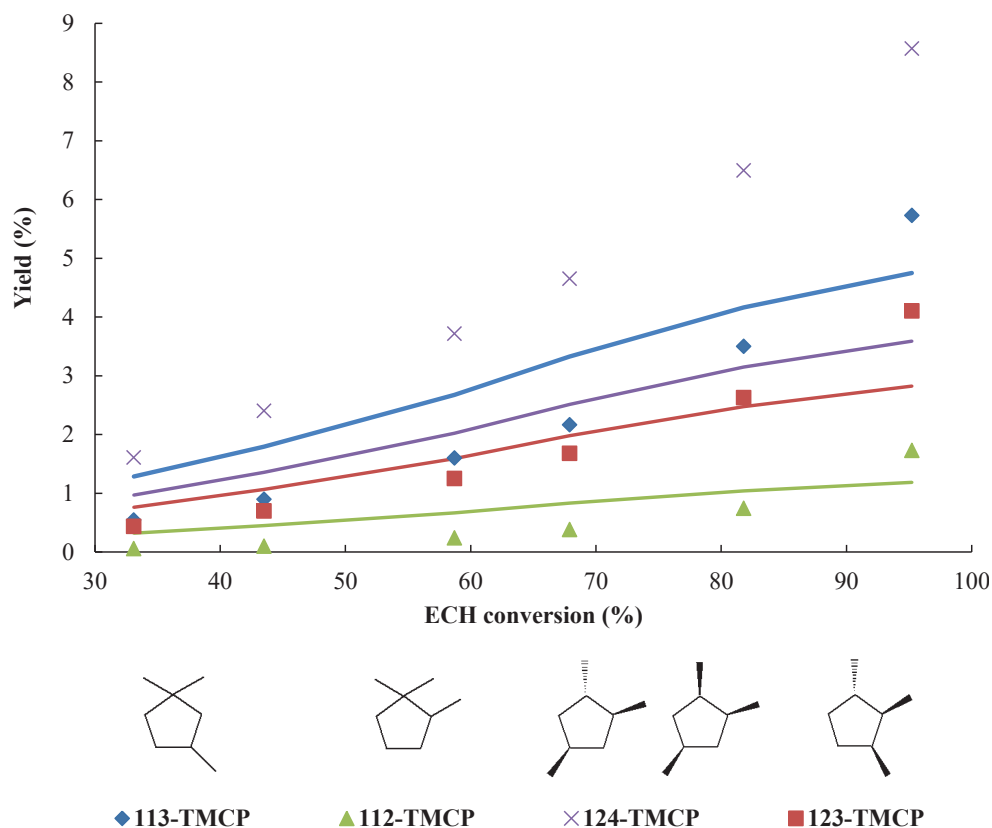


**Figure 5.26. Isomers yield within the TMCP family vs ECH conversion at 285°C. Full lines: kinetic data; dots: experimental data.**

The TMCP family is probably the one in which the model fits worst the experimental data. Even so, within this group, the 112-TMCP model yield is pretty close to the experimental data. Besides, 123-TMCP yield is well defined as well by the model even if at higher ECH conversion is slightly underestimated. Regarding, 133-TMCP model yield, it is overestimated at lower ECH conversion whereas at higher conversion is a little bit underestimated. Finally, the 124-TMCP yield is underestimated at all ECH conversion being this difference maxima at higher conversion.

Figure 5.20 shows the reaction network and the net rates for all steps. Within the reaction network a very fast interconversion between 5 surface species occurs (represented in Figure 5.20 with orange arrows). This "loop" stores 50% of all the surface species inside the zeolite. The overall coverage is very small, as expected based on the concentration of olefins.

Overall, the relevance of the kinetic model with respect to experimental product distribution as a function of the contact time / ECH conversion is very well rendered by the model. This agreement shows that for type B naphthene isomerization reactions, the kinetic parameters provided by ab initio calculations at the channel site are satisfactory. Other parameters (prefactors in bold in Table 5.3) were lumped and fitted, which also explains why the model performs well. Reducing the number of fitted parameters thanks to ab initio calculations is however of great help to obtain a robust and chemically relevant multi-scale kinetic model.

## 5.5. Conclusion

The evolution of the conversion and selectivity vs the contact times at some given temperatures is measured in the ethylcyclohexane hydroconversion on the EU-1 zeolite. The target of this analysis is to confirm the apparent mechanisms proposed in chapter 3 by a more rigorous kinetic investigation and then, to investigate in more detail the composition of the isomerization and ring opening products lumps. The results confirm the mechanisms and show a more detailed description of the isomerization products distribution within each family and of the ring opening products. The mechanism involves reactions of cycle expansion-contraction through protonated cyclopropyl (PCP), hydride and methyl shifts. According to this mechanism, the first primary products appearing are the ethylmethycyclopentanes (EMCP) followed by the dimethylcyclohexanes (DMCH) and at last by the trimethylcyclopentanes (TMCP). The analysis of the isomers within the EMCP family reveals the 13-EMCP as the first product appearing followed by the 12-EMCP in lower amount and the 11-EMCP at last in a very small amount. Regarding the isomers within the DMCH family, 13-DMCH and 14-DMCH appear first followed by lower amounts of 12-DMCH in second place and 11-DMCH at last in really low amount. The TMCP family results, reveal the 124-TMCP as the first isomer appearing followed by 113-TMCP and 123-TMCP and 112-TMCP appearing at last. Furthermore, the ring opening products distribution is analyzed as well. 25-Dimethylhexane and 2-methylheptane are revealed as the major ring opening products appearing. These products are expected to be obtained respectively from the opening of 133-



TMCP and 13-DMCH respectively. n-octane appeared as well within the ring opening products family, however its production is believed to come from the isomerization of the ring opening products instead of being the products of the  $\text{ECH}^+$  opening. From these results, several pathways of the isomerization reaction scheme (containing the isomers observed experimentally) are depicted and studied with *ab initio* calculations in two different active sites of the zeolite: the pocket (T9O6) and the channel (T1O1). These calculations reveal the energy barriers of each elementary step and thermodynamic data such as Gibbs adsorption energy, enthalpy and entropy energies. The first step of the isomerization of  $\text{ECH}^-$  appears as critical for the production of 24DMCH.

The analysis of the different pathways in the channel, does not allow us to define a major pathway occurring during the reaction. Even the analysis of the Gibbs adsorption energies does not put out to any favorite pathway. In the case of the pocket, Path I is clearly favored since the other paths (involving the TS1II) include a first step with a really high energy barrier. However, even if the pocket active site, possesses lower intermediate adsorption energies and many of the transition states have as well lower adsorption energy values, a part of the reaction products rests quite impeded. Thus, in order to build up a microkinetic model able to clarify the reactional scheme, only the thermodynamic data of the channel active site is employed in a preliminary kinetic modeling. With regards to the ring opening reaction, it is calculated in the different active sites from the intersection (T10O12), channel (T1O1) and pocket (T9O6). The only successful ring opening reaction carried out is the 113-TMCP ring opening into 25-dimethylhexane. Nevertheless, the transition state is not isolated because it is really close in energy to the product. Then, the energy barrier is finally calculated as an energy difference between the reactive and the product. These forward energy barriers reveal the ring opening as a difficult reaction since even if the forward barrier is not too high (such as in the pocket site), the backward energy is 0. From all the active sites tested within the zeolite, the ring opening is more favored in the pocket than in the channel or the intersection.

From the thermokinetic *ab initio* data, the kinetic constants of each individual step are calculated and introduced into the model. According to the model, the reaction would have an apparent activation energy of 131 kJ/mol assuming a first order reaction and using the integral rate equation for a fixed bed reactor. Applying this procedure to the experimental conversion at the lowest W/F, an activation energy of 115 kJ/mol was calculated. The initial activation barrier to convert ethyl-cyclohexane in the model equals 127 kJ/mol for Path I

(steps (1a) + (15)) and 147 kJ/mol for Path II (steps (1b) + (19)), respectively. Following with the mechanisms, the model fits quite well the experimental data of the general mechanism. The data concerning the isomerization mechanism is well fitted as well by the model, even if at higher ECH conversion the DMCP yield is a little bit overestimated in detriment of the TMCP yield which is underestimated. Going further into detail, the EMCP product distribution within this family reveals as well a good correlation between the experimental and the modelled data. Within this family, in a range between 30-80 % of ECH conversion, the model underestimates the 13-EMCP yield while at higher conversion the kinetic model overestimates it if compared to the experience. Following with this detailed analysis and regarding the DMCH family, the kinetic model fits quite well the experimental yields. Only at lower conversion 13-DMCH model yield is overestimated if compared to experimental data whereas at higher conversion it is overestimated. Finally, the TMCP family is probably the one in which the model fitted worst the experimental data. Even so, within this group, the 112-TMCP and 123-TMCP model yields are pretty close to the experimental data, even if at higher ECH conversion 123-TMCP yield is slightly underestimated. Regarding, 133-TMCP model yield, it is overestimated at lower ECH conversion whereas at higher conversion is a little bit underestimated. Finally, the 124-TMCP yield is underestimated at all ECH conversion being this difference maximal at higher conversion.

To sum up, the general mechanism and the isomerization and ring opening mechanisms are unraveled. Besides, thanks to the *ab initio* calculations, a deep knowledge of the mechanism has been achieved and the rate constants calculated. Including these rate constants in the microkinetic model, a well correlation between the experimental and modelled data has been found for describing the global and the isomerization mechanisms.

A perspective of this kinetic modeling is related to a hybrid channel-pocket scheme. Since the first step of Path II in the pocket has a first energy barrier that makes this step really unfavorable, we can imagine that this first step could occur in the channel. Afterwards, the product intermediate ( $\pi$ -complex  $i^*$ ) of this reaction would diffuse through the intersection into the channel where the rest of the reaction would take place. Furthermore, another perspective is to split up the lump of  $\pi$  and carbenium complexes in order to have access to the reaction intermediates concentration.



## 6. ECH HYDROISOMERIZATION: Evaluation of various zeolite topologies

---

### 6.1. Introduction

The zeolites topology has been revealed as an important factor in the catalytic selectivity as reported by several authors.<sup>5,187</sup> The previous chapter 4 also showed that the local topology, depending on the active site location within the EUO framework, is a key parameter playing on the catalytic activity. In the following study, the evaluation of the impact of the zeolitic topology in the ethylcyclohexane hydroisomerization, using eleven different zeolites, has been performed. The zeolites have been selected in order to maximize the diversity of the topologies in terms of dimensionality (1D, 2D, 3D) and pore size (10 MR and 12 MR). The availability of the zeolite was also taken into account for practical reasons (Section 2.1). The zeolites are presented in Table 6.1. according to this classification. The bifunctional catalysts are synthesized under the same protocol followed in Chapter 3. The catalysts are mechanical mixtures of alumina and zeolite, though in this case the Pt is always deposited on the alumina. For each zeolite (acidic phase) considered, three different amounts of Pt (HD/DHD function) are used: 0.2, 1 and 2 wt.% Pt. The purpose of testing three different Pt amounts is to find “ideal catalysts” as defined in Chapter 3. Then, for each zeolite one “ideal catalyst” was identified. Catalytic results of the ideal catalysts are presented hereafter. The results obtained with the other catalysts are provided in the appendix VI. The bifunctional catalysts are tested under the conditions gathered in section 2.3.2.2. Furthermore, preliminary DFT ab initio calculations have been carried out over some zeolites structures (only the ones whose framework is known), taking into account the key intermediates and TS of the reaction in order to see if the differences of activity / selectivity can be rationalized / anticipated. The zeolites structures will be shown in this section.

**Table 6.1. Zeolites employed in this study classified as a function of the pore size and dimensionality.**

Zeolite	Framework type	Ring-size/Dimensionality	D <sub>max</sub> <sup>a</sup> (Å)	D <sub>diff</sub> <sup>b</sup> (Å)
ZSM-23	MTT	10MR/1D	6.2	5.1
EU-1, ZSM-50	EUO	10MR-12 MR pockets/1D	7.0	5.0
ZSM-12	MTW	12MR/1D	6.1	5.7
ZSM-5	MFI	10MR/3D	6.4	4.7
ZSM-57	MFS	10MR-8MR/2D	6.8	5.4
IZM-2	Unknown	10-12 MR /1-2D ?*	—	—
NU-86	Unknown	10-11-12MR/3D**	—	—
BETA	BEA	12MR/3D	6.7	6.0
MOR-15, MOR-50	MOR	12MR-8 MR/2D	6.7	6.5

<sup>a</sup> maximal sphere diameter suitable in the framework, from IZA online.

<sup>b</sup> maximal sphere diameter able to diffuse inside the framework, from IZA online.

\* IZM-2 structure is unknown at the moment. It is believed to possess 10 and 12 MR pores and a low dimensionality.<sup>135</sup> \*\* NU-86 structure is unknown at the moment, it is believed to possess 10, 11 and 12 MR pores.<sup>224</sup>

## 6.2. Zeolites characterization

Table 6.2 reports the main physical-chemical properties of the zeolites employed for the catalytic evaluation. All the zeolites are in the protonic form and have been subjected to calcination and ion exchange when necessary. Information about calcination and ion exchange protocols is provided in Appendix I. In the case of HMOR, two different global Si/Al ratio have been tested in order to evaluate the influence of the acidity. For all the zeolites, crystallinity was around 100% (Appendix VI). The amount of sodium after ionic exchange was low, below 100 ppm in many cases except HZSM-50, HZSM-57 and HZSM-5, the sodium amount of which were 448, 132, 227 ppm., respectively. All the zeolites can be considered in the protonic form as their Na/Al ratio is below 5% mol. The BET surface area varied from one zeolite to the other even if many zeolites exhibited BET surface areas between 400 and 500 m<sup>2</sup> g<sup>-1</sup>. The highest BET surface area corresponded to HBETA zeolite (726 m<sup>2</sup> g<sup>-1</sup>) and the lower to HZSM-23 (220 m<sup>2</sup> g<sup>-1</sup>). Regarding the microporous volumes, they were not so different in many zeolites varying from 0.07 to 0.19 mL g<sup>-1</sup>. Again the highest value of microporous volume was found for the HBETA zeolite, 0.19 mL g<sup>-1</sup> and the lowest for the HZSM-23, 0.08 mL g<sup>-1</sup>. Such results are in accordance with the dimensionality and pore size of the two zeolites. Concerning the external surface area, it was found that one-dimensional zeolites had lower surface area than the two- or three-dimensional zeolites. With regards to the mesoporous volume, somehow the same tendency was observed. The acidity

was calculated removing the amount of Na from the amount of  $Al^{IV}$ . Most of the zeolites had an amount of acid sites in between 500 and 600  $\mu\text{mol g}^{-1}$ . Nonetheless, some zeolites showed lower amount of acid sites such as HIZM-2, HZSM-12 and HMOR50. These values were expected since these zeolite possessed the highest Si/Al ratio of the all set. HNU-86 and HBETA showed the highest values of total amount of acid sites.

According to SEM characterization, the crystals size strongly depended on the zeolite. In the case of the 10MR zeolites (Figure 6.1), the HZSM-23 crystals exhibits a needle shape morphology with a size in between 100 and 700 nm, whereas HZSM-57 particles are platelets constituted of very small round crystals (lower than 50 nm). At last, HZSM-5 crystals exhibits sizes ranging from 20 to 60 nm with a round shape.

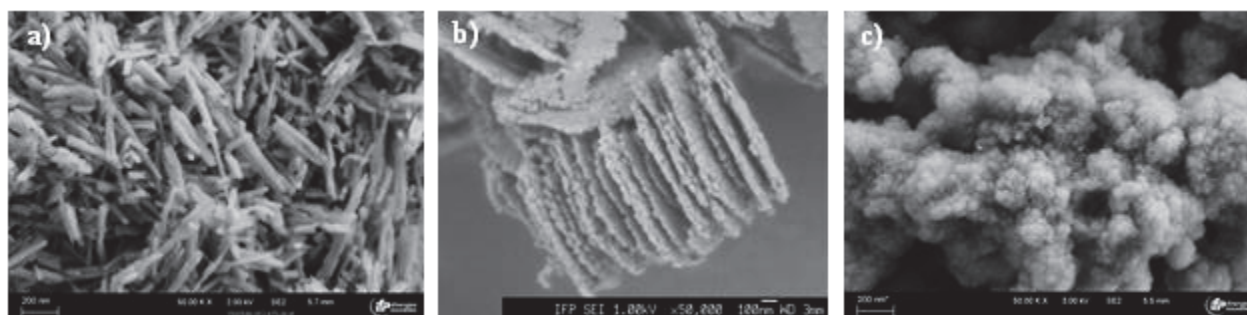


Figure 6.1. SEM images of a) ZSM-23, b) ZSM-57 and c) ZSM-5.

Table 6.2. Zeolites characterization

Sample	$S_{BET}$ ( $\text{m}^2 \text{g}^{-1}$ )	$V_{micro}$ ( $\text{mL g}^{-1}$ )	$V_{meso}$ ( $\text{mL g}^{-1}$ )	$S_{ext}$ ( $\text{m}^2 \text{g}^{-1}$ )	Crystal size (nm)	Na*	Na/Al	(Si/Al) <sub>g</sub>	Al*	Al <sup>IV</sup>	$n_A^{*,**}$
						(ppm)	(%)	mol/mol	(%)	(%)	( $\mu\text{mol g}^{-1}$ )
HZSM-23	220	0.07	0.42	66	100-700	46	0.34	26	1.56	100	607
HZSM-57	434	0.15	0.17	148	<50	132	0.84	26	1.58	95	556
HZSM-5	459	0.12	0.30	161	20-60	227	1.74	25	1.53	100	622
HEU-1	438	0.14	0.19	75	30-60	52	2.35	18	2.10	91	735
HZSM50	356	0.13	0.05	28	200	448	3.57	29	1.38	91	529
HIZM-2	291	0.08	0.26	100	40-100	55	1.24	73	0.58	92	214
HNU-86	498	0.13	0.83	174	—	73	0.38	14	2.49	91	981
HZSM-12	370	0.11	0.31	92	20-70	94	1.28	46	0.97	100	359
HMOR15	565	0.19	0.12	55	100	50	0.33	17	2.05	88	756
HMOR50	490	0.16	0.17	95	50-200	75	1.00	45	0.93	97	335
HBETA	726	0.19	0.62	280	20	24	0.17	13	1.38	100	1015

\* corrected from loss on ignition, \*\* calculated removing the amount of Na from the amount of  $Al^{IV}$ .

The SEM images concerning the 10-12 MR zeolites group are reported in Figure 6.2. As it has been already mentioned in chapter 4, HEU-1 particles are round and their nano crystals



typical size estimated by SEM is about 30-60 nm, whereas the HZSM-50 crystals are much bigger rods, about several  $\mu\text{m}$  of length and 200 nm of thickness. On the other hand, HIZM-2 exhibits oblong shape crystals, the size of which is between 40 and 100 nm approximately, and HNU-86 crystals have a leaflets shape. Typical crystallite size were difficult to measure due to agglomeration.

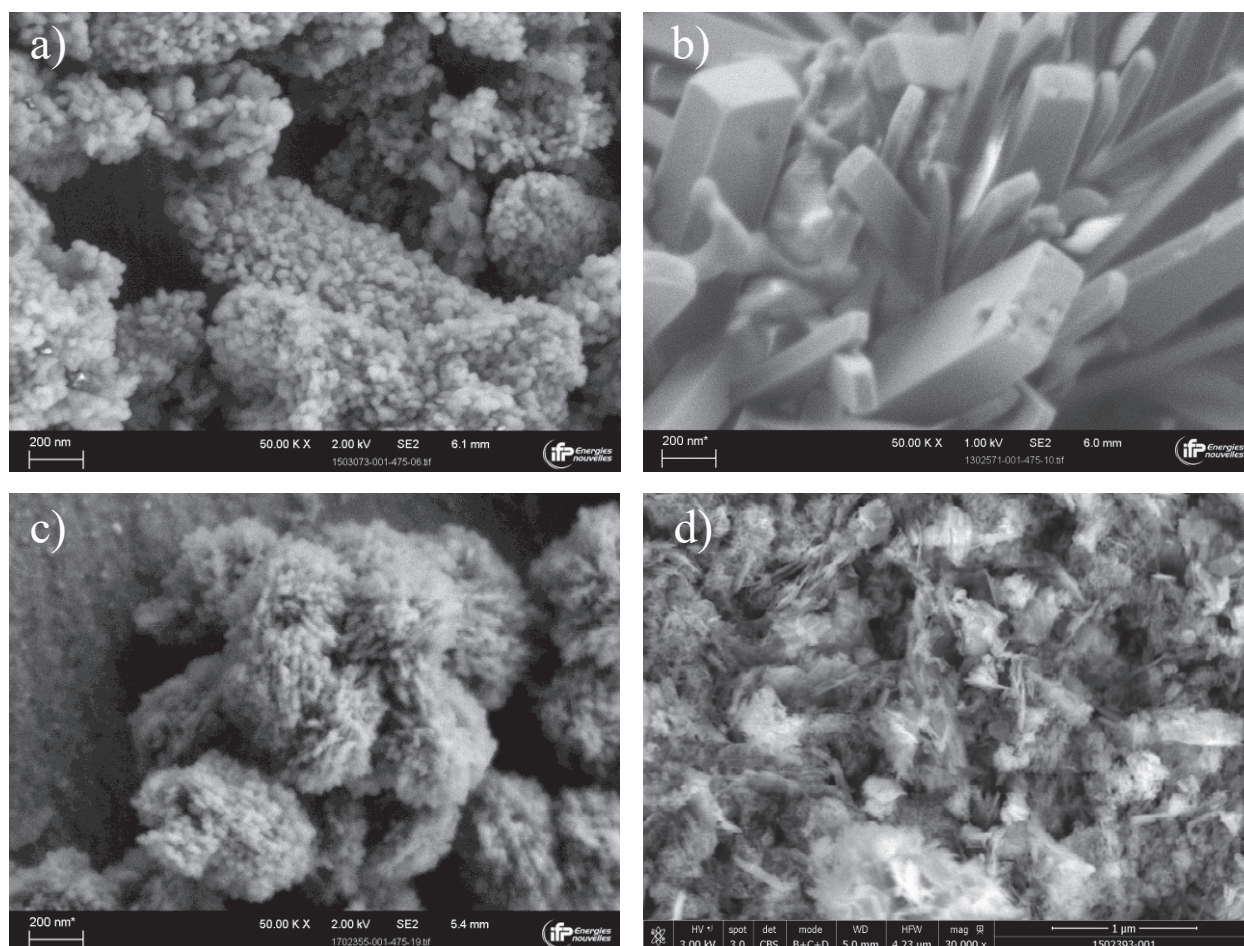


**Figure 6.2.** SEM images of a) EU-1, b) ZSM-50, c) IZM-2 and d) NU-86.

Regarding the 12MR zeolites group (Figure 6.4), HZSM-12 revealed crystallites with a size between 20 and 70 nm, HMOR15 has faceted polyhedral crystals between 50 and 500 nm in size with an average size of 100 nm, whereas HMOR50 has crystals of 50 to 200 nm in diameter. With regards to HBETA zeolite, their crystals with somehow a rounded shape, are of small size around 20 nm. However, sometimes these crystals had a not well-defined shape.

As conclusion from the SEM analysis, the lower crystallite size were found for the HBETA, HZSM-5, HZSM-12 and HEU-1 zeolites whereas bigger crystallites were found for HZSM-23 and HZSM-50. If we relate this values to the textural properties, it is found that

HBETA zeolite exhibits the highest external surface area and mesoporous volume. This is in agreement with the small crystallites size observed for this sample. It occurred similarly with HZSM-5, their crystallites were small, therefore the external surface area and mesoporous volume were quite high. On the other hand, larger crystallites such as the ones corresponding to HZSM-50 provide a smaller external surface area and mesoporous volume.

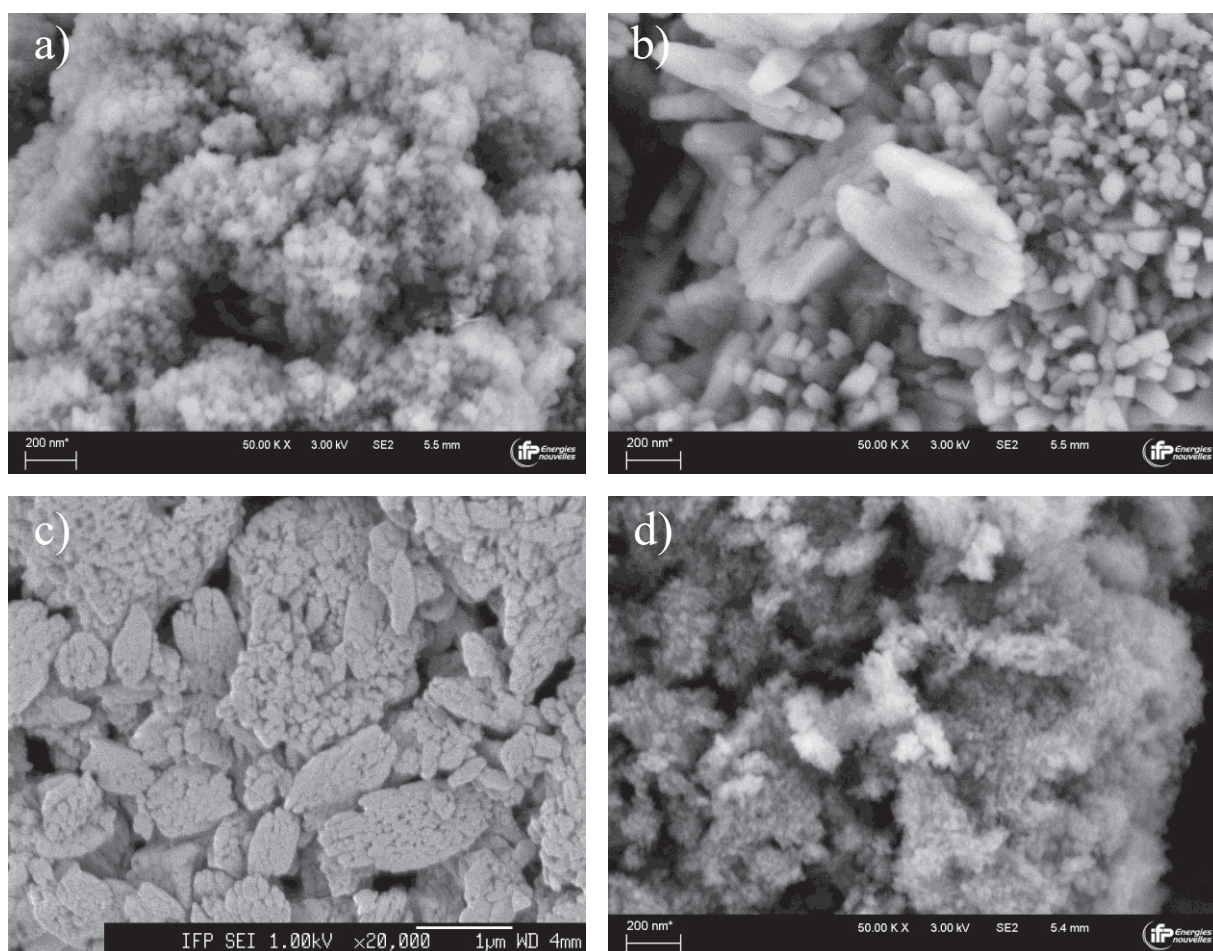


Figure 6.3. SEM images of a) ZSM-12, b) MOR15, c) MOR50 and d) BETA.

### 6.3. Well-balanced bifunctional catalysts selection

The description of all the bifunctional catalysts is enclosed in Table 6.3. For each zeolite, three mechanical mixtures (zeolite-alumina) with alumina containing three different amounts of Pt deposited were prepared and tested. Catalytic evaluation was performed using a High Throughput Experimentation Unit. Details about the unit, catalytic test protocol and operating conditions are provided in Chapter 2. In Chapter 3, it was observed for HEU-1 that the catalytic activity and selectivity plateau were reached for the 1%Pt-Al<sub>2</sub>O<sub>3</sub>/HEU-1 catalyst.



This tendency is also observed for most of the zeolites screened: 0.2% Pt is below the plateau whereas 1% and 2 %Pt/Alumina are located on the plateau. An example based on the results containing HMOR as acidic function (1%Pt- Al<sub>2</sub>O<sub>3</sub>/HMOR15) is depicted in figures 6.4. and 6.5. From these figures it is observed how two catalysts are located at the plateau, 1 and 2%Pt-Al<sub>2</sub>O<sub>3</sub>/HMOR15, whereas the 0.2%Pt- Al<sub>2</sub>O<sub>3</sub>/HMOR15 is not. Even if this is observed in terms of catalytic activity, it is not the case in terms of selectivity towards the isomerization, cracking, ring opening and dehydrogenation reactions. Selectivity plateaus seem to be reached even at 0.2%. This is in agreement with the affirmation of Chapter 3 according to which, the metal/acid balance required for reaching an activity plateau was lower than the metal/acid balance required for reaching the isomerization plateau.

When the same performances are obtained for a set of catalyst, the selected well balanced catalyst is the one containing the lower amount of platinum. The selected catalysts are provided in table 6.3. All the well balanced catalysts are containing the same amount of platinum (1.05wt% Pt deposited on Al<sub>2</sub>O<sub>3</sub>).

**Table 6.3. Bifunctional catalysts tested in this study. The selected well balanced catalyst are labeled in italic and bold.**

	Composition	Catalyst name
<b>BIFUNCTIONAL CATALYSTS</b>	80% 0.26wt%Pt-Al <sub>2</sub> O <sub>3</sub> - 20% HZSM-23	0.2%Pt- Al <sub>2</sub> O <sub>3</sub> /HZSM-23
	<b>80% 1.05wt%Pt- Al<sub>2</sub>O<sub>3</sub>- 20% HZSM-23</b>	<b>1%Pt- Al<sub>2</sub>O<sub>3</sub>/HZSM-23</b>
	80% 1.76wt%Pt- Al <sub>2</sub> O <sub>3</sub> - 20% HZSM-23	2%Pt- Al <sub>2</sub> O <sub>3</sub> /HZSM-23
	80% 0.26wt%Pt- Al <sub>2</sub> O <sub>3</sub> - 20% HZSM-57	0.2%Pt- Al <sub>2</sub> O <sub>3</sub> /HZSM-57
	<b>80% 1.05wt%Pt- Al<sub>2</sub>O<sub>3</sub>- 20% HZSM-57</b>	<b>1%Pt- Al<sub>2</sub>O<sub>3</sub>/HZSM-57</b>
	80% 1.76wt%Pt- Al <sub>2</sub> O <sub>3</sub> - 20% HZSM-57	2%Pt- Al <sub>2</sub> O <sub>3</sub> /HZSM-57
	80% 0.26wt%Pt- Al <sub>2</sub> O <sub>3</sub> - 20% HZSM-5	0.2%Pt- Al <sub>2</sub> O <sub>3</sub> /HZSM-5
	<b>80% 1.05wt%Pt- Al<sub>2</sub>O<sub>3</sub>- 20% HZSM-5</b>	<b>1%Pt- Al<sub>2</sub>O<sub>3</sub>/HZSM-5</b>
	80% 1.76wt%Pt- Al <sub>2</sub> O <sub>3</sub> - 20% HZSM-5	2%Pt- Al <sub>2</sub> O <sub>3</sub> /HZSM-5
	80% 0.26wt%Pt- Al <sub>2</sub> O <sub>3</sub> - 20% HEU-1	0.2%Pt- Al <sub>2</sub> O <sub>3</sub> /HEU-1
	<b>80% 1.05wt%Pt- Al<sub>2</sub>O<sub>3</sub> 20% HEU-1</b>	<b>1%Pt- Al<sub>2</sub>O<sub>3</sub>/HEU-1</b>
	80% 1.76wt%Pt- Al <sub>2</sub> O <sub>3</sub> - 20% HEU-1	2%Pt- Al <sub>2</sub> O <sub>3</sub> /HEU-1
	<b>80% 1.05wt%Pt- Al<sub>2</sub>O<sub>3</sub>- 20% HZSM-50</b>	<b>1%Pt- Al<sub>2</sub>O<sub>3</sub>/HZSM-50</b>
	80% 0.26wt%Pt- Al <sub>2</sub> O <sub>3</sub> - 20% HIZM-2	0.2%Pt- Al <sub>2</sub> O <sub>3</sub> /HIZM-2
	<b>80% 1.05wt%Pt- Al<sub>2</sub>O<sub>3</sub>- 20% HIZM-2</b>	<b>1%Pt- Al<sub>2</sub>O<sub>3</sub>/HIZM-2</b>
	80% 1.76wt%Pt- Al <sub>2</sub> O <sub>3</sub> - 20% HIZM-2	2%Pt- Al <sub>2</sub> O <sub>3</sub> /HIZM-2
	80% 0.26wt%Pt- Al <sub>2</sub> O <sub>3</sub> - 20% HNU-86	0.2%Pt- Al <sub>2</sub> O <sub>3</sub> /HNU-86
	<b>80% 1.05wt%Pt- Al<sub>2</sub>O<sub>3</sub>- 20% HNU-86</b>	<b>1%Pt- Al<sub>2</sub>O<sub>3</sub>/HNU-86</b>
	80% 1.76wt%Pt- Al <sub>2</sub> O <sub>3</sub> - 20% HNU-86	2%Pt- Al <sub>2</sub> O <sub>3</sub> /HNU-86
	80% 0.26wt%Pt- Al <sub>2</sub> O <sub>3</sub> - 20% HZSM-12	0.2%Pt- Al <sub>2</sub> O <sub>3</sub> /HZSM-12

	<b>80% 1.05wt%Pt- Al<sub>2</sub>O<sub>3</sub>- 20% HZSM-12</b>	<b>1%Pt- Al<sub>2</sub>O<sub>3</sub>/HZSM-12</b>
	80% 1.76wt%Pt- Al <sub>2</sub> O <sub>3</sub> - 20% HZSM-12	2%Pt- Al <sub>2</sub> O <sub>3</sub> /HZSM-12
	80% 0.26wt%Pt- Al <sub>2</sub> O <sub>3</sub> - 20% HMOR15	0.2%Pt- Al <sub>2</sub> O <sub>3</sub> /HMOR15
	<b>80% 1.05wt%Pt- Al<sub>2</sub>O<sub>3</sub>- 20% HMOR15</b>	<b>1%Pt- Al<sub>2</sub>O<sub>3</sub>/HMOR15</b>
	80% 1.76wt%Pt- Al <sub>2</sub> O <sub>3</sub> - 20% HMOR15	2%Pt- Al <sub>2</sub> O <sub>3</sub> /HMOR15
	80% 0.26wt%Pt- Al <sub>2</sub> O <sub>3</sub> - 20% HMOR50	0.2%Pt- Al <sub>2</sub> O <sub>3</sub> /HMOR50
	<b>80% 1.05wt%Pt- Al<sub>2</sub>O<sub>3</sub>- 20% HMOR50</b>	<b>1%Pt- Al<sub>2</sub>O<sub>3</sub>/HMOR50</b>
	80% 1.76wt%Pt- Al <sub>2</sub> O <sub>3</sub> - 20% HMOR50	2%Pt- Al <sub>2</sub> O <sub>3</sub> /HMOR50
	80% 0.26wt%Pt- Al <sub>2</sub> O <sub>3</sub> - 20% HBETA	0.2%Pt- Al <sub>2</sub> O <sub>3</sub> /HBETA
	<b>80% 1.05wt%Pt- Al<sub>2</sub>O<sub>3</sub>- 20% HBETA</b>	<b>1%Pt- Al<sub>2</sub>O<sub>3</sub>/HBETA</b>
	80% 1.76wt%Pt- Al <sub>2</sub> O <sub>3</sub> - 20% HBETA	2%Pt- Al <sub>2</sub> O <sub>3</sub> /HBETA

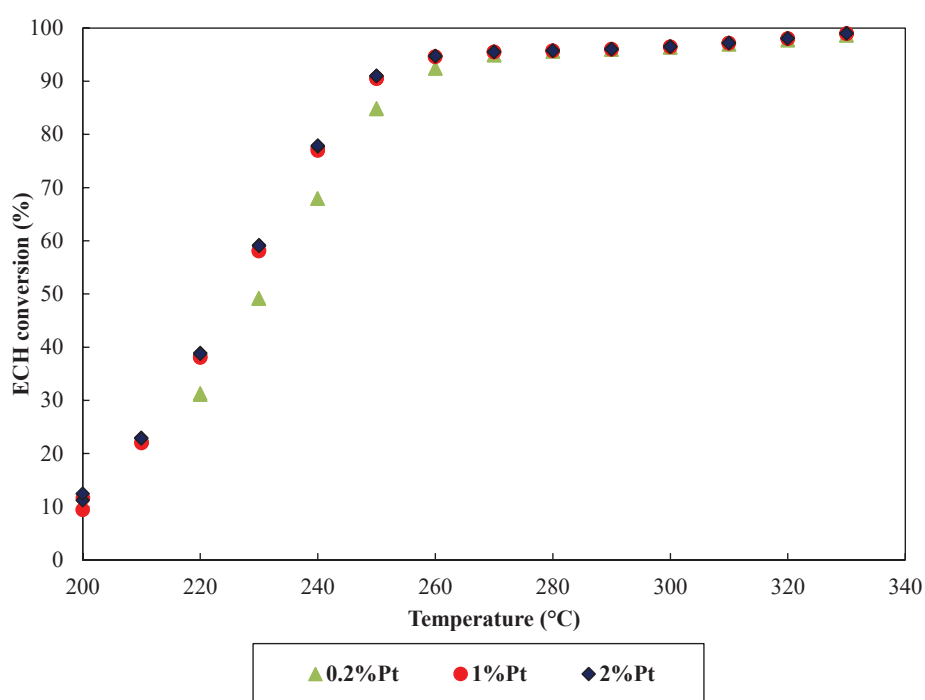
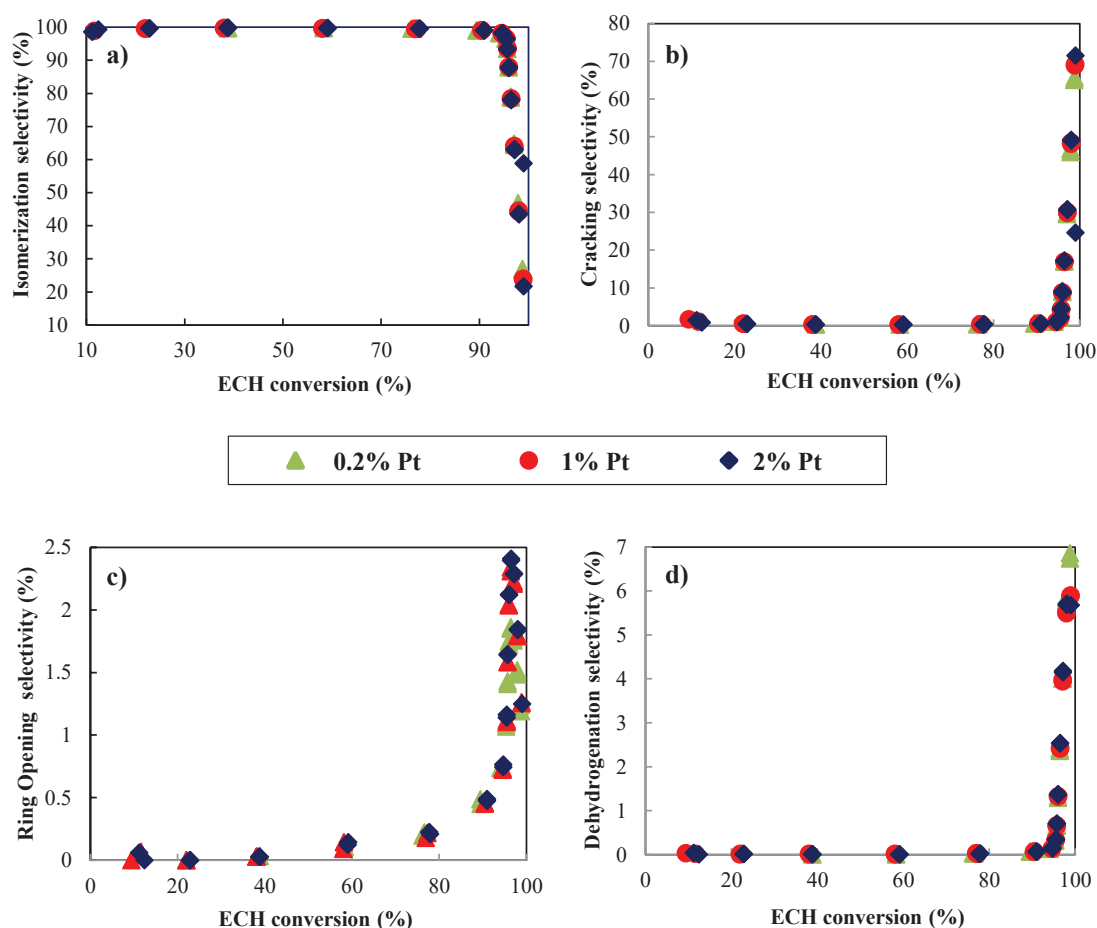


Figure 6.4. ECH conversion vs temperature for the 1%Pt- Al<sub>2</sub>O<sub>3</sub>/HMOR15 catalyst.



**Figure 6.5.** Evolution of the selectivity versus ECH conversion for the 1%Pt-Al<sub>2</sub>O<sub>3</sub>/HMOR15 catalysts; a) isomerization; b) cracking; c) ring opening; d) dehydrogenation.

#### 6.4. Performances of the well-balanced bifunctional catalysts

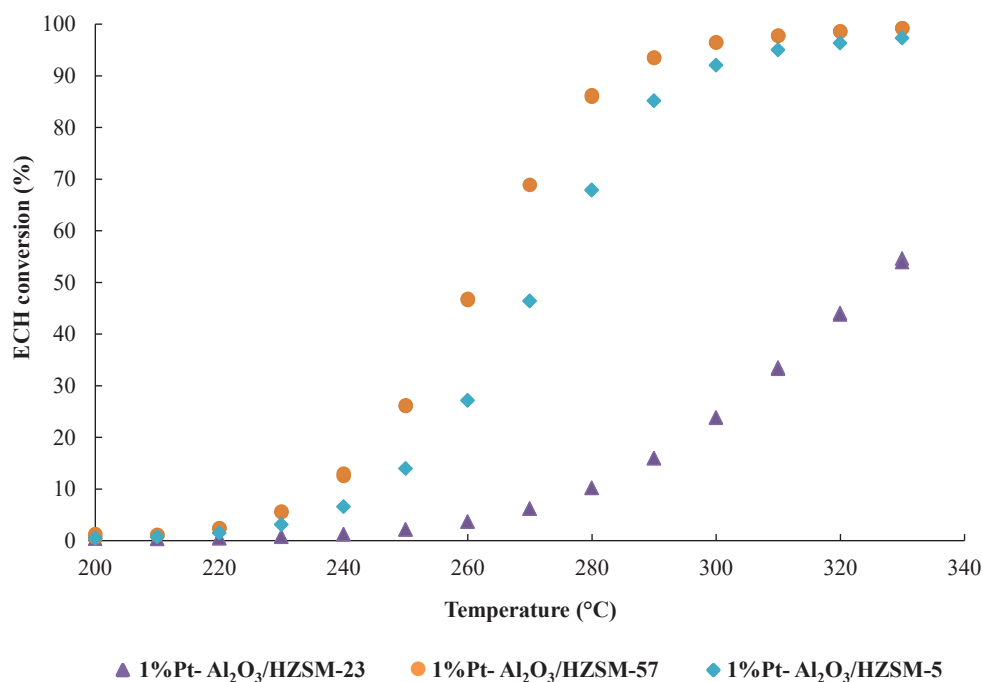
The performances of the bifunctional catalysts are herein discussed according to:

- the catalytic activity, firstly on weight basis and then on the turnover frequency per Brønsted acid site of the zeolite basis
- the catalytic selectivity. The evolution of the various product yields with conversion will be discussed.

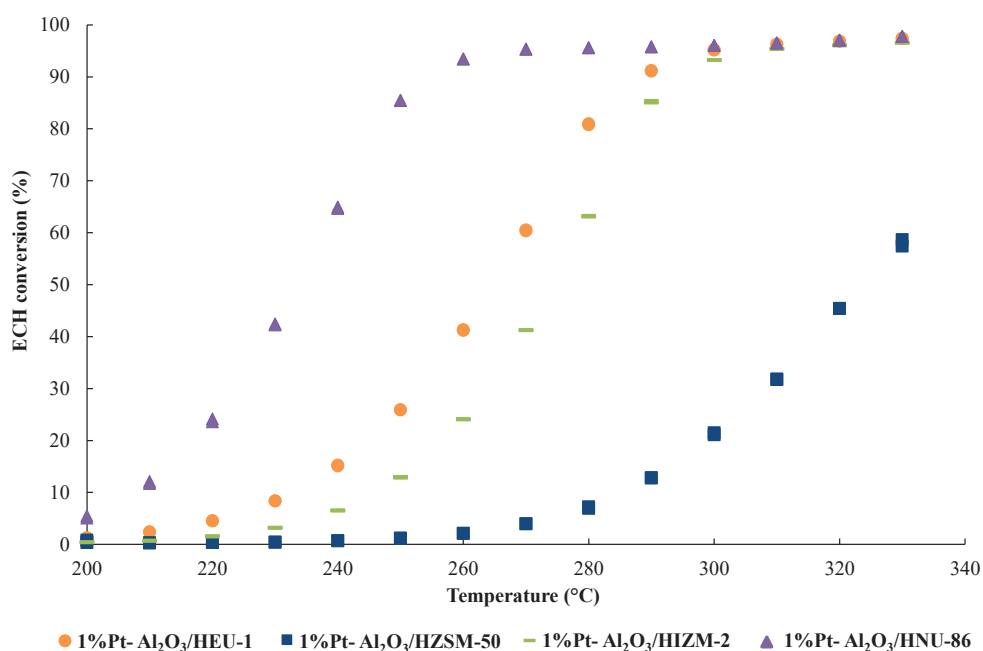
##### 6.4.1. Catalytic activity

Figure 6.6, 6.7 and 6.8 depict the evolution of reactant conversion with temperature for all the catalysts considered.

Figure 6.6 represents the evolution of ECH conversion with the temperature of the zeolites possessing 10 MR pores. For a given temperature, higher ECH conversion are obtained with the catalysts containing two- and three- dimensional zeolites (1% Pt-Al<sub>2</sub>O<sub>3</sub> /HZSM-57 and 1% Pt-Al<sub>2</sub>O<sub>3</sub> /HZSM-5 respectively) compared to the ECH conversion found with the catalyst containing the one-dimensional zeolite (1% Pt-Al<sub>2</sub>O<sub>3</sub> /HZSM-23). In this group, the HZSM-57 zeolite-based catalyst is the most active one.



**Figure 6.6.** Evolution of the ECH conversion with the temperature for the 10MR zeolite-based catalysts.



**Figure 6.7. Evolution of the ECH conversion with the temperature for the 10-12MR zeolite-based catalysts.**

Figure 6.7 is the same as Figure 6.6 but for the 10-12MR zeolites. The main feature of this figure is that all the catalyst except the one containing HZSM-50 zeolite, reach the same ECH conversion from 310°C (around 98%). Something remarkable in this group is the huge difference of activity found for the two one-dimensional zeolites sharing the same framework: HEU-1 and HZSM-50 zeolite-based catalysts. This difference assigned to the location of the active sites, had been already explained in Chapter 4. In this group, the HNU-86 zeolite-based catalyst is the most active one.

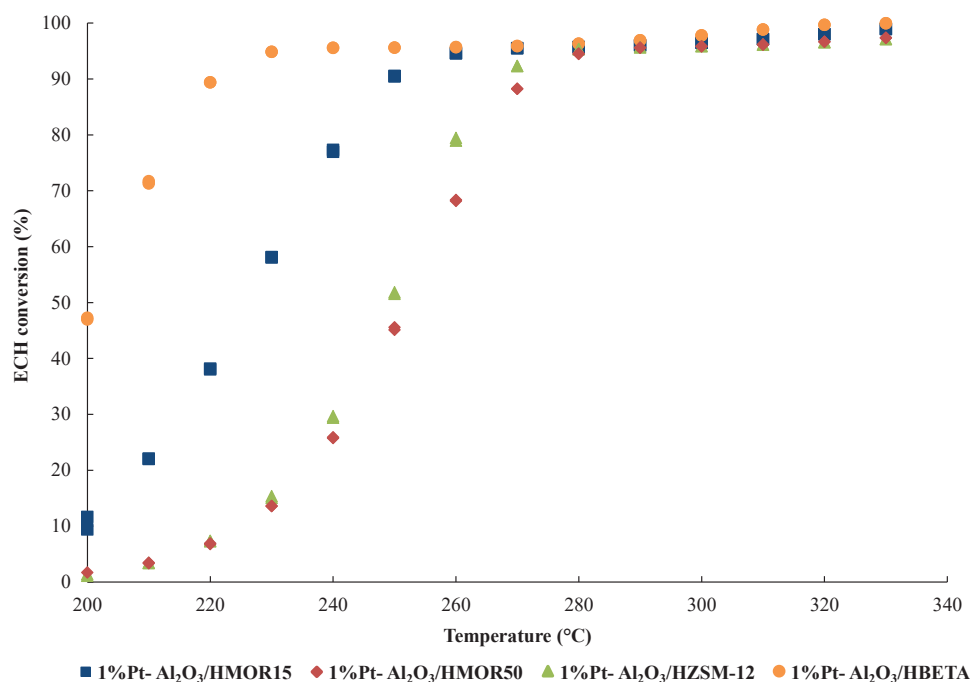


**Figure 6.8. Evolution of the ECH conversion with the temperature for the 12MR zeolite-based catalysts.**

Figure 6.8 depicts the evolution of the ECH conversion with the temperature for the 12MR zeolites. The low temperature (230°C) at which the maximal ECH conversion is reached with the HBETA zeolite it is above all associated to its higher acidity. Regarding the mordenite zeolites, it is observed that mordenite with lower Si/Al ratio (more acidic zeolite) is substantially more active than the one with the higher Si/Al ratio. For example at 240°C 77% ECH conversion are obtained with HMOR15 zeolite-based catalyst whereas for HMOR50 zeolite-based catalyst, only 14% of ECH conversion is obtained. Thus, this observation confirms the influence of the acidity in the reaction. In here, both HBETA and HMOR15 zeolite-based catalyst are the most active ones.

In a nutshell, the catalysts evaluated in this study exhibit very different levels of activities for ECH conversion. The temperature necessary to reach 50% conversion of ECH is then a convenient descriptor of the catalytic activity.<sup>225</sup> (provided in table 6.4. for all the catalysts). The temperature range between the most (1%Pt- Al<sub>2</sub>O<sub>3</sub>/HBETA) and the less (1%Pt- Al<sub>2</sub>O<sub>3</sub>/HZSM-23) active catalyst of the studied zeolites is typically 120°C. For a well-balanced catalyst, apparent activation energy  $E_{app}$  should be related to the enthalpies associated to the elementary steps of ECH conversion on the zeolite, according to Eq. 6.1.<sup>226</sup>:

$$E_{app} = \Delta H_{DSH} + \Delta H_{phys} + \Delta H_{prot} + E_{int} \quad \text{Eq 6.1.}$$

$\Delta H_{DSH}$  : ethylcyclohexane dehydrogenation over Pt site enthalpy;  $\Delta H_{phys}$  : ethylcyclohexene adsorption in the zeolite pore physisorption enthalpy;  $\Delta H_{prot}$  protonation for adsorbed ethylcyclohexene on Brønsted acid site enthalpy;  $E_{int}$  formation enthalpy of the protonated cyclopropane transition state.

Figure 6.9. represents the different elementary steps gathered in Equation 6.1.

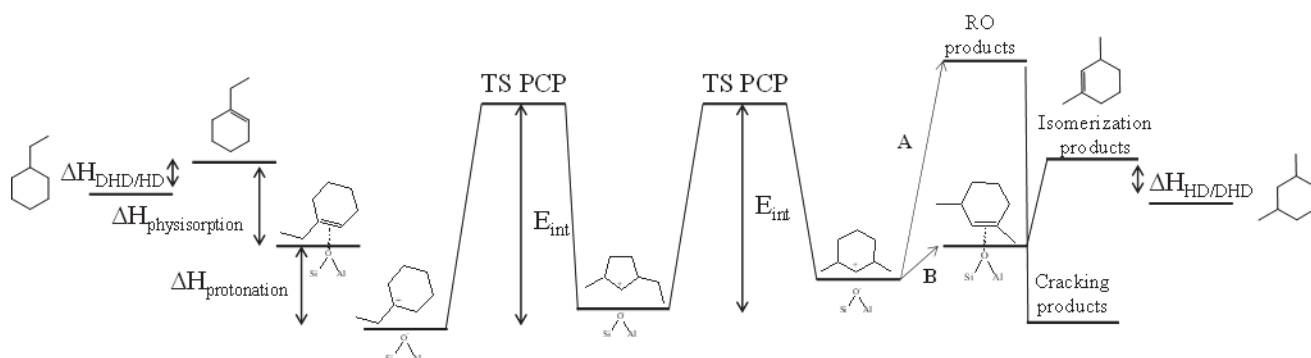


**Figure 6.9. Elementary steps of the ethylcyclohexane hydroconversion highlighting the two competing pathways controlling the selectivity. Adapted from ref <sup>227</sup>.**

Apparent activation energies were calculated for the well balanced catalysts and are reported in table 6.4. To minimize any bias in the calculation, only ECH conversions below 80% and isomerization selectivities higher than 90% were considered. Significant differences are observed. The lowest  $E_{app}$  is observed for HZSM-23 (124 kJ/mol) and the highest for HZSM-5 (174 kJ/mol). It is difficult to draw any significant conclusion because of the lack of data for physisorption, protonation and protonated cyclopropane formation enthalpies (even if some data about protonation and PCP formation enthalpies is available from DFT calculations).

The Arrhenius plot is provided in figure 6.9. It can be observed that the difference of activity between the catalysts can reach one order of magnitude. This was expected according to the large range of temperature observed to reach 50% of ECH conversion.

**Table 6.4. Temperature required to reach 50% ECH conversion and apparent activation energy for each well balanced catalyst.**

	Temperature required to reach 50%ECH conversion (°C)	$E_{app}$ (kJ/mol)
1%Pt- Al <sub>2</sub> O <sub>3</sub> /HZSM-23	325	124
1%Pt- Al <sub>2</sub> O <sub>3</sub> /HZSM-57	272	158
1%Pt- Al <sub>2</sub> O <sub>3</sub> /HZSM-5	262	178

1%Pt- Al <sub>2</sub> O <sub>3</sub> /HEU-1	264	137
1%Pt- Al <sub>2</sub> O <sub>3</sub> /HZSM50	324	147
1%Pt- Al <sub>2</sub> O <sub>3</sub> /HIZM-2	274	159
1%Pt- Al <sub>2</sub> O <sub>3</sub> /HNU-86	233	155
1%Pt- Al <sub>2</sub> O <sub>3</sub> /HZSM-12	247	174
1%Pt- Al <sub>2</sub> O <sub>3</sub> /HMOR15	226	139
1%Pt- Al <sub>2</sub> O <sub>3</sub> /HMOR50	262	149
1%Pt- Al <sub>2</sub> O <sub>3</sub> /HBETA	201	135

Considering the catalyst that show better performance in each group, it is easily observable how the best catalyst of 10MR group is not competitive with the catalyst of the 10-12MR, neither with the 12MR catalysts. This is the case not only in terms of ECH conversion reached, but also in terms of the activation energy demanded and TOF values showed at lower temperatures (Figure 6.10).

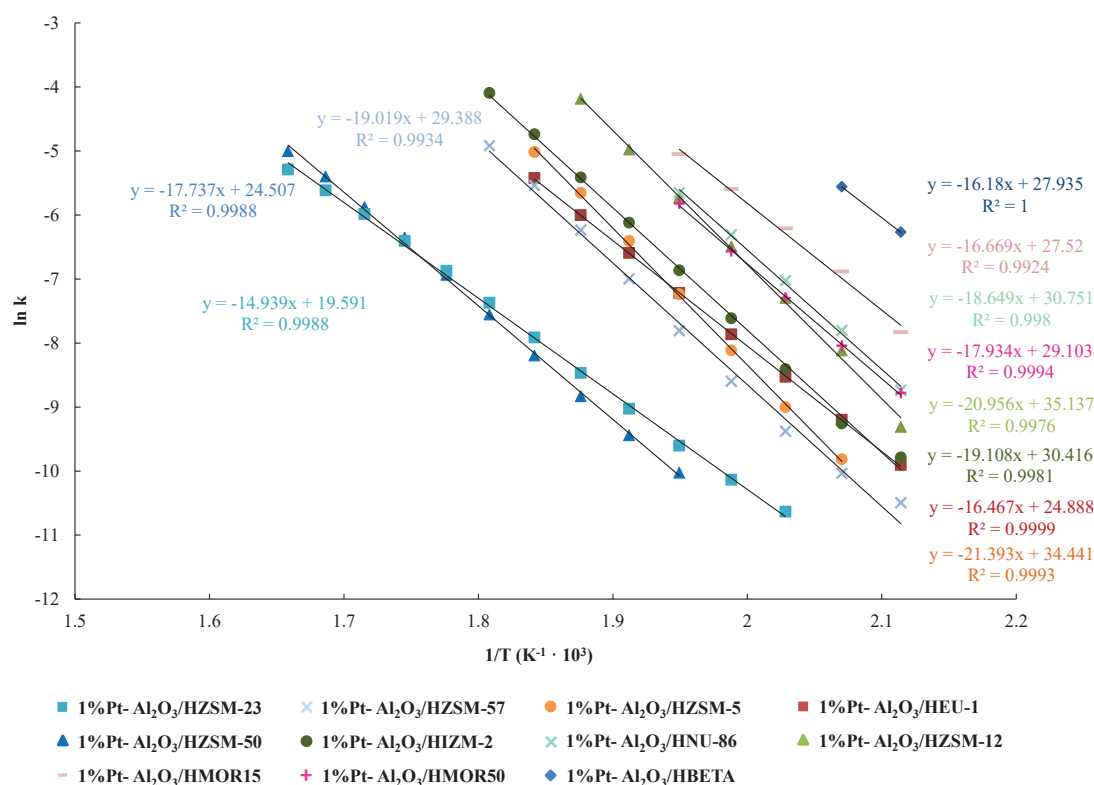
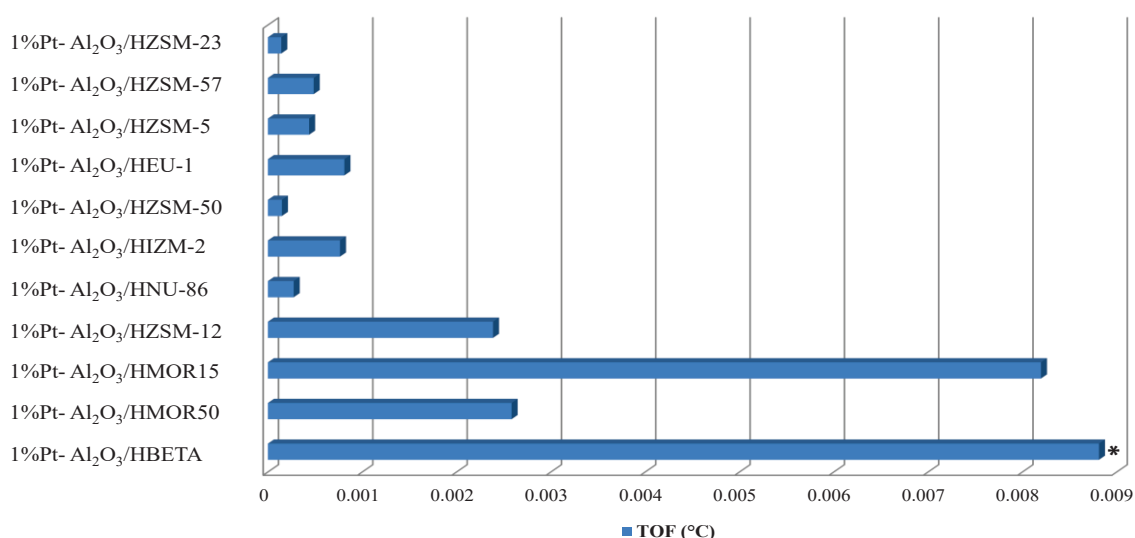


**Figure 6.9.** Arrhenius plot for zeolite based catalysts. The rate constant  $k$  [ $\text{m}^3 \text{mol}^{-1} \text{s}^{-1}$ ] is on a concentration basis and calculated from the integral expression for a first order reaction in a fixed-bed reactor.

The average turnover frequency per Brønsted acid site at 210°C is provided figure 6.10 for all the zeolites. According to the striking differences observed, the variation of activity reported previously cannot be explained solely based on the amount of Brønsted acid sites per



gram of zeolite. Straightforward explanation for the observed TOF differences is not possible as the Brønsted site activity depends on numerous parameters such as the acid site strength, the extraframework aluminium species and the position of the active sites. The possible contribution of diffusional problems can also not be excluded. Regarding the strength of the acid site, it increases with the Si/Al molar ratio of a given zeolite structure until reaching a quasi-plateau (for Si/Al ratio higher than 7).<sup>22</sup> In this study, all the investigated zeolites possess Si/Al ratios higher than 13. Then, the impact of this parameter can then be disregarded. A synergetic effect between Brønsted acid sites and extraframework aluminum species at the vicinity is also claimed.<sup>228</sup> The investigated zeolites possess low percentages of extraframework aluminum, so then, such effect could be disregarded as well. As emphasized in Chapter 4 for EUO zeolites, the localization of the Brønsted sites in non-equivalent T sites, can also impact the average TOF. According to table 6.2, the zeolite samples exhibit very different crystallite sizes whereas the determination of the real position of Al in T sites still remains a challenge.<sup>204,206</sup> According to figure 6.10., HBETA possess by far the higher TOF of all the group of zeolites. This solid combines a high framework dimensionality (3D), micropore size (12 MR) and small nanocrystals (20 nm). A second group formed by zeolites with 12 MR micropores but with lower dimensionality (1-2D), (i.e. ZSM-12, MOR-15 and MOR-50) can be considered. Besides, a third less active group is formed by zeolites of 10 MR micropores such as ZSM-23, EU-1, ZSM-50 and ZSM-57. Whatever the dimensionality, ZSM-23 and ZSM-50 have the lowest TOF of all the zeolites. These two zeolites combine a low framework dimensionality (1D), 10 MR micropores and are formed by big crystals (100-700 and 200 nm respectively).



\*TOF · 10<sup>-1</sup>

**Figure 6.10.** TOF values for the zeolite-based catalysts considered at 210 °C.

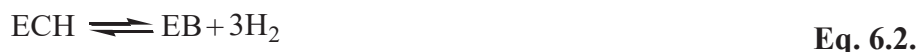
Therefore, from this evaluation of the catalysts, it seems that the ones showing better performances in terms of activity are the HBETA and HMOR15 zeolites. However, studying the zeolites selectivity towards desired and undesired products is also of prime importance. This point is addressed in the following section.

### 6.4.2. Catalytic selectivity

The primary objective of this PhD work is to assess the impact of the zeolite topology on the ethylcyclohexane hydroisomerization and cracking plus ring opening selectivities. Ethylbenzene and xylenes can also be formed by naphthenes dehydrogenation over the metallic function and were lumped as dehydrogenation products in previous chapters. However, in this chapter the results has lead us to consider these products differently as explained below.

#### 6.4.2.1. Contribution of dehydrogenation reactions

For a well-balanced catalyst, hydro-dehydrogenation reactions should be at thermodynamic equilibrium. Dehydrogenation reaction of the ethylcyclohexane and can be written as follow:



**EB:** ethylbenzene.

In the gas phase the equilibrium constant  $K_{(\text{DHD})}$  of Eq. 6.2. can written as follow:

$$K_{(\text{DHD})} = (\text{P}_{\text{EB}} * \text{P}_{\text{H}_2}^3) / \text{P}_{\text{ECH}} = \exp (-\Delta G^\circ / RT) \quad \text{Eq. 6.3.}$$

$\text{P}_{\text{EB}}$  ethylbenzene partial pressure,  $\text{P}_{\text{ECH}}$  ethylcyclohexane partial pressure,  $\text{P}_{\text{H}_2}$  hydrogen partial pressure,  $\Delta G^\circ$  dehydrogenation reaction free enthalpy,  $T$  reaction temperature.

The hydrogen partial pressure can be considered constant, and  $\text{P}_{\text{EB}}/\text{P}_{\text{ECH}}$  is also proportional to  $\text{wt}\%\text{EB} / \text{wt}\%\text{ECH}$ . Therefore Eq. 6.3. can be rewritten as:

$$\ln (\text{wt}\%\text{EB}/\text{wt}\%\text{ECH}) = A - \Delta G^\circ / RT \quad \text{Eq. 6.4}$$

**wt% EB:** weight percentage of ethylbenzene in the hydrocarbon effluent, **wt% ECH** weight percentage of ethylcyclohexane in the hydrocarbon effluent, **A:** constant.

The experimental evolution of  $\ln(\text{wt}\%\text{EB}/\text{wt}\%\text{ECH})$  with  $1/T$  is plotted for all the catalysts figure 6.11. As expected from Eq. 6.4., a single straight line is obtained, regardless of the zeolite at stake in the catalyst. This result sustains the fact that hydro and

dehydrogenation products are indeed at thermodynamic equilibrium. The thermodynamic equilibrium has been confirmed with PROII. The  $\Delta G^\circ$  results obtained are 211 and 209 kJ/mol experimentally and with PROII (Appendix VI.III) respectively, which is an excellent agreement.

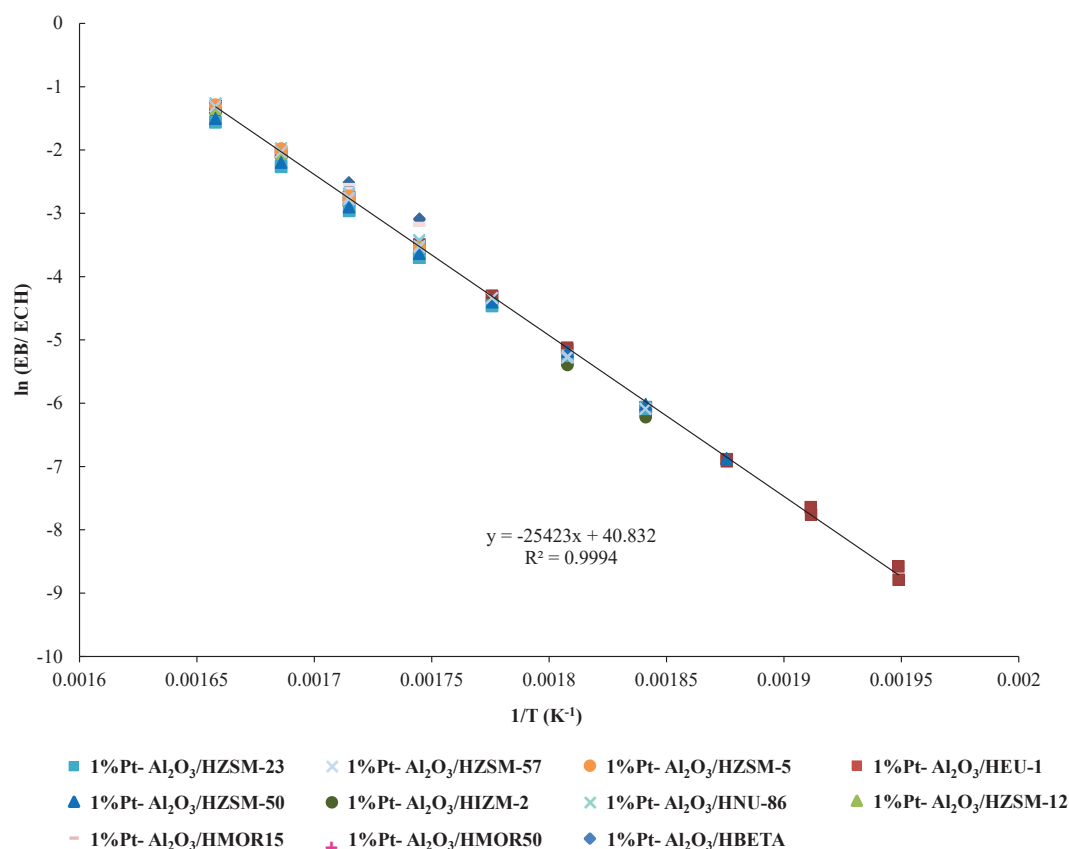


**Figure 6.11. Evolution of  $\ln(\text{wt}\% \text{EB} / \text{wt}\% \text{ECH})$  with  $1/T$  for the zeolite-based catalyst.**

The relative contribution of the monofunctional dehydrogenation pathway compared to the bifunctional pathway increases when the activity of the zeolite at stake in the bifunctional catalyst decreases. Indeed, for a zeolite showing low activity, a higher temperature will be required to reach a given ECH conversion. Since dehydrogenation is thermodynamically favored at high temperatures, dehydrogenation products will be then favored by the less active zeolites. This is nicely illustrated by the results obtained over 1%Pt-Al<sub>2</sub>O<sub>3</sub>/HZSM-23 compared to 1%Pt- Al<sub>2</sub>O<sub>3</sub>/HMOR15. The first one is the less active catalyst and the second is one of the most active catalyst of the investigated zeolites (Table 6.4.). Figure 6.12 represent the evolution of the isomerization, cracking + ring opening and dehydrogenation yields versus ECH conversion for the two catalysts. The difference between the two catalysts is very strong: at 50% of ECH conversion, the dehydrogenation products yield is about 13.5% for HZSM-23 based catalyst and less than 1% for the HMOR15 based catalyst. For HZSM-23 the

production of ECH isomers is clearly impacted by the dehydrogenation pathway as dimethylcyclohexanes are partially dehydrogenated to corresponding xylenes.

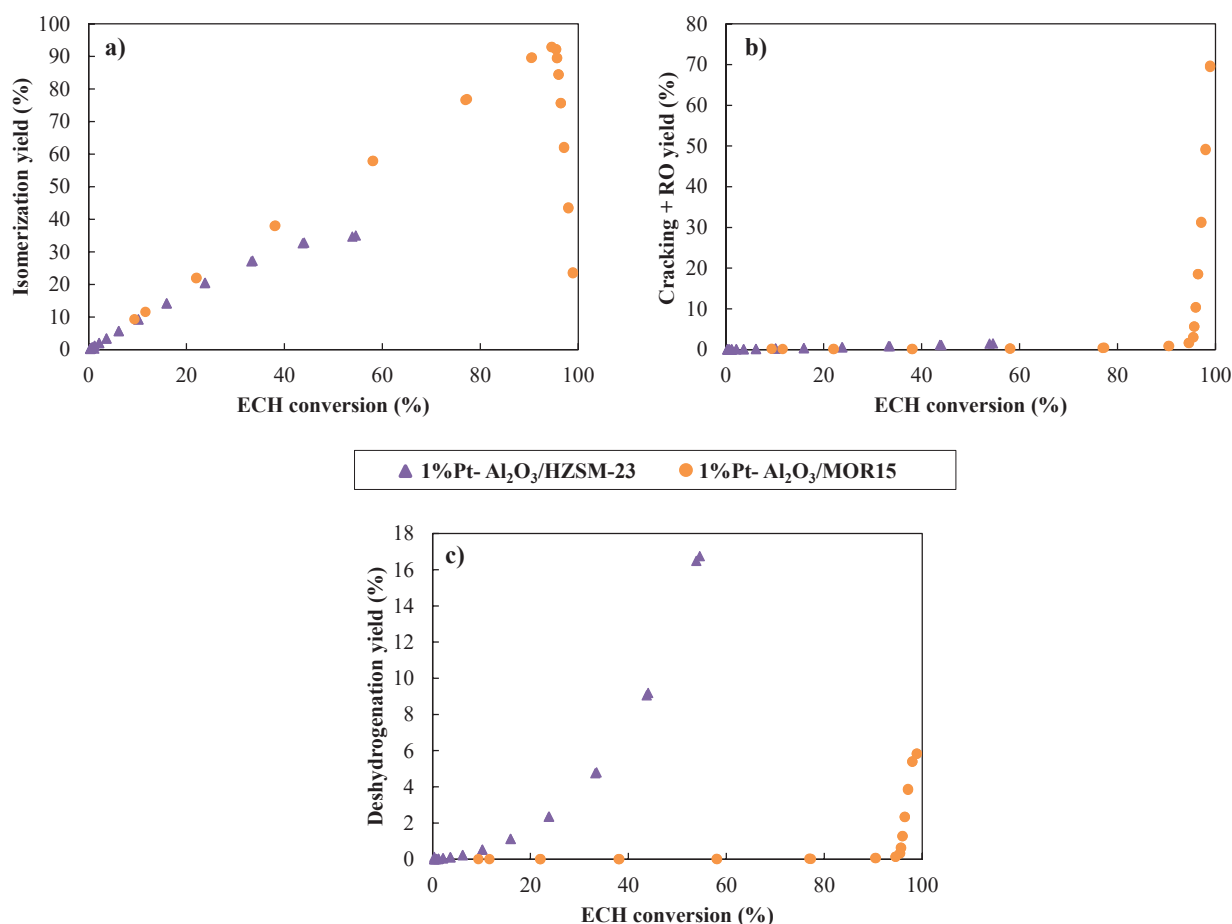


**Figure 6.12.** Evolution of isomerization, cracking + RO and dehydrogenation yields versus ECH conversion over 1%Pt-Al<sub>2</sub>O<sub>3</sub>/HZSM-23 and 1%Pt-Al<sub>2</sub>O<sub>3</sub>/HMOR15 based catalysts.

#### 6.4.2.2. Evaluation of catalysts selectivity isomerization vs ring opening and cracking

Because of the dehydrogenation reaction, the comparison of the catalysts isomerization selectivities cannot be done by solely considering the ECH isomers. Therefore, it was decided to lump the ECH isomers and the structurally corresponding xylenes. Indeed xylenes are formed by dehydrogenation of some ECH isomers, namely dimethylcyclohexanes. In the following discussion the lump is labeled iN<sub>8</sub>+iA<sub>8</sub>. Furthermore, ring opening and cracking products are also lumped as both kind of products formation involves the breakage of a C-C ring bond. It should be mentioned that the amount of ring opening products remains low (max yield < 6.6%) for all the catalysts, in accordance with previous observations of Chapter 3. Again this is in agreement with the fact that naphthenes ring opening is slow compared to

naphthenes isomerization and paraffin cracking. In the following discussion the lump is labeled CR+RO. Figure 6.13 depicts the evolution of the CR+RO yield with the  $iN_8+iA_8$  yield for all the investigated catalysts.

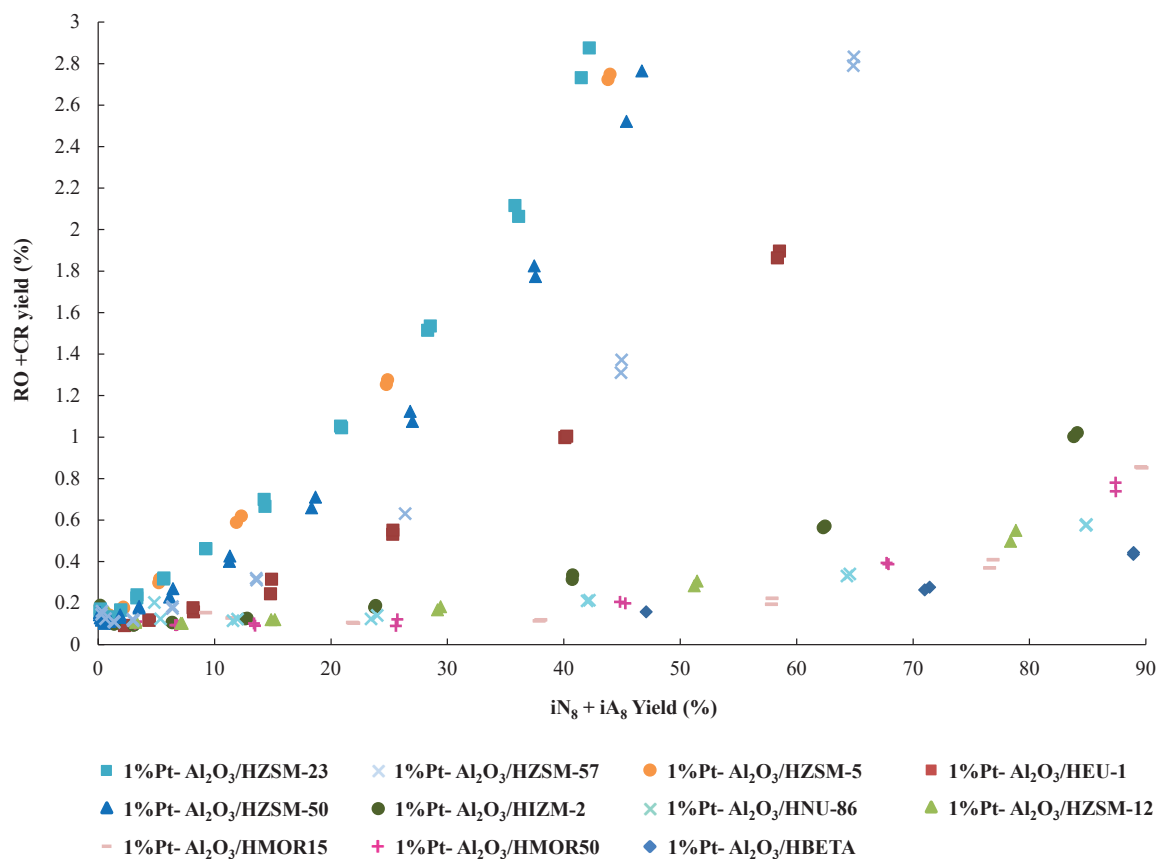


**Figure 6.13. Evolution of ring opening and cracking product yield with the ECH isomers and xylenes yield for the zeolite based catalysts.**

The most selective catalyst produces the smallest CR+ RO products yield for a given  $iN_8+iA_8$  products yield. By convention, the CR+RO yield at 40%  $iN_8+iA_8$  yield is used as a descriptor of the catalyst selectivity (Table 6.5). Significant differences can be observed. It must be borne in mind that the activity of the catalysts are very different. Therefore, a given yield in  $iN_8+iA_8$  is obtained at different temperatures depending on the catalyst considered. However, the reaction temperature does not seem to be a critical factor to explain these differences of selectivity. Indeed, HZSM-5, HEU-1 and HMOR-50 based catalysts have similar activities for a given temperature (table 6.4.) whereas their selectivities are very different. Thus, the selectivity of the catalyst may largely be related to the properties of the zeolite. The most selective zeolites have 12 MR pores framework: Beta (12 MR, 3D), Mordenite (12 MR, 2D), ZSM-12 (12 MR, 1D), NU-86 (10-11-12 MR, 3D) and IZM-2 (10-

12 MR / 1D, 2D ?). The acid sites density does not seem to be a critical factor as the two HMOR samples exhibit similar selectivity behavior. HZSM-23 and HZSM-5 based catalysts are the least selective zeolites studied. These two zeolites have 10 MR pore frameworks.

HEU1 is significantly more selective than HZSM50. Both zeolites are of the EUO type. The EUO type framework is 1-dimensional possessing 10 MR pores and 12 MR side pockets. The improved selectivity of HEU1 could be either ascribed to the different position of the Brønsted acid sites in the T sites and/or to its smaller crystallites size compared to HZSM50. It has been shown in Chapter 4 that the active sites located at the intersection between the channel and the pocket have different catalytic properties. An analysis of the DFT results (enclosed in the following section) was carried out in an attempt to explain this difference of selectivity in that spirit. Besides, the diffusion of the reactant was found as a non-limiting process in both zeolites, but we cannot exclude that for products (in particular non-cyclic ring-opening products), this could be the case. Indeed, diffusion of the products was shown to have an impact in the selectivity of EU-1 for the nC7 hydroconversion selectivity.<sup>60</sup>

**Table 6.5. Ring opening and cracking products yield at 40% ECH isomers and xylenes yield for the zeolite based catalysts.**

	RO+CR products yield (%)
1%Pt- Al <sub>2</sub> O <sub>3</sub> /HZSM-23	2.6
1%Pt- Al <sub>2</sub> O <sub>3</sub> /HZSM-57	1.1
1%Pt- Al <sub>2</sub> O <sub>3</sub> /HZSM-5	2.4
1%Pt- Al <sub>2</sub> O <sub>3</sub> /HEU-1	1.0
1%Pt- Al <sub>2</sub> O <sub>3</sub> /HZSM50	2.0
1%Pt- Al <sub>2</sub> O <sub>3</sub> /HIZM-2	0.3
1%Pt- Al <sub>2</sub> O <sub>3</sub> /HNU-86	0.2
1%Pt- Al <sub>2</sub> O <sub>3</sub> /HZSM-12	0.22
1%Pt- Al <sub>2</sub> O <sub>3</sub> /HMOR15	0.12
1%Pt- Al <sub>2</sub> O <sub>3</sub> /HMOR50	0.18
1%Pt- Al <sub>2</sub> O <sub>3</sub> /HBETA	0.10

The investigated zeolites do not only have different framework topologies but also the crystallite size density of acid sites and even the strength of the acid sites can also differ. Therefore, straightforward explanation to the observed differences in selectivity is not possible. However, confinement effects within the pores of the zeolite may play a major role. As a matter of fact, the most opened zeolites (with 12MR pores) appears to be the most selective ones. Adsorption effects have been proposed to be of prime importance for

controlling the selectivity in phenanthrene hydroconversion.<sup>227</sup> After the isomerization step, the isomerized products can either be desorbed or cracked. If the isomerized product is too strongly adsorbed at the vicinity of the acid site, the consecutive cracking (or ring opening and cracking reaction in our case, Figure 6.9.) will be favored.

As a rule of the thumb, for a given molecule that can be suited in the zeolite microporosity, the absolute value of the adsorption energy is expected to increase when the pore aperture of the zeolite is smaller.<sup>227</sup> This is due to the confinement effect.<sup>229</sup> Nevertheless, it should be borne in mind that there is an optimal size. If the microporosity is too tight, the repulsive terms will take over (and in the extreme case, because of this, the molecule does not fit the microporosity). Therefore, isomerization selectivity should decrease for the less opened zeolite structures as the isomerization products are too strongly adsorbed. Figure 6.15. depicts the evolution of the RO+CR products yield at 40% iN<sub>8</sub>+iA<sub>8</sub> products yield versus the maximal sphere diameter of a molecule able to diffuse inside the corresponding zeolite framework. Such diameter is considered as a convenient descriptor of the pore aperture of the zeolite. Indeed the less opened zeolite are less selective than the more opened ones. Diffusional limitations could also be studied for all the zeolites in order to rule out (or not) their impact on the zeolite selectivity.

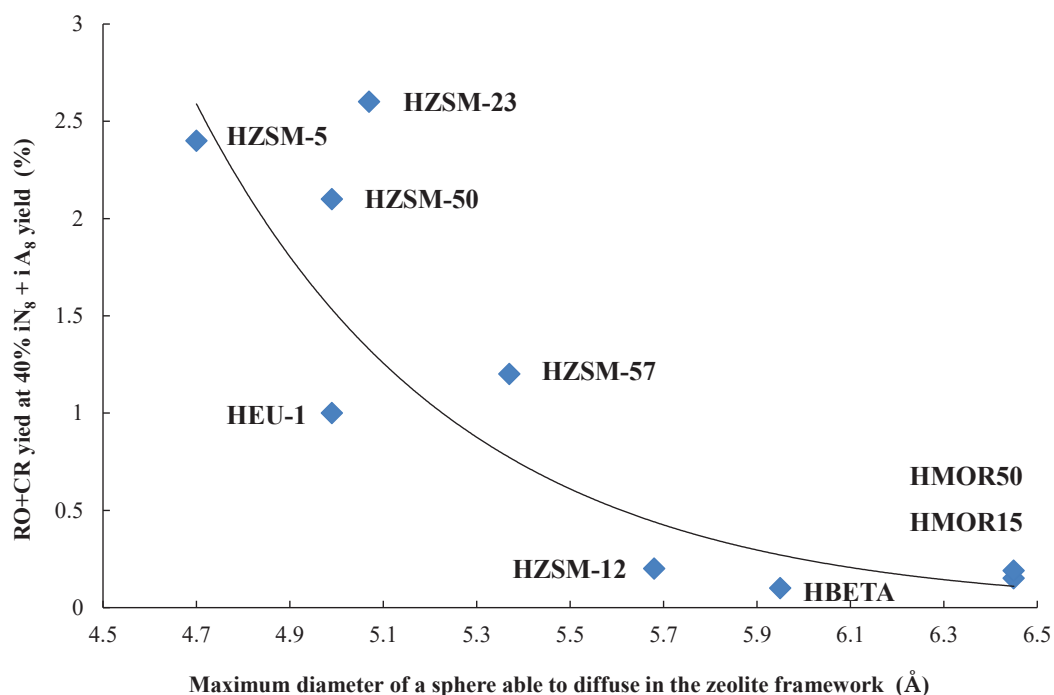


**Figure 6.15.** evolution of the RO+CR products yield at 40% iN<sub>8</sub>+iA<sub>8</sub> products yield with the maximal sphere diameter of a molecule able to diffuse inside the corresponding zeolite framework.

### 6.5. DFT analysis of the stability of key intermediates and TS for isomerization and ring opening

Preliminary DFT ab initio calculations have been carried out over some zeolites structures whose framework is known. Therefore, IZM-2 and NU-86 are not considered since their structures have not been yet resolved. Considering some key intermediates and TS of the reaction, the purpose was to see if the differences of activity / selectivity can be rationalized / anticipated. Table 6.6 contains some information about the different zeolite structures considered. In some zeolites, several active sites have been taken into account for the calculations. The number of Aluminum atoms has been calculated according to the Si/Al ratio of the real zeolites employed in the experimental work.

All the zeolite structures possess from 2 to 5 aluminum atoms per unit cell considered. For the one-dimensional zeolites, only one active site has been taken into account such is the case of HZSM-23 and HZSM-12. However in two- and three-dimensional zeolites two or three active sites have been considered in order to take into account at least one type of typical locations. For instance, in the HZSM-5 structure three different active site were considered: one in the straight channel (T11O25), one in the sinusoidal channel (T10O23) and other in the intersection of both channels (T1O3).

**Table 6.6. Zeolites structure properties considered in the DFT study.**

Zeolite	Active site	Si/Al	Si	Al	O	Unit cell considered*
ZSM-12	T1O1	27	84	3	168	x3Y
ZSM-23	T2O1	36	72	2	144	x3X
Mordenite	T1O1 (chan)	19	96	5	192	x2Z
	T4O10 (int)	19	96	5	192	x2Z
ZSM-57	T2O2 (chan)	16	72	4	144	x2X
	T8O8 (int)	16	72	4	144	x2X
	T1O3 (int)	24	96	4	192	—
ZSM-5	T10O23(sin)	24	96	4	192	—
	T11O25(st)	24	96	4	192	—
Beta	T4O11(int)	16	64	4	128	--
	T6O12(chan)	16	64	4	128	—

**chan:** channel, **int:** intersection, **sin:** sinusoidal, **st:** straight,\* the unit cells have been sometimes multiplied in order to obtain a big enough structure to limit the proximity between different Al atoms.



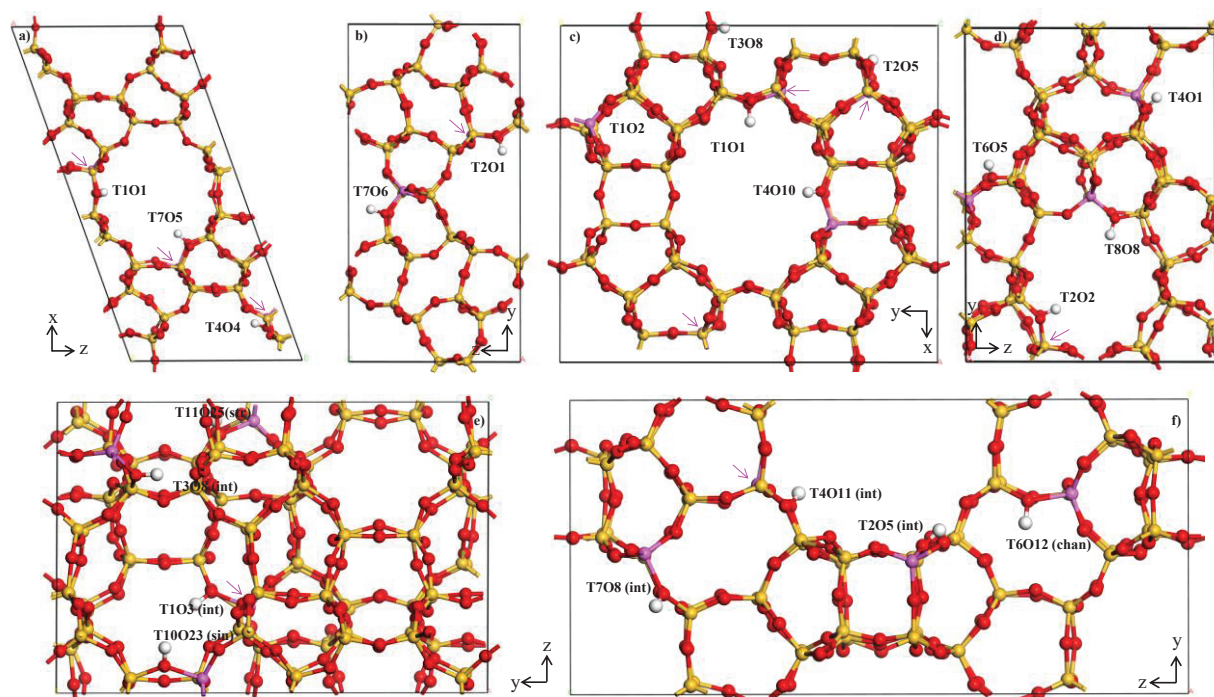


Figure 6.16. Unit cells of a)HZSM-12, b)HZSM-23, c)HMOR, d)HZSM-57, e)HZSM-5, f) HBETA. the purple arrows are pointing out the hidden aluminum atoms.

Figure 6.16. shows the unit cells corresponding to the studied zeolite structures.

The study in all the frameworks has been focused in a different way than the study over the HEU-1. The reaction intermediates and the TS analyzed are depicted in figure 6.17.

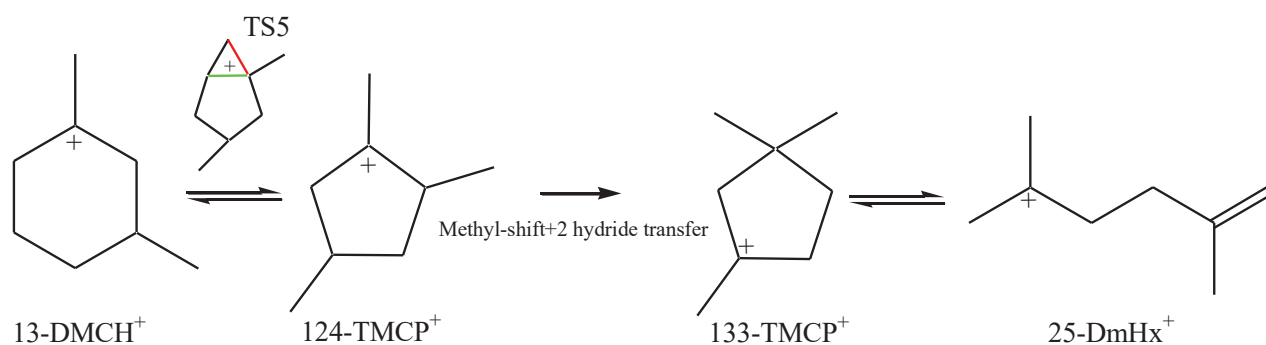
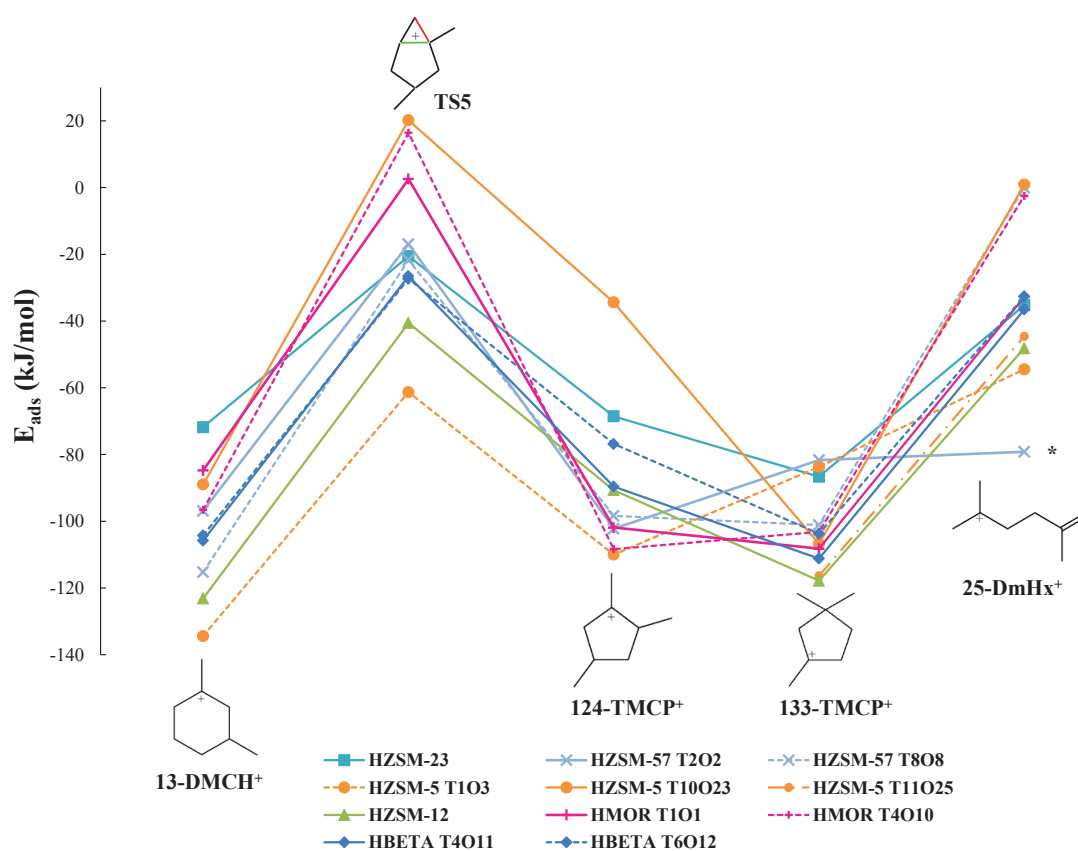


Figure 6.17. Reaction considered in the DFT study the different zeolite structures.

Only one transition state being a PCP has been considered, and it is the one passing from 13-DMCH<sup>+</sup> to 124-TMCP<sup>+</sup>. This path has been chosen not only because it involves tertiary carbocations, but also because 133-TMCP<sup>+</sup> can be obtained from 124-TMCP<sup>+</sup> by methyl-shift and hydride transfer. The importance of the latter molecule has already been highlighted in previous chapters because it can be opened into 25-DmHx. To sum up, only one reaction of

isomerization (passing from 13-DMCH<sup>+</sup> to 124-TMCP<sup>+</sup>) and one of ring opening (passing from 133-TMCP<sup>+</sup> to 25-DmHx) have been considered. In the isomerization reaction, the procedure followed has been exactly the same as the procedure employed for the calculations over the HEU-1 (transition state search by a NEB calculation, refining by a quasi-Newton algorithm, then IRC calculation to connect with reactant and products). In the case of the ring opening reaction, the hypothesis that the ring opening product is at the same level of energy than the TS (as it occurred for the HEU-1 zeolite) has been considered (Chapter 5) and then we have not search for the TS. Note also that for the sake of time, we did not evaluate so far the Gibbs free energy of all species, but the energy only. Indeed, after the optimization procedure described above, a few spurious imaginary mode remained, preventing the accurate evaluation of the entropy components. Removing those modes would have been possible according to the line minimization method (employed in chapters 4 and 5). Nonetheless, it has not been yet undertaken in the framework screening approach performed in the present chapter. Figure 6.18 represents the adsorption energies of the compounds represented in figure 6.17 for each zeolite structure studied.



**Figure 6.18.** Adsorption energies for all the zeolite structures active sites evaluated in this study. \* diolefin (with spontaneous back-proton transfer to the zeolite framework in the course of the geometry optimization).

The first remarkable thing from this figure 6.18. is the lower or similar energy of the isomerization transition state compared to the ring opening product. However it should be bear on mind, that the TS of ring opening has been considered close in energy to the 25-DmHx intermediate and then, this intermediate could not be very representative as TS. The last affirmation comes from the analysis of the 25-DmHx structure in some zeolites. When the cycle is opened, the ring opening product is folded and in some zeolite frameworks analyzed, this ring opening products folded are not stable. Hence, after a geometry optimization in many cases they become unfolded. For instance, this occurred systematically in the zeolites possessing smaller pores such as HZSM-23 and HZSM-57 since the folded ring opening product has not space enough to be suited in a stable conformation. Figure 6.19 represents a folded and an unfolded ring opening product structure corresponding to HZSM-12 and HZSM-23 respectively. Another explanation of this fact had been already highlighted in Chapter 5 where it has been shown that the only way to obtain cracking products from only one isomer ( $133\text{-TMCP}^+$ ) was not enough. On the HEU-1, it was also necessary, to take into account the distribution of products, invoking other ways that are not considered here.

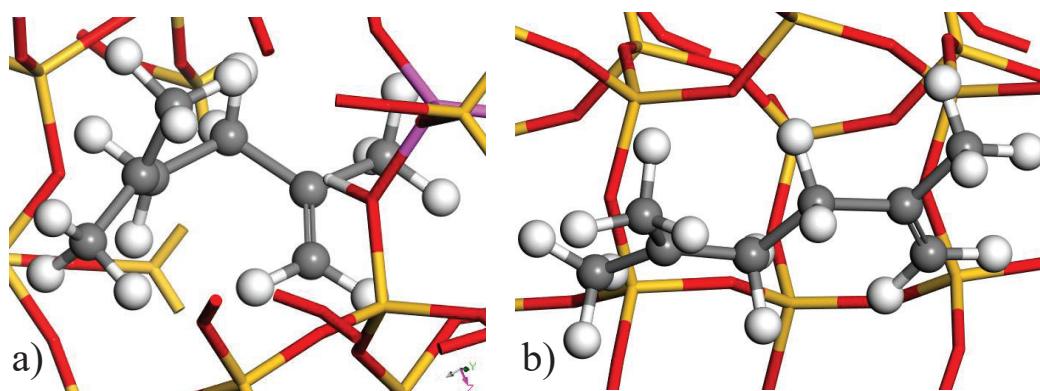


**Figure 6.19. a) Folded and b)unfolded 25-DmHx structures in HZSM-12 and HZSM-23 zeolite structures.**

Another thing that catch the eye is the difference between active sites of the HZSM-5 zeolite framework: T1O3, located in the intersection and T1O23, located in the sinusoidal channels. Whereas the HZSM-5 T1O3 active site possesses one of the lowest isomerization energy barriers to pass from  $13\text{-DMCH}^+$  to  $124\text{-TMCP}^+$ , the HZSM-5 T1O23 possesses the highest isomerization energy barrier of all the zeolites studied. Furthermore, the intermediates of this reaction are much more stable in the intersection active site (T1O3) than in the sinusoidal channel (T1O23). Within this zeolite, the straight channel was as well investigated. However the calculations concerning the isomerization did not converge in this

active site. On the other hand, HBETA active sites reveal a similar behavior regardless the location and it occurs similarly in the case of the HMOR zeolite. The HZSM-57 active sites exhibit as well a similar behavior regarding the isomerization reaction. Nonetheless, the ring opening product 25-DmHx is much more stable in the channel than in the intersection. This fact is attributed to the non-charged character of the stabilized 25-DmHx product in the channel since in this case, the energy optimization gives a diolefin instead a carbocation.

## 6.6. Comparison between experimental and calculated catalytic features

### a. Level of activity

We looked at possible correlations between the activity (temperature at 50% conversion, or TOF) and the energy levels of the calculated intermediates and transition states. None of these correlation appeared to be satisfactory, only giving rise to scattered points as it can be observed in figure 6.20.

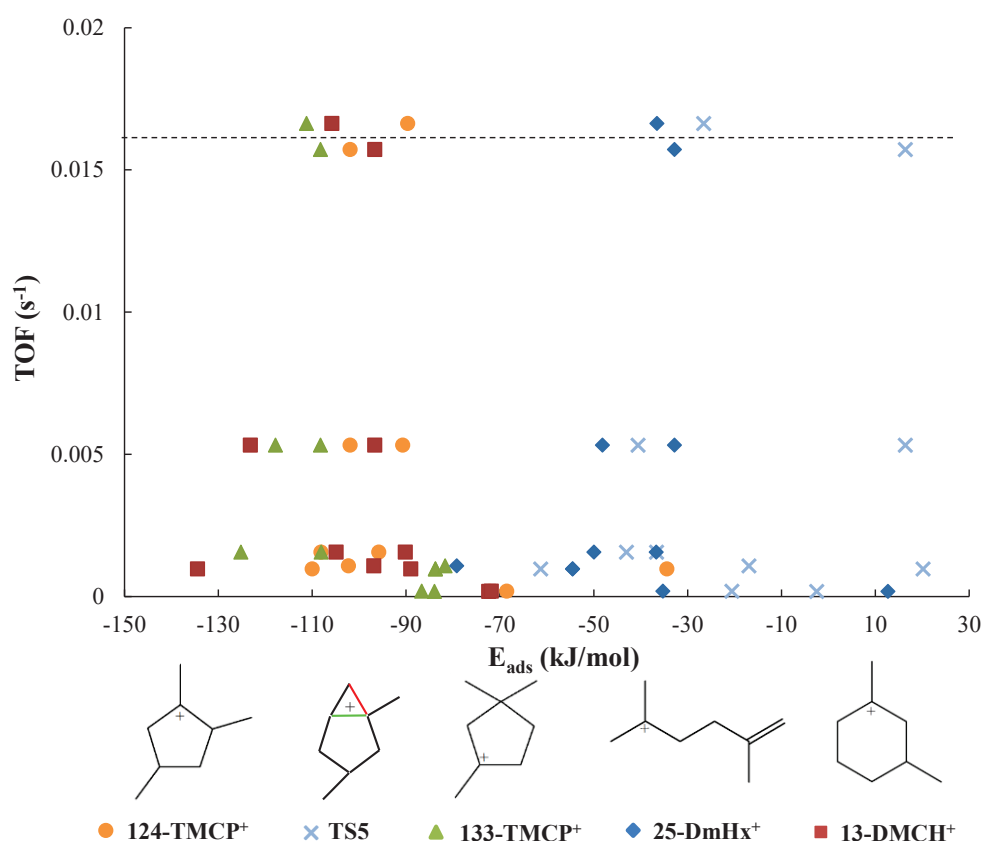


**Figure 6.20.** Experimental TOF at 220°C *versus* adsorption energies for all the zeolite structures active sites evaluated by DFT in this study. The results over the dashed line corresponds to BETA zeolite and they are multiplied by  $10^{-1}$  in order to have a TOF value comparable to the others.

Several explanations can be tentatively given for such a discrepancy:

- As shown in Chapter 4, and illustrated again in Figure 6.18, not all sites for a given framework are equally active. The TOF determined experimentally assumes that this is however the case. Considering that a portion of the sites only plays a role (that may differ from one zeolite to another), the intrinsic TOF (for a given site) will vary easily by one order of magnitude. By the DFT calculation, we estimate the reactivity of individual sites only. Note also that the location of the sites modeled was not exhaustively sampled.
- Entropy components (pre-factors in rate constants) may have an important role, in particular comparing several zeolitic frameworks of various topologies. The degrees of freedom of the species may strongly vary from a 1D 10MR zeolite to a 3D 12MR one. This was not estimated in the present DFT study.
- Finally, possible diffusion limitation may take place within some of the zeolites. We don't have a quantification of these effects for all the solids investigated here.
- Possible zeolite-dependent diffusion limitation may also affect the selectivity pattern.

### **b. Selectivity**

In the same spirit, some correlations were looked at to correlate the selectivity with computational features. Again, this led to non-conclusive results as depicted in figure 6.21.

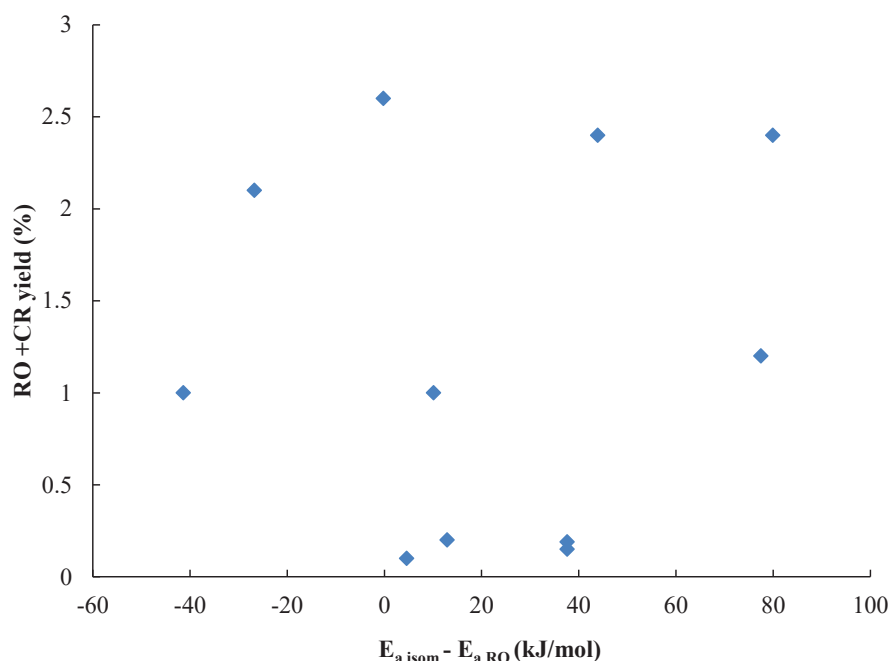


**Figure 6.20.** Ring opening and cracking products yield at 40% ECH isomers and xylenes yield *versus* isomerization activation energies minus ring opening activation energy. for all the zeolite structures active sites evaluated by DFT in this study.

The proportion of active sites may not be a relevant parameter explaining the discrepancy, as the selectivity refers to a ratio of rates. Other aspects need to be further investigated to understand why we do not reach a prediction ability by DFT in the present case:

- We have only simulated one of the ring-opening products, whereas we showed in Chapter 5 that considering at least two is required to correctly depict the distribution of products.
- We did not simulate the cracking products that rapidly form after ring-opening. The confinement effect of these cracking products may express differently as for RO products, affecting the selectivity.
- We focused on a single isomerization reaction, which may not be the rate limiting isomerization reaction.
- As for the activity, entropy components (pre-factors in rate constants) may have an important role for the selectivity. In particular, the ring-opening reaction converts a naphthene-like molecule (cyclic) into an alkene-like molecule (acyclic). This may be accompanied by a strong change in entropy, not estimated here. Probably, this change strongly depends on the zeolite framework considered. This is notably

illustrated by the fact that in some of the calculations, unfolded forms of the open molecules had to be calculated, and that some spontaneous proton transfer to the framework was also observed.

- For the open molecules, static DFT approaches to reactivity may be insufficient to estimate both enthalpies and entropies, whereas we obtained very satisfactory results for cyclic compounds in chapter 4 and 5. Biased Ab Initio Molecular Dynamics (AIMD) may be required in such cases. This was recently illustrated by Van Speybroeck et al.,<sup>230</sup> and leads to current developments at IFPEN (Jérôme Rey's thesis, in collaboration with Tomas Bucko from the University of Bratislava). These methods are however very expensive from the computational point of view, preventing a systematic screening of zeolite structures at present time.

As an example, we compared the two zeolites sharing the same framework (EUO), HEU-1 and HZSM-50. The quantification of the differences of isomerization and ring opening activation energies (-26.7 kJ/mol in the intersection *versus* 10.1 kJ/mol in the pocket and -41.4 kJ/mol in the channel), would suggest that the channel should be the most selective site followed by the intersection site (the one corresponding to the HZSM-50 zeolite) whereas the pocket should be the less selective one. Then the EU-1 zeolite would possess at the same time the most and less selective types of active sites. Experimental results where the HEU-1 zeolite possessing active sites at the channel and inside the pocket is significantly more selective than the HZSM-50 could then be attributed to the sites located in the channel and not in the pocket according to DFT results. However, this is impossible to discern from experience.

This opens perspectives both for the computational and the experimental aspects of the work.

## 6.7. Conclusion

The evaluation of the impact of the zeolitic topology structure in the ethylcyclohexane hydroisomerization using eleven different zeolites has been performed. These eleven zeolites possess different pore size and dimensionality. The objective of this study is to reveal which are the zeolites features being the key parameters to control the selectivity towards isomerization.



The characterization of the zeolites reveals that all of them are really different. They have different morphology, acidity and physical properties. Then, the results of activity and selectivity are going to be a result of the combination of all of that parameters.

In order to compare the intrinsic properties of the zeolites, ideal catalysts are required. Therefore three different amounts of Pt have been tested in order to find an ideal catalyst for each zeolite. In this study the Pt is deposited over the alumina and after the evaluation of all the catalysts, the catalysts chosen as ideal ones were the ones containing 1% Pt - Al<sub>2</sub>O<sub>3</sub>/ zeolite.

The activity of each catalyst was analyzed separately in different groups concerning the ring size: 10MR, 10-12MR and 12MR. Within each group one or two catalysts exhibit better performance than the others. For instance, in the 10MR group the HZSM-57 zeolite is the most active one (on a weight basis) whereas in the 10-12MR group they are HNU-86 and HIZM-2. The last group 12MR, evidences the HBETA and HMOR15 as the most active zeolite-based catalysts (per gram). Very different activities (on a weight basis) were recorded. The temperature necessary to reach 50% of ECH conversion is 201°C in the case of the most active catalyst (1%Pt- Al<sub>2</sub>O<sub>3</sub>/HBETA) whereas it is 325°C for the less active one (1%Pt-Al<sub>2</sub>O<sub>3</sub>/HZSM-23). The difference of activity observed could not be explained solely based on the amount of Brønsted acid sites per gram of zeolite. Zeolites exhibited very different average turnover frequency per Brønsted acid site. Straightforward explanation could not be proposed as the Brønsted site activity depends on numerous parameter. As a matter of fact, the solid with by far the higher TOF of the investigated zeolites (HBETA) combines a high framework dimensionality (3D), micropore size (12 MR) and small nanocrystals (20 nm). Solids with the lowest TOF of the all zeolites (HZSM-23 and HZSM-50) combine a low framework dimensionality (1D), 10 MR micropores and big crystals (100-700 and 200 nm respectively).

The evaluation of the catalysts selectivities towards ECH isomerization, ring opening and cracking was scrutinized next. It appeared that the contribution of naphthenes dehydrogenation reaction to produce the corresponding aromatics could be significant, depending on the catalyst at stake. Therefore, the comparison of the catalysts selectivities towards isomerization could not be done by solely considering the ECH isomers. For this reason, ECH isomers and xylenes were lumped as a single family since xylenes are formed by dehydrogenation of some ECH isomers, namely dimethylecylcohexanes. Ring opening and cracking products were lumped together as well because both kind of product formation involves the breakage of a C-C ring bond. The cracking and ring opening yield at 40% of



ECH isomers and xylenes yield was used as a descriptor of the catalyst selectivity. The different zeolites exhibited marked differences in selectivity. It was observed that the most opened structure were the most selective ones. Preliminary results suggest that the confinement effects within the pores of the zeolite plays a key role to govern the zeolite selectivity. After the isomerization step, isomerized product can either be desorbed or cracked. If the isomerized product is too strongly adsorbed at the vicinity of the acid site, the consecutive cracking and ring opening reaction will be favored. The latter observation is in agreement with a previous proposal done for phenanthrene hydroconversion.<sup>227</sup> This was continued by complementary simulations to calculate the adsorption energies of the various zeolites towards isomerized products that are prone to ring opening in order to see if the differences of activity and/or selectivity can be rationalized and/or anticipated. The analysis of these data shows no correlation in between experimental and DFT results. However many hypothetical explanations have been found which open many perspectives for further studies. Furthermore, we consider that diffusional limitations should also be studied for all the zeolites in order to rule out (or not) their impact on the zeolite selectivity.

## CONCLUSIONS AND PERSPECTIVES

---

Para-xylene is a valuable product since it is used in the manufacture of terephthalic acid employed in the production of polyester. Para-xylene can be produced by isomerization of the C<sub>8</sub> aromatic cut composed by the xylenes isomers and ethylbenzene. Ethylbenzene isomerization follows a bifunctional mechanism, thus requiring the use of a bifunctional catalyst. Such catalyst contains two catalytic functions, an acidic one (provided for example by EU-1 zeolite) and a hydro/dehydrogenating one (provided by platinum). Because of the strong hydrogenating function, C<sub>8</sub> naphthenes are formed during ethylbenzene hydroisomerization. Then, naphthenes can undergo undesired side reactions such as ring opening and cracking. Isomerization, ring opening and cracking reactions are taking place on the acidic function.

This work has been started with the first aim to understand the mechanism of isomerization, ring opening and cracking of the C<sub>8</sub> naphthenes, revealing which are the main features of the zeolite affecting the kinetics of these reactions. With this purpose, the hydroconversion of ethylcyclohexane was studied over EU-1/platinum bifunctional catalysts. Two groups of bifunctional catalysts with different metal/acid distances (nanometer and micrometer scale) were tested in this study. Within each group, the metal to acid sites ratio was varied. We have shown that the catalytic activity and selectivity are strongly influenced by the metal to acid site ratio. However, no influence of the distance between both functions was observed, up to micrometer scale. This means that both groups of catalysts, at either nano- or microscale distances, exhibit the same catalytic performance, provided that the metal to acid site ratio is the same. Thus, the Weisz intimacy criterion can be fulfilled in both cases. An ideal bifunctional catalyst is obtained when the metal to acid sites ratio is sufficiently high. Therefore, a well balanced catalyst in which the acid phase is rate controlling and the distance between metal/acid sites fits the Weisz intimacy criterion was found. Therefore, we succeeded to have access to the intrinsic kinetics of the zeolite.

To quantify the effect on the metal to acid sites ratio on the catalytic performance (activity and isomerization selectivity), a dual-function kinetic model was employed. The model describes the experimental catalytic performances with good accuracy. It shows that the catalyst activity plateau is reached at a higher metal to acid sites ratio compared to the catalyst isomerization selectivity plateau. This is interpreted as a consequence of the lower value of the ring-opening kinetic constant in comparison to the isomerization kinetic constant.

## CONCLUSIONS AND PERSPECTIVES

A preliminary study of the products distribution (isomerization, ring opening and cracking) has revealed a first isomerization apparent reaction scheme. According to this scheme, the ethylmethylcyclopentanes products are the primary products which are converted into dimethylcyclohexanes and after into trimethylcyclopentanes. This apparent isomerization scheme was then taken into consideration for a first DFT study. Based on experimental results, some ring opening pathways involving the 1,1,3 trimethylcyclopentane for instance, were proposed to be studied with DFT methods.

The preliminary DFT study, dealing with chosen tertiary carbenium ions, has shed some light about the mechanism and has given some precious information. The first surprising thing was to find out that the naphthenic alkoxide species are not stable whereas is not the case of the olefins ( $\pi$ -complex), when investigated by static DFT approaches. Besides, the secondary carbocations are local energy minima in the zeolite framework even if they are not very stable. This is probably due to their structure that makes the cavities very adapted to that disposition of the molecule. Regarding the apparent reaction scheme, the proton and hydride transfers reactions, as expected, are not the rate-determining step of the reaction. Therefore, the cycle contraction-expansion is shown as the rate determinant step of the isomerization reaction.

The location of the most active sites (for ethylcyclohexene isomerization, within the ethylcyclohexane hydroconversion bi-functional framework) within a given zeolitic framework (EUO) is elucidated by DFT calculations. Then, it was also confirmed experimentally by the experimental catalytic evaluation of two zeolites (EU-1 and ZSM50) depicting this framework (EUO) but with different positions of the Brønsted acid sites. The active sites in the EU-1 zeolite are mainly found inside 12MR side-pockets and in 10MR channels, whereas in the ZSM-50 zeolite they are located at the intersection between the channel and the side-pocket. The DFT evaluation of the intermediates and transition states stability revealed the intersection between the channel and the pocket as the most unfavorable active site for the reaction. On the contrary, the side pocket is found as the preferred place for the reaction to happen. These results were as well confirmed by the calculation of the Gibbs adsorption energy profile. Consistently, HEU-1 shows an average turnover frequency per Brønsted acid site 15 times higher than HZSM50 in the experimental hydroconversion of ethylcyclohexane. This difference in activity could be attributed either to diffusional limitations or to the active site location. However, TAP experiments to measure diffusional limitations revealed that the difference in catalytic performance between the two zeolites can

## CONCLUSIONS AND PERSPECTIVES

not be attributed to transport phenomena. Hence, the difference of activity is attributed to the different active sites location.

This study also provides detailed computational information about the reaction network for the bi-functional isomerization of naphthenes. The transition structures are PCP-like, the cyclopropane being connected edge-to-edge to a cyclopentane unit. A typical feature of the transition states is the presence of an edge proton, migrating along the cycle contraction-expansion step.

Therefore, our DFT study supported by our experimental study allows us to conclude that confinement is optimal to promote isomerization of ethylcyclohexene (obtained from dehydrogenation of ethylcyclohexane) for active sites located in the side pockets. From the later study, the thermodynamic data and kinetic constants were calculated in order to use them in the construction of a microkinetic model. In order to build this microkinetic model, a experimental study of the ethylcyclohexane hydroconversion at different contact times has been carried out. The target of this analysis was to confirm the apparent mechanisms proposed by a more rigorous kinetic investigation and then, to investigate in more detail the composition of the isomerization and ring opening products lumps. The results confirm the isomerization mechanisms and show a more detailed description of the isomerization products distribution within each family and of the ring opening products. The mechanism involves reactions of cycle expansion-contraction through protonated cyclopropyl (PCP), hydride and methyl shifts. According to this mechanism, the first primary products appearing are the ethylmethycyclopentanes (EMCP) followed by the dimethylcyclohexanes (DMCH) and at last by the trimethylcyclopentanes (TMCP). The analysis of the isomers within the EMCP family reveals the 13-EMCP as the first product appearing followed by the 12-EMCP in lower amount and the 11-EMCP at last in a very small amount. Regarding the isomers within the DMCH family, 13-DMCH and 14-DMCH appear first followed by lower amounts of 12-DMCH in second place and 11-DMCH at last in much lower amount. The 124-TMCP is the first isomer appearing in the TMCP family followed by 113-TMCP, 123-TMCP and 112-TMCP appearing at last. Furthermore, the ring opening products distribution is analyzed as well. 25-Dimethylhexane and 2-methylheptane are revealed as the major ring opening products appearing. These products may come respectively from the opening of 133-TMCP and 13-DMCH. n-octane appeared as well within the ring opening products family, however its production is believed to come from the isomerization of the ring opening products instead of being the products of the  $\text{ECH}^+$  opening. From these results, several pathways of the

## CONCLUSIONS AND PERSPECTIVES

isomerization reaction (containing the isomers observed experimentally) and ring opening scheme are depicted and studied with *ab initio* calculations in two different active sites of the zeolite: the pocket (T9O6) and the channel (T1O1). These calculations reveal the energy barriers of each elementary step and thermodynamic data such as Gibbs adsorption energy, enthalpy and entropy energies.

The very complex *ab initio* reaction energy and Gibbs free energy profiles did not allow us to define a major pathway occurring during the isomerisation reaction for the active sites located in the channel. Four different paths have been identified: Path I, Path II, Path II bis et Path II ter. The Path I involves only tertiary carbocations whereas the other three involve as well secondary carbocations. All the transition states involving PCP were really similar except the first one corresponding to Path II, Path II bis et Path II ter. In the case of the pocket, Path I is clearly favored since the other paths include a first step, to convert the  $\text{ECH}^+$ , with a really high energy barrier. However, even if the pocket active site, possesses lower intermediate adsorption energies and many of the transition states have as well lower adsorption energy values, a part of the reaction products rests quite impeded (the energy barrier required to obtain a key intermediate in the pathways involving secondary carbocations is very high). Thus, in order to build up a preliminary microkinetic model able to clarify the reactional scheme, only the thermodynamic data of the channel active site is employed. Furthermore, the ring opening reaction was studied in the different active sites from the intersection (T10O12), channel (T1O1) and pocket (T9O6). The only successful ring opening reaction carried out is the 113-TMCP ring opening into 25-dimethylhexane. Nevertheless, the transition state is not isolated because it is really close in energy to the product. Then, the energy barrier is finally calculated as an energy difference between the reactive (113-TMCP) and the product (25-dimethylhexane). These forward energy barriers reveal the ring opening as a difficult reaction since even if the forward barrier is not too high (such as in the pocket site), the backward reaction is non-activated. From all the active sites tested within the zeolite, the ring opening is more favored in the pocket than in the channel or the intersection. Then, even if the pocket is the most active site, it is the less selective one.

From the thermodynamic data, the kinetic constants of each individual step taking place in channel sites are calculated and introduced into the kinetic model. According to the model, the reaction would have an apparent activation energy of 131 kJ/mol assuming a first order reaction and using the integral rate equation for a fixed bed reactor. Applying this procedure to the experimental conversion at the lowest W/F, an activation energy of 115 kJ/mol was

## CONCLUSIONS AND PERSPECTIVES

calculated. The initial activation barrier to convert ethyl-cyclohexane in the model equals 127 kJ/mol for Path I (steps (1a) + (15)) and 147 kJ/mol for Path II (steps (1b) + (19)), respectively. Following with the mechanisms, the model fits quite well the experimental data concerning the general mechanism. The data concerning the isomerization mechanism is well fitted as well by the model, even if at higher ECH conversion the DMCH yield is a little bit overestimated in detriment of the TMCP yield which is underestimated. Going further into detail, the EMCP product distribution within this family reveals as well a good correlation between the experimental and the modelled data. Within this family the 13-EMCP model yield is slightly overestimated at higher ECH conversion. Following with this detailed analysis and regarding the DMCH family, the kinetic model fits quite well the experimental yields. Only at higher conversion 13-DMCH model yield is overestimated if compared to experimental data whereas at lower conversion it is underestimated. Finally, the TMCP family is probably the one in which the model fitted worst the experimental data. Even so, within this group, the 112-TMCP and 123-TMCP model yields are pretty close to the experimental data, even if at higher ECH conversion 123-TMCP yield is slightly underestimated. Regarding, 133-TMCP model yield, it is a little bit underestimated at higher conversions whereas the 124-TMCP yield is underestimated at all ECH conversion being this difference maximal at higher conversion.

To sum up, the general mechanism and the isomerization and ring opening mechanisms are unraveled for EUO type zeolites. Besides, thanks to the *ab initio* calculations, a deep knowledge of the mechanism has been achieved and key rate constants calculated. Including these rate constants in the microkinetic model, a good correlation between the experimental and modelled data has been found for describing the isomerization and ring opening mechanisms.

Finally, the evaluation of the impact of the zeolitic topology structure in the ethylcyclohexane hydroisomerization using eleven different zeolites has been performed. These zeolites possess different pore size and dimensionality. The objective of this study is to reveal which are the features of the zeolites contributing to the fatal losses of this reaction (ring opening and cracking side reactions). Once known these features, these reactions could be reduced by promoting the zeolites less selective towards these undesired side reactions. In order to compare the zeolite performances, ideal catalysts are required. Therefore three different amounts of Pt have been tested in order to find an ideal catalyst for each zeolite. In

## CONCLUSIONS AND PERSPECTIVES

this study the Pt is deposited over the Alumina and after the evaluation of all the catalysts, the catalysts chosen as ideal ones were the ones containing 1% Pt - Al<sub>2</sub>O<sub>3</sub>/ zeolite.

The characterization of the zeolites reveals their diversity. They have different morphology, acidity and physical properties. Then, the results of activity and selectivity are going to be a result of the combination of all of that parameters. The activity of each catalyst was analyzed separately in different groups concerning the ring size: 10MR, 10-12MR and 12MR. Within each group one or two catalysts exhibit better performance than the others. For instance, in the 10MR group the HZSM-57 zeolite is the most active one whereas in the 10-12MR group it is HNU-86. The last group 12MR, evidences the HBETA and HMOR15 as the most active zeolite-based catalysts.

The temperature necessary to reach 50% of ECH conversion is 201°C in the case of the most active catalyst (1%Pt- Al<sub>2</sub>O<sub>3</sub>/HBETA) whereas it is 325°C for the less active one (1%Pt- Al<sub>2</sub>O<sub>3</sub>/HZSM-23). The difference of activity observed could not be explained solely based on the amount of Brønsted acid sites per gram of zeolite. Straightforward explanation could not be proposed as the Brønsted site activity depends on numerous parameter. As a matter of fact, the solid with by far the higher TOF of the investigated zeolites (HBETA) combines a high framework dimensionality (3D), micropore size (12 MR) and small nanocrystals (20 nm). Solids with the lowest TOF of the all zeolites (HZSM-23 and HZSM-50) combine a low framework dimensionality (1D), 10 MR micropores and big crystals (100-700 and 200 nm respectively).

The evaluation of the catalysts selectivities towards ECH isomerization, ring opening and cracking was scrutinized next. It appeared that the contribution of naphthenes dehydrogenation reaction to produce the corresponding aromatics could be significant, depending on the catalyst at stake. Therefore, the comparison of the catalysts selectivities towards isomerization has been done considering ECH isomers and xylenes lumped as a single family. Ring opening and cracking products were lumped together as well because both kind of product formation involves the breakage of a C-C ring bond. The cracking and ring opening yield at 40% of ECH isomers and xylenes yield was used as a descriptor of the catalyst selectivity. The different zeolites exhibited marked differences in selectivity. It was observed that the most opened structure were the most selective ones. Preliminary results suggest that the confinement effects within the pores of the zeolite plays a key role to govern the zeolite selectivity. After the isomerization step, isomerized product can either be desorbed or cracked. If the isomerized product is too strongly adsorbed at the vicinity of the acid site,



## CONCLUSIONS AND PERSPECTIVES

the consecutive cracking and ring opening reaction will be favored. The latter observation is in agreement with a previous proposal done for phenanthrene hydroconversion.<sup>227</sup> This was continued by complementary simulations to calculate the adsorption energies in the various zeolites of isomerized products that are prone to ring opening in order to see if the differences of activity and/or selectivity can be rationalized and/or anticipated. The analysis of these data shows no correlation in between experimental and DFT results. However many hypothetical explanations have been found which open many perspectives for further studies. Furthermore, we consider that diffusional limitations should also be studied for all the zeolites in order to rule out (or not) their impact on the zeolite selectivity.

To conclude, according to this study the choice of the zeolite has been not only influenced by the topology but also by the location of the acid sites. The results make us to think that there is a ring size adapted to this process and it involves 12MR which allow to accommodate not only the reaction intermediates but also the transition states. Besides, this size is big enough to avoid the possibility of diffusional problems, decreasing then the residence time of the molecules inside the zeolitic structure. Higher residences times will promote cracking products. The fact of having a one-dimensional zeolite the movements of the molecule inside the zeolite are more restraint than in two- or three-dimensional zeolites. The sum of all of these conclusions makes the HBETA zeolite as the most adapted zeolites to this hydroconversion of ethylcyclohexane reaction.

The **perspectives** of this project are large. Some of them are described below:

Concerning the analysis of the acidity on zeolites, and its strength a wide study can be carried out by IR pyridine and CO. However it should be bear on mind that pyridine sometimes will not enter to the all porosity of small pore zeolites since its dimension will induce diffusional problems<sup>231–233</sup>.

In this work it has been shown the difference of activity depending on the active site of the EUO framework. However the phenomenon of pore mouth catalysis has not been investigated. This line of work could be followed not only from a DFT point of view (the building of external surface models would be needed for the EUO framework, in the spirit of previous studies on other zeolites<sup>212,234–236</sup>) but also from an experimental point of view. The proper passivation treatment of the zeolite could deactivate acid sites at the surface of the zeolite crystals, leaving only the microporosity available for catalysis.<sup>237–239</sup> This will allow to measure not only the remaining active sites inside the porosity, but also if they are active and selective in catalysis by comparing with the non-passivated zeolite.



## CONCLUSIONS AND PERSPECTIVES

Following with that difference of activity depending on the location of active sites within the EUO framework, it will be really interesting to make an analog of Chapter 5 (kinetic study and model) on the intersection (active sites concerning the ZSM-50 zeolite) to anticipate the possible differences in selectivity between EU-1 and ZSM50.

Besides, the kinetic model could be expanded considering more reactions than the ones already considered in the present work because they were out of scope. By introducing the hydro/dehydrogenation reactions (metallic function) and also calculating by DFT all the thermodynamic data concerning the less activated steps of the reaction such as the protonation and hydride or methyl-shifts the model will be more complete. In the model developed so far the HD/DHD reactions are supposed to be at equilibrium. An extension of the work could be to generalize the kinetic model to situation where the rate determining steps of the reaction can occur both on the acidic phase and on the metallic phase. This situation applies when the acidic function is not balanced by the metallic function. Kinetics of HD and DHD reactions must be then taken into account as these reactions are no more at thermodynamic equilibrium. Such situation could be encountered in industrial like conditions and catalysts. The quantification of the effects of deviation to equilibrium to the catalyst performance can be of practical interest. Note that this is actually what makes the kinetic model of Mendes,<sup>174</sup> in a very "macro" way. Besides, Froment has also generalized the single event model for non-ideal cases for hydroconversion of paraffins.<sup>59</sup> Another perspective of the kinetic modeling is related to a hybrid channel-pocket scheme. Since the first step of Path II in the pocket has a first energy barrier that makes this step really unfavorable, we can imagine that this first step could occur in the channel. Afterwards, the product intermediate ( $\pi$ -complex) of this reaction would diffuse through the intersection into the channel where the rest of the reaction would take place. Furthermore, the model will be more complete if the lump of  $\pi$  and carbenium complexes is split up, which will allow to have access to the reaction intermediates concentration.

With regards to the last part of this study concerning the zeolites screening, diffusion TAP experiments should be carried in order to identify possible diffusional problems affecting to the catalytic performance in some of the zeolites. Besides since by the DFT calculation, we estimate only the reactivity of some specific individual sites, this study could also be expanded in an exhaustive way to other zeolite framework sites.

Regarding the DFT ab initio calculations, a first perspective will be the use of a biased molecular dynamic approach in order to estimate the kinetic constants in a more accurate way.

## CONCLUSIONS AND PERSPECTIVES

However, it should be borne in mind that this perspective is not be fully realistic to date due to the long time of calculation required. On the other hand, based on the number of studied cases in this thesis, some descriptors able to predict the behavior of zeolites could be looked for. Such approach appeared to be successful for several zeolite-catalyzed reactions<sup>240,241</sup>.

On the other hand, for the open molecules, static DFT approaches to reactivity may be insufficient to estimate both enthalpies and entropies, whereas we obtained very satisfactory results for cyclic compounds in chapter 4 and 5. Biased Ab Initio Molecular Dynamics (AIMD) may be required in such cases. This was recently illustrated by Van Speybroeck et al.,<sup>230</sup> and leads to current developments at IFPEN (Jérôme Rey's thesis, in collaboration with Tomas Bucko from the University of Bratislava). These methods are however very expensive from the computational point of view, preventing a systematic screening of zeolite structures at present time.



## REFERENCES

---

- (1) Guillon, E.; Leflaive, P. Traitement des essences aromatiques pour la pétrochimie. *Techniques de l'ingénieur* **2011**, J 5 920v2, 1–16.
- (2) Hsu, Y. S.; Lee, T. Y.; Hu, H. C. Isomerization of Ethylbenzene and m-xylene on zeolites. *Ind. Eng. Chem. Prod. Res.* **1988**, 27, 942–947.
- (3) Fernandes, L.; Monteiro, J.; Sousa-Aguiar, E.; Martinez, A.; Corma, A. Ethylbenzene hydroisomerization over bifunctional zeolite based catalysts. *J. Catal.* **1998**, 177, 363–377.
- (4) Vermeiren, W., Gilson, J.-P. Impact of Zeolites on the Petroleum and Petrochemical Industry. *Top Catal.* **2009**, 52, 1131–1161.
- (5) Guillon, E.; Lacombe, S.; Sozinho, T.; Magnoux, P.; Gnep, S.; Moreau, P.; and Guisnet, M. How to Improve the Selectivity of Zeolitic Catalysts in C8 Aromatic Cut Isomerization. *Oil Gas Sci. Technol.- Rev. IFP* **2009**, 64, 731–744.
- (6) Guisnet, M. Catalyse bifonctionnelle redox-acide -Applications en raffinage du pétrole et pétrochimie. *Techniques de l'ingénieur* **2015**, J 1 217, 1–22.
- (7) Pitts, P. M.; Connor, J.; and Leum, L. Isomerization of Alkyl Aromatic hydrocarbons. *Industrial and engineering chemistry* **1955**, 47, 770–773.
- (8) Weisz, P. B. Polyfunctional Heterogeneous Catalysis. *Adv. Catal.* **1962**, 13, 137–190.
- (9) Cannella, W. J. Xylenes and Ethylbenzene. in *Kirk-Othmer Encyclopedia of Chemical Technology*, John Wiley & Sons, Inc., Suppl. Vol. 2007.
- (10) Silva, J.M.; Ribeiro, M.F.; Ramôa Ribeiro, F.; Benazzi, E.; Guisnet, M. Transformation of an ethylbenzene-o-xylene mixture on HMOR and Pt-HMOR catalysts. Comparison with ZSM-5 catalysts. *Appl. Catal., A.* **1995**, 125, 15–27.
- (11) Moreau, F.; Gnep, N. S.; Lacombe, S.; Merlen, E.; Guisnet, M. Ethylbenzene transformation on bifunctional Pt/Al<sub>2</sub>O<sub>3</sub>-NaHMOR catalysts. *Appl. Catal., A.* **2002**, 230, 253–262.
- (12) Moreau, F.; Bernard, S.; Gnep, N.; Lacombe, S.; Merlen, E.; Guisnet, M. Ethylbenzene Isomerization on Bifunctional Platinum Alumina–Mordenite Catalysts. *J. Catal.* **2001**, 202, 402–412.

## REFERENCES

- (13) Moreau, F.; Bernard, S.; Gnep, N.; Lacombe, S.; Merlen, E.; Guisnet, M. Ethylbenzene Isomerization on Bifunctional Platinum Alumina-Mordenite Catalysts. 2. Influence of the Pt Content and of the Relative Amounts of Platinum Alumina and Mordenite Components. *Ind. Eng. Chem. Prod. Res.* **2002**, 41, 1469–1476.
- (14) Geetha Bhavani, A.; Pandurangan, A. Hydroisomerization of ethylbenzene over bimetallic bifunctional zeolite catalysts. *J. Mol. Catal.* **2007**, 267, 209–217.
- (15) Moreau, F.; Moreau, P.; Gnep, N.S.; Magnoux, P.; Lacombe, S.; Guisnet, M. Ethylbenzene isomerization over bifunctional platinum alumina–EUO catalysts: Location of the active sites. *Micropor. Mesopor. Mat.* **2006**, 90, 327–338.
- (16) Martens, J. A.; Souverijns, W.; Verrelst, W.; Parton, R.; Froment, G. F.; Jacobs, P. A. Selective Isomerization of Hydrocarbon Chains on External Surfaces of Zeolite Crystals. *Angew. Chem. Int. Ed. Engl.* **1995**, 34, 2528–2530.
- (17) Martens, J. A.; Vanbutsele, G.; Jacobs, P. A.; Denayer, J.; Ocakoglu, R.; Baron, G.; Muñoz Arroyo, J. A.; Thybaut, J.; Marin, G. B. Evidences for pore mouth and key–lock catalysis in hydroisomerization of long n-alkanes over 10-ring tubular pore bifunctional zeolites. *Catal. Today* **2001**, 65, 111–116.
- (18) Tanabe, K. Industrial application of solid acid–base catalysts. *Appl. Catal., A.* **1999**, 181, 399–434.
- (19) Corma, A. Inorganic Solid Acids and Their Use in Acid-Catalyzed Hydrocarbon Reactions. *Chem. Rev.* **1995**, 95, 559–614.
- (20) Corma, A. State of the art and future challenges of zeolites as catalysts. *J. Catal.* **2003**, 216, 298–312.
- (21) Csicsery, S. M. Shape-selective catalysis. *Zeolites* **1984**, 4, 202–213.
- (22) Marcilly, C. in *Acid-basic catalysis: Application to refining and petrochemistry*; IFP publications, Editions Technip: Paris 2006.
- (23) Patriceon, A.; Benazzi, E.; Travers, C.; Bernhard, J. Y. Influence of the zeolite structure and acidity on the hydroisomerization of n-heptane. *Catal. Today* **2001**, 65, 149–155.
- (24) Arroyo, J.; Martens, G. G.; Froment, G. F.; Marin, G. B.; Jacobs, P. A.; Martens, J. A. Hydrocracking and isomerization of n-paraffin mixtures and a hydrotreated gasoil on Pt/ZSM-22. *Appl. Catal., A.* **2000**, 192, 9–22.

## REFERENCES

- (25) Souverijns, W.; Martens, J. A.; Froment, G. F.; Jacobs, P. A. Hydrocracking of Isoheptadecanes on Pt/H-ZSM-22: An Example of Pore Mouth Catalysis. *J. Catal.* **1998**, 174, 177–184.
- (26) Gola, A. Influence des techniques de désalumination de la zéolithe Y sur ses propriétés physico-chimiques et sur ses performances catalytiques en hydrocraquage de N-decane, Université Pierre et Marie Curie, 1996.
- (27) Weisz, P. B. Zeolites-New horizons in catalysis. *Chemtech* **1973**, 493–505.
- (28) Webster, C. E.; Drago, R. S.; Zerner, M. C. A Method for Characterizing Effective Pore Sizes of Catalysts. *J. Phys. Chem. B* **1999**, 103, 1242–1249.
- (29) Nelson, P. H.; Kaiser, A. B.; Bibby, D. M. Simulation of diffusion and adsorption in zeolites. *J. Catal.* **1991**, 127, 101–112.
- (30) Theodorou, D.; Wei, J. Diffusion and reaction in blocked and high occupancy zeolite catalysts. *J. Catal.* **1983**, 83, 205–224.
- (31) Derouane, E. G. A novel effect of shape selectivity. *J. Catal.* **1980**, 65, 486–489.
- (32) Derouane, E. G. Shape Selectivity in Catalysis by Zeolites: The Nest Effect. *J. Catal.* **1986**, 100, 541–544.
- (33) Derouane, E. G.; André, J. M.; Lucas, A. A. A simple van der waals model for molecule-curved surface interactions in molecular-sized microporous solids. *Chem. Phys. Lett.* **1987**, 137, 336–340.
- (34) Blomsma, E.; Martens, J. A.; Jacobs, P. A. Isomerization and Hydrocracking of Heptane over Bimetallic Bifunctional PtPd/H-Beta and PtPd/USY Zeolite Catalysts. *J. Catal.* **1997**, 165, 241–248.
- (35) Weitkamp, J.; Jacobs, P. A.; Martens, J. A. Isomerization and hydrocracking of C9 through C16 n-alkanes on Pt/HZSM-5 zeolite. *Appl. Catal.* **1983**, 8, 123–141.
- (36) Pedro S.F.M.; Lapisardi, G.; Bouchy, C.; Rivallan, M.; Silva, J. M.; Ribeiro, M. F. Hydrogenating activity of Pt/zeolite catalysts focusing acid support and metal dispersion influence. *Appl. Catal., A* **2015**, 504, 17–28.
- (37) Donnis, B. Platinum/Alumina Catalysts in Reforming Methylcyclopentane. *Ind. Eng. Chem. Prod. Res. Dev.* **1976**, 15, 254–258.

## REFERENCES

- (38) Bond, G. C. The origins of particle size effects in heterogeneous catalysis. *Surf. Sci.* **1985**, 156, 966–981.
- (39) Boudart, M. in *Kinetics of heterogeneous catalytic reactions*, Princeton University Press: New Jersey 2016.
- (40) Borgna, A.; Garetto, T. F.; Monzón, A. Modelling of sulfur deactivation of naphtha-reforming catalysts Structure sensitivity in cyclopentane hydrogenolysis. *J. Chem. Soc., Faraday Trans.* **1997**, 93, 2445–2450.
- (41) Koussathana, M.; Vamvouka, D.; Economou, H.; Verykios, X. Slurry-phase hydrogenation of aromatic compounds over supported noble metal catalysts. *Appl. Catal.* **1991**, 77, 283–301.
- (42) Madon, R. J.; O'Connell, J. P.; Boudart, M. Catalytic hydrogenation of cyclohexene. *AIChE J.* **1978**, 24, 904–911.
- (43) Schwarz, J. A.; Contescu, C.; Contescu, A. Methods for Preparation of Catalytic Materials. *Chem. Rev.* **1995**, 95, 477–510.
- (44) Ertl, G.; Knözinger, H.; Weitkamp, J. in *Preparation of solid acids*, Wiley-VCH, Germany 1999.
- (45) Cañizares, P.; Lucas, A. d.; Dorado, F.; Durán, A.; Asencio, I. Characterization of Ni and Pd supported on H-mordenite catalysts. *Appl. Catal., A.* **1998**, 169, 137–150.
- (46) T. Sozinho. étude mecanistique et cinetique des reactions de craquage dans les conditions d'isomerization de la coupe C8 aromatique sur catalyseur bifonctionnel, Poitiers University//IFPEN, 2010.
- (47) Weitkamp, J.; Ernst. S.; Karge. H. G. Peculiarities in the Conversion of Napthenes on Bifunctional Catalysts. *Erdöl, Kohle –Erdgas -Petrochem* **1984**, 457–462.
- (48) Weitkamp, J.; Jacobs, P. A.; Ernst. S. Shape Selective Isomerization and Hydrocracking of Napthenes Over Pt/HZSM-5 Zeolite. in *Structure and Reactivity of Modified Zeolites*, Elsevier Science Publishers B.V.; Jacobs, P. A. Ed.; 1984.
- (49) Weitkamp, J.; Ernst. S. Comparison of the Reactions of Ethylcyclohexane and 2-Methylheptane on PdY Zeolite. in *Catalysis by Acids and Bases*, Elsevier Science Publishers B.V.; Imelik, B., Naccache, C., Coudurier, G., Ben Taarit, Y., Vedrine, J. C. Eds.; 1985.

## REFERENCES

- (50) Cerqueira, H. S.; Mihindou-Koumba. P.C.; Magnoux, P.; Guisnet, M. Methylcyclohexane Transformation over HFAU, HBEA, and HMFI Zeolites. *Ind. Eng. Chem. Res.* **2001**, 40, 1032–1041.
- (51) Martens. G.G.; Joris W. T.; Marin, G. B. Single-Event Rate Parameters for the Hydrocracking of Cycloalkanes on Pt/US-Y Zeolites. *Ind. Eng. Chem. Prod. Res.* **2001**, 40, 1832–1844.
- (52) Guisnet, M. “Ideal” bifunctional catalysis over Pt-acid zeolites. *Catal. Today* **2013**, 218-219, 123–134.
- (53) McVicker. G.B.; Feeley. O.C.; Ziemiak. J.J.; Vaughan. DEW.; Strohmaier. K.C.; Klier. W.R.; Leta. D.P. Methylcyclohexane Ring-Contraction: A Sensitive Solid Acidity and Shape Selectivity Probe Reaction. *J. Phys. Chem. B.* **2005**, 109, 2222–2226.
- (54) Cook, B. R.; Wilkinson, B. B.; Culross, C. C.; Holmes, S. M.; Martinez, L. E. Hydrogen Transfer Induced Cleavage of Biaryl Bonds. *Energy Fuels* **1997**, 11, 61–75.
- (55) Gault, F. G. Mechanisms of Skeletal Isomerization of Hydrocarbons on Metals. *Advances in catalysis and related*, 1–95.
- (56) Brandenberger, S. G.; Callender, W. L.; Meerbott, W. K. Mechanisms of methylcyclopentane ring opening over platinum-alumina catalysts. *J. Catal.* **1976**, 42, 282–287.
- (57) Smith, R. L.; Naro, P. A.; Silvestri, A. J. Reaction paths for decyclization of methylcyclopentane over Pt/Al<sub>2</sub>O<sub>3</sub> catalyst. *J. Catal.* **1971**, 20, 359–366.
- (58) Galperin, L. B.; Bricker, J. C.; Holmgren, J. R. Effect of support acid–basic properties on activity and selectivity of Pt catalysts in reaction of methylcyclopentane ring opening. *Appl. Catal., A.* **2003**, 239, 297–304.
- (59) Kumar, H.; Froment, G. F. A Generalized Mechanistic Kinetic Model for the Hydroisomerization and Hydrocracking of Long-Chain Paraffins. *Ind. Eng. Chem. Res.* **2007**, 46, 4075–4090.
- (60) Raybaud, P.; Patriceon, A.; Toulhoat, H. The Origin of the C<sub>7</sub>-Hydroconversion Selectivities on Y,  $\beta$ , ZSM-22, ZSM-23, and EU-1 Zeolites. *J. Catal.* **2001**, 197, 98–112.
- (61) Samad, J. E.; Blanchard, J.; Sayag, C.; Louis, C.; J.R. Regalbuto. The controlled synthesis of metal-acid bifunctional catalysts. *J. Catal.* **2016**, 342, 203–212.



## REFERENCES

- (62) Calemma. V.; Carati. A.; Flego. C.; Giardino. R.; Gagliardi. F.; Millini. R.; Bellussi. G. Ring Opening of Methylcyclohexane over Platinum-Loaded Zeolites. *ChemSusChem* **2008**, 1, 548–557.
- (63) Brouwer, D. M.; Hogeveen, H. The importance of orbital orientation as a rate-controlling factor in intramolecular reactions of carbonium ions. *Recl. Trav. Chim. Pays-Bas* **1970**, 89, 211–224.
- (64) Weitkamp, J. Isomerization of Long-chain n -Alkanes on a Pt/CaY Zeolite Catalyst. *Ind. Eng. Chem. Prod. Res. Dev.* **1982**, 21, 550–558.
- (65) Bouchy, C., Hastoy, G., Guillon, E., Martens, J. A. Fischer-Tropsch Waxes Upgrading via Hydrocracking and Selective Hydroisomerization. *Oil Gas Sci. Technol.- Rev. IFP* **2009**, 64, 91–112.
- (66) Pichler. H.; Schulz. H.; Reitemeyer. H.O.; Weitkamp, J. über das hydrocracken gesättigter kohlenwasser stoffe. *Erdöl, Kohle –Erdgas -Petrochem*, 1972.
- (67) Thybaut, J. W.; Laxmi Narasimhan, C. S.; Denayer, J. F.; Baron, G. V.; Jacobs, P. A.; Martens, J. A.; Marin, G. B. Acid–Metal Balance of a Hydrocracking Catalyst. *Ind. Eng. Chem. Res.* **2005**, 44, 5159–5169.
- (68) Batalha, N.; Pinard, L.; Bouchy, C.; Guillon, E.; Guisnet, M. n-Hexadecane hydroisomerization over Pt-HBEA catalysts. Quantification and effect of the intimacy between metal and protonic sites. *J. Catal.* **2013**, 307, 122–131.
- (69) Batalha, N.; Pinard, L.; Pouilloux, Y.; Guisnet, M. Bifunctional Hydrogenating/Acid Catalysis: Quantification of the Intimacy Criterion. *Catal. Lett.* **2013**, 143, 587–591.
- (70) Ben Moussa, O.; Tinat, L.; Jin, X.; Baaziz, W.; Durupthy, O.; Sayag, C.; Blanchard, J. Heteroaggregation and Selective Deposition for the Fine Design of Nanoarchitected Bifunctional Catalysts. *ACS Catal.* **2018**, 8, 6071–6078.
- (71) Alvarez, F.; Ribeiro, F. R.; Perot, G.; Thomazeau, C.; Guisnet, M. Hydroisomerization and Hydrocracking of Alkanes. *J. Catal.* **1996**, 162, 179–189.
- (72) Guisnet, M.; Alvarez, F.; Giannetto, G.; Perot, G. Hydroisomerization and hydrocracking of n-heptane on Pth zeolites. Effect of the porosity and of the distribution of metallic and acid sites. *Catal. Today* **1987**, 1, 415–433.

## REFERENCES

- (73) Mignard, S.; and Marchal-George, N. Décyclisation du méthylcyclohexane en des conditions d'hydroconversion sur des catalyseurs de type Pt/USY : influence du rapport H/A. *Rapport IFP* **1995**, n°42061,
- (74) Zečević, J.; Vanbutsele, G.; P. de Jong, K.; Martens, J. A. Nanoscale intimacy in bifunctional catalysts for selective conversion of hydrocarbons. *Nature* **2015**, 528, 245–254.
- (75) Mojet, B. L.; Miller, J. T.; Ramaker, D. E.; Koningsberger, D. C. A New Model Describing the Metal–Support Interaction in Noble Metal Catalysts. *J. Catal.* **1999**, 186, 373–386.
- (76) Regali, F.; Liotta, L. F.; Venezia, A. M.; Boutonnet, M.; Järås, S. Hydroconversion of n-hexadecane on Pt/silica-alumina catalysts. *Appl. Catal., A* **2014**, 469, 328–339.
- (77) Samant, M. G.; Boudart, M. Support effects on electronic structure of platinum clusters in Y zeolite. *J. Phys. Chem.* **1991**, 95, 4070–4074.
- (78) Hafner, J.; Benco, L.; Bučko, T. Acid-based Catalysis in Zeolites Investigated by Density-Functional Methods. *Top Catal* **2006**, 37, 41–54.
- (79) Sauer, J.; Kölmel, C. M.; Hill, J.-R.; Ahlrichs, R. Brønsted sites in zeolitic catalysts. An ab initio study of local geometries and of the barrier for proton jumps between neighbouring sites. *Chem. Phys. Lett.* **1989**, 164, 193–198.
- (80) Kazansky, V. B.; Frash, M. V.; van Santen, R. A. Quantumchemical study of the isobutane cracking on zeolites. *Appl. Catal., A* **1996**, 146, 225–247.
- (81) Guo, Y. H.; Pu, M.; Wu, J.; Zhang, J. Y.; Chen, B. H. Theoretical study of the cracking mechanisms of linear  $\alpha$ -olefins catalyzed by zeolites. *Appl. Surf. Sci.* **2007**, 254, 604–609.
- (82) Ryder, J. A.; Chakraborty, A. K.; Bell, A. T. Density Functional Theory Study of Proton Mobility in Zeolites. *J. Phys. Chem. B* **2000**, 104, 6998–7011.
- (83) Cuán, A.; Martínez-Magadán, J. M.; García-Cruz, I.; Galván, M. DFT—Quantum chemical study of the HZSM-5-cyclohexene interaction pathways. *J. Mol. Catal. A: Chem.* **2005**, 236, 194–205.
- (84) van Santen, R. A.; Kramer, G. J. Reactivity Theory of Zeolitic Brønsted Acidic Sites. *Chem. Rev.* **1995**, 95, 637–660.

## REFERENCES

- (85) Fermann, J. T.; Moniz, T.; Kiowski, O.; McIntire, T. J.; Auerbach, S. M.; Vreven, T.; Frisch, M. J. Modeling Proton Transfer in Zeolites: Convergence Behavior of Embedded and Constrained Cluster Calculations. *J. Chem. Theory Comput.* **2005**, 1, 1232–1239.
- (86) Sauer, J. Molecular models in ab initio studies of solids and surfaces. *Chem. Rev.* **1989**, 89, 199–255.
- (87) Stave, M. S.; Nicholas, J. B. Density Functional Studies of Zeolites. 2. Structure and Acidity of [T]-ZSM-5 Models (T = B, Al, Ga, and Fe). *J. Phys. Chem.* **1995**, 99, 15046–15061.
- (88) Cook, S. J.; Chakraborty, A. K.; Bell, A. T.; Theodorou, D. N. Structural and electronic features of a Brønsted acid site in H-ZSM-5. *J. Phys. Chem.* **1993**, 97, 6679–6685.
- (89) Farnworth, K. J.; O'Malley, P. J. Brønsted acid site models for zeolites. *Electron. J. Theor. Chem.* **1996**, 1, 172–182.
- (90) Gu, J.; Gorb, L.; Leszczynski, J. A DFT Study of the Models of the Brønsted Acid Sites of Zeolite Catalysts. *Struct. Chem.* **1998**, 9, 319–326.
- (91) Demuth, T.; Hafner, J.; Benco, L.; Toulhoat, H. Structural and Acidic Properties of Mordenite. An ab Initio Density-Functional Study. *J. Phys. Chem. B* **2000**, 104, 4593–4607.
- (92) Vollmer, J. M.; Truong, T. N. Mechanisms of Hydrogen Exchange of Methane with H-Zeolite Y. *J. Phys. Chem. B* **2000**, 104, 6308–6312.
- (93) Sharkas, K. Développement de nouvelles méthodes hybrides en théorie de la fonctionnelle de la densité par séparation linéaire de l'interaction électronique. Chimie théorique, UPMC, 2013.
- (94) Demuth, T.; Rozanska, X.; Benco, L.; van Santen, R. A.; Toulhouat, H. Catalytic isomerization of 2-pentene in H-ZSM-22—A DFT investigation. *J. Catal.* **2003**, 214, 68–77.
- (95) Demuth, T.; Raybaud, P.; Lacombe, S.; Toulhouat, H. Effects of zeolite pore sizes on the mechanism and selectivity of xylene disproportionation—a DFT study. *J. Catal.* **2004**, 222, 323–337.
- (96) Ivanova, I. I.; Kolyagin, Y. G. Impact of in situ MAS NMR techniques to the understanding of the mechanisms of zeolite catalyzed reactions. *Chem. Soc. Rev.* **2010**, 39, 5018–5050.

## REFERENCES

- (97) Kazansky, V. B. Adsorbed carbocations as transition states in heterogeneous acid catalyzed transformations of hydrocarbons. *Catal. Today* **1999**, 51, 419–434.
- (98) Rigby, A. M.; Frash, M. V. Ab initio calculations on the mechanisms of hydrocarbon conversion in zeolites. *J. Mol. Catal. A: Chem.* **1997**, 126, 61–72.
- (99) Rozanska, X.; van Santen, R. A.; Demuth, T.; Hutschka, F.; Hafner, J. A Periodic DFT Study of Isobutene Chemisorption in Proton-Exchanged Zeolites. *J. Phys. Chem. B.* **2003**, 107, 1309–1315.
- (100) Tuma, C.; Sauer, J. Protonated Isobutene in Zeolites: tert-Butyl Cation or Alkoxide? *Angew. Chem. Int. Ed. Engl.* **2005**, 44, 4769–4771.
- (101) Hajek, J.; van der Mynsbrugge, J.; Wispelaere, K. d.; Cnudde, P.; Vanduyfhuys, L.; Waroquier, M.; van Speybroeck, V. On the stability and nature of adsorbed pentene in Brønsted acid zeolite H-ZSM-5 at 323K. *J. Catal.* **2016**, 340, 227–235.
- (102) Cnudde, P.; Wispelaere, K. d.; van der Mynsbrugge, J.; Waroquier, M.; van Speybroeck, V. Effect of temperature and branching on the nature and stability of alkene cracking intermediates in H-ZSM-5. *J. Catal.* **2017**, 345, 53–69.
- (103) Boronat, M.; Corma, A. Are carbenium and carbonium ions reaction intermediates in zeolite-catalyzed reactions? *Appl. Catal., A.* **2008**, 336, 2–10.
- (104) Tuma, C.; Kerber, T.; Sauer, J. The tert-Butyl Cation in H-Zeolites: Deprotonation to Isobutene and Conversion into Surface Alkoxides. *Angew. Chem. Int. Ed. Engl.* **2010**, 49, 4678–4680.
- (105) Boronat, M.; Viruela, P. M.; Corma, A. Reaction Intermediates in Acid Catalysis by Zeolites: Prediction of the Relative Tendency To Form Alkoxides or Carbocations as a Function of Hydrocarbon Nature and Active Site Structure. *J. Am. Chem. Soc.* **2004**, 126, 3300–3309.
- (106) Yang, S.; Kondo, J. N.; Domen, K. Formation of alkenyl carbenium ions by adsorption of cyclic precursors on zeolites. *Catal. Today* **2002**, 73, 113–125.
- (107) Yang, S.; Kondo, J. N.; Domen, K. 12-P-06 - Infrared observation of the stable carbenium ions formed by adsorption of olefins on zeolite Y at low temperatures. *Stud. Surf. Sci. Catal.* **2001**, 135, 217.

## REFERENCES

- (108) Jeffrey H.P.; Redondo, A.; Guo, Y. Theoretical studies of pentene cracking on zeolites. *Catal. Today* **1999**, 50, 517–523.
- (109) Guo, Y. H.; Pu, M.; Chen, B. H.; Cao, F. Theoretical study on the cracking reaction catalyzed by a solid acid with zeolitic structure. *Appl. Catal., A* **2013**, 455, 65–70.
- (110) Svelle, S.; Kolboe, S.; Swang, O. Theoretical Investigation of the Dimerization of Linear Alkenes Catalyzed by Acidic Zeolites. *J. Phys. Chem. B* **2004**, 108, 2953–2962.
- (111) Namuangruk, S.; Pantu, P.; Limtrakul, J. Investigation of ethylene dimerization over faujasite zeolite by the ONIOM method. *Chemphyschem* **2005**, 6, 1333–1339.
- (112) Chu, Y.; Han, B.; Zheng, A.; Deng, F. Influence of Acid Strength and Confinement Effect on the Ethylene Dimerization Reaction over Solid Acid Catalysts. *J. Phys. Chem. C* **2012**, 116, 12687–12695.
- (113) Li, Q.; East, A. Catalyzed  $\beta$  scission of a carbenium ion II — Variations leading to a general mechanism. *Can. J. Chem.* **2006**, 84, 1159–1166.
- (114) Li, Q.; East, A. Catalyzed  $\beta$  scission of a carbenium ion —Mechanistic differences from varying catalyst basicity. *Can. J. Chem.* **2005**, 83, 1146–1157.
- (115) Leydier, F.; Chizallet, C.; Costa, D.; Raybaud, P. Revisiting carbenium chemistry on amorphous silica-alumina: Unraveling their milder acidity as compared to zeolites. *J. Catal.* **2015**, 325, 35–47.
- (116) Saeys, M.; Reyniers, M. F.; Thybaut, J. W.; Neurock, M.; Marin, G. B. First-principles based kinetic model for the hydrogenation of toluene. *J. Catal.* **2005**, 236, 129–138.
- (117) Sabbe, M. K.; Canduela-Rodriguez, G.; Joly, J.-F.; Reyniers, M.-F.; Marin, G. B. Ab initio coverage-dependent microkinetic modeling of benzene hydrogenation on Pd(111). *Catal. Sci. Technol.* **2017**, 7, 5267–5283.
- (118) Saliccioli, M.; Stamatakis, M.; Caratzoulas, S.; Vlachos, D. G. A review of multiscale modeling of metal-catalyzed reactions. *Chemical Engineering Science* **2011**, 66, 4319–4355.
- (119) Reuter, K. Ab Initio Thermodynamics and First-Principles Microkinetics for Surface Catalysis. *Catal Lett* **2016**, 146, 541–563.
- (120) Maestri, M.; Reuter, K. Semiempirical rate constants for complex chemical kinetics. *Angew. Chem. Int. Ed. Engl.* **2011**, 50, 1194–1197.

## REFERENCES

- (121) Christiansen, M. A.; Mpourmpakis, G.; Vlachos, D. G. DFT-driven multi-site microkinetic modeling of ethanol conversion to ethylene and diethyl ether on  $\gamma$ -Al<sub>2</sub>O<sub>3</sub> (1 1 1). *J. Catal.* **2015**, 323, 121–131.
- (122) Larmier, K.; Chizallet, C.; Maury, S.; Cadran, N.; Abboud, J.; Lamic-Humblot, A.-F.; Marceau, E.; Lauron-Pernot, H. Isopropanol Dehydration on Amorphous Silica-Alumina: Synergy of Brønsted and Lewis Acidities at Pseudo-Bridging Silanols. *Angew. Chem. Int. Ed. Engl.* **2017**, 56, 230–234.
- (123) Larmier, K.; Nicolle, A.; Chizallet, C.; Cadran, N.; Maury, S.; Lamic-Humblot, A.-F.; Marceau, E.; Lauron-Pernot, H. Influence of Coadsorbed Water and Alcohol Molecules on Isopropyl Alcohol Dehydration on  $\gamma$ -Alumina: Multiscale Modeling of Experimental Kinetic Profiles. *ACS Catal.* **2016**, 6, 1905–1920.
- (124) Sabbe, M. K.; van Geem, K. M.; Reyniers, M.-F.; Marin, G. B. First Principle-Based Simulation of Ethane Steam Cracking. *AIChE J.* **2011**, 57, 482–496.
- (125) Rankovic, N.; Chizallet, C.; Nicolle, A.; Da Costa, P. Multiscale Modeling of Barium Sulfate Formation from BaO. *Ind. Eng. Chem. Res.* **2013**, 52, 9086–9098.
- (126) Rankovic, N.; Chizallet, C.; Nicolle, A.; Berthout, D.; Da Costa, P. Sulfur Deactivation of NO<sub>x</sub> Storage Catalysts. *Oil Gas Sci. Technol.- Rev. IFP* **2013**, 68, 995–1005.
- (127) Matera, S.; Blomberg, S.; Hoffmann, M. J.; Zetterberg, J.; Gustafson, J.; Lundgren, E.; Reuter, K. Evidence for the Active Phase of Heterogeneous Catalysts through In Situ Reaction Product Imaging and Multiscale Modeling. *ACS Catal.* **2015**, 5, 4514–4518.
- (128) Sabbe, M. K.; Reyniers, M.-F.; Reuter, K. First-principles kinetic modeling in heterogeneous catalysis. *Catal. Sci. Technol.* **2012**, 2, 2010.
- (129) Maestri, M. Escaping the trap of complication and complexity in multiscale microkinetic modelling of heterogeneous catalytic processes. *Chem Commun (Camb)*. **2017**, 53, 10244–10254.
- (130) Foppa, L.; Margossian, T.; Kim, S. M.; Müller, C.; Copéret, C.; Larmier, K.; Comas-Vives, A. Contrasting the Role of Ni/Al<sub>2</sub>O<sub>3</sub> Interfaces in Water-Gas Shift and Dry Reforming of Methane. *JACS*. **2017**, 139, 17128–17139.
- (131) Jasper, A. W.; Pelzer, K. M.; Miller, J. A.; Kamarchik, E.; Harding, L. B.; Klippenstein, S. J. Predictive a priori pressure-dependent kinetics. *Science* **2014**, 346, 1212–1215.

## REFERENCES

- (132) John, M.; Alexopoulos, K.; Reyniers, M.-F.; Marin, G. B. Effect of zeolite confinement on the conversion of 1-butanol to butene isomers. *Catal. Sci. Technol.* **2017**, 7, 2978–2997.
- (133) John, M.; Alexopoulos, K.; Reyniers, M.-F.; Marin, G. B. Mechanistic insights into the formation of butene isomers from 1-butanol in H-ZSM-5: DFT based microkinetic modelling. *Catal. Sci. Technol.* **2017**, 7, 1055–1072.
- (134) John, M.; Alexopoulos, K.; Reyniers, M.-F.; Marin, G. B. Reaction path analysis for 1-butanol dehydration in H-ZSM-5 zeolite. *J. Catal.* **2015**, 330, 28–45.
- (135) Marques Mota, F.; Bouchy, C.; Guillon, E.; Fécant, A.; Bats, N.; Martens, J. A. IZM-2: A promising new zeolite for the selective hydroisomerization of long-chain n-alkanes. *J. Catal.* **2013**, 301, 20–29.
- (136) Faraldos, M.; Goberna, C. in *Técnicas de análisis y caracterización de materiales*, 2a. edición revisada y aumentada; Biblioteca de ciencias, 39, Editorial CSIC Consejo Superior de Investigaciones Científicas: Madrid 2011.
- (137) Bertin, E. P. in *Introduction to X-Ray Spectrometric Analysis*, Springer US 2013.
- (138) Brunauer, S.; Emmett, P. H.; Teller, E. Adsorption of Gases in Multimolecular Layers. *J. Am. Chem. Soc.* **1938**, 60, 309–319.
- (139) Lynch, J. in *Physico-chemical analysis of industrial catalysts: A practical guide to characterisation*; Institut français du pétrole publications, Editions Technip: Paris 2003.
- (140) Galarneau, A.; Villemot, F.; Rodriguez, J.; Fajula, F.; Coasne, B. Validity of the t-plot method to assess microporosity in hierarchical micro/mesoporous materials. *Langmuir* **2014**, 30, 13266–13274.
- (141) Georgia State University. HyperPhysics(©C.R. Nave, 2017). <http://hyperphysics.phy-astr.gsu.edu/>.
- (142) Vannice, M. A.; Twu, C. C. Extinction coefficients and integrated intensities for linear- and bridged-bonded CO on platinum. *J. Chem. Phys.* **1981**, 75, 5944–5948.
- (143) Eischens, R. P.; Pliskin, W. A.; Francis, S. A. Infrared Spectra of Chemisorbed Carbon Monoxide. *J. Chem. Phys.* **1954**, 22, 1786–1787.
- (144) Alia, A.; Ganapathy, S.; Groot, H. J. M. de. Magic Angle Spinning (MAS) NMR: a new tool to study the spatial and electronic structure of photosynthetic complexes. *Photosynth. Res.* **2009**, 102, 415–425.



## REFERENCES

- (145) Benson, J.; Boudart, M. Hydrogen-oxygen titration method for the measurement of supported platinum surface areas. *J. Catal.* **1965**, 4, 704–710.
- (146) Bartholemew, C. H. in *H<sub>2</sub> adsorption on supported noble metals and its use in determining metal dispersion*; A Specialist periodical report; Spivey, J. J., Agarwal, S. K., Eds.; Royal Society of Chemistry: Cambridge, England 1994, 93–126.
- (147) Freel, J. Chemisorption on supported platinum I. Evaluation of a pulse method. *J. Catal.* **1972**, 25, 139–148.
- (148) Dorling, T. A. Hydrogen adsorption on platinum/silica catalysts. *J. Catal.* **1968**, 12, 207–209.
- (149) Dann, S. E. in *Reactions and characterization of solids*; Tutorial chemistry texts, 2, Royal Society of Chemistry: Cambridge 2000.
- (150) Fadoni, M.; Lucarelli, L. Temperature programmed desorption, reduction, oxidation and flow chemisorption for the characterisation of heterogeneous catalysts. Theoretical aspects, instrumentation and applications. *Stud. Surf. Sci. Catal.* **1998**, 120, 177–225.
- (151) Niwa, M.; Katada, N. New method for the temperature-programmed desorption (TPD) of ammonia experiment for characterization of zeolite acidity. *Chemical record (New York, N.Y.)* **2013**, 13, 432–455.
- (152) Javier Pérez-Ramirez, Rob J. Berger, Guido Mul, Freek Kapteijn, Jacob A. Moulijn. The six-flow reactor technology A review on fast catalyst screening and kinetic studies. *Catal. Today* **2000**, 60, 93–109.
- (153) Perdew, J.P., Burke, K., Ernzerhof M. Generalized Gradient Approximation Made Simple. *Phys. Rev. Lett.* **1996**, 77, 3865–3868.
- (154) Grimme, S. Semiempirical GGA-Type Density Functional Constructed with a Long-Range Dispersion Correction. *J. Comput. Chem.* **2006**, 27, 1787–1799.
- (155) Kohn, W.; Sham, L. J. Self-Consistent Equations Including Exchange and Correlation Effects. *Phys. Rev.* **1965**, 140, A1133-A1138.
- (156) Hafner, J. Ab-initio simulations of materials using VASP. *J. Comput. Chem.* **2008**, 29, 2044–2078.
- (157) Blöchl, P. E. Projector augmented-wave method. *Phys. Rev. B* **1994**, 50, 17953–17979.



## REFERENCES

- (158) Kresse, G., Furthmüller, J. Efficiency of ab-initio total energy calculations for metals and semiconductors using a plane-wave basis set. *Comput. Mater. Sci.* **1996**, 6, 15–50.
- (159) IZA database. <http://www.iza-structure.org/databases/>.
- (160) Fleurat-Lessard, P. Reaction path construction and determination , Opt'n-Path. <http://pfleurat.free.fr/ReactionPath.php>.
- (161) Hannes, J.; Mills, G.; Jacobsen, K. W. Nudged elastic band method for finding minimum energy paths of transitions. in *Classical and Quantum Dynamics in Condensed Phase Simulations* ,1998, 385–404.
- (162) Henkelman, G.; Uberuaga, B. P.; Jónsson, H. A climbing image nudged elastic band method for finding saddle points and minimum energy paths. *J. Chem. Phys.* **2000**, 113, 9901–9904.
- (163) Henkelman, G.; Jónsson, H. A dimer method for finding saddle points on high dimensional potential surfaces using only first derivatives. *J. Chem. Phys.* **1999**, 111, 7010–7022.
- (164) Heyden, A.; Bell, A. T.; Keil, F. J. Efficient methods for finding transition states in chemical reactions: Comparison of improved dimer method and partitioned rational function optimization method. *J. Chem. Phys.* **2005**, 123, 224101.
- (165) Fukui, K. Formulation of the Reaction Coordinate. *J. Phys. Chem.* **1970**, 74, 4161–4163.
- (166) Hratchian, H. P.; Schlegel, H. B. Following Reaction Pathways Using a Damped Classical Trajectory Algorithm. *J. Phys. Chem. A* **2002**, 106, 165–169.
- (167) Frenkel, D.; Smit, B. in *Understanding molecular simulation: From algorithms to applications* / Daan Frenkel, Berend Smit, 2nd ed.; Computational science series, 1, Academic Press: San Diego, London 2002.
- (168) Eyring, H. The Activated Complex in Chemical Reactions. *Chemphyschem* **1935**, 3, 107–115.
- (169) Dumesic, J. A., Rudd, D.D., Aparicio, L. M., Rekoske, J.E. ,Treviño A. A. in *The microkinetics of heterogeneous catalysis*; ACS professional reference book, American Chemical Society: Washington, DC 1993.

## REFERENCES

- (170) Stoltze, P. Microkinetic simulation of catalytic reactions. *Prog. Surf. Sci.* **2000**, 65, 65–150.
- (171) Levenberg, K. A method for the solution of certain non-linear problems in least squares. *Quart. Appl. Math.* **1944**, 2, 164–168.
- (172) Marquardt, D. W. An Algorithm for Least-Squares Estimation of Nonlinear Parameters. *SIAM J. Appl. Math.* **1963**, 11, 431–441.
- (173) Froment, G. F. Single Event Kinetic Modeling of Complex Catalytic Processes. *Catal. Rev. -Sci. Eng* **2005**, 47, 83–124.
- (174) Mendes, P. S. F. Silva, J. M. Ribeiro, M. F. Duchêne, P. Daudin, A. Bouchy, C. Quantification of metal-acid balance in hydroisomerization catalysts. *AIChE J.* **2017**, 63, 2864–2875.
- (175) Guisnet, M.; Gilson, J. P. in *Zeolites for cleaner technologies*; Catalytic science series, 3, Imperial College Press: London 2002.
- (176) Kuchar, P. J.; Bricker, J. C.; Reno, M. E.; Haizmann, R. S. Paraffin isomerization innovations. *Fuel Process Technol.* **1993**, 35, 183–200.
- (177) Primo, A.; Garcia, H. Zeolites as catalysts in oil refining. *Chem. Soc. Rev.* **2014**, 43, 7548–7561.
- (178) Rana, M. S.; Sámano, V.; Ancheyta, J.; Diaz, J. A review of recent advances on process technologies for upgrading of heavy oils and residua. *Fuel* **2007**, 86, 1216–1231.
- (179) Bertoncini, F.; Bonduelle-Skrzypcak, A.; Francis, J.; Guillon, E. Hydrocracking. in *Catalysis by transition metal sulphides: from molecular theory to industrial applications*, Editions Technip; Toulhoat, H., Raybaud, P. Eds., Paris 2013.
- (180) Huber, G. W.; O'Connor, P.; Corma, A. Processing biomass in conventional oil refineries. *Appl. Catal., A.* **2007**, 329, 120–129.
- (181) Sotelo-Boyás, R.; Liu, Y.; Minowa, T. Renewable Diesel Production from the Hydrotreating of Rapeseed Oil with Pt/Zelite and NiMo/Al<sub>2</sub>O<sub>3</sub> Catalysts. *Ind. Eng. Chem. Res.* **2011**, 50, 2791–2799.
- (182) Davis, B. H.; Occelli, M. L. in *Fischer-Tropsch synthesis, catalysts and catalysis*, Studies in surface science and catalysis, 163, Elsevier: Amsterdam, London 2007.

## REFERENCES

- (183) Böhringer, W.; Kotsiopoulos, A.; Boer, M. de; Knottenbelt, C.; Fletcher, J. Selective Fischer-Tropsch wax hydrocracking - opportunity for improvement of overall gas-to-liquids processing. *Stud. Surf. Sci. Catal.* **2007**, 163, 345–365.
- (184) Huber, G. W.; Cortright, R. D.; Dumesic, J. A. Renewable alkanes by aqueous-phase reforming of biomass-derived oxygenates. *Angew. Chem. Int. Ed. Engl.* **2004**, 43, 1549–1551.
- (185) Guan, G.; Kaewpanha, M.; Hao, X.; Abudula, A. Catalytic steam reforming of biomass tar. *Renew. Sust. Energ. Rev.* **2016**, 58, 450–461.
- (186) Héroguel, F.; Rozmysłowicz, B.; Luterbacher, J. S. Improving Heterogeneous Catalyst Stability for Liquid-phase Biomass Conversion and Reforming. *Chimia* **2015**, 69, 582–591.
- (187) Chareonpanich, M.; Zhang, Z.-G.; Tomita, A. Hydrocracking of Aromatic Hydrocarbons over USY-Zeolite. *Energy Fuels* **1996**, 10, 927–931.
- (188) Alvarez, F.; Giannetto, G.; Guisnet, M.; Perot, G. Hydroisomerization and hydrocracking of n-Alkanes. 2. n-Heptane transformation on a Pt-dealuminated Y zeolite - comparison with a Pt-Y zeolite. *Appl. Catal.* **1987**, 34, 353–365.
- (189) Hadjiivanov, K. I.; Vayssilov, G. N. Characterization of oxide surfaces and zeolites by carbon monoxide as an IR probe molecule. *Adv. Catal.* **2002**, 47, 307–511.
- (190) Antos, G. J.; Aitani, A. M. in *Catalytic naphtha reforming*, 2nd ed.; Chemical industries, 100, Marcel Dekker; London: Taylor & Francis: New York 2004.
- (191) Weitkamp, J. Catalytic Hydrocracking-Mechanisms and Versatility of the Process. *ChemCatChem.* **2012**, 4, 292–306.
- (192) Ribeiro, F.; Marcilly, C.; Guisnet, M. Hydroisomerization of n-Hexane on Platinum Zeolites I. Kinetic Study of the Reaction on Platinum/Y-Zeolite Catalysts: Influence of the Platinum Content. *J. Catal.* **1982**, 78, 267–274.
- (193) Chevalier F., Guisnet M., Maurel R. in *Tracer study of the isomerization of paraffins on bifunctional catalysts*, Proceedings of the Sixth International Congress on Catalysis, 1,
- (194) Deka, U.; Lezcano-Gonzalez, I.; Weckhuysen, B. M.; Beale, A. M. Local Environment and Nature of Cu Active Sites in Zeolite-Based Catalysts for the Selective Catalytic Reduction of NO<sub>x</sub>. *ACS Catal.* **2013**, 3, 413–427.

## REFERENCES

- (195) Jacobs, P. A.; Dusselier, M.; Sels, B. F. Will Zeolite-Based Catalysis be as Relevant in Future Biorefineries as in Crude Oil Refineries? *Angew. Chem. Int. Ed. Engl.* **2014**, *53*, 8621–8626.
- (196) Li, C.; Vidal-Moya, A.; Miguel, P. J.; Dedecek, J.; Boronat, M.; Corma, A. Selective Introduction of Acid Sites in Different Confined Positions in ZSM-5 and Its Catalytic Implications. *ACS Catal.* **2018**, *8*, 7688–7697.
- (197) Gallego, E. M.; Portilla, M. T.; Paris, C.; Leon-Escamilla, A.; Boronat, M.; Moliner, M.; Corma, A. "Ab initio" synthesis of zeolites for preestablished catalytic reactions. *Science* **2017**, *355*, 1051–1054.
- (198) Knott, B. C.; Nimlos, C. T.; Robichaud, D. J.; Nimlos, M. R.; Kim, S.; Gounder, R. Consideration of the Aluminum Distribution in Zeolites in Theoretical and Experimental Catalysis Research. *ACS Catal.* **2018**, *8*, 770–784.
- (199) Pinar, A. B.; Verel, R.; Pérez-Pariente, J.; van Bokhoven, J. A. Direct evidence of the effect of synthesis conditions on aluminum siting in zeolite ferrierite: A  $^{27}\text{Al}$  MQ MAS NMR study. *Micropor. Mesopor. Mat.* **2014**, *193*, 111–114.
- (200) van Bokhoven, J. A.; Koningsberger, D. C.; Kunkeler, P.; van Bekkum, H.; Kentgens, A. P. M. Stepwise Dealumination of Zeolite Beta at Specific T-Sites Observed with  $^{27}\text{Al}$  MAS and  $^{27}\text{Al}$  MQ MAS NMR. *J. Am. Chem. Soc.* **2000**, *122*, 12842–12847.
- (201) Vjunov, A.; Fulton, J. L.; Huthwelker, T.; Pin, S.; Mei, D.; Schenter, G. K.; Govind, N.; Camaioni, D. M.; Hu, J. Z.; Lercher, J. A. Quantitatively Probing the Al Distribution in Zeolites. *J. Am. Chem. Soc.* **2014**, *136*, 8296–8306.
- (202) Brus, J.; Kobera, L.; Schoefberger, W.; Urbanová, M.; Klein, P.; Sazama, P.; Tabor, E.; Sklenak, S.; Fishchuk, A. V.; Dědeček, J. Structure of Framework Aluminum Lewis Sites and Perturbed Aluminum Atoms in Zeolites as Determined by  $^{27}\text{Al}\{^1\text{H}\}$  REDOR (3Q) MAS NMR Spectroscopy and DFT/Molecular Mechanics. *Angew. Chem. Int. Ed. Engl.* **2015**, *54*, 541–545.
- (203) Sklenak, S.; Dedecek, J.; Li, C.; Wichterlová, B.; Gábová, V.; Sierka, M.; Sauer, J. Aluminum Siting in Silicon-Rich Zeolite Frameworks: A Combined High-Resolution  $^{27}\text{Al}$  NMR Spectroscopy and Quantum Mechanics / Molecular Mechanics Study of ZSM-5. *Angew. Chem. Int. Ed. Engl.* **2007**, *46*, 7286–7289.

## REFERENCES

- (204) Holzinger, J.; Beato, P.; Lundegaard, L. F.; Skibsted, J. Distribution of Aluminum over the Tetrahedral Sites in ZSM-5 Zeolites and Their Evolution after Steam Treatment. *J. Phys. Chem. C*. **2018**, 122, 15595–15613.
- (205) Perea, D. E.; Arslan, I.; Liu, J.; Ristanović, Z.; Kovarik, L.; Arey, B. W.; Lercher, J. A.; Bare, S. R.; Weckhuysen, B. M. Determining the location and nearest neighbours of aluminium in zeolites with atom probe tomography. *Nat. Commun.* **2015**, 6, 7589–7596.
- (206) van Bokhoven, J. A.; Lee, T.-L.; Drakopoulos, M.; Lamberti, C.; Thieß, S.; Zegenhagen, J. Determining the aluminium occupancy on the active T-sites in zeolites using X-ray standing waves. *Nat. Mater.* **2008**, 7, 551–555.
- (207) Agostini, G.; Lamberti, C.; Palin, L.; Milanesio, M.; Danilina, N.; Xu, B.; Janousch, M.; van Bokhoven, J. A. In Situ XAS and XRPD Parametric Rietveld Refinement To Understand Dealumination of Y Zeolite Catalyst. *J. Am. Chem. Soc.* **2010**, 132, 667–678.
- (208) Souverijns, W.; Rombouts, L.; Martens, J. A.; Jacobs, P. A. Molecular shape selectivity of EUO zeolites. *Micropor. Mat.* **1995**, 4, 123–130.
- (209) Peral, I.; Jones, C. Y.; Varkey, S. P.; Lobo, R. F. Structural comparison of two EUO-type zeolites investigated by neutron diffraction. *Micropor. Mesopor. Mat.* **2004**, 71, 125–133.
- (210) Gutierrez-Acebo, E.; Leroux, C.; Chizallet, C.; Schuurman, Y.; Bouchy, C. Metal/Acid Bifunctional Catalysis and Intimacy Criterion for Ethylcyclohexane Hydroconversion. *ACS Catal.* **2018**, 8, 6035–6046.
- (211) Rigby, A. M.; Kramer, G. J.; van Santen, R. A. Mechanisms of Hydrocarbon Conversion in Zeolites: A Quantum Mechanical Study. *J. Catal.* **1997**, 170, 1–10.
- (212) Rey, J.; Raybaud, P.; Chizallet, C. Ab Initio Simulation of the Acid Sites at the External Surface of Zeolite Beta. *ChemCatChem*. **2017**, 9, 2176–2185.
- (213) Gleaves, J. T.; Yablonskii, G. S.; Phanawadee, P.; Schuurman, Y. TAP-2: An interrogative kinetics approach. *Appl. Catal., A*. **1997**, 160, 55–88.
- (214) Kresse, G.; Hafner, J. Ab initio molecular-dynamics simulation of the liquid-metal–amorphous-semiconductor transition in germanium. *Phys. Rev. B*. **1994**, 49, 14251–14269.
- (215) Kresse, G.; Joubert, D. From ultrasoft pseudopotentials to the projector augmented-wave method. *Phys. Rev. B*. **1999**, 59, 1758–1775.

## REFERENCES

- (216) Martins, J.; Birot, E.; Guillon, E.; Lemos, F.; Ramôa Ribeiro, F.; Magnoux, P.; Laforge, S. Sodium exchange over H-EU-1 zeolite. Part I: Physicochemical characterization. *Micropor. Mesopor. Mat.* **2013**, 171, 230–237.
- (217) Pulay, P. Convergence Acceleration of Iterative Sequences. The Case of SCF Iteration. *Chem. Phys. Lett.* **1980**, 73, 393–398.
- (218) Bučko, T.; Benco, L.; Hafner, J.; Ángyán, J. G. Monomolecular cracking of propane over acidic chabazite. *J. Catal.* **2011**, 279, 220–228.
- (219) Fukui, K. The Path of Chemical Reactions - The IRC Approach. *Acc. Chem. Res.* **1981**, 14, 363–368.
- (220) Coutanceau, C.; Da Silva, J. M.; Alvarez, M. F.; Ribeiro, F. R.; Guisnet, M. Dealumination of zeolites. Part VII. Influence of the acid treatment of a HBEA zeolite on the framework composition and on the porosity. *J. Chim. Phys.* **1997**, 94, 765–781.
- (221) Jentoft, F. C.; Gates B.C. Solid-acid-catalyzed alkane cracking mechanisms: evidence from reactions of small probe molecules. *Top. Catal.* **1997**, 4, 1–13.
- (222) Pines, H.; Hoffman, N. E. in *Isomerization of saturated Hydrocarbons*, 2; Olah, G. A. Ed.; 1964.
- (223) Rey, J. Identification of acid sites sensitive descriptors for the kinetic modeling of cracking and isomerization in aluminosilicates in presence of inhibitors Mid-thesis report. Theoretical chemistry, IFPEN, 2018.
- (224) Casci, J.L., Cox, P.A., Shannon, M.D. in *The preparation, characterization and properties of zeolite NU-86*; Ballmoos, R. v., Higgins, J. B., Treacy, M. M. J., Eds.; Butterworth-Heinemann: Boston 1992, 514–520.
- (225) Marques Mota, F. Synergetic and antagonistic effects in hydroconversion catalysts composed of mixtures of solid acids, Leuven University, 2013.
- (226) Benazzi, E.; Leite, L.; Marchal-George, N.; Toulhoat, H.; Raybaud, P. New insights into parameters controlling the selectivity in hydrocracking reactions. *J. Catal.* **2003**, 217, 376–387.
- (227) Benazzi, E.; Leite, L.; Marchal-George, N.; Toulhoat, H.; Raybaud, P. New insights into parameters controlling the selectivity in hydrocracking reactions. *J. Catal.* **2003**, 217, 376–387.

## REFERENCES

- (228) Biaglow, A. I.; Parrillo, D. J.; Kokotailo, G. T.; Gorte, R. J. A Study of Dealuminated Faujasites. *J. Catal.* **1994**, 148, 213–223.
- (229) Derouane, E. G.; André, J. M.; Lucas, A. A. Surface curvature effects in physisorption and catalysis by microporous solids and molecular sieves. *J. Catal.* **1988**, 110, 58–73.
- (230) Cnudde, P.; Wispelaere, K. de; Vanduyfhuys, L.; Demuynck, R.; van der Mynsbrugge, J.; Waroquier, M.; van Speybroeck, V. How chain length and branching influence the alkene cracking reactivity on H-ZSM-5. *ACS Catal.* **2018**, Just Accepted Manuscript.
- (231) Trombetta, M.; Armaroli, T.; Gutiérrez Alejandro, A.; Ramirez Solis, J.; Busca, G. An FT-IR study of the internal and external surfaces of HZSM5 zeolite. *Appl. Catal., A* **2000**, 192, 125–136.
- (232) Trombetta, M.; Busca, G.; Rossini, S. A.; Piccoli, V.; Cornaro, U. FT-IR Studies on Light Olefin Skeletal Isomerization Catalysis. *J. Catal.* **1998**, 179, 581–596.
- (233) Pieterse, J. A.; Veeffkind-Reyes, S.; Seshan, K.; Domokos, L.; Lercher, J. A. On the Accessibility of Acid Sites in Ferrierite for Pyridine. *J. Catal.* **1999**, 187, 518–520.
- (234) Bucko, T.; Benco, L.; Demuth, T.; Hafner, J. Ab initio density functional investigation of the (001) surface of mordenite. *The Journal of chemical physics* **2002**, 117, 7295–7305.
- (235) Bučko, T.; Benco, L.; Hafner, J. Defect sites at the (001) surface of mordenite. *The Journal of chemical physics* **2003**, 118, 8437–8445.
- (236) Hernandez-Tamargo, C. E.; Roldan, A.; Leeuw, N. H. de. A density functional theory study of the structure of pure-silica and aluminium-substituted MFI nanosheets. *J. Solid State Chem.* **2016**, 237, 192–203.
- (237) Kunkeler, P. J.; Moeskops, D.; van Bekkum, H. Zeolite Beta: characterization and passivation of the external surface acidity. *Micropor. Mat.* **1997**, 11, 313–323.
- (238) Čejka, J.; Richter, M.; Kölsch, P. in *Characterization of external surface properties of zeolite ZSM-5 modified by 12-tungstosilicic acid* vol. 94; Studies in Surface Science and Catalysis; Beyer, H. K., Ed.; Elsevier: Amsterdam 1995, 246–253.
- (239) Bauer, F.; Chen, W.-H.; Ernst, H.; Huang, S.-J.; Freyer, A.; Liu, S.-B. Selectivity improvement in xylene isomerization. *Micropor. Mesopor. Mat.* **2004**, 72, 81–89.



## REFERENCES

- (240) Bai, P.; Jeon, M. Y.; Ren, L.; Knight, C.; Deem, M. W.; Tsapatsis, M.; Siepmann, J. I. Discovery of optimal zeolites for challenging separations and chemical transformations using predictive materials modeling. *Nat. Commun.* **2015**, 6, 5912–5921.
- (241) Siahrostami, S.; Falsig, H.; Beato, P.; Moses, P. G.; Nørskov, J. K.; Studt, F. Exploring Scaling Relations for Chemisorption Energies on Transition-Metal-Exchanged Zeolites ZSM-22 and ZSM-5. *ChemCatChem*. **2016**, 8, 767–772.
- (242) Frenkel, D.; Smit, B. in *Understanding Molecular Simulation: From Algorithms to Applications*; Computational science series, Academic Press 2002.
- (243) Schuurman, Y. Assessment of kinetic modeling procedures of TAP experiments. *Catal. Today* **2007**, 121, 187–196.
- (244) Keipert, O. P.; Baerns, M. Determination of the intracrystalline diffusion coefficients of alkanes in H-ZSM-5 zeolite by a transient technique using the temporal-analysis-of-products (TAP) reactor. *Chem. Eng. Sci.* **1998**, 53, 3623–3634.
- (245) Schuurman, Y.; Pantazidis, A.; Mirodatos, C. The TAP-2 reactor as an alternative tool for investigating FCC catalysts. *Chem. Eng. Sci.* **1999**, 54, 3619–3625.
- (246) Schuurman, Y.; Delattre, C.; Pitault, I.; Reymond, J. P.; Forissier, M. Effect of coke deposition on transport and sorption in FCC catalysts studied by temporal analysis of products. *Chem. Eng. Sci.* **2005**, 60, 1007–1017.
- (247) Nayak, S. V.; Ramachandran, P. A.; Dudukovic, M. P. TAP Study of Adsorption and Diffusion of 2,2,4-Trimethylpentane and 2,5-Dimethylhexane on  $\beta$  and USY Zeolites. *Ind. Eng. Chem. Res.* **2011**, 51, 1570–1578.
- (248) Denayer, J. F.; Baron, G. V.; Vanbutsele, G.; Jacobs, P. A.; Martens, J. A., Evidence for Alkylcarbenium Ion Reaction Intermediates from Intrinsic Reaction Kinetics of C<sub>6</sub>–C<sub>9</sub>n-Alkane Hydroisomerization and Hydrocracking on Pt/H–Y and Pt/USY Zeolites, *J. Catal.* **2000**, 190, 469-473.
- (249) Thybaut, J.; Narasimhan, C. S. L.; Marin, G.; Denayer, J. M.; Baron, G.; Jacobs, P.; Martens, J., Alkylcarbenium Ion Concentrations in Zeolite Pores During Octane Hydrocracking on Pt/H-USY Zeolite, *Catal. Lett.* **2004**, 94, 81-88.
- (250) Huang, B.; Bai, P.; Neurock, M.; Davis, R. J., Conversion of n-Hexane and n-Dodecane over H-ZSM-5, H-Y and Al-MCM-41 at Supercritical Conditions, *Appl. Catal. A* **2017**, 546, 149-158.



## REFERENCES

- (251) McCann, D. M.; Lesthaeghe, D.; Kletnieks, P. W.; Guenther, D. R.; Hayman, M. J.; Van Speybroeck, V.; Waroquier, M.; Haw, J. F., A Complete Catalytic Cycle for Supramolecular Methanol-to-Olefins Conversion by Linking Theory with Experiment, *Angew. Chem., Int. Ed.* **2008**, *47*, 5179.
- (252) Van Speybroeck, V.; De Wispelaere, K.; Van der Mynsbrugge, J.; Vandichel, M.; Hemelsoet, K.; Waroquier, M., First principle chemical kinetics in zeolites: the methanol-to-olefin process as a case study, *Chem. Soc. Rev.* **2014**, *43*, 7326-7357.
- (253) Wang, C.-M.; Wang, Y.-D.; Liu, H.-X.; Xie, Z.-K.; Liu, Z.-P., Theoretical Insight into the Minor Role of Paring Mechanism in the Methanol-to-Olefins Conversion within HSAPO-34 Catalyst, *Microporous Mesoporous Mater.* **2012**, *158*, 264-271.
- (254) Sun, Y.; Zheng, D.; Pei, S.; Fan, D., New Theoretical Insights into the Contributions of Poly(methylbenzene) and Alkene Cycles to the Methanol to Propene Process in H-FAU Zeolite, *J. Phys. Chem. C* **2017**, *121*, 16216-16237.
- (255) Wang, S.; Chen, Y.; Wei, Z.; Qin, Z.; Ma, H.; Dong, M.; Li, J.; Fan, W.; Wang, J., Polymethylbenzene or Alkene Cycle? Theoretical Study on Their Contribution to the Process of Methanol to Olefins over H-ZSM-5 Zeolite, *J. Phys. Chem. C* **2015**, *119*, 28482-28498.
- (256) Mansoor, E.; Van der Mynsbrugge, J.; Head-Gordon, M.; Bell, A. T., Impact of Long-Range Electrostatic and Dispersive Interactions on Theoretical Predictions of Adsorption and Catalysis in Zeolites, *Catal. Today* **2018**, *312*, 51-65.
- (257) Fang, H.; Zheng, A.; Xu, J.; Li, S.; Chu, Y.; Chen, L.; Deng, F., Theoretical Investigation of the Effects of the Zeolite Framework on the Stability of Carbenium Ions, *J. Phys. Chem. C* **2011**, *115*, 7429-7439.
- (258) Song, B.; Chu, Y.; Li, G.; Wang, J.; Lo, A.-Y.; Zheng, A.; Deng, F., Origin of Zeolite Confinement Revisited by Energy Decomposition Analysis, *J. Phys. Chem. C* **2016**, *120*, 27349-27363.
- (259) De Moor, B. A.; Reyniers, M.-F. o.; Sierka, M.; Sauer, J.; Marin, G. B., Physisorption and Chemisorption of Hydrocarbons in H-FAU Using QM-Pot(MP2//B3LYP) Calculations, *J. Phys. Chem. C* **2008**, *112*, 11796-11812.

## REFERENCES

## **APPENDIX**

<b>APPENDIX</b>	<b>i</b>
<b>APPENDIX I</b>	<b>i</b>
<b><u>I.I. TEMPERATURE PROFILES FOR CALCINATION</u></b>	i
<b><u>I.II. LOSS ON IGNITION</u></b>	iv
<b><u>I.III. WATER UPTAKE VOLUME (WUV)</u></b>	iv
<b>APPENDIX II</b>	<b>vi</b>
<b><u>II.I. DIFFERENT TYPES OF ISOTHERMS</u></b>	vi
<b><u>II.II. H<sub>2</sub>/O<sub>2</sub> DOUBLE TITRATION PRODEDURE</u></b>	vii
<b>APPENDIX III</b>	<b>viii</b>
<b>APPENDIX IV</b>	<b>xxi</b>
<b>APPENDIX V</b>	<b>xliii</b>
<b><u>V.I. GENERAL FEATURES</u></b>	xliii
<b><u>V.II. HYDRIDE- AND METHYL- SHIFT</u></b>	xliv
<b><u>V.III. DFT STUDY</u></b>	xlvii
<b>APPENDIX VI</b>	<b>lxi</b>
<b><u>VI.I CHARACTERIZATION</u></b>	lxi
<b><u>VI.II CATALYTIC TESTS</u></b>	lxiii
<b><u>VI.III PROII RESULTS</u></b>	lxxxi
<b><u>VI.IV PRODUCTS DISTRIBUTION</u></b>	lxxxii
<b><u>VI.I ZEOLITES STRUCTURES BY MATERIALS STUDIO</u></b>	lxxxvii
<b>REFERENCES</b>	<b>xcviii</b>

## APPENDIX

---

### APPENDIX I

#### I.I. TEMPERATURE PROFILES FOR CALCINATION

The zeolites that still have the template have been calcined according to different protocols depicted in figures 1, 4,5 and 6. After ionic exchange, zeolites have been calcined according to protocol depicted in figure 2.

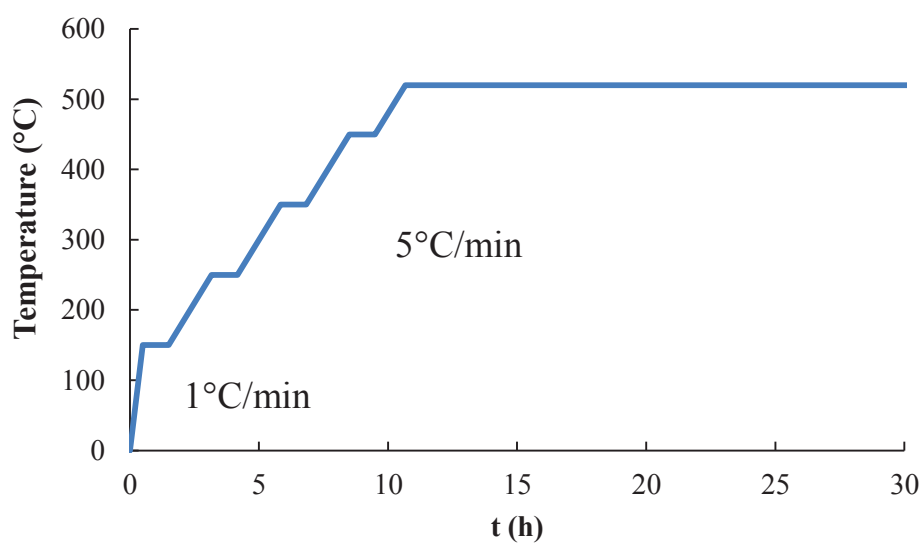


Figure 1. Temperature profile for EU-1 calcination.

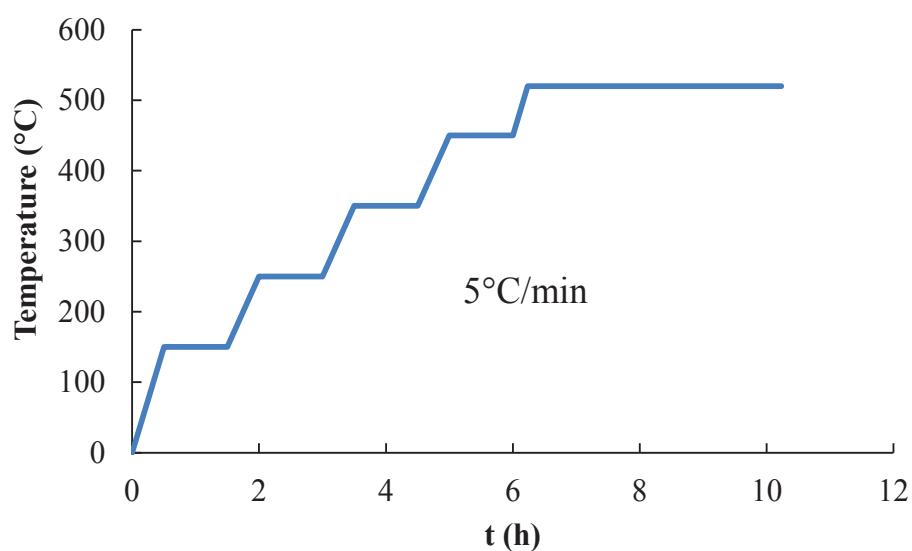


Figure 2. Temperature calcination profile for all the zeolites after ionic exchange.

## APPENDIX

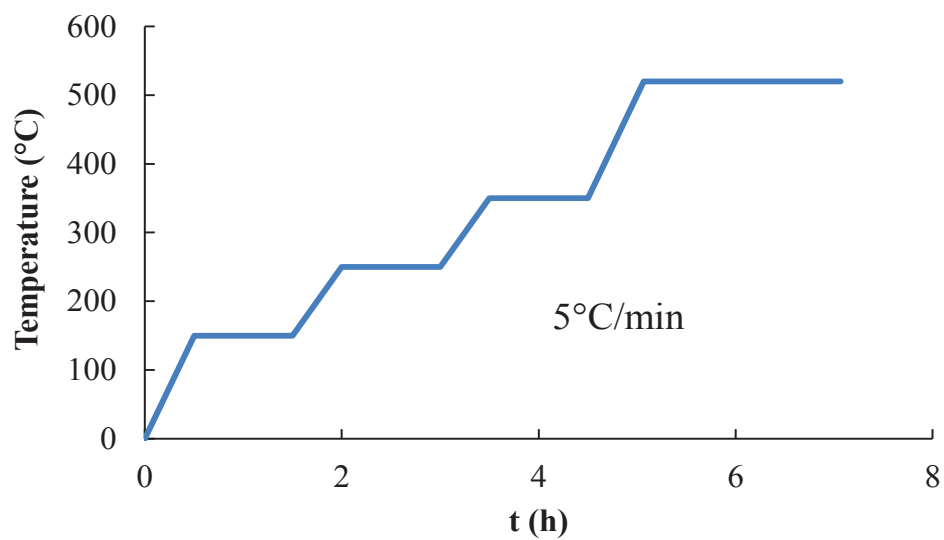


Figure 3. Temperature profile for Pt-EU-1 calcination.

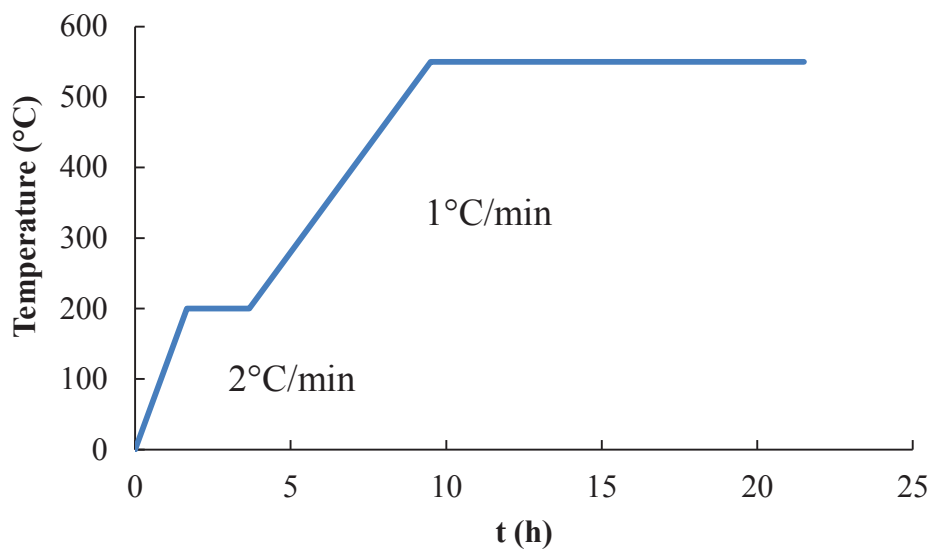
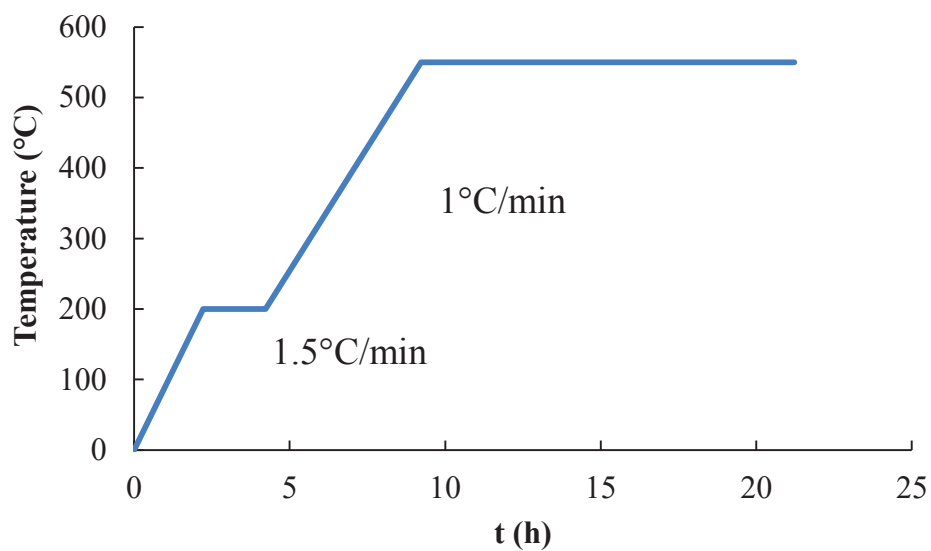
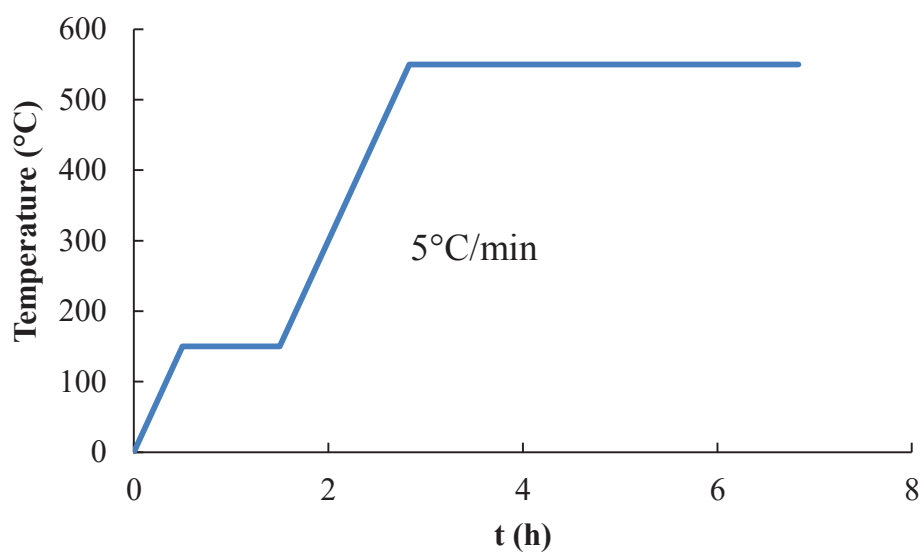


Figure 4. Temperature profile for NU-86 and IZM-2\_80 calcination.

## APPENDIX



**Figure 5. Temperature profile for ZSM-57 and ZSM-50 calcination.**



**Figure 6. Temperature profile for BETA calcination.**

## APPENDIX

### I.II. LOSS ON IGNITION

The loss on ignition is performed as follows:

A vide recipient is weighed and the mass noted as  $m_e$  (empty mass), afterwards the solid is added in the same recipient and the mass is noted as well but this time as  $m_{fh}$  (full humid mass)

Note that the difference between  $m_f$  and  $m_e$  is the humid mass ( $m_h$ ). Later the recipient is introduced into the muffle furnace where the temperature will be increased until 500°C with a temperature ramp of 10°C/min and once that this temperature is reached is kept for 2 hours and after descended to 150°C.

When the ramp is finished (at 150°C), the recipient is taken out from the muffle and weighed again. The mass is noted as  $m_{fd}$  (full dry mass). The dry mass ( $m_d$ ) is defined as the difference between  $m_{fd}$  and  $m_e$ .

Finally the LOI is calculated as shown in Eq.1

$$LOI(\%) = \frac{m_h - m_d}{m_h} \cdot 100 \quad \text{Eq. 1}$$

### I.III. WATER UPTAKE VOLUME (WUV)

This technique will give the volume of a liquid solution needed for the preparation of impregnation solutions in incipient wetness impregnation either if they have been or not matured.

Multiplied for the mass of the solid the WUV will give us the real volume of liquid solution to impregnate over the solid partially humid or not in the way to fulfill the total porous volume of our support. This volume of solution help to dissolve the desired metal salt to impregnate

In order to carry out this analysis a known mass ( $m_s$ ) is deposited inside a rotatory vessel and water is added with a graduated burette dropwise over the solid whereas is also mixed manually with the help of a spatula. When the solid starts to get stuck to the walls of the vessel and the color is homogeneous the dropwise is stopped and the water volume employed is noted as  $V_w$



## APPENDIX

The WUV (cm<sup>3</sup>/g) is calculated as illustrated in Eq.2.

$$WUV = \frac{V_w}{m_s} \quad \text{Eq. 2}$$

## APPENDIX II

## II.I. DIFFERENT TYPES OF ISOTHERMS

- **Isotherm I** is characteristic of microporous materials with low external surface area.
- **Isotherm II** can be observed with macroporous or non-porous solids. B point represents the moment when the monolayer is complete and starts the adsorption in the multilayer.
- **Isotherm III** doesn't have any B point. It is a rare case in which the adsorbate-adsorbate interactions are stronger than adsorbate-solid interactions.
- **Isotherm IV** shows hysteresis related to the capillary condensation in the mesoporous materials at high relative pressures.
- **Isotherm V** is not really common. It is related to the Isotherm 3 in which the adsorbate-solid interaction is weak; mixed with the presence of mesoporous.
- **Isotherm VI** represents different adsorption steps on multilayer in a uniform non-porous area.

Figure 7 includes the different isotherms explained before.

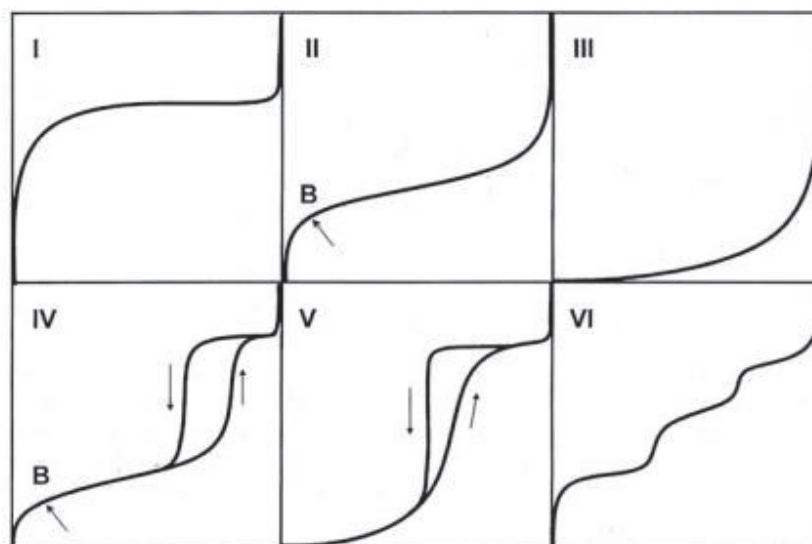


Figure 7. Types of isotherms classified by IUPAC.<sup>136</sup>

According to t-plot the external surface and the microporous volume are calculated according to Eq. 3 and Eq. 4.

## APPENDIX

$$S_{\text{ext}} = (S \cdot 10^{10} \cdot D) / (F \cdot 10^6) \quad \text{Eq. 3}$$

$$V_{\mu} = Y_{\text{int}} \cdot D \quad \text{Eq. 4}$$

**D** density conversion factor = 0.0015468 in our conditions it corresponds to the index to transform mL of gas in mL of liquid, **F** surface area correction factor = 1 in our conditions, **S** slope of the line (g/cm<sup>3</sup>/Å) determined during the calculation of the microporous surface, **10<sup>10</sup>** conversion factor to transform Å into m, **10<sup>6</sup>** conversion factor to transform cm<sup>3</sup> into m<sup>3</sup>, **S<sub>ext</sub>** in m<sup>2</sup>/g, **Y<sub>int</sub>** = Y axis value at the origin determined when calculating the microporous surface (mL/g), **V<sub>μ</sub>** = microporous volume (mL/g)

### II.II. H<sub>2</sub>/O<sub>2</sub> DOUBLE TITRATION PRODEDURE

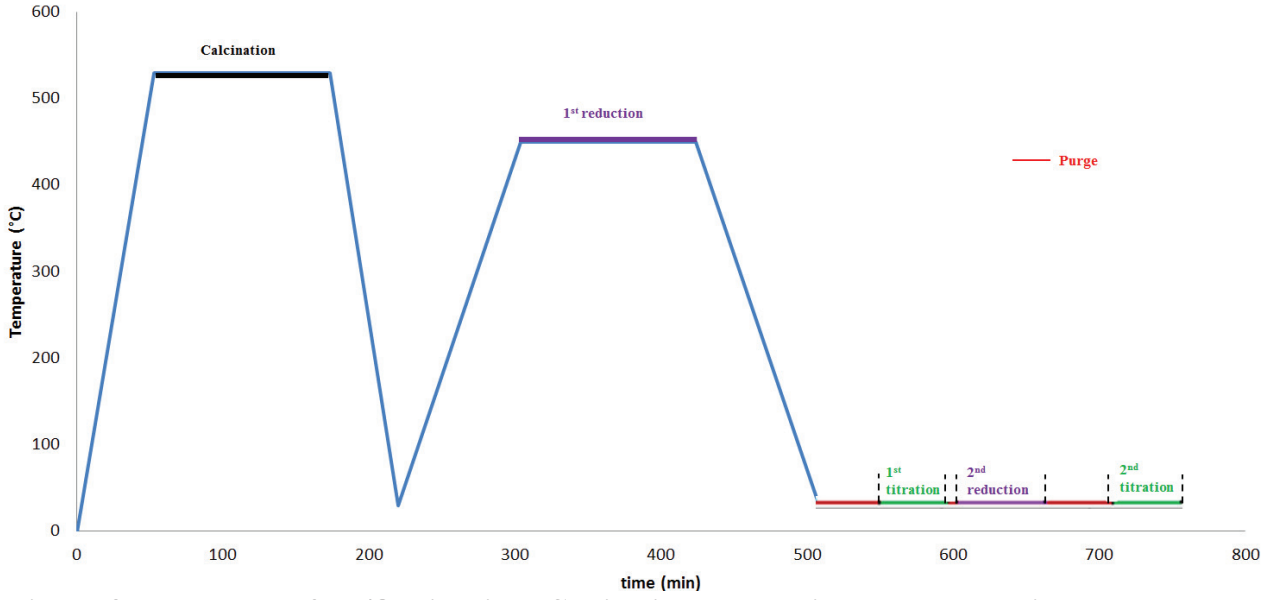


**Figure 8. Procedure of H<sub>2</sub>/O<sub>2</sub> titration. Calcination under air and purges with He at room temperature. The first reduction with H<sub>2</sub> was done with a flow of 20 NmL min<sup>-1</sup>. Afterwards a first oxygen titration is done followed of a second H<sub>2</sub> titration.**

APPENDIX III

**Supporting information**

***Metal/acid bifunctional catalysis and intimacy criterion for ethylcyclohexane hydroconversion: when proximity does not matter***

*Ester Gutierrez-Acebo,<sup>1</sup> Charles Leroux,<sup>1</sup> Céline Chizallet,<sup>1</sup> Yves Schuurman,<sup>2</sup> Christophe Bouchy<sup>1,\*</sup>*

<sup>1</sup>IFP Energies nouvelles, Rond-point de l'échangeur de Solaize, BP 3, Solaize, 69360, France

<sup>2</sup> IRCELYON, Institut de recherches sur la catalyse et l'environnement de Lyon, CNRS, UMR 5256, Université Lyon 1, 2 avenue Albert Einstein, F-69626 Villeurbanne, France

\*Corresponding author: christophe.bouchy@ifpen.fr

**Table S1. List of products of ECH hydroconversion.**

# APPENDIX

Reaction	Product Family	Products
Isomerization	TMCP	1,1,3-trimethylcyclopentane
		1-trans-2-cis-4-trimethylcyclopentane
		1-cis-2-cis-4-trimethylcyclopentane *a
		1,trans-2-cis-3-trimethylcyclopentane
		1,1,2-trimethylcyclopentane
	DMCH	1,trans-4-dimethylcyclohexane
		1,cis-3-dimethylcyclohexane *
		1,trans-2-dimethylcyclohexane
		1,cis-4-dimethylcyclohexane
		1,1-dimethylcyclohexane
		1 ,cis-2-dimethylcyclohexane
	EMCP	1-methyl-trans-3-ethylcyclopentane
		1-methyl-cis-3-ethylcyclopentane
		1-methyl-trans-2-ethylcyclopentane
		1-methyl-cis-2-ethylcyclopentane
		1-ethyl-1-methylcyclopentane
	PCP	isocyclopentane
		n-propyl-cyclopentane *b
	MCHP	methylcycloheptane
Ring opening	P8	2-methylheptane
		4-methylheptane
		2,3-dimethylhexane
		2,4-dimethylhexane
		2,5-dimethylhexane*
		n-Octane
		3,4-dimethylhexane
Cracking	C1	ethane

# APPENDIX

	C2	methane
	C3	propane
	C4	n-butane
		isobutane
	C5	n-pentane
		isopentane
		cyclopentane
	C6	methylcyclopentane
		2-methylpentane
		3-methylpentane
		cyclohexane
		n-hexane
	C7	1,1-dimethylcyclopentane
		1,cis-3-dimethylcyclopentane
		1,trans-3-dimethylcyclopentane
		2-methylhexane
		3-methylhexane
		3-methylpentane
		ethylcyclohexane
		n-heptane
Dehydrogenation	A8	ethylbenzene
		m-xylene
		p-xylene
		o-xylene

\* In coelution with low amounts of paraffin C<sub>8</sub>

\*a In coelution with low amounts of 3-methylheptane

\*b In coelution with the ECH. Compound in negligible amount.

## APPENDIX

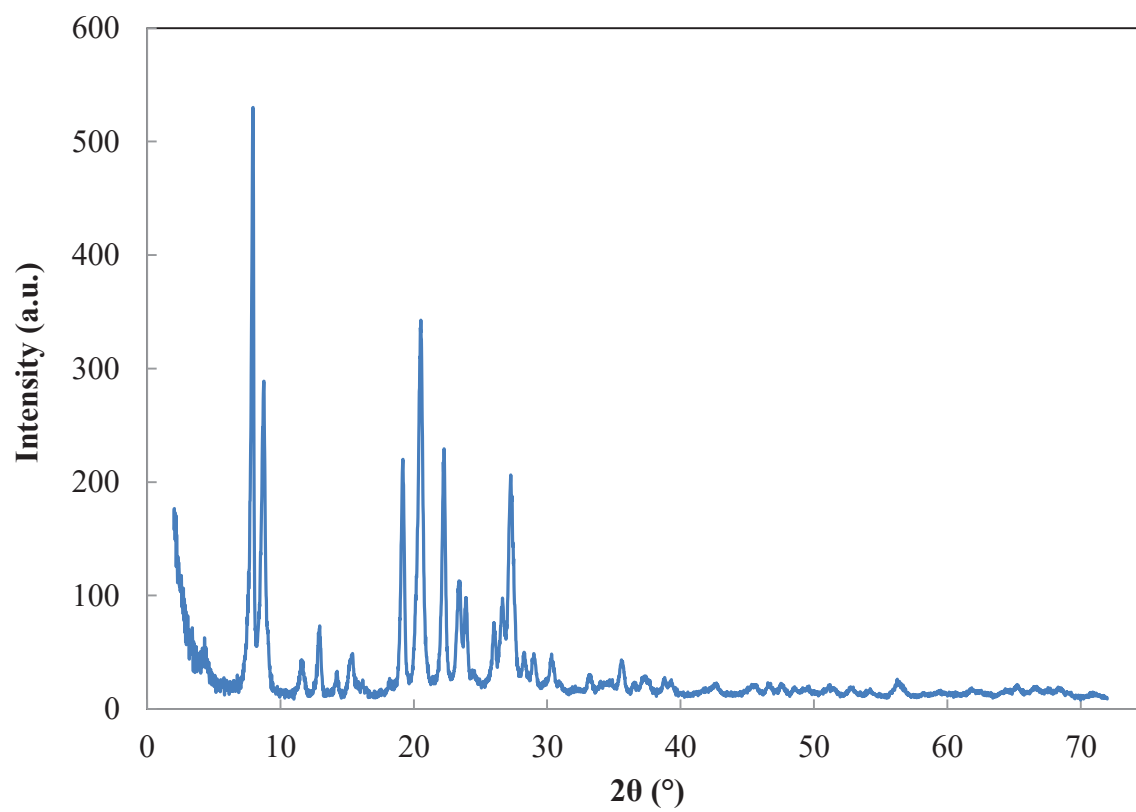


**Figure S1. XRD diffractogram for HEU-1**

## APPENDIX

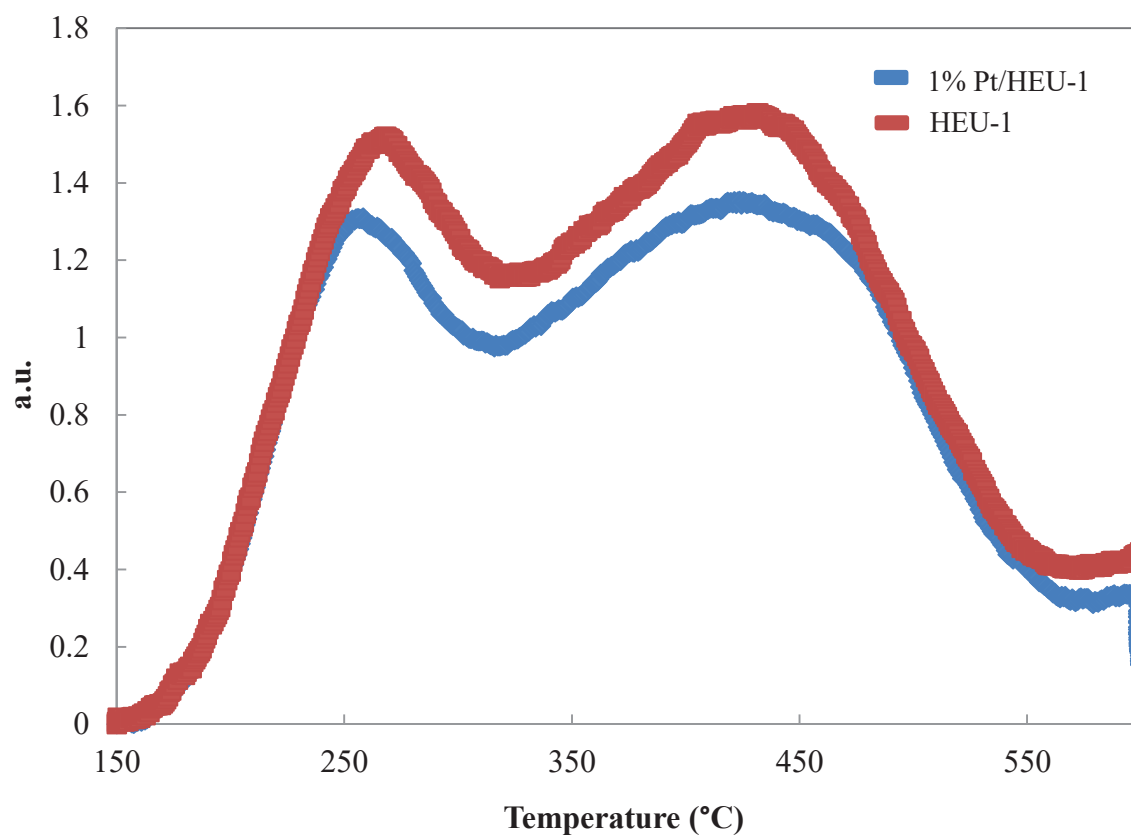


**Figure S2. NH<sub>3</sub>-TPD profiles for the parent HEU-1 zeolite and the zeolite impregnated with platinum (1% Pt-HEU-1/Al<sub>2</sub>O<sub>3</sub>)**



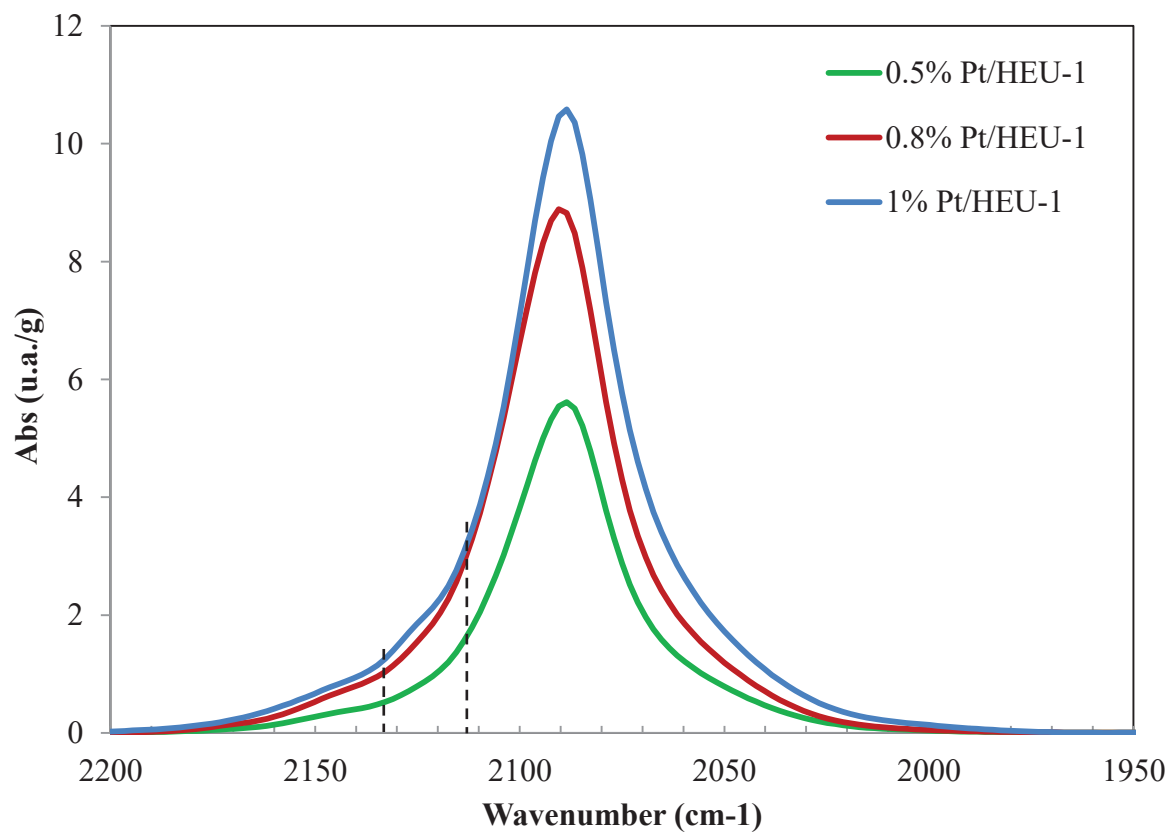


**Figure S3.** IR spectra at CO saturation plus desorption at 25°C in the CO region (2300-1900)-common scale for the Pt-HEU-1/Al<sub>2</sub>O<sub>3</sub> samples.

## APPENDIX

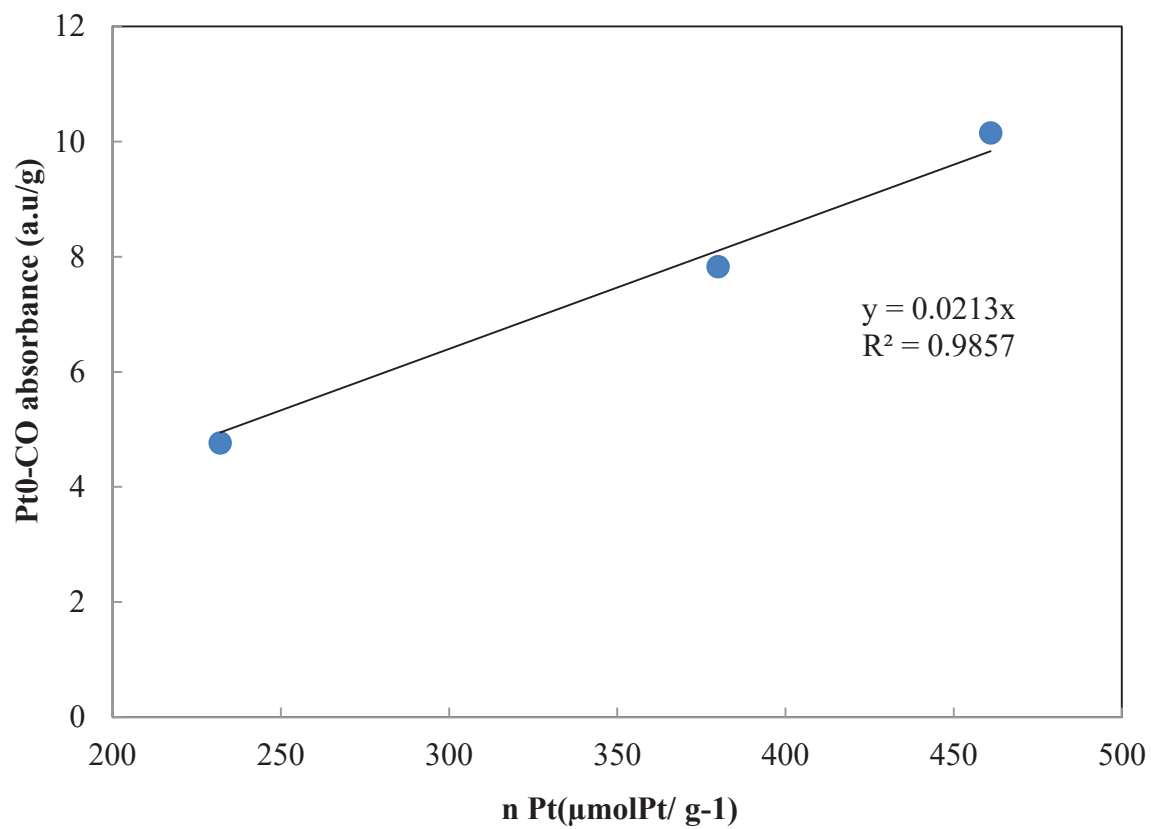
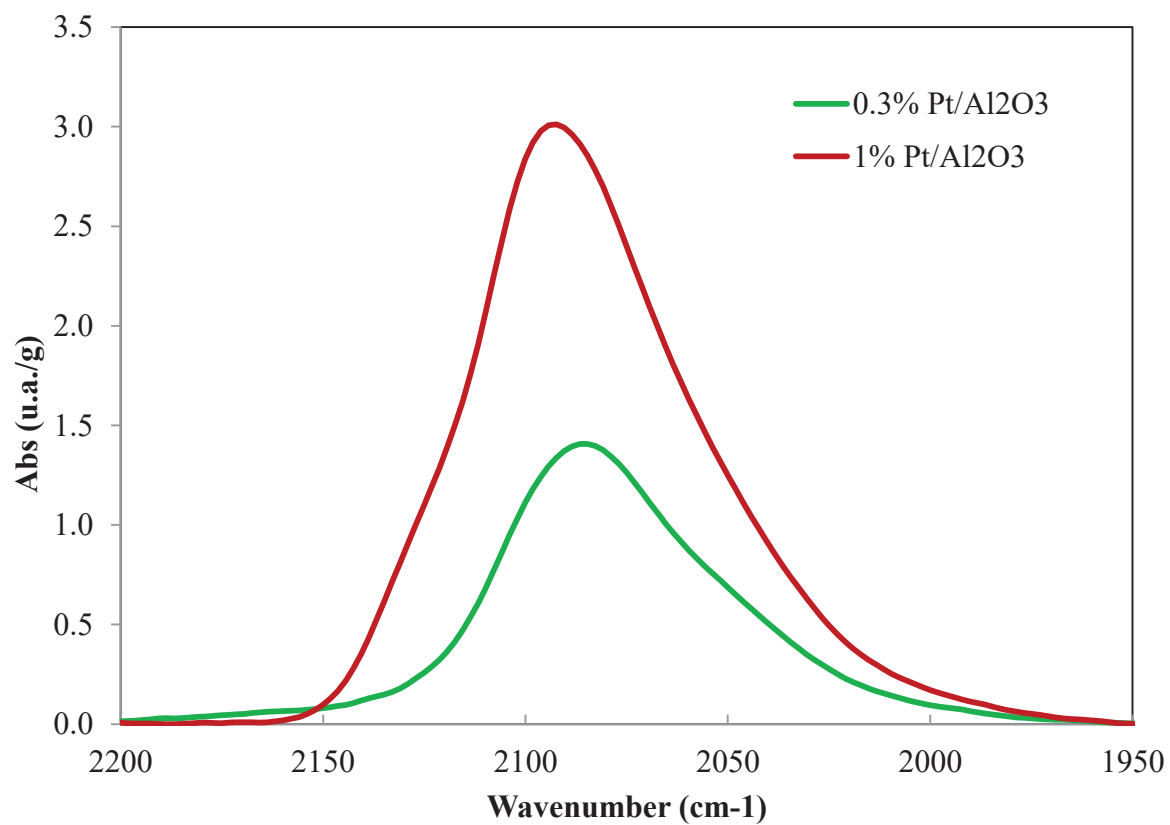


Figure S4. Amount of micromoles of platinum plotted as a function of the peak area of CO at  $2090\text{ cm}^{-1}$  from  $\text{Pt}^0\text{-CO}$  species for HEU-1 impregnated samples

## APPENDIX



**Figure S5.** IR spectra at CO saturation plus desorption at 25°C in the CO region (2300-1900)-common scale for the Pt-Al<sub>2</sub>O<sub>3</sub>/ HEU-1 samples.

# APPENDIX

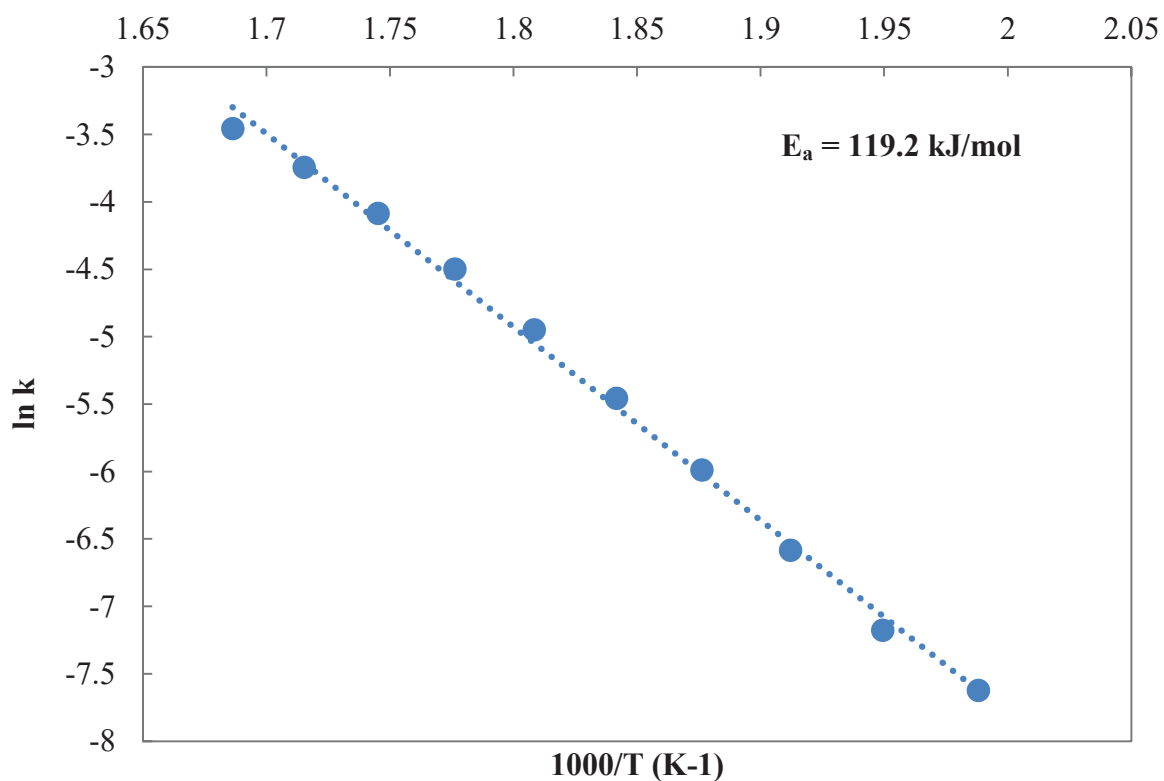


Figure S6. Arrhenius plot for 1 %Pt-HEU-1/Al<sub>2</sub>O<sub>3</sub>. The rate constant  $k$  [m<sup>3</sup>mol<sup>-1</sup>s<sup>-1</sup>] is on a concentration basis and calculated from the integral expression for a first order reaction in a fixed-bed reactor. The corresponding pre-exponential factor,  $A^0$ , is equal to  $1.2 \cdot 10^9$  [m<sup>3</sup>mol<sup>-1</sup>s<sup>-1</sup>].

# APPENDIX

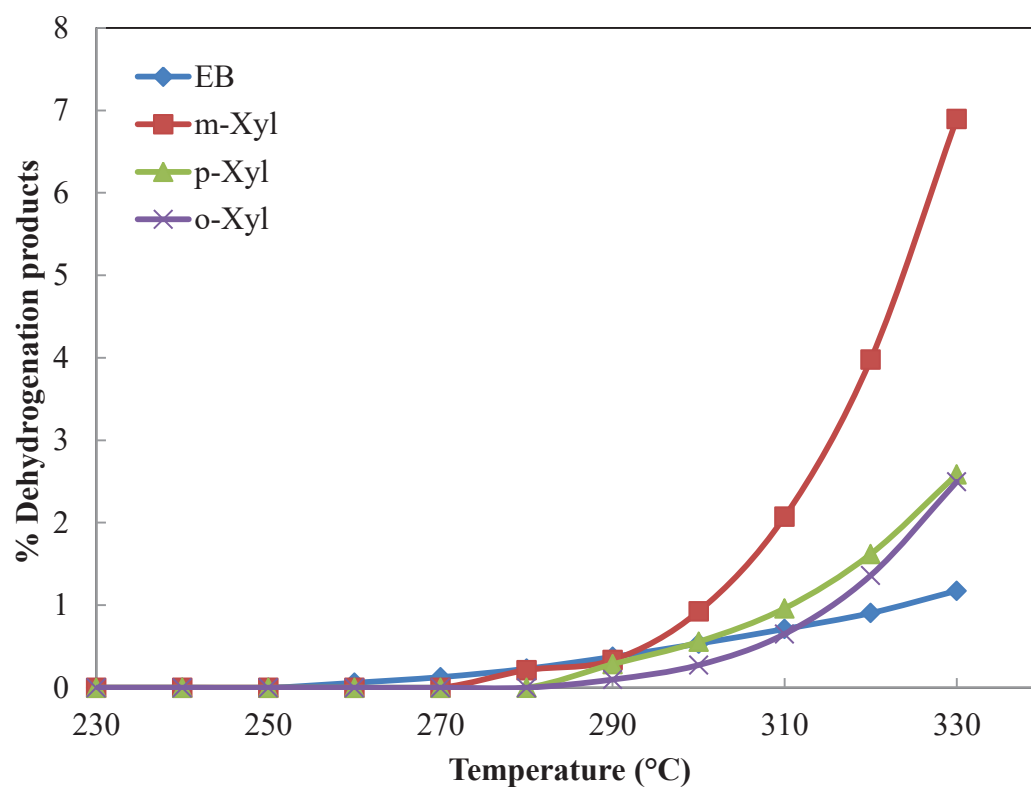
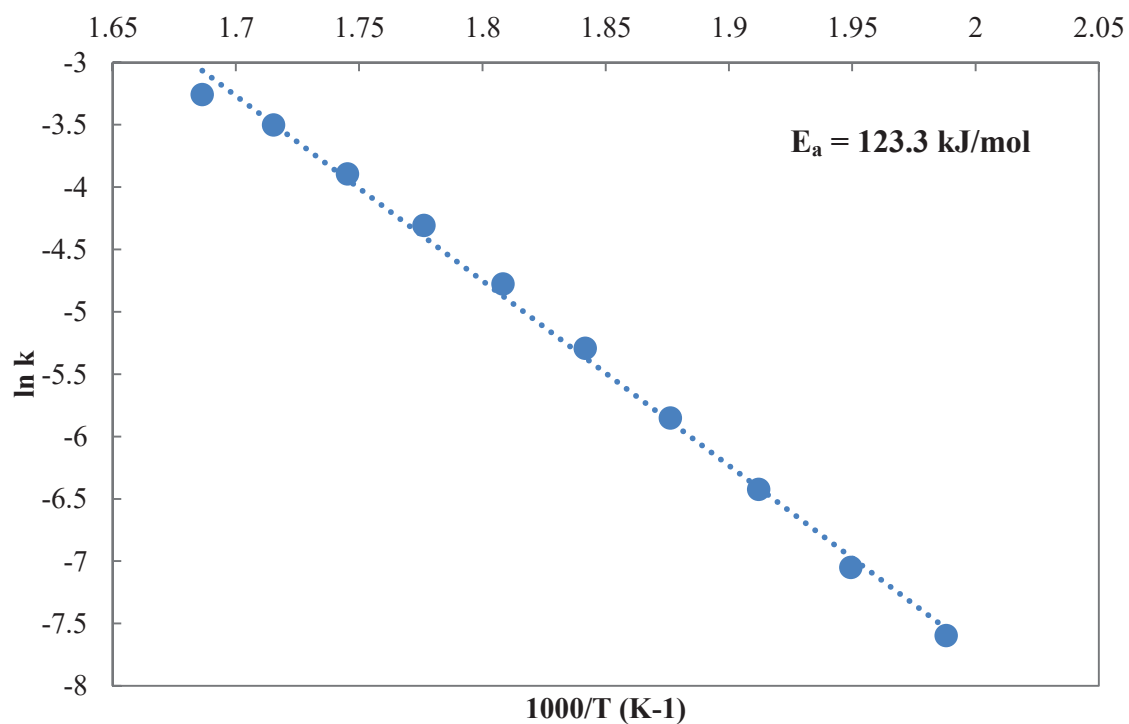


Figure S7. Evolution of different dehydrogenation products for the 1% Pt-HEU-1/Al<sub>2</sub>O<sub>3</sub> catalyst.

# APPENDIX



**Figure S8.** Arrhenius plot for 1% Pt-Al<sub>2</sub>O<sub>3</sub>/HEU-1. The rate constant  $k \text{ [m}^3\text{mol}^{-1}\text{s}^{-1}\text{]}$  is on a concentration basis and calculated from the integral expression for a first order reaction in a fixed-bed reactor. The corresponding pre-exponential factor,  $A^0$ , is equal to  $3.4 \cdot 10^9 \text{ [m}^3\text{mol}^{-1}\text{s}^{-1}\text{]}$ .

## APPENDIX

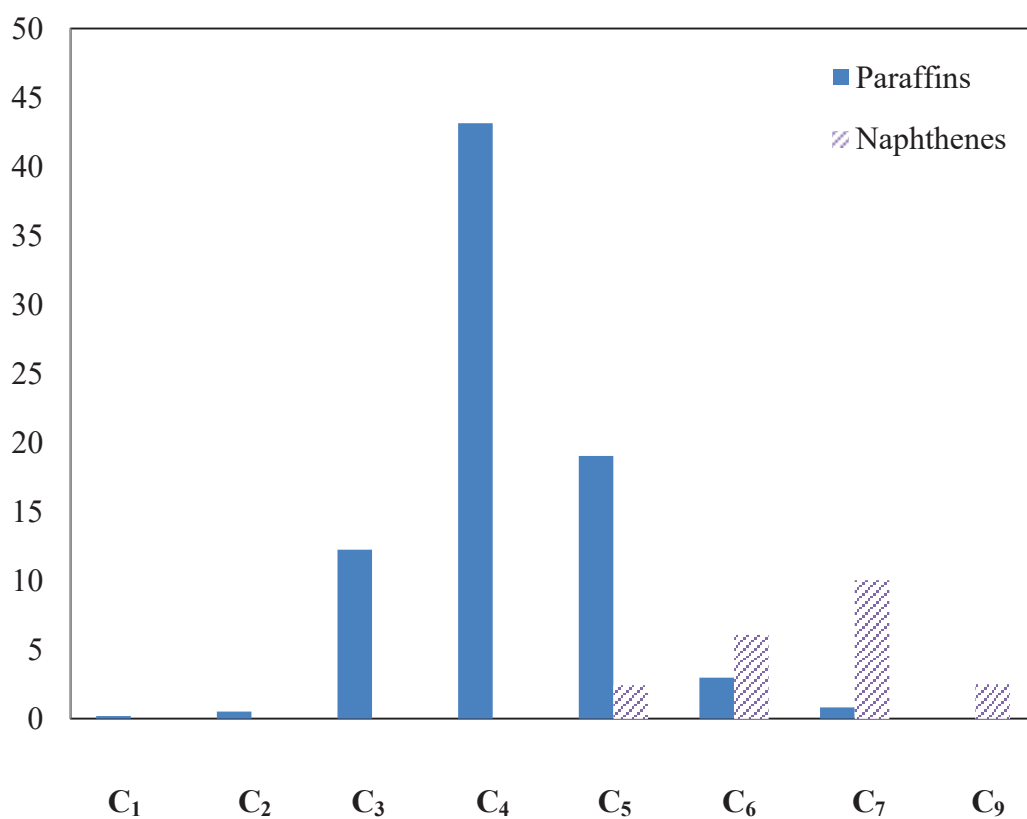


**Figure S9.** Cracking product distribution at 300°C for the reference catalyst 1% Pt-Al<sub>2</sub>O<sub>3</sub>/HEU-1.

# APPENDIX

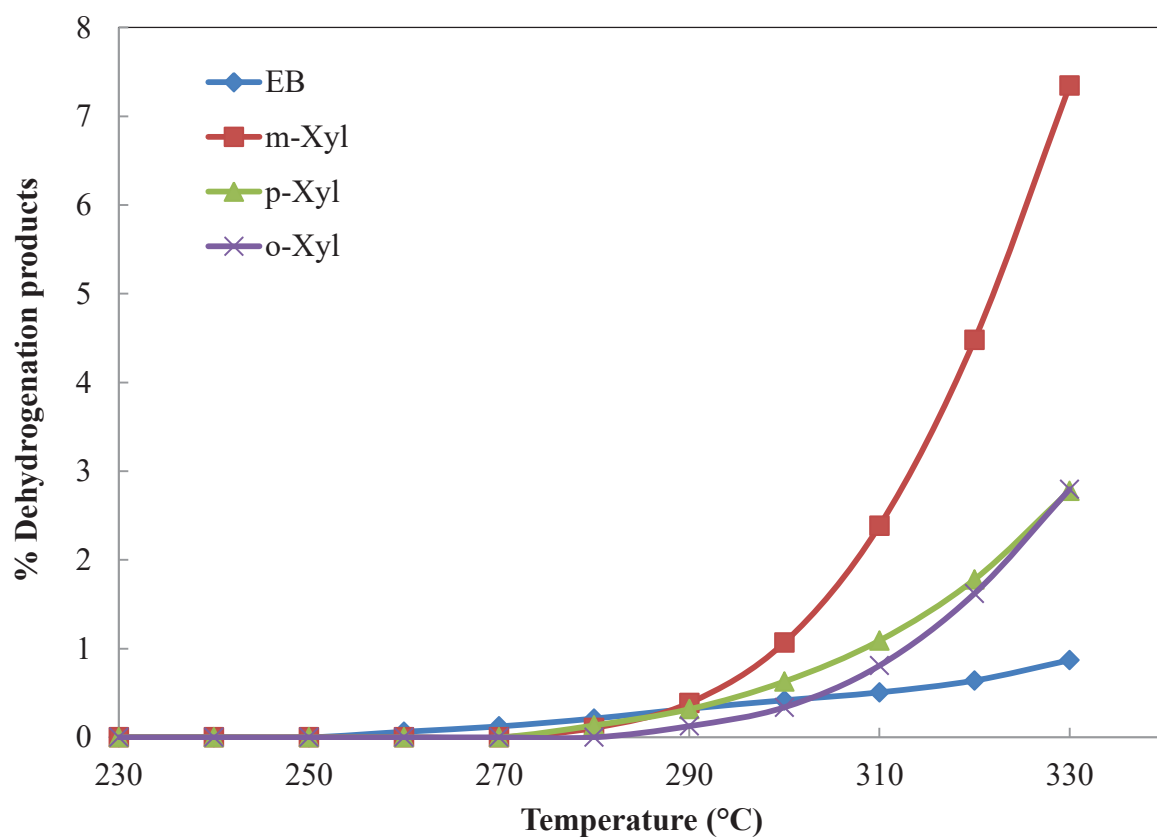


Figure S10. Evolution of different dehydrogenation products for the reference catalyst 1% Pt- $\text{Al}_2\text{O}_3$ /HEU-1.



APPENDIX IV

**Supporting information**

***Location of the Active Sites for Ethylcyclohexane Hydroisomerization by Ring***

***Contraction and Expansion in the EUO Zeolitic Framework***

*Ester Gutierrez-Acebo,<sup>1</sup> Jérôme Rey,<sup>1</sup> Christophe Bouchy<sup>1</sup>, Yves Schuurman,<sup>2</sup> Céline Chizallet,<sup>1\*</sup>*

<sup>1</sup>IFP Energies nouvelles, Rond-point de l'échangeur de Solaize, BP 3, Solaize, 69360, France

<sup>2</sup> IRCELYON, Institut de recherches sur la catalyse et l'environnement de Lyon, CNRS, UMR 5256, Université Lyon 1, 2 avenue Albert Einstein, F-69626 Villeurbanne, France

\*Corresponding author: [celine.chizallet@ifpen.fr](mailto:celine.chizallet@ifpen.fr)

## APPENDIX

**Table S1. Substituted active sites and initial systems for the sites analysis of TS2.**

Initial system	T site changed	Oxygen changed	Final system
T10T1T9	T9 --> T2	O6 --> O6	T10T1T2
T10T1T9	T9 --> T3	O6 --> O9	T10T1T3
T10T1T9	T10 --> T4	O12 --> O12	T4T1T9
T10T1T9	T1 --> T5	O1 --> O13	T10T5T6
T10T1T9	T1 --> T6	O1 --> O3	T10T6T9
T10T1T9	T9 --> T7	O6 --> O7	T10T1T7
T10T1T9	T9 --> T8	O6 --> O9	T10T1T8

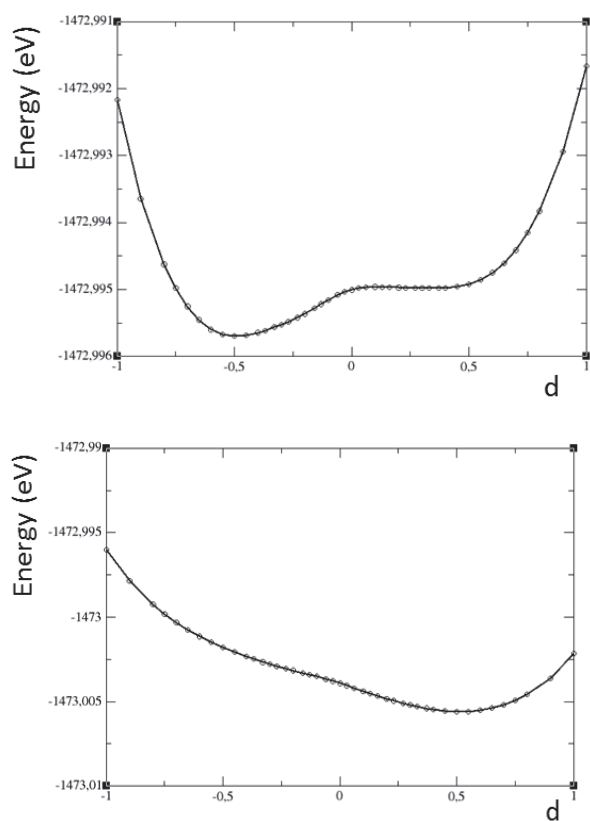
## S1. LINE MINIMIZATION PROCEDURE

This procedure allows to explore energy along a specific direction in the  $3N$  dimensional configuration space. We employ this technique to eliminate the residual imaginary frequencies often remaining after the geometry optimizations. These imaginary frequencies are usually due to an incomplete energy minimization along one or more directions. This problem is often related to a relative flatness of potential energy landscape in some parts of the configuration space, hence even very tight convergence criteria used in atomic relaxations may not lead to elimination of all undesired imaginary frequencies.

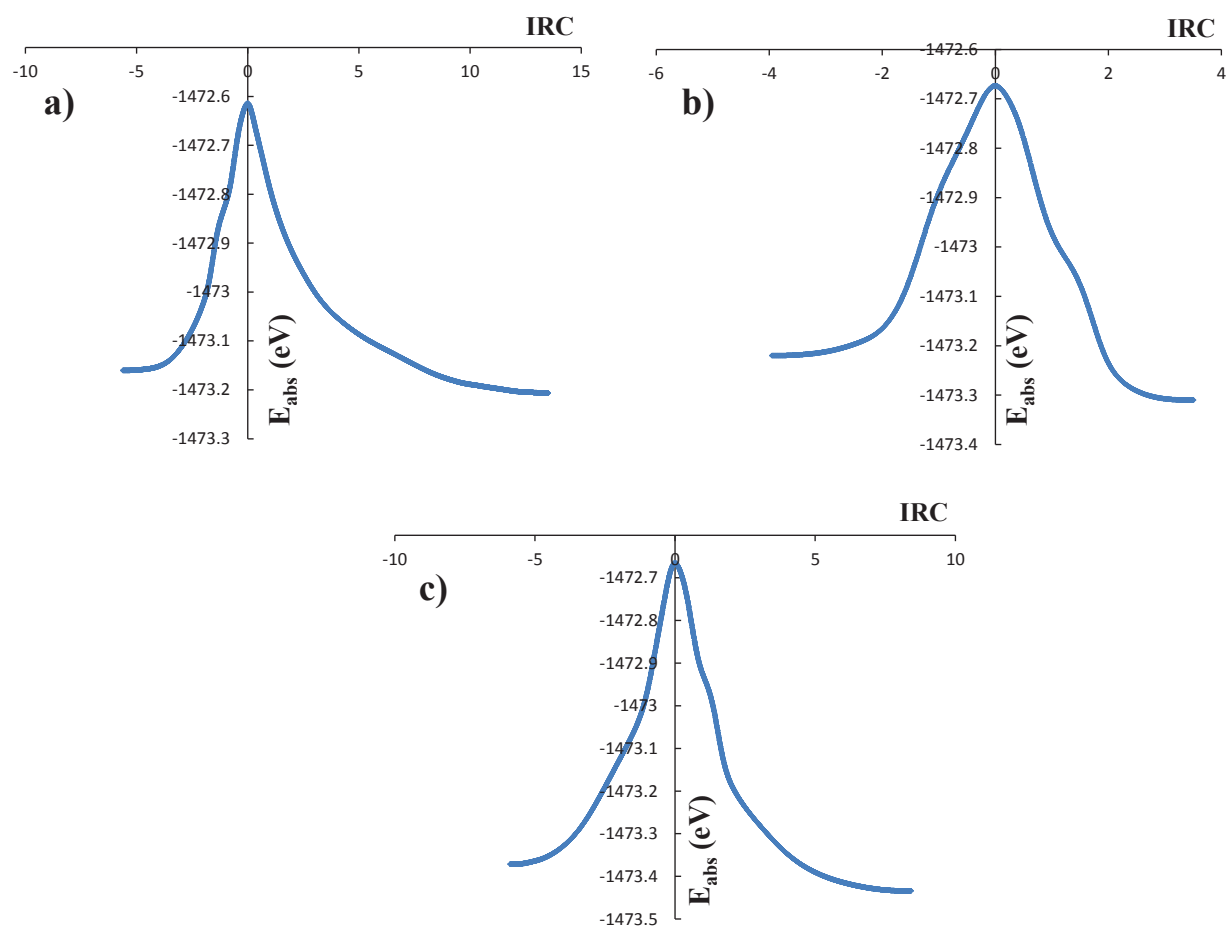
For a periodic solid with  $N$  atoms, there are no global rotations and 3 global translations. The total momentum is taken to be zero in simulations, and there are  $3N - 3$  vibrational degrees of freedom.<sup>242</sup> Importantly, the potential energy of the system is translationally and rotationally invariant. In order to identify and efficiently eliminate the residual imaginary vibrations, the translational (and, in the case of the gas phase molecules, also rotational) degrees of freedom have to be decoupled from vibrations. As this is not done by the VASP code (the  $3N$  modes are considered to be vibrational modes), we use a program developed by Tomas Bucko (Univ. Bratislava) for this purpose. The program reads the forces in the output file of the VASP calculation and computes and diagonalizes the Hesse and dynamical matrices in translationally and rotationally invariant internal coordinates. Translations (and rotations in the case of the gas phase molecules) are thus effectively decoupled from vibrations. In the next step, the energy landscape is sampled along the direction of the eigenvector with the largest undesired eigenvalue by a sequence of single point energy calculations (see Figure S1 for examples of successive sampling during the optimization of a transition state). The structure corresponding to the energy minimum is re-optimized and the vibrational frequencies are re-computed at each step. The procedure is repeated until the configuration with a correct vibrational spectrum is identified (typically 1 to 6 repeated cycles are needed).

This line minimization procedure has been successfully applied to some structures investigated in this work.

## APPENDIX



**Figure S1.** Successive sampling of the potential energy along Hesse matrix eigenvector with negative eigenvalue.  $d$  is a scaling dimensionless parameter for displacement. Two successive line minimizations for the same transition state are shown. Upon each line minimization, the structures with the lowest energy (for  $d = -0.55$  (left) and  $d = 0.50$  (right)) have been re-optimized and the Hesse matrix has been re-calculated.

**S2. INTRINSIC REACTION COORDINATE (IRC)**

**Figure S2. IRC curves for each ring contraction/expansion elementary steps at the channel-pocket intersection T10O12 site: a) TS1, b) TS2, c) TS3.**

## APPENDIX

### S3. ESTIMATION OF GIBBS FREE ENERGIES

Gibbs free energy was calculated with the following equations, with E the electronic energy, S the entropies, U internal energies, P the pressure and  $V_m$  the molar volume.

$$G(T, p) = E + U_{trans}(T, p) + U_{vib}(T, p) + U_{rot}(T, p) + PV_m - T(S_{trans}(T, p) + S_{vib}(T, p) + S_{rot}(T, p)) \quad (\text{Equation S1})$$

$$H_{vib}(T) = N_A \left[ \sum_n \frac{1}{2} h\nu_n + \sum_n \frac{h\nu_n \times \exp\left(-\frac{h\nu_n}{k_B T}\right)}{1 - \exp\left(-\frac{h\nu_n}{k_B T}\right)} \right] \quad (\text{Equation S2})$$

For gas phase ethylcyclohexene, equation S3 is used. In the case of condensed systems, these terms are considered to be zero, as well as rotational and translational entropies given by equations (S5) and (S6).

$$U_{trans}(T) + U_{rot}(T) + PV_m(T) = 4RT \quad (\text{Equation S3})$$

$$S_{vib}(T) = N_A k_B \left[ \sum_n \frac{\frac{h\nu_n}{k_B T} \times \exp\left(-\frac{h\nu_n}{k_B T}\right)}{1 - \exp\left(-\frac{h\nu_n}{k_B T}\right)} - \sum_n \ln \left( 1 - \exp \left( -\frac{h\nu_n}{k_B T} \right) \right) \right] \quad (\text{Equation S4})$$

$$S_{rot}(T) = N_A k_B \left( \frac{3}{2} + \ln \left[ \frac{\sqrt{\pi}}{\sigma} \left( \frac{8\pi^2 k_B T}{h^2} \right)^{\frac{3}{2}} \sqrt{A_e \times B_e \times C_e} \right] \right) \quad (\text{Equation S5})$$

$$S_{trans}(T, p) = N_A k_B \left( \frac{5}{2} + \ln \left( \frac{RT}{p} \left( \frac{2\pi M}{h^2} \right)^{3/2} \right) \right) \quad (\text{Equation S6})$$

With  $\nu_n$  the vibrational frequencies of the system (vibration eigenvalues),  $k_B$  the Boltzmann constant,  $N_A$  the Avogadro constant, T the temperature, h the Planck constant and M the molar weight.  $\sigma$  corresponds to the symmetry number of the system and  $A_e$ ,  $B_e$  and  $C_e$  the moments of inertia according to the eigenaxes of the molecule.

# APPENDIX

**Table S2. Distance values between isomers molecules / carbenium ions and the zeolite framework at the intersection channel-pocket site T10O12.**

Starting molecule	Distance (Å)		
	pi complex		carbenium
	C <sub>1</sub> -H	C <sub>2</sub> -H	O <sub>12</sub> -H
ECH <sup>−</sup>	2.365	1.9	3.766
12-EMCP <sup>−</sup>	3.105	3.757	2.644
12-DMCH <sup>−</sup>	2.271	2.298	2.747
123-TMCP <sup>−</sup>	3.06	3.643	3.101

C<sub>1</sub> and C<sub>2</sub> are the carbons of the double bond.

## S4. STRUCTURAL AND VIBRATIONAL DATA FOR TRANSITION STRUCTURES

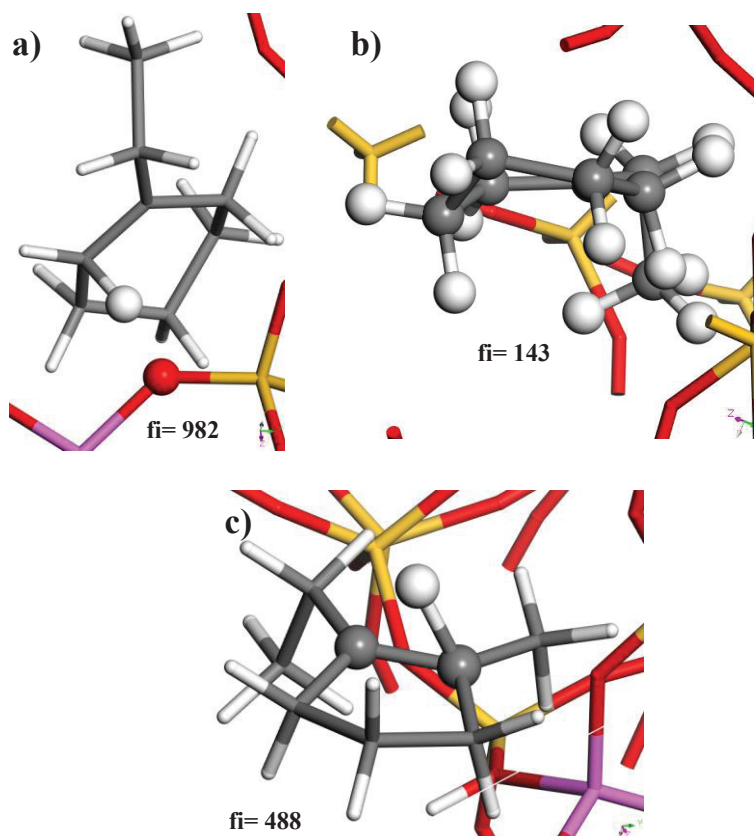


Figure S3. Transition structures at the intersection active site T10O12 and their imaginary frequencies (given in  $\text{cm}^{-1}$ ). a) ts1 (proton transfer from the framework), b) ts2 (distorted chair to boat conformation change), c) ts3 (hydride shift). The energy corresponding to these structures is shown in Figure 7.



# APPENDIX

**Table S3. TS distances at the channel active site T1O1 and their imaginary frequencies ( $\text{cm}^{-1}$ ).**

	Distance ( $\text{\AA}$ )					fi
	C1-C2	C2-C3	C1-C3	C2-H	C3-H	
TS1	1.476	1.71	1.542	1.426	1.259	414
TS2	1.576	1.734	1.462	1.209	1.576	196
TS3	1.463	1.709	1.558	1.468	1.239	292

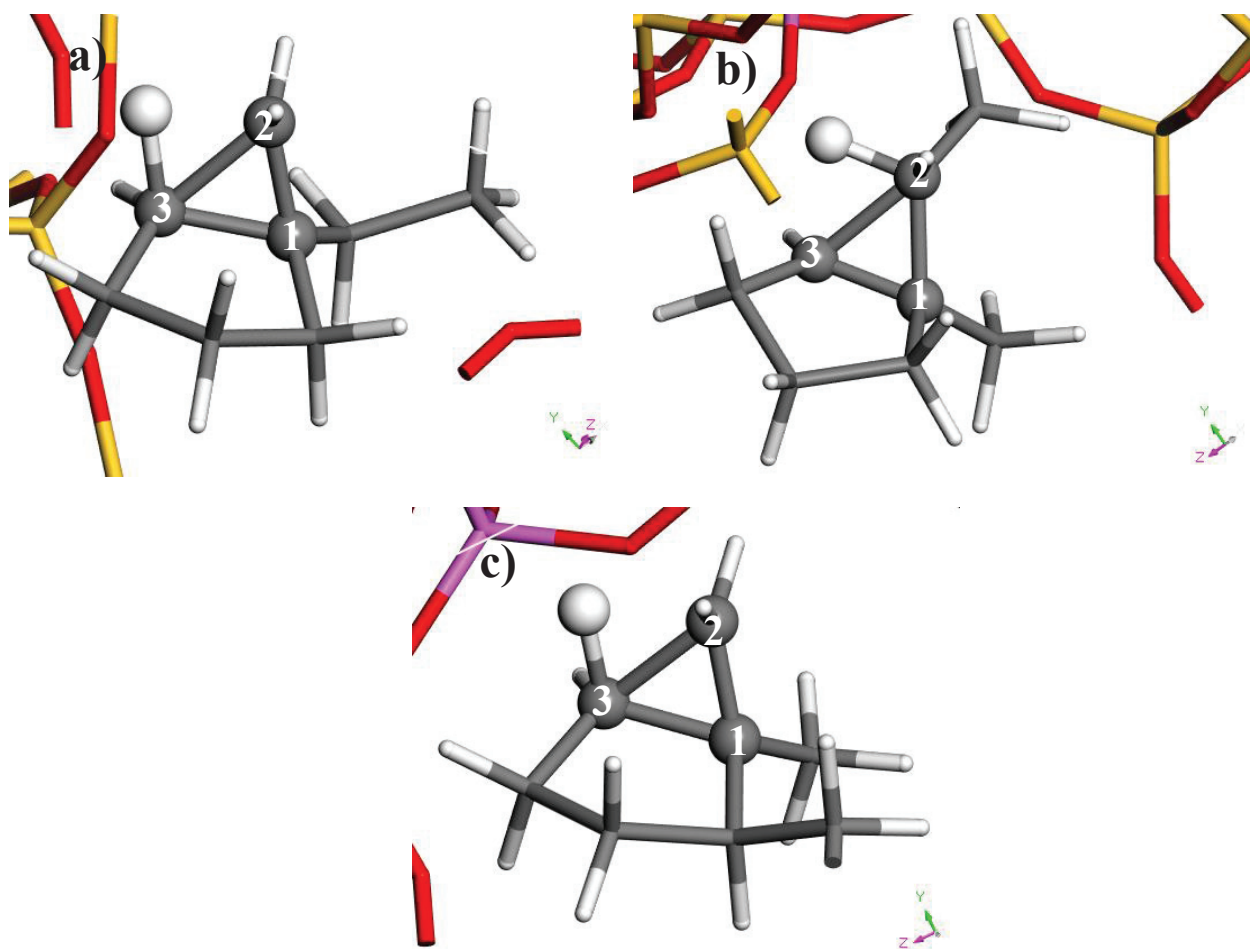


**Figure S4. TS distances at the channel active site T1O1. a) TS1, b) TS2, c) TS3.**

# APPENDIX

**Table S4.** TS distances at the pocket active site T9O6 and their imaginary frequencies ( $\text{cm}^{-1}$ ).

	Distance ( $\text{\AA}$ )					fi
	C1-C2	C2-C3	C1-C3	C2-H	C3-H	
TS1	1.479	1.751	1.544	1.393	1.236	401
TS2	1.532	1.797	1.503	1.261	1.351	322
TS3	1.469	1.741	1.558	1.446	1.215	469

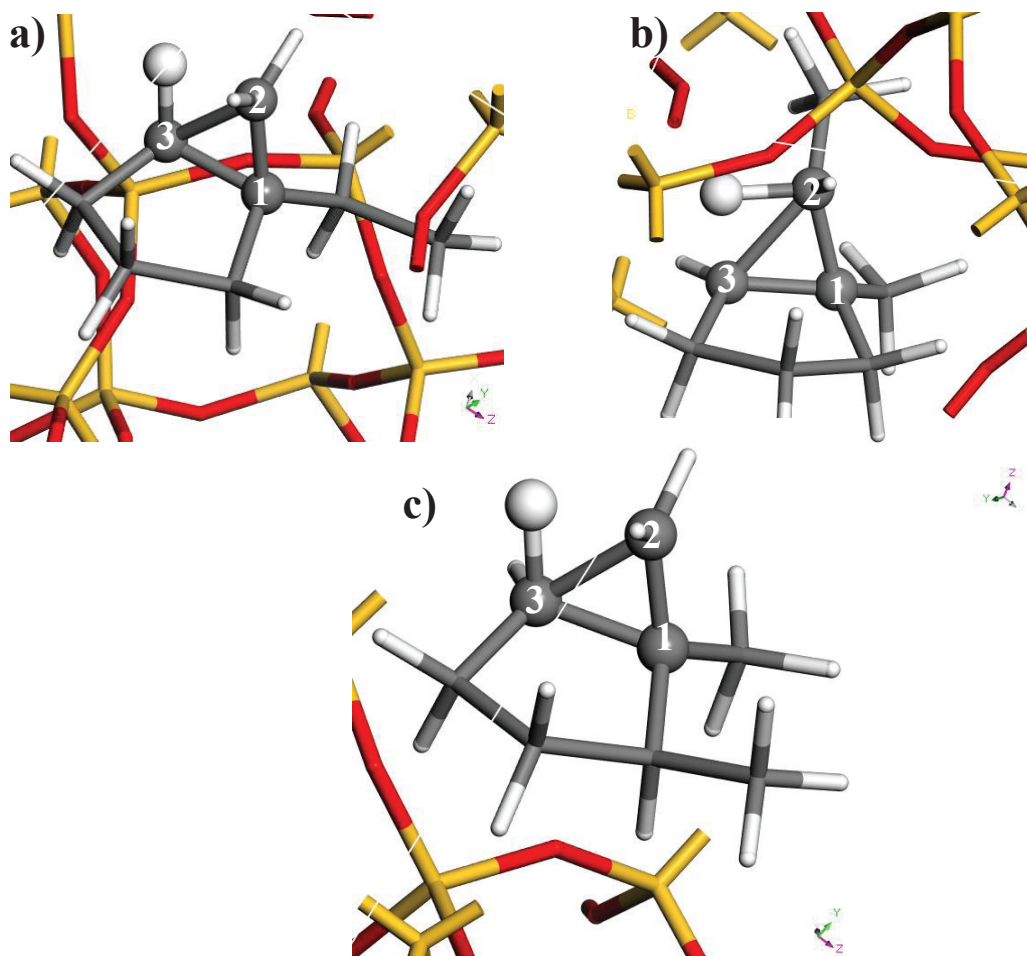


**Figure S5.** TS at the pocket active site T9O6. a) TS1, b) TS2, c) TS3 and d) TS4

# APPENDIX

**Table S5. Distances (Å) for TS2 at all other active sites and their imaginary frequencies (cm<sup>-1</sup>).**

	C1-C2	C2-C3	C1-C3	C2-H	C3-H	f <sub>i</sub>
T2	1.514	1.794	1.518	1.308	1.298	275
T3	1.537	1.800	1.495	1.243	1.381	363
T4	1.557	1.806	1.481	1.210	1.450	442
T7	1.553	1.791	1.482	1.212	1.452	374
T8	1.537	1.781	1.488	1.251	1.377	273

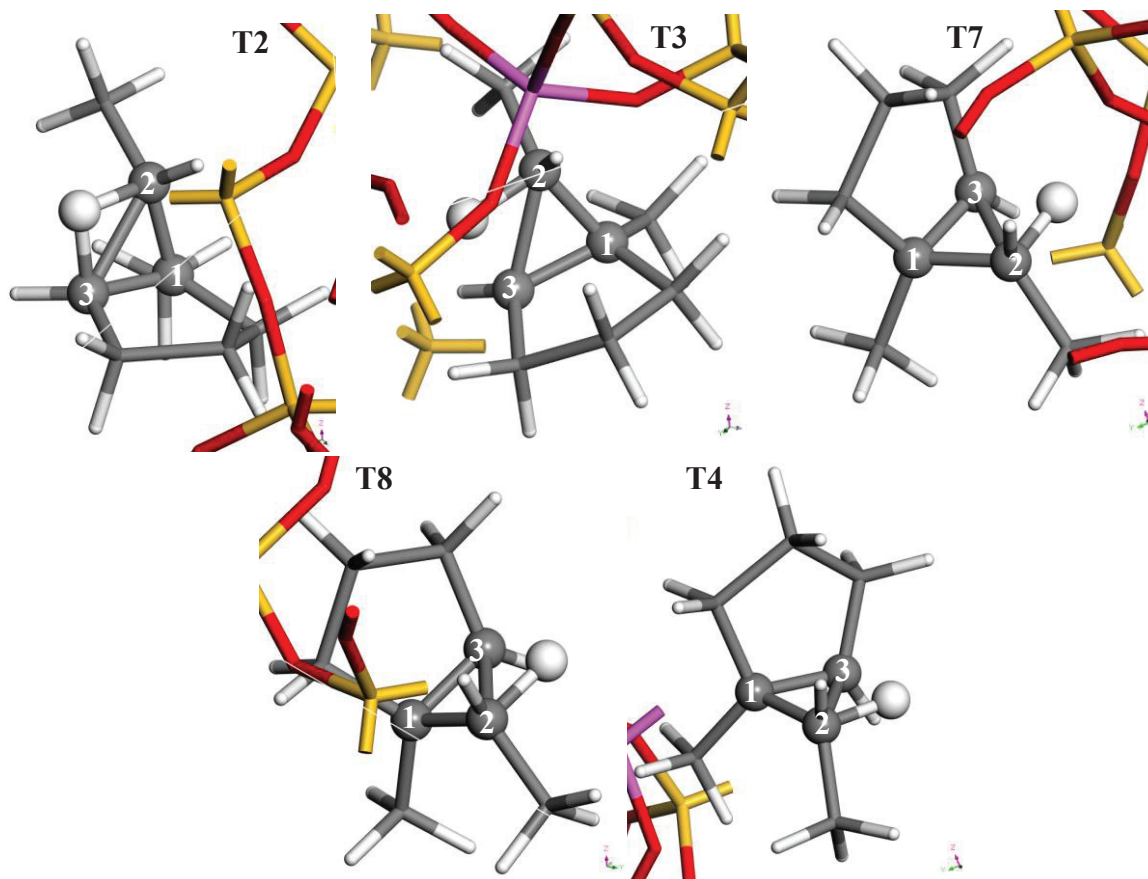


**Figure S6. TS2 at the pocket different active sites: T2, T3, T7, T8 and T4.**

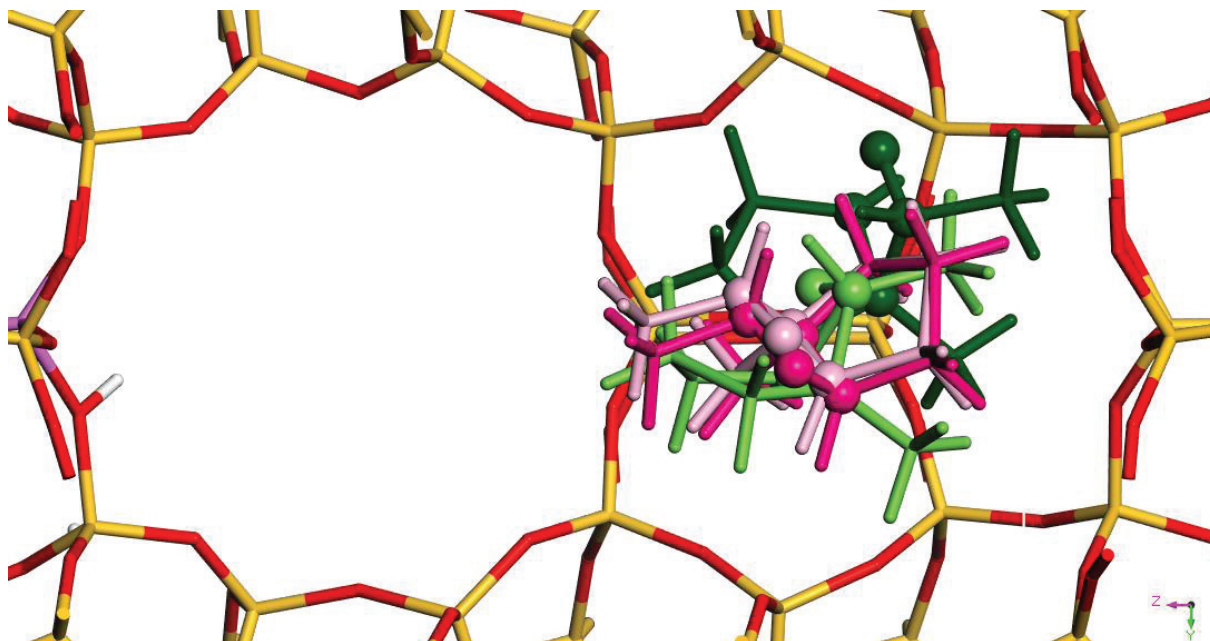


Figure S7. A wider view of the location of the transition structures (TS2) within the pocket (dark pink: T2, light pink: T3, dark green: T7, purple: T8, light green: T9).

# APPENDIX

**Table S6. Distances between the aluminum atoms in the zeolite and the PCP and between the corresponding oxygen releasing the proton and the PCP for T4 and T10.**

	Distance (Å)		
	Al-C2	Al-H	O12-H
T4	3.996	5.140	4.933
T10	4.008	4.590	3.437

**S5. ENERGY AND THERMODYNAMIC DATA****Table S7. Forward and backward energies barriers for all the active sites.**

	$E_{\text{for}}$	$E_{\text{back}}$
T1	77	88
T2	55	61
T3	67	67
T4	59	73
T7	50	67
T8	59	69
T9	49	56
T10	53	67

# APPENDIX

**Table S8. Gibbs energies for the selected active sites in the pocket (T9O6), in the channel (T1O1) and in the intersection (T10O12)**

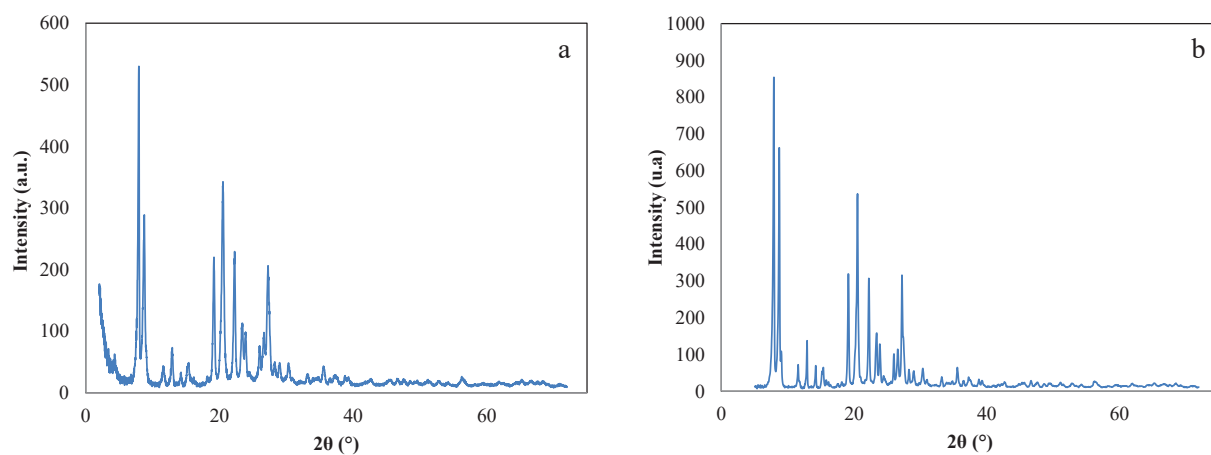
	T9O6 (pocket)	T1O1 (channel)	T10O12 (intersection)
ECH <sup>+</sup>	-13.02	-16.69	15.68
TS1	56.22	70.64	74.19
21-EMCP <sup>+</sup>	-0.92	-34.24	2.78
TS2	27.30	71.41	61.60
12-DMCH <sup>+</sup>	-14.51	-22.17	0.40
TS3	38.72	53.93	78.40
125-TMCP <sup>+</sup>	-32.95	-17.45	-24.86

# APPENDIX

**Table S9. Activation data for the selected active sites in the pocket (T9O6), in the channel (T1O1) and in the intersection (T1O12), estimated thanks to DFT calculations.**

		Forward			Backward		
		$\Delta G_f$ (kJ/mol)	$\Delta H_f$ (kJ/mol)	$\Delta S_f$ (J/molK)	$\Delta G_b$ (kJ/mol)	$\Delta H_b$ (kJ/mol)	$\Delta S_b$ (J/molK)
T1O12 (intersection)	TS1	58.5	54.0	-8.24	71.4	52.1	-35.18
	TS2	58.8	47.8	-19.96	61.2	61.4	4.430E-01
	TS3	78.0	60.6	-31.62	103.3	68.8	-62.69
T1O1 (channel)	TS1	87.3	51.5	-65.13	104.9	67.4	-68.21
	TS2	105.6	74.9	-55.84	93.6	81.5	-21.88
	TS3	76.1	64.7	-20.74	71.4	45.6	-46.94
T9O6 (pocket)	TS1	69.2	52.4	-30.7	57.1	52.6	-8.3
	TS2	30.1	41.5	20.8	43.7	46.6	5.4
	TS3	53.2	35.8	-31.7	71.7	46.9	-45



**S6. CHARACTERIZATION OF THE CATALYSTS**

**Figure S8. XRD diffractograms for a) EU-1, b) ZSM-50.**

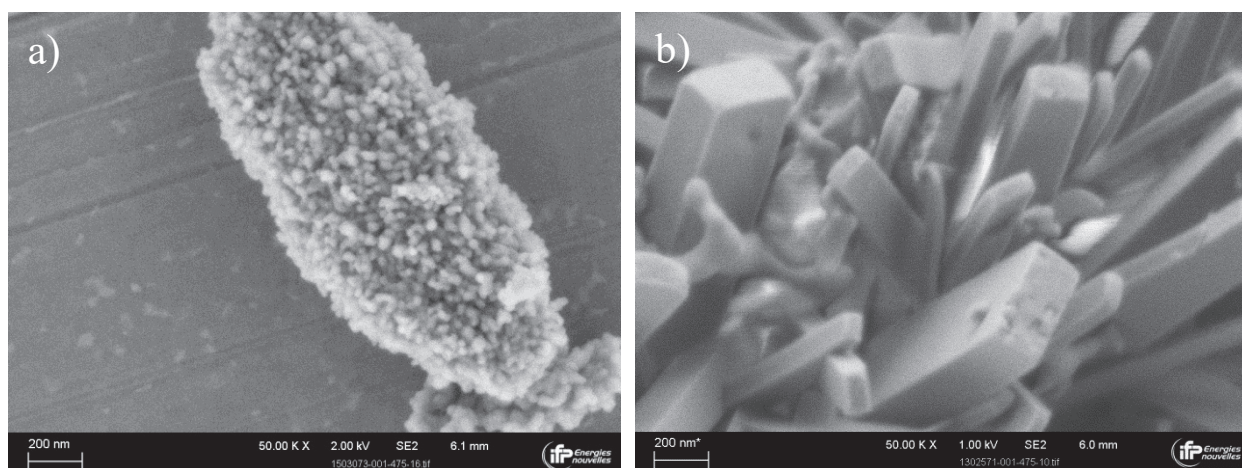


**Figure S9. SEM images for a) EU-1 and b) ZSM-50.**

## S7. DIFFUSSIONAL TAP EXPERIMENTS

### Micropore diffusion measurements

Temporal Analysis of Products (TAP) experiments were carried out to estimate the characteristic diffusion time of ethyl-cyclohexane inside EU-1 and ZSM-50 zeolites. TAP experiments consist of introducing a very narrow nanomole sized pulses into a fixed bed reactor under reduced pressure conditions.<sup>213</sup> A quadrupole mass spectrometer is located directly at the reactor exit inside a vacuum chamber. At these low pressures the gas transport through the reactor is by Knudsen diffusion only. Interaction of the gas with a catalyst surface or diffusion inside the micropores of the zeolite will lead to pulse broadening at the reactor outlet compared to an inert gas. By modeling the exit pulse response, the sorption and diffusion parameters can be estimated.<sup>213,243–247</sup> TAP experiments for micropore diffusion studies present several advantages: Knudsen flow guarantees the absence of external mass transfer limitations, the small pulse size leads to negligible heat effects and low surface coverages, assuring to be in the linear part of the adsorption curve and therefore a Darken factor of 1. The mathematical model for micropore diffusion in a TAP reactor is rather straightforward, coupling two diffusion equations through an adsorption equilibrium.<sup>244–247</sup>

### Modeling

For the modeling the data were baseline corrected and then normalized with respect to the curve area. No noise reduction methods were applied. The parameters were estimated through regression analysis of the pulse response data. The Knudsen coefficients for the diffusion of ethyl-cyclohexane through the quartz particles were calculated from Ar pulses over a bed of quartz particles. The Knudsen diffusion coefficient through the zeolite layer was set at a similar value as that for the quartz layer, as the zeolite zone is very small (0.6-0.8 mm) compared to the overall reactor length (25.4 mm). Simulations showed indeed that a variation of +/- 20% of this value did not lead to significantly different parameter estimates.

The diffusion inside the micropores is usually described as an activated diffusion process:

$$D = D^0 \exp(-E_{\text{act}}/RT) \quad (\text{Equation S7})$$

The adsorption equilibrium at the outside of the zeolite particles is described by the van 't Hoff equation:

$$K = K^0 \exp(-\Delta H/RT) \quad (\text{Equation S8})$$

## APPENDIX

Modeling of the TAP response curves gives access to the characteristic time of diffusion,  $t_D$ , which is equal to:

$$t_D = r^2/D \quad (\text{Equation S9})$$

where  $r$  is the characteristic diffusion length. The model is based on diffusion into a spherical particle with radius  $r$ . The characteristic diffusion time can only be extracted from TAP data within a window of approximately 3-4 orders of magnitude.<sup>244,246,247</sup> This was carefully checked during the modeling procedure, by varying the value of the characteristic diffusion time after the optimization procedure. A significant change in the model fit with increasing value of the characteristic diffusion time indicates that the model is sensitive to this parameter.

By simultaneous regression analysis of the pulse responses at different temperatures both the adsorption enthalpy and the activation energy for diffusion can be estimated. To reduce the correlation between the pre-exponential factor and energy term in equations S7 and S8, these equations were re-parametrized with respect to a reference temperature of 175°C. More details on modeling of TAP experiments can be found in [<sup>243–247</sup>].

## Results

Figure S1-S2 compares the experimental and model normalized TAP pulse responses for ethyl-cyclohexane over ZSM-50 and EU-1 as a function of temperature. As shown in the Figures, an adequate description of the experimental data is obtained by the model.

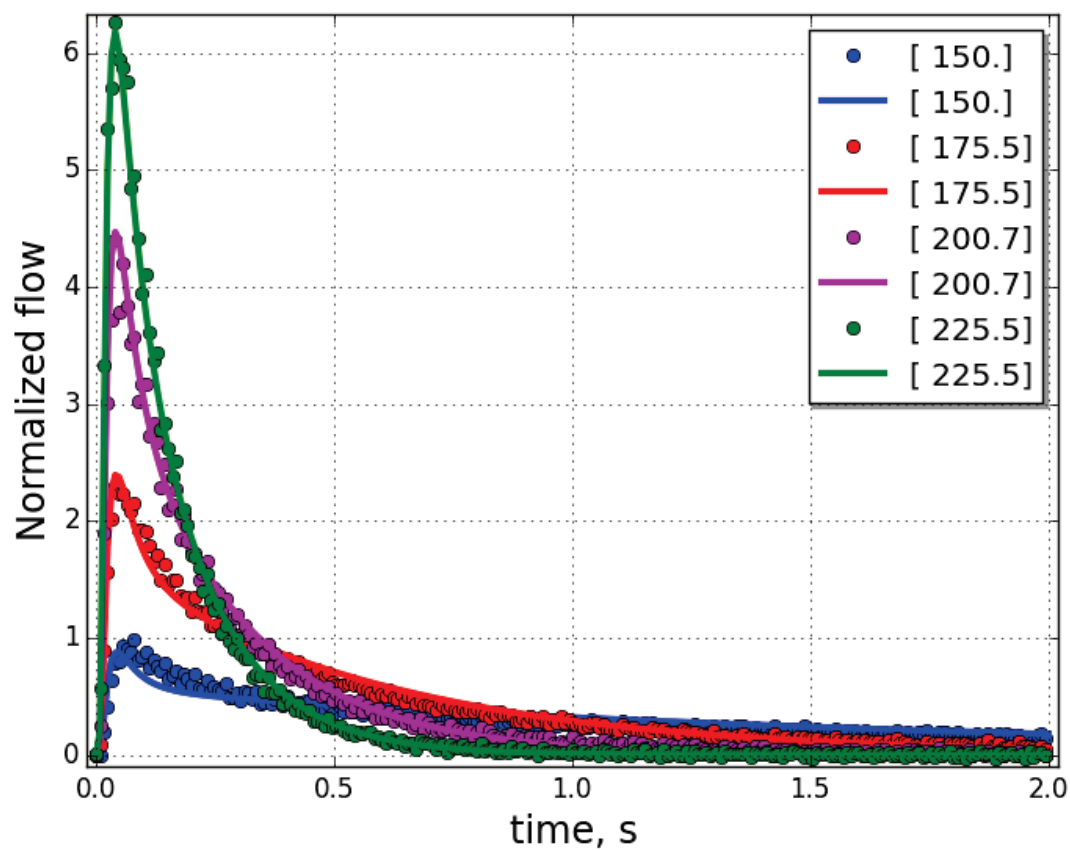


Figure S1. The experimental (symbols) and model (lines) normalized pulse responses for ethyl-cyclohexane over ZSM-50 as a function of temperature. Note that the data were recorded for 20 s, while the plot zooms in on the first 2 seconds.

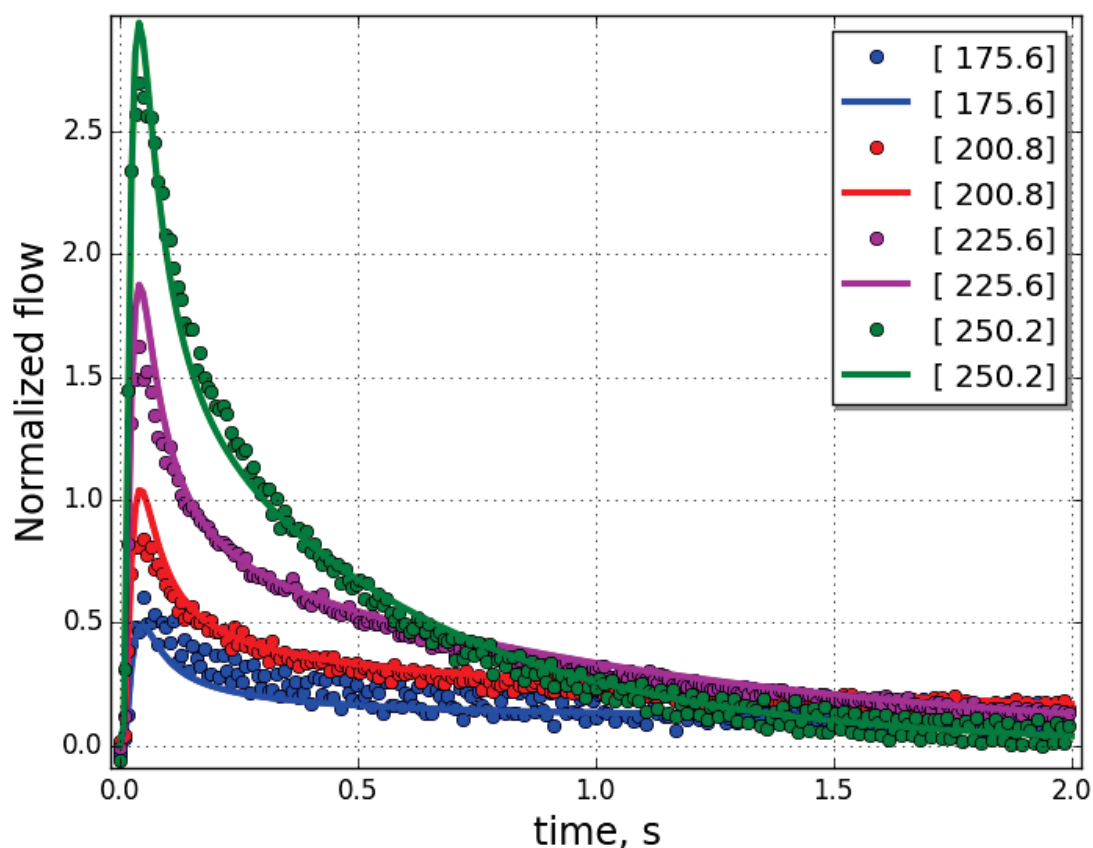


Figure S2. The experimental (symbols) and model (lines) normalized pulse responses for ethyl-cyclohexane over EU-1 as a function of temperature. Note that the data were recorded for 20 s, while the plot zooms in on the first 2 seconds.

Table S1. Parameters estimates from ethyl-cyclohexane TAP pulse response experiments.

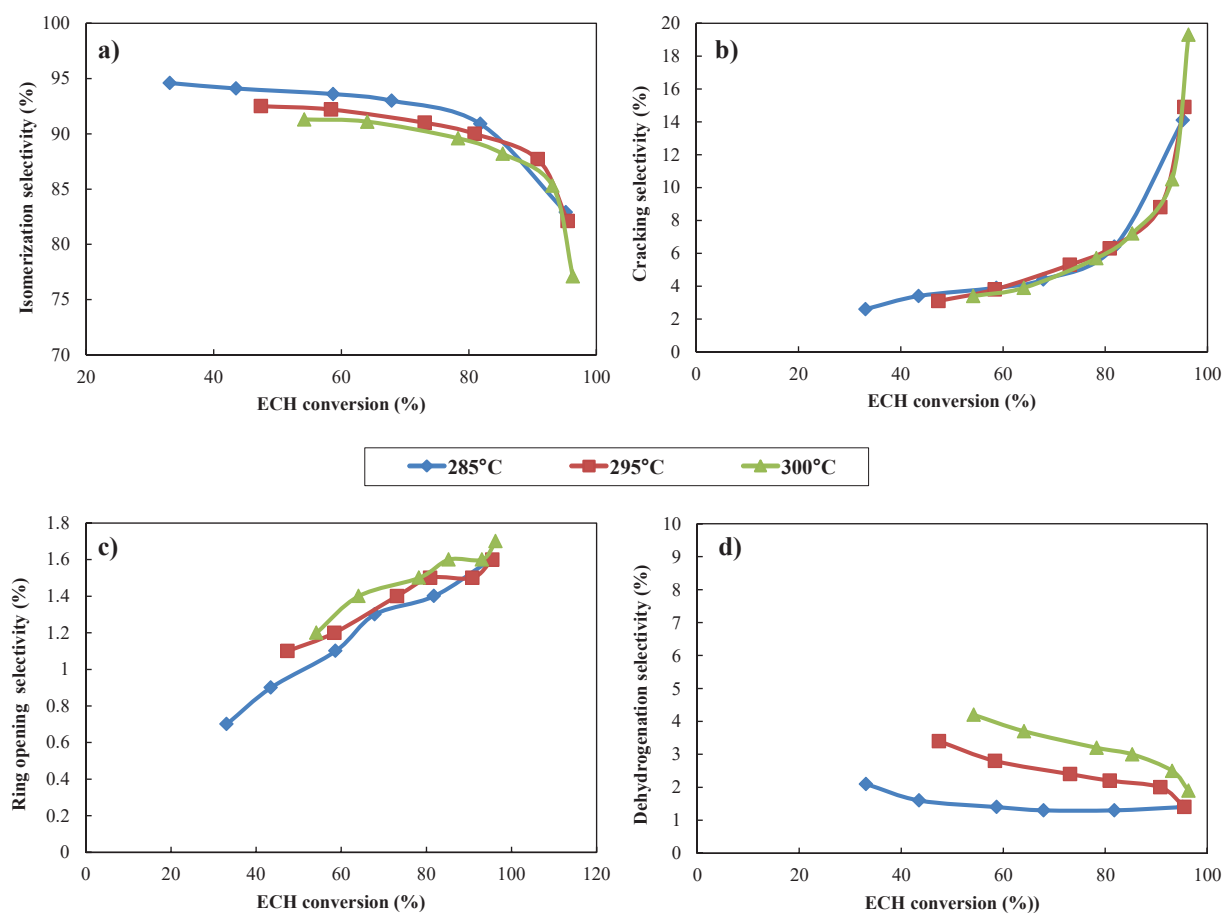
Sample	$-\Delta H$ (kJ/mol)	$t_D$ (s) @ 175°C	$E_{act}$ (kJ/mol)
ZSM-50	$78 \pm 8$	$1 \pm 0.4$	$20 \pm 10$
EU-1	$71 \pm 7$	$5 \pm 2$	$50 \pm 20$

Table S1 reports the parameter estimates from the TAP data. Rather similar adsorption enthalpies were found for both zeolite samples, as expected for zeolites with similar structures. The characteristic diffusion times are, on the other hand, different for the two zeolites. At equal crystallite sizes, the diffusion of ethyl-cyclohexane inside the micropores of ZSM-50 is faster than for EU-1 at 175°C.



## APPENDIX V

## V.I. GENERAL FEATURES



**Figure 9. Selectivity Evolution of the selectivity versus ECH conversion for the 1% Pt-Al<sub>2</sub>O<sub>3</sub>/HEU-1 catalysts group; a) isomerization; b) cracking; c) ring opening; d) dehydrogenation.**

It should be borne on mind that a high percentage of the dehydrogenation products are the desired “dehydrogenated isomers”

## V.II. HYDRIDE- AND METHYL- SHIFT

In the case of the methyl-shift reactions only one barrier for two tertiary carbocations was calculated and it was 17 kJ / mol. However in this case we do not have the thermodynamic data. In the kinetic model, a activation energy of 17 kJ / mol is going to be considered in all the methyl-shift reactions.

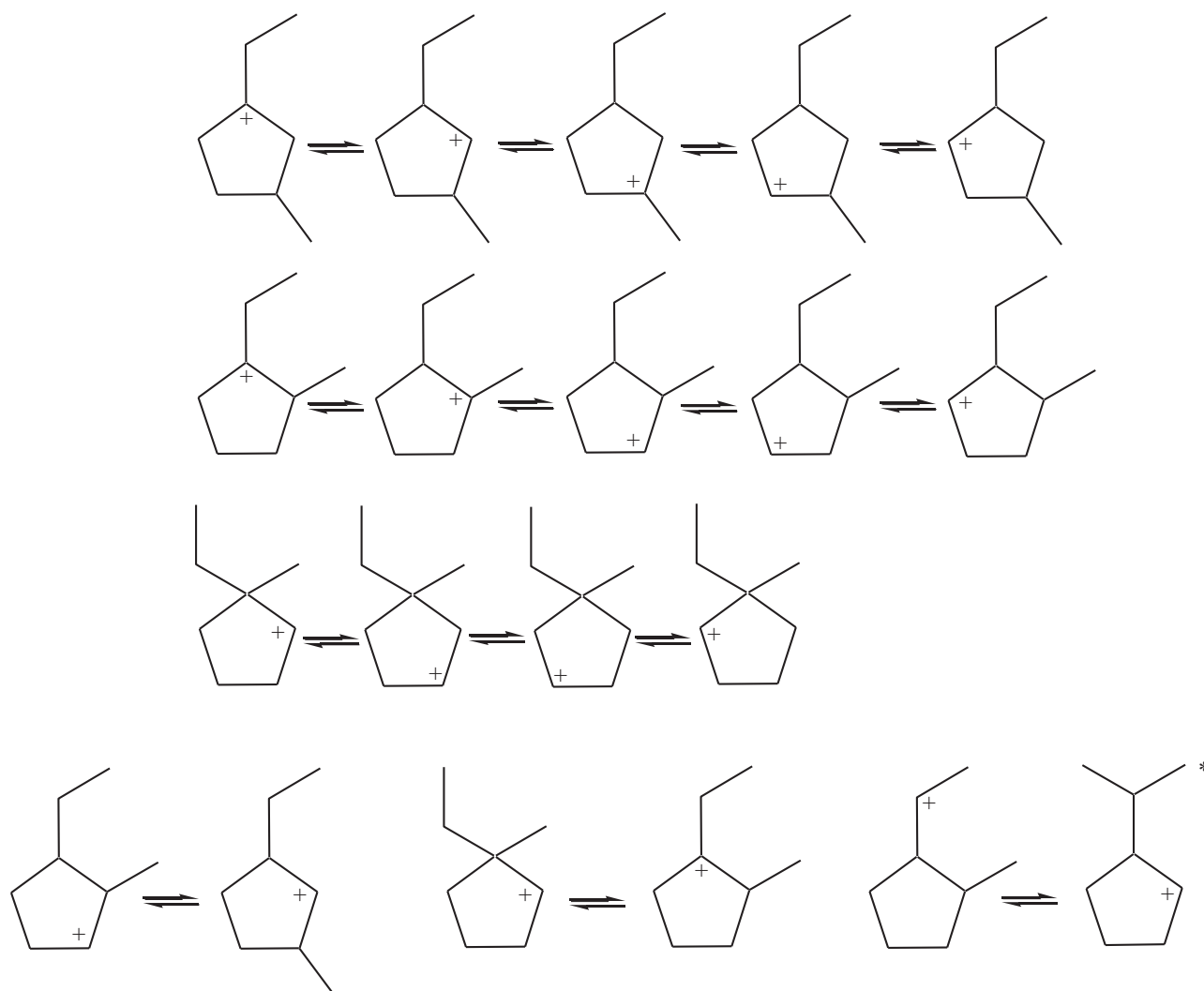
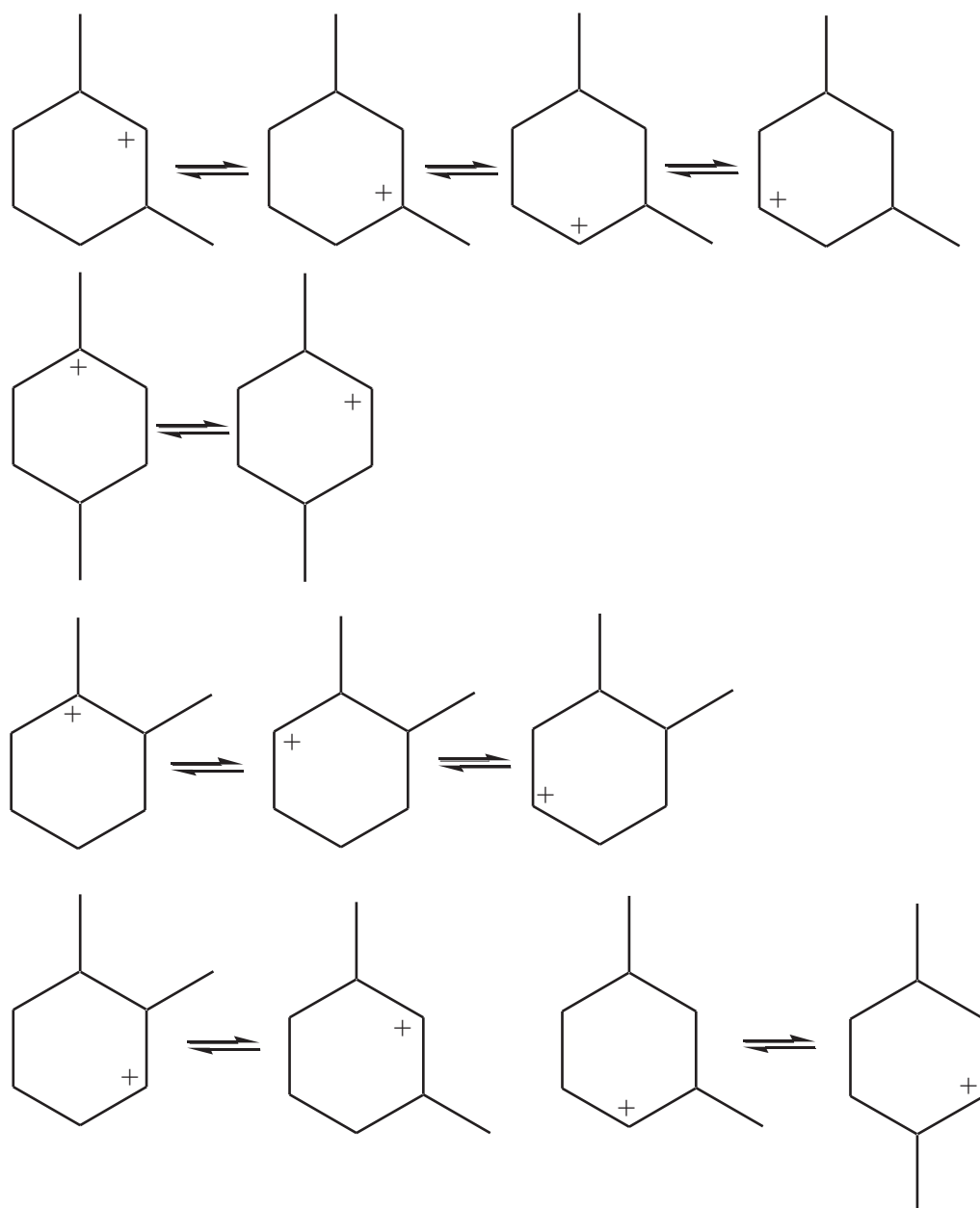


Figure 10. Hydride- and methyl-shifts within the EMCP family (\*IPCP).



# APPENDIX



**Figure 11. Hydride- and methyl-shifts within the DMCH family**

# APPENDIX

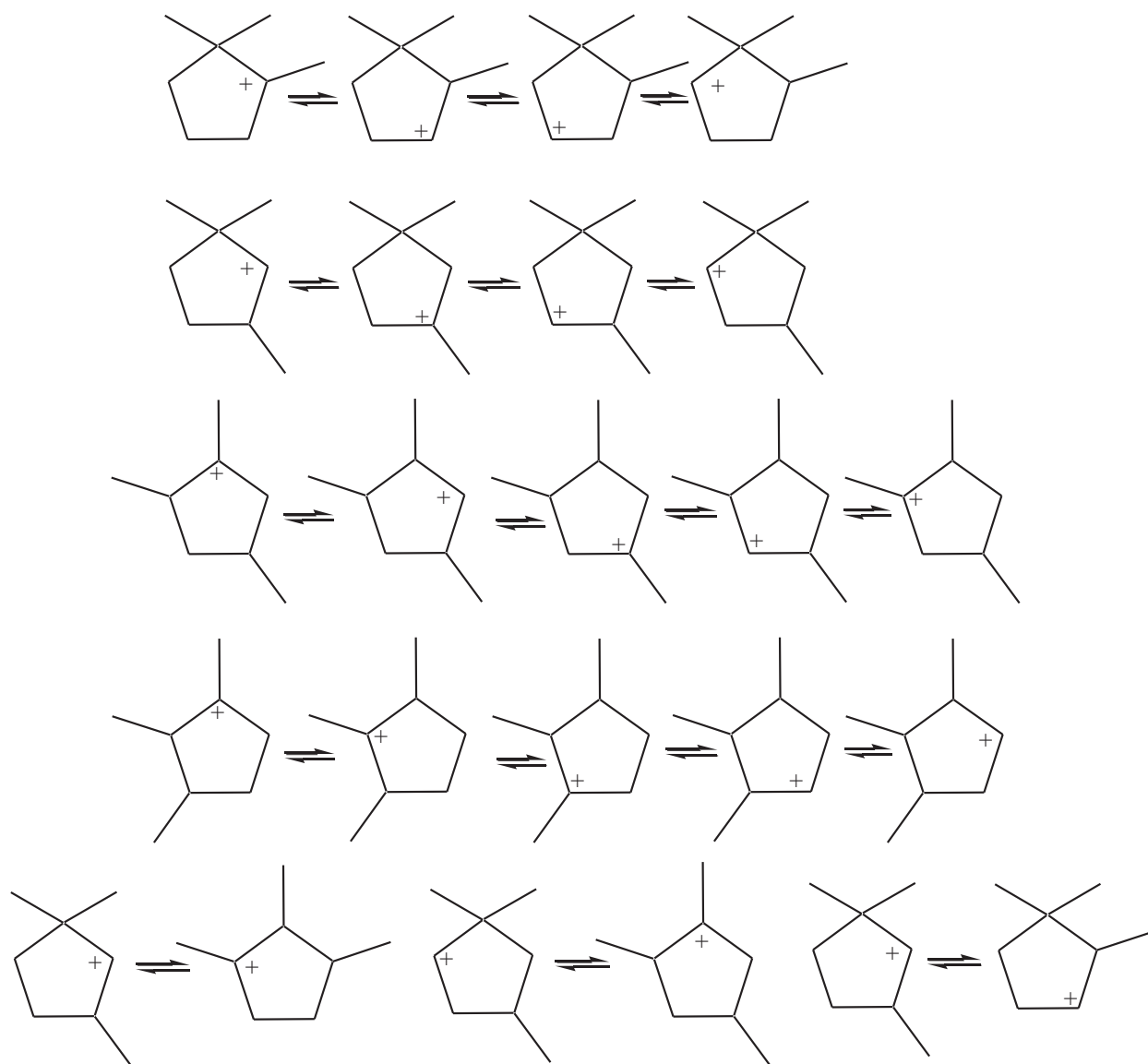


**Figure 12. Hydride- and methyl-shifts within the TMCP family**

# APPENDIX

## V.III. DFT STUDY

**Table 1. Activation data for the reactional scheme and the selected active sites in the pocket (T9O6), in the channel (T1O1) and in the intersection (T10O12), estimated thanks to DFT calculations.**

		Forward			Backward		
		$\Delta G_f$ (kJ/mol)	$\Delta H_f$ (kJ/mol)	$\Delta S_f$ (J/molK)	$\Delta G_b$ (kJ/mol)	$\Delta H_b$ (kJ/mol)	$\Delta S_b$ (J/molK)
T10O12 (intersection)	TS1	58.5	54	-8.2	71.4	52.1	-35.2
	TS2	58.8	47.8	-20.0	61.2	61.4	0.4
	TS3	78.0	60.6	-31.6	103.3	68.8	-62.7
	TS4	86.5	66.2	-36.8	64.2	60.5	-6.7
	TS5	70.7	64.0	-12.1	70.1	64.1	-11.0
	TS1II	NC	NC	NC	NC	NC	NC
	TS2II	NC	NC	NC	NC	NC	NC
	TS2bisII	NC	NC	NC	NC	NC	NC
	TS4II	NC	NC	NC	NC	NC	NC
T1O1 (channel)	TS1	87.3	51.5	-65.1	104.9	67.4	-68.2
	TS2	105.6	74.9	-55.8	93.6	81.5	-21.9
	TS3	76.1	64.7	-20.7	71.4	45.6	-67.7
	TS4	77.2	57.5	-35.9	65.1	46.7	-33.5
	TS5	52.0	39.6	-22.7	67.8	43.9	-43.4
	TS1II	102	99.7	-4.3	114.8	95.5	-35.2
	TS2II	_____	_____	_____	_____	_____	_____
	TS2bisII	_____	_____	_____	_____	_____	_____
	TS4II	_____	_____	_____	_____	_____	_____
T9O6 (pocket)	TS1	69.2	52.4	-30.7	57.1	52.6	-8.3
	TS2	30.1	41.5	20.8	43.7	46.6	5.4
	TS3	53.2	35.8	-31.7	71.7	46.9	-45.0
	TS4	84.3	70.8	-24.7	100.8	65.5	-64.2
	TS5	3.8	-6.7	-13.7	80.4	67.8	-22.9
	TS1II	_____	_____	_____	_____	_____	_____
	TS2II	19.5	3.9	-28.4	35.9	19.0	-30.6
	TS2bisII	-4.7	-14.8	-18.5	11.1	1.9	-16.7
	TS4II	_____	_____	_____	_____	_____	_____

NC: non- calculated; the gaps correspond to calculations that still have more than one imaginary frequency.

# APPENDIX

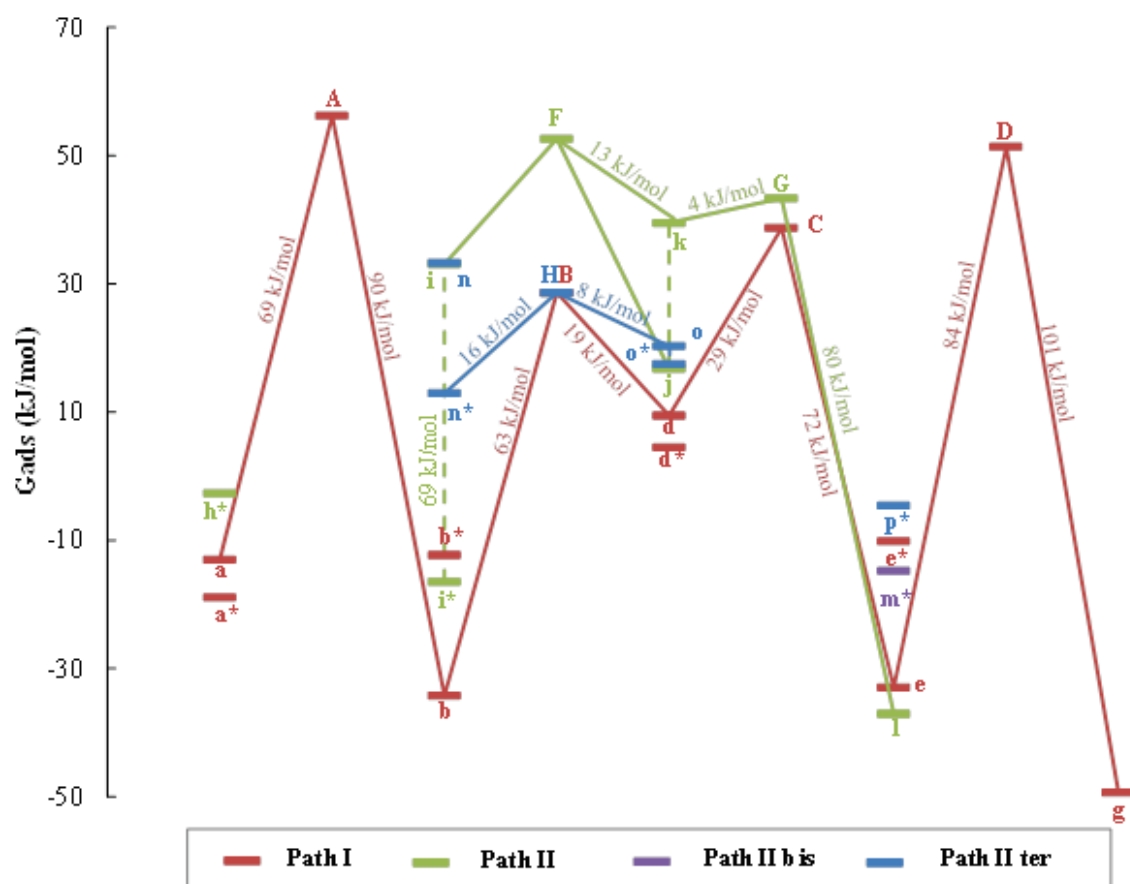
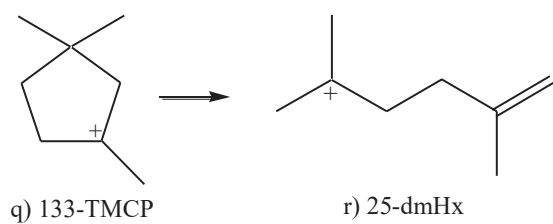
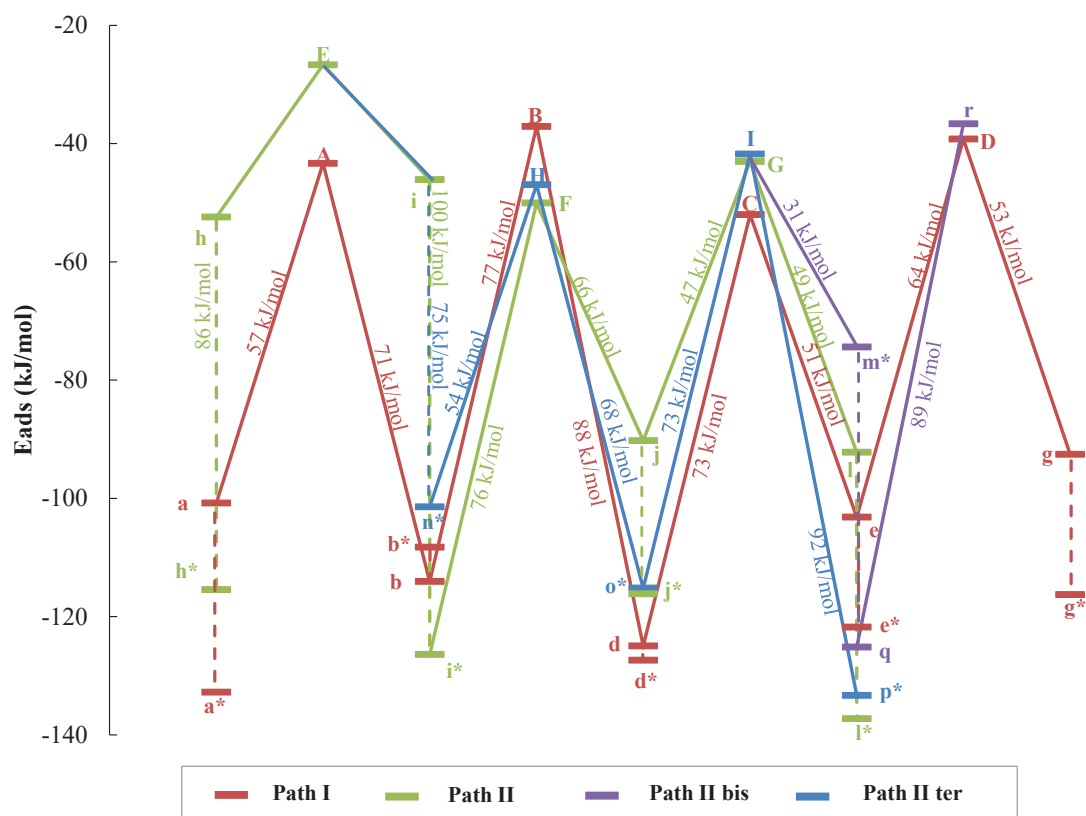


Figure 13. Adsorption Gibbs energy profile for the cycle contraction-expansions pathways through PCPs, at the pocket T9O6 active site. (\* pi-complex).

# APPENDIX



**Figure 14. RO reaction.**



**Figure 15. Energy profile for the cycle contraction-expansions pathways through PCPs, at the channel T1O1 active site. (\* pi-complex).**

# APPENDIX

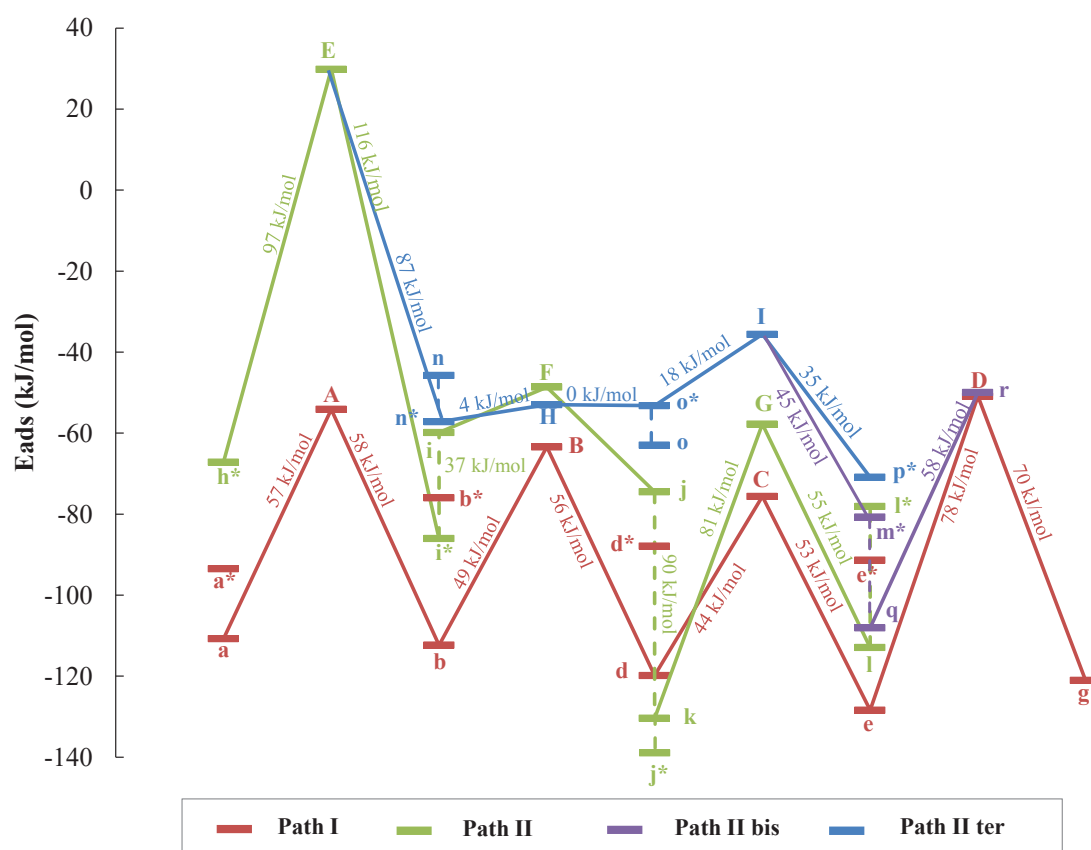


Figure 16. Energy profile for the cycle contraction-expansions pathways through PCPs, at the pocket T9O6 active site. (\* pi-complex).

# APPENDIX

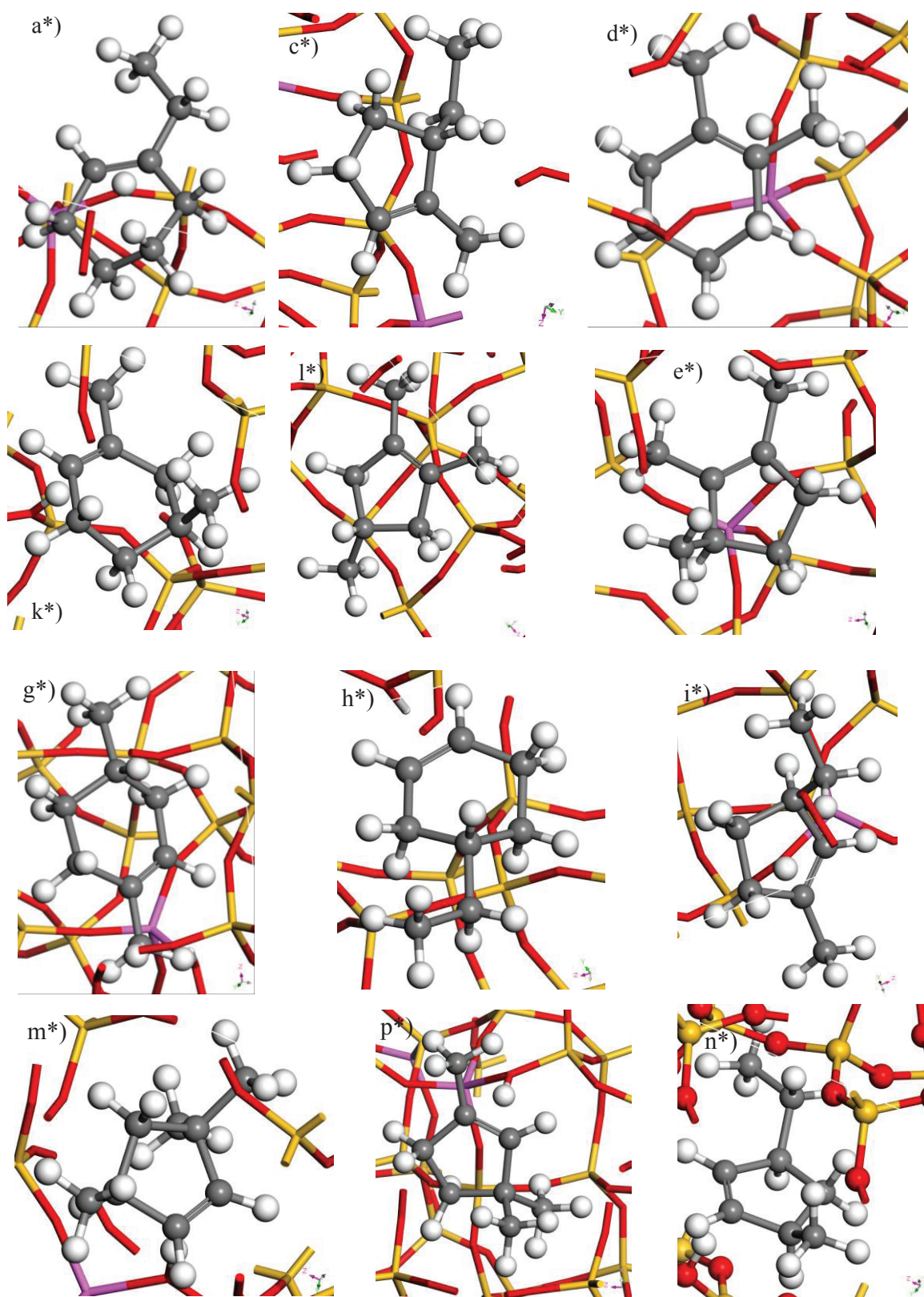
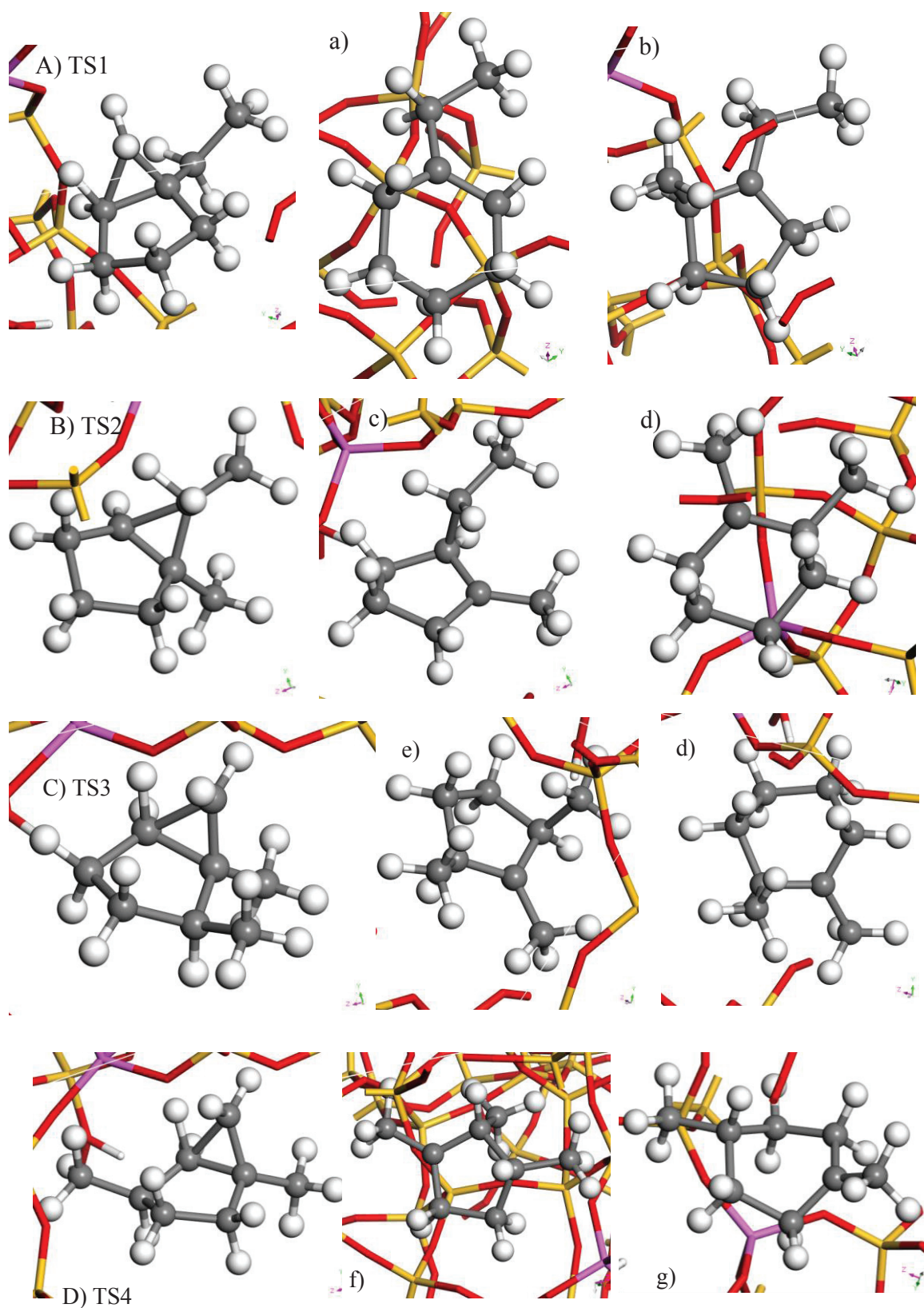


Figure 17. Optimized structures of all the molecules appearing in the reactional scheme in the channel T1O1.



# APPENDIX



**Figure 17.** Optimized structures of all the molecules appearing in the reactional scheme in the channel T1O1.



# APPENDIX

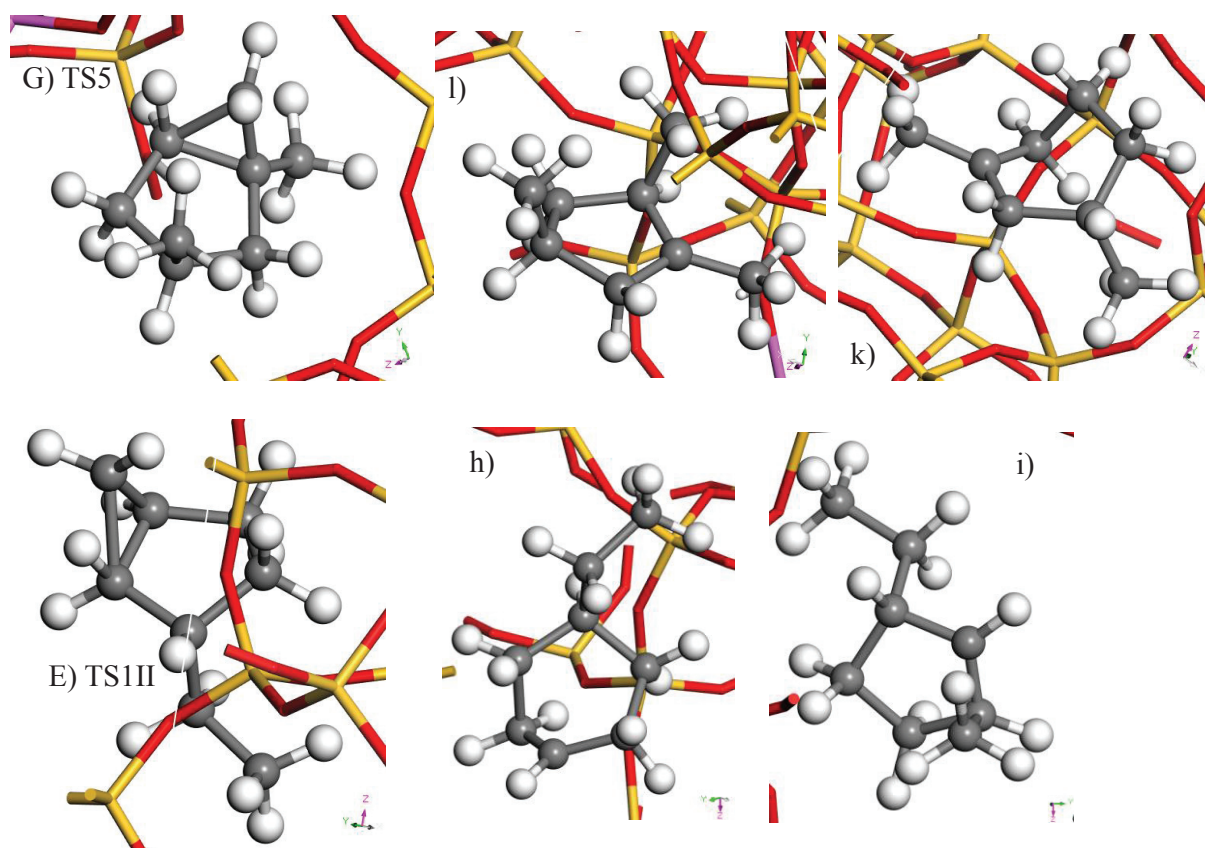


**Figure 17. Optimized structures of all the molecules appearing in the reactional scheme in the channel T1O1.**

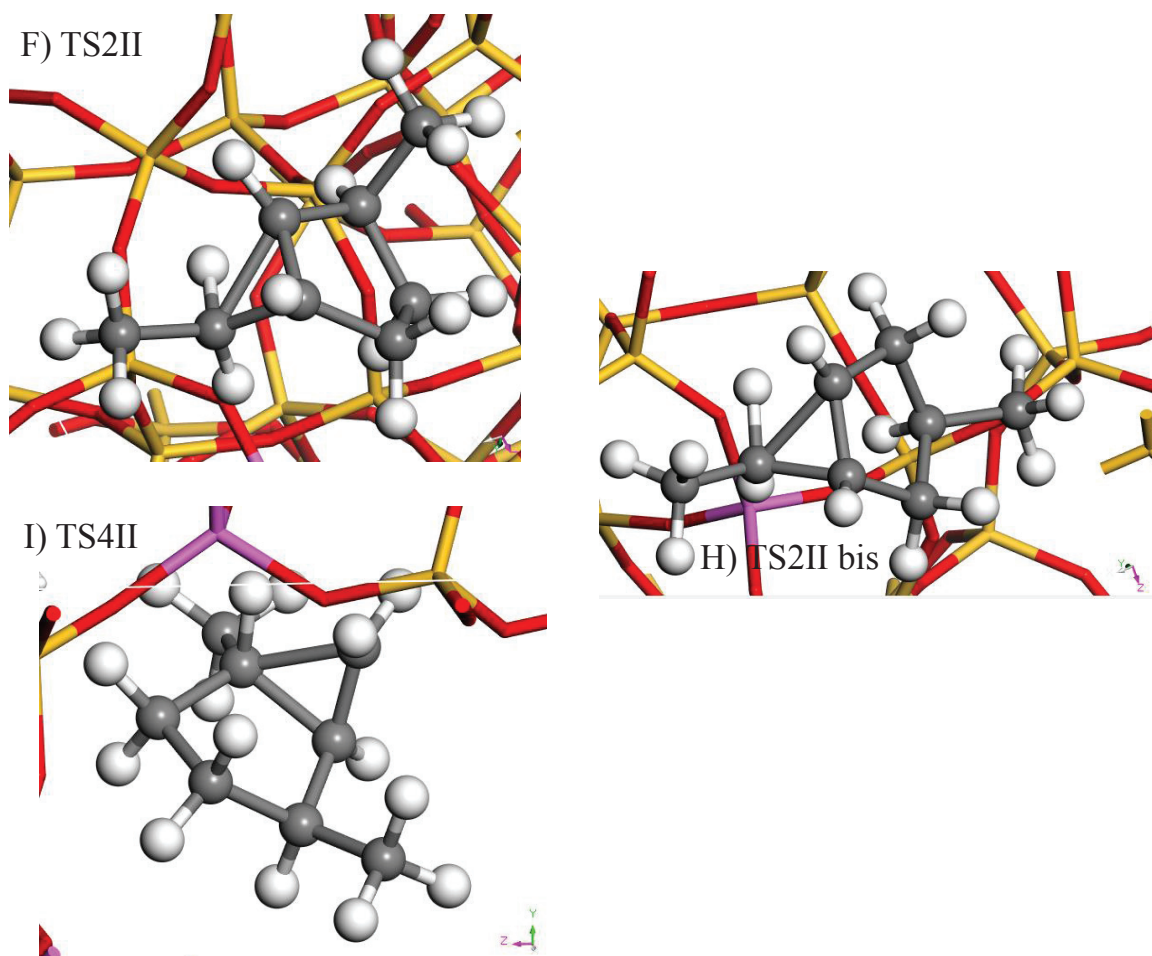


**Figure 18.** Optimized structures of some TS considered in the reactional scheme in the channel T1O1, but not well optimized (more than one imaginary frequency).

# APPENDIX

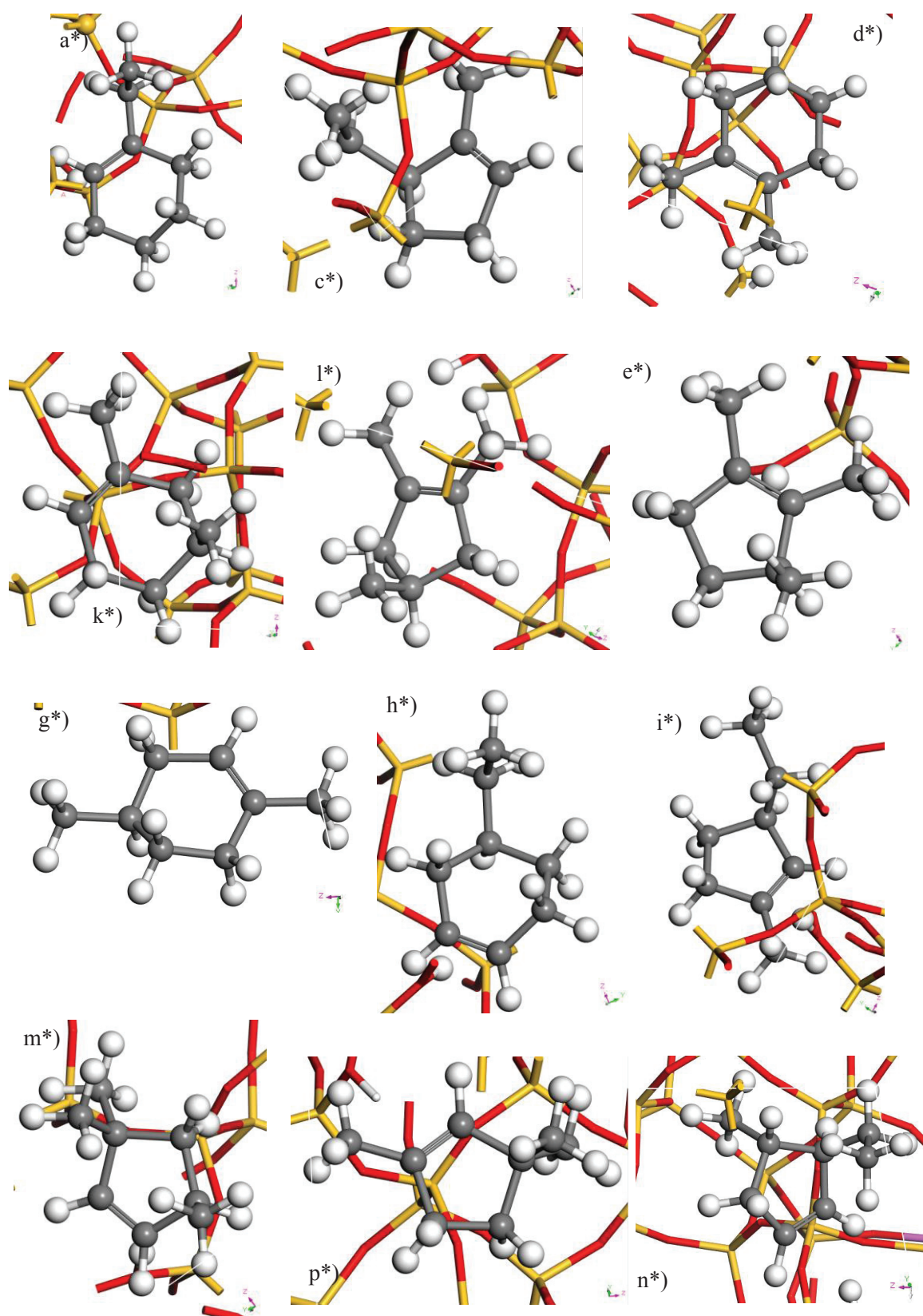
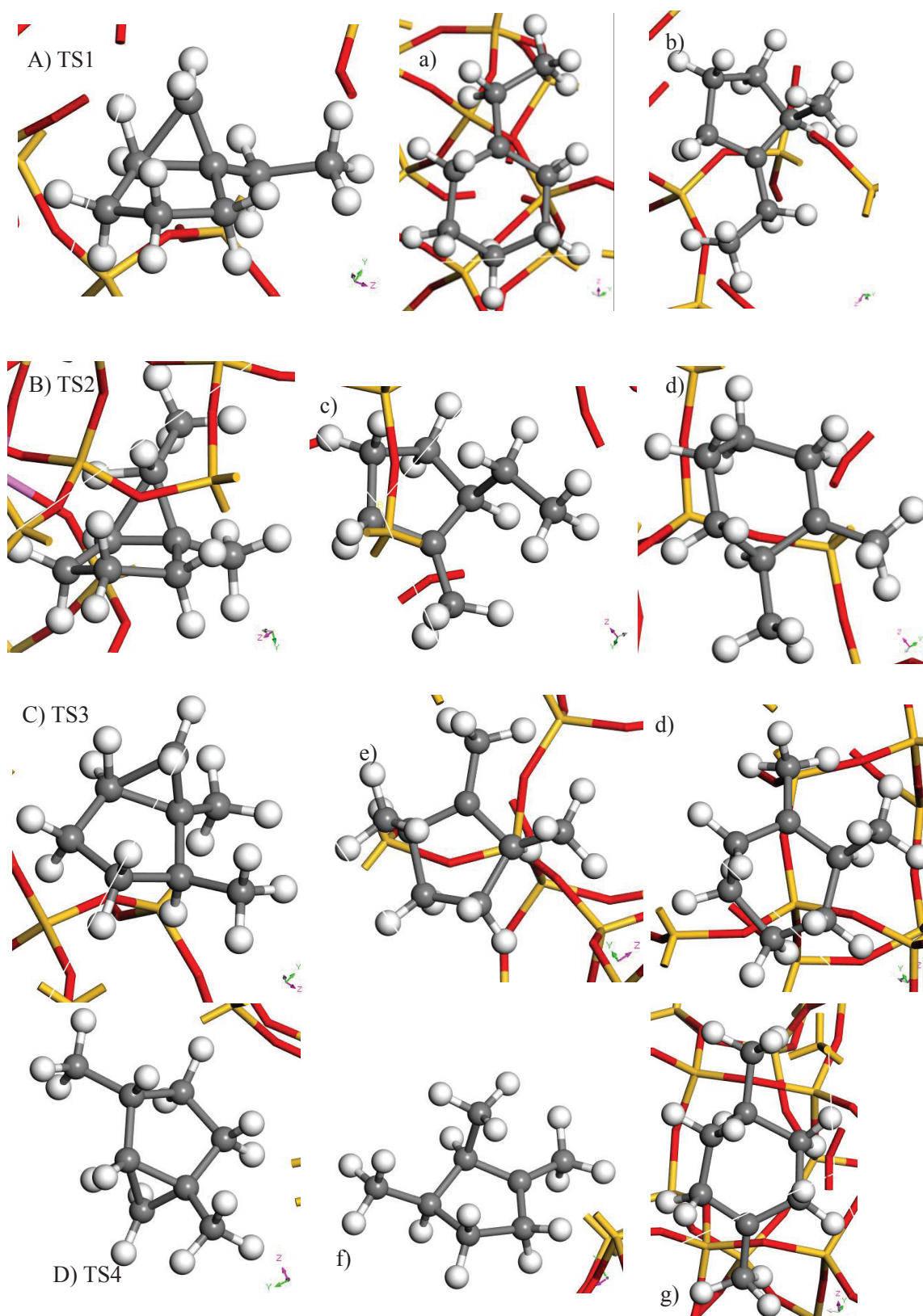


Figure 19. Optimized structures of all the molecules appearing in the reactional scheme in the pocket T9O6.



# APPENDIX



**Figure 19.** Optimized structures of all the molecules appearing in the reactional scheme in the pocket T9O6.

# APPENDIX

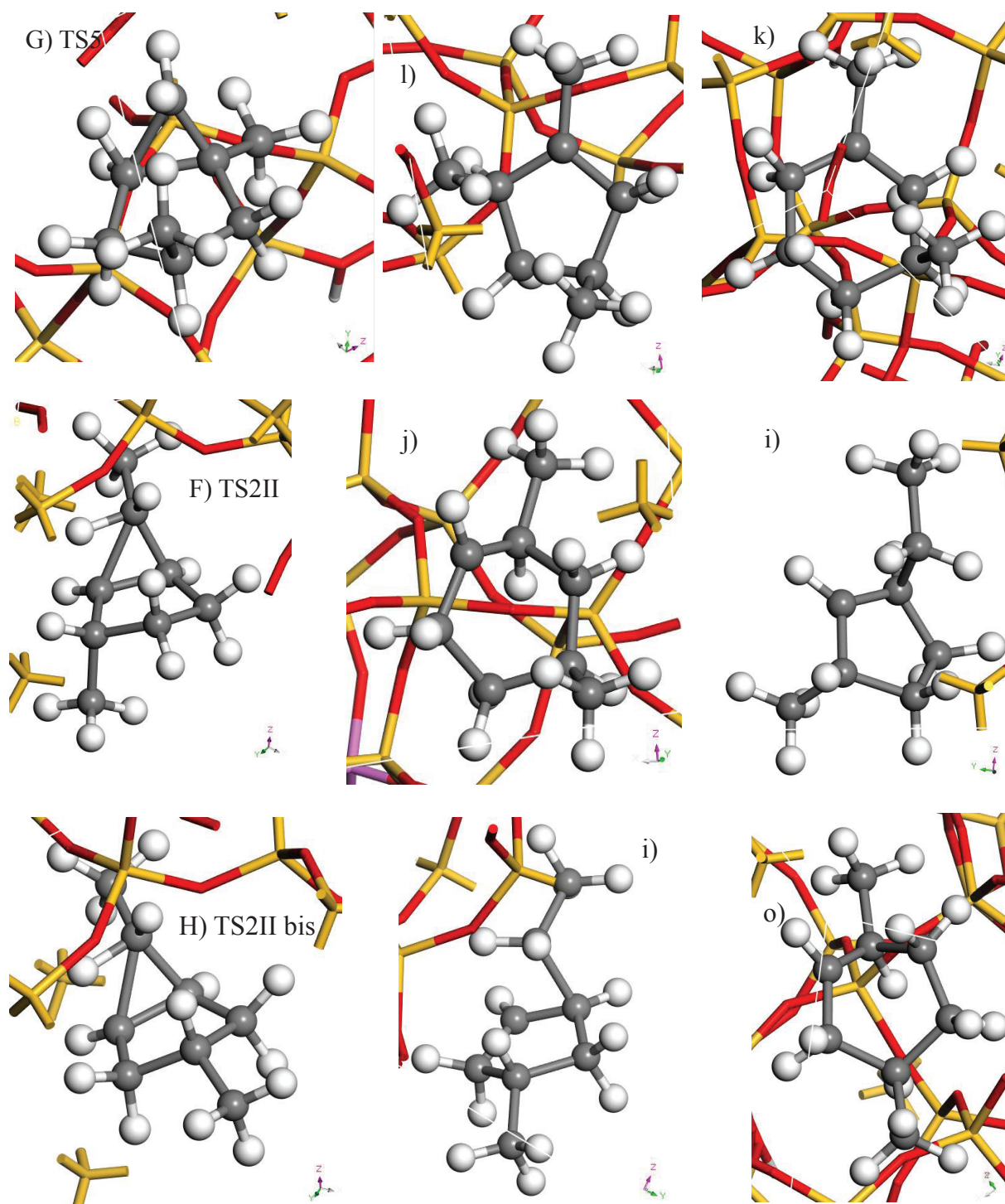


**Figure 19.** Optimized structures of all the molecules appearing in the reaction scheme in the pocket T9O6.

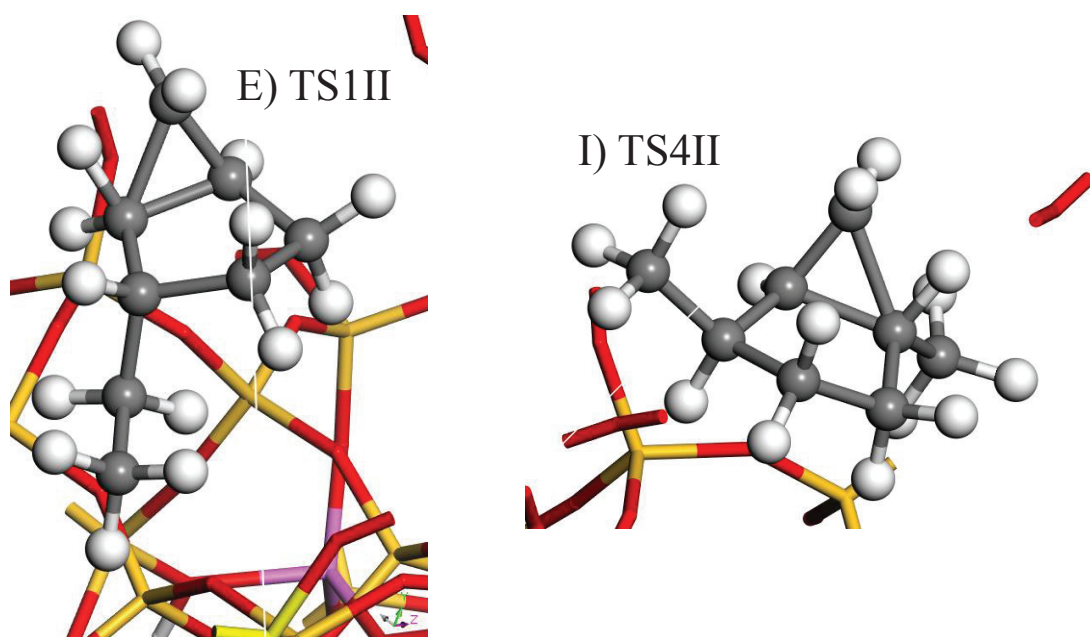


**Figure 20.** Optimized structures of some TS considered in the reactional scheme in the pocket T9O6 but not well optimized (more than one imaginary frequency).

## APPENDIX

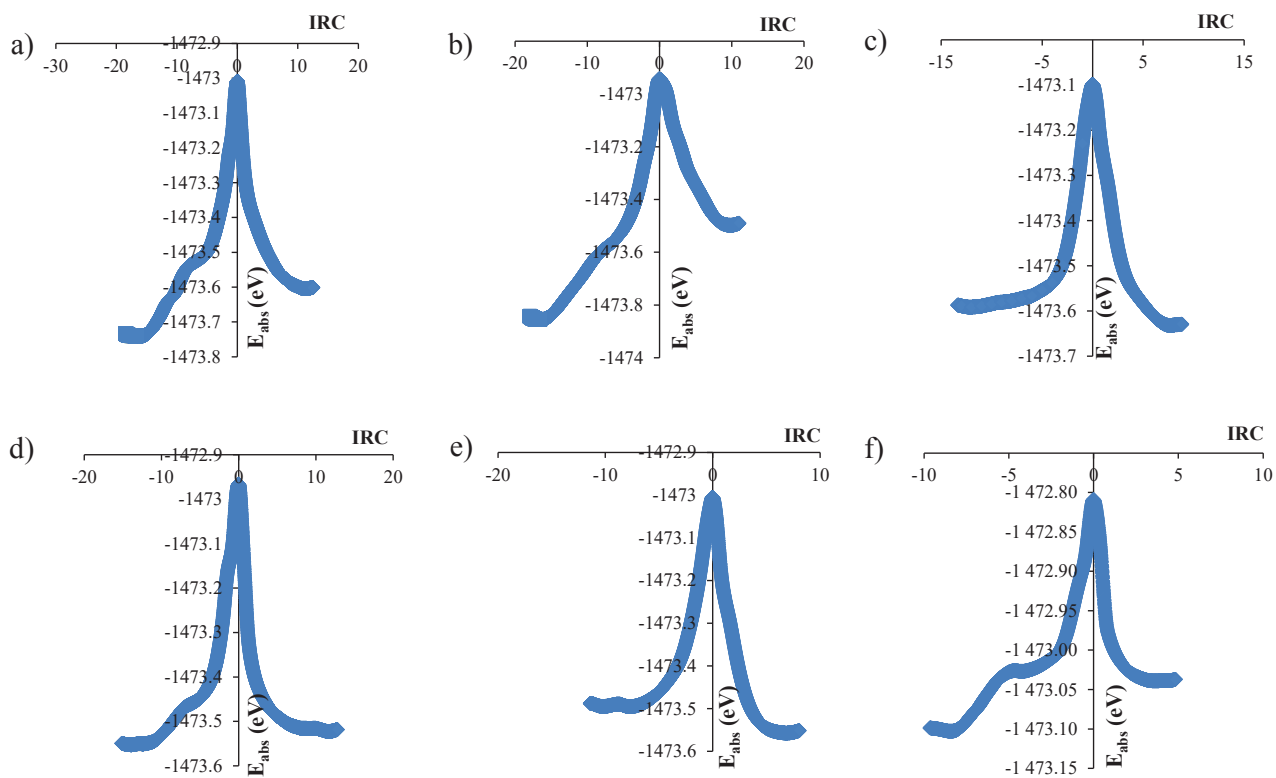


**Figure 21. IRC curves for each ring contraction/expansion elementary steps at the channel T1O1 site: a) TS1, b) TS2, c) TS3, d) TS4, e) TS5, f) TS1II.**

# APPENDIX

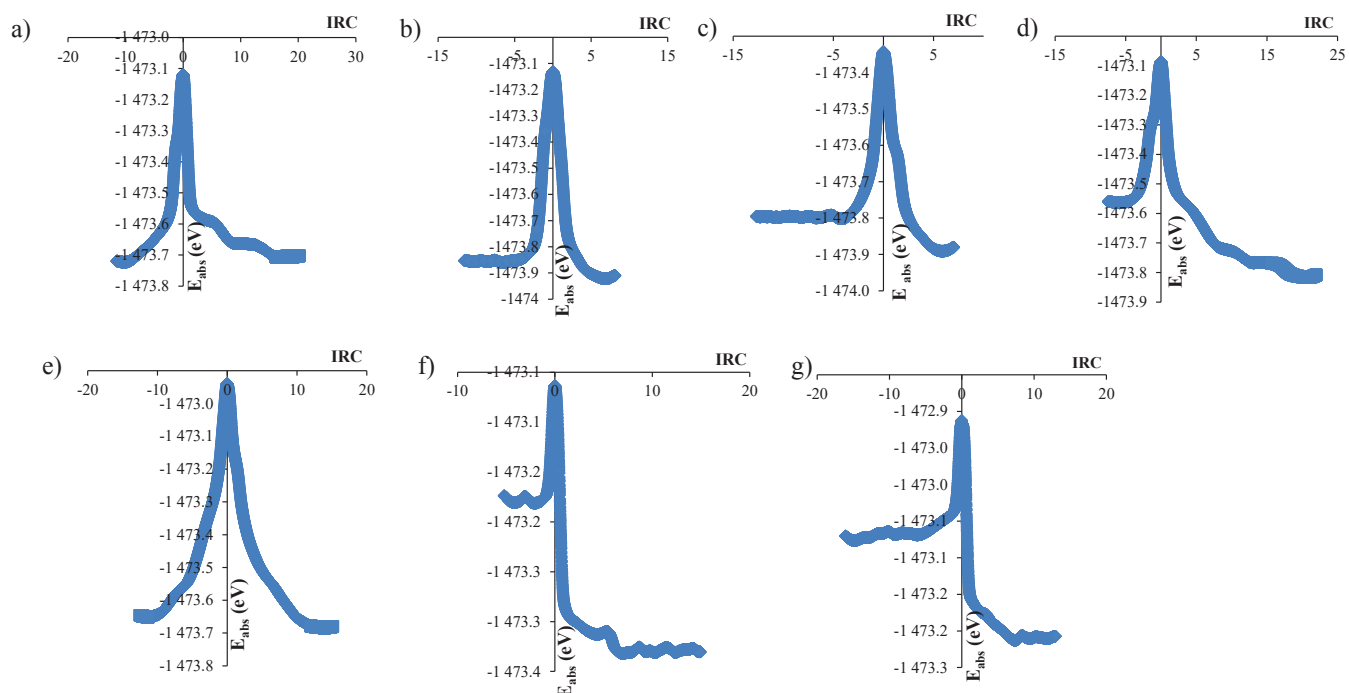
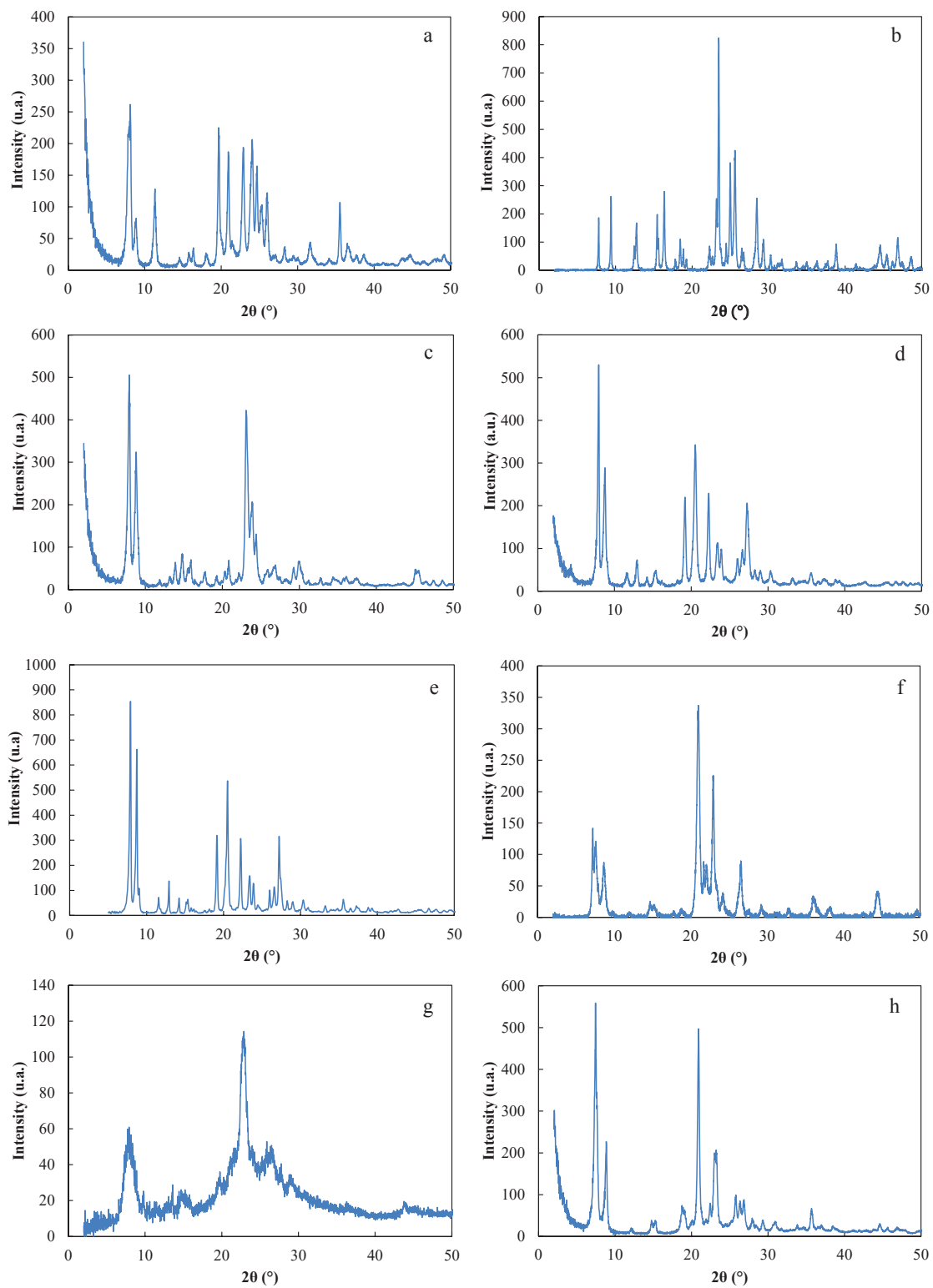


**Figure 22.** IRC curves for each ring contraction/expansion elementary steps in the pocket T9O6 site: a) TS1, b) TS2, c) TS3, d) TS4, e) TS5, f) TS2II, g) TS2bisII.



## APPENDIX VI

## VI.I CHARACTERIZATION



## APPENDIX

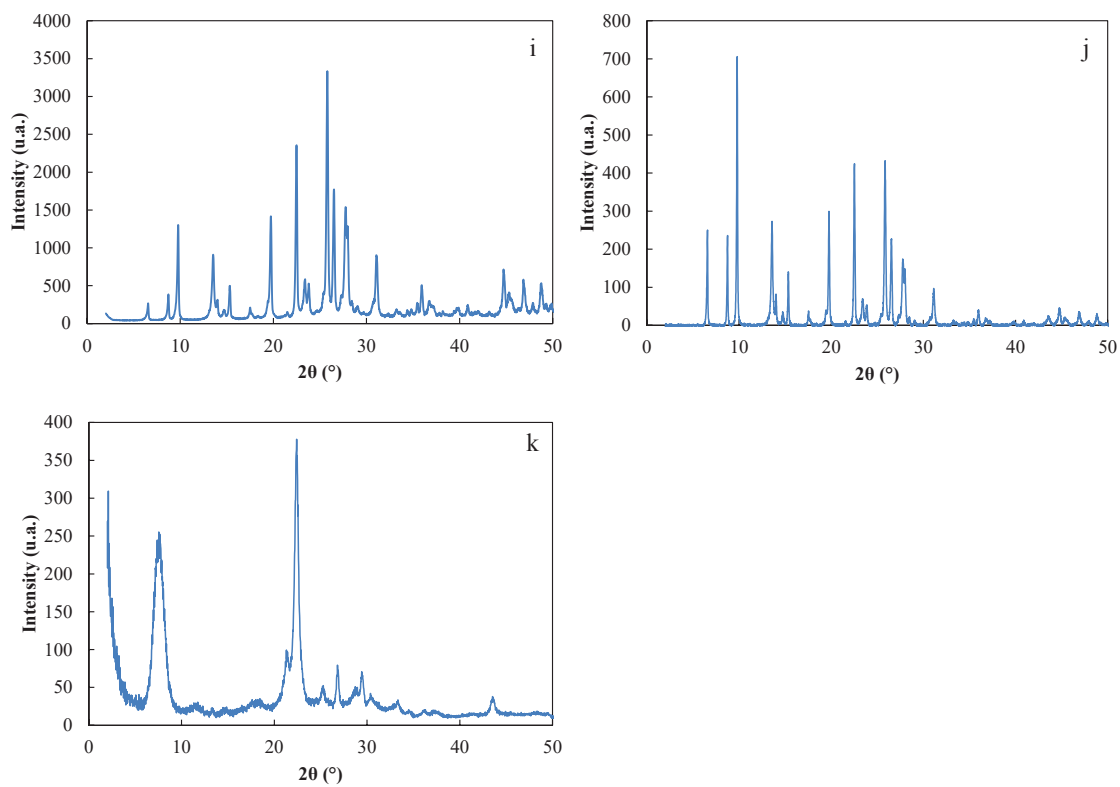


**Figure 23. XRD diffractograms for a) ZSM-23, b) ZSM-57, c) ZSM-5, d) EU-1, e) ZSM-50, f) IZM-2, g) NU-86, h) ZSM-12, i) MOR15, j) MOR50, k) BETA.**

## VI.II CATALYTIC TESTS

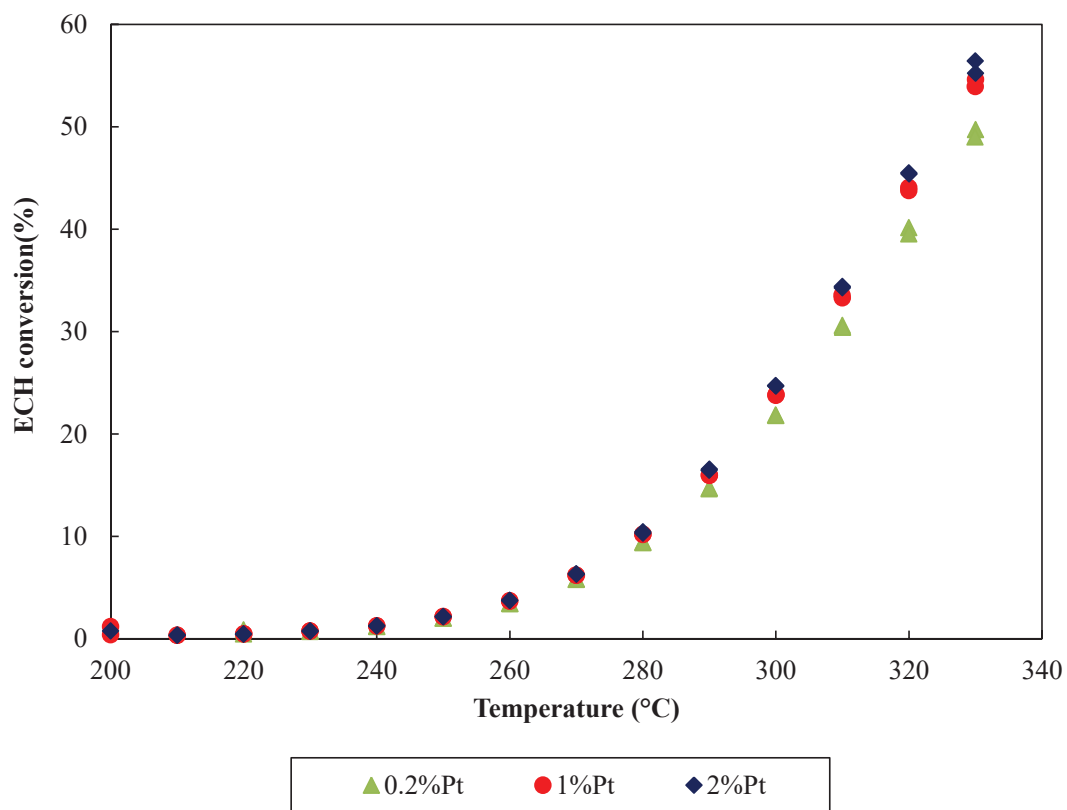
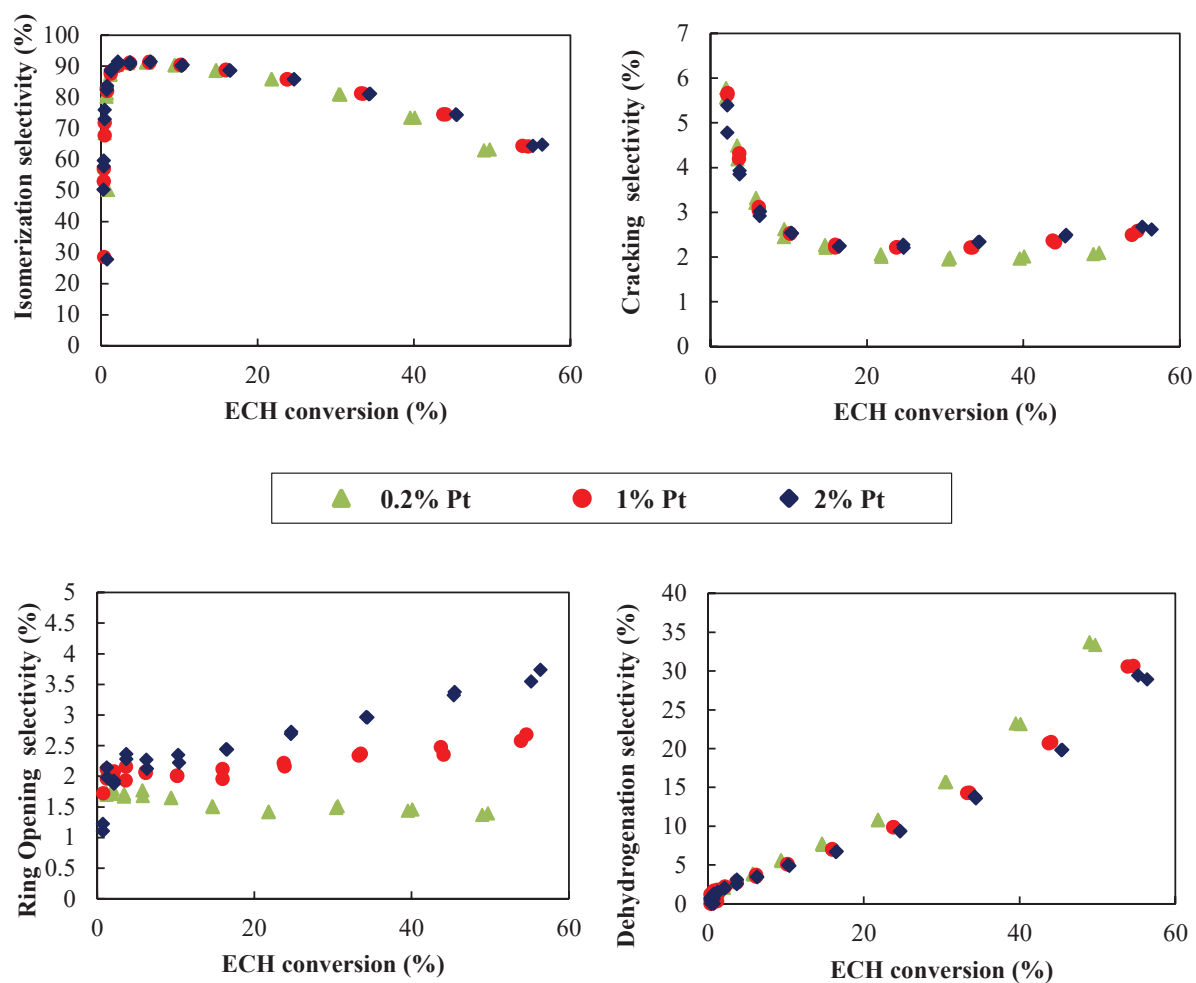


Figure 24. ECH conversion vs temperature for the 1%Pt-  $\text{Al}_2\text{O}_3$ / HZSM-23 catalyst.

## APPENDIX



**Figure 25.** Evolution of the selectivity versus ECH conversion for the 1%Pt-  $\text{Al}_2\text{O}_3$ / HZSM-23 catalyst; a) isomerization; b) cracking; c) ring opening; d) dehydrogenation.

## APPENDIX

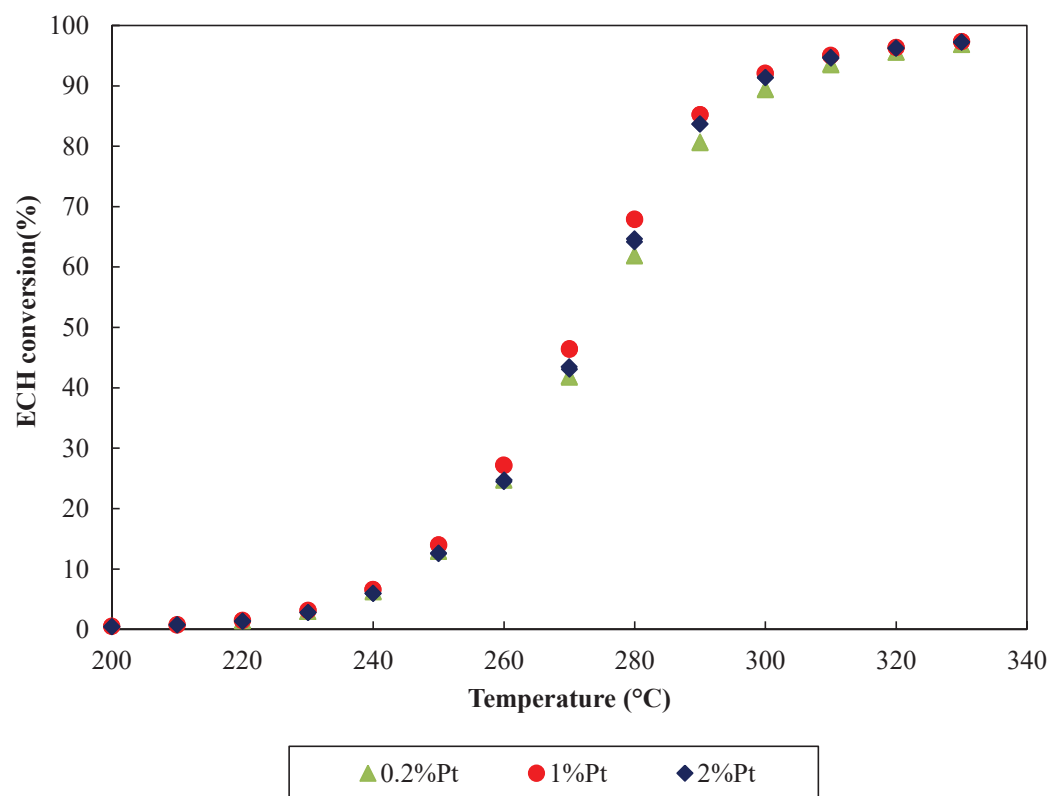
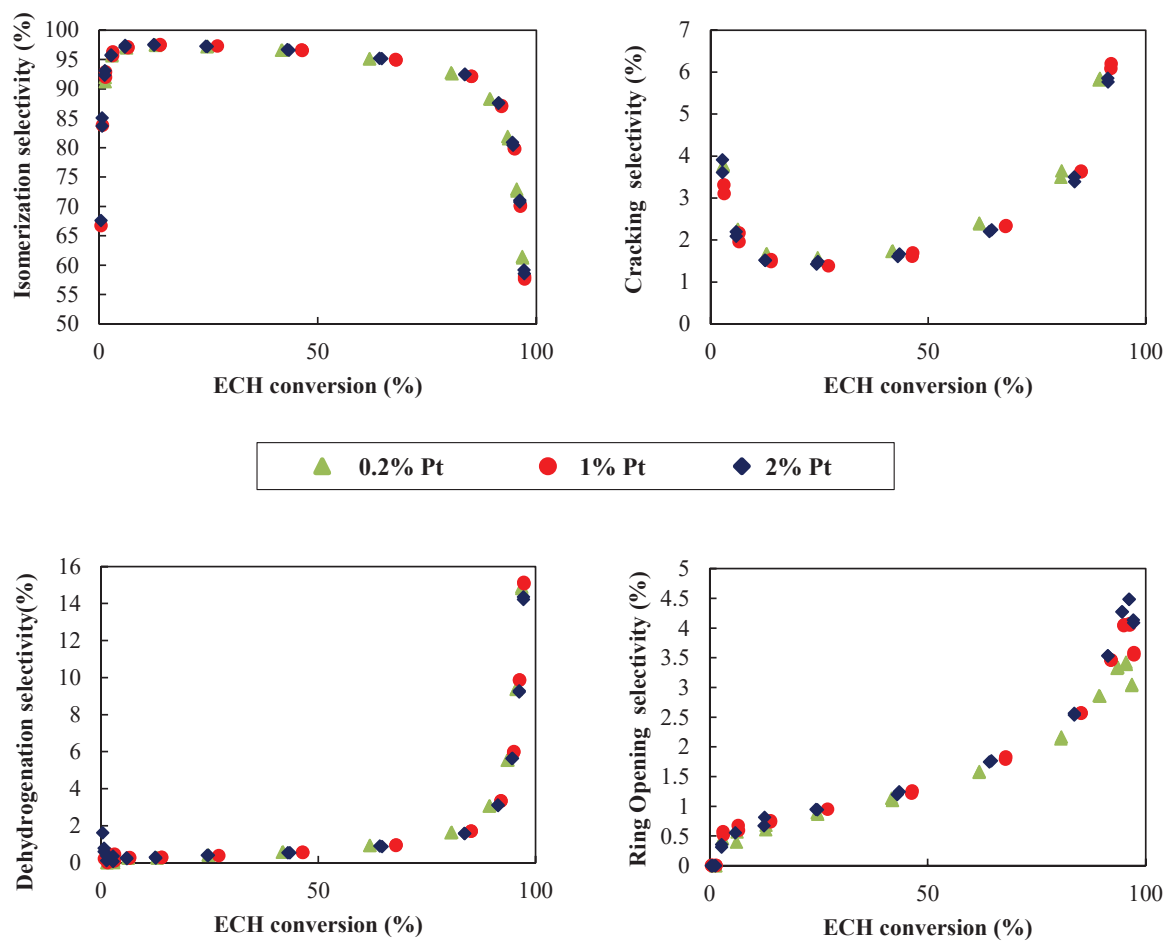


Figure 26 . ECH conversion vs temperature for the 1%Pt-  $\text{Al}_2\text{O}_3$ / HZSM-57 catalyst.

# APPENDIX



**Figure 27. Evolution of the selectivity versus ECH conversion for the 1%Pt- Al<sub>2</sub>O<sub>3</sub>/ HZSM-57 catalyst; a) isomerization; b) cracking; c) ring opening; d) dehydrogenation**

## APPENDIX

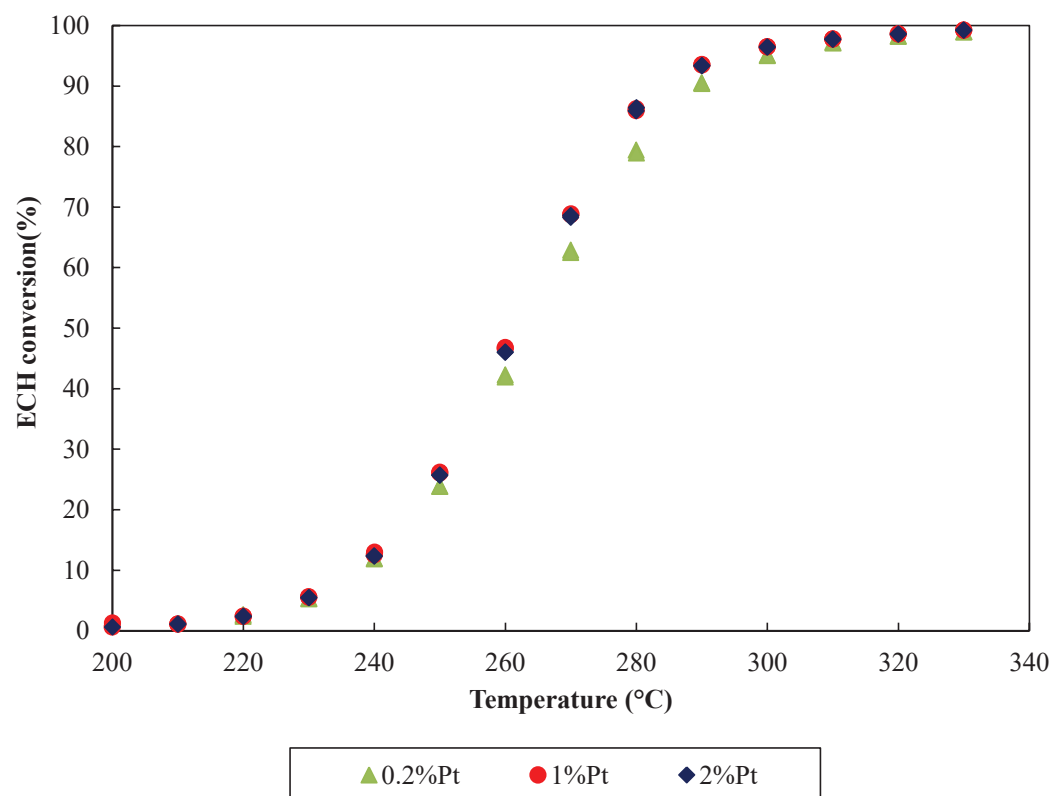


**Figure 28 . ECH conversion vs temperature for the 1%Pt-  $\text{Al}_2\text{O}_3$ / HZSM-5 catalyst.**

## APPENDIX

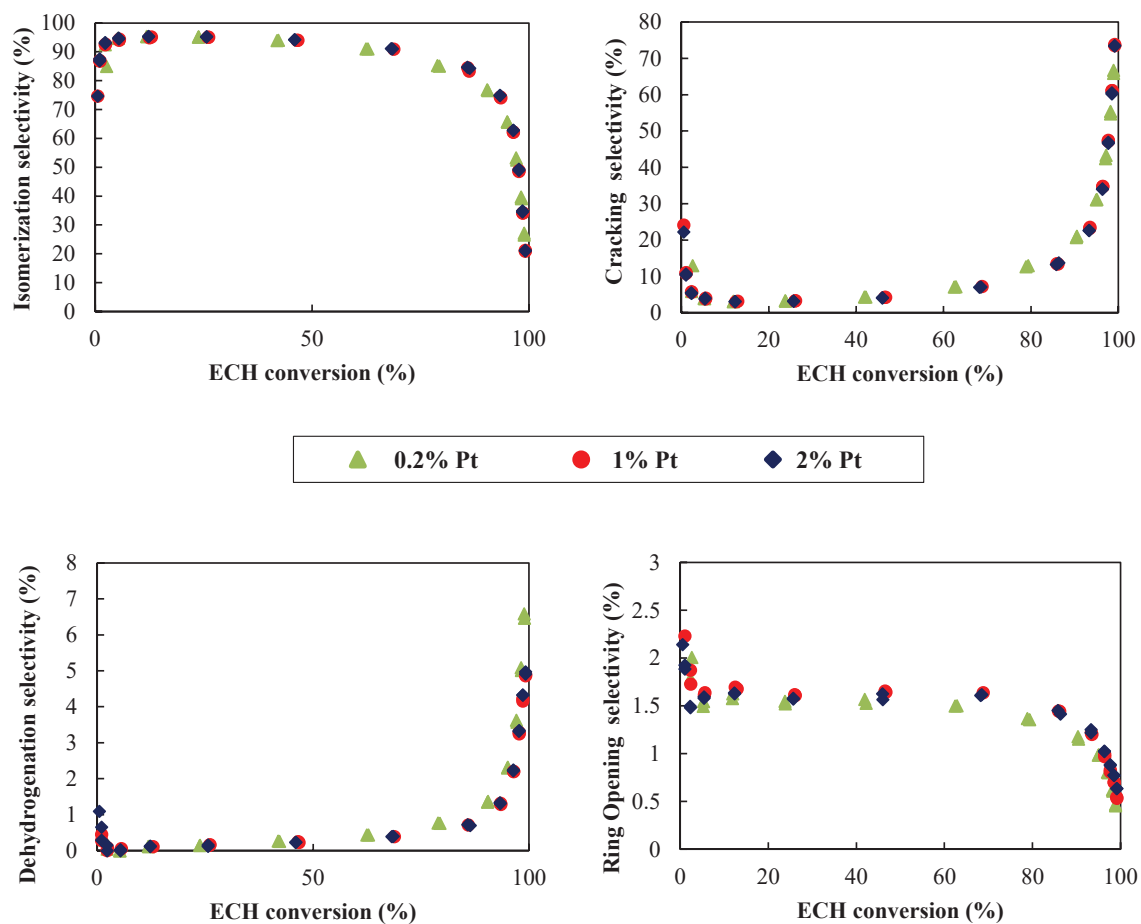


**Figure 29.** Evolution of the selectivity versus ECH conversion for the 1%Pt- Al<sub>2</sub>O<sub>3</sub>/ HZSM-5 catalyst; a) isomerization; b) cracking; c) ring opening; d) dehydrogenation



## APPENDIX

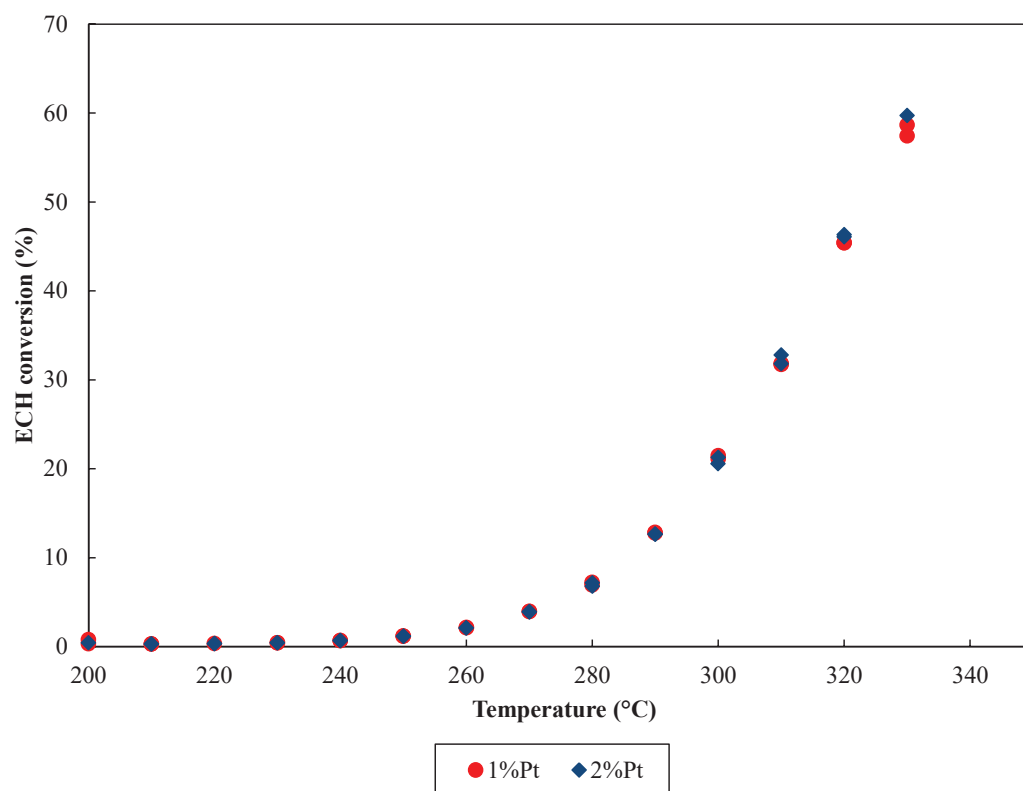


**Figure 30. ECH conversion vs temperature for the 1%Pt-  $\text{Al}_2\text{O}_3$ / HZSM-50 catalyst.**

## APPENDIX

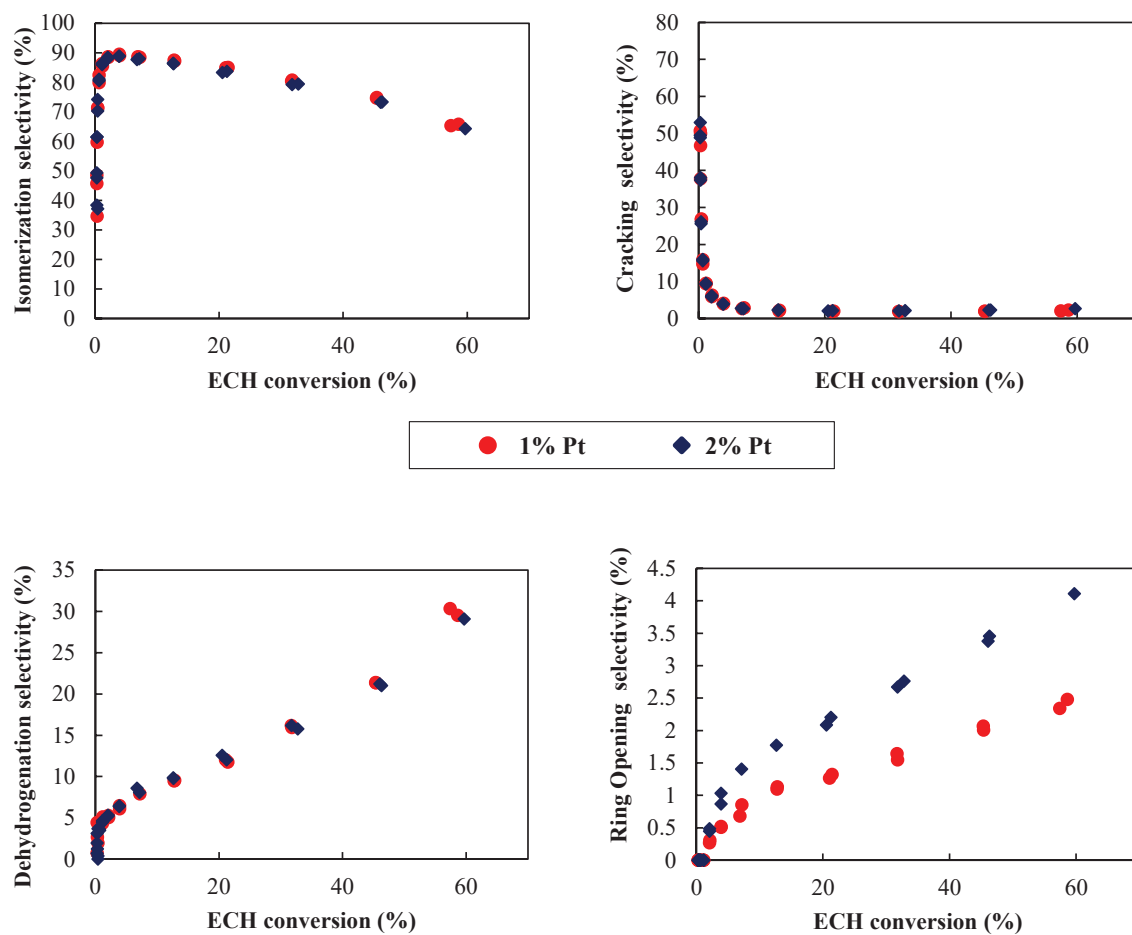


**Figure 31.** Evolution of the selectivity versus ECH conversion for the 1%Pt- Al<sub>2</sub>O<sub>3</sub>/ HZSM-50 catalyst; a) isomerization; b) cracking; c) ring opening; d) dehydrogenation

## APPENDIX

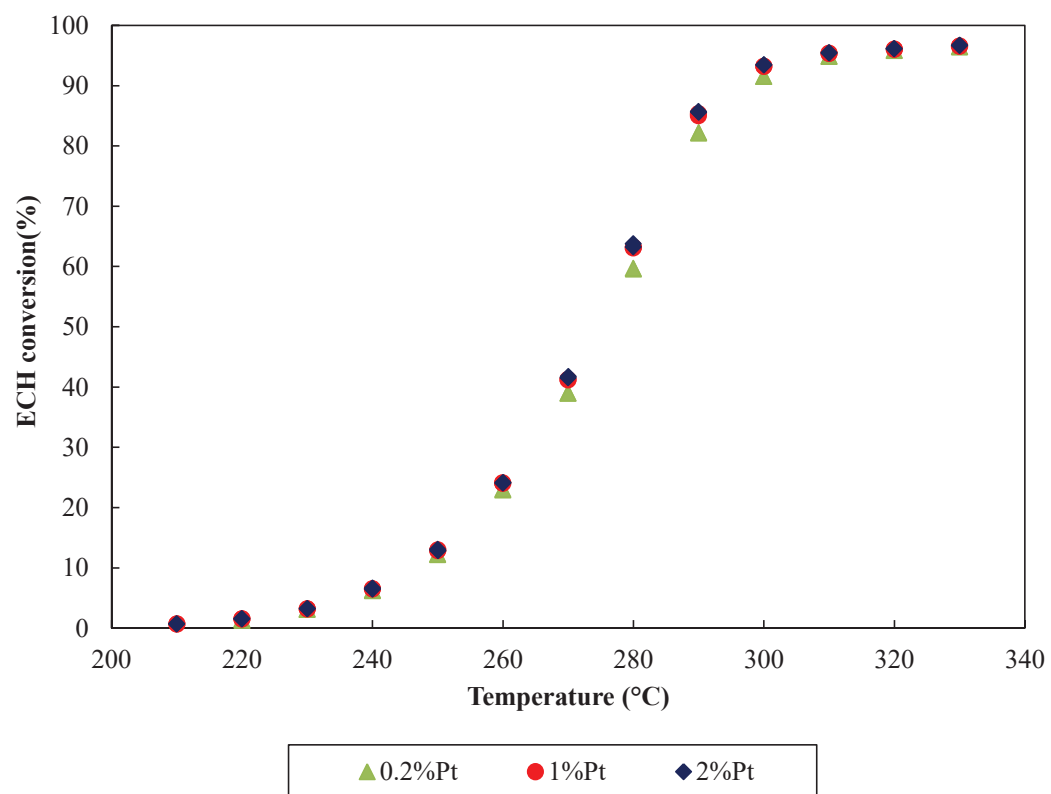


**Figure 32 . ECH conversion vs temperature for the 1%Pt- Al<sub>2</sub>O<sub>3</sub>/ HIZM-2 catalyst.**

## APPENDIX

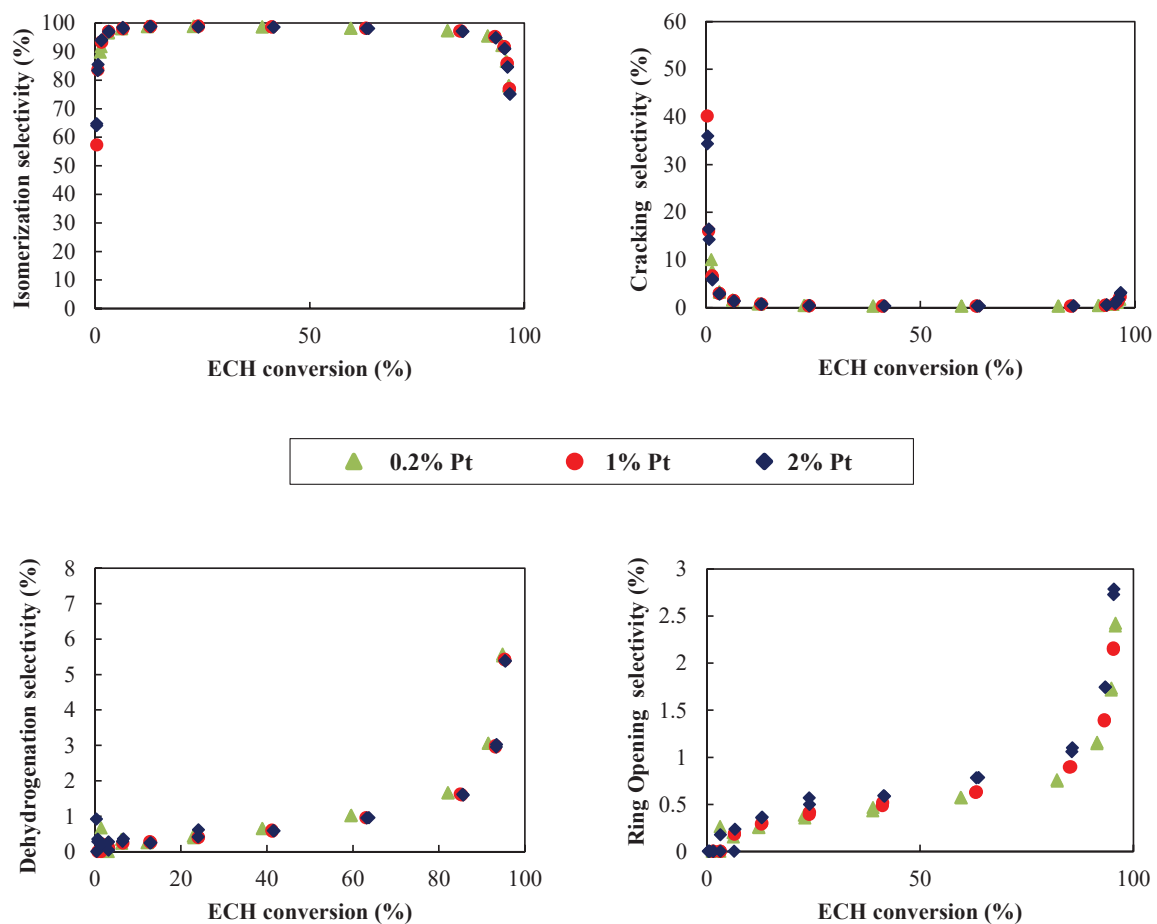


**Figure 33. Evolution of the selectivity versus ECH conversion for the 1%Pt- Al<sub>2</sub>O<sub>3</sub>/ HIZM-2 catalyst; a) isomerization; b) cracking; c) ring opening; d) dehydrogenation.**

## APPENDIX

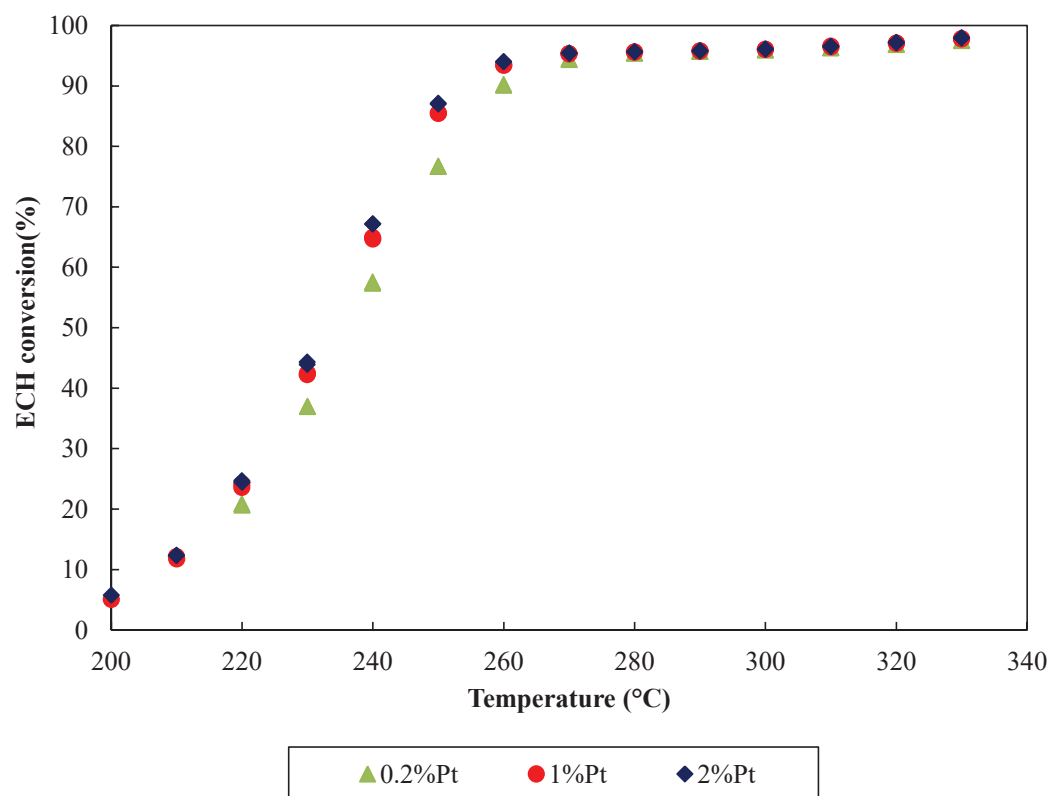


**Figure 34. ECH conversion vs temperature for the 1%Pt-  $\text{Al}_2\text{O}_3$ / HNU-86 catalyst.**

## APPENDIX

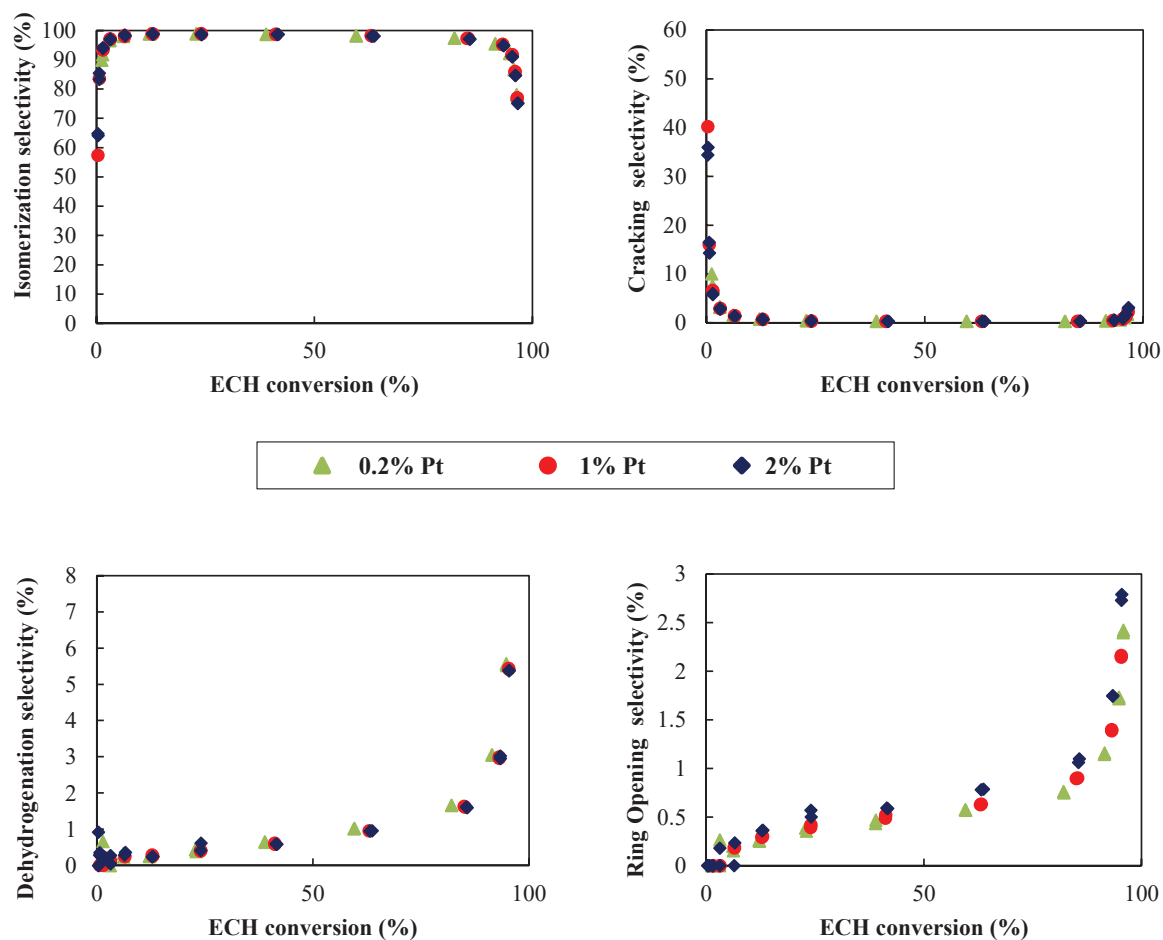


**Figure 35.** Evolution of the selectivity versus ECH conversion for the 1%Pt-  $\text{Al}_2\text{O}_3$ / HNU-86 catalyst; a) isomerization; b) cracking; c) ring opening; d) dehydrogenation.

# APPENDIX

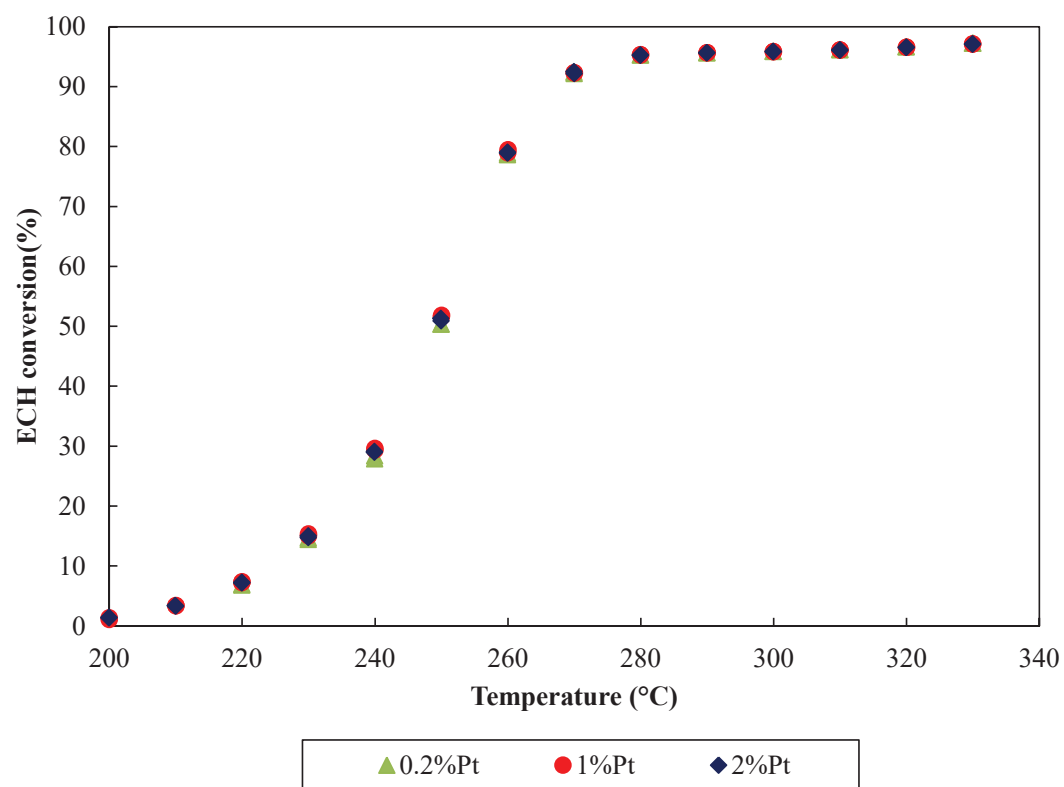


**Figure 36. ECH conversion vs temperature for the 1%Pt-  $\text{Al}_2\text{O}_3$ / HZSM-12 catalyst.**

## APPENDIX

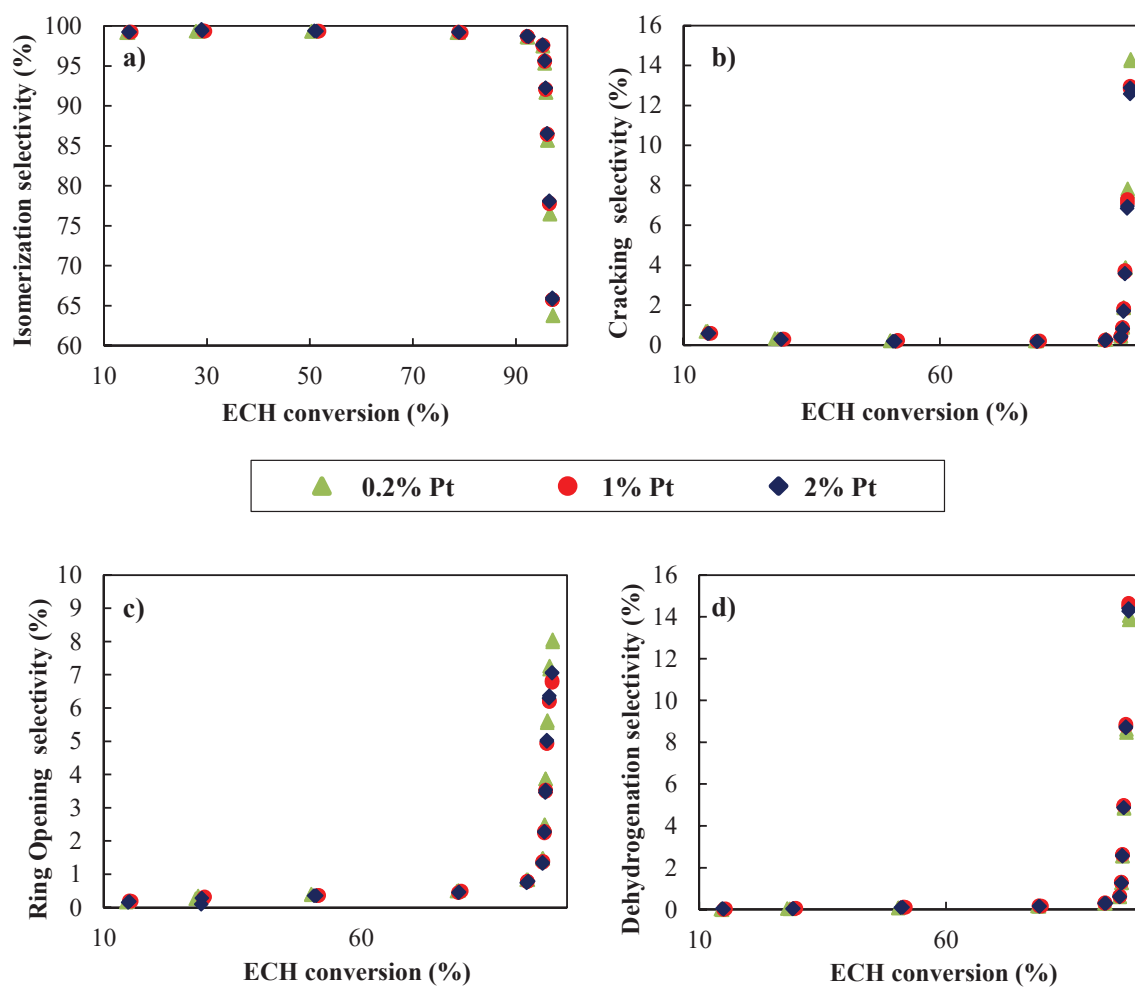


**Figure 37. Evolution of the selectivity versus ECH conversion for the 1%Pt- Al<sub>2</sub>O<sub>3</sub>/HZSM-12 catalyst; a) isomerization; b) cracking; c) ring opening; d) dehydrogenation.**



## APPENDIX

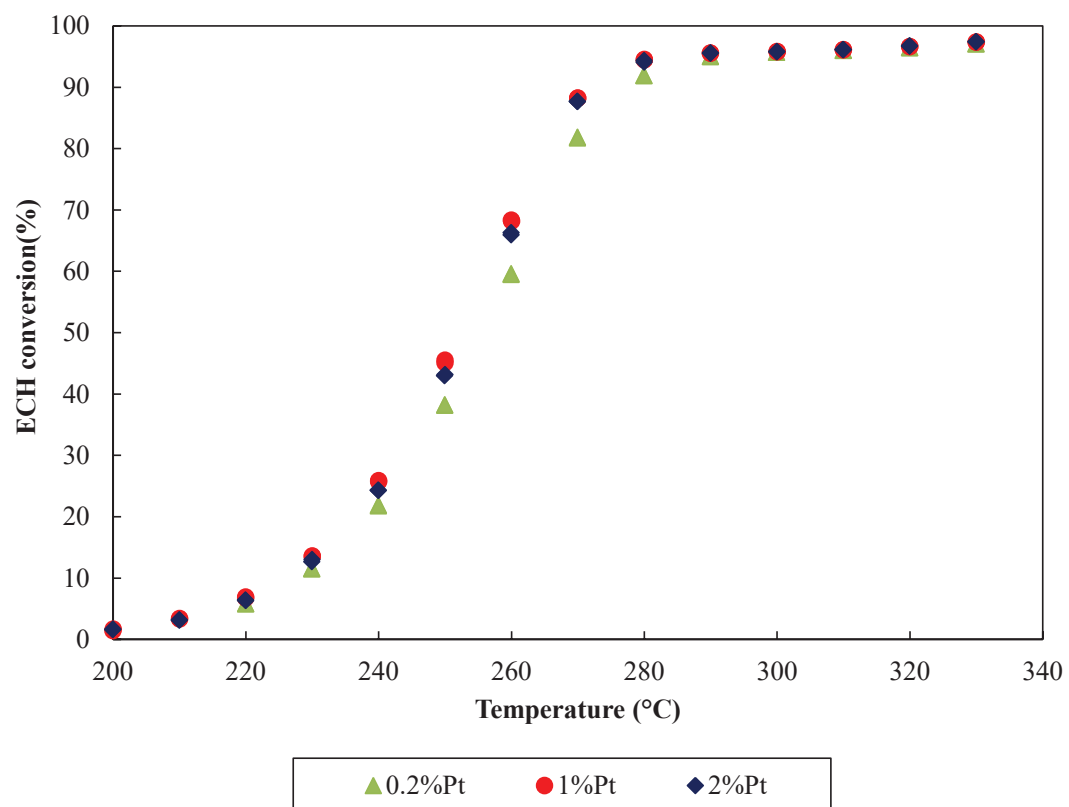


**Figure 38.** ECH conversion vs temperature for the 1%Pt-  $\text{Al}_2\text{O}_3$ / HMOR50 catalyst.

## APPENDIX

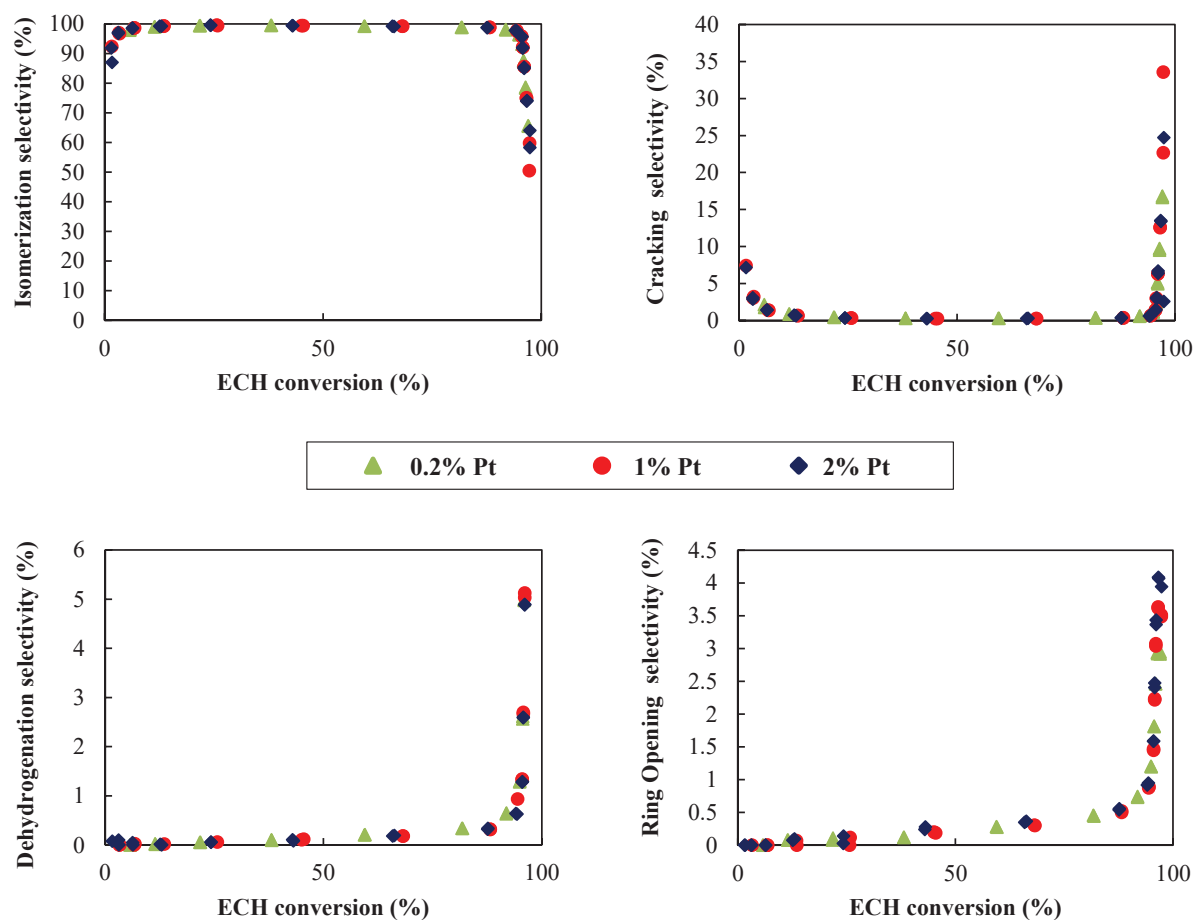


**Figure 39.** Evolution of the selectivity versus ECH conversion for the 1%Pt-  $\text{Al}_2\text{O}_3/\text{HMOR50}$  catalyst; a) isomerization; b) cracking; c) ring opening; d) dehydrogenation.

# APPENDIX

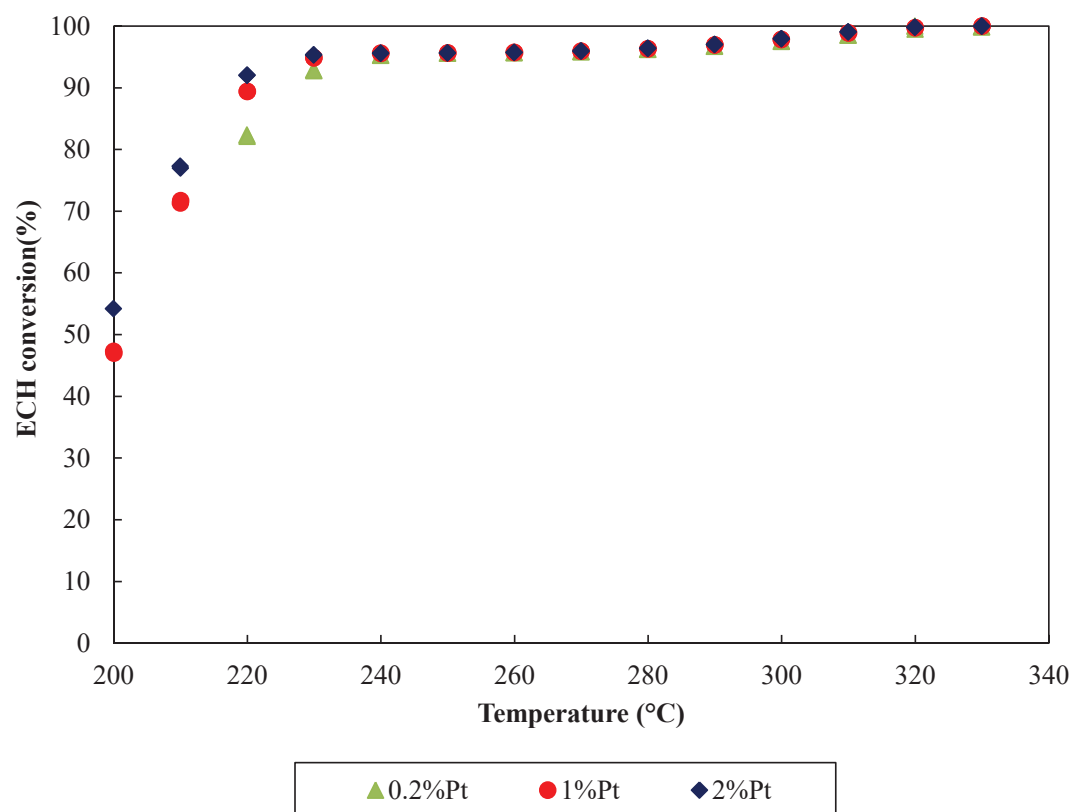


**Figure 40. ECH conversion vs temperature for the 1%Pt-  $\text{Al}_2\text{O}_3$ / HBETA catalyst.**

## APPENDIX

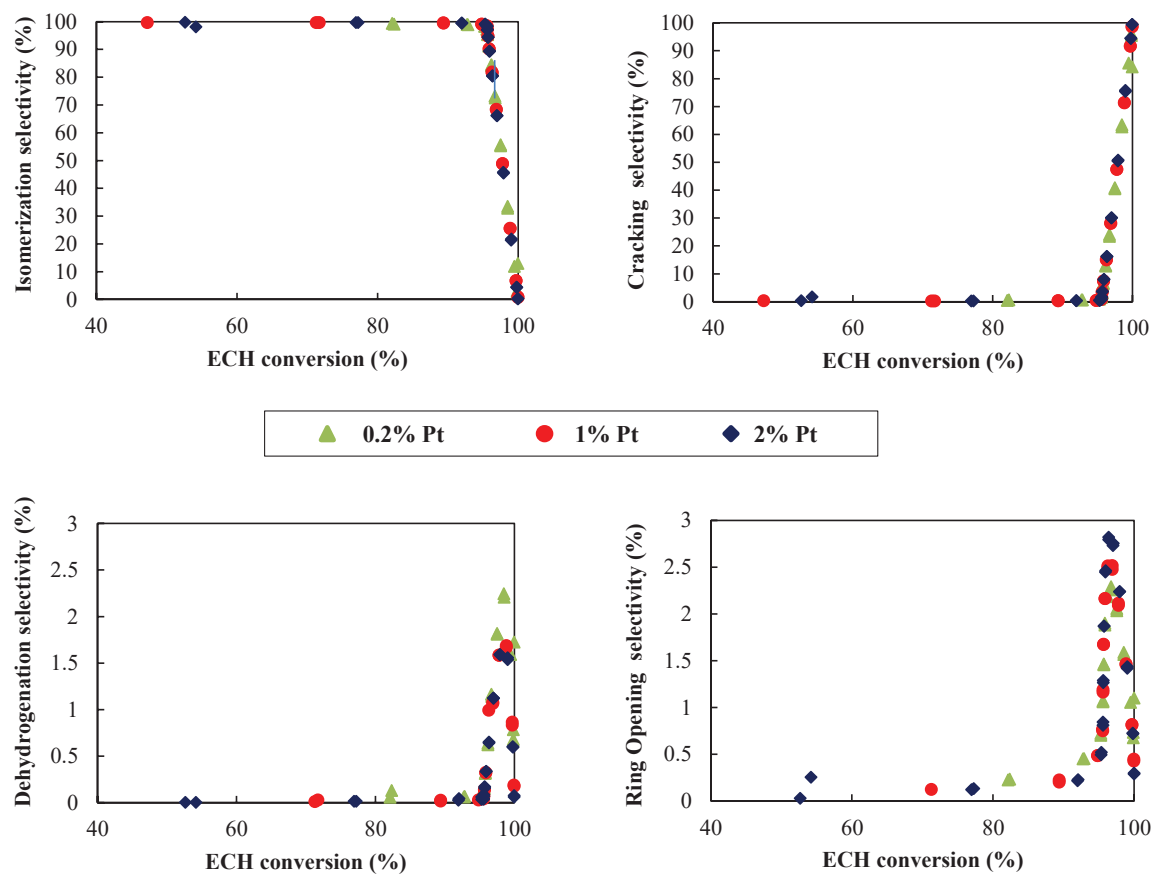


**Figure 41.** Evolution of the selectivity versus ECH conversion for the 1%Pt-  $\text{Al}_2\text{O}_3/\text{HBETA}$  catalyst; a) isomerization; b) cracking; c) ring opening; d) dehydrogenation.

## VI.III PROII RESULTS

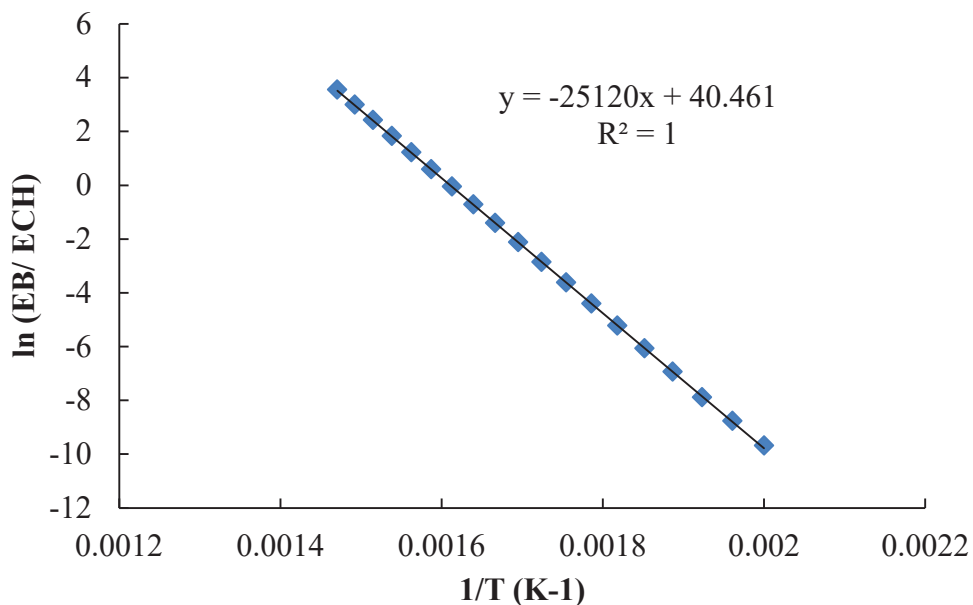


Figure 42. Evolution of  $\ln(\text{wt}\%\text{EB}/\text{wt}\%\text{ECH})$  with  $1/T$  evaluated with PROII (p=10 bar,  $\text{H}_2/\text{ECH} = 30$ )

## VI.IV PRODUCTS DISTRIBUTION

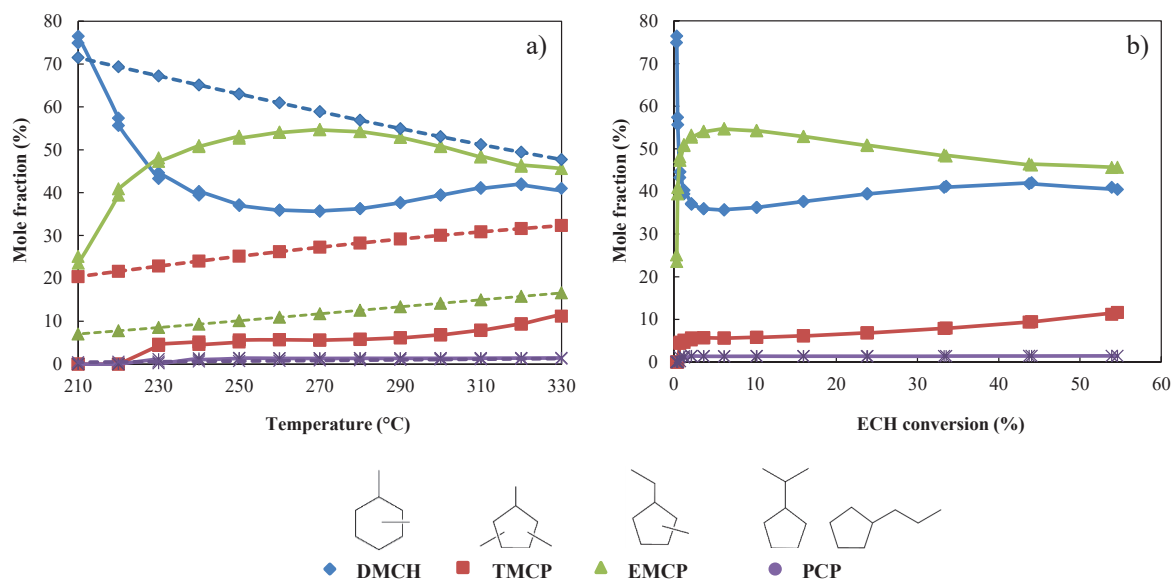
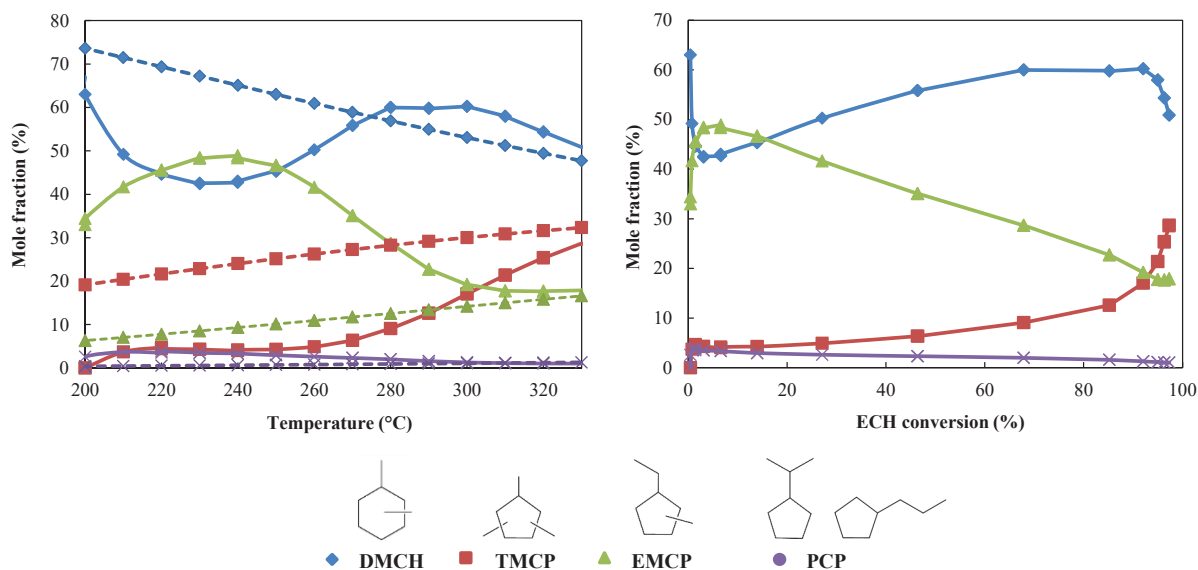
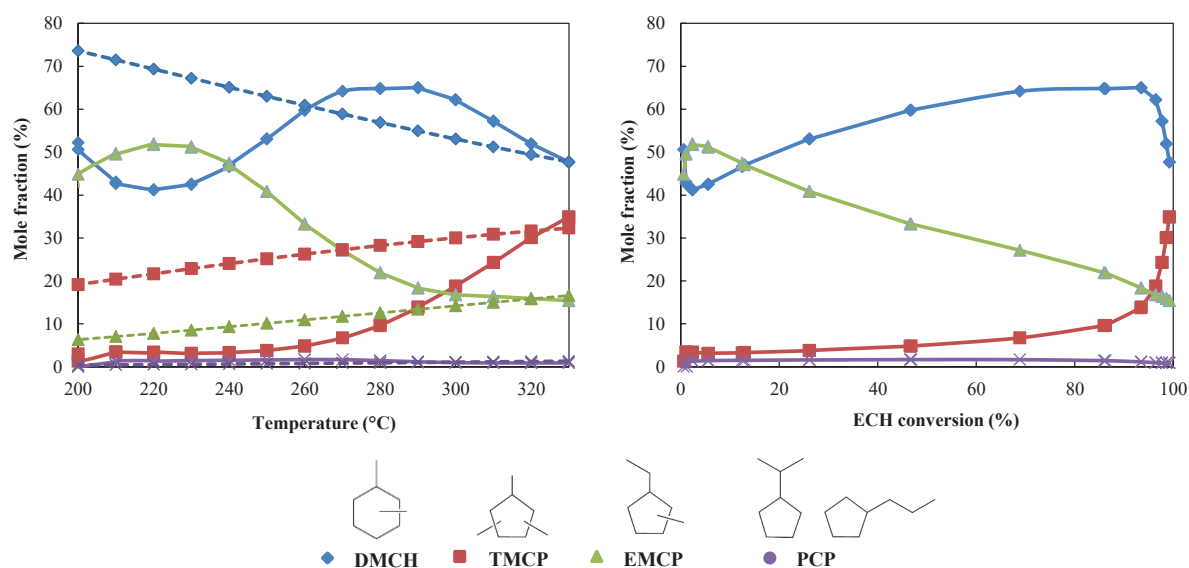


Figure 43. Evolution of the mole fraction of the grouped isomers a) versus temperature at thermodynamic equilibrium (dashed line, PRO II simulation) and as observed experimentally (full line) b) versus conversion for 1% Pt-Al<sub>2</sub>O<sub>3</sub>/HZSM-23 catalyst.

## APPENDIX



**Figure 44.** Evolution of the mole fraction of the grouped isomers a) versus temperature at thermodynamic equilibrium (dashed line, PRO II simulation) and as observed experimentally (full line) b) versus conversion for 1% Pt-Al<sub>2</sub>O<sub>3</sub>/HZSM-57 catalyst.



**Figure 45.** Evolution of the mole fraction of the grouped isomers a) versus temperature at thermodynamic equilibrium (dashed line, PRO II simulation) and as observed experimentally (full line) b) versus conversion for 1% Pt-Al<sub>2</sub>O<sub>3</sub>/HZSM-5 catalyst.

# APPENDIX

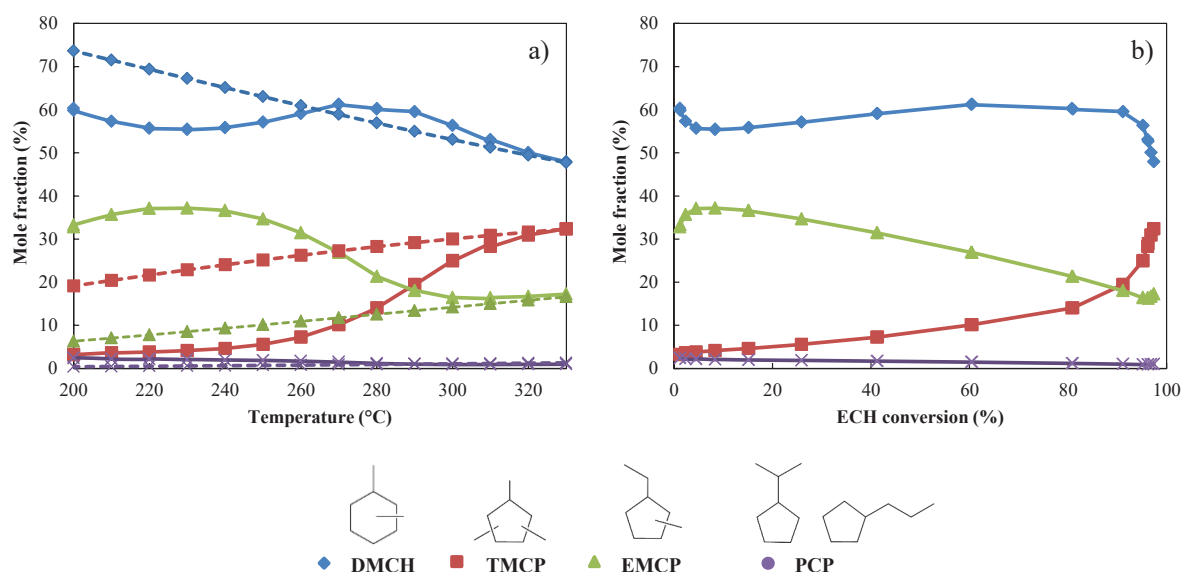


Figure 46. Evolution of the mole fraction of the grouped isomers a) versus temperature at thermodynamic equilibrium (dashed line, PRO II simulation) and as observed experimentally (full line) b) versus conversion for 1% Pt-Al<sub>2</sub>O<sub>3</sub>/HEU-1 catalyst.

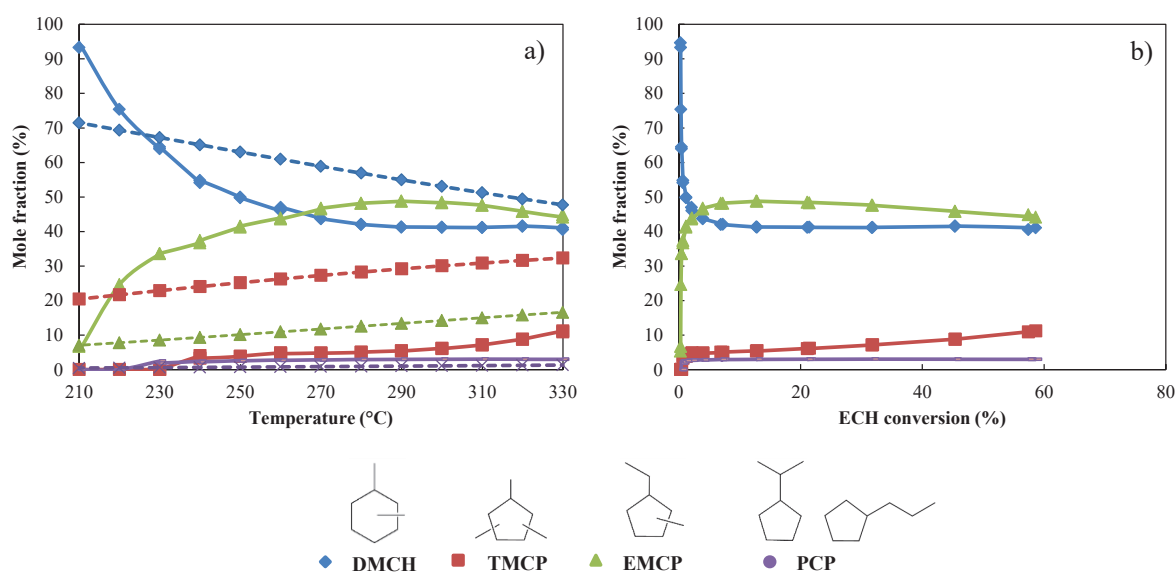


Figure 47. Evolution of the mole fraction of the grouped isomers a) versus temperature at thermodynamic equilibrium (dashed line, PRO II simulation) and as observed experimentally (full line) b) versus conversion for 1% Pt-Al<sub>2</sub>O<sub>3</sub>/HZSM-50 catalyst.

# APPENDIX

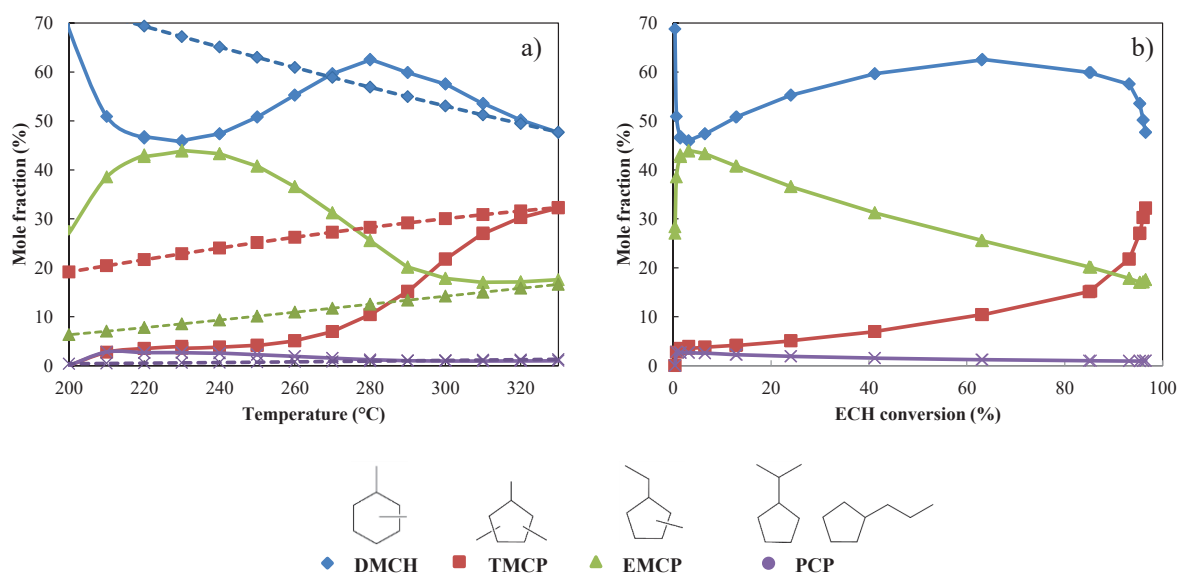


Figure 48. Evolution of the mole fraction of the grouped isomers a) versus temperature at thermodynamic equilibrium (dashed line, PRO II simulation) and as observed experimentally (full line) b) versus conversion for 1% Pt-Al<sub>2</sub>O<sub>3</sub>/HIZM-2 catalyst.

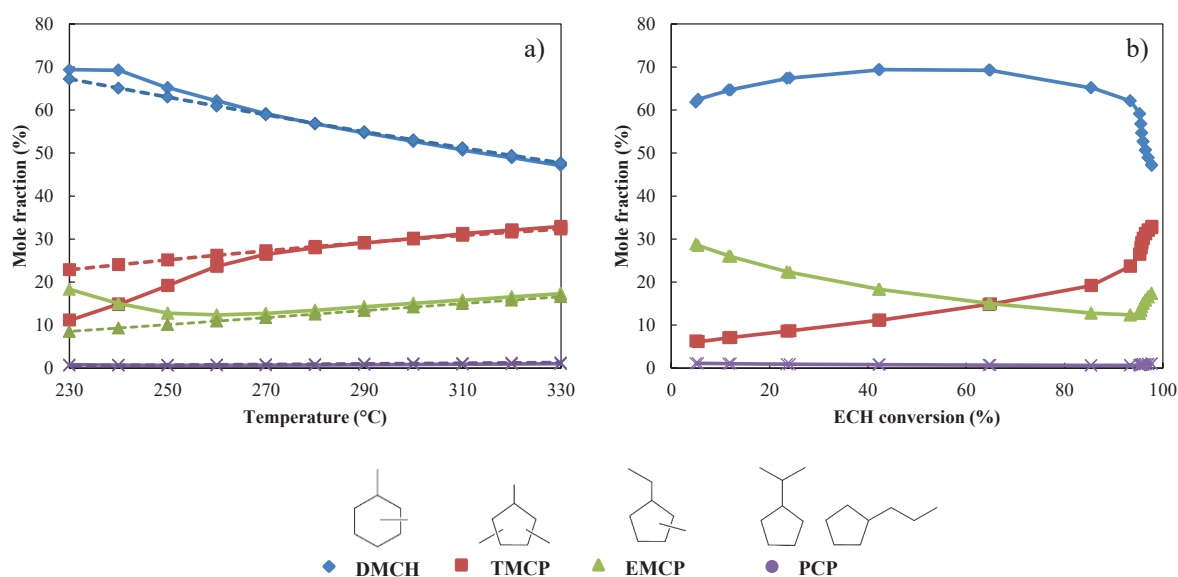
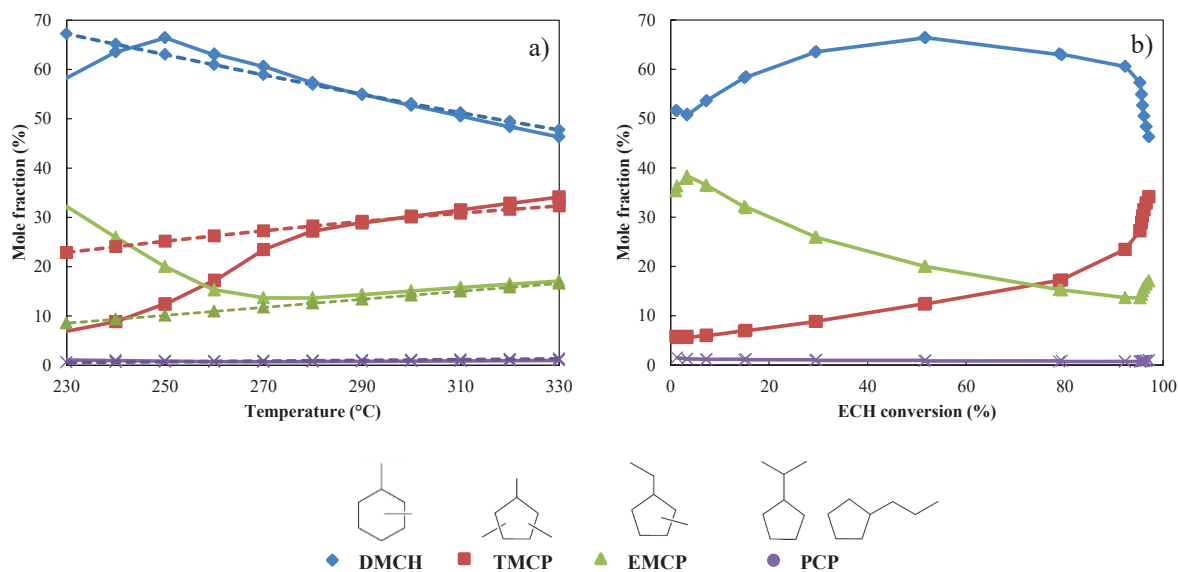


Figure 49. Evolution of the mole fraction of the grouped isomers a) versus temperature at thermodynamic equilibrium (dashed line, PRO II simulation) and as observed experimentally (full line) b) versus conversion for 1% Pt-Al<sub>2</sub>O<sub>3</sub>/HNU-86 catalyst.



## APPENDIX



**Figure 50.** Evolution of the mole fraction of the grouped isomers a) versus temperature at thermodynamic equilibrium (dashed line, PRO II simulation) and as observed experimentally (full line) b) versus conversion for 1% Pt-Al<sub>2</sub>O<sub>3</sub>/HZSM-12 catalyst.

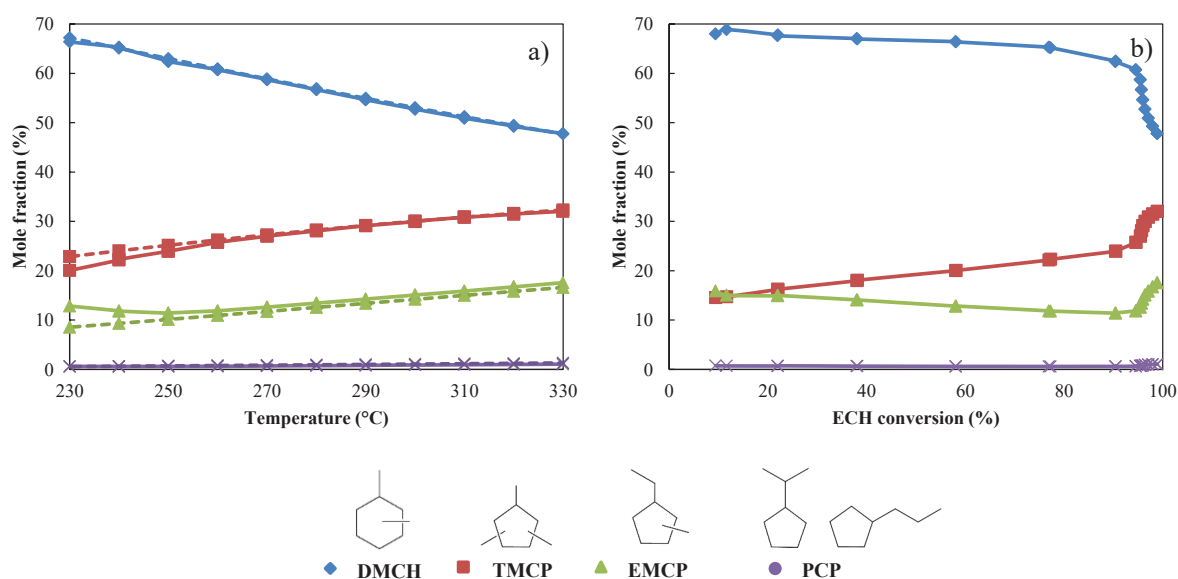


**Figure 51.** Evolution of the mole fraction of the grouped isomers a) versus temperature at thermodynamic equilibrium (dashed line, PRO II simulation) and as observed experimentally (full line) b) versus conversion for 1% Pt-Al<sub>2</sub>O<sub>3</sub>/HMOR15 catalyst.

## APPENDIX

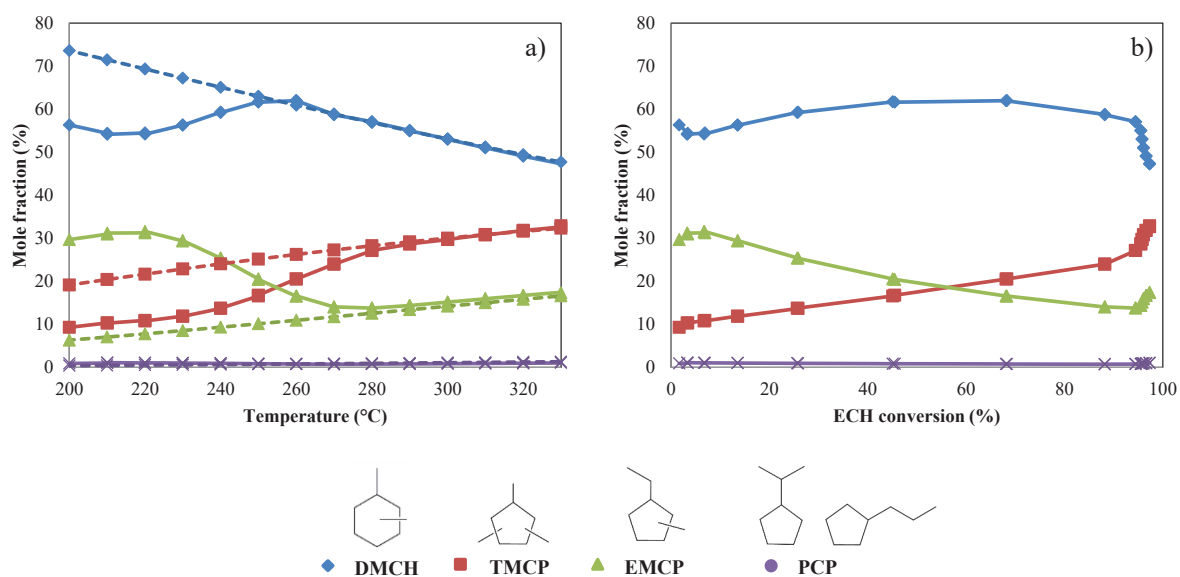


Figure 52. Evolution of the mole fraction of the grouped isomers a) versus temperature at thermodynamic equilibrium (dashed line, PRO II simulation) and as observed experimentally (full line) b) versus conversion for 1% Pt-Al<sub>2</sub>O<sub>3</sub>/HMOR50 catalyst.

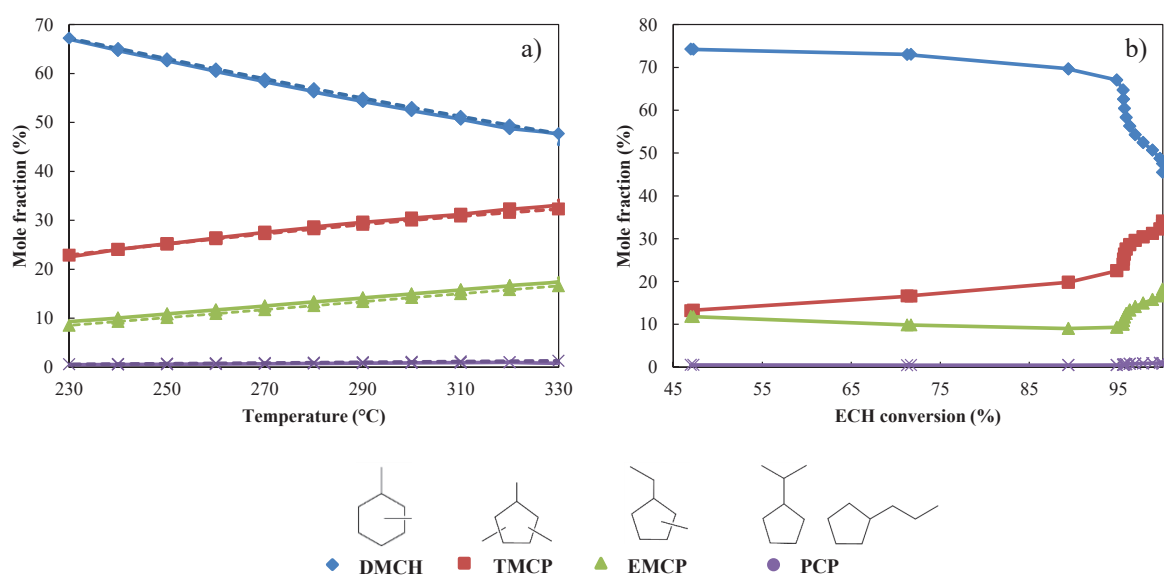


Figure 53. Evolution of the mole fraction of the grouped isomers a) versus temperature at thermodynamic equilibrium (dashed line, PRO II simulation) and as observed experimentally (full line) b) versus conversion for 1% Pt-Al<sub>2</sub>O<sub>3</sub>/HBETA catalyst.

## VI.I ZEOLITES STRUCTURES BY MATERIALS STUDIO

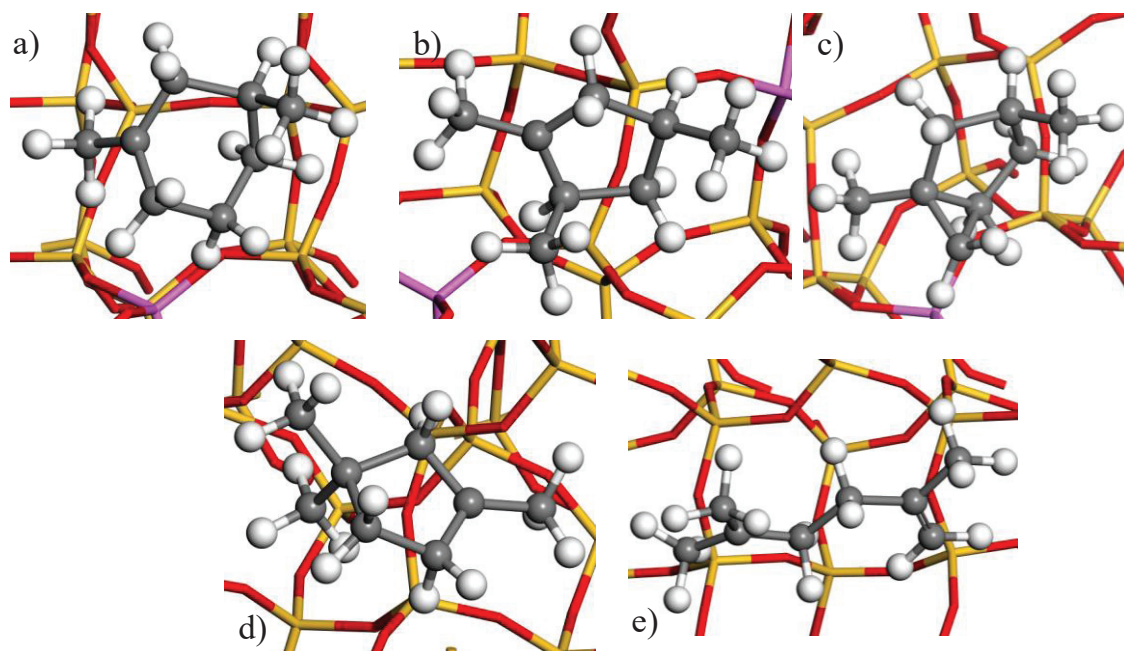


Figure 54. Optimized structures of all the molecules analyzed in the T2O1 active site of HZSM-23 zeolite. a) 13-DMCH<sup>+</sup>, b) 124-TMCP<sup>+</sup>, c) TS5, d) 133-TMCP and e) 25-DmHx.

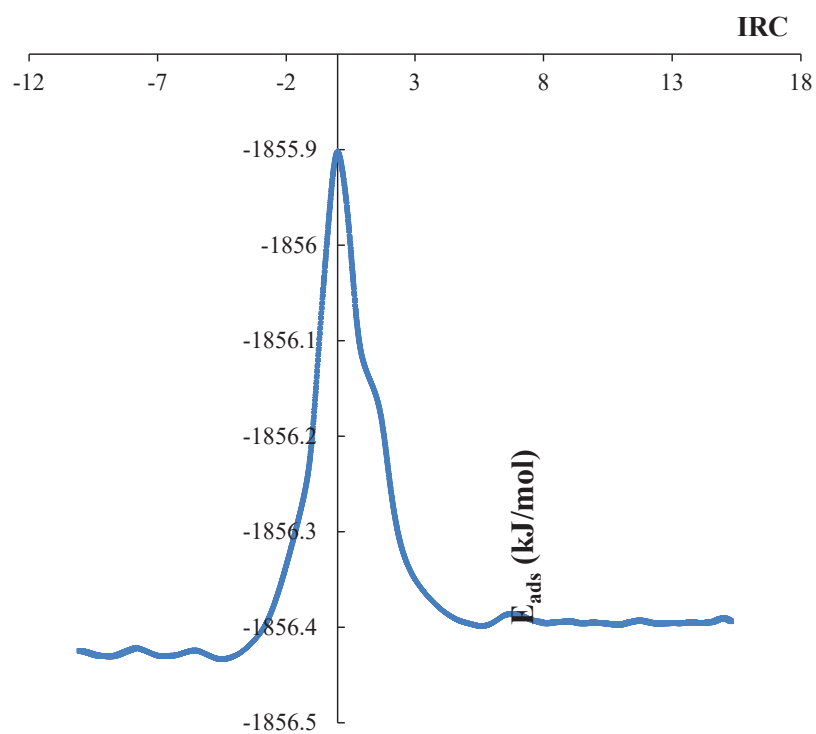


Figure 55. IRC curves for ring contraction from 13-DMCH<sup>+</sup> to 124-TMCP<sup>+</sup> in HZSM-23 zeolite (T2O1).

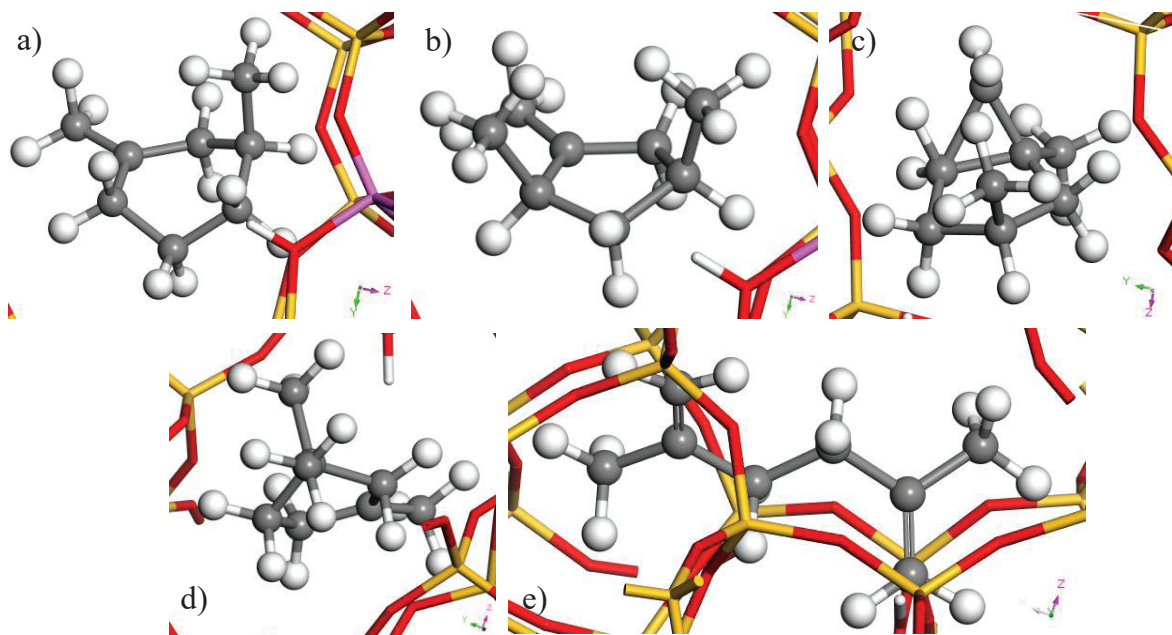


Figure 56. Optimized structures of all the molecules analyzed in the T2O2 active site of HZSM-57 zeolite. a) 13-DMCH<sup>+</sup>, b) 124-TMCP<sup>+</sup>, c) TS5, d) 133-TMCP and e) 25-DmHx.

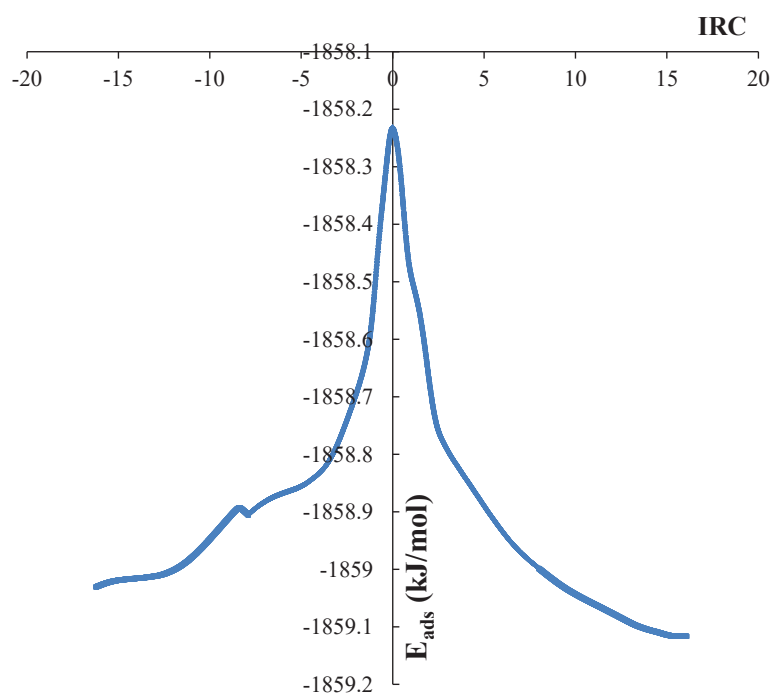


Figure 57. IRC curves for ring contraction from 13-DMCH<sup>+</sup> to 124-TMCP<sup>+</sup> in HZSM-57 zeolite (T2O2).

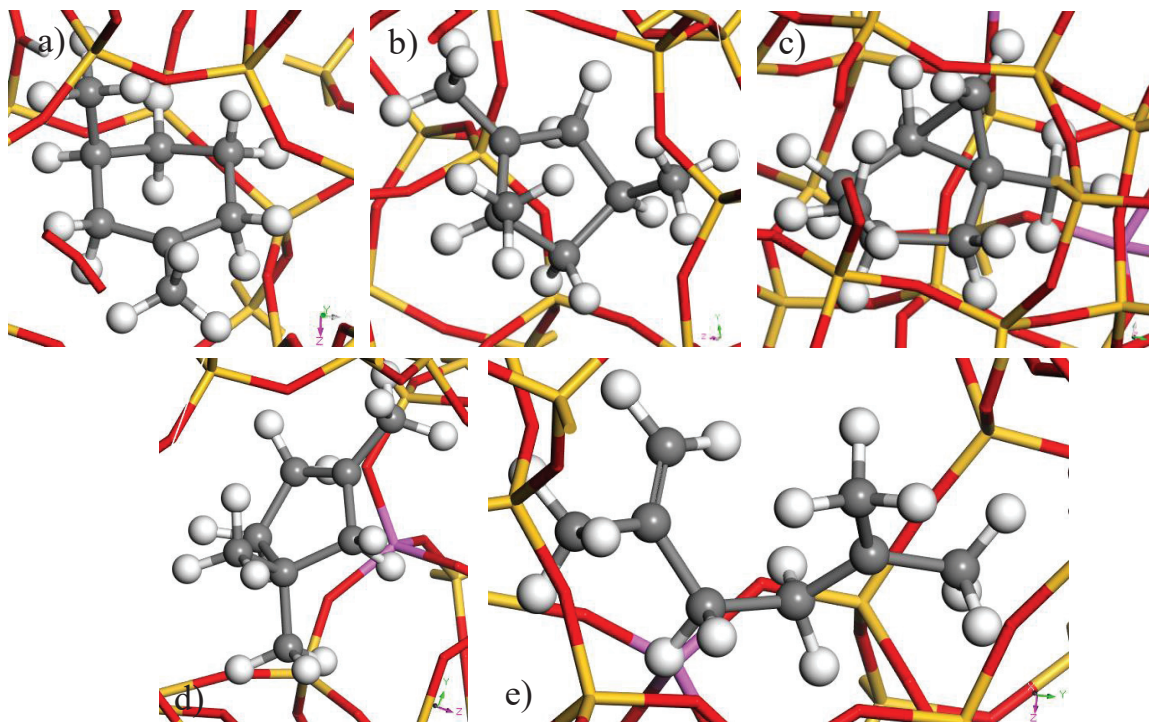


Figure 58. Optimized structures of all the molecules analyzed in the T8O8 active site of HZSM-57 zeolite. a) 13-DMCH<sup>+</sup>, b) 124-TMCP<sup>+</sup>, c) TS5, d) 133-TMCP and e) 25-DmHx.

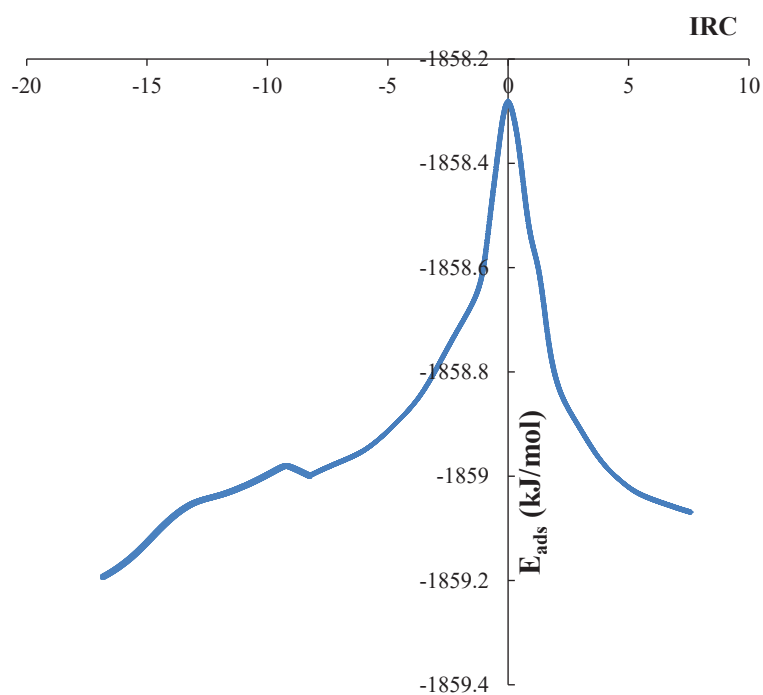


Figure 59. IRC curves for ring contraction from 13-DMCH<sup>+</sup> to 124-TMCP<sup>+</sup> in HZSM-57 zeolite (T8O8).

## APPENDIX

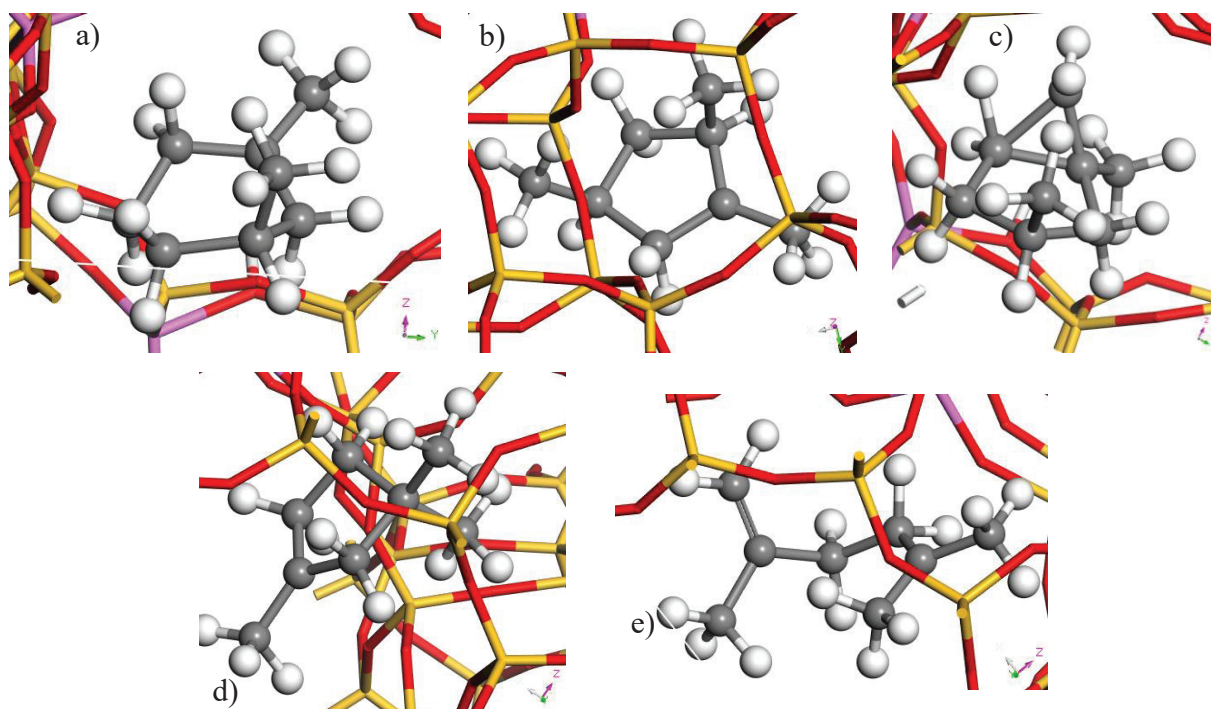


Figure 60. Optimized structures of all the molecules analyzed in the T1O3 active site of HZSM-5 zeolite. a) 13-DMCH<sup>+</sup>, b) 124-TMCP<sup>+</sup>, c) TS5, d) 133-TMCP and e) 25-DmHx.

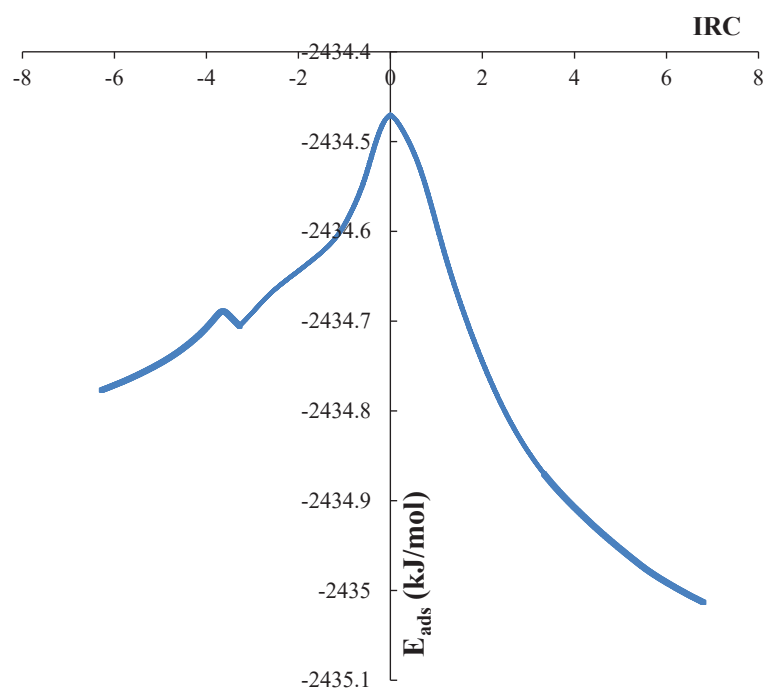


Figure 61. IRC curves for ring contraction from 13-DMCH<sup>+</sup> to 124-TMCP<sup>+</sup> in HZSM-5 zeolite (T1O3).



## APPENDIX

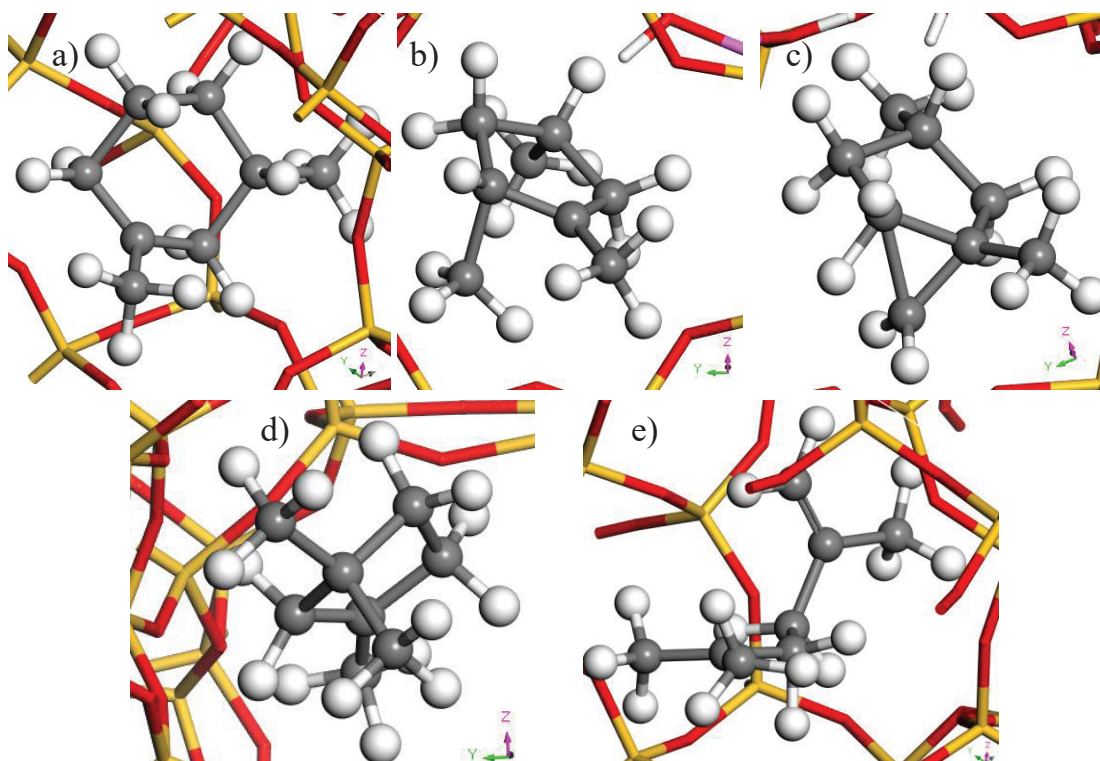


Figure 62. Optimized structures of all the molecules analyzed in the T10O23 active site of HZSM-5 zeolite. a) 13-DMCH<sup>+</sup>, b) 124-TMCP<sup>+</sup>, c) TS5, d) 133-TMCP and e) 25-DmHx.

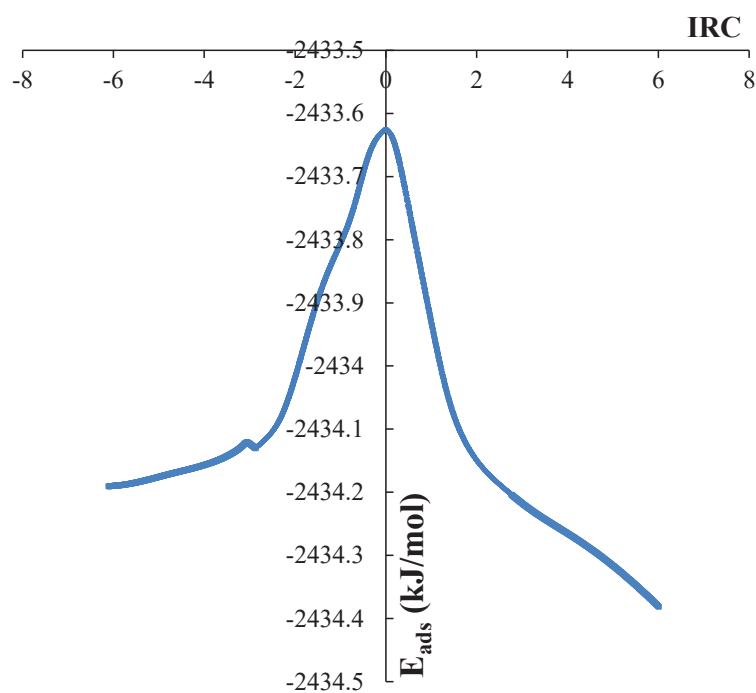


Figure 63. IRC curves for ring contraction from 13-DMCH<sup>+</sup> to 124-TMCP<sup>+</sup> in HZSM-5 zeolite (T10O23).

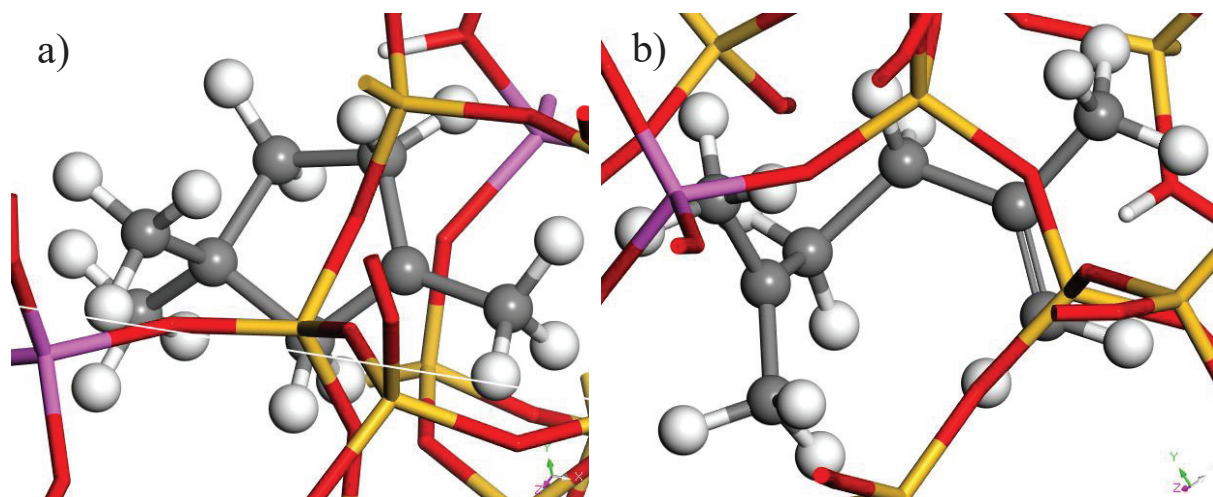


Figure 64. Optimized structures of all the molecules analyzed in the T11O25 active site of HZSM-5 zeolite. a) 133-TMCP and b) 25-DmHx.



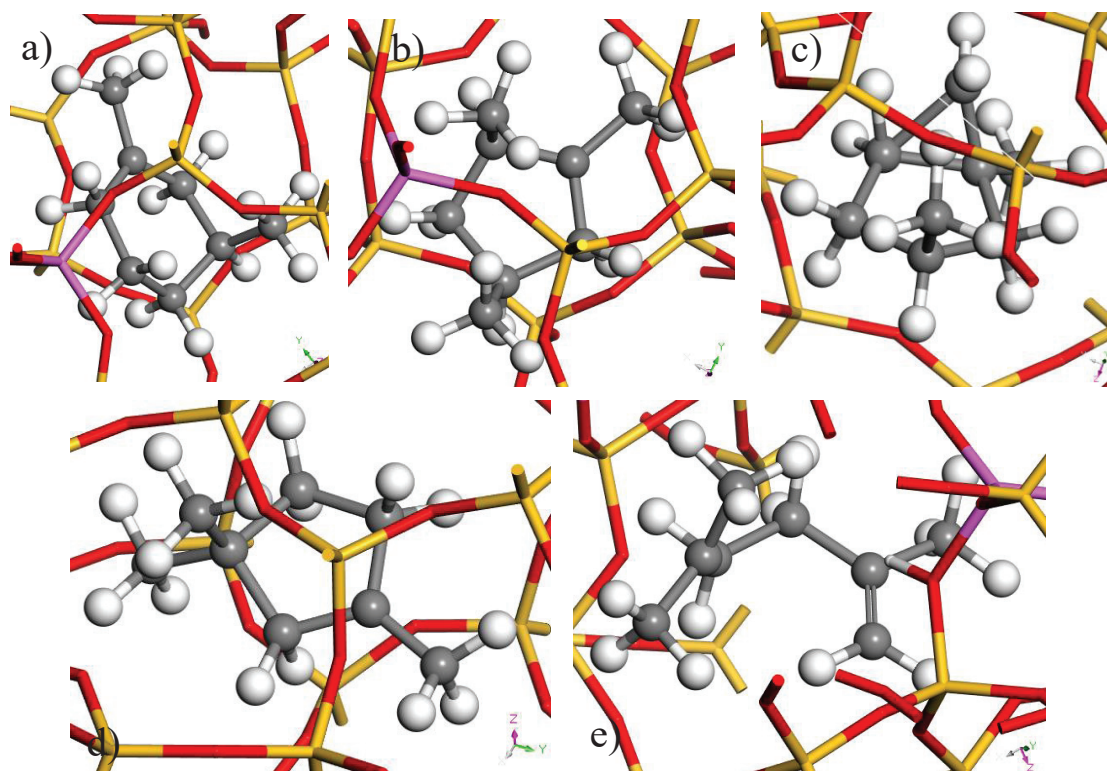


Figure 65. Optimized structures of all the molecules analyzed in the T1O1 active site of HZSM-12 zeolite. a) 13-DMCH<sup>+</sup>, b) 124-TMCP<sup>+</sup>, c) TS5, d) 133-TMCP and e) 25-DmHx.

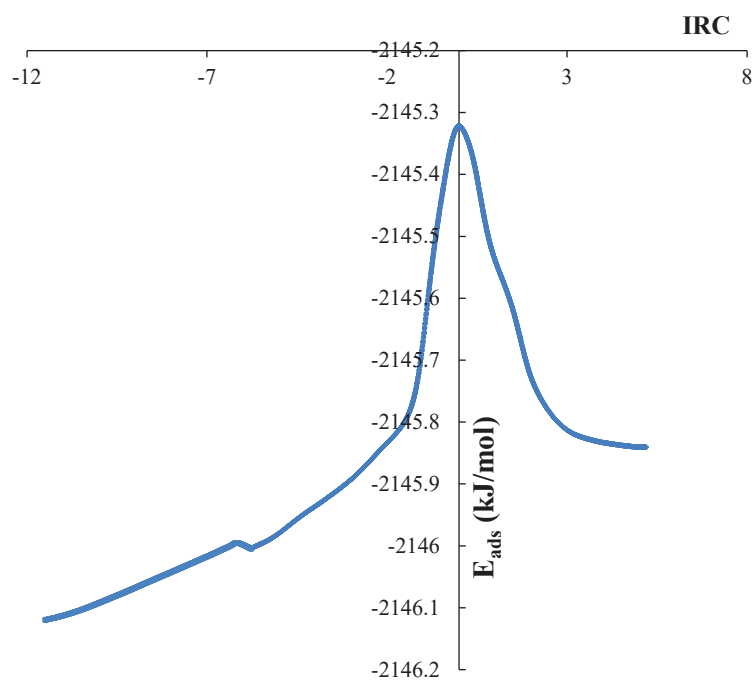


Figure 66. IRC curves for ring contraction from 13-DMCH<sup>+</sup> to 124-TMCP<sup>+</sup> in HZSM-12 zeolite (T1O1).

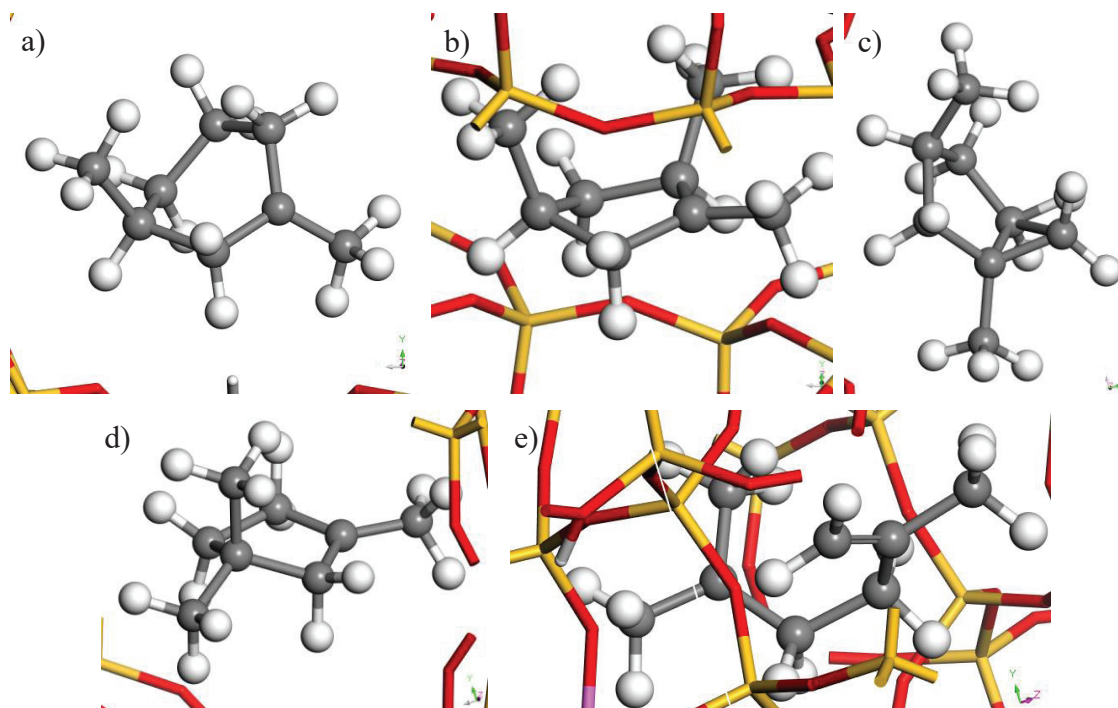


Figure 67. Optimized structures of all the molecules analyzed in the T1O1 active site of HMOR zeolite. a) 13-DMCH<sup>+</sup>, b) 124-TMCP<sup>+</sup>, c) TS5, d) 133-TMCP and e) 25-DmHx.

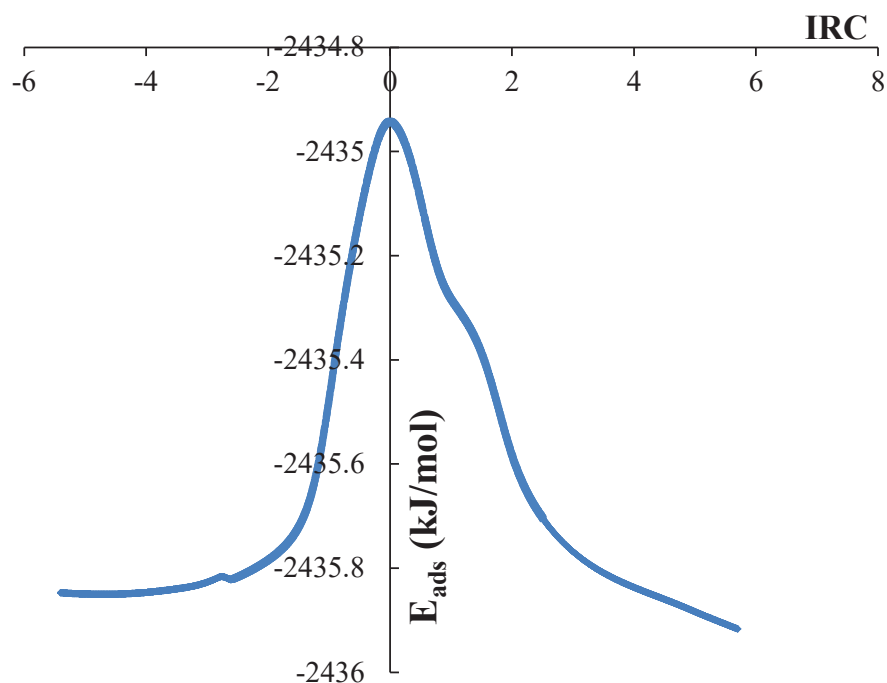


Figure 68. IRC curves for ring contraction from 13-DMCH<sup>+</sup> to 124-TMCP<sup>+</sup> in HMOR zeolite (T1O1).

## APPENDIX

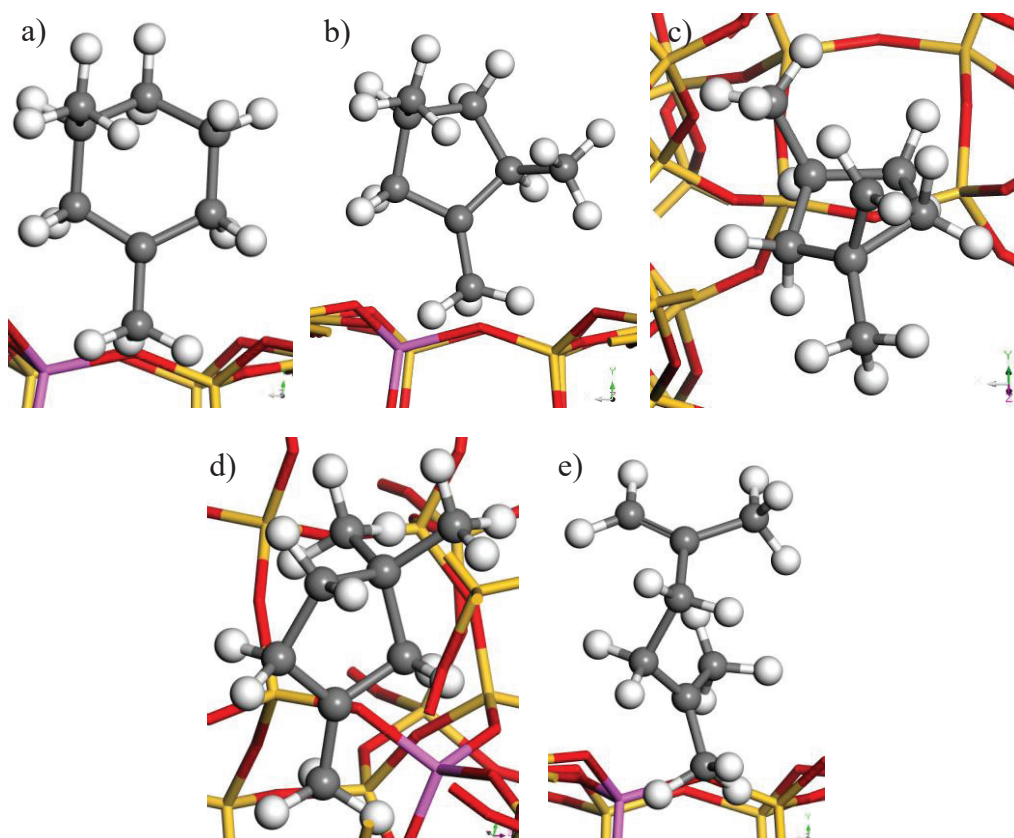


Figure 69. Optimized structures of all the molecules analyzed in the T4O10 active site of HMOR zeolite. a) 13-DMCH<sup>+</sup>, b) 124-TMCP<sup>+</sup>, c) TS5, d) 133-TMCP and e) 25-DmHx.

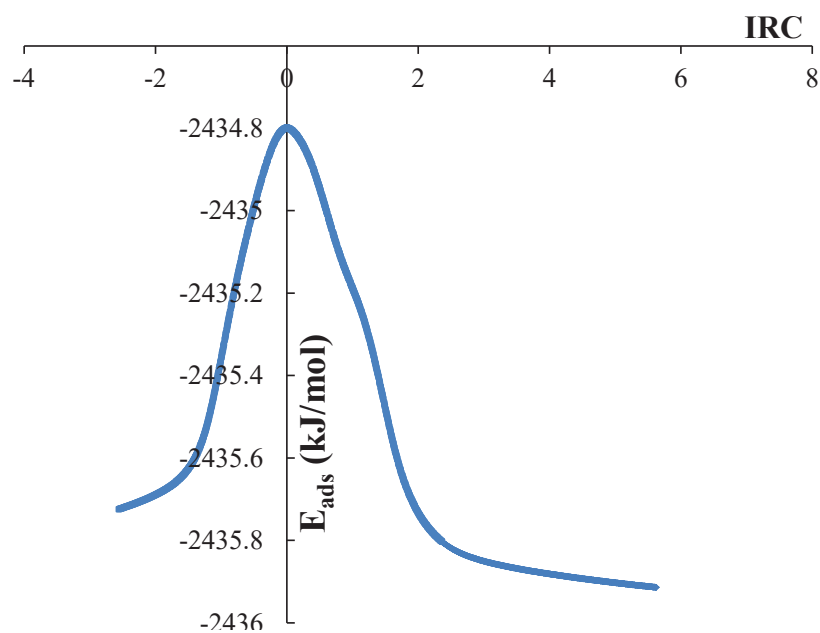


Figure 70. IRC curves for ring contraction from 13-DMCH<sup>+</sup> to 124-TMCP<sup>+</sup> in HMOR zeolite (T4O10).

## APPENDIX

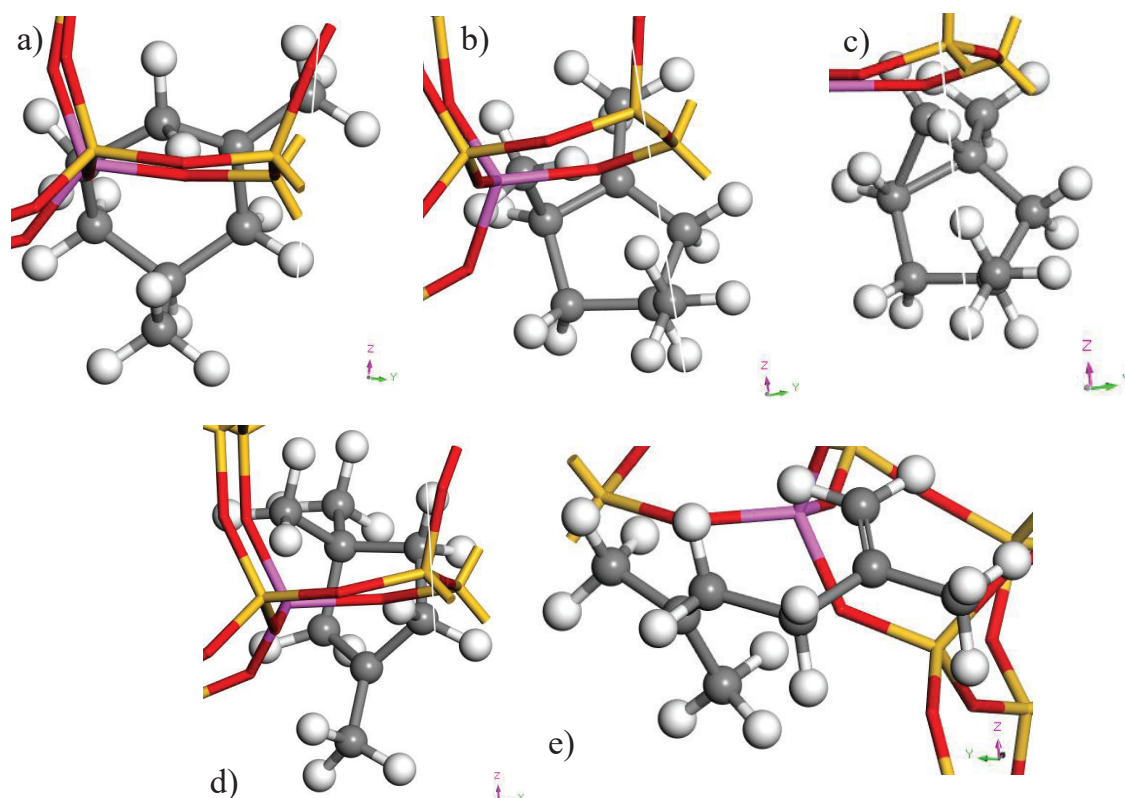


Figure 71. Optimized structures of all the molecules analyzed in the T4O11 active site of HBETA zeolite. a) 13-DMCH<sup>+</sup>, b) 124-TMCP<sup>+</sup>, c) TS5, d) 133-TMCP and e) 25-DmHx.

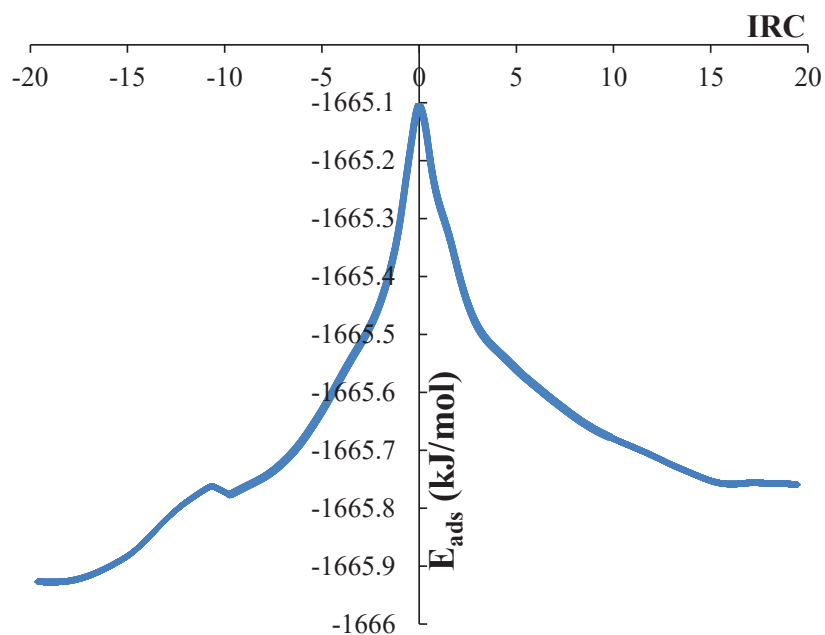


Figure 72. IRC curves for ring contraction from 13-DMCH<sup>+</sup> to 124-TMCP<sup>+</sup> in HBETA zeolite (T4O11).

## APPENDIX

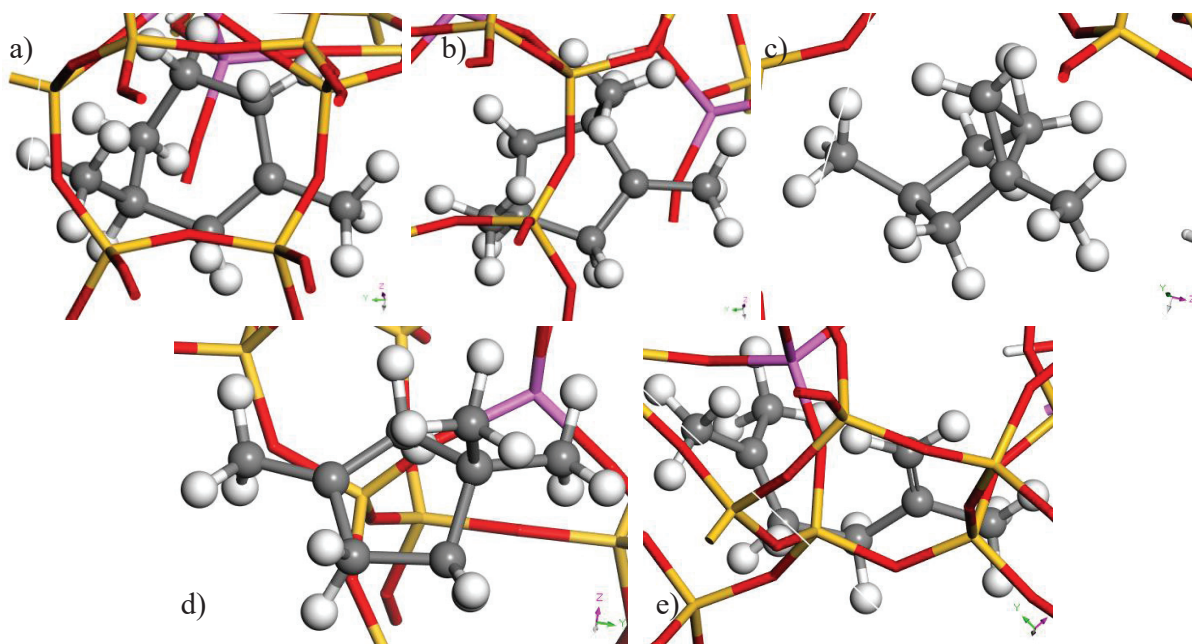


Figure 73. Optimized structures of all the molecules analyzed in the T6O12 active site of HBETA zeolite. a) 13-DMCH<sup>+</sup>, b) 124-TMCP<sup>+</sup>, c) TS5, d) 133-TMCP and e) 25-DmHx.

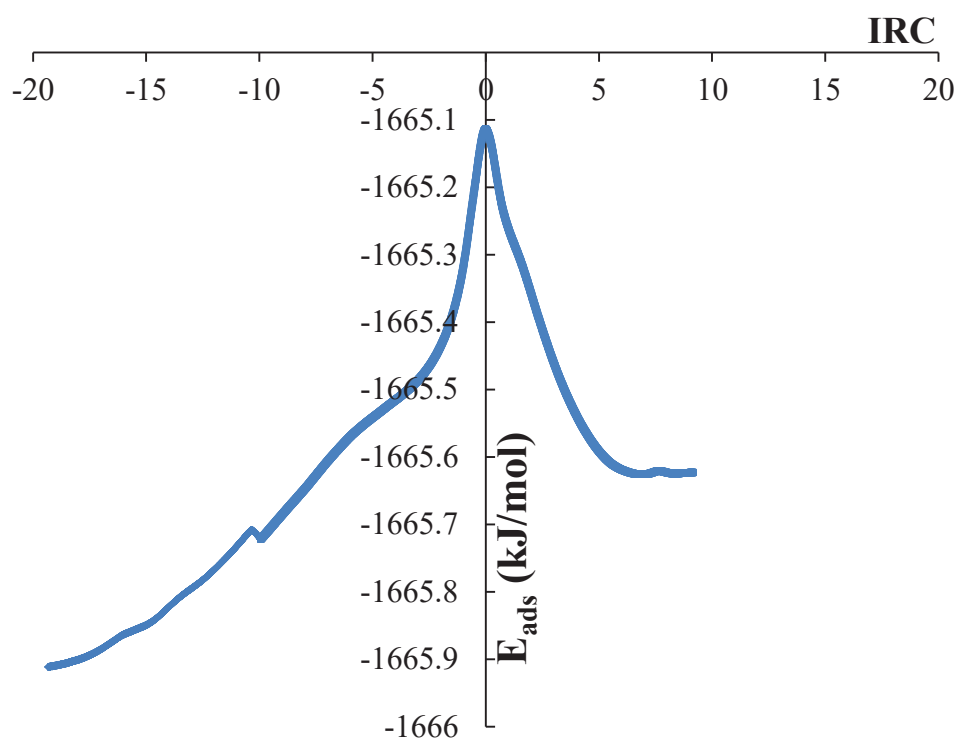


Figure 74. IRC curves for ring contraction from 13-DMCH<sup>+</sup> to 124-TMCP<sup>+</sup> in HBETA zeolite (T6O12)



## REFERENCES

- (1) Chareonpanich, M.; Zhang, Z.-G.; Tomita, A. Hydrocracking of Aromatic Hydrocarbons over USY-Zeolite. *Energy Fuels* 1996, 10, 927–931.
- (2) Guillon, E.; Lacombe, S.; Sozinho, T.; Magnoux, P.; Gnep, S.; Moreau, P.; and Guisnet, M. How to Improve the Selectivity of Zeolitic Catalysts in C8 Aromatic Cut Isomerization. *Oil Gas Sci. Technol.- Rev. IFP* 2009, 64, 731–744.
- (3) Marques Mota, F.; Bouchy, C.; Guillon, E.; Fécant, A.; Bats, N.; Martens, J. A. IZM-2: A promising new zeolite for the selective hydroisomerization of long-chain n-alkanes. *J. Catal.* 2013, 301, 20–29.
- (4) Marques Mota, F. Synergetic and antagonistic effects in hydroconversion catalysts composed of mixtures of solid acids, Leuven University, 2013.
- (5) Benazzi, E.; Leite, L.; Marchal-George, N.; Toulhoat, H.; Raybaud, P. New insights into parameters controlling the selectivity in hydrocracking reactions. *J. Catal.* 2003, 217, 376–387.
- (6) Marcilly, C. Acid-basic catalysis: Application to refining and petrochemistry; IFP publications; Editions Technip: Paris, 2006.
- (7) Biaglow, A. I.; Parrillo, D. J.; Kokotailo, G. T.; Gorte, R. J. A Study of Dealuminated Faujasites. *J. Catal.* 1994, 148, 213–223.
- (8) van Bokhoven, J. A.; Lee, T.-L.; Drakopoulos, M.; Lamberti, C.; Thieß, S.; Zegenhagen, J. Determining the aluminium occupancy on the active T-sites in zeolites using X-ray standing waves. *Nat. Mater.* 2008, 7, 551–555.